IMPACTS OF GLOBAL WARMING ON ECOLOGY AND METEOROLOGY AND THE RELATED PHYSICAL MECHANISMS, EVALUATION AND PREDICTION

EDITED BY: Gui-Quan Sun, Yongping Wu, Bai-Lian Li and Yipeng Guo
PUBLISHED IN: Frontiers in Physics and Frontiers in Climate

frontiers Research Topics

ISSN 1664-8714
ISBN 978-2-83250-853-4
DOI 10.3389/978-2-83250-853-4

About Frontiers

Frontiers is more than just an open-access publisher of scholarly articles: it is a pioneering approach to the world of academia, radically improving the way scholarly research is managed. The grand vision of Frontiers is a world where all people have an equal opportunity to seek, share and generate knowledge. Frontiers provides immediate and permanent online open access to all its publications, but this alone is not enough to realize our grand goals.

Frontiers Journal Series

The Frontiers Journal Series is a multi-tier and interdisciplinary set of open-access, online journals, promising a paradigm shift from the current review, selection and dissemination processes in academic publishing. All Frontiers journals are driven by researchers for researchers; therefore, they constitute a service to the scholarly community. At the same time, the Frontiers Journal Series operates on a revolutionary invention, the tiered publishing system, initially addressing specific communities of scholars, and gradually climbing up to broader public understanding, thus serving the interests of the lay society, too.

Dedication to Quality

Each Frontiers article is a landmark of the highest quality, thanks to genuinely collaborative interactions between authors and review editors, who include some of the world's best academicians. Research must be certified by peers before entering a stream of knowledge that may eventually reach the public - and shape society; therefore, Frontiers only applies the most rigorous and unbiased reviews.
Frontiers revolutionizes research publishing by freely delivering the most outstanding research, evaluated with no bias from both the academic and social point of view. By applying the most advanced information technologies, Frontiers is catapulting scholarly publishing into a new generation.

What are Frontiers Research Topics?

Frontiers Research Topics are very popular trademarks of the Frontiers Journals Series: they are collections of at least ten articles, all centered on a particular subject. With their unique mix of varied contributions from Original Research to Review Articles, Frontiers Research Topics unify the most influential researchers, the latest key findings and historical advances in a hot research area! Find out more on how to host your own Frontiers Research Topic or contribute to one as an author by contacting the Frontiers Editorial Office: frontiersin.org/about/contact

IMPACTS OF GLOBAL WARMING ON ECOLOGY AND METEOROLOGY AND THE RELATED PHYSICAL MECHANISMS, EVALUATION AND PREDICTION

Topic Editors:
Gui-Quan Sun, North University of China, China
Yongping Wu, Yangzhou University, China
Bai-Lian Li, University of California, Riverside, United States
Yipeng Guo, Nanjing University, China

Citation: Sun, G.-Q., Wu, Y., Li, B.-L., Guo, Y., eds. (2022). Impacts of Global Warming on Ecology and Meteorology and the Related Physical Mechanisms, Evaluation and Prediction. Lausanne: Frontiers Media SA. doi: 10.3389/978-2-83250-853-4

Table of Contents

frontiers | Frontiers in Physics

TYPE Editorial
PUBLISHED 10 November 2022
DOI 10.3389/fphy.2022.1041941

OPEN ACCESS

EDITED AND REVIEWED BY
Alex Hansen,
Norwegian University of Science and Technology, Norway

*CORRESPONDENCE
Gui-Quan Sun,
gquansun@126.com

SPECIALTY SECTION
This article was submitted to Interdisciplinary Physics, a section of the journal Frontiers in Physics

RECEIVED 11 September 2022
ACCEPTED 29 September 2022
PUBLISHED 10 November 2022

CITATION
Sun G-Q, Wu Y, Li B-L and Guo Y (2022), Editorial: Impacts of global warming on ecology and meteorology and the related physical mechanisms, evaluation and prediction.
Front. Phys. 10:1041941.
doi: 10.3389/fphy.2022.1041941

Editorial: Impacts of global warming on ecology and meteorology and the related physical mechanisms, evaluation and prediction

Gui-Quan Sun[1]*, Yongping Wu[2], Bai-Lian Li[3] and Yipeng Guo[4,5]

[1]Department of Mathematics, North University of China, Taiyuan, China, [2]College of Physics Science and Technology, Yangzhou University, Yangzhou, China, [3]Department of Botany and Plant Sciences, University of California, Riverside, Riverside, CA, United States, [4]Key Laboratory of Mesoscale Severe Weather/Ministry of Education, School of Atmospheric Sciences, Nanjing University, Nanjing, China, [5]Nanjing Normal University Nanjing, Nanjing, China

KEYWORDS

global warming, ecology, meteorology, physical mechanisms, prediction

Editorial on the Research Topic
Impacts of global warming on ecology and meteorology and the related physical mechanisms, evaluation and prediction

Global warming refers to changes in climate over a period of time in which the temperatures of the atmosphere and seas on Earth dramatically rise due to the greenhouse effect, and it plays a dominant role in climate change, rising sea levels, increasing frequency and intensity of extreme events, ecological imbalances, and loss of biodiversity [1–4]. Consequently, global warming has an adverse effect on meteorology and ecology, both of which inevitably affect human life and social development. As a result, how we can effectively mitigate global warming has become an urgent problem for the survival and development of mankind. In this sense, analysis of the features of meteorological and ecological change, quantification of the influence of climate warming on ecology and meteorology, and the uncovering of the underlying physical mechanisms contribute to a much deeper comprehension of the impact of global warming.

This Research Topic accepted many manuscripts across multiple research fields, including mathematics, meteorology, and ecology. These research studies mainly focus on construction or using models to quantify influence and predict future trends. For instance, Zhao et al. have, based on the CMIP6 model, evaluated the performance of wind speed in China, providing available guidance for wind prediction in specific regions; Hou et al. developed a model based on a three-dimensional Copula function to quantify the effects of drought on cropland area and assess the risk of drought, which is important for understanding and reducing the negative effects associated with drought; Feng et al. used a

nonlinear time series analysis method of phase space reconstruction to quantify the snow depth over the Tibetan Plateau; Chou et al. proposed an economic climate model to quantify the effects of climate change on the economy; Wang et al. utilized Earth system model simulations to assess oceanic CO_2 uptake, surface temperature, and acidity for Zhejiang offshore; and, to investigate the influence of saturated water absorption on vegetation systems, Li et al. established a vegetation-water model with a saturated water absorption effect.

This Research Topic has also received some papers that use a variety of data to analyze the characteristics of meteorological elements. Su et al. used a multi-dataset to analyze trends—seasonal and irregular variations of actual evapotranspiration. Wang et al. analyzed the climate change characteristics of coastal wind energy resources in Zhejiang Province based on ERA-medium-term data. Based on wind speed data and machine learning, Yan et al. studied the daily characteristics of wind speed changes in Beijing and analyzed the spatial and temporal characteristics of wind speed diurnal changes, which is conducive to predicting pollutant emissions.

We also collected some papers on the physical mechanisms of climate change. Guo et al. utilized Chinese meteorological station data and reanalysis data to explore the physical mechanism behind the variation of precipitation cycling rate in the middle and lower reaches of the Yangtze River. Zhao et al. explored the dominant factors causing the subtropical atmospheric anomaly in the western Pacific.

The situation of global warming is becoming more and more serious, and the impact on ecology and meteorology is intensifying, which means human beings and our development are facing unprecedented threats. The purpose of this research topic is to use a variety of methods to analyze the characteristics of meteorological and ecological changes in the context of global warming, quantify the impact of extreme events on agriculture, meteorology, and oceans, and reveal the physical mechanisms of their changes. We hope that this Research Topic will provide a platform to promote multidisciplinary and integrated research at a deeper level in the fields of meteorology, ecology, epidemiology, and mathematics.

Author contributions

G-QS wrote the manuscript. YW, B-LL, and YG contributed to the manuscript edits. All authors read, contributed to the research design, and approved the final manuscript.

Funding

The project is funded by the National Key Research and Development Program of China (Grant no. 2018YFE0109600), National Natural Science Foundation of China under Grant nos. 42075029 and 42275034.

Conflict of interest

The authors declare that the research was conducted in the absence of any commercial or financial relationships that could be construed as a potential conflict of interest.

Publisher's note

References

1. Landsea CW. Hurricanes and global warming. *Nature* (2005) 438:E11–2. doi:10.1038/nature04477

2. Kerr RA. Global warming is changing the world. *Science* (2007) 361:188–90. doi:10.1126/science.316.5822.188

3. Tebaldi C, Ranasinghe R, Vousdoukas M, Rasmussen DJ, Vega-Westhoff B, Kirezci E, et al. Extreme sea levels at different global warming levels. *Nat Clim Chang* (2021) 11: 746–51. doi:10.1038/s41558-021-01127-1

4. Sun GQ, Zhang HT, Song YL, Li L, Jin Z. Dynamic analysis of a plant-water model with spatial diffusion. *J Differential Equations* (2022) 329:395–430. doi:10.1016/j.jde.2022.05.009

frontiers in Physics

ORIGINAL RESEARCH
published: 01 April 2021
doi: 10.3389/fphy.2021.656253

A 3D Copula Method for the Impact and Risk Assessment of Drought Disaster and an Example Application

Wei Hou[1], *Pengcheng Yan*[2], *Guolin Feng*[3,4] *and Dongdong Zuo*[5]*

[1] National Climate Center, China Meteorological Administration, Beijing, China, [2] Institute of Arid Meteorology, China Meteorological Administration, Lanzhou, China, [3] Southern Marine Science and Engineering Guangdong Laboratory, Zhuhai, China, [4] Institute of Physics Science and Technology, Yangzhou University, Yangzhou, China, [5] School of Mathematics and Physics, Yancheng Institute of Technology, Yancheng, China

Droughts have more impact on crops than any other natural disaster. Therefore, drought risk assessments, especially quantitative drought risk assessments, are significant in order to understand and reduce the negative impacts associated with droughts, and a quantitative risk assessment includes estimating the probability and consequences of hazards. In order to achieve this goal, we built a model based on the three-dimensional (3D) Copula function for the assessment of the proportion of affected farmland areas (PAFA) based on the idea of internally combining the drought duration, drought intensity, and drought impact. This model achieves the "internal combination" of drought characteristics and drought impacts rather than an "external combination." The results of this model are not only able to provide the impacts at different levels that a drought event (drought duration and drought intensity) may cause, but are also able to show the occurrence probability of impact at each particular level. We took Huize County and Mengzi County in Yunnan Province as application examples based on the meteorological drought index (SPI), and the results showed that the PAFAs obtained by the method proposed in this paper were basically consistent with the actual PAFAs in the two counties. Moreover, due to the meteorological drought always occurring before an agricultural drought, we can get SPI predictions for the next month or months and can further obtain more abundant information on a drought warning and its impact. Therefore, the method proposed in this paper has values both on theory and practice.

Keywords: drought, risk assessment, three-dimensional Copula function, Huize county, Mengzi County

OPEN ACCESS

Edited by:
Gui-Quan Sun,
North University of China, China

Reviewed by:
Qiang Zhang,
Gansu Meteorological Bureau, China
Eric Josef Ribeiro Parteli,
University of
Duisburg-Essen, Germany

***Correspondence:**
Dongdong Zuo
dongdz_vow@163.com

Specialty section:
This article was submitted to Interdisciplinary Physics, a section of the journal Frontiers in Physics

Received: *25 January 2021*
Accepted: *10 March 2021*
Published: *01 April 2021*

Citation:
Hou W, Yan P, Feng G and Zuo D (2021) A 3D Copula Method for the Impact and Risk Assessment of Drought Disaster and an Example Application. Front. Phys. 9:656253. doi: 10.3389/fphy.2021.656253

INTRODUCTION

Droughts are a complex and recurrent natural disaster that result in widespread effects on humans and natural systems, including agriculture, ecosystems, energy, economics, and so forth [1–8]. A drought can be commonly classified into four types: meteorological, agricultural, hydrological, and socioeconomic, and the meteorological drought has received more attention as it usually occurs before the other three types of drought [1, 9].

Over the past decades, droughts around the world have caused tremendous economic losses on an annual basis [10, 11]; furthermore, droughts are a major cause of unexpected crop failure (in corn, rice, and wheat). In China, problematically frequent occurrences of drought have resulted in great impacts on social and economic development and human life [12, 13], and historical disaster data show that the average annual area of crop damage due to drought accounted for 50% of all areas affected by meteorological disasters over the period of 2004–2013 [14]. Due to rising temperatures and increasing climatic variability [15–18], it is widely recognized that droughts may become more frequent and more serious globally in the coming decades on regional and temporal levels [17, 19, 20]. In this context, the challenges faced by agricultural production will become more severe. In addition, the possibility of soil desertification will increase under prolonged drought, so sand prevention and control also face major challenges [21, 22]. Therefore, drought risk assessment, especially quantitative drought risk assessment, is required in order to reduce the negative impacts associated with droughts [23–26].

Quantitative drought risk assessment includes estimating the probability and consequences of a drought disaster [27]. To achieve this, we need on three levels to (i) characterize the drought statistically in terms of its relative severity; e.g., exceeding probability [28], (ii) quantify the consequences of a given drought event [29], and (iii) estimate the consequences of droughts with varying severity. The key point here is to separate "droughts" from "non-droughts" [30]. Although studies have proven that risk assessment results on the impacts or losses provided by statistical methods and physical models are reliable and valid [31–36], the accurate assessment of drought impacts on agricultural production is not easy to calculate, and there are still various data-related and methodological problems that need to be solved [37, 38]. In particular, these include the requirement of (i) the time series of drought index with sufficient spatial and temporal details in order to obtain enough information on the local meteorological and hydrological conditions, and (ii) the accurate, high-resolution, long-term yield or economic loss databases [36]. Therefore, a complete description of a drought disaster requires multiple related variables, and the appropriate option is a multivariate analysis using the Copula function [39]. The Copula function is a statistical tool, which can used to construct a multivariate joint distribution function for analyzing the statistical characteristics of dependent variables. However, the applications of the Copula technique in assessing the impacts of droughts on agricultural production are very limited in published literature, and almost all research has been performed to obtain the qualitative relationships between drought characteristics and the degree of a potential disaster [32, 40–46]. Moreover, most previous studies use two-dimensional Copula functions, and crop damage data are not often used as a variable to be substituted into the Copula function, but are instead used as an independent variable in combination with the comprehensive features of a drought obtained by the Copula function.

The goal pursued by many international researchers is to obtain objective results and reduce subjective judgments through the use of statistical methods and physical models to provide more accurate drought information and warnings for the prevention of disasters and to reduce losses. It is of more practical significance to assess the specific impacts of droughts with different severities and durations, and to see how crop damage data are substituted directly into the Copula function as one of the variables in assessing the impact of droughts. However, there is no published work that uses the above ideas to study the impact of droughts, so it is, therefore, worth studying in further detail. Therefore, the objective of this paper is to make a breakthrough in this respect.

Combining the above reasons, in this paper we propose a three-dimensional (3D) Copula model for the assessment of drought risks in terms of agriculture. We built a model based on the three-dimensional (3D) Copula function for the assessment of the proportion of affected farmland areas for the purpose of quantitative drought risk assessment. We calculated the proportion of affected farmland areas (PAFA) based on the farmland areas affected by droughts and the annual agricultural planting area, and then obtained the PAFA time series caused by each drought event. The reason behind using PAFA as the assessment object is that the affected area is a result of drought; thus, the impacts of "droughts" can be clearly separated from those of "non-droughts." Next, we extracted drought events from a monthly standardized precipitation index (SPI) time series, which is calculated based on precipitation data and satisfies a standard normal distribution. After, we calculated the parameters of the duration and the severity of a drought, as well as the PAFA, and thus, the marginal distribution functions of duration, severity, and PAFA were obtained, and their joint distribution function was then computed using a three-dimensional Copula function. The joint probability and the classification of these three variables were both achieved using this 3D statistical model. Different types of drought events were identified based on the combination of these variables, and the probabilities of occurrence of the drought events were calculated. Thus, the estimation of the PAFA of a drought event could be obtained by integrating this method with the monitoring of current droughts and the prediction of future droughts.

STUDY AREA AND DATA

Study Area

Yunnan Province, located in the southwest of China, is influenced primarily by the South Asian monsoon and also impacted by the East Asian monsoon, the Tibetan Plateau monsoon, and westerlies [47]. The soil in Yunnan Province is covered by a large area of karst landforms and characterized by poor water conservation. Due to the complicated land surface terrain, as well as the control and influence of different general circulation patterns, the seasonal and geographical distributions of precipitation are extremely uneven in Yunnan, and droughts have become one of the most extensive, frequent, and severe natural disasters in Yunnan Province [48–50]. Yunnan's crops mainly include rice, wheat, and corn, among others, and the crops are normally fed and cultivated with rain.

Because in this article we are trying to build a Copula-based three-dimensional (3D) risk analysis model, including the

duration and intensity of the drought, as well as the PAFA, only the areas where the three types of data (SPI, affected farmland areas caused by droughts, and annual agricultural planting area) that meet the following three requirements can therefore be used as the research area in this article: (i) the daily precipitation series as long as possible without missing values, (ii) the number of disaster loss records (affected farmland areas caused by droughts) from 1984 to 2012 should be as much as possible, and (iii) the annual agricultural planting area from 1984 to 2012 requires as much continuous data as possible. **Figure 1** shows the spatial distribution of the number of disaster loss records caused by droughts from 1984 to 2012 submitted by each county in Yunnan Province, and the stations that comply with the requirement in Yunnan Province are also shown in **Figure 1**. After a survey of all the stations (counties) in Yunnan Province, it was found that two stations (counties) met the above three requirements: Huize county and Mengzi county.

In this paper, we take Huize County and Mengzi County in Yunnan Province as examples to demonstrate the three-dimensional (3D) Copula model for the assessment of drought risk on agriculture.

Data

The data used in this study on damages caused by droughts come from China's Meteorological Disaster Loss Databases at County Level (1984–2012, including county name, geographic location, category of meteorological disasters, starting and ending time of meteorological disaster, number of affected populations, affected farmland areas, and direct economic losses) compiled by the China Meteorological Administration (CMA). Currently, the database is stored in the National Climate Center, and applied to the scientific research [51] and operational works (http://10.28.107.46:8084/MDMIS_oneMap/) of meteorological disaster risk management. The data on the affected farmland areas caused by drought was obtained between 1986 and 2012; of these, there are 20 records in Huize County and 21 records in Mengzi County. The two counties did not experience drought in 1984 and 1985.

It is known that agricultural yields vary continuously with the hydro-climatic conditions; it is also influenced by many other factors such as field management and specific varieties of crops. In addition, the direct economic loss of agriculture caused by droughts is also related to the current price of crops, and the factors affecting prices are so complex that they far exceed the drought itself. Therefore, in this study, we used the data of affected farmland areas caused by droughts because they have an intuitive cut-off between "drought" and "non-drought" conditions.

The exposure of crops to drought will also change with changes in the agricultural planting areas. Even if a drought occurs with the same duration and intensity, the larger the agricultural planting area, the larger affected the farmland area is. This makes it difficult to compare and analyze the impact of droughts when the data on the affected farmland areas in different years are used directly. Thus, the PAFA in each year was used for analysis in this study. In order to cooperate with the data on the affected farmland areas, we also need the continuous data of annual agricultural planting areas to calculate the PAFA. The data on the annual agricultural planting areas were taken between 1986 and 2012 (**Figure 2**) in Huize and from 1995 to 2012 in Mengzi. These data were obtained from the yearbook of Huize and Mengzi. Because of the establishment of the marginal distribution functions of duration and intensity of drought, it is necessary to use a time series of drought index. The monthly SPI [52] was calculated after processing daily precipitation data into monthly data. It should be noted that the Gamma distribution is used as the distribution function of precipitation in the calculation of SPI. The Kolmogorov-Smirnov distribution test results show that all stations in **Figure 1** have passed the distribution test. In order to obtain more accurate and stable marginal distribution functions of drought duration and drought intensity, the daily precipitation data without missing values from 1961 to 2012 from Huize County and Mengzi County were acquired from the National Meteorological Information Center of the China Meteorological Administration (http://www.nmic.cn).

Methods

Description of Drought Characteristics

We described drought events based on the two major characteristics: drought duration and severity, which were both extracted from monthly SPIs. The most applied index is the SPI that concerns meteorological drought. As a powerful index, the SPI has been widely used to analyze droughts in different parts of the world, and the advantage of the SPI over other indices is that the SPI depends only on precipitation, the flexibility of timescales at which this index can be calculated, as well as being comparable in time and space. The SPI obtained based on the precipitation of 1 month is called a monthly scale index, the SPI obtained based on the precipitation of 3 months is called a seasonal scale index, and the SPI obtained based on the precipitation of 6 months is called an semi-annual scale index. SPI for 1 month is suitable for describing meteorological drought, SPI for 3 months is suitable for describing agricultural drought, and SPI for more than 6 months is suitable for describing drought in watersheds or groundwater. Since the SPI can characterize short- and long-term droughts, various research on drought risk assessment has been carried out using the SPI, and the results show that the SPI is ideal for performing a risk assessment in comparison to other drought indices [53–56]. Recently, a piece of research applied six drought indices to estimate the drought onset, and the results showed that meteorological drought indices predict the onset of a drought earlier than hydrological and agricultural drought indices [57]. Therefore, in this paper, we use the SPI to allow the method to be more practical in terms of risk warnings of droughts.

For an SPI time series, the definitions of drought duration and drought intensity that are adopted in the run theory [58] are shown in **Figure 3**. Run theory is a method of time series analysis, which is widely used in the identification of drought events [44, 59–61]. Drought duration (d) represents the number of months during which the SPI index is continuously below the threshold value ($s_0 = 0$). Because the SPI of the monthly scale is used in this paper, the drought duration lasts for at least 1 month, and the range of the d value is within $[1, +\infty]$

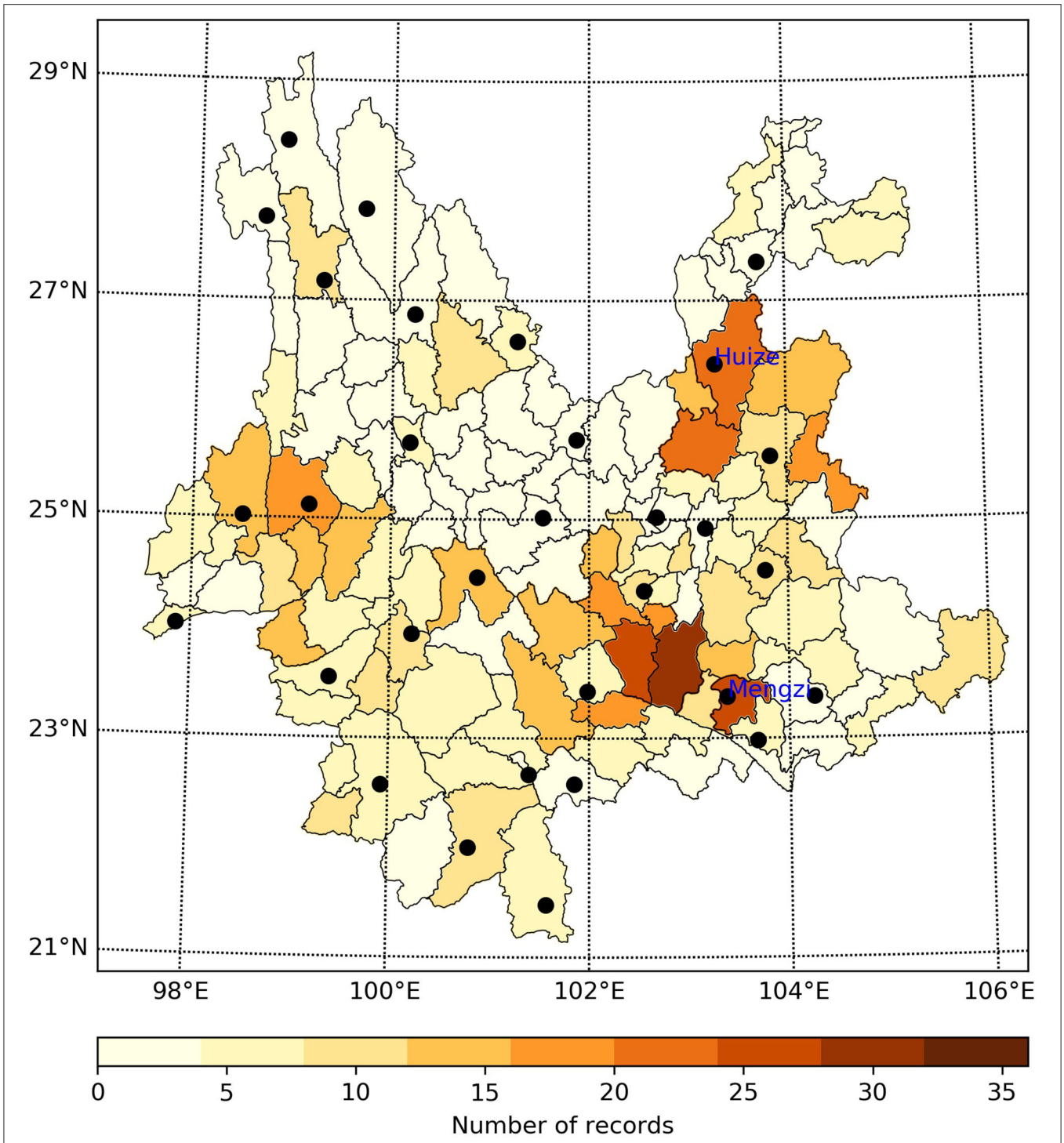

FIGURE 1 | The distribution of the number of damage records (affected farmland areas by drought, 1984–2012) in the counties of Yunnan Province, China (black symbols represent the location of meteorological stations).

month. Drought severity refers to the accumulation of the value of the SPI index within the ranges of the drought duration, and can be calculated by using the formula $s = -\sum_{i=1}^{d} SPI_i$, and the range of the s value is within $(0, +\infty)$. Thus, the duration $(d_1, d_2, d_3 \cdots)$ and severity $(s_1, s_2, s_3 \cdots)$ of drought events can be extracted from an SPI time series [62, 63]. Based on previous studies, the classification of drought duration and severity was defined, and is shown in **Tables 1**, **2**.

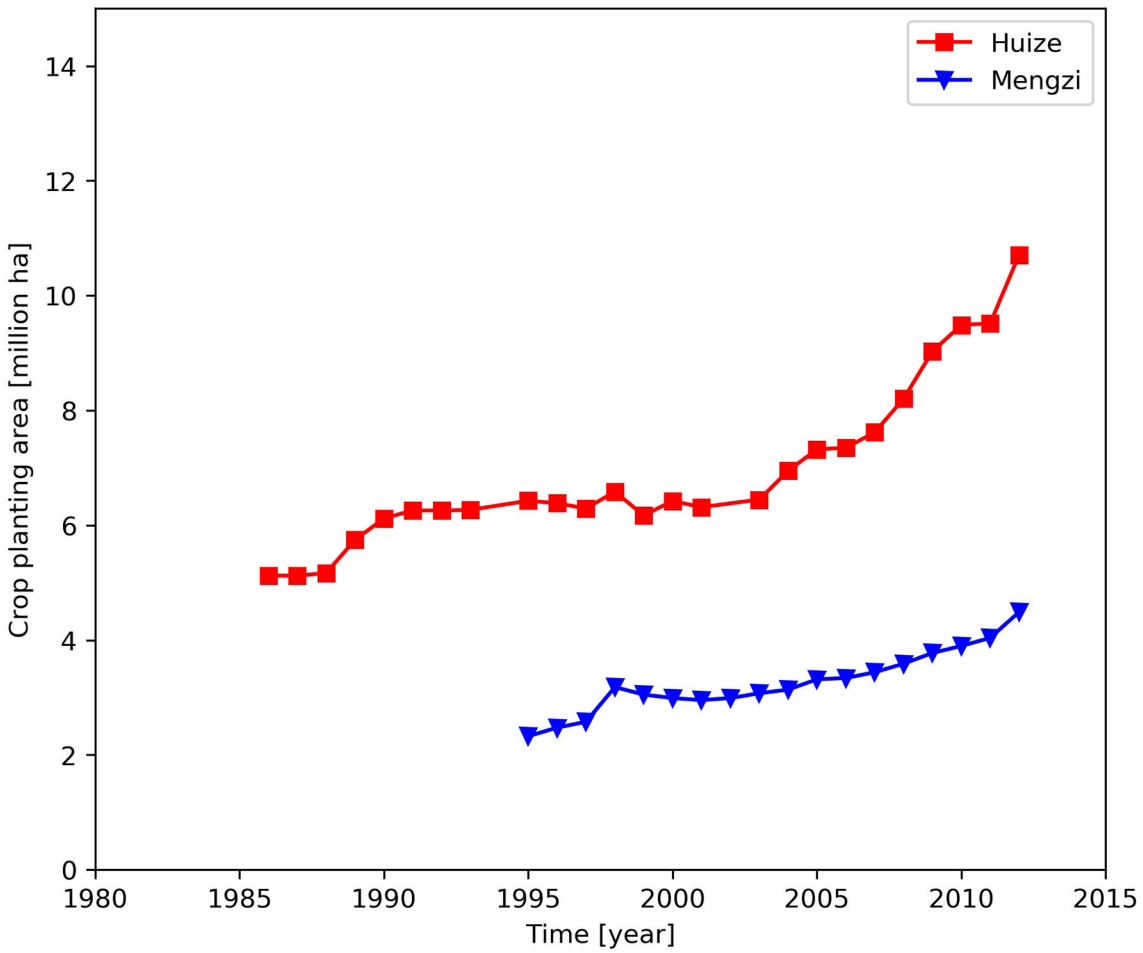

FIGURE 2 | Changes of the agricultural planting areas over time.

The Distribution Characteristics of Three Variables

The proportion of affected farmland area (PAFA) in each year was used for analysis. The mathematical expression is:

$$I = \frac{A_d}{A_P} \times 100\%, \tag{1}$$

where I refers to PAFA, A_d is the affected farmland area, and A_P is the annual agricultural planting area. An exponential function is applied to describe the distribution of the index I, and the mathematical expression is defined as:

$$F_I(i) = 1 - e^{-\lambda i}, \tag{2}$$

Some studies [62, 64] have reported that drought duration and severity follow exponential and Gamma distributions, respectively. The mathematical expressions of the two distributions are:

$$F_D(d) = 1 - e^{-\lambda d}, \tag{3}$$

$$F_S(s) = \int_0^s \frac{s^{\alpha-1}}{\beta^\alpha \Gamma(\alpha)} e^{-\frac{s}{\beta}} ds, \tag{4}$$

where D and S refer to the sample set of drought duration and severity, respectively, d and s denote the element in the sample set of drought duration and severity, respectively, $F_D(d)$ refers to the probability that drought duration d is equal to or less than D, $F_S(s)$ denotes the probability that drought severity s is equal to or less than S, and λ, α, and β are the distribution parameters.

According to Equations (2–4), the Copula function was used to establish the joint distribution function of the three variables (the duration and intensity of the drought, as well as the PAFA caused by drought) in this study.

Copula Function

The Copula function is an effective method that uses the marginal distribution functions of different random variables to build a joint distribution function. As each marginal distribution of the variables is known, the joint distribution can be constructed with the Copula function. According to the theory of Sklar [39], the joint distribution function $F(x_1, x_2, \cdots, x_n)$ can be decomposed into marginal distribution functions $F(x_1), F(x_2), \cdots, F(x_n)$ and

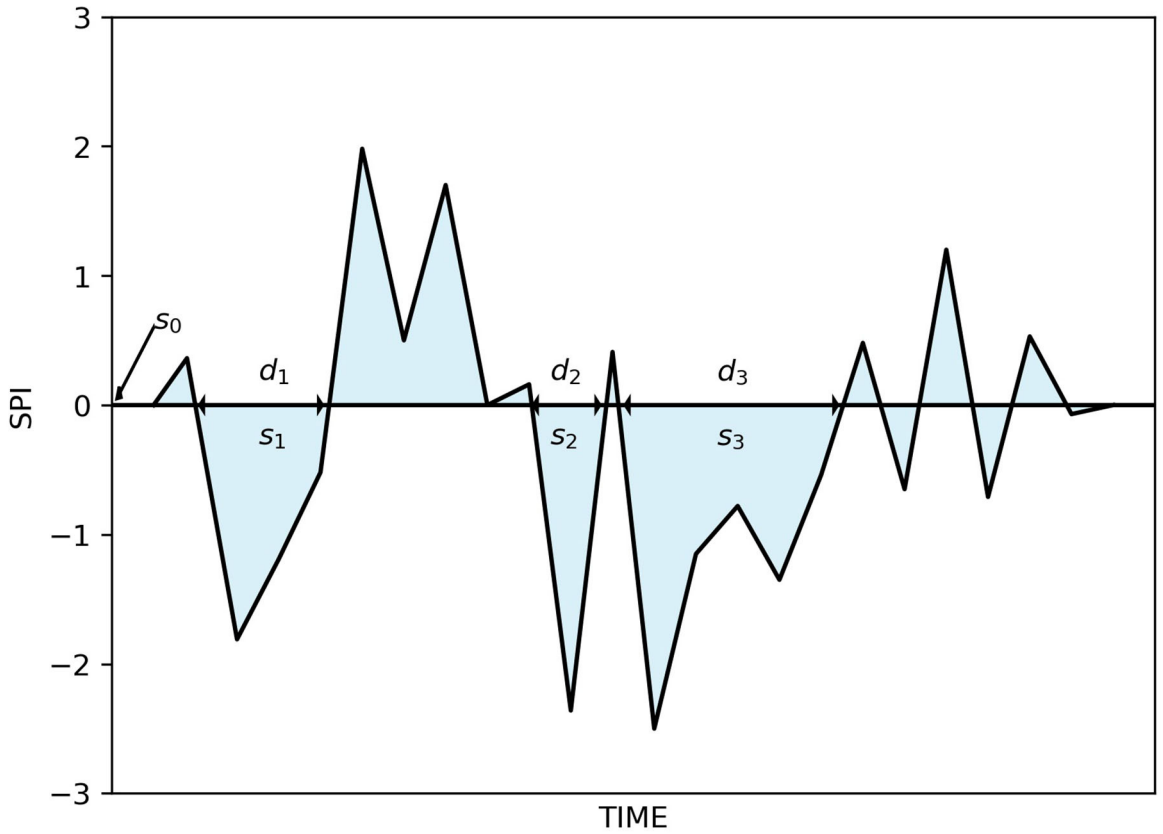

FIGURE 3 | Descriptions of drought characteristics.

TABLE 1 | The classification of drought duration.

D (month)	Level
$0 < D \leq 1$	1 (within 1 month)
$1 < D \leq 3$	2 (within one season)
$3 < D \leq 6$	3 (cross-quarter)
$6 < D$	4 (over 6 months)

TABLE 2 | The classification of drought severity.

S	Level
$0 < S \leq 0.5$	0 (Normal)
$0.5 < S \leq 1$	1 (Slight drought)
$1 < S \leq 1.5$	2 (Moderate drought)
$1.5 < S \leq 2.0$	3 (Severe drought)
$2.0 < S$	4 (Extreme drought)

a Copula function $C(\cdot)$. The mathematical expression is:

$$F(x_1,x_2,\cdots,x_n) = C(F(x_1), F(x_2), \cdots, F(x_n)), \quad (5)$$

The Copula function can be classified into three classes: the elliptic type, Archimedean family, and quadric form. The Archimedean Copula function has been widely used [62, 64], and therefore, it has also been used in our study. The common 3D Archimedean Copulas functions [40, 65] are as follows.

Clayton

$$C_\theta(\mu, v, \omega) = \left(\mu^{-\theta} + v^{-\theta} + \omega^{-\theta} - 2\right)^{\frac{-1}{\theta}}, \quad (6)$$

Frank

$$C_\theta(\mu, v, \omega) = -\frac{1}{\theta}\ln\left[1 + \frac{\left(e^{-\mu\theta}-1\right)\left(e^{-v\theta}-1\right)\left(e^{-w\theta}-1\right)}{\left(e^{-\theta}-1\right)^2}\right], \quad (7)$$

Gumbel-Hougaard

$$C_\theta(\mu, v, \omega) = exp\left\{-\left[\left(-ln\mu\right)^\theta + \left(-lnv\right)^\theta + \left(-ln\omega\right)^\theta\right]^{\frac{1}{\theta}}\right\}, \quad (8)$$

Where, μ, v, ω are the marginal distribution functions, and θ is the parameter of the Copula function.

In this study, the parameter θ is estimated through the maximum log-likelihood estimation. The function can be written

TABLE 3 | The statistical characteristics of the drought events.

County	Size	ρ (**D**, **S**)	Drought duration (month)				Drought severity			
			Mean	Std	Min	Max	Mean	Std	Min	Max
Huize	161	0.80	1.88	1.38	1	8	1.53	1.48	0.01	8.43
Mengzi	153	0.88	1.95	1.71	1	12	1.60	1.79	0.03	12.12

as follows:

$$\ln L(\theta)=\sum_{i=1}^{n}\ln c(\mu_i,\nu_i,\omega_i,\theta)+\sum_{i=1}^{n}\left(\ln \mu_i^{'}+\ln \nu_i^{'}+\ln \omega_i^{'}\right), \quad (9)$$

where μ, ν, ω are marginal distributions, and $c(\mu, \nu, \omega, \theta)$ is defined as $c(\mu, \nu, \omega, \theta) = \frac{\partial C(\mu,\nu,\omega,\theta)}{\partial\mu\partial\nu\partial\omega}$. The log-likelihood function $\ln L$ can be maximized in order to obtain the estimation of Copula parameter $\hat{\theta}$. Furthermore, the root-mean-square error method [66, 67] was used to select the optimal Copula function:

$$RMSE=\sqrt{\frac{1}{n}\sum_{i=1}^{n}(Pe_i-P_i)^2}, \quad (10)$$

where Pe_i is the empirical probability value obtained directly from the sample size, and P_i is the theoretical probability value under different Copula functions.

We compared and analyzed three Archimedes Copula functions, suggesting that the difference between the three Copula functions is not significant. However, the Gumbel-Hougaard function has an upper tail dependency, which is more suitable for the analysis of the dependence among three variables (the duration and intensity of a drought, as well as the PAFA caused by a drought). Thus, our subsequent analyses were all based on the Gumbel-Hougaard type Copula function.

Joint Distribution

In recent years, some researchers have begun to use three-dimensional Copula functions in their research [68, 69]. The joint distribution function can be obtained from the marginal distribution functions $F_D(d)$, $F_S(s)$, and $F_I(i)$, as well as the Copula function of drought duration, severity, and PAFA.

$$F(d,s,i)=P(D\le d,S\le s,I\le i)=C\left[F_D(d),F_S(s),F_I(i)\right], \quad (11)$$

The joint distribution describes the probability that the drought duration, severity, and PAFA are all equal to or less than a given value of the drought event.

Analysis Process

The main analysis process in this paper is as follows: first, the Run theory was used to extract the drought events by using the SPI sequences in Huize County and Mengzi County from 1961 to 2011. Then, the marginal distribution functions and their parameters were obtained using the data on drought durations and drought intensities, respectively. After that, we calculated the PAFA, and the marginal distribution functions and their parameters of PAFA were obtained by using the data from Huize County from 1986 to 2011 and Mengzi County from 1995 to 2011. Finally, by using the data on drought durations, drought intensities, and the PAFA of Huize County from 1986 to 2011 and Mengzi County from 1995 to 2011, the 3D joint distribution functions and the parameters of the two counties were obtained, respectively, based on a maximum likelihood estimation. The data on drought durations, drought intensities, and the PAFA for 2012 would be used to verify the evaluation of the model.

TABLE 4 | Kendall's tau among drought duration (D), drought severity (S), and PAFA (I).

County	τ (**D**, **S**)	τ (**D**, **I**)	τ (**S**, **I**)
Huize	0.63	0.10	0.63
Mengzi	0.47	0.42	0.47

RESULTS AND DISCUSSION

The Establishment and Analysis of the 3D Joint Probability Distribution

The SPI sequences of the Huize and Mengzi counties were applied to extract drought events during the period between 1961 and 2011. Statistical characteristics were obtained and shown in **Table 3**, with $s_0 = 0$ set as the threshold.

The number of drought events extracted from the SPI sequence were 161 (Huize County) and 153 (Mengzi County) from 1961 to 2011. The statistical indicators of drought duration and severity in Mengzi County were slightly larger than in Huize County. The average drought duration of both counties was close to 2 months, and the average drought severity of both counties reached the level of severe drought. The longest drought duration in Mengzi County was 12 months, and its cumulative drought severity reached the maximum recorded value (12.12) in history. The Pearson correlation coefficient of drought duration and drought severity indicated that there was a strong correlation between the two variables in the two counties, showing that the duration and severity of the droughts in the two counties were both strongly synchronized (**Table 3**). Moreover, each pairwise relationship among drought duration, drought severity, and PAFA is measured using Kendall's tau coefficient (**Table 4**), the results indicating that there exists a positive interrelated relationship between any two of these three variables in the two counties because the values of Kendall's tau are all > 0.

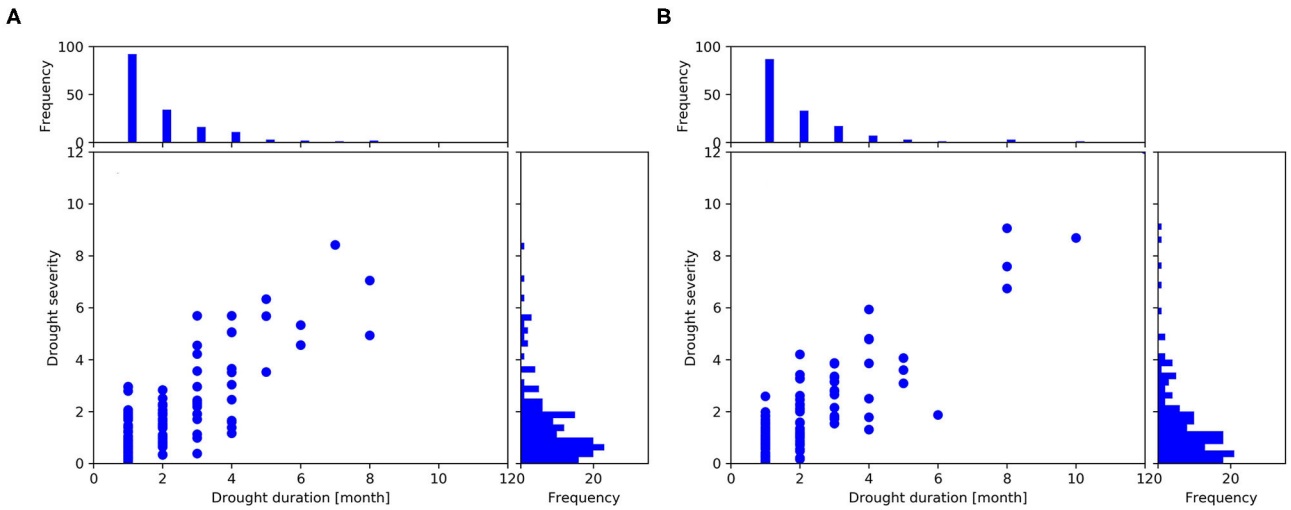

FIGURE 4 | The scatter diagrams and the frequency diagrams of the drought duration and severity in **(A)** Huize County and **(B)** Mengzi County.

TABLE 5 | The *P*-value of goodness of fit based on the KS test for drought duration severity, PAFA.

County	Drought duration	Drought severity	PAFA
Huize	0.999	0.984	0.998
Mengzi	0.957	0.955	0.997

Figure 4 shows the scatter diagrams and statistical histograms of the drought duration and severity in the two counties, respectively. The distribution characteristics of drought duration and severity in the two counties were basically consistent (**Figure 4**). In most cases, the drought durations were all under 2 months and the drought severities were lower than the level of a severe drought in the two counties.

In order to confirm that the distributions of the drought durations of the two counties satisfy the exponential distribution, drought severities of the two counties satisfy the gamma distribution, as well as having the distributions of the PAFA of the two counties satisfy the exponential distribution, the Kolmogorov-Smirnov (KS) test was used to analyze the difference between the empirical distribution function and the theoretical distribution function at the 0.05 significance level. The results according to the KS test are shown in **Table 5**. **Table 5** shows that the results had passed the statistical test and were reliable; namely, the distributions of the drought durations of the two counties were subject to exponential distribution, the distributions of the drought severities of the two counties were subject to gamma distribution, and PAFA of the two counties were subject to exponential distribution.

In this study, Copulas are employed to construct the joint distribution function. A three-variable joint distribution function was obtained by using Equations (1–11), and the probability distributions of PAFA were then calculated based on different drought durations and severities. **Figure 5** shows the three-variable joint probability distribution of different PAFAs in Huize County, and the distribution characteristics were similar in Mengzi County.

The Z coordinate in **Figure 5** represents the probability when the random variables are less than given values. Taking **Figure 5A** as an example, the meaning of the curved surface in the figure is the probability $P\left(D \leq d, S \leq s, PAFA \leq 10\%\right)$. The meaning in **Figure 5B** is the same as **Figure 5A**, except that the PAFA is less than a different value. As shown in **Figure 5A**, with regard to all drought events, 40% of the drought events caused PAFAs of no more than 10%; in other words, the farmland areas affected by 40% of the drought events did not exceed 10% of the planted areas. In addition, 80% of the drought events caused PAFAs of no more than 30%, meaning that the drought events, which caused PAFA to exceed 30% occurred rarely in history (**Figure 5B**). Then, the 3D joint probability distribution and the statistical relationships between the PAFA, the drought duration, and the drought severity could be obtained.

In this paper, more attention was actually paid to the practical application of the 3D joint probability distribution rather than the statistical relationships between the PAFA, the drought duration, and the drought severity, so we propose a classification scheme. By combining the classification method of drought duration and severity (**Tables 1**, **2**) with the classification standard of PAFA (**Table 6**) (National Standard of the People's Republic of China: Grade of drought disaster GB/T 34306-2017), the probability distribution of various combinations of different drought durations, severities, and PAFAs could be determined, as shown in **Figure 6**.

Figure 6 shows the joint probability distributions of Huize County that drought duration and drought severity are within a given interval. **Figure 6A** shows the occurrence probability $(P\left(d_1 < D \leq d_2, s_1 < S \leq s_2, 10\% < PAFA \leq 30\%\right))$ of drought events with different durations and severities when the PAFA is

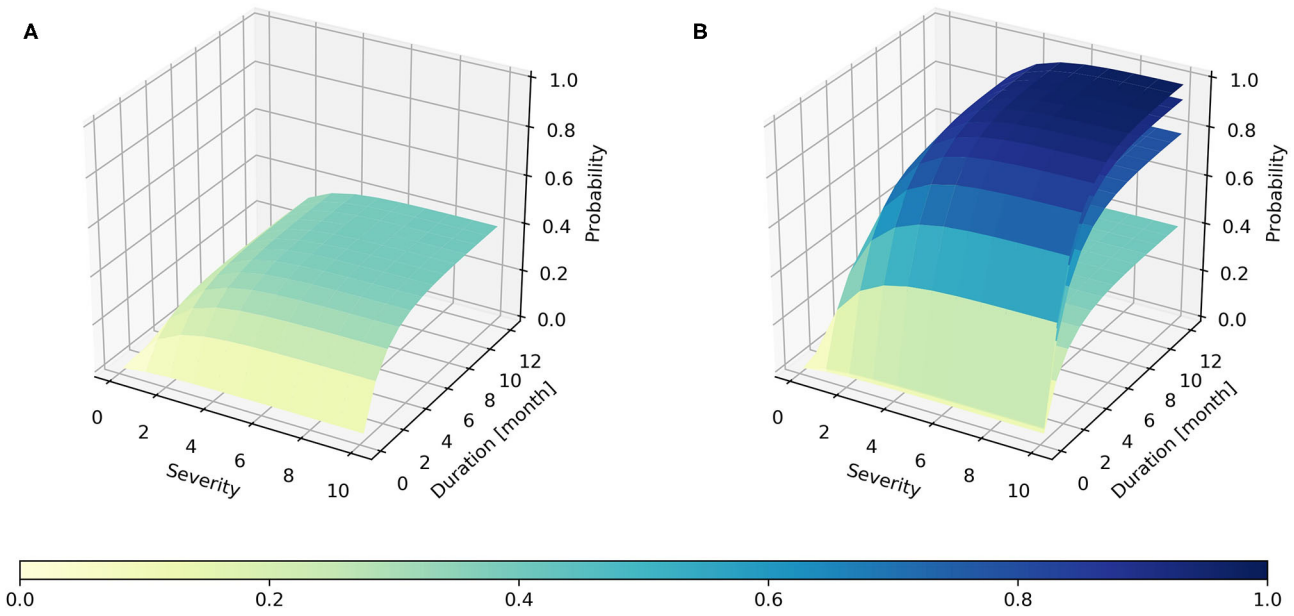

FIGURE 5 | The 3D joint probability distribution **(A)** when PAFA is 10%, and **(B)** when PAFA is 10, 30, 50, and 80% in Huize County.

at the level of 2. The durations of drought events with a high probability of occurrence are at levels 1 ($0 < D \leq 1$ within 1 month) and 2 ($1 < D \leq 3$ within one season); that is, the durations do not exceed one season. If the drought duration is in level 1 ($0 < D \leq 1$ within 1 month), the severity of the most likely drought events is in level 1 ($0.5 < S \leq 1$ slight drought), but the severity of the most likely drought events is in level 4 ($2.0 < S$ extreme drought) while the drought duration is in level 2 ($1 < D \leq 3$ within one season). The probability of drought events with other durations and severities is very small. Similarly, **Figures 6B–D** gives the occurrence probability of drought events with different durations and severities when the PAFA is at three other levels. When the PAFA is at level 3 ($30\% < I \leq 50\%$) (**Figure 6B**), the durations of drought events with a high probability of occurrence are at levels 2 ($1 < D \leq 3$ within one season) and 3 ($3 < D \leq 6$ cross-quarter), as well as severity level 4 ($2.0 < S$ extreme drought); when the PAFA is at level 4 ($50\% < I \leq 80\%$) (**Figure 6C**), the durations of drought events with a high probability of occurrence are at levels 3 ($3 < D \leq 6$ cross-quarter) and 4 ($6 < D$ over 6 months), as well as severity level 4 ($2.0 < S$ extreme drought). The conclusion of **Figure 6D** is similar to **Figure 6C** but for the PAFA being at level 5 ($80\% < I$). As the PAFA increases, the joint probability of drought duration and severity also increases with the increase in their levels.

The Application of the 3D Joint Probability Distribution

Figure 7 shows the SPI index sequences in Huize and Mengzi counties in 2012. According to **Figure 7**, Huize (**Figure 7A**) and Mengzi (**Figure 7B**) counties experienced several drought events during this period, especially between January and March 2012. Huize County experienced a drought event with a duration of 2 months and a severity of 1.9 from January 2012 to February 2012. Similarly, Mengzi County experienced a drought event with a duration of 5 months and a severity of 3.09 from February 2012 to June 2012. Furthermore, the disaster data indicated that drought disasters occurred in Huize and Mengzi counties from January to April in 2012. **Table 7** shows the disaster data during this period.

There was one piece of recorded disaster drought data in Huize County in 2012 (during the period between January and March); at the same time, there were three records in Mengzi County in 2012 (**Table 7**). By comparison, it was found that the start and end times of the drought disasters given by the recorded disaster data were basically consistent with the calculation results of the SPI index sequences in the two counties. The calculation result of the SPI index shows that the drought event in Huize County lasted for 2 months from January to February 2012 and the severity was 1.90, and the drought event in Mengzi County lasted for 5 months from February to June 2012 and the severity was 3.09, although the drought intensity in April-June was weak. The levels of drought duration and severity in Huize County were 2 ($1 < D \leq 3$ within one season) and 3 ($1.5 < S \leq 2$ Moderate drought), respectively, while the levels of drought duration and severity in Mengzi County were 3 ($3 < D \leq 6$ cross-quarter) and 4 ($2 < S$ Extreme drought), respectively. Equation (8) was used to estimate the occurrence probability of PAFAs that correspond to the two drought events in the two counties in 2012, respectively, and the results are shown in **Table 8**.

Table 8 shows that in Huize County, the highest probability of an occurrence of a PAFA was $10\% < I \leq 30\%$; that is, the maximum risk corresponded to a PAFA of 10%; and in Mengzi County, the highest probability of an occurrence of PAFA was

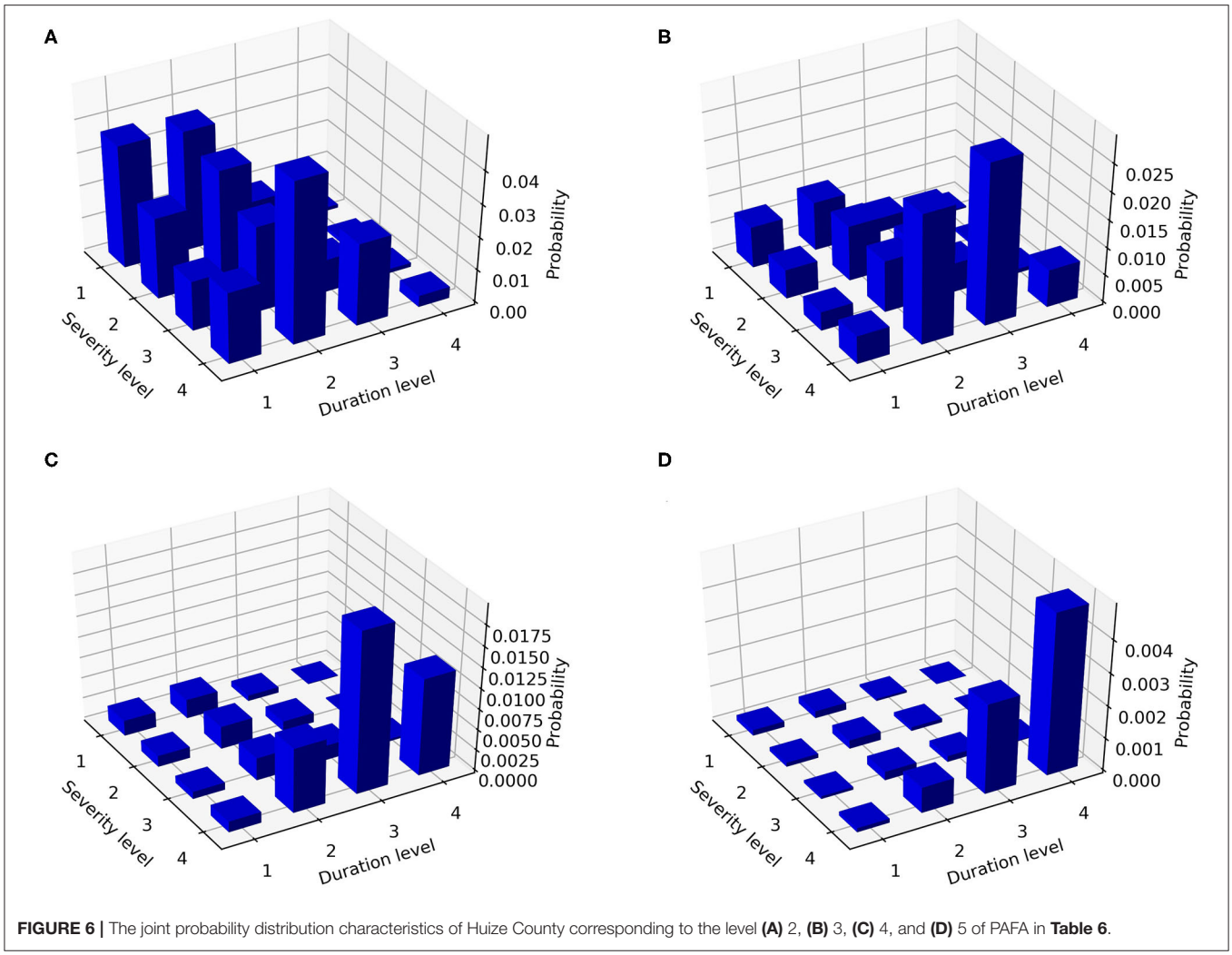

FIGURE 6 | The joint probability distribution characteristics of Huize County corresponding to the level **(A)** 2, **(B)** 3, **(C)** 4, and **(D)** 5 of PAFA in **Table 6**.

TABLE 6 | The classification of PAFA.

Level	1	2	3	4	5
I	$I \leq 10\%$	$10\% < I \leq 30\%$	$30\% < I \leq 50\%$	$50\% < I \leq 80\%$	$80\% < I$

$30\% < I \leq 50\%$; i.e., the maximum risk corresponded to a PAFA of $30\% < I \leq 50\%$. In a practical situation, the actual PAFA in Huize County was 14.3%, and in Mengzi County it was 50.3%. The PAFA results obtained by the method proposed in this paper were consistent with the actual PAFAs in the two counties, the PAFA of Huize County was evaluated well, and the PAFA of Mengzi County was slightly underestimated.

On the one hand, the underestimation of Mengzi County can be understood from a statistical point of view because we gave the occurrence probabilities of different levels of PAFA in a certain drought event, and while the probability is precisely an expression of risk, and on the other hand, the drought index used in this study (i.e., the SPI) is a meteorological drought index rather than a direct indicator of agricultural drought. Therefore, there is still a certain difference between the duration/severity of a drought obtained through the SPI index and the actual agricultural drought. However, a meteorological drought always occurs before an agricultural drought, so a meteorological drought index could be used to forecast and forewarn farmers of an agricultural drought and its effects in advance. In practical applications, compared with simple drought monitoring indicators, we can get SPI predictions for the following month or months based on monthly or seasonal precipitation forecasts, and can further obtain more abundant information about a drought warning and its impact through the method proposed in this paper so that relevant countermeasures

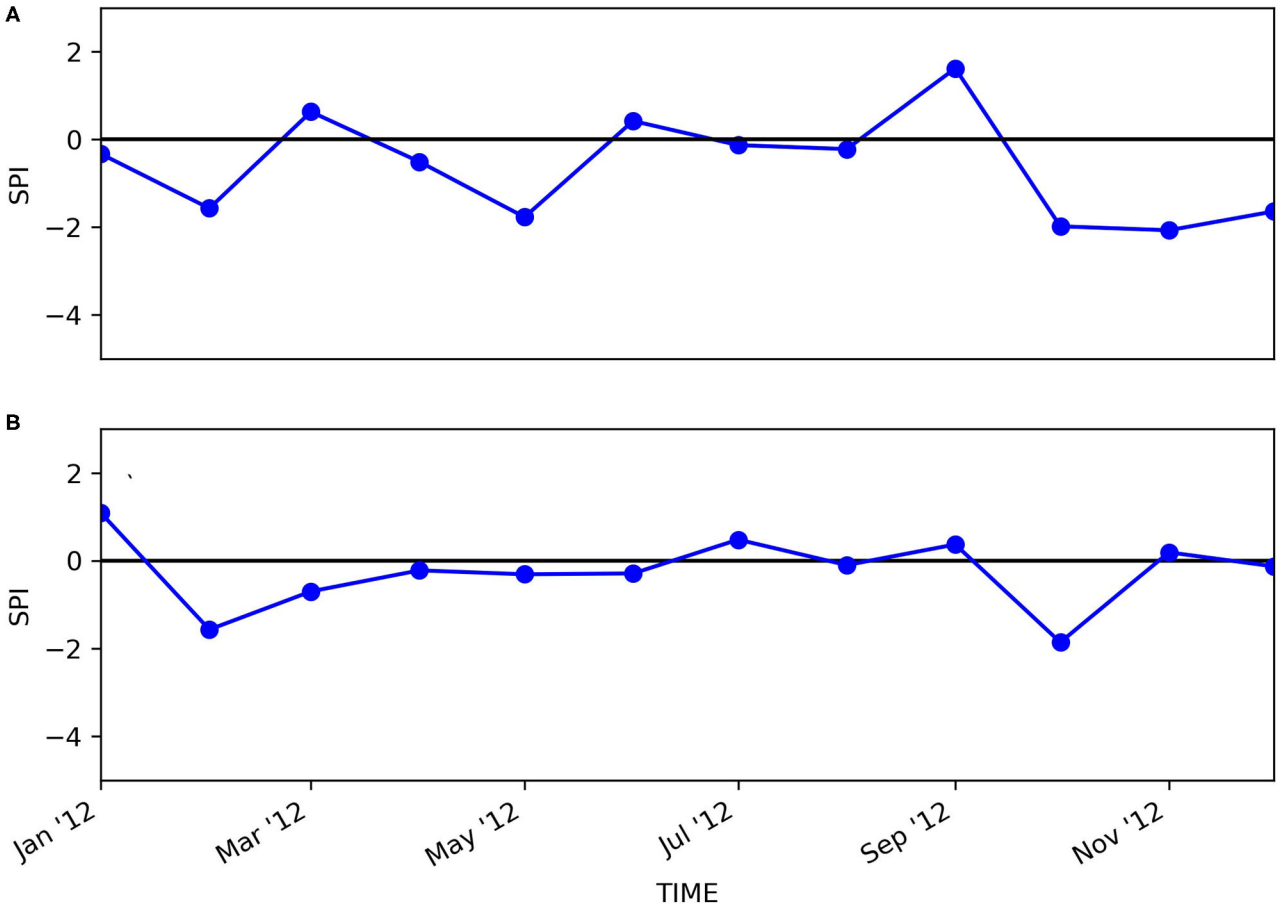

FIGURE 7 | The SPI sequences of **(A)** Huize County and **(B)** Mengzi County from January to December 2012.

can be taken according to the probability of occurrence of different levels of PAFA in order to achieve the purpose of disaster prevention, mitigation, and relief.

CONCLUSIONS AND DISCUSSIONS

Copula-based distribution has been used by researchers from different countries around the world in multivariate analyses of hydrological or meteorological events such as droughts due to its advantages in modeling the non-linear dependence structure of variables regardless of their marginal distributions. However, the applications of the Copula technique in assessing the impacts of a drought on agricultural production are very limited in published literature, and the damage data are often not used as a variable to be substituted into the Copula function, but are instead used as an independent variable in combination with the comprehensive features of a drought obtained by the Copula function. This assessment is actually based on an "external combination" of drought characteristics and drought impacts.

In order to achieve the "internal combination" of drought characteristics and drought impacts, as well as assessing the specific impacts of droughts with different severities and durations, we used three variables of drought events and their impacts; namely, the drought duration, drought intensity, and the proportion of affected farmland areas (PAFA), and built a model based on the three-dimensional (3D) Copula function

TABLE 7 | The disaster data of droughts in Huize County and Mengzi counties.

County	Start Time	End Time	The areas of affected farmland (hectare)
Huize	2012-1-15	2012-3-2	15296.7
Mengzi	2012-1-21	2012-2-17	19093.3
Mengzi	2012-2-21	2012-2-29	3077.2
Mengzi	2012-3-1	2012-3-31	405.5

TABLE 8 | The occurrence probability of PAFAs.

County	$I \leq 10\%$	$10\% < I \leq 30\%$	$30\% < I \leq 50\%$	$50\% < I \leq 80\%$	$80\% < I$
Huize	0.0145	0.0264	0.0095	0.0028	0.0003
Mengzi	0.0049	0.0396	0.0403	0.0147	0.0009

for the assessment of the PAFA for the purpose of quantified drought risk analysis. The result of the model can provide occurrence probabilities for different levels of PAFA in a certain drought event, and while probability is precisely an expression of risk, we took Huize County and Mengzi County in Yunnan Province as application examples, and the results showed that the PAFAs obtained by the method proposed in this paper were both consistent with the actual PAFAs in the two counties.

Based on this model, the loss size and uncertainty (probability) under a given drought intensity can be well-expressed, which is the expected result of risk analysis. What's more, according to the division of drought grade, what kind of loss and its probability caused by a certain type of drought event can be clearly given. Moreover, in order to take risk control and mitigation measures, it is necessary to assess the impacts of a drought on agricultural production based on current drought conditions, and, more importantly, based on the forecast and predicted drought conditions in the future. A meteorological drought always occurs before an agricultural drought. In practical applications, we can obtain SPI predictions for the following month or months and can obtain further abundant information on drought warnings and their impact according to the probability of occurrence of different levels of PAFA. Therefore, the method proposed in this paper has values both on theory and practice.

DATA AVAILABILITY STATEMENT

The original contributions presented in the study are included in the article/supplementary material, further inquiries can be directed to the corresponding author/s.

AUTHOR CONTRIBUTIONS

WH, DZ, and PY: methodology. WH and DZ: writing original draft preparation. GF and WH: writing review and editing. DZ and PY: visualization. All authors contributed to the article and approved the submitted version.

FUNDING

This work was funded by National key research and development program of China (Grant no. 2017YFC1502402), National Natural Science Foundation of China (Grant No. 41775078), Natural science research project of higher education in Jiangsu provinces (Grant No. 20KJB170004), and School-level research projects of Yancheng Institute of Technology (Grant No. xjr2019052).

REFERENCES

1. Wilhite DA, Glantz MH. Understanding: the drought phenomenon: the role of definitions. *Water Int.* (1985) 10:111–20. doi: 10.1080/02508068508686328
2. Wilhite DA, Svoboda MD, Hayes MJ. Understanding the complex impacts of drought: a key to enhancing drought mitigation and preparedness. *Water Resour Manag.* (2007) 21:763–74. doi: 10.1007/s11269-006-9076-5
3. Quiring SM. Developing objective operational definitions for monitoring drought. *J Appl Meteorol Climatol.* (2009) 48:1217–29. doi: 10.1175/2009JAMC2088.1
4. Mishra AK, Singh VP. A review of drought concepts. *J Hydrol.* (2010) 391:202–16. doi: 10.1016/j.jhydrol.2010.07.012
5. Al-Qinna MI, Hammouri NA, Obeidat MM, Ahmad FY. Drought analysis in Jordan under current and future climates. *Clim Change.* (2011) 106:421–40. doi: 10.1007/s10584-010-9954-y
6. Schwalm CR, Anderegg WRL, Michalak AM, Fisher JB, Biondi F, Koch G, et al. Global patterns of drought recovery. *Nature.* (2017) 548:202–5. doi: 10.1038/nature23021
7. Sun GQ, Wang SF, Li MT, Li L, Feng GL. Transmission dynamics of COVID-19 in Wuhan, China: effects of lockdown and medical resources. *Nonlinear Dyn.* (2020) 101:1981–93. doi: 10.1007/s11071-020-05770-9
8. Sun GQ, Zhang HT, Wang JS, Li J, Wang Y, Li L, et al. Mathematical modeling and mechanisms of pattern formation in ecological systems: a review. *Nonlinear Dyn.* (2021). doi: 10.1007/s11071-021-06314-5. [Epub ahead of print].
9. Van Loon AF, Gleeson T, Clark J, Dijk AIJMV, Stahl K, Hannaford J, et al. Drought in the anthropocene. *Nat Geosci.* (2016) 9:89–91. doi: 10.1038/ngeo2646
10. Wilhite DA. *Drought as a Natural Hazard: Concepts and Definitions*. London: Routledge (2000).
11. Aghakouchak A, Feldman D, Hoerling M, Huxman T, Lund J. Recognize anthropogenic drought. *Nature.* (2015) 524:409–11. doi: 10.1038/524409a
12. Wang XJ, Shahid S, Elmahdi A, He RM, Bao ZX, Ali M. Water resources management strategy for adaptation to droughts in China. *Mitig Adapt Strateg Glob Change.* (2012) 17:923–37. doi: 10.1007/s11027-011-9352-4
13. Yu M, Li Q, Hayes MJ, Svoboda MD, Heim RR. Are droughts becoming more frequent or severe in China based on the Standardized Precipitation Evapotranspiration Index: 1951–2010? *Int J Climatol.* (2014) 34:545–58. doi: 10.1002/joc.3701
14. Wang X, Hou X, Li Z, Wang Y. Spatial and temporal characteristics of meteorological drought in Shandong Province, China, from 1961 to 2008. *Adv Meteorol.* (2014) 2014:1–11. doi: 10.1155/2014/685971
15. Trinh T, Ishida K, Kavvas ML, Ercan A, Carr K. Assessment of 21st century drought conditions at Shasta Dam based on dynamically projected water supply conditions by a regional climate model coupled with a physically-based hydrology model. *Sci Total Environ.* (2017) 586:197–205. doi: 10.1016/j.scitotenv.2017.01.202
16. Ahmed K, Shahid S, Nawaz N. Impacts of climate variability and change on seasonal drought characteristics of Pakistan. *Atmos Res.* (2018) 214:364–74. doi: 10.1016/j.atmosres.2018.08.020
17. Hao Z, Singh VP, Hao F. Compound extremes in hydroclimatology: a review. *Water.* (2018) 10:718. doi: 10.3390/w10060718
18. Lloret F, Kitzberger T. Historical and event-based bioclimatic suitability predicts regional forest vulnerability to compound effects of severe drought and bark beetle infestation. *Glob Change Biol.* (2018) 24:39. doi: 10.1111/gcb.14039
19. Royer PD, Villegas JC. Extreme climatic event-triggered overstorey vegetation loss increases understorey solar input regionally: primary and secondary ecological implications. *J Ecol.* (2011) 99:714–23. doi: 10.1111/j.1365-2745.2011.01804.x
20. Hui-Mean F, Yusop Z, Yusof FJAR. Drought analysis and water resource availability using standardised precipitation evapotranspiration index. *Atmosp Res.* (2018) 201:102–15. doi: 10.1016/j.atmosres.2017.10.014
21. Li B, Sherman DJ. Aerodynamics and morphodynamics of sand fences: a review. *Aeolian Res.* (2015) 17:33–48. doi: 10.1016/j.aeolia.2014.11.005
22. Lima IA, Parteli EJR, Shao Y, Andrade JS, Araújo AD. CFD simulation of the wind field over a terrain with sand fences: critical spacing for the wind shear velocity. *Aeolian Res.* (2020) 43:100574. doi: 10.1016/j.aeolia.2020.100574
23. Li YP, Wei Y, Meng W, Yan XD. Climate change and drought: a risk assessment of crop-yield impacts. *Clim Res.* (2009) 39:31–46. doi: 10.3354/cr00797

24. Ferrise R, Moriondo M, Bindi M. Probabilistic assessments of climate change impacts on durum wheat in the Mediterranean region. *Nat Hazards Earth Syst Sci.* (2011) 11:1293–302. doi: 10.5194/nhess-11-1293-2011
25. Capa-Morocho M, Ines AVM, Baethgen WE, Rodríguez-Fonseca B, Han E, Ruiz-Ramos M. Crop yield outlooks in the Iberian Peninsula: connecting seasonal climate forecasts with crop simulation models. *Agric Syst.* (2016) 149:75–87. doi: 10.1016/j.agsy.2016.08.008
26. Madadgar S, Aghakouchak A, Farahmand A, Davis SJ. Probabilistic estimates of drought impacts on agricultural production: Drought impacts on agricultural. *Geophys Res Lett.* (2017) 44:7799–807. doi: 10.1002/2017GL073606
27. Willner SN, Otto C, Levermann A. Global economic response to river floods. *Nat Clim Change.* (2018) 8:594–8. doi: 10.1038/s41558-018-0173-2
28. Volpi E. On return period and probability of failure in hydrology. *Wiley Interdiscip Rev Water.* (2019) 6:1–13. doi: 10.1002/wat2.1340
29. Freire-González J, Christopher AD, Jim WH. A scenario-based framework for assessing the economic impacts of potential droughts. *Water Econ Policy.* (2017) 3:1–27. doi: 10.1142/S2382624X17500072
30. Hall JW, Leng G. Can we calculate drought risk and do we need to? *Wiley Interdiscip Rev Water.* (2019) 6:e1349. doi: 10.1002/wat2.1349
31. Hagenlocher M, Castro MC. Mapping malaria risk and vulnerability in the United Republic of Tanzania: a spatial explicit model. *Popul Health Metr.* (2015) 13:2. doi: 10.1186/s12963-015-0036-2
32. Sun Z, Zhang JQ, Yan DH, Lan W, Guo E. The impact of irrigation water supply rate on agricultural drought disaster risk: a case about maize based on EPIC in Baicheng City, China. *Nat Hazards.* (2015) 78:23–40. doi: 10.1007/s11069-015-1695-9
33. Welle T, Birkmann J. The world risk index – an approach to assess risk and vulnerability on a global scale. *J Extreme Events.* (2015) 2:34. doi: 10.1142/S2345737615500037
34. Zhang Q, Sun P, Li J, Xiao M, Singh VP. Assessment of drought vulnerability of the Tarim River basin, Xinjiang, China. *Theor Appl Climatol.* (2015) 121:337–47. doi: 10.1007/s00704-014-1234-8
35. Feizizadeh B, Kienberger S. Spatially explicit sensitivity and uncertainty analysis for multicriteria-based vulnerability assessment. *J Environ Plann Manag.* (2017) 60:1–23. doi: 10.1080/09640568.2016.1269643
36. García-León D, Contreras S, Hunink J. Comparison of meteorological and satellite-based drought indices as yield predictors of Spanish cereals. *Agric Water Manag.* (2019) 213:388–96. doi: 10.1016/j.agwat.2018.10.030
37. Siebert S, Webber H, Rezaei EE. Weather impacts on crop yields - searching for simple answers to a complex problem. *Environ Res Lett.* (2017) 12:081001. doi: 10.1088/1748-9326/aa7f15
38. Hagenlocher M, Meza I, Anderson C, Min A, Renaud F, Walz Y, et al. Drought vulnerability and risk assessments: state of the art, persistent gaps, and research agenda. *Environ Res Lett.* (2019) 14:083002. doi: 10.1088/1748-9326/ab225d
39. Sklar, A. Fonctions de répartition à n dimensions et leurs marges publications de l'Institut de Statistique de l'Université de Paris. *Sci Res.* (1959) 8:229–31.
40. Nelsen RB. *An Introduction to Copulas.* New York, NY: Springer (2006).
41. Okhrin O, Odening M, Wei X. Systemic weather risk and crop insurance: the case of China. *J Risk Insur.* (2013) 80:351–72. doi: 10.1111/j.1539-6975.2012.01476.x
42. Bokusheva R, Kogan F, Vitkovskaya I, Conradt S, Batyrbayeva M. Satellite-based vegetation health indices as a criteria for insuring against drought-related yield losses. *Agric For Meteorol.* (2016) 220:200–6. doi: 10.1016/j.agrformet.2015.12.066
43. Mehdikhani H, Saghafian B, Arasteh PD. A new damage-probability approach for risk analysis of rain-fed agricultural systems under meteorological drought. *KSCE J Civil Eng.* (2016) 21:1453–61. doi: 10.1007/s12205-016-0510-y
44. Guo E, Liu X, Zhang J, Wang Y, Wang C, Rui W, et al. Assessing spatiotemporal variation of drought and its impact on maize yield in Northeast China. *J Hydrol.* (2017) 553:231–47. doi: 10.1016/j.jhydrol.2017.07.060
45. Nguyen-Huy T, Deo RC, Mushtaq S, An-Vo DA, Khan S. Modeling the joint influence of multiple synoptic-scale, climate mode indices on Australian wheat yield using a vine copula-based approach. *Eur J Agron.* (2018) 98:65–81. doi: 10.1016/j.eja.2018.05.006
46. Nguyen-Huy T, Deo RC, Mushtaq S, Kath J, Khan S. Copula statistical models for analyzing stochastic dependencies of systemic drought risk and potential adaptation strategies. *Stoch Environ Res Risk Assess.* (2019) 33:779–99. doi: 10.1007/s00477-019-01662-6
47. Li Z, He Y, Wang P, Theakstone WH, An W, Wang X, et al. Changes of daily climate extremes in southwestern China during 1961–2008. *Glob Planet Change.* (2012) 80:255–72. doi: 10.1016/j.gloplacha.2011.06.008
48. Huang K, Tao Z, Xiang Z. Extreme drought-induced trend changes in MODIS EVI time series in Yunnan, China. *IOP Conf Ser Earth Environ Sci.* (2014) 17:012070. doi: 10.1088/1755-1315/17/1/012070
49. Long D, Shen Y, Sun A, Hong Y, Longuevergne L, Yang Y, et al. Drought and flood monitoring for a large karst plateau in Southwest China using extended GRACE data. *Remote Sens Environ.* (2014) 155:145–60. doi: 10.1016/j.rse.2014.08.006
50. Yan Z, Zhang Y, Zhou Z, Ning H. The spatio-temporal variability of droughts using the standardized precipitation index in Yunnan, China. *Nat Hazards.* (2017) 88:1–20. doi: 10.1007/s11069-017-2904-5
51. Wang Y, Wen S, Li X, Thomas F, Su B, Wang R, et al. Spatiotemporal distributions of influential tropical cyclones and associated economic losses in China in 1984–2015. *Nat Hazards.* (2016) 84:2009–30. doi: 10.1007/s11069-016-2531-6
52. McKee TB, Doesken NJ, Kleist J. The relationship of drought frequency and duration to time scales Preprints. In: *8th Conference on Applied Climatology.* Anaheim (1993). p. 179–84.
53. Mishra AK, Desai VR. Drought forecasting using stochastic models. *Stoch Environ Res Risk Assess.* (2005) 19:326–39. doi: 10.1007/s00477-005-0238-4
54. Cancelliere A, Mauro GD, Bonaccorso B, Rossi G. Drought forecasting using the standardized precipitation index. *Water Resour Manag.* (2007) 21:801–19. doi: 10.1007/s11269-006-9062-y
55. Bordi I, Fraedrich K, Sutera A. Observed drought and wetness trends in Europe: an update. *Hydrol Earth Syst Sci.* (2009) 13:1519–30. doi: 10.5194/hess-13-1519-2009
56. Golian S, Mazdiyasni O, Aghakouchak A. Trends in meteorological and agricultural droughts in Iran. *Theor Appl Climatol.* (2015) 119:679–88. doi: 10.1007/s00704-014-1139-6
57. Bayissa Y, Maskey S, Tadesse T, Andel SJV, Moges S, Griensven AV, et al. Comparison of the performance of six drought indices in characterizing historical drought for the upper blue Nile Basin, Ethiopia. *Geosciences.* (2018) 8:81. doi: 10.3390/geosciences8030081
58. Herbst PH, Bredenkamp DB, Barker HMG. A technique for the evaluation of drought from rainfall data. *J Hydrol.* (1966) 4:264–72. doi: 10.1016/0022-1694(66)90084-9
59. Cancelliere A, Salas JD. Drought length properties for periodic-stochastic hydrologic data. *Water Resour Res.* (2004) 40:389–91. doi: 10.1029/2002WR001750
60. Chang J, Li Y, Wang Y, Meng Y. Copula-based drought risk assessment combined with an integrated index in the Wei River Basin, China. *J Hydrol.* (2016) 540:824–34. doi: 10.1016/j.jhydrol.2016.06.064
61. Wu L, Feng L, Li Y, Wang J, Wu L. A yield-related agricultural drought index reveals spatio-temporal characteristics of droughts in Southwestern China. *Sustainability.* (2019) 11:714. doi: 10.3390/su11030714
62. Shiau JT. Fitting drought duration and severity with two-dimensional copulas. *Water Resour Manag.* (2006) 20:795–815. doi: 10.1007/s11269-005-9008-9
63. Liu CL, Zhang Q, Singh VP, Cui Y. Copula-based evaluations of drought variations in Guangdong, South China. *Nat Hazards.* (2011) 59:1533–46. doi: 10.1007/s11069-011-9850-4
64. Serinaldi F, Bonaccorso B, Cancelliere A, Grimaldi S. Probabilistic characterization of drought properties through copulas. *Phys Chem Earth A/B/C.* (2009) 34:596–605. doi: 10.1016/j.pce.2008.09.004
65. Bezak N, Mikoš M, Šraj M. Trivariate frequency analyses of peak discharge, hydrograph volume and suspended sediment concentration data using copulas. *Water Resour Manag.* (2014) 28:2195–212. doi: 10.1007/s11269-014-0606-2
66. Willmott CJ, Ackleson SG, Davis RE, Feddema JJ, Klink KM, Legates DR, et al. Statistics for the evaluation and comparison of models. *J Geophys Res Oceans.* (1985) 90:8995–9005. doi: 10.1029/JC090iC05p08995

67. Jeong DI, Sushama L, Khaliq MN, Roy R. A copula-based multivariate analysis of Canadian RCM projected changes to flood characteristics for northeastern Canada. *Clim Dyn.* (2014) 42:2045–66. doi: 10.1007/s00382-013-1851-4
68. Song S, Singh VP. Frequency analysis of droughts using the Plackett copula and parameter estimation by genetic algorithm. *Stoch Environ Res Risk Assess.* (2010) 24:783–805. doi: 10.1007/s00477-010-0364-5
69. Ma M, Song S, Ren L, Jiang S, Song J. Multivariate drought characteristics using trivariate Gaussian and Student t copulas. *Hydrol Process.* (2013) 27:1175–90. doi: 10.1002/hyp.8432

Conflict of Interest: The authors declare that the research was conducted in the absence of any commercial or financial relationships that could be construed as a potential conflict of interest.

frontiers in Physics

ORIGINAL RESEARCH
published: 01 June 2021
doi: 10.3389/fphy.2021.675922

Typical Modes of the Wind Speed Diurnal Variation in Beijing Based on the Clustering Method

Pengcheng Yan[1,2], Dongdong Zuo[3], Ping Yang[4]* and Suosuo Li[2]*

[1]Key Laboratory of Arid Climatic Change and Reducing Disaster of Gansu Province/Key Laboratory of Arid Climatic Change and Reducing Disaster of China Meteorological Administration, Institute of Arid Meteorology, China Meteorological Administration, Lanzhou, China, [2]Key Laboratory of Land Surface Process and Climate Change in Cold and Arid Regions, Chinese Academy of Sciences, Lanzhou, China, [3]School of Mathematics and Physics, Yancheng Institute of Technology, Yancheng, China, [4]China Meteorological Administration Training Center, Beijing, China

Wind speed is an important meteorological condition affecting the urban environment. Thus, analyzing the typical characteristics of the wind speed diurnal variation is helpful for forecasting pollutant diffusion. Based on the K-means clustering method, the diurnal variation characteristics of the wind speed in Beijing during 2008–2017 are studied, and the spatiotemporal characteristics of the wind speed diurnal variations are analyzed. The results show that there are mainly five to seven clusters of typical characteristics of the wind speed diurnal variation at different stations in Beijing, and the number of clusters near the city is smaller than that in the suburbs. The typical number of the wind speed diurnal variation during 2013–2015 is smaller than that in other periods, which means the anomalous clusters of the diurnal variation are reduced. Besides, the numbers of different clusters in different years are often switched. Especially, the switch between clusters five and six and the switch between clusters six and seven are frequent. Based on the second cluster analysis of the clustering results at the Beijing station, we find 12 clusters of the diurnal variation, including nine clusters of "large in the daytime, while small at night," two clusters of "monotonous," and one cluster of "strong wind." Furthermore, the low-speed clusters of wind mainly locate in the city with a significant increasing trend, while the high-speed clusters and the monotonous clusters of wind locate in the suburbs with a decreasing trend.

Keywords: diurnal variation of wind speed, typical wind modes, K-means, clustering method, second clustering

OPEN ACCESS

Edited by:
Gui-Quan Sun,
North University of China, China

Reviewed by:
Pengfei Lin,
Institute of Atmospheric Physics (CAS), China
Jianping Li,
Ocean University of China, China

****Correspondence:***
Ping Yang
zz96998@163.com

Specialty section:
This article was submitted to Interdisciplinary Physics, a section of the journal Frontiers in Physics

Received: *04 March 2021*
Accepted: *05 May 2021*
Published: *01 June 2021*

Citation:
Yan P, Zuo D, Yang P and Li S (2021) Typical Modes of the Wind Speed Diurnal Variation in Beijing Based on the Clustering Method. Front. Phys. 9:675922. doi: 10.3389/fphy.2021.675922

1 INTRODUCTION

There are significant environmental problems in big cities and industrial areas [1]. Surface meteorological conditions are important factors affecting the air quality [2], and the strong wind is associated with the rapid diffusion of the pollutant [3]. With the rapid expansion of cities, the urban heat island effect is significant, and the heat island circulation in the daytime is more significant than that at night, which means the characteristics of the wind speed diurnal variation have been changed [4, 5]. Beijing is one of the largest cities in China located at the northern foot of the North China Plain, which is the intersection of the Taihang Mountains and the Yanshan Mountains. The special terrain leads to increasingly serious environmental problems, which become more significant with the expansion of the city [6]. In Beijing, the main concentration of pollutants is

a two-peak pattern being coincident with rush hour [7]. If the wind speed is not big enough during these two periods, the pollutants are not easy to dissipate. The appearance time of strong wind is important for pollution.

Extracting the typical modes of daily variation of wind speed is helpful to study the appearance time of strong wind. The classification method has been verified to be useful to extract the typical modes, which can obtain more information from the system [8, 9]. In the classification, the typical spatial modes can be extracted by taking the spatial field as the sample (Makra et al. [10]). Taking the diurnal variation as the sample, the typical diurnal variation modes can be extracted. The clustering is an effective technique for extracting the typical modes. The K-means clustering method [11, 12] is the most widely used clustering method, which classifies a set of samples into k clusters according to the average distance from each sample to the cluster center. The clustering method is unsupervised learning, which does not rely on predefined samples and can automatically learn and label samples through iteration [13]. At present, it is widely used in fields such as machine learning [14], image recognition [15, 16], speech recognition [17], and climate change [18]. Because the K-means clustering method is based on calculating the spatial distance, it is generally used in numerical samples. Therefore, when it comes to texts, risk levels, and logical decisions, quantification is needed [19]. The clustering analysis algorithm is simple and easy to operate. However, on the one hand, clustering tends to fall into the local optimization and instability due to the randomness of the initial value; that is, the clustering result depends on the selection of the initial value [20]. On the other hand, the selection of the k value is generally subjective and lacks self-adaptability. To solve the problem of selecting the initial values, improved K-means algorithms such as the Kd-tree [21], the K-means++ [22], the cluster center initialization algorithm [23], and the fast search and find of density peaks [24] were proposed.. For self-adaptation of the k value, the author in Ref. 13 proposed a new method based on the degree of dispersity and aggregation, which automatically determines the k value by presetting a large k value and then degenerating. The authors in Ref. 25 also proposed a support vector machine decision tree method to determine the k value based on the dichotomy K-means. In addition, the elbow method is widely used to determine the k value because it is simple to operate. The authors in Ref. 26 proposed a new method to automatically obtain the k value based on the elbow method. The application of these new methods makes up the shortcoming of the K-means method, and effectively promotes the development and application of the K-means clustering method. Time consumption of the clustering algorithm in the iteration process is another problem that must be considered. Time consumption increases linearly along with the increase of the database. Therefore, a second clustering method is proposed in this study to reduce time consumption and promote clustering efficiency.

In this study, the clustering analysis of characteristics of the wind speed diurnal variation in Beijing is carried out based on the K-means clustering method. In "*Results and Analyses*" section, the data and the method are introduced briefly. In "*First Clustering: The Number of Clustering*" section, the clustering analysis is carried out for each station based on the hourly wind speed data at 160 observation stations during 2008–2017.

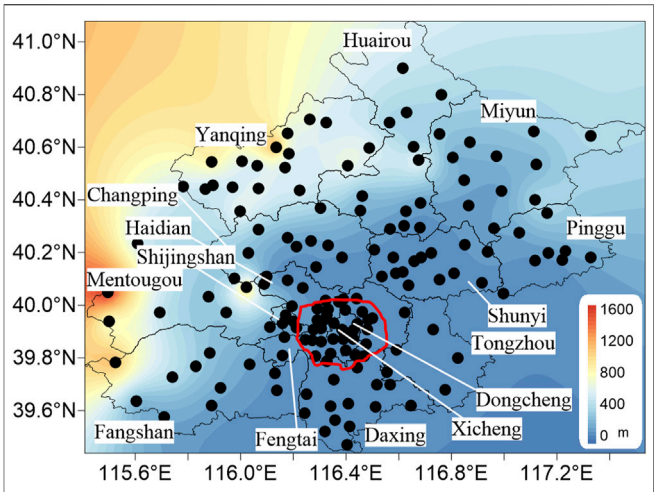

FIGURE 1 | The distribution of 16 districts and stations in Beijing. The red line indicates the Fifth Ring Road.

The typical characteristics of the diurnal variation and the number of main clusters are obtained. In "*Second Clustering: Typical Characteristics of the Wind Speed Diurnal Variation*" section, according to the classification results, a second clustering is carried out to obtain the typical modes of the characteristics of the wind speed diurnal variation in Beijing. The temporal and spatial variations of the typical modes are analyzed too.

2 DATA AND METHOD

2.1 Data

Based on the observed meteorological data at Beijing station, relatively complete hourly wind speed data at 160 stations are retained after the quality control, covering the period from January 1, 2008 to December 31, 2017. The distribution of the stations is shown in **Figure 1**. Most of them are in the flat region in Beijing. The altitudes at some stations in Yanqing district, Mentougou district, and Fangshan district are more than 1, 000 m above sea level. The city and suburbs are divided by the Fifth Ring Road. The stations in the city are significantly more than those in the suburbs.

2.2 K-Means Clustering Method and Its Improvements

The K-means algorithm is an unsupervised learning algorithm, which is often applied to the field of data mining [26], and it is a common clustering algorithm. The calculation steps are as follows:

1) The number of samples is N, and k samples are selected randomly as the initial cluster centers.
2) Do calculation of Euclidean distances ($D_{i,j}$) from one sample represented with x_i to each clustering center represented with c_j according to **Eq. 1**. The sample x_i is assigned to the cluster center c_j when the Euclidean distance $D_{i,J}$ is the shortest.

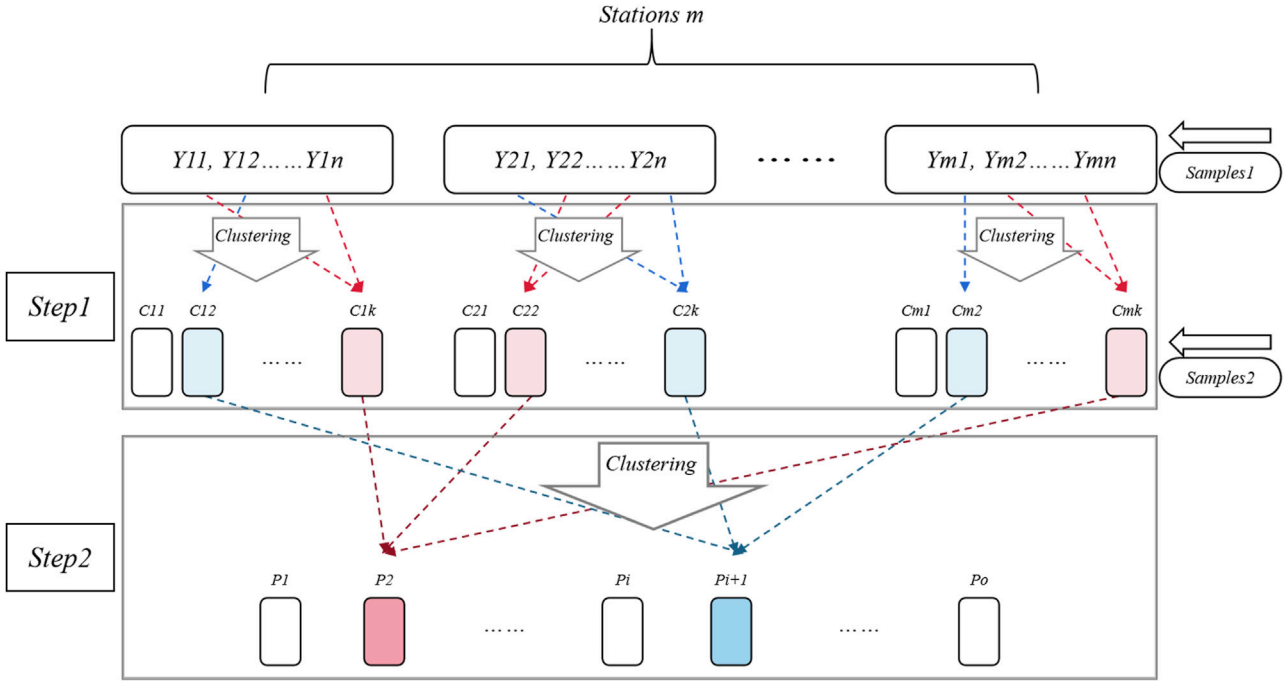

FIGURE 2 | The schematic diagram of the two-step clustering analysis.

Calculate all the samples like this and assign them to different cluster centers.

3) In order to ensure that the cluster centers can be representative as much as possible, the cluster centers are recalculated by using the samples assigned in different clusters.
4) Repeat steps 2 and 3 until the cluster centers of each sample no longer change.

$$D_{i,j} = \left|x_i - c_j\right|, \quad i \in [1, N], \quad j \in [1, k], \tag{1}$$

$$x_i \to c_J, D_{i,J} = \min|_{j=1}^{k} D_{i,j}, \quad i \in [1, N]. \tag{2}$$

There are two shortcomings of the K-means method. The first is that the randomness of selecting the initial value results in different results. The method of the ensemble is used in this study. We repeat the clustering several times (the random selection of the initial value), then calculate the ensemble results, and finally determine the clustering results. The second shortcoming is that the selection of the k value directly impacts the clustering results. The optimal number of the samples is related to the structure of the data themselves, but the latter is hard to determine. It is very difficult to determine the optimal solution of the k value. Therefore, the elbow method is used to determine the k value in this study.

2.3 Second Clustering

If the number of samples is too large to be clustered directly, a second clustering method can be used. According to the characteristics of samples, the first clustering is carried out first. Then, the clustering results are used as samples for the second clustering. As shown in **Figure 2**, the cluster of each station is carried out first, and the second clustering is taken by using the clusters' results. The distributed clustering can greatly reduce the calculating time and save computing resources. Y_{ij} (i = 1, 2, 3,..., m; j = 1, 2, 3, ..., n) represents the samples for the first clustering, where m represents a station and n represents moment. C_{il} (i = 1, 2, 3, ..., m; l = 1, 2, 3, ..., k) represents the first clustering results, and it also represents the samples of second clustering, where k represents the number of first clustering for each station. Pt (t = 1, 2,3, ...,o) represents the clustering result of second clustering.

3 RESULTS AND ANALYSES

3.1 First Clustering: The Number of Clustering

3.1.1 Analyses of the Clustering Results at a Single Station

Taking Shunyi station as an example, we illustrate the process of the K-means clustering. The hourly data during 2008–2017 are taken as samples, and the total number of samples is 87,600. First, the elbow method is used to determine the k value, as shown in **Figure 3A**. The X-axis represents the k value, and the Y-axis is the average of the Euclidean distance between different samples and their corresponding clusters. It is noted that the average distance is 0 when $k = N$. In the actual clustering analyses, we hope that k is as small as possible, but the clusters can represent the samples. In **Figure 3**, with the increase of k, the average distance decreases

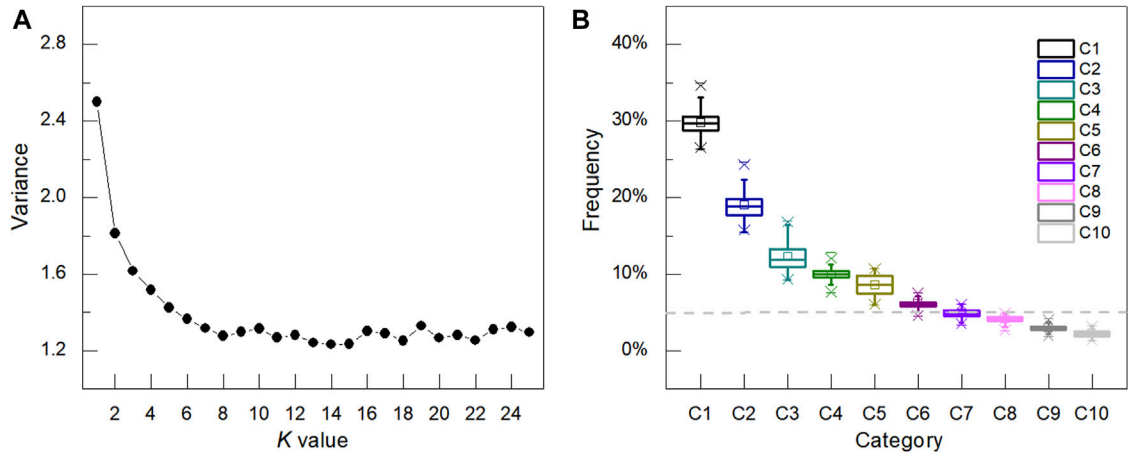

FIGURE 3 | (A) The average distance between the sample and the center corresponding to different *k* values. **(B)** Percentage box line chart of clustering samples (k = 10).

continuously. When k>10, the average distance is nearly constant. Thus, k is set to 10. Next, the ensemble method is used to minimize the influence of the initial value selection. In this study, the initial values are selected randomly 100 times, and the cluster frequency of each time is shown in **Figure 3B** with the percentage box line chart. The 10 clusters are marked as *C1*, *C2*,. . ., and *C10*, respectively. Their average sample proportions are 29.80, 19.01, 12.25, 9.96, 8.56, 6.10, 4.90, 4.14, 3.03, and 2.25%, respectively. However, their variances are small, which means that the clustering of most samples has not changed. For one sample, it may belong to different cluster center. We assign this sample to the cluster center which appears most in 100 clusters. Finally, 10 cluster centers of wind speed at Shunyi station are obtained and shown in **Figure 4**. Among them, the wind speed cluster of *C1* shows the diurnal variation characteristic of "small at night and large in the daytime" with the maximum wind speed around 12:00 CST (China Standard Time; the same below). The wind speed cluster of *C2* shows a skewed distribution, with the maximum wind speed in the afternoon. The diurnal variation characteristic of the wind speed cluster of *C3* is similar to that of *C1*, but the wind speed is higher than that of *C1*. The diurnal variation of *C4* is similar to that of *C2*, but the wind speed is higher than that of *C2*. The wind speed cluster of *C5* is different from other clusters, showing a monotonous increasing diurnal variation. The diurnal variation cluster of *C7* is significantly different from that of other clusters, showing a decreasing characteristic. The wind speed of *C8* keeps low before 10:00 CST and increases rapidly from 11:00 to 16:00 CST. The wind speed diurnal characteristic of *C9* presents the characteristics of linear increasing and linear decreasing. The diurnal variation of wind speed of *C10* is similar to that of *C6*.

Using the clustering method, we can obtain the typical characteristics of the wind speed diurnal variation. However, the temporal and spatial distributions of the typical characteristics are not clear. Also, the number of the typical characteristics (clusters) that can be obtained at different stations is not clear. Therefore, the observed wind speed data of other 159 stations in Beijing are clustered like those of Shunyi station.

3.1.2 Numbers of the Clusters at Different Stations

The above analyses show that the diurnal variation of the wind speed in Beijing is diverse. The sample numbers of different clusters can be greatly different from those of each other. Thus, typical clusters are analyzed. Cluster analyses are carried out based on the diurnal variations of the wind speed at 160 stations in Beijing. The cluster number (k) is 10. According to **Figure 3B**, the frequencies of the first few clusters' samples are larger, which can represent more samples, and these clusters are considered to be typical clusters. In this study, if the sample percentage of one cluster is greater than 5%, the cluster is considered as a typical cluster.

The spatial distribution of the typical cluster number at different stations is shown in **Figure 5A**. The number of typical clusters in urban and flat areas is less than that of clusters in suburban mountainous areas. There are six stations with four clusters, which are mainly in the suburbs including Shunyi district, Huairou district, and Daxing district, with a low average altitude of 80.83 m (**Figure 5B**). There are 29 stations with 5 clusters, which are mainly located in the city (including Chaoyang district, Haidian district, Fengtai district, Shijingshan district, Dongcheng district, and Xicheng district) and areas near the city (including Shunyi district, Changping district, and the south of Huairou district). Their average altitude is 113.17 m. There are 79 stations with 6 clusters, which are mainly in the urban area, and the average altitude is 172.85 m. There are 31 stations with 7 clusters. Parts of them are located in the city, and the others are in the area far away from the city, including Miyun district, Pinggu district, and the south of Daxing district. The average altitude is 243.48 m. There are 12 stations with eight and three stations with nine clusters, respectively, which are mainly in the northern area such as Yanqing district, Miyun district, and Pinggu district. The average altitudes are 335.75 and 588.00 m, respectively.

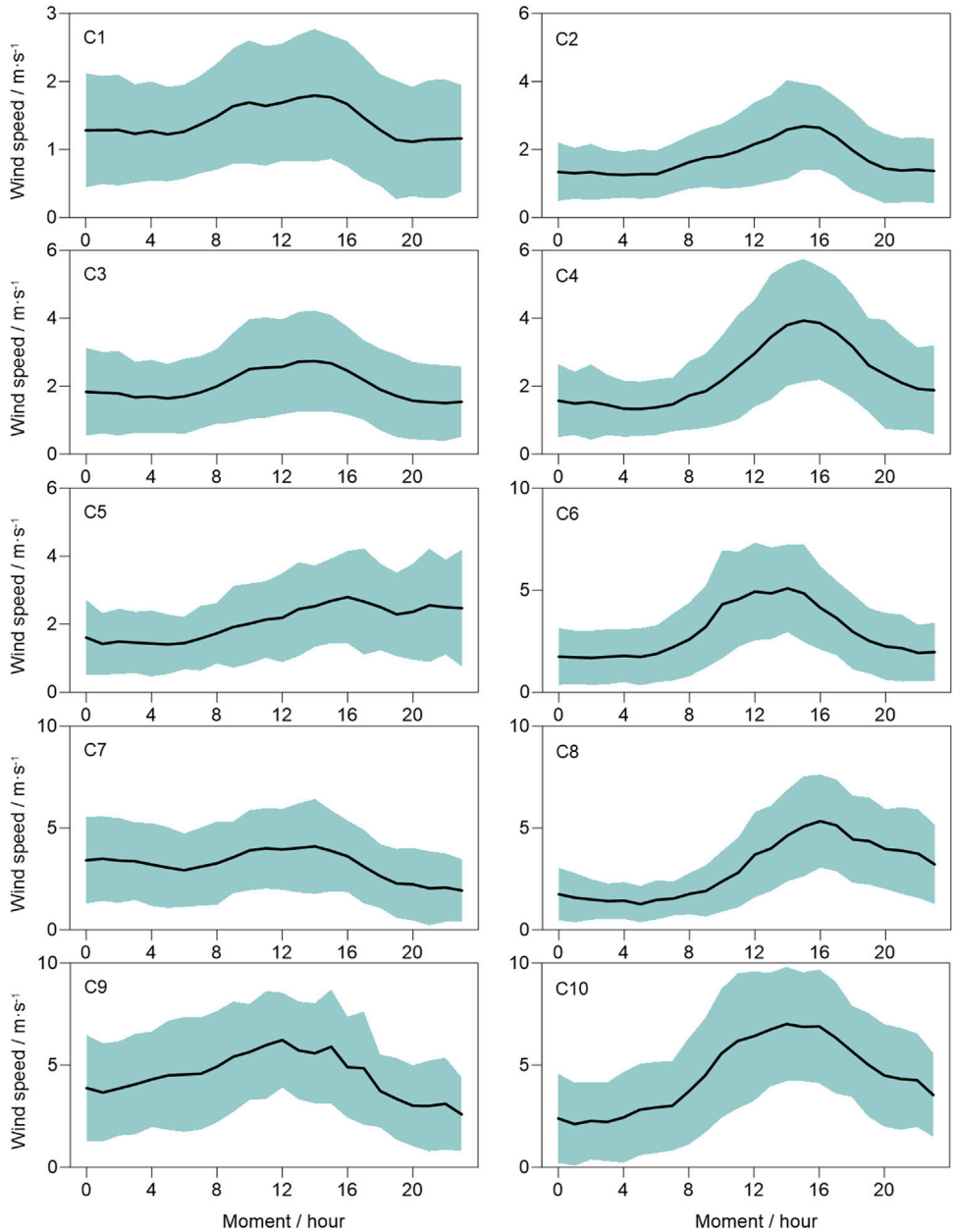

FIGURE 4 | The cluster analysis results of the hourly wind speed in 3,650 days at Shunyi station in Beijing. The *X*-axis is 00:00–23:00 CST, the *Y*-axis is the wind speed, and C1–C10 represent the 10 clusters, respectively. The black line represents the sample average at different times, and the shade represents one standard deviation of the corresponding sample.

In conclusion, the number of clusters with a lower altitude is less, including five clusters in urban areas and seven clusters in the suburb area. In the areas with high altitudes, there are mainly 8 and 9 clusters.

3.1.3 The Interannual Variation of the Cluster Number at Different Stations

The spatial and temporal variations of the typical cluster numbers in different years are further studied. The relationship between the typical cluster number and the station number is shown in **Figure 6**. During 2008–2012, the station numbers with four clusters (abbreviated to four clusters) and 5 clusters hardly changed. The average station numbers were 6.00 and 30.00, respectively. The station numbers with six to nine clusters were significantly different before and after 2010. The average station numbers during 2008–2010 were 48.00, 41.67, 22.67, and 10.33, respectively. During 2011–2012, the average station numbers were 69.50, 29.50, 15.50, and 4.00, respectively. The stations with 6 clusters increased significantly, while the stations with seven to nine clusters decreased significantly. During

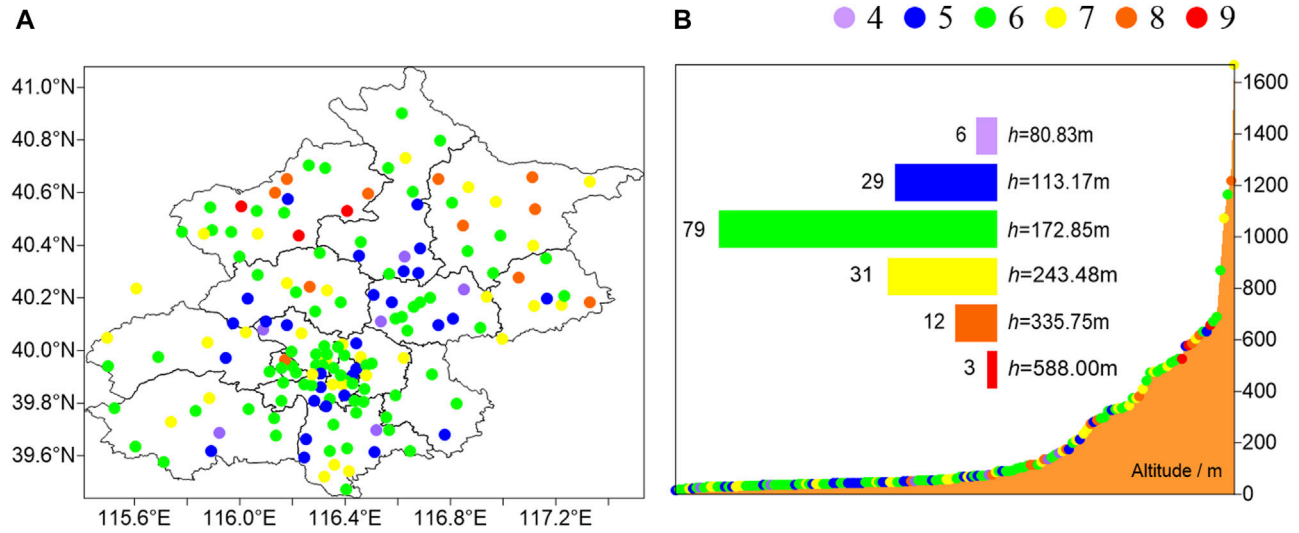

FIGURE 5 | (A) Spatial distribution of typical cluster numbers at different stations. **(B)** Relationship between the typical cluster number and the station altitude. The orange contour represents the station altitude, the scatter chart represents the cluster number of the corresponding station, and the histogram is the number of different clusters and the average altitude of the number. The *x*-axis represents the stations, and the *y*-axis represents these stations' altitude.

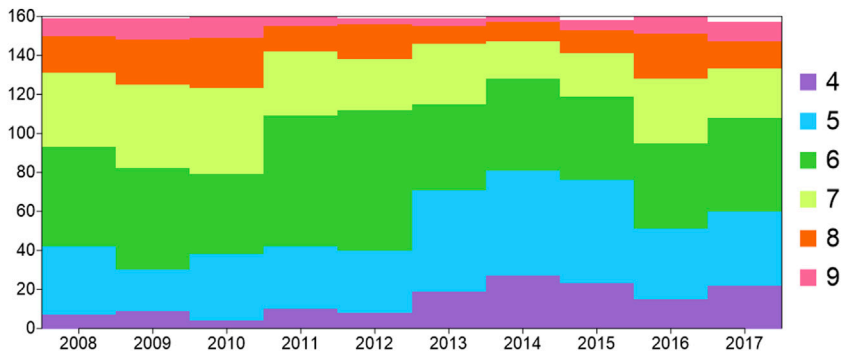

FIGURE 6 | Interannual variation characteristics of the total clustering numbers in different years. The *x*-axis represents time (year), and the *y*-axis represents the number of stations.

2013–2015, the stations with four to five clusters increased significantly, reaching 20.67 and 53.00, respectively. The stations with six to eight clusters decreased to 44.67, 24.00, and 10.33, respectively. During 2016–2017, the stations with four to five clusters decreased to 16.00 and 37.00, respectively. The stations with six to nine clusters increased. Among them, the station numbers with seven to nine clusters increased significantly by 5.00, 8.17, and 5.50, respectively. Therefore, in the past 10 years, during 2011–2012, the stations with six clusters increased, and during 2013–2015, the stations with four to five clusters increased, which indicates that the clustering numbers at stations in Beijing are decreasing. However, after 2016, the clustering numbers are increasing.

The spatial distribution of the annual cluster numbers is shown in **Figure 7**. Before 2011, the cluster numbers in Yanqing district, Miyun district, Pinggu district, and Tongzhou district, which are all suburban areas, were mainly seven to nine, while those in the other areas were mainly 5–6. During 2011–2012, the cluster numbers in the urban area, including Yanqing district, and Miyun district changed from 8–9 to 6, while the cluster numbers in the urban area and Shunyi district changed from 7 to 6. During 2013–2015, the cluster numbers in Yanqing district, Huairou district, Fangshan district, and Daxing district, and the urban area changed from 6–7 to 4–5. The variation shows that the number of main clusters was decreasing. While during 2016–2017, the cluster numbers in the urban areas, including Yanqing district, Changping district, and Pinggu district, changed from four to five to six to seven, which means the diurnal variation of wind speed has become more significant. The variation of the cluster numbers in recent years is further studied, as shown in **Figure 8**. Five to seven clusters remain unchanged before and after the transformation.

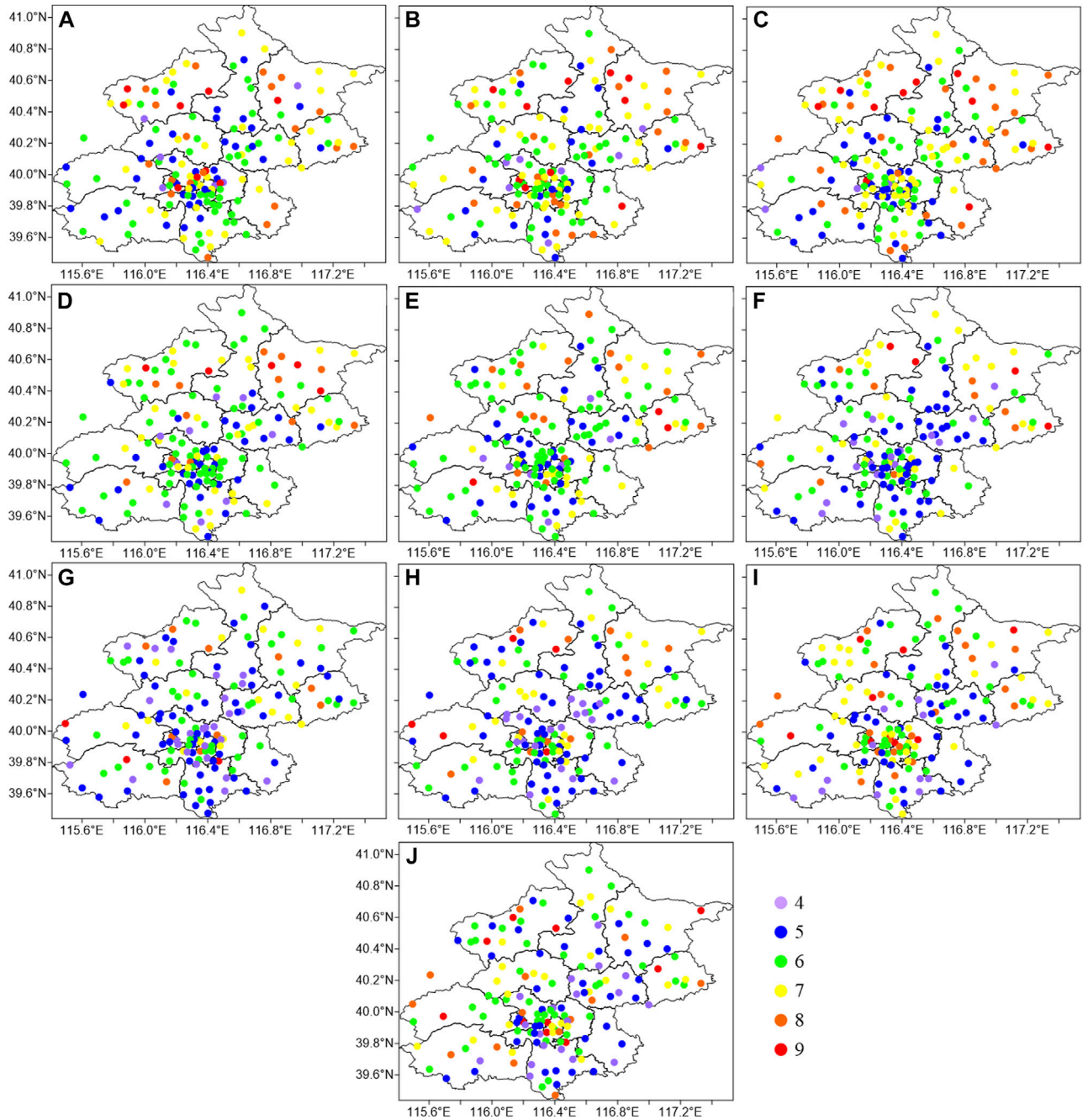

FIGURE 7 | Spatial distribution of typical cluster numbers at different stations in different years. **(A–J)** 2008–2017.

The annual average station numbers are 17.44, 23.56, and 10.11. The frequency of decreased clusters is 450 after the transformation, that is, 50 stations per year on average. Among them, there are 12.22 stations per year with cluster numbers changing from 6 to 5 and 11.11 stations changing from 7 to 6 per year. The frequency of increased clusters is 400 after the transformation, that is, 44.44 stations per year on average. Among them, 10.11 stations change from 5 to 6, and 9.00 stations change from 6 to 7 per year.

In summary, the cluster numbers of the wind speed diurnal variation in different regions of Beijing are significantly different. In urban areas, the cluster numbers are mainly 5 and 6. In the suburbs, the cluster numbers are mainly 7–9. Before 2015, the cluster numbers mainly changed from 7–9 to 4–5. The numbers increased after 2016. In the recent 10 years, the cluster numbers at most stations change from 5 to 6 and from 6 to 7, and the decreasing transformations are more than the increasing ones.

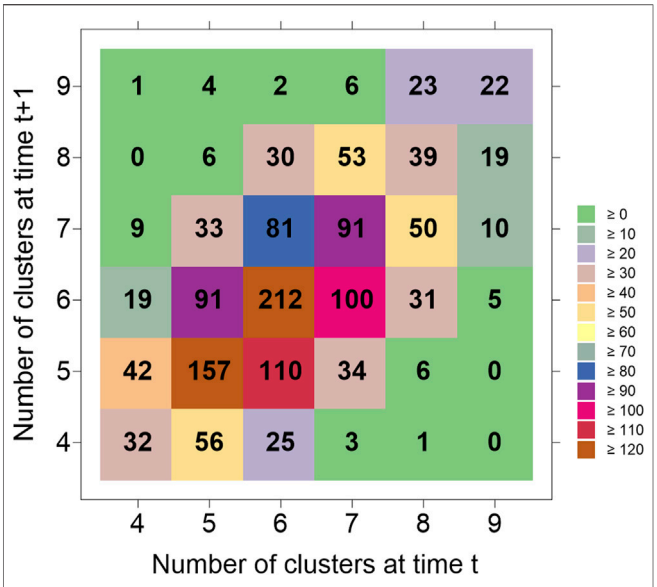

FIGURE 8 | Transformation of clustering numbers in different years. *t* represents the cluster number in the current year, and *t+1* represents the cluster number in the next year.

3.2 Second Clustering: Typical Characteristics of the Wind Speed Diurnal Variation

3.2.1 Classification and Diurnal Variation of Different Wind Speeds

The cluster results at different stations are simplified by the second clustering. The cluster results at all stations in Beijing are used as new samples for the second clustering analyses. **Figure 9A** is the elbow diagram of the second cluster. When the cluster number *k* is larger than 12, the average distance is almost the same. Therefore, the cluster number is set to 12, and different clusters are marked as *P1*, *P2*,. . ., and *P12*, respectively. **Figure 9B** shows the percentage of cumulative days at stations with different clusters. *P1–P3* clusters are more than 10%, accounting for 39.85, 21.04, and 11.39%, respectively. The cumulative percentage is 72.28%, representing most of the wind speed diurnal variation. The proportions of *P4*, *P5*, and *P6* are 9.04, 4.64, and 4.31%, respectively. The days represented by *P7–P12* are less than the others, accounting for only 9.73% as shown in **Figure 10**.

The wind speed diurnal variations of different types are shown in **Figure 10**. The wind speeds of *P1–P3* clusters are significantly lower than those of other clusters, and the diurnal average wind speeds are 1.07, 1.56, and 1.95 m s^{-1}, respectively. The wind speed diurnal variation of *P1* cluster presents a quasi-symmetric structure, which is in a stable stage (about 1.00 m s^{-1}) during 18:00–08:00 CST and increases during 8:00–14:00 CST. The maximum wind speed is 1.46 m s^{-1}. Then, the wind speed decreases during 14:00–18:00. The wind speed of *P2* cluster is asymmetric. The wind speed is almost constant (1.00 m s^{-1}) during 00:00 to 8:00 CST and increases during 08:00–15:00 CST, with a maximum of 2.63 m s^{-1}. The wind speed decreases during 15:00–19:00 CST and decreases slowly during 19:00–23:00 CST. The wind speed of *P3* cluster is also distributed asymmetrically. The wind speed is about 2 m s^{-1} during 00:00–8:00 CST and then increases. The maximum wind speed is at 11:00 and 12:00 CST (both are 2.53 m s^{-1}). Then, the wind speed decreases slowly and remains constant after 19:00 CST (the average wind speed is 1.43 m s^{-1}).

Compared with the average wind speeds of *P1–P3* clusters, the average wind speeds of *P4–P6* clusters are higher, which are 2.24, 3.03, and 2.14 m s^{-1}, respectively. The wind speed diurnal variation of *P4* cluster is similar to that of *P2* cluster. The wind speed hardly changes during 00:00–8:00 CST (the average wind speed is 1.31 m s^{-1}), and then increases. The maximum wind speed is at 15:00 CST, which is 3.99 m s^{-1}. The wind speed decreases at 15:00–19:00 CST and becomes constant during 19:00–23:00. The wind speeds of *P5* and *P6* clusters are monotonous. *P5* cluster is a monotonously decreasing type, and *P6* is a monotonously increasing type. The wind speed diurnal variation of *P7* and *P8* is slightly similar to that of *P4*, but the maximum wind speeds appear at different times. The maximum wind speeds of *P7* and *P8* clusters occur at 12:00 and 15:00 CST, with the maximum wind speeds of 4.41 and 5.07 m s^{-1}, respectively. Before reaching the

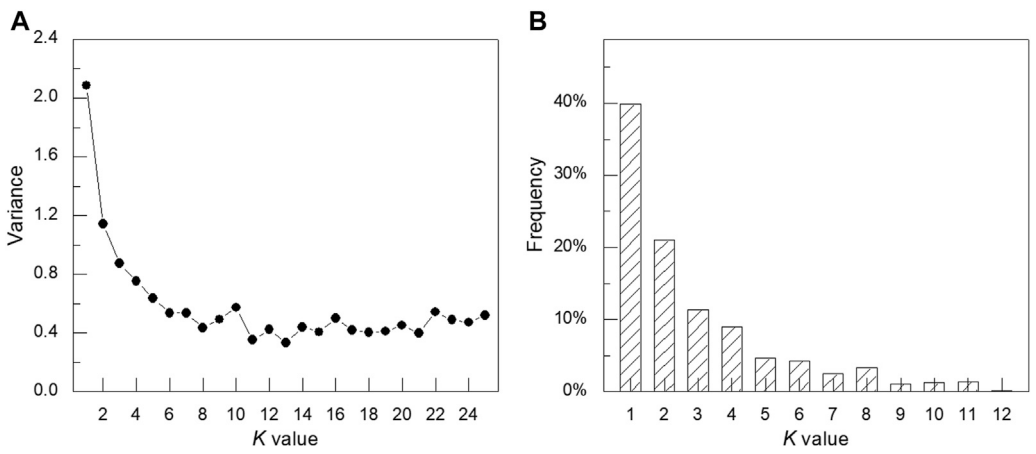

FIGURE 9 | (A) Sum of square error of different cluster numbers. **(B)** Experiments for the cluster number of 10.

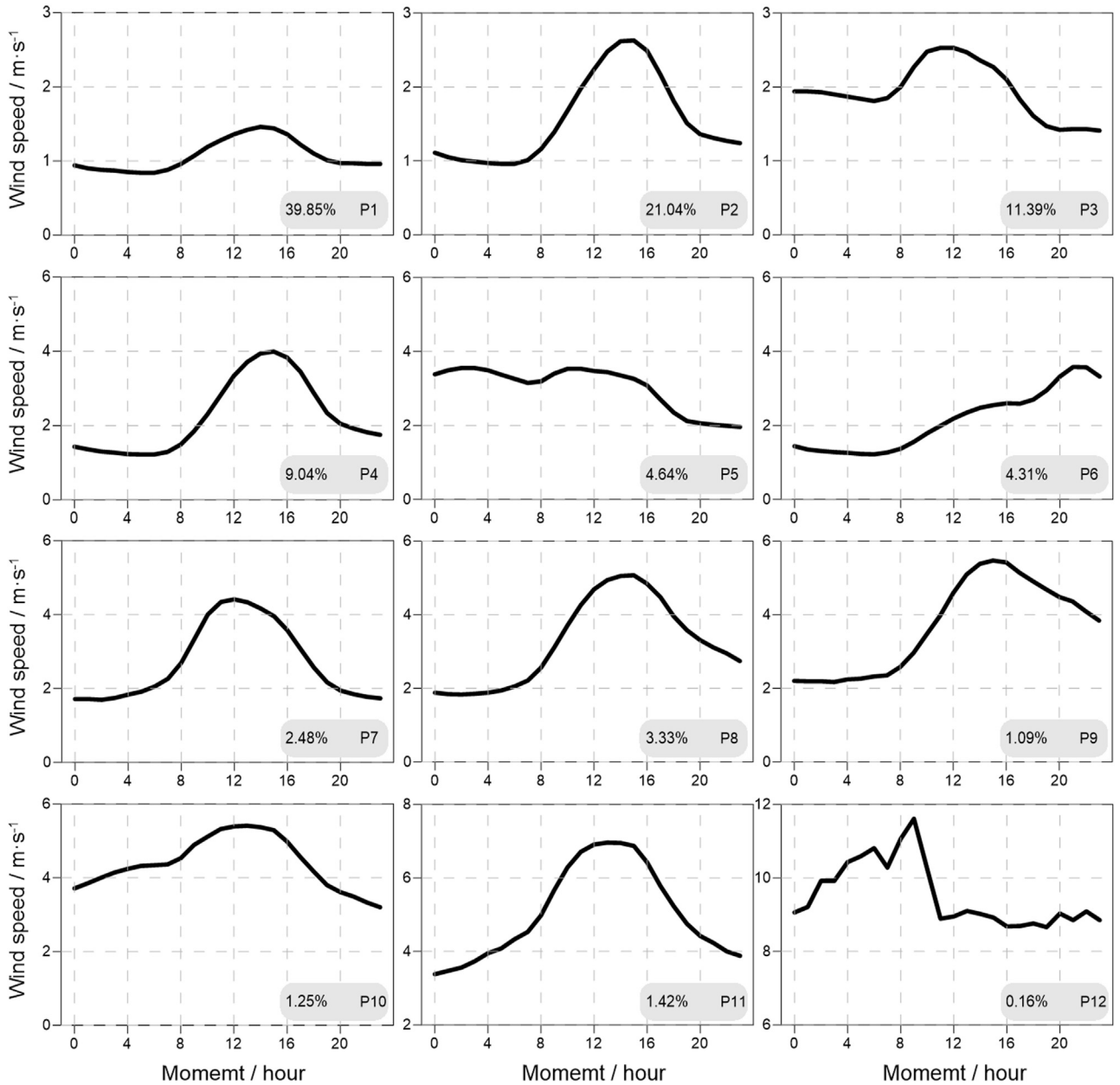

FIGURE 10 | Diurnal variation characteristics of different clusters.

maximum wind speed, the wind speed of *P9* cluster also keeps constant (the average wind speed is 2.24 m s^{-1} during 00:00–8:00 CST) at first and then increases. The maximum wind speed of 5.47 m s^{-1} appears at 15:00 CST. The wind speed decreases rapidly during 15:00–23:00 CST to 3.84 m s^{-1} at 23:00, which is higher than 2.20 m s^{-1} at 00:00 CST. The average wind speeds of *P10–P12* are significantly higher than those of other clusters, which are 4.39, 5.05, and 9.53 m s^{-1}, respectively. The wind speed of *P10* cluster reaches 3.71 m s^{-1} at 00:00 CST and reaches the maximum value (5.41 m s^{-1}) at 13:00 CST. Then, the wind speed decreases and reaches the minimum value (3.20 m s^{-1}) at 23:00 CST. The wind speed of *P11* cluster increases during 00:00–13:00 CST with the maximum of 6.96 m s^{-1}, which decreases during 13:00–23:00 CST. The variation of *P12* cluster is different from that of other clusters. The diurnal variation is insignificant. The wind speed shows a linear increasing trend during 00:00–8:00 CST. Then, the wind speed decreases rapidly during 08:00–10:00 CST and nearly remains constant during 11:00–23:00 CST, which is 8.88 m s^{-1}.

To sum up, the diurnal variation of wind speed at all stations in Beijing can be divided into 11 clusters. Except for *P5*, *P6*, and *P12*, the wind speed diurnal variations of other clusters show the characteristics of "large in the daytime and small at night." However, the different time of the maximum wind speed and the different wind speed lead to multiple clusters of the wind

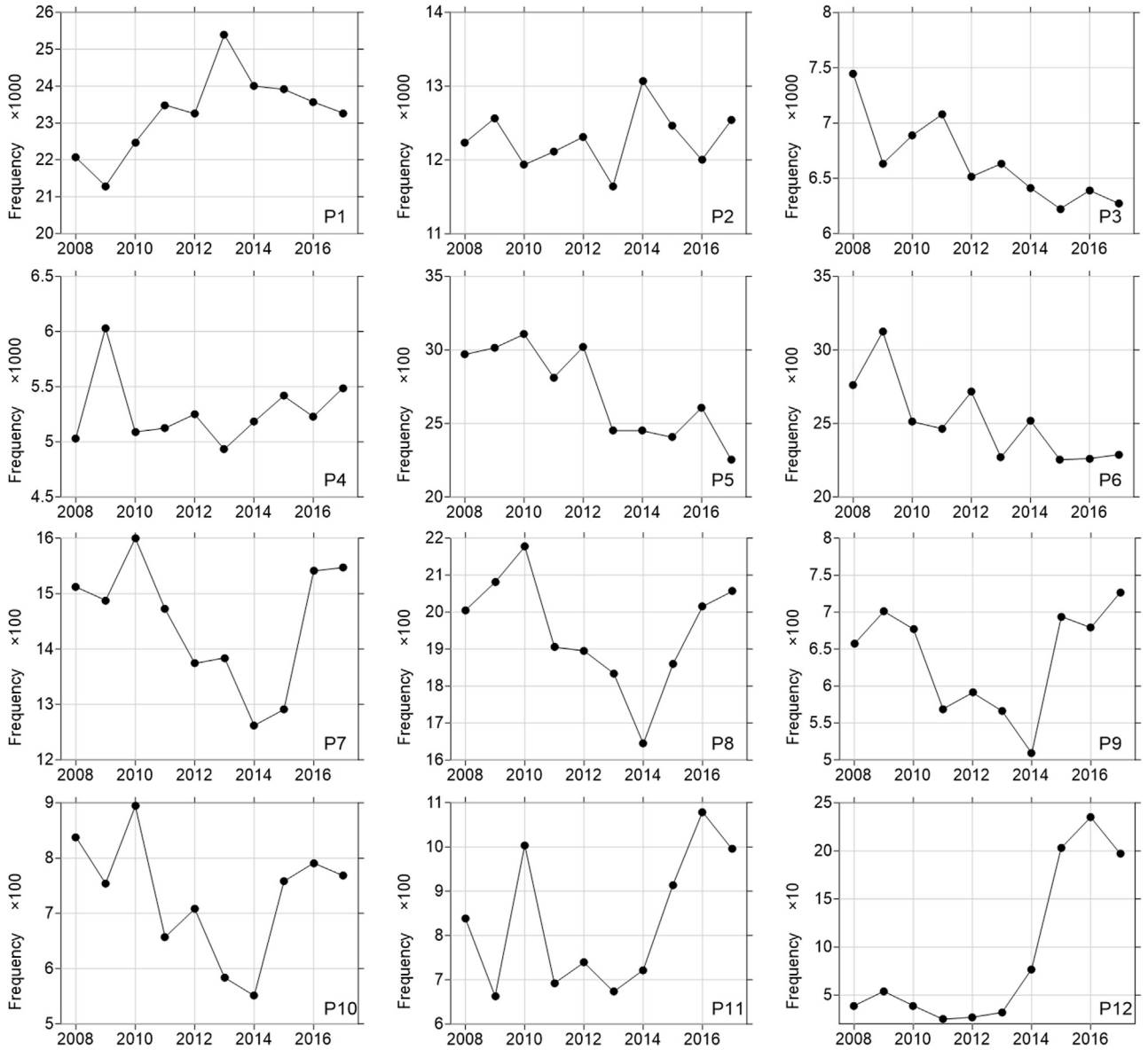

FIGURE 11 | Interannual variation of different wind speed clusters (P1–P12). The *X*-axis represents time, and the *Y*-axis represents the total frequency (unit: days) of one wind speed cluster at all stations. The coefficient in the figure represents the multiple of the actual data.

speed diurnal variation of this type. *P5* is a monotonic increasing cluster. *P6* is a monotonic decreasing cluster. The wind speed of *P12* is high without significant diurnal variation.

3.2.2 Interannual Variation and Trend of Different Wind Speed Clusters

Furthermore, the interannual variations of different wind speed cluster frequencies are analyzed, as shown in **Figure 11**. For *P1* cluster, the frequency increases rapidly during 2008–2013, with a trend of 672.54 a^{-1} (significant at the 98% confidence level, according to the linear trend regression test (LTRT)), which means more and more wind speed is getting smaller. In 2014–2017, the increasing trend stops (the annual average frequency is 2.37×10^4). *P1* cluster is mainly distributed in the fifth ring, which might be related to the larger roughness of the city. The frequency of *P2* cluster does not increase or decrease significantly in the past 10 years, with an annual average frequency of 1.23×10^4. The frequency of *P3* cluster shows a significant negative trend of −105.89 a^{-1} (significant at the 95% confidence level, according to the LTRT). The frequency of *P4* cluster in 2009 (6,062 times) is significantly higher than the annual average (5,193.44 times). After removing this year, there is a significant increasing trend of 42.39 a^{-1} (significant at the 95% confidence level, according to the LTRT). The frequencies of *P5* and *P6* significantly decrease with the trends of −87.55 a^{-1} and −71.99 a^{-1}, respectively (both significant at the

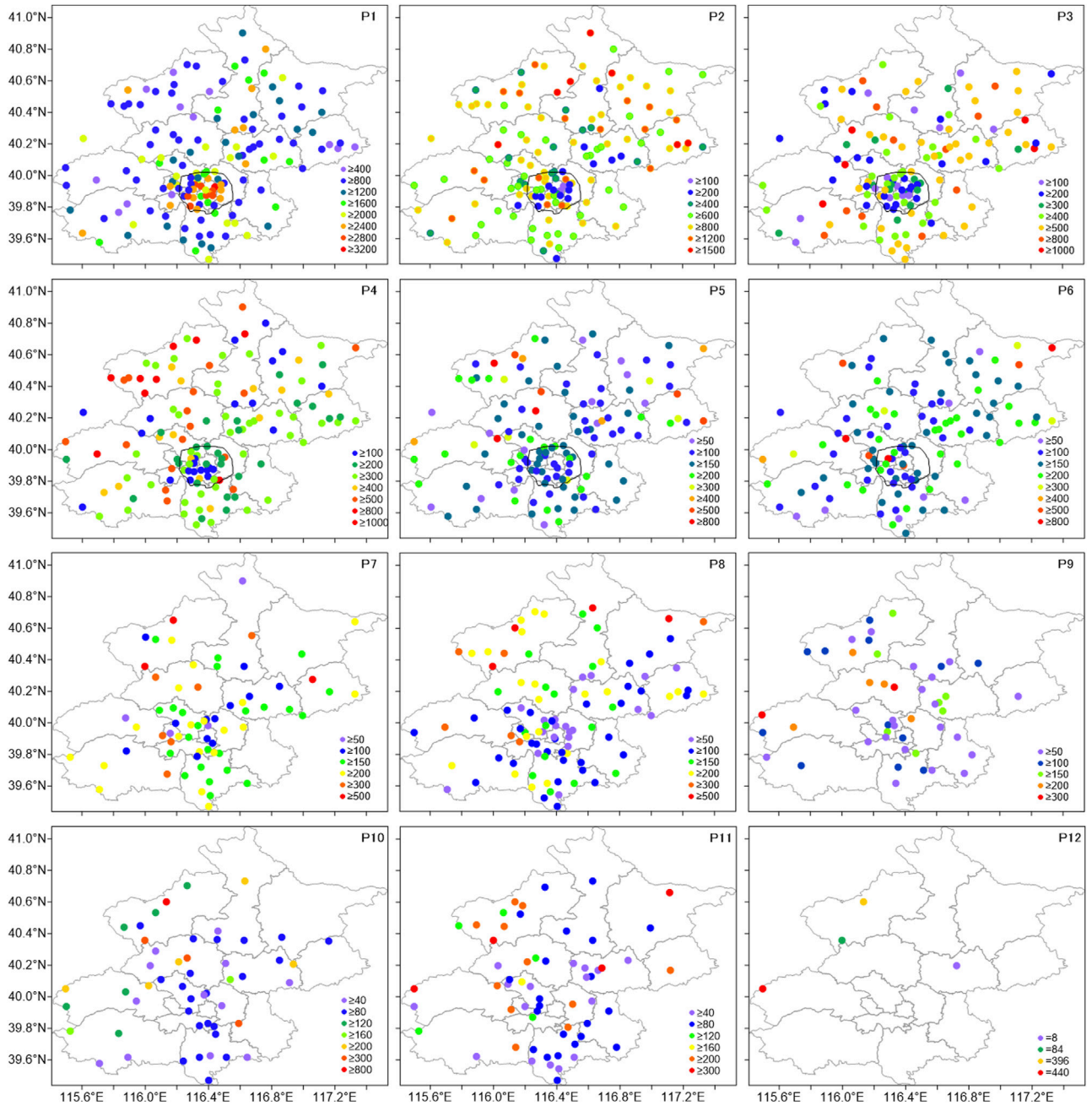

FIGURE 12 | Cluster frequency at different stations. The black line is the Fifth Ring Road.

99% confidence level, according to the LTRT). The frequencies of *P7–P10* clusters show the variation characteristics of "first decrease and then increase," with the minimum frequency in 2014. The frequency trends of the four clusters during 2008–2014 are −42.29, −66.39, −28.57, and −49.54 a^{-1} (all significant at the 98% confidence level, according to the LTRT), respectively. The frequencies of the four clusters increase to varying degrees during 2015–2017. The frequency of *P11* is significantly higher in 2010 and during 2015–2017. The frequency of *P12* increases significantly during 2015–2017.

In conclusion, there are significant differences in the variation trend of different wind speed clusters in different years. The variation trend of *P2* is not significant. *P1* and *P4* show significant increasing trends. *P3*, *P5*, and *P6* show significant decreasing trends. The frequencies of *P7–P10* decrease before 2014 and then increase. The frequencies of *P11* and *P12* increase after 2014.

3.2.3 Clusters of Wind Speed at Different Stations

There are regional differences in the frequency of the wind speed clusters at different stations. The frequencies of *P1–P12* clusters at

each station during 2008–2017 are calculated, as shown in **Figure 12**. *P1* cluster is the most common type. As for the spatial distribution, the frequencies at stations in urban areas are significantly higher than those in suburban areas. There are 25 stations more than 2,400 times. The station number with the frequency more than 1,200 times in the whole area is 81, showing that *P1* cluster is the main cluster at most stations. Stations with frequencies less than 800 times are mainly in Yanqing district, Pinggu district, and Fangshan district, and the total number is 12. The stations of *P2* cluster with a frequency more than 1,200 times are mainly distributed in Yanqing district, Huairou district, Miyun district, and Pinggu district, and the station number is 24. However, the frequency at most urban stations is less than 400. The stations with high frequencies of *P3* cluster are mainly in the suburbs. There are 56 stations with frequencies more than 500 times, which are mainly distributed in Fangshan district, Changping district, Yanqing district, Miyun district, Pinggu district, and Shunyi district. The frequency of *P3* cluster in most urban areas is less than 400 times. *P4* cluster mainly occurs in the northwest of Beijing, including Mentougou district, Yanqing district, and Changping district. The number of stations with more than 500 times is 26. The frequency of *P4* cluster in most urban stations is less than 300. As for *P5* cluster, the number of stations with more than 400 times is 17, which are mainly distributed in Yanqing district, Changping district, and Pinggu district. As for *P6* cluster, the number of stations with more than 400 times is 12, which are mainly distributed in the urban area and Miyun district. The frequencies of *P7* and *P8* clusters are low. There are 9 and 10 stations with more than 300 times, respectively, which distribute in the west and northwest of Beijing. There are few stations with *P9*–*P12* clusters. As for *P9* cluster, there are seven stations with a frequency of more than 200 times, which are mainly in Changping district, and most of the other stations are less than 100 times. As for *P10* cluster, there are nine stations with a frequency of more than 200 times, which are mainly in Changping district and Yanqing district. As for *P11* cluster, there are 15 stations with a frequency of more than 200 times, which are mainly distributed in Yanqing district. There are only four stations with *P12* cluster. Among them, the frequency at Lingshan station in Mentougou district is 440 times, and the frequency at Foyeding station in Yanqing district is 396 times. At these two stations, the altitudes are 1,669 and 1,217 m, respectively. Therefore, the wind speeds are always high.

To sum up, there are differences in the main areas of different clusters of wind speed. *P1* cluster mainly appears in urban areas. *P2* cluster is mainly distributed in urban areas and northern areas. *P3* cluster is mainly distributed in the central and northern areas. *P4* and *P5* clusters are mainly distributed in the northwest. *P6* cluster is mainly distributed in the central area.

4 CONCLUSION AND DISCUSSION

In this study, the initial value of the K-means clustering method is selected using an ensemble method. The hourly observation data at 160 observation stations in Beijing in recent 10 years are used for cluster analyses. The different clusters of the wind speed diurnal variation at different stations are studied, and the spatial and temporal variations of the cluster numbers and types at different stations are analyzed. The conclusions are as follows.

1) The cluster analyses are carried out at each station. The wind speed at most stations can be divided into four to nine clusters, and the main clusters are five to seven clusters. There are mainly five to six clusters near the urban area and seven clusters far away from the urban area. The altitudes are high at the stations with 8 and 9 clusters.

2) As for the long-term variation, the number of stations with cluster numbers of four to five increased significantly during 2013–2015, and the number of stations with cluster numbers of six to eight decreased, which means the total number of the wind speed clusters decreased during this period. As for the transformation of cluster numbers in the recent 10 years, the stations with five to six clusters and six to seven clusters tend to transform more than the others, and the transformation to fewer cluster numbers is more than that to more cluster numbers.

3) For all stations, the diurnal variation of the wind speed can be divided into 12 clusters including 9 clusters of "large in the daytime and small at night," with 1 cluster of monotonous increase, 1 cluster of monotonous decrease, and 1 cluster of strong wind. Among them, nine different clusters of "large in the daytime and small at night" are mainly caused by the different time and value of the maximum wind speed.

4) As for the long-term variation trend, *P1* and *P4* increase significantly. *P3*, *P5*, and *P6* decrease. *P7*–*P12* show opposite trends before and after 2014. As for the spatial distribution, *P1* cluster is mainly in urban areas, while other types are mainly in suburbs.

The daily variation of wind speed at the station near the urban area is consistent, while in the suburban area, the diurnal variation of wind speed at different stations is quite different, especially for the stations with high altitude. The difference of daily variation of wind speed at more and more stations is small, and the wind speed is small too. Under the background of urbanization, more and more buildings increase the surface roughness, reduce the wind speed, and reduce the difference of daily variation of wind speed at different stations [27]. It is not conducive to the dissipation of urban pollutants and should be paid more attention by the government.

DATA AVAILABILITY STATEMENT

The raw data supporting the conclusions of this article will be made available by the authors, without undue reservation.

AUTHOR CONTRIBUTIONS

PY and PY contributed to the conception of the study. PY and DZ performed the data analyses and wrote the manuscript. DZ and SL helped preform the analysis with constructive discussions.

FUNDING

This research has been supported by the Ministry of Science and Technology of China (2018YFA0606302), the Open

Project of Key Laboratory of Land Surface Process and Climate Change in Cold and Arid Regions (LPCC2019002), and the National Natural Science Foundation of China (41775078, 42005058, 41675092). The data used in this study can be obtained by contacting the corresponding author: Ping Yang (zz96998@163.com).

REFERENCES

1. Cassiani M, Stohl A, Eckhardt S, Stohl A, and Eckhardt S. The Dispersion Characteristics of Air Pollution from the World's Megacities. *Atmos Chem Phys* (2013) 13:9975–96. doi:10.5194/acp-13-9975-2013
2. Li XF, Zhang MJ, Wang SJ, Zhao AF, Ma Q, Zhang MJ, et al. [Variation Characteristics and Influencing Factors of Air Pollution index in China]. *Environ. Sci.* (2012) 33:1936–43. doi:10.13227/j.hjkx.2012.06.035
3. Šinik N, and Lončar E. An Estimation of Pollutant Diffusion Rates during Calm Conditions. *IL Nuovo Cimento C* (1990) 13:917–21. doi:10.1007/bf02514780
4. Alan S, and Evgeni F. An Analytical Model of an Urban Heat Island Circulation in Calm Conditions. *Environ. Fluid Mech.* (2019). 19:111–135. doi:10.1007/s10652-018-9621-9
5. Yang P, Ren GY, Yan PC, Ren G, and Yan P. Evidence for a Strong Association of Short-Duration Intense Rainfall with Urbanization in the Beijing Urban Area. *J Clim* (2017) 30:5851–70. doi:10.1175/JCLI-D-16-0671.1
6. Wang W, Tang DG, Liu HJ, Yue X, Pan Z, and Ding Y. Research on Current Pollution Sataus and Pollution Characteristics of PM2.5 in China. *Res Environ Sci* (2000) 13:1–5. doi:10.3321/j.issn:1001-6929.2000.01.001
7. Miao L, Liao XN, Wang YC, Liao XN, and Wang YC. [Diurnal Variation of PM2.5 Mass Concentration in Beijing and Influence of Meteorological Factors Based on Long Term Date]. *Huan Jing Ke Xue* (2016) 37(8):2836–46. doi:10.13277/j.hjkx.2016.08.003
8. Sun G-Q, Zhang HT, Wang JS, Li J, Wang Y, Li L, et al.Mathematical Modeling and Mechanisms of Pattern Formation in Ecological Systems: a Review. *Nonlinear Dyn* (2021) 104:1677–96. doi:10.1007/s11071-021-06314-5
9. Xue Q, Liu C, Li L, Sun GQ, Liu C, Li L, et al.Interactions of Diffusion and Nonlocal Delay Give Rise to Vegetation Patterns in Semi-arid Environments. *Appl Math Comput* (2021) 399:126038. doi:10.1016/j.amc.2021.126038
10. Makra L, Puskás J, Matyasovszky I, Csépe Z, Lelovics E, Bálint B, et al.Weather Elements, Chemical Air Pollutants and Airborne Pollen Influencing Asthma Emergency Room Visits in Szeged, Hungary: Performance of Two Objective Weather Classifications. *Int J Biometeorol* (2015) 59:1269–89. doi:10.1007/s00484-014-0938-x
11. Forgy EW. Cluster Analysis of Multivariate Data: eIciency versus Interpretability of Classi7cations. *Biometrics* (1965) 21. doi:10.1080/00207239208710779
12. Michael RA. *Cluster Analysis for Applications: Probability and Mathematical Statistics*. New York: Academic Press (1973). p. 347–53.
13. Li F. *Research of the Adaptive Optimization Method about K Value of K-Means Algorithm*. Anhui: Anhui University (2015). doi:10.2991/isci-15.2015.29
14. Yovan AF, Vinay GSS, and Akhik G. K-means Cluster Using Rainfall and Storm Prediction in Machine Learning Technique. *J Comput Theor Nanoence* (2019). 16(8):3265–3269. doi:10.1166/jctn.2019.8174
15. Liu KP, Ying ZL, and Zhai YK. SAR Image Target Recognition Based on Unsupervised K-Means Feature and Data Augmentation. *J Signal Process* (2017) 33(3):452–8. doi:10.16798/j.issn.1003-0530.2017.03.029
16. Kim H-G, Yu YW, Yang Y, Park MH, Yu YW, Yang Y, et al.Portable Environmental Microfluidic Chips with Colorimetric Sensors: Image Recognition and Visualization. *Toxicol Environ Health Sci* (2019) 11(4):320–6. doi:10.1007/s13530-019-0419-z
17. Mao B, and Li BC. Building Façade Semantic Segmentation Based on K-Means Classification and Graph Analysis. *Arab J Geosci* (2019) 12(7):253. doi:10.1007/s12517-019-4431-z
18. Salehnia N, Salehnia N, Salehnia N, Ansari H, Kolsoumi S, Bannayan M, et al.Climate Data Clustering Effects on Arid and Semi-arid Rainfed Wheat Yield: a Comparison of Artificial Intelligence and K-Means Approaches. *Int J Biometeorol* (2019) 63:861–72. doi:10.1007/s00484-019-01699-w
19. Mao JL. Text Clustering Algorithm Based on K-Means. *Comput Syst Appl* (2009) 18(10):85–7. doi:10.3969/j.issn.1003-3254.2009.10.020
20. Saxena A, Prasad M, Gupta A, Bharill N, Patel OP, Tiwari A, et al. A Review of Clustering Techniques and Developments. *Neurocomputing* (2017) 267(6):664–81. doi:10.1016/j.neucom.2017.06.053
21. Redmond SJ, and Heneghan C. A Method for Initialising the K-Means Clustering Algorithm Using Kd-Trees. *Pattern Recognition Lett* (2007) 28(8):965–73. doi:10.1016/j.patrec.2007.01.001
22. Arthur D, and Vassilvitskii S. K-Means++: The Advantages of Careful Seeding. *Proc Annu Acm-siam Symp Discrete Algorithms* (2007) 8:1027–35. doi:10.1145/1283383.1283494
23. Khan SS, and Ahmad A. Cluster center Initialization Algorithm for K-Means Clustering. *Pattern Recognition Lett* (2004) 25(11):1293–302. doi:10.1016/j.patrec.2004.04.007
24. Rodriguez A, and Laio A. Clustering by Fast Search and Find of Density Peaks. *Science* (2014) 344(6191):1492–6. doi:10.1126/science.1242072
25. Qiu GY, and Zhang J. Adaptive SVM Decision Tree Classification Algorithm Based Om Bisecting K-Means. *Appl Res Comput* (2012) 29(10):3685–7. doi:10.3969/j.issn.1001-3695.2012.10.021
26. Wu GJ, and ZhangYuan JLD. Automatically Obtaining K Value Based on K-Means Elbow Method. *Comput Eng Softw* (2019) 40(5):167–70.
27. Yang P, Ren GY, Yan PC, Deng JM, Ren G, Yan P, et al.Tempospatial Pattern of Surface Wind Speed and the "Urban Stilling Island" in Beijing City. *J Meteorol Res* (2020) 34(5):986–96. doi:10.1007/s13351-020-9135-5

Conflict of Interest: The authors declare that the research was conducted in the absence of any commercial or financial relationships that could be construed as a potential conflict of interest.

frontiers in Physics

ORIGINAL RESEARCH
published: 11 June 2021
doi: 10.3389/fphy.2021.672288

Combining Snow Depth From FY-3C and *In Situ* Data Over the Tibetan Plateau Using a Nonlinear Analysis Method

Aixia Feng[1], Feng Gao[1], Qiguang Wang[2], Aiqing Feng[3], Qiang Zhang[1], Yan Shi[1], Zhiqiang Gong[4,5]*, Guolin Feng[5,6] and Yufei Zhao[1]*

[1]Data Service Office, National Meteorological Information Center, China Meteorological Administration, Beijing, China, [2]China Meteorological Administration Training Center, China Meteorological Administration, Beijing, China, [3]Meteorological Disaster Risk Management Division, National Climate Center, China Meteorological Administration, Beijing, China, [4]College of Physics and Electronic Engineering, Changshu Institute of Technology, Changshu, China, [5]Laboratory for Climate Studies, National Climate Center, China Meteorological Administration, Beijing, China, [6]College of Physics Science and Technology, Yangzhou University, Yangzhou, China

OPEN ACCESS

Edited by:
Yipeng Guo,
Nanjing Normal University, China

Reviewed by:
Hongxing Cao,
Chinese Academy of Meteorological Sciences, China
Anna Carbone,
Politecnico di Torino, Italy
Shixuan Zhang,
Pacific Northwest National Laboratory (DOE), United States

***Correspondence:**
Qiguang Wang
photon316@163.com
Zhiqiang Gong
gzq0929@126.com

Specialty section:
This article was submitted to Interdisciplinary Physics, a section of the journal Frontiers in Physics

Received: *25 February 2021*
Accepted: *17 May 2021*
Published: *11 June 2021*

Citation:
Feng A, Gao F, Wang Q, Feng A, Zhang Q, Shi Y, Gong Z, Feng G and Zhao Y (2021) Combining Snow Depth From FY-3C and In Situ *Data Over the Tibetan Plateau Using a Nonlinear Analysis Method. Front. Phys. 9:672288. doi: 10.3389/fphy.2021.672288*

Snow cover over the Tibetan Plateau plays a vital role in the regional and global climate system because it affects not only the climate but also the hydrological cycle and ecosystem. However, high-quality snow data are hindered due to the sparsity of observation networks and complex terrain in the region. In this study, a nonlinear time series analysis method called phase space reconstruction was used to obtain the Tibetan Plateau snow depth by combining the FY-3C satellite data and *in situ* data for the period 2014–2017. This method features making a time delay reconstruction of a phase space to view the dynamics. Both of the grids and their nearby *in situ* snow depth time series were reconstructed with two appropriate parameters called time delay and embedding dimension. The values of the snow depth for grids were averaged over the *in situ* observations and retrieval of the satellite if their two parameters were the same. That implies that the two trajectories of the time series had the same evolution trend. Otherwise, the snow depth values for grids were averaged over the *in situ* observation. If there were no *in situ* sites within the grids, the retrieval of the satellite remained. The results show that the integrated Tibetan Plateau snow depth (ITPSD) had an average bias of −1.35 cm and 1.14 cm, standard deviation of the bias of 3.96 cm and 5.67 cm, and root mean square error of 4.18 cm and 5.79 cm compared with the *in situ* data and FY-3C satellite data, respectively. ITPSD expressed the issue that snow depth is usually overestimated in mountain regions by satellites. This is due to the introduction of more station observations using a dynamical statistical method to correct the biases in the satellite data.

Keywords: snow depth, Tibetan Plateau, phase space reconstruction, FY-3C satellite, nonlinear analysis method

INTRODUCTION

Snow over the Tibetan Plateau plays a prominent role in the climate system, hydrological cycle, and biogeochemical cycle [1–5]. It is also a primary indicator of climate change and significantly impacts local and global climate, water resources, and economic and society development [1, 6, 7]. Long-term and high-resolution data are prerequisites for climate change monitoring and assessments, and climate forecast, especially for snow depth [1, 8, 9] because snow depth can provide quantitative information about the material and energy of snow. Thus, there is an urgent need for operations and research on climatology and hydrology.

Conventional snow measurement through *in situ* devices has a long history [10]. For China, systematic observations can be traced back to the 1950s. The measure is high in accuracy and usually used to validate satellite retrieval snow products and reanalysis products. However, observational networks suffer from low station density in complex terrains due to the Tibetan Plateau's remoteness, high altitude, and harsh weather conditions, especially for the western and middle Tibetan Plateau. The installation and maintenance of stations in the Tibetan Plateau are the main challenges [11, 12].

The past four decades witnessed the development of passive microwave remote sensing to acquire large-scale snow datasets [13]. It has become an effective way to estimate snow depth for providing all-day and all-weather monitoring and spatially continuous information of snow depth variation derived from the Scanning Multichannel Microwave Radiometer (SMMR), the Special Sensor Microwave/Imager (SSM/I), the Advanced Microwave Sounding Unit (AMSU), the Advanced Microwave Scanning Radiometer for EOS (AMSR-E), and the Microwave Radiation Imager (MWRI). The MWRI is onboard the FY-3 series satellite. It is important for snow monitoring of the Tibetan Plateau. However, it usually overestimates the snow depth by mistaking the cold surface as snow cover in the retrieval algorithms in the Tibetan Plateau. This issue needs to be investigated.

One way is to combine the snow depth from the remote sensing data and station observations. There are two classical approaches to do this. One includes using a semiempirical snow emission model. In the model, the passive microwave brightness between 20 and 150 GHz is assimilated and the *in situ* snow depth values are used as input to estimate snow grain size at the station locations. The disadvantages of this method are as follows: the model is in the progress stage and forward modeling of the microwave brightness in the above frequency range exhibits large uncertainties [14]. Another approach is statistical interpolation taking both satellite and *in situ* snow depth increments and terrain-dependent error correlations of snow depth increments into consideration. However, currently, snow depth is not assimilated due to the perceived unreliability of satellite estimates [15].

Phase space reconstruction is a nonlinear time series analysis method to reveal dynamic characteristics by expanding the time series to high dimensions, that is, a state space reconstruction method of delayed coordinates. This is a common method to predict the now and future state based on the past state in nonlinear time series analysis [7, 16]. It has achieved great success in climate prediction and analysis [17–22]. However, phase space reconstruction has rarely been applied to blend and analyze snow depth from satellites and *in situ* data. This study aimed to obtain accurate snow depth by integrating FY-3C satellite data and *in situ* data based on phase space reconstruction.

The remainder of the article is organized as follows. In Section 2, the study area and data used are described. The nonlinear analysis method—phase space reconstruction—and integrated Tibetan Plateau snow depth (ITPSD) bias correction model are introduced in Section 3. Section 4 presents the processes of combining snow depth observations from the FY-3C satellite and meteorological stations. In Section 5, the evaluation criteria of ITPSD are presented and the validation results are also provided in this section. The discussion and conclusion are presented in Section 6.

STUDY AREA AND DATA

The study area is located at 25°N–40°N and 73°E–105°E and confines the Tibetan Plateau. It is about 2.6 million square kilometers in area. Most of it lies at an altitude of more than 4,000 m above sea level, making it peculiarly cold for its latitude—colder than anywhere else outside the polar regions, leading it to be known as the Third Pole [23]. It has an abundance of snow and ice cover. When they melt, the runoff from the region's mountain feeds major rivers in Asia, such as the Yangtze, Yellow, Mekong, and Indus rivers. With the warming climate, snow cover is becoming even more important to gauge what is happening to the Tibetan Plateau and understand its potential impact on regional or global climate and water supply.

Due to the region's remoteness, high altitude, and harsh weather conditions, there are only 340 meteorological stations which is much fewer than that in East China. The locations of the stations can be found in **Figure 1**. Some of the stations began operating in the 1950s. But they are insufficient to meet the needs for understanding the snow spatial variation of the Tibetan Plateau. The other common source of snow cover observation is remote sensing data. The Microwave Radiometer Imager (MWRI) is onboard the FY-3C satellite which was launched in 2014. Therefore, the study period was from 2014 to 2017. The MWRI daily product of snow depth and snow water equivalent was produced by the National Satellite Meteorological Center and is available at http://satellite.nsmc.org.cn/portalsite/default.aspx?currentculture=en-US#.

METHODOLOGY

A nonlinear prediction method called phase space reconstruction was used here to retrieve ITPSD. For nonlinear systems, it is a common method to view the dynamical factors of their evolution. For a grid point or an *in situ* site, its time series can be described by $x_1, x_2, ..., x_t, ..., x_m$, where m is the length of the record time. To reduce noise and view the dynamics of the time series, it was

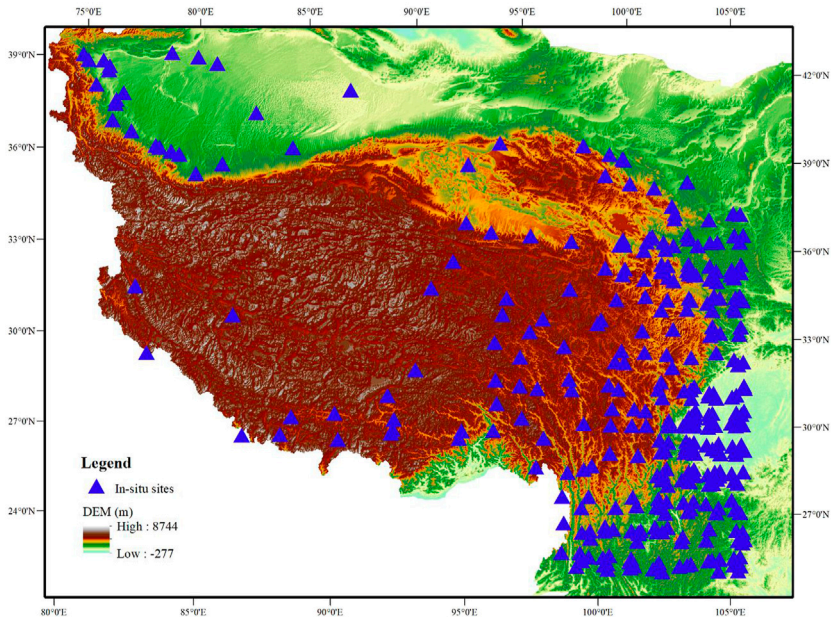

FIGURE 1 | Location of the *in situ* sites over the Tibetan Plateau.

extended to three or even more dimensions, that is, a delayed coordinates phase space reconstruction (DCPSRC) was created. For a f (n), the vector time series is given by the following equation:

$$X(t_i) = (x(t_i), x(t_i + \tau), \cdots, x(t_i + (n-1)\tau)), \quad (1)$$

where i denotes a grid point or an *in situ* site and τ is an appropriate time delay. Based on the decay of the auto-correlation function to 1/e, the appropriate time delay can be determined for each time series [24]. As for embedding dimension, the false nearest neighbor (FNN) approach was used to calculate the optimal embedding dimension [25].

In this study, to obtain ITPSD, DCPSRC was first applied to the time series of the *in situ* sites and grids from FY-3C, respectively. Then the optimal time delay (τ) and embedding dimension (n) for each site and grid were given and analyzed. Finally, ITPSD data were combined as per the following strategy. For a grid, if there were matched sites and its dynamic factors (i.e., the time delay and the embedding dimension) were similar to those of the sites, snow depth values of the grid were averaged over all the sources. If its dynamic factors were far from those of the sites, snow depth values of the grid were averaged over all the sites. If there were no matched sites, then its original values were referred to as the ITPSD.

PROCESSES OF COMBINING INTEGRATED TIBETAN PLATEAU SNOW DEPTH

The process of integrating data from multiple sources into the ITPSD dataset takes four steps: 1) choosing stations for whose snow depth is greater than zero and include records of more than 30 days, and match the snow depth from FY-3C; 2) applying DCPSRC to the time series of the stations and grids from FY-3C; 3) deriving all the dynamic factors of the stations and grids; and 4) combining the data from the *in situ* sites and FY-3C satellite according to the strategy in part 3 to form comprehensive records.

In the initial step, records that have snow fall for more than 30 days from stations and the satellite are considered to meet the statistics of applying DCPSRC. There are 5,461 records meeting the conditions in total. The statement of records of snow cover of the stations and FY-3C satellite are shown in **Table 1**: 1) the missing rate of snow cover in stations is low, accounting for only 0.19%, while that of the FY-3C satellite is much higher and accounts for 37.98%; 2) both rates of no snow cover for the two sources are very high and that of the stations is higher with the value of 97.2%; 3) for trace snow, the rate of station records is 0.63%. However, it is hard for the satellite to retrieve this kind of snow information and the rate of satellite records is 0; and 4) as for snow depth greater than 1 cm, the rates of the stations and satellite are 1.98% and 1.30%, which are closer to each other than in other situations. This type of snow is concentrated on in this study. The records chosen in the first step match the records of the stations and satellite of this type.

The second and third steps are key to determining how to integrate the station and satellite data in the final step. The second step is to construct the delayed phase space for all the data to find their dynamic factors. The third step is to give the time delay and the embedding dimension of the stations and the grids. **Table 2** shows the site information of 18 stations and their dynamic factors. Meanwhile, these stations have matched satellite grids and these grids' dynamic factors are identified with those of

TABLE 1 | Snow cover of stations and FY-3C satellite over the Tibetan Plateau.

Source	No snow cover		Snow depth greater than 1 cm		Trace snow		Missing	
	Number of records	Rate	Number of records	Rate	Number of records	Rate	Number of records	Rate
Stations	41,2679	97.20%	8,388	1.98%	2,688	0.63%	811	0.19%
FY-3C satellite	25,7783	60.72%	5,537	1.30%	0	0	16,1246	37.98%

Note: trace snow means that the daily snow depth was less than 0.1 mm.

TABLE 2 | Site information and dynamic factors of 18 stations which have the same dynamic factors as that of the satellite.

ID	Province	Station name	Latitude (°)	Longitude (°)	Elevation(m)	Time delay	Embedding dimension
1	Xinjiang	Wuqia	39.7	75.2	2,175.7	4	9
2	Gansu	Subei	39.5	94.9	2,137.2	4	8
3	Gansu	Minle	38.5	100.8	2,281.4	4	9
4	Gansu	Gulang	37.5	102.9	2072.4	3	9
5	Qinghai	Zeku	35	101.5	3,662.8	4	8
6	Gansu	Hezheng	35.4	103.3	2,162.8	3	8
7	Gansu	Huajialing	35.4	105	2,450.6	3	8
8	Xizang	Nielamu	28.2	86	3,810	4	9
9	Qinghai	Qumalai	34.1	95.8	4,175	4	8
10	Qinghai	Maduo	34.9	98.2	4,272.3	3	9
11	Qinghai	Qingshuihe	33.8	97.1	4,415.4	3	9
12	Sichuan	Shiqu	33	98.1	4,200	4	9
13	Qinghai	Gande	34	99.9	4,050	3	9
14	Qinghai	Dari	33.8	99.7	3,967.5	3	9
15	Qinghai	Jiuzhi	33.4	101.5	3,628.5	3	8
16	Gansu	Hezuo	35	102.9	2,910	3	9
17	Sichuan	Hongyuan	32.8	102.6	3,491.6	3	8
18	Sichuan	Emeishan	29.5	103.3	3,047.4	4	9

TABLE 3 | Comparison of different types of FY-3C satellite data and *in situ* data. The number of samples, CC, AB, SDB, and RMSE are listed.

Type of snow	Samples	CC	AB(cm)	SDB(cm)	RMSE(cm)
Blizzard and heavy snow	1,565	–0.17	3.34	10.43	10.95
Blizzard	721	–0.07	7.40	3.38	8.13
Heavy snow	844	–0.23	–0.13	12.87	12.87

stations. Their time delay is between 3 and 4, and the embedding dimension is between 8 and 9.

As shown in the **Figure 2**, the stations are Alpine stations and located at the edge of the Tibetan Plateau. This can be contributed to the fact that these sites have an abundance of snow cover and the atmosphere is clean due to less pollution. Therefore, the MWRI onboard the FY-3C satellite can penetrate the atmosphere more easily and reach the surface, and the bias correction effect is better.

ASSESSMENT AND RESULTS

Evaluation Matrices

To evaluate the data, four statistical accuracy measures were applied. The averaged bias (AB) was used for an assessment of the whole dataset bias between ITPSD, FY-3C satellite data, and *in situ* data. Standard deviation of the bias (SDB) evaluated the amount of variation or dispersion of the AB. Root mean square error (RMSE) measured their differences. Correlation coefficient (CC) assessed their relationships.

$$ab_i = I_i - D_i, \tag{2}$$

$$AB = \frac{1}{N}\sum_{i=1}^{N} ab_i, \tag{3}$$

$$SDB = \sqrt{\frac{1}{N}(ab_i - AB)^2}, \tag{4}$$

$$RMSE = \sqrt{\frac{1}{N}ab_i^2}. \tag{5}$$

Here, I_i means the ITPSD or FY-3C at site i or grid i, D_i means the snow depth of the site or the FY-3C of the grid i, and ab_i means the bias of them.

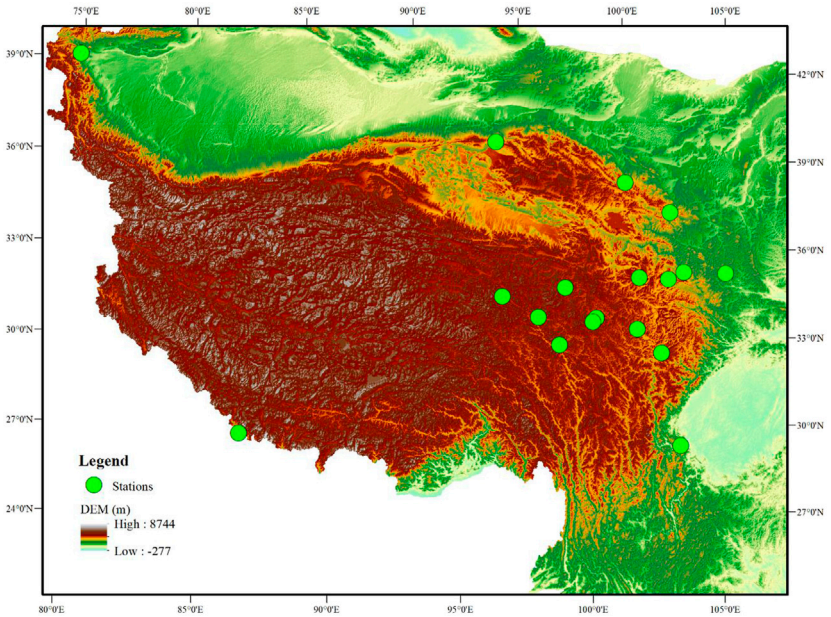

FIGURE 2 | Location of 18 stations with the same dynamic factors as satellite data.

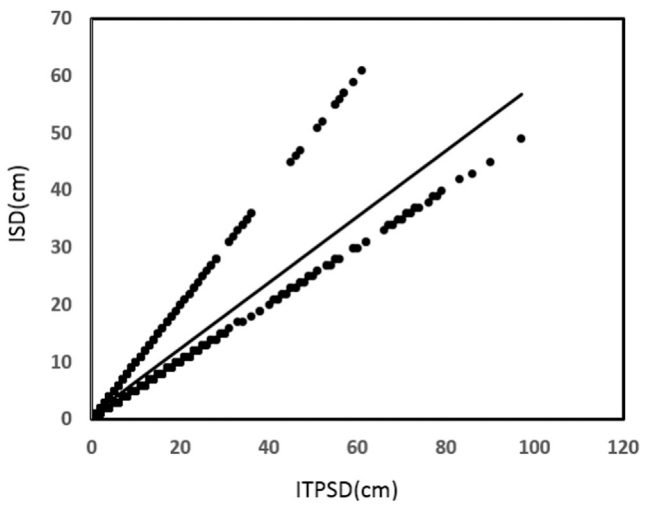

FIGURE 3 | Scatter plots of ITPSD and *in situ* data. The corresponding RMSE and other statistics can be found in **Table 4**.

TABLE 4 | Comparison of ITPSD with FY-3C satellite data and *in situ* data. The CC, AB, SDB, and RMSE are listed.

Data	CC	AB(cm)	SDB(cm)	RMSE(cm)
In situ data	0.93	−1.35	3.96	4.18
FY-3C satellite data	0.30	1.14	5.67	5.79

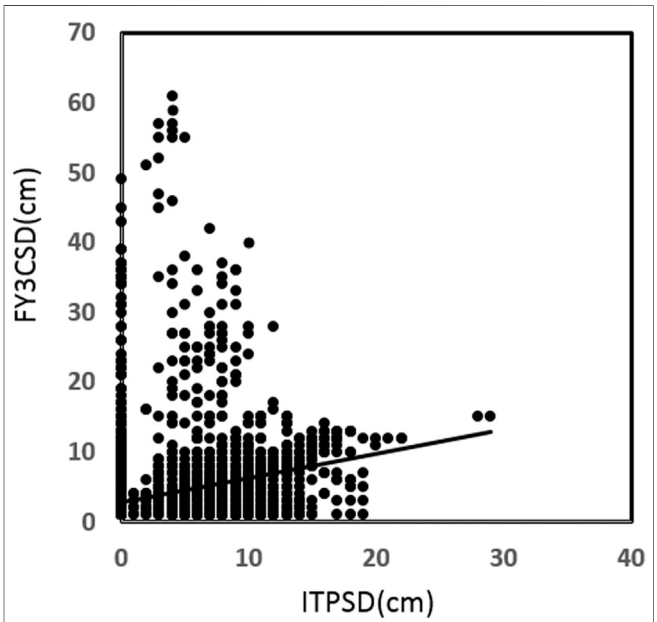

FIGURE 4 | Scatter plots of ITPSD and FY-3C satellite data.

Assessment Results of Snow Depth

Blizzards and heavy snow were of great concern in the assessment (details just shown in **Table 3**), that is, when the snow depth was between 1 cm and 3 cm for blizzards and greater than 3 cm for heavy snow. The FY-3C satellite data and *in situ* data were not well correlated with negative values of CC around 0. The AB of them for heavy snow was rather low with a value of –0.13 cm, which meant that the FY-3C could easily identify heavy snow with little negative bias. The bias of blizzards between the FY-3C satellite data and *in situ* data was higher and the value was up to 7.4 cm. This indicates

that blizzards were overestimated by the satellite, and blizzards also had low variation (SDB equaled 3.38 cm) but heavy snow had large variability (SDB was up to 12.87 cm). The RMSE was large both for blizzards and heavy snow.

The ITPSD and *in situ* data were highly correlated with the value of 0.93 for CC. While ITPSD and FY-3C satellite data were positively correlated, their CC was much lower with a value of 0.30 cm. The AB between the ITPSD and *in situ* data was −1.35 cm, while that between the ITPSD and FY-3C satellite data was 1.14 cm. The absolute value of them was around 1 cm, which meant that ITPSD had low bias both between the FY-3C satellite data and the *in situ* data. The variation of their bias was low with an SDB of 5.67 cm and 3.96 cm, respectively. The differences of the ITPSD between the FY-3C satellite data and *in situ* data were not apparently significant with an RMSE of 5.79 cm and 4.18 cm, respectively. **Figure 3** shows the comparison of ITPSD and *in situ* data. The scatter plot is concentrated along two lines. And the slopes of them are about 1 and 0.3, respectively, as shown in **Table 4**. As for **Figure 4**, the ITPSD and FY-3C satellite data have moderate positive linear association with more outlier points.

DISCUSSION AND CONCLUSION

In this study, a nonlinear time series analysis method called phase space reconstruction was introduced to improve the accuracy of the snow depth over the Tibetan Plateau by combining FY-3C satellite data and *in situ* data in the period 2014–2017. The results show that the method can integrate the FY-3C satellite data and *in situ* data effectively. This can be attributed to considering the evolution facts of snow with time to correct satellite bias and introducing more *in situ* observations. Other useful conclusions are as follows:

1) Eighteen stations and their matched FY-3C satellite grids were identified with the same dynamic factors (time delay and embedding dimension) of the method. The time delays were between 3 and 4 days.

This meant the snow depth time series had a short range of correlation. The embedding dimensions were between 8 and 9 indicating that in those dimensions the snow depth time series was ideal and noise free. The locations of the stations are at the edge of the Tibetan Plateau and they are Alpine stations. This can be attributed to the abundance of snow cover and the cleanness of the atmosphere in these stations. Therefore, the FY-3C satellite could retrieve snow data better.

2) A negative bias and a positive bias between the FY-3C snow depth and *in situ* snow depth for heavy snow and blizzards indicated that the FY-3C underestimated heavy snow but overestimated blizzards. For heavy snow, it was less underestimated with a value of −0.13 cm for the averaged bias. Blizzards were more likely to be overestimated with a value of 7.4 cm.
3) Integrated Tibetan Plateau snow depth had a positive linear association with the FY-3C snow depth and *in situ* snow depth. This relationship was strong between the integrated Tibetan Plateau snow depth and *in situ* snow depth, while that between the integrated Tibetan Plateau snow depth and the FY-3C snow depth was moderate.

Although the integrated Tibetan Plateau snow depth dataset is much accurate than that of the *in situ* and FY-3C data, more work needs to be done to extend the time span and density of the dataset. Furthermore, more datasets should be included, such as the ERA5 reanalysis dataset, to increase the samples of the data on dynamic integration.

DATA AVAILABILITY STATEMENT

The datasets presented in this article are not readily available because the data are only used for the operation in CMA. Requests to access the datasets should be directed to fengax@cma.gov.cn.

AUTHOR CONTRIBUTIONS

QW and ZG designed the study. AF performed the study and wrote the manuscript. FG, AF, QZ, YS, GF, and YZ provided suggestions and took part in the discussion.

FUNDING

This work is supported by the National Natural Science Foundation of China under grant numbers 41775081, 41975100, 41901016, 41875100, and 41675107, the Climate Change Project of the China Meteorological Administration under grant numbers CCSF202042, and the National Key Research and Development Program of China under grant number 2018YFC1507702.

ACKNOWLEDGMENTS

We thank the National Satellite Meteorological Center for providing the MWRI daily product of snow depth retrieved from FY-3C.

REFERENCES

Gao L, Bernhardt M, and Schulz K. Elevation Correction of ERA-Interim Temperature Data in Complex Terrain. *Hydrol Earth Syst Sci* (2012) 16: 4661–73. doi:10.5194/hess-16-4661-2012

Gao L, Hao L, and Chen X-w. Evaluation of ERA-Interim Monthly Temperature Data over the Tibetan Plateau. *J Mt Sci* (2014) 11:1154–68. doi:10.1007/s11629-014-3013-5

Ma Y, Hong Y, Chen Y, Yang Y, Tang G, Yao Y, et al. Performance of Optimally Merged Multisatellite Precipitation Products Using the Dynamic Bayesian Model Averaging Scheme over the Tibetan Plateau. *J Geophys Res Atmos* (2018) 123:814–34. doi:10.1002/2017jd026648

Yang K, Wu H, Qin J, Lin C, Tang W, and Chen Y. Recent Climate Changes over the Tibetan Plateau and Their Impacts on Energy and Water Cycle: A Review. *Glob Planet Change* (2014) 112:79–91. doi:10.1016/j.gloplacha.2013.12.001

Zhu Y, and Ding Y. Influences of Snow Cover over Tibetan Plateau on Weather and Climate: Advances and Problems. *Meteorol Sci Technol* (2007) 35:1–8.

Gao L, Schulz K, and Bernhardt M. Statistical Downscaling of ERA-Interim Forecast Precipitation Data in Complex Terrain Using LASSO Algorithm. *Adv Meteorology* (2014) 2014:1–16. doi:10.1155/2014/472741

Gao L, Deng H, Lei X, Wei J, Chen Y, Li Z, et al. Evidence for Elevation-dependent Warming from the Chinese Tianshan Mountains. *The Cryosphere* (2020). doi:10.5194/tc-2020-188

Gao L, Bernhardt M, Schulz K, Chen X, Chen Y, and Liu M. A First Evaluation of ERA-20CM over China. *Mon Weather Rev* (2016) 144:45–57. doi:10.1175/mwr-d-15-0195.1

Gao L, Bernhardt M, Schulz K, and Chen X. Elevation Correction of ERA-Interim Temperature Data in the Tibetan Plateau. *Int J Climatol* (2017) 37:3540–52. doi:10.1002/joc.4935

Rasmussen R, Baker B, Kochendorfer J, Meyers T, Landolt S, Fischer AP, et al. How Well Are We Measuring Snow: The NOAA/FAA/NCAR winter Precipitation Test Bed. *Bull Amer Meteorol Soc.* (2012) 93:811–29. doi:10.1175/bams-d-11-00052.1

Kunkel KE. Simple Procedures for Extrapolation of Humidity Variables in the Mountainous Western United States. *J Clim* (1989) 2:656–70. doi:10.1175/1520-0442(1989)002<0656:spfeoh>2.0.co;2

Rolland C. Spatial and Seasonal Variations of Air Temperature Lapse Rates in Alpine Regions. *J Clim* (2003) 16:1032–46. doi:10.1175/1520-0442(2003)016<1032:sasvoa>2.0.co;2

Rostosky P, Spreen G, Farrell SL, Frost T, Heygster G, and Melsheimer C. Snow Depth Retrieval on Arctic Sea Ice from Passive Microwave Radiometers-Improvements and Extensions to Multiyear Ice Using Lower Frequencies. *J Geophys Res Oceans* (2018) 123:7120–38. doi:10.1029/2018jc014028

Grody N. Relationship between Snow Parameters and Microwave Satellite Measurements: Theory Compared with Advanced Microwave Sounding Unit Observations from 23 to 150 GHz. *J Geophys Res* (2008) 113:D22108. doi:10.1029/2007jd009685

Kongoli C, Key J, and Smith TM. Mapping of Snow Depth by Blending Satellite and In-Situ Data Using Two-Dimensional Optimal Interpolation-Application to AMSR2. *Remote sensing* (2019) 11:3049. doi:10.3390/rs11243049

Feng G, Dong W, Gong Z, Hou W, Wan S, and Zhi R. *The Nonlinear Spatiotemporal Theory and Method of Observations*. Beijing: China Meteorological Press (2006).

Feng G-L, Yang J, Zhi R, Zhao J-H, Gong Z-Q, Zheng Z-H, et al. Improved Prediction Model for Flood-Season Rainfall Based on a Nonlinear Dynamics-Statistic Combined Method. *Chaos, Solitons & Fractals* (2020) 140:110160. doi:10.1016/j.chaos.2020.110160

Feng A, Gong Z, Huang Y, and Wang Q. Spatiotemporal Analysis of Information Entropy of the Global Temperatur. *Acta Phys Sin* (2011) 60:099204.

Feng A, Wang Q, Gong Z, and Feng G. Vertical Structure of Predictability and Information Transport over the Northern Hemisphere. *Chin Phys B* (2014) 23(2):029202. doi:10.1088/1674-1056/23/2/029202

Tsonis AA, and Elsner JB. Mapping the Channels of Communication between the Tropics and Higher Latitudes in the Atmosphere. *Physica D: Nonlinear Phenomena* (1996) 92:237–44. doi:10.1016/0167-2789(95)00265-0

Wang G, and Yang P. A Compound Reconstructed Prediction Model for Nonstationary Climate Processes. *Int J Climatol* (2005) 25:1265–77. doi:10.1002/joc.1158

Wang G, Yang P, Bian J, and Zhou X. A Novel Approach in Predicting Non-stationary Time Series by Combining External Forces. *Chin Sci Bull* (2011) 56: 3053–6. doi:10.1007/s11434-011-4638-1

Qiu J. China: The Third Pole. *Nature* (2008) 454:393–6. doi:10.1038/454393a

Kantz H, and Schreiber T. *Nonlinear Time Series Analysis*. Cambridge University Press (2004). p. p80.

Kantz H, and Schreiber T. *Nonlinear Time Series Analysis*. Cambridge University Press (2004). p. p37.

Conflict of Interest: The authors declare that the research was conducted in the absence of any commercial or financial relationships that could be construed as a potential conflict of interest.

frontiers in Physics

ORIGINAL RESEARCH
published: 23 July 2021
doi: 10.3389/fphy.2021.688801

The Physical Mechanisms Behind the Change in the Precipitation Recycling Rate in the Mid- and Lower Reaches of the Yangtze River

Wen-Kang Guo[1], Xi-Yu Wang[1], Wang-Ze Gao[1], Jia-Hua Yong[1], Xin-Yue Bao[2], Yong-Ping Wu[1], Guo-Lin Feng[1,3,4]* and Wen-Jie Dong[4,5]*

[1]College of Physical Science and Technology, Yangzhou University, Yangzhou, China, [2]Yangzhou Shuren School, Yangzhou, China, [3]Laboratory for Climate Studies, National Climate Center, China Meteorological Administration, Beijing, China, [4]Guangdong Provincial Laboratory of Marine Science and Engineering, Zhuhai, China, [5]School of Atmospheric Sciences and Guangdong Province Key Laboratory for Climate Change and Natural Disaster Studies, Sun Yat-sen University, Zhuhai, China

The precipitation recycling rate (PRR) is an important index when trying to understand the physical mechanisms behind the effects of different sources of water vapor on regional precipitation. We studied the change in the PRR in the mid- and lower reaches of the Yangtze River (MLRYR), the correlation between the PRR and the external source of water vapor and local evaporation, and the possible reasons for the interannual variation of the PRR. Our study was based on an evaluation model of the PRR and used precipitation data from meteorological stations in China and NCEP/NCAR reanalysis datasets. Our results show that the mean PRR in the MLRYR for the time period 1961–2017 was largest in autumn (about 0.3) and smallest in summer (about 0.23), with a clear upward trend (passed the 95% significance *F*-test), except in summer. The highest trend coefficient of the PRR was in autumn (0.38), indicating that the contribution of an external source of water vapor to local precipitation was reduced. The PRR of the MLRYR was strongly correlated with the input of water vapor through the western and southern boundaries. Water vapor was mainly sourced from the Northwest Pacific Ocean, the South China Sea and the Bay of Bengal. The anomalous Northwest Pacific cyclone induced by the Pacific sea surface temperature restrained the input of water vapor into the MLRYR from the Western Pacific, the South China Sea and the Bay of Bengal, contributing to the upward trend in the PRR. We suggest that increases in the sea surface temperature in the Pacific Ocean, South China Sea and especially the Indian Ocean will have an important impact on precipitation in East Asia.

Keywords: the middle and lower reaches of the Yangtze River, precipitation recycling rate, water vapor flux, regression analysis, influence mechanism

OPEN ACCESS

Edited by:
Umberto Lucia,
Politecnico di Torino, Italy

Reviewed by:
Kaiming Hu,
Institute of Atmospheric Physics (CAS), China
Bo Sun,
Nanjing University of Information Science and Technology, China

****Correspondence:***
Yong-Ping Wu
ypwu@yzu.edu.cn
Guo-Lin Feng
fenggl@cma.gov.cn

Specialty section:
This article was submitted to Interdisciplinary Physics, a section of the journal Frontiers in Physics

Received: *31 March 2021*
Accepted: *21 May 2021*
Published: *23 July 2021*

Citation:
Guo W-K, Wang X-Y, Gao W-Z, Yong J-H, Bao X-Y, Wu Y-P, Feng G-L and Dong W-J (2021) The Physical Mechanisms Behind the Change in the Precipitation Recycling Rate in the Mid- and Lower Reaches of the Yangtze River. Front. Phys. 9:688801. doi: 10.3389/fphy.2021.688801

INTRODUCTION

The mid- and lower reaches of the Yangtze River (MLRYR) are located in the East Asian monsoon region and have a higher annual precipitation than most other regions of China. The global climate has significantly warmed in recent decades [1]. Many studies have shown that the total rainfall in the MLRYR has not changed significantly, but the number of extreme precipitation events has

significantly increased [2–5], which poses new challenges in the prediction of precipitation [6]. The source of water vapor for regional precipitation depends on the amount of water vapor produced by local evaporation and the amount of water vapor transported into the region by horizontal movement through the atmosphere [7–12]. Many researchers have used the precipitation recycling rate (PRR) to quantitatively evaluate the contribution of these two sources of water vapor to regional precipitation. The PRR is defined as the proportion of precipitation formed by the local evaporation of water vapor in the total precipitation [7, 13–17]. However, water vapor that forms precipitation through local evaporation cannot be observed, so numerous precipitation recycling models have been developed to assess the regional PRR [7, 8, 13–19].

Budyko [13, 14] developed a one-dimensional linear model to estimate the recycling of precipitation in large-scale regions and analyzed the PRR in the former Soviet Union, showing that the annual average PRR was about 10%. Brubaker et al. [7] extended the Budyko model to the two-dimensional plane and evaluated the PRR in some parts of the global continent. The highest PRR was seen in Africa (up to 48% in August) and the lowest in Eurasia (almost zero in February) and the PRR in dry areas was higher than that in humid areas. Guo et al. [20] adopted this two-dimensional model to study the trend of PRR over the Qinghai–Tibetan Plateau. They showed that, with increasing temperatures, the PRR in the arid region of the western Qinghai–Tibetan Plateau showed a downward trend (−2.5%/10a), whereas that in other regions presented an upward trend. The PRR in the northeastern Qinghai–Tibetan Plateau showed the strongest growth trend of 3.1%/10a.

Burde et al. expanded the Budyko model into a two-dimensional model [15] and refined and improved it [21], showing that the average annual PRR in the Amazon basin was 41% [22]. Eltahir et al. [16, 17] fundamentally improved the Budyko model by eliminating the influence of the non-uniformity of the regional spatial distribution and studied the precipitation recycling process in the Amazon region. Their results showed that the average annual PRR in the Amazon basin was about 35%.

Hai et al. [23] used the Eltahir model to study the characteristics of the hydrological cycle in the Tarim river basin. They showed that about 14% of the water vapor for the annual precipitation came from evaporation in the Tarim river basin and 86% from the surrounding area. Schär et al. [18] simplified the Brubaker model based on the whole-layer moisture balance model. Li et al. [24] then used this model to study the PRR in arid and semi-arid regions in the northern hemisphere and showed that the PRR in arid regions has a clear seasonal variation (from <1 to >25%) and that the PRR in arid regions showed a significant negative correlation with precipitation.

Dominguez et al. [8] considered the influence of the water vapor content of the atmosphere on the recirculation of precipitation and established a dynamic recirculation model to study the spatiotemporal distribution of the summer PRR in the United States. They concluded that the average summer PRR in the United States was between 11 and 28% and that the PRR in the southeastern United States was the highest in August, reaching 36%.

Amey Pathak et al. [25] used the Dominguez dynamic recirculation model to study the recirculation of precipitation in the Indian subcontinent during the monsoon period and showed that the PRR in India was high in the northeast and low in the southwest. The PRR in northern India was highest in August, with some areas >40%. Hua et al. [26] used this model to conduct a systematic study on precipitation recycling in China and concluded that the PRR in China was low in the southeast and high in the west (range 8–28%). Van der Ent et al. [19] proposed a complex numerical scheme to evaluate the PRR of the global continent. They showed that the PRR of the whole continent was about 40% and the regional PRR increased with an increase in the regional spatial scale.

Previous studies have shown that the PRR is helpful in understanding the causes of changes in precipitation in the MLRYR. It is therefore important to discuss the variation of the PRR in the MLRYR. Yi et al. [27] calculated and analyzed different sources of water vapor for precipitation in the MLRYR based on the Eltahir and Brubaker models and found that the average annual PRR in the Yangtze river basin was about 10% and the PRR was highest (about 19%) in late summer and early autumn and lowest (about 3%) in early spring.

Fu Xiang et al. [28] used the Eltahir model to study precipitation recycling in the MLRYR in the context of global climate change and found that, on average, about 30% of the precipitation in the MLRYR in the summer rainstorm period came from local evaporation. Kang et al. [29] used the Eltahir model to evaluate the PRR in central and southern China. They showed that 20% of the precipitation in the upper reaches of the Yangtze River was from the evaporation of water vapor in central and southern China, as was 40% of the precipitation in the MLRYR. The PRR was highest (about 40%) in August, September and October and was <25% in May, June and July. The PRR has shown an increasing trend over the last 20 years.

These studies on the PRR of the MLRYR reflect the contribution of the circulation of internal and external sources of atmospheric water, but the models are calculated based on the average value for the whole region and the results are approximate. Previous research on the PRR of the MLRYR has mostly been limited to annual changes and the interannual and trend analyses need to be supplemented. The mechanism for the changes in the PRR of the MLRYR requires further study.

We improved the evaluation model for the PRR based on gridded data and studied the characteristics of the annual and trend changes of the PRR in the MLRYR. We then analyzed the mechanism for the variation in the PRR in the MLRYR from the perspective of the sea surface temperature (SST) and atmospheric circulation.

Datasets and Methods

We used the specific humidity (q), wind field ($\vec{V}$), surface pressure ($p_{surface}$) and other daily data from the National Centers for Environmental Prediction/National Center for Atmospheric Research NCEP/NCAR (2.5° × 2.5°) reanalysis dataset [30] to calculate the water vapor flux in the whole layer $\vec{Q}$:

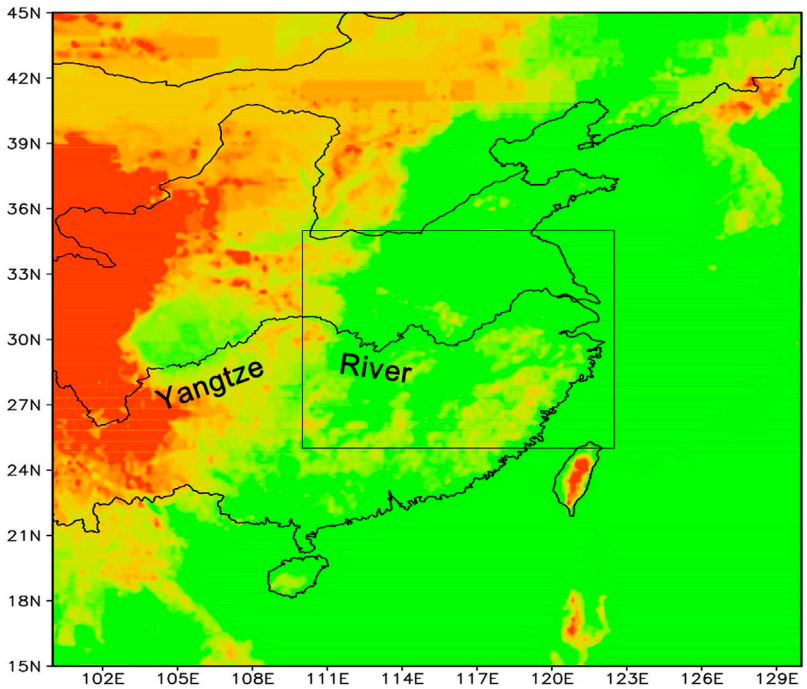

FIGURE 1 | Location of the study area. The color shading indicates the altitude (units: m) and the black rectangle indicates the MLRYR.

$$\overrightarrow{Q} = -\frac{1}{g}\int_{P_{surface}}^{300\,\mathrm{hPa}} q\overrightarrow{V}\,dp. \tag{1}$$

The evaporation data were calculated using the method proposed by Su et al. [31], who integrated multiple datasets, including the NCEP-R1, NCEP-R2, MERRA (Modern-Era Retrospective analysis for Research and Applications), ERA-Interim and JRA-55 (Japanese 55-year Reanalysis) datasets. Su et al. [31] showed that evaporation data calculated by this method are more reliable because it avoids dependence on a single dataset.

The precipitation data were daily data from meteorological stations in China between 1961 and 2017, which were interpolated onto a (2.5° × 2.5°) grid for subsequent calculations. The Western Pacific subtropical high index was provided by the National Climate Center, China Meteorological Administration. The SST was from the monthly mean COBE-SST data provided by the National Oceanic and Atmospheric Administration (NOAA). The research area was the MLRYR (110–122.5° E, 25–35° N) (**Figure 1**).

We based the calculation of the PRR on the evaluation model proposed by Eltahir [16, 17]. The water vapor provided by region Ω forms the proportion of precipitation in subregion ΔA—that is, the contribution rate of region Ω to precipitation in the subregion is $\rho = (I_\Omega + e)/(I + e)$, where I is the total amount of water vapor flowing into subregion ΔA through the advection term, I_Ω is that part of I sourced from the parent region Ω and e is the evaporation in the subregion. Because this model is calculated based on the average value for the whole region, the settlement result is approximate. Based on gridded data within the region, we improved this calculation as follows:

$$\rho_\Omega(x,y) = \frac{I(x,y)\frac{e(\Omega)-e(x,y)}{e(\Omega)-e(x,y)+I(\Omega)} + e(x,y)}{I(x,y)+e(x,y)}. \tag{2}$$

where $I(x,y)$ is the water vapor input to the grid point (x,y), $I(\Omega)$ is the total water vapor input to region Ω, region Ω is regarded as a whole and the total water vapor input through each boundary represents the water vapor input into the whole region, $e(x,y)$ is the water vapor evaporated from grid point (x,y) and $e(\Omega)$ is the total water vapor evaporated from area Ω. I_Ω is the water vapor input into the study area from outside through the four boundaries. It can be calculated from the vertically integrated water vapor flux, which can be expressed as **Eq. 1**. It is worth noting that only the water vapor flowing into the region needs to be calculated as I_Ω.

The PRR $r_\Omega(\Delta t)$ in the region within time Δt is then:

$$r_\Omega(\Delta t) = \frac{\sum_{t=t_{begin}}^{t=t_{end}}\left[\sum_{(x,y)\in\Omega} P(x,y,t)\cdot\rho_\Omega(x,y,t)\right]}{\sum_{t=t_{begin}}^{t=t_{end}}\left[\sum_{(x,y)\in\Omega} P(x,y,t)\right]}. \tag{3}$$

In this equation, $t_{end} = t_{begin} + \Delta t$ and $P(x,y,t)$ is the precipitation of grid point (x,y). As long as the improved $\rho_\Omega(x,y,t)$ is substituted into **Eq. 3**, the PRR can be calculated. We also compared several other major PRR models, include the Schär and Brubaker models, which are based on Euler hydrodynamics. However, these models may underestimate the

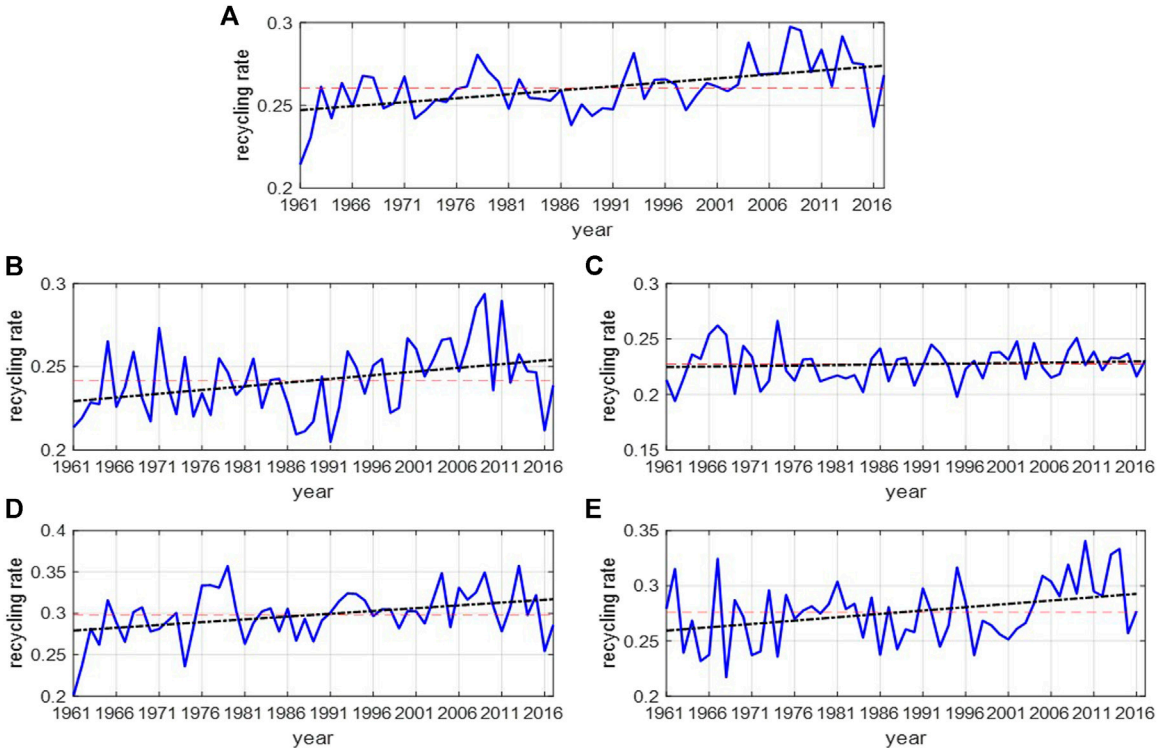

FIGURE 2 | (A) Annual PRR and the PRR in **(B)** spring, **(C)** summer, **(D)** autumn and **(E)** winter in the MLRYR. The blue line is the time series of the PRR, the black line is the linear fit of the PRR and the red line is the mean of the PRR.

PRR, so we improved the calculation scheme of the model based on its physical meaning and then compared the results with those of the Lagrange trajectory tracking method [32]. The results for the PRR in summer using the Schär, Brubaker, our model and the Lagrange method were 16.8, 9.3, 22.7 and 23.97%, respectively. The results of our PRR model (22.7%) were therefore close to those of the Lagrange method (23.97%). This further verifies the rationality of our model from the perspective of both Euler and Lagrange.

We used conventional meteorological statistical methods—such as regression and correlation analysis, the climatic trend coefficient and the climatic tendency rate (regression coefficient) [33]—to analyze the increase and decrease in the time series.

RESULTS

Temporal Variation of the Precipitation Recycling Rate in the Mid- and Lower Reaches of the Yangtze River

Figure 2 shows the annual mean and seasonal PRR in the MLRYR. The average annual PRR in the MLRYR was about 0.26 and there were clear interannual variations. From 1961 to 2016, the linear trend was increasing with a trend coefficient of 0.51 (regression coefficient 0.48%/10a) that passed the 95% significance test. The PRR in spring, summer, autumn and winter were about 0.24, 0.23, 0.3 and 0.28, respectively, and all seasons showed an upward trend with trend coefficients of 0.36, 0.09, 0.38 and 0.35, respectively (regression coefficients 0.44, 0.09, 0.68 and 0.61%/10a, respectively). The 95% significance test was passed in spring, autumn and winter.

TABLE 1 | Correlation coefficients between the seasonal PRR in the MLRYR and the input of water vapor through each boundary and local evaporation.

	MAM	JJA	SON	DJF
Eastern boundary	0.2	−0.12	−0.09	0.02
Western boundary	−0.7**	−0.41**	−0.76**	−0.68**
Northern boundary	0.3*	0.14	0.26	−0.06
Southern boundary	−0.78**	−0.27*	−0.63**	−0.51**
Evaporation	0.42**	−0.02	0.28*	0.33**

**Passed the 95% significance test; **passed the 99% significance test.*

Correlation Between the Precipitation Recycling Rate and External Sources of Water Vapor and Local Evaporation

The PRR was affected by the input of external sources of water vapor and local evaporative water vapor: the greater the input of external sources of water vapor, the smaller the PRR and the larger the local evaporative water vapor, the larger the PRR.

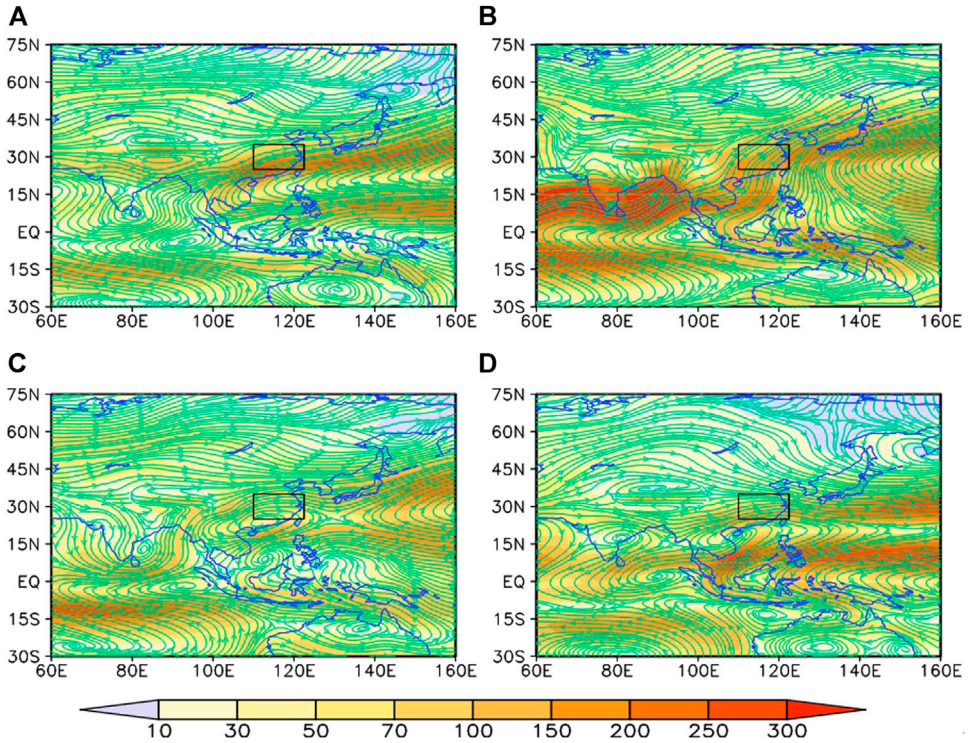

FIGURE 3 | Water vapor flux of the whole layer in **(A)** spring, **(B)** summer, **(C)** autumn and **(D)** winter in the MLRYR (units: kg m^{-1} s^{-1}). The vectors represent the direction of the water vapor flux in the whole layer and the color shading indicates its specific value. The black rectangular box represents the MLRYR.

The correlation between the PRR in each season along the MLRYR and the input of water vapor at each boundary and local evaporation (**Table 1**) shows that the PRR of the MLRYR was mainly related to the input of water vapor through the western and southern boundaries. This further suggests that the PRR of the MLRYR is mainly affected by the input of water vapor from the western and southern boundaries and local evaporation.

The water vapor transported into the MLRYR was mainly from the Northwest Pacific Ocean, the South China Sea and the Bay of Bengal (**Figure 3**), which is consistent with previous research [32, 34–37]. The input of water vapor into the MLRYR was mainly from the western and southern boundaries, with less water vapor from the northern and eastern boundaries (**Figure 3**).

Possible Reasons of the Interannual Variation of the Precipitation Recycling Rate

Anomalous Northwest Pacific anticyclones (cyclones) promote (inhibit) the transport of water vapor over the Northwest Pacific, the South China Sea and the Bay of Bengal [38, 39]. The Mongolian cyclonic (anticyclonic) anomaly promotes (inhibits) the transport of water vapor by westerly winds. The regression coefficients of the PRR and the 850 hPa wind field show that, in the lower troposphere, the PRR in the MLRYR is affected by the Northwest Pacific cyclone in every season. This means that the MLRYR is dominated by northerly winds, which inhibits the input of water vapor from the Western Pacific, the South China Sea and the Bay of Bengal. The anticyclone near Lake Baikal also weakens the input of water vapor in the zone of westerly winds. The PRR in the MLRYR is therefore higher under the combined action of the Northwest Pacific cyclone and the anticyclone near Lake Baikal. By contrast, the input of water vapor through the southern and western boundaries is promoted, which favors a lower PRR in the MLRYR (**Figure 4**).

Figure 5 shows the regression coefficient field of the PRR and the 500 hPa height field in the mid-troposphere in each season. The spatial distribution of the Northwest Pacific to East Asia continent mainly presents a "– +" pattern. Previous studies [40] have shown that when the mid- and high-latitude height field of Eurasia presents a "+ – +" distribution from west to east, then Eurasia has a "two ridges and one trough" distribution, which favors the frequent formation of a blocking high in Central Asia. The distribution of the regression field for spring and summer is similar.

There are significant negative anomalies in the Northwest Pacific, which weaken the Northwest Pacific subtropical high. When the Northwest Pacific subtropical high is strong, the southwesterly air flow in the west of the Northwest Pacific enhances the transport of water vapor, whereas a weak Northwest Pacific subtropical high weakens the transport of water vapor. **Table 2** shows that the PRR in the MLRYR was mainly negatively correlated with the area index, intensity index and ridge index of the Western Pacific subtropical high (the correlation between the PRR and the ridge index was better). At

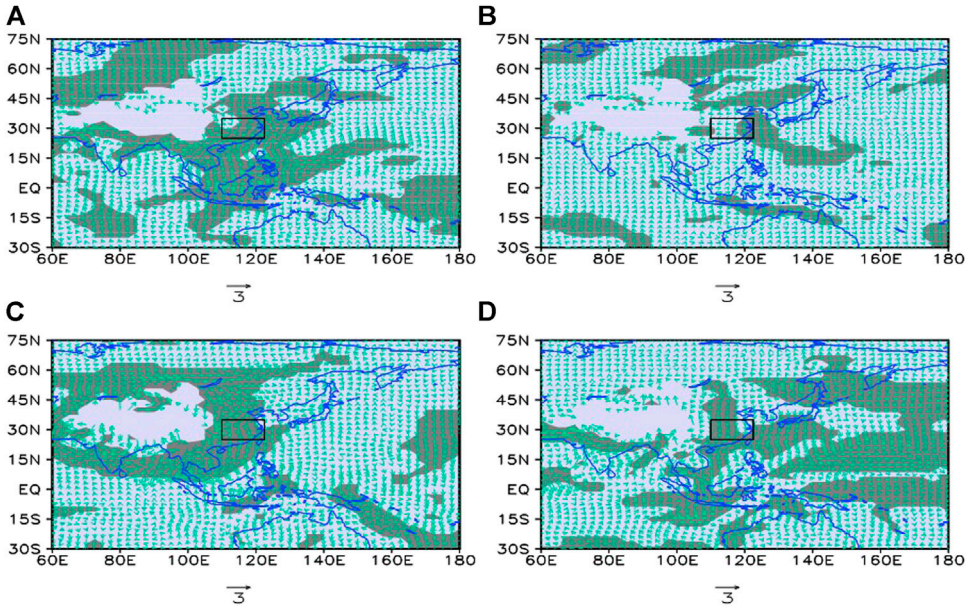

FIGURE 4 | Regression coefficients of the PRR and the 850 hPa wind field in **(A)** spring, **(B)** summer, **(C)** autumn and **(D)** winter in the MLRYR [units: %/(m/s)]. The shaded area indicates that the results passed the 95% significance test and the black rectangle box represents the MLRYR.

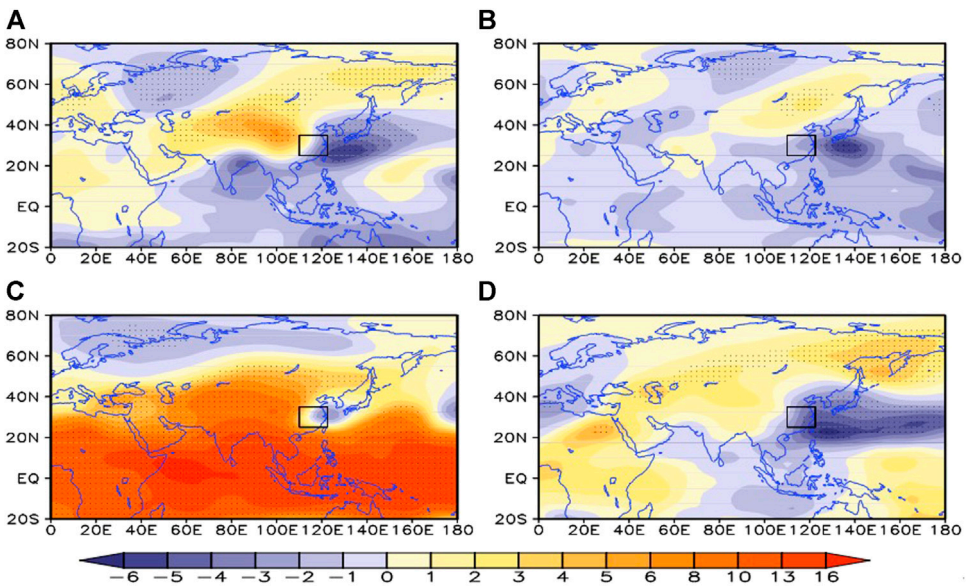

FIGURE 5 | Regression coefficient field of the PRR in the MLRYR and the 500 hPa height field in **(A)** spring, **(B)** summer, **(C)** autumn and **(D)** winter in the MLRYR (units: 10^{-4}/m). The color shading represents the regression coefficient, the dotted area represents the 95% significance test and black rectangular box represents the MLRYR.

the same time (except in autumn), East Asia showed a "+ −" dipole distribution from north to south, which suppressed the transport of water vapor to the north.

The SST is an important factor affecting the atmospheric circulation, regional precipitation and its recycling through atmospheric circulation. Previous studies have shown that the anomalous anticyclone in the Philippine Sea may be caused by the response of Rossby waves to restrained convective heating. It is induced by both *in situ* cooling of the ocean surface and the subsidence forced remotely by warming of the central Pacific. The development of the anticyclone almost coincides with the increased local cooling of the sea surface [41, 42].

Huang et al. [43] showed that the dynamic effect of the atmospheric circulation and zonal wind anomalies in the lower troposphere over the tropical Western Pacific on the El Niño Southern Oscillation cycle may be through the excitation of

TABLE 2 | Correlation coefficients of the seasonal PRR in the MLRYR with the Northwest Pacific subtropical high index (area index, intensity index, ridge line index, ridge point index) and oceanic El Niño index.

	MAM	JJA	SON	DJF
Area	−0.09	−0.16	0.23	−0.06
Intensity	−0.13	−0.15	0.16	−0.08
Ridge line	−0.31*	−0.13	−0.33*	−0.47**
Ridge point	0.13	0.21	−0.29*	−0.04
Oceanic El Niño index	−0.32*	−0.05	0.23	−0.30*

**Passed the 95% significance test; **passed the 99% significance test.*

equatorial oceanic Kelvin waves and Rossby waves in the equatorial Pacific. Wu et al. [44] showed that the western North Pacific anticyclone is maintained by the combined effects of local forcing of the negative SST anomalies in the western North Pacific and remote forcing from the Indian Ocean basin mode. During the mature phase of El Niño, the convective cooling anomalies over the western tropical Pacific caused by weakened convection trigger an atmospheric Rossby wave response, resulting in the generation of the western North Pacific anticyclone [45]. The western North Pacific anticyclone can persist from the winter when El Niño is at its peak to the subsequent summer. It is maintained by a number of factors, including the sustained presence of convective cooling anomalies, the local air–sea interaction over the western tropical Pacific and the persistent SST anomalies in the tropical Indian and tropical North Atlantic oceans.

The western North Pacific anticyclone can influence atmospheric circulation over East Asia and rainfall in China, not only simultaneously, but also in the subsequent summer after an El Niño year, leading to more rainfall over southern China. The El Niño Southern Oscillation is an important system for transporting water vapor from the Northwest Pacific and the South China Sea to China. We therefore analyzed the regression coefficient field of the PRR in the MLRYR and the SST in the same time period (**Figure 6**). The regression field was similar to the La Niña distribution. This is shown in **Table 2**, where the PRR is negatively correlated with the oceanic El Niño index. The equatorial Central Eastern Pacific and the northern Indian Ocean present negative anomalies, whereas the Northwest Pacific presents positive anomalies. This suppresses the anomalous anticyclone near the Philippines and inhibits the northward transport of water vapor. The situation is the opposite in autumn and the specific reasons for this need further investigation.

Combined with the regression coefficient field of the PRR and the 500 hPa vertical velocity (**Figure 7**), the SST of the Northwest Pacific is abnormally warm, which favors ascending motion and inhibits the development of the anomalous anticyclone in the Northwest Pacific. The downdraft near Lake Baikal also favors the development of the anticyclone.

Previous studies [46, 47] have shown that precipitation, temperature, cloud cover and wind speed are important factors affecting evaporation. In general, evaporation is higher when precipitation is abundant in arid areas, whereas there is an inverse correlation between precipitation and evaporation in humid regions such as the MLRYR [48]. **Table 3** shows that the PRR of the MLRYR is inversely correlated with precipitation in all seasons, with more precipitation leading to less evaporation and a lower PRR, which also conforms to this relationship. There is a good inverse correlation between the PRR and cloud cover because more cloud cover means more precipitation in humid regions. The PRR is also related to both temperature and wind as a result of their influence on evaporation. Higher temperatures mean greater local evaporation and therefore a higher regional PRR. By contrast, a higher the wind speed leads to higher local evaporation and a higher

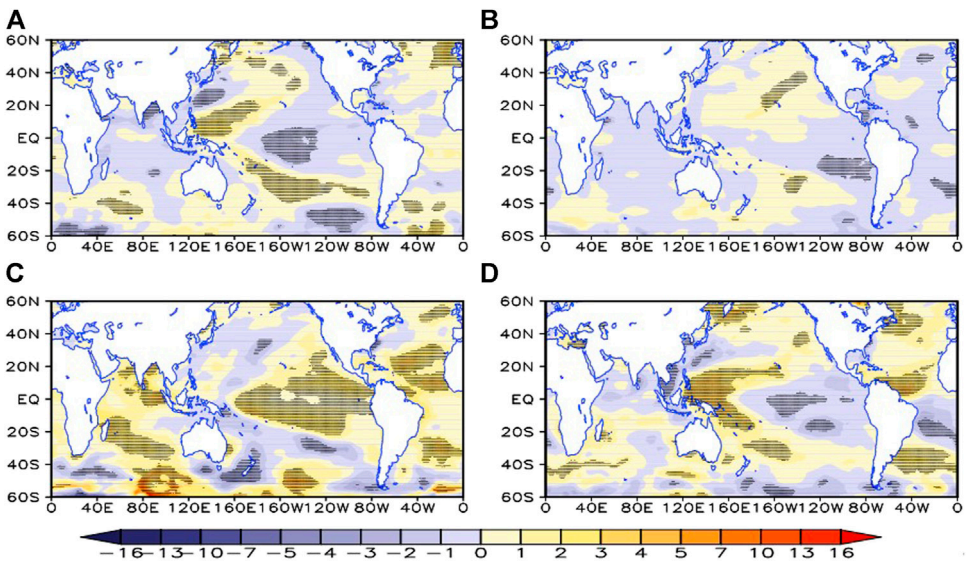

FIGURE 6 | Regression coefficient field of the PRR in the MLRYR and the SST in **(A)** spring, **(B)** summer, **(C)** autumn and **(D)** winter (units: %/K). The dotted area indicates that it passed the 95% significance test.

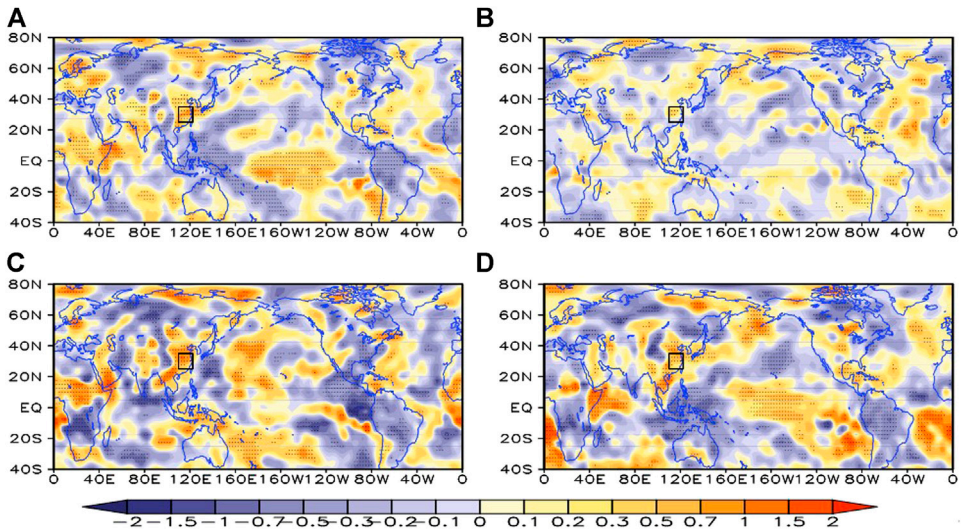

FIGURE 7 | Regression coefficient field of the PRR in the MLRYR and the 500 hPa vertical velocity in **(A)** spring, **(B)** summer, **(C)** autumn and **(D)** winter [units: /(Pa/s)]. The dotted area indicates that it passed the 95% significance test and the black rectangular box represents the MLRYR.

TABLE 3 | Correlation coefficients of the PRR in different seasons with the local average precipitation, total cloud cover, surface temperature and surface wind speed in the MLRYR.

	MAM	JJA	SON	DJF
Precipitation	−0.62**	−0.14	−0.54**	−0.49**
Cloud cover	−0.74**	−0.47**	−0.67**	−0.74**
Temperature	0.29*	0.14	0.23	−0.17
Wind	−0.34**	−0.26	−0.43**	−0.03

**Passed the 95% significance test; **passed the 99% significance test.*

regional PRR. There is an inverse correlation between the PRR and the surface wind speed in the MLRYR (**Table 3**), which may be because the influence of the monsoon on the external input of water vapor is greater than that on local evaporation.

DISCUSSION AND CONCLUSION

We improved the calculation method in the previously proposed PRR evaluation model. We used precipitation data from stations in China from 1961 to 2017 and the corresponding NCEP/NCAR specific humidity and wind field reanalysis datasets to study the change in the PRR in the MLRYR. Our results showed that the PRR in the MLRYR was largest in autumn (0.3), followed by winter (0.28) and the smallest in summer (0.23). The PRR in the MLRYR showed an upward trend in all seasons (all, except summer, passed the 95% significance test). The trend coefficient of the PRR was largest (0.38) in autumn and smallest (0.09) in summer. The regression coefficient was highest in autumn (0.68%/10a), followed by winter (0.61%/10a) and the smallest in summer (0.09%/10a). The PRR showed a clear interannual variation.

We analyzed the physical factors influencing the change in the PRR in the MLRYR from the perspectives of the SST and atmospheric circulation using the reanalysis and SST datasets. We found that a high SST in the Northwest Pacific promotes local upward motion, which favors the development of cyclones and inhibits the input of water vapor from the Western Pacific, the South China Sea and the Bay of Bengal. The anomalous anticyclone near Lake Baikal inhibits the input of water vapor from westerly winds.

In the regression coefficient field of the PRR and the 500 hPa height field, the Northwest Pacific–Asian continent mainly presents a "+ −" spatial distribution, which weakens the Northwest Pacific subtropical high. By contrast, East Asia (except in autumn) presents a "+ −" dipole distribution from north to south, which inhibits the northward transport of water vapor and leads to a higher PRR in the MLRYR.

In terms of local factors, the PRR in the MLRYR is mainly affected by precipitation and cloud cover. When precipitation and cloud cover are small, evaporation is high, increasing the PRR in the MLRYR. By contrast, the PRR is low when precipitation and cloud cover are high and evaporation is low.

The anticyclonic circulation of the Northwest Pacific Ocean is the key system for the transport of water vapor from the Western Pacific, the South China Sea and the Bay of Bengal to the MLRYR. Previous studies have linked the anticyclonic circulation in the Northwest Pacific with the local wind–evaporation–SST feedback in the western North Pacific and the propagation of Kelvin waves caused by warming of the tropical Indian Ocean [41–45, 49]. However, the characteristics of the regression field of the PRR and SST in the MLRYR in autumn are almost the opposite of those in other seasons (**Figure 7**). Yoo [50] showed that climate change caused by global warming weakened the atmospheric response in the central Pacific during El Niño years and atmospheric feedback increased during La Niña years. Huang et al [51] showed that the response of the vertical circulation of the atmosphere to local SST anomalies may be

weakened under global warming. These results may explain the abnormal situation of the regression field of the PRR and SST in autumn and require further research.

Previous studies have shown that the East Asian winter and summer monsoons have both weakened with global warming [52–55]. The MLRYR are located in the monsoon region and the weaker monsoon has led to a decrease in the input of water vapor to this region. Global warming has also increased evaporation, which favors an increase in the PRR. These factors may explain the increasing trend of the PRR in the MLRYR. The contribution and influence of different sources of water vapor on the regional precipitation were evaluated using the PRR, which provides a new perspective for analyzing the cause of precipitation and further improving our ability to predict precipitation [7]. Future work will analyze the respective roles of water vapor from external advection and local evaporation in the precipitation process and the contribution of external inputs of b water vapor and local evaporation to precipitation in different stages of the meiyu in the MLRYR on an hourly scale.

DATA AVAILABILITY STATEMENT

The original contributions presented in the study are included in the article/supplementary material, further inquiries can be directed to the corresponding authors.

AUTHOR CONTRIBUTIONS

Y-P W and G-L F were responsible for the improvement of the model of rainfall recycling rate assessment and the editing andrevision of the paper. G-L F and W-J D provided meteorological data, climate background and theoretical guidance for the middleand lower reaches of the Yangtze River. W-K G was responsible for drawing, analysis and writing of the paper. And X-Y W and W-Z G collected, sorted and analyzed the responsible data. J-H Y and X-Y B have recalculated and analyzed the data in our manuscript to demonstrate the correctness of the original results and helped to verify the language grammar and edit the references according to our editor's commend.

FUNDING

This work was supported by National Key Research and Development Program of China (grant no. 2018YFE0109600, 2017YFC1502303), National Natural Science Foundation of China through grants 41875097, 41875096, High-level Talent Support Program funding of Yangzhou University and Six Talent Peaks of Jiangsu Province (Grant no. JNHB-071) and Selective Support for Scientific and Technological Activities of Overseas Scholars of Shanxi province, and Outstanding Young Talents Support Plan of Shanxi province, and College Students' scientific innovation project (X20190247, 201911117030Z).

REFERENCES

1. Hansen J, Sato M, Ruedy R, Lo K, Lea DW, and Medina-Elizade M. Global Temperature Change. *Proc Natl Acad Sci* (2006) 103:14288–93. doi:10.1073/pnas.0606291103
2. Su B, Xiao B, Zhu D, and Jiang T. Trends in frequency of precipitation extremes in the Yangtze River basin, China: 1960-2003 / Tendances d'évolution de la fréquence des précipitations extrêmes entre 1960 et 2003 dans le bassin versant du Fleuve Yangtze (Chine). *Hydrological Sci J* (2005) 50: 479–92. doi:10.1623/hysj.50.3.479.65022
3. Su BD, Jiang T, and Jin WB. Recent Trends in Observed Temperature and Precipitation Extremes in the Yangtze River basin, China. *Theor Appl Climatol* (2006) 83:139–51. doi:10.1007/s00704-005-0139-y
4. Quan D, Chen X, and Chen T. Characteristics and Changes of Extreme Precipitation in the Yellow-Huaihe and Yangtze-Huaihe Rivers Basins, China. *J Clim* (2011) 24:3781–95. doi:10.1175/2010JCLI3653.1
5. Chen H. Projected Change in Extreme Rainfall Events in China by the End of the 21st century Using CMIP5 Models. *Chin Sci Bull* (2013) 58:1462–72. doi:10.1007/s11434-012-5612-2
6. Feng GL, Yang J, Zhi R, Zhao J-H, Gong Z-Q, Zheng Z-H, et al. Improved Prediction Model for Flood-Season Rainfall Based on a Nonlinear Dynamics-Statistic Combined Method. *Chaos, Solitons and Fractals* (2020) 140:110–60. doi:10.1016/j.chaos.2020.110160
7. Brubaker KL, Entekhabi D, and Eagleson PS. Estimation of continental Precipitation Recycling. *J Clim* (1993) 6:1077–89. doi:10.1175/1520-0442(1993)006<1077:EOCPR>2.0.CO;2
8. Dominguez F, Kumar P, Liang X-Z, and Ting M. Impact of Atmospheric Moisture Storage on Precipitation Recycling. *J Clim* (2006) 19:1513–30. doi:10.1175/JCLI3691.1
9. Tiwari V, Tripathi JP, Upadhyay RK, Wu Y-P, Wang J-S, and Sun G-Q. Predator-prey Interaction System with Mutually Interfering Predator: Role of Feedback Control, Predator–Prey Interaction System with Mutually Interfering Predator: Role of Feedback Control. *Appl Math Model* (2020) 87:222–44. doi:10.1016/j.apm.2020.04.024
10. Zou M, Qiao S, Feng T, Wu Y, and Feng G. The Inter-decadal Change in Anomalous Summertime Water Vapor Transport Modes over the Tropical Indian Ocean-Western Pacific in the Mid-1980s. *Int J Climatology* (2018) 13: 1–14. doi:10.1002/joc.5452
11. Wu Y-P, Feng G-L, and Li B-L. Interactions of Multiple Atmospheric Circulation Drive the Drought in Tarim River Basin. *Scientific Rep* (2016) 6:26470. doi:10.1038/srep26470
12. Wu Y-P, and Feng G-L. A New Algorithm for Seasonal Precipitation Forecast Based on Global Atmospheric Hydrological Water Budget. *Appl Maths Comput* (2015) 268:478–88. doi:10.1016/j.amc.2015.06.059
13. Budyko MI, and Drozdov OA. Regularities of the Hydrologic Cycle in the Atmosphere. *Izv Akad Nauk Sssr, Ser Geogr* (1953) 4:5–14.
14. Budyko MI. *Climate and Life*. London: Academic Press New York (1974). p. 507.
15. Burde GI, Zangvil A, and Lamb PJ. Estimating the Role of Local Evaporation in Precipitation for a Two-Dimensional Region. *J Clim* (1996) 9:1328–38. doi:10.1175/1520-0442(1996)009<1328:etrole>2.0.co;2
16. Eltahir EAB, and Bras RL. Precipitation Recycling in the Amazon Basin. *Q.J R Met. Soc.* (1994) 120:861–80. doi:10.1002/qj.49712051806
17. Eltahir EAB, and Bras RL. Precipitation Recycling. *Rev Geophys* (1996) 34: 367–78. doi:10.1029/96RG01927
18. Schär C, Lüthi D, and Beyerle U. The Soil Precipitation Feedback: A Process Study with a Regional Climate Model. *J Clim* (1999) 12:722–41. doi:10.1175/1520-0442(1999)012<0722:TSPFAP>2.0.CO;2
19. Van der Ent RJ, Savenije HHG, Schaefli B, and Steele-Dunne SC. Origin and Fate of Atmospheric Moisture over Continents. *Water Resour Res* (2010) 46: w09525. doi:10.1029/2010WR009127
20. Guo Y, and Wang C. Trends in Precipitation Recycling over the Qinghai-Xizang Plateau in Last Decades. *J Hydrol* (2014) 517:826–35. doi:10.1016/j.jhydrol.2014.06.006

21. Burde GI, and Zangvil A. The Estimation of Regional Precipitation Recycling. Part II: A New Recycling Model. *J Clim* (2001) 14:2509–27. doi:10.1175/1520-0442(2001)014<2509:TEORPR>2.0.CO;2
22. Burde GI, Gandush C, and Bayarjargal Y. Bulk Recycling Models with Incomplete Vertical Mixing. Part II: Precipitation Recycling in the Amazon Basin. *J Clim* (2006) 19:1473–89. doi:10.1175/JCLI3688.1
23. Hai HE, and Guihua LU. Precipitation Recycling in Tarim River Basin. *J Hydrol Eng* (2013) 18:1549–56. doi:10.1061/(ASCE)HE.1943-5584.0000503
24. Li R, Wang C, and Wu D. Changes in Precipitation Recycling over Arid Regions in the Northern Hemisphere. *Theor Appl Climatol* (2018) 131: 489–502. doi:10.1007/s00704-016-1978-4
25. Pathak A, Ghosh S, and Kumar P. Precipitation Recycling in the Indian Subcontinent during Summer Monsoon. *J Hydrometeorology* (2014) 15: 2050–66. doi:10.1175/JHM-D-13-0172.1
26. Hua L, Zhong L, and Ke Z. Characteristics of the Precipitation Recycling Ratio and its Relationship with Regional Precipitation in China. *Theor Appl Climatol* (2017) 127:513–31. doi:10.1007/s00704-015-1645-1
27. Lan Y, and Tao S. Construction and Analysis of a Precipitation Recycling Model. *Adv Water Sci* (1997) 8:205–11. [in Chinese]. doi:10.14042/j.cnki.32.13.9.1997.03.001
28. Fu X, Xu X, and Kang H. Research on Precipitation Recycling during Meiyu Season over Middle-Lower Reaches of Changjiang River in 1998. *Meteorol Sci Techn* (2006) 34:394–9. [in Chinese]. doi:10.19517/j.1671-6345.2006.04.010
29. Kang H, Gu X, Zhu C, and Paul W. Precipitation Recycling in Southern and Central China. *Chin J Atmos Sci* (2004) 28:892–900. [in Chinese]. doi:10.3878/j.issn.1006-9895.2004.06.08
30. Kalnay E, Kanamitsu M, Kistler R, Collins W, Deaven D, Gandin L, et al. The NCEP/NCAR 40-Year Reanalysis Project. *Bull Am Meteorol Soc* (1996) 77: 437–70. doi:10.1175/1520-0477(1996)077<0437:TNYRP>2.0.CO;2
31. Su T, Feng T, and Feng G. Evaporation Variability under Climate Warming in Five Reanalyses and its Association with pan Evaporation over Chinafive Reanalyses and its Association with pan Evaporation over China. *J Geophys Res Atmos* (2015) 120:8080–98. doi:10.1002/2014JD023040
32. Chu Q-c., Zhi R, Wang Q-g., and Feng G-l. Roles of Moisture Sources and Transport in Precipitation Variabilities during Boreal Summer over East China. *Clim Dyn* (2019) 53:5437–57. doi:10.1007/s00382-019-04877-z
33. Shi N, Chen J, and Tu Q. 4-phase Climate Change Features in the Last 100 Years over china. *Acta Meteologica Sinica* (1995) 53:431–9. [in Chinese].
34. Zhou T-J, and Yu R-C. Atmospheric Water Vapor Transport Associated with Typical Anomalous Summer Rainfall Patterns in China. *J Geophys Res* (2005) 110:D08104. doi:10.1029/2004JD005413
35. Chen B, Xu X-D, and Zhao T. Main Moisture Sources Affecting Lower Yangtze River Basin in Boreal Summers during 2004-2009. *Int J Climatology* (2013) 33: 1035–46. doi:10.1002/joc.3495
36. Wang N, Zeng X-M, Guo W-D, Chen C, You W, Zheng Y, et al. Quantitative Diagnosis of Moisture Sources and Transport Pathways for Summer Precipitation over the Mid-lower Yangtze River Basin. *J Hydrol* (2018) 559: 252–65. doi:10.1016/j.jhydrol.2018.02.003
37. Shi Y, Jiang Z, Liu Z, and Li L. A Lagrangian Analysis of Water Vapor Sources and Pathways for Precipitation in East China in Different Stages of the East Asian Summer Monsoon. *J Clim* (2020) 33:977–92. doi:10.1175/JCLI-D-19-0089.1
38. Huang S, and Huang F. Spatial-Temporal Variations of Dominant Drought/Flood Modes and the Associated Atmospheric Circulation and Ocean Events in Rainy Season over the East of China. *J Ocean Univ China* (2012) 11:137–46. doi:10.1007/s11802-012-1813-1
39. Yao H, Zhong Z, Zhang Y, Ding J, and Yang X. Relationship between Interannual Changes of Summer Rainfall over Yangtze River Valley and South China Sea–Philippine Sea: Possible Impact of Tropical Zonal Sea Surface Temperature Gradient. *Int J Climatology* (2019) 39:5522–38. doi:10.1002/joc.6169
40. Sun LH, and He M. The Relationship between Summer Precipitation in China and Circulation Anomaly in Eurasia and its Application in Precipitation Prediction. *Acta Meteorologica Sinica* (2004) 62:355–64. [in Chinese]. doi:10.3321/j.issn:0577-6619.2004.03.010
41. Wang B, Wu R, and Fu X. Pacific–East Asian Teleconnection: How Does ENSO Affect East Asian Climate. *J Clim* (2000) 13:1517–36. doi:10.1175/1520-0442(2000)013<1517:PEATHD>2.0.CO;2
42. Wang B, Wu RG, and Li T. Atmosphere-warm Ocean Interaction and its Impacts on Asian-Australian Monsoon Variation. *J Clim* (2003) 16:1195–211. doi:10.1175/1520-0442(2003)16<1195:AOIAII>2.0.CO;2
43. Huang R, Wen C, Yang B, and Zhang R. Recent Advances in Studies of the Interaction between the East Asian Winter and Summer Monsoons and ENSO Cycle. *Adv Atmos Sci* (2004) 21:407–24. doi:10.1007/BF02915568
44. Wu B, Li T, and Zhou T. Relative Contributions of the Indian Ocean and Local SST Anomalies to the Maintenance of the Western North Pacific Anomalous Anticyclone during the El Niño Decaying Summer*. *J Clim* (2010) 23:2974–86. doi:10.1175/2010JCLI3300.1
45. Zhang R, Min Q, and Su J. Impact of El Niño on Atmospheric Circulations over East Asia and Rainfall in China: Role of the Anomalous Western North Pacific Anticyclone. *Sci China Earth Sci* (2017) 60:1124–32. doi:10.1007/s11430-016-9026-x
46. Davarzani H, Smits K, Tolene RM, and Illangasekare T. Study of the Effect of Wind Speed on Evaporation from Soil through Integrated Modeling of the Atmospheric Boundary Layer and Shallow Subsurface. *Water Resour Res* (2014) 50:661–80. doi:10.1002/2013WR013952
47. Wang J, Wang Q, Zhao Y, Li H, Zhai J, and Shang Y. Temporal and Spatial Characteristics of pan Evaporation Trends and Their Attribution to Meteorological Drivers in the Three-River Source Region, China. *J Geophys Res Atmos* (2015) 120:6391–408. doi:10.1002/2014JD022874
48. Li N, Li Y, and Yao N. Bias Correction of the Observed Daily Precipitation and Re-division of Climatic Zones in China. *Int J Climatol* (2018) 38:3369–87. doi:10.1002/joc.5506
49. Xie S-P, Hu K, Hafner J, Tokinaga H, Du Y, Huang G, et al. Indian Ocean Capacitor Effect on Indo-Western Pacific Climate during the Summer Following El Niño. *J Clim* (2009) 22:730–47. doi:10.1175/2008JCLI2544.1
50. Ham Y-G. A Reduction in the Asymmetry of ENSO Amplitude Due to Global Warming: The Role of Atmospheric Feedback. *Geophys Res Lett* (2017) 44: 8576–84. doi:10.1002/2017GL074842
51. Huang P, Chen D, and Ying J. Weakening of the Tropical Atmospheric Circulation Response to Local Sea Surface Temperature Anomalies under Global Warming. *J Clim* (2017) 30:8149–58. doi:10.1175/JCLI-D-17-0171.1
52. Hori ME, and Ueda H. Impact of Global Warming on the East Asian winter Monsoon as Revealed by Nine Coupled Atmosphere-Ocean GCMs. *Geophys Res Lett* (2006) 33:L03713. doi:10.1029/2005GL024961
53. Liu J, Xu H, and Deng J. Projections of East Asian Summer Monsoon Change at Global Warming of 1.5 and 2 °C. *Earth Syst Dynam* (2018) 9:427–39. doi:10.5194/esd-9-427-2018
54. Gong H, Wang L, Zhou W, Chen W, Wu R, Liu L, et al. Revisiting the Northern Mode of East Asian Winter Monsoon Variation and its Response to Global Warming. *J Clim* (2018) 31:9001–14. doi:10.1175/JCLI-D-18-0136.1
55. Sun B, and Wang H. Analysis of the Major Atmospheric Moisture Sources Affecting Three Sub-regions of East China. *Int J Climatol* (2015) 35(9): 2243–57. doi:10.1002/joc.4145.(SCI)

Conflict of Interest: The authors declare that the research was conducted in the absence of any commercial or financial relationships that could be construed as a potential conflict of interest.

frontiers in Physics

ORIGINAL RESEARCH
published: 17 August 2021
doi: 10.3389/fphy.2021.723306

An Economy-Climate Model for Quantitatively Projecting the Impact of Future Climate Change and Its Application

Jieming Chou[1,2], *Yuan Xu*[1]*, *Wenjie Dong*[3,2], *Weixing Zhao*[1], *Jiangnan Li*[1] *and Yuanmeng Li*[1]

[1]State Key Laboratory of Earth Surface Processes and Resource Ecology, Faculty of Geographical Science, Beijing Normal University, Beijing, China, [2]Southern Marine Science and Engineering Guangdong Laboratory (Zhuhai), Zhuhai, China, [3]School of Atmospheric Sciences, Sun Yat-Sen University, Zhuhai, China

Quantitatively projecting the impact of future climate change on the socio-economy and exploring its internal mechanism are of great practical significance to adapt to climate change and prevent climate risks. Based on the economy-climate (C-D-C) model, this paper introduces a yield impact of climate change (YICC) model that can quantitatively project the climate change impact. The model is based on the YICC as its core concept and uses the impact ratio of climate change (IRCC) indicator to assess the response of the economic system to climate change over a long period of time. The YICC is defined as the difference between the economic output under changing climate condition and that under assumed invariant climate condition. The IRCC not only reflects the sensitivity of economic output to climate change but also reveals the mechanism of the nonlinear interaction between climate change and non-climatic factors on the socio-economic system. Using the main grain-producing areas in China as a case study, we use the data of the ensemble average of 5 GCMs in CMIP6 to project the possible impact of climate change on grain production in the next 15–30 years under three future scenarios (SSP1-2.6, SSP2-4.5, SSP5-8.5). The results indicate that the long-term climate change in the future will have a restraining effect on production in North region and enhance production in South region. From 2021 to 2035, climate change will reduce production by 0.60–2.09% in North region, and increase production by 1.80–9.01% in South region under three future scenarios. From 2021 to 2050, compared with the climate change impact in 2021–2035, the negative impact of climate change on production in North region will weaken, and the positive impact on production in South region will enhance with the increase in emission concentration. Among them, climate change will reduce grain output in North region by 0.52–1.99%, and increase output in South region by 1.35–9.56% under the three future scenarios. The combination of economic results and climate change research is expected to provide scientific support for further revealing the economic mechanism of climate change impacts.

Keywords: climate change, economy-climate model, mechanism, grain production, impact assessment

OPEN ACCESS

Edited by:
Gui-Quan Sun,
North University of China, China

Reviewed by:
Yinpeng Li,
International Global Change Institute (IGCI), New Zealand
Xiong Zhe,
Institute of Atmospheric Physics, Chinese Academy of Sciences (CAS), China

****Correspondence:***
Yuan Xu
xuyuan01@mail.bnu.edu.cn

Specialty section:
This article was submitted to Interdisciplinary Physics, a section of the journal Frontiers in Physics

Received: *10 June 2021*
Accepted: *03 August 2021*
Published: *17 August 2021*

Citation:
Chou J, Xu Y, Dong W, Zhao W, Li J and Li Y (2021) An Economy-Climate Model for Quantitatively Projecting the Impact of Future Climate Change and Its Application. Front. Phys. 9:723306. doi: 10.3389/fphy.2021.723306

INTRODUCTION

The impact of climate change on the social economy is an important field and a main link in research on climate change impacts. The sustainable development of human society and the economy has been severely affected by climate change, and this phenomenon will continue. From the Chinese region at the small scale to the global region at the large scale, climate not only has the characteristics of drastic seasonal and interannual changes at the short time scale [1–3] but also has obvious interdecadal changes at the long time scale [4,5]. Climate change not only indirectly affects the economic system through direct impacts on water resources, ecosystems, and land surface conditions but also increases the negative effects of meteorological disasters caused by extreme events on the economic system [6]. The risk climate change poses for the economic system is expected to increase with global warming at 1.5°C and further increase with warming at 2°C [1]. How humans respond and adapt to climate change is an issue of combining natural science with socioeconomic applications. It is necessary to link the results of climate change with economic theories to conduct multidisciplinary studies on the impact of future climate change [7,8]. Therefore, exploring a quantitative method for projecting the impact of future climate change on the economic system is of great significance to the prevention of climate change risks.

In the future, the impact of climate change on the socioeconomic system may become greater under different greenhouse gas emission scenarios [3]. At present, there are many methods used to study the economic impact of climate change in China and abroad, which mainly include non-model methods and model-based methods. Non-model methods include statistical regression [9,10], historical experience comparison [11], questionnaire survey [12], literature review [13], and meteorological output methods [14]. However, most statistical regression methods have the disadvantages of ignoring the long-term trend climatic changes and the nonlinear interaction between climate change and the economy. The other methods are subjective and uncertain. The model methods include empirical statistical models [15], natural mechanism models [16,17], and economic mechanism models, which are currently common methods for studying the impact of future climate change. Among them, the natural mechanism model based on crop models is a purely natural experimental research method, which requires a solid experimental observation basis and generally does not involve socioeconomic factors. Economic mechanism models quantitatively assess the impact of climate change on different economic systems from an economic perspective, including the Ricardian model [18–20], computable general equilibrium (CGE) model [21,22], and economy-climate (C-D-C) model [23,24]. Among them, the C-D-C model can integrate climatic and economic factors and deal with the climatic factor parameters on the average climate state, taking into account the long-term trend of climatic factors. In addition, the model is relatively simple, with convenient data acquisition and easy operation. Therefore, we select the economy-climate model to develop a model that can project the impact of future climate change on the economic system on a long-term scale.

The C-D-C model is mainly applicable for evaluating the impact of climate change on economic output by the incorporation of climatic and socioeconomic factors. Essentially, it does not focus on the natural science of climate change itself but uses climate change as an economic factor to analyze its contribution to economic development. Its effectiveness has been tested mostly on wheat, maize, and rice in China's grain-producing areas [25,26]. The climate change impact assessment part of the model focuses on analyzing the impact of climate change on economic output based on the output elasticity of climatic factors. In recent years, studies have used the C-D-C model to analyze the effects of temperature and precipitation changes on the rice yield in different regions [27,28], initially developed the concept and method of "the yield impact of climate change" [24], and assessed the regional sensitivity of crop yields to changes in comprehensive climate factors [26]. The persistent improvement in the simulation capabilities of climatic models and the continuous emergence of future prediction data of CMIP6 have enabled the use of the C-D-C model, and prediction data have made it possible to quantitatively predict the impact of future climate change.

Based on the above, this study aims to further introduce and popularize the yield impact of the climate change (YICC) model to explore the impact of future climate change on economic output. In addition, it carries out a case study on the model in the North and South regions of China's main grain-producing areas. In other words, this study's objective is to derive a YICC model based on the C-D-C model, use the impact ratio of the climate change index to project the impact of future climate change on economic output, and apply it to China's main grain-producing areas. As critical areas in China, the main grain-producing areas are a breadbasket but also areas vulnerable to climate change. Among them, the North region presents a warm, dry trend with increasing temperature and decreasing precipitation, while the South region presents a warm-humidification trend with increasing temperature and precipitation [29]. This uneven and obvious trend of climate change inevitably affects agricultural production and economic development. The goal is therefore to use the findings to inform and support policies towards preventing the risk climate change poses to crops and improving the sustainable development of the agricultural economy. The section that follows discusses the methods and case study.

THEORETICAL BASIS OF THE ECONOMY-CLIMATE MODEL

The economic system is a complex system, an organic combination of the relationships among economic elements [24]. Economic output is subject to the combined influence of socio-economic and climatic factors. Climate change impacts are a complex nonlinear system that is subject to the interaction of many factors, and it is necessary to integrate

economics and climatology for cross-disciplinary study [30,31]. In addition, climate change has economic characteristics. First, climate change is an exogenous factor and has external effects. As a public natural resource, climate change is regarded as a public good in the field of economics and is not controlled by any individual or state. Therefore, it has randomness and uncertainty. Climate change, characterized by rising global temperatures, is mainly caused by excessive emissions of greenhouse gases in certain countries, and its impacts not only involve the emitting regions but also spread across borders to other countries and regions [32]. Climate change has no borders. Second, climate resources are not restricted by national boundaries, so they are shared natural resources. They do not require investment or payment of any usage fees and entail no cost and profit calculations. Third, economic growth is mainly caused by external environmental factors and internal economic activities. As one of the external factors, climate change needs to be combined with economic activity factors to take effect. Evaluation of the economic impact of climate change does not focus on the natural science of climate change itself but uses climate change as an economic factor to analyze its contribution to or impact on economic development, that is, to analyze the economic impact of climate change from a socio-economic perspective [30]. Climate change has these economic characteristics that are basically consistent with economic growth. Scholars have used "climate change" as an economic input factor to construct an economy-climate (C-D-C) model to evaluate the impact of climate change on economic growth [23].

The Cobb-Douglas production function model (C-D model) is a classic mathematical model in the field of economics. It is easy to operate and widely used and has the advantages of convenient parameter retrieval in modeling [33]. The C-D-C model is based on the C-D production function model and adds climatic factors to construct an econometric model to evaluate the impact of climate change on the economic system [23]. In addition, with this study, we introduce into the model the comprehensive climate factor (CCF), a new factor constructed in previous studies, and analyze the economic impact of changes in the comprehensive climate factor on the yields of different crops in China's main grain-producing areas over the past 35 years (1981–2015) [5]; [26]. The C-D-C model represents the functional relationship between the number of input factors and the economic output in the production process over a long period of time (more than 10 years), and its formula is shown in **Eq. 1**. where Y is the economic output, x_i is the economic factor ($i \geq 3$), β_i is the output elasticity corresponding to the economic factor, C is the comprehensive climate factor, γ is the output elasticity corresponding to the climatic factor (also called "climatic output elasticity"), α represents the sum of the influence of factors other than economic and climatic factors, and $N = \alpha \cdot x_1^{\beta_1} \cdot x_2^{\beta_2} \cdots x_i^{\beta_i}$ is expressed as the sum of the effects of factors other than climate change on economic output. This model has some advantages:

A. The dimension of variables does not need to be considered in modeling, and the function formula can be logarithmically linearized into **Eq. 2**, which is easier to process and calculate.
B. Both short time scale meteorological factors and long time scale climatic factors can be added as input factors.
C. The comprehensive climate factor is a combination of a variety of climate factors (such as temperature, precipitation, sunshine hours), reflecting the main change trend of a variety of climatic factors, and its formula is shown in **Eq. 3**, where n represents the number of climate factor variables, c_i is the i-th climatic factor, and δ_i is the weight corresponding to the i-th climatic factor. This factor was calculated by principal component analysis (PCA) method.
D. The model expresses the relationship between economic output and its influencing factors in the form of an exponential product, reflecting the nonlinear interaction between economic and climatic factors in the production process.
E. Output elasticity is an economic concept. It reveals the change rate of economic output caused by the change rate of an input factor under the condition that other input factors remain unchanged. The sensitivity to changes in the input factors can also simply distinguish the influence of climatic and economic factors on economic output. For example, the output elasticity corresponding to the climate change factor is γ, which means that under the condition that non-climatic factors remain unchanged, every 1% increase in climatic factors increases economic output by γ%.

$$\boldsymbol{Y = \alpha \cdot x_1^{\beta_1} \cdot x_2^{\beta_2} \cdots x_i^{\beta_i} \cdot C^{\gamma} = N \times C^{\gamma}} \quad (1)$$

$$\boldsymbol{lnY = \beta_1 lnx_1 + \beta_2 lnx_2 + \cdots\cdots + \beta_i lnx_i + \gamma lnC + ln\alpha} \quad (2)$$

$$\boldsymbol{C = \sum_{i=1}^{n} (\delta_i \times c_i) = \delta_1 \times c_1 + \delta_2 \times c_2 + \cdots + \delta_n \times c_n} \quad (3)$$

When assessing the impact of climate change on economic output, we mainly use climatic output elasticity as the evaluation index to focus on the analysis of the impact of changes in climatic factor C, and use the output elasticity of climate change factors to reflect the contribution of climate change to economic output. The model schematic diagram is shown in **Figure 1**, which mainly includes three parts. The first part is the selection of indicators, including input and output factors. The input factors are composed of climatic and non-climatic factors. The second part is the construction of the model. The selected indicators are introduced into the model for calculation and simulation to obtain the output elasticity corresponding to the climatic factor. The third part is the impact assessment, which analyzes the impact of climate change on economic output by the output elasticity of the climatic factors.

From **Equations 1–2**, it can be seen that as long as the economic data and climate change data are obtained, the output elasticity of each input element can be calculated. Historical economic data can be obtained through the National Bureau of Statistics and the Statistical Yearbook in China. Historical and future climatic data can be obtained not only through observational data from the National Meteorological Administration in China but also through

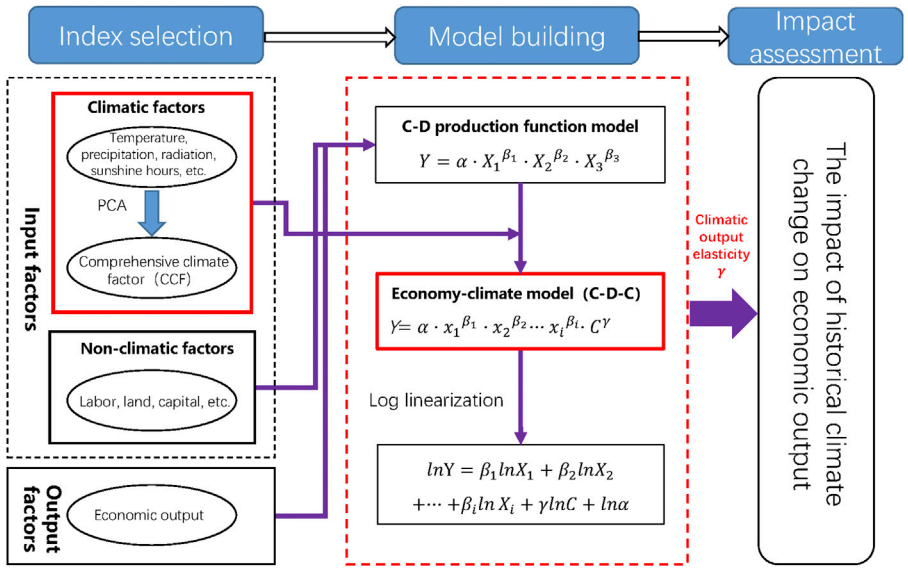

FIGURE 1 | Schematic diagram of the economy-climate (C-D-C) model. Y is an economic output, x_i is an economic factor ($i \geq 3$), β_i is an output elasticity corresponding to the economic factor, C is a climatic factor, γ is an output elasticity corresponding to climatic factor (called "climatic output elasticity"), α represents the sum of the influence of factors other than economic and climatic factors.

simulations using different climate models in the international CMIP6 experiment. However, due to the randomness and uncertainty of the economic development laws of the country and society, it is difficult to obtain future economic data. Therefore, the C-D-C model has been widely used to assess the impact of historical climate change on food production [26–28]. To solve the difficulty of predicting the impact of future climate change, it is necessary to further explore a new method based on the C-D-C model.

MECHANISM OF THE YICC MODEL

Global climate change has significant interdecadal characteristics, and there are multiple time-scale changes in China [4]. Climate has its own changing trend on the interdecadal time scale, which affects the economic system. As the output of the production system, economic output is the result of the nonlinear interaction between socio-economic factors and natural factors rather than the linear superposition of their individual effects. To distinguish the impact of climate change on economic output under nonlinear conditions and to compensate for the limitations of the C-D-C model in predicting the impact of future climate change, we introduce a method for projecting the impact of climate change—the yield impact of climate change (YICC) model.

The Yield Impact of Climate Change

The yield impact of climate change is different from the meteorological yield, which linearly decomposes crop yield into three parts: technical yield, meteorological yield and random yield. However, it does not consider the long-term trend of climatic factors and the changes in yield caused by factors such as crop sown area [14,34]. On decadal or even longer time scales (decades or even hundreds of years), the climate has a changing trend. Therefore, in the process of studying the impact of future climate change, long-term climate change cannot be ignored and must be considered.

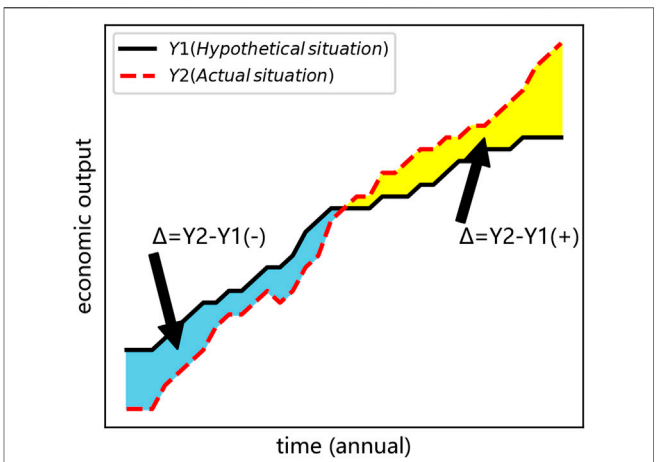

FIGURE 2 | Schematic diagram of the yield impact of climate change. Y_1 is the economic growth state (idealized state) when the climate does not change, and Y_2 is the actual state of future economic growth. Δ represents the impact of climate change on economic output, that is, the difference between Y_2 and Y_1. (–) indicates that the impact of climate change is negative, (+) indicates that the impact of climate change is positive.

The variation in economic output not only depends on the input of production factors but is also affected by many factors, such as the scientific level, technological progress, policies, and

the natural environment. It is the result of the combined effects of various factors. Therefore, under the comprehensive effects of climatic and economic factors, the following method quantitatively distinguishes the effects caused by climatic factors.

After n years (the first n years, $n \geq 15$), economic output presents a state of economic growth. After another n years (next n years), we assume that the climatic state remains unchanged in the first n years, and the economic output will have another state of economic growth under continuous changes in nonclimatic factors, denoted as Y_1. It is important to emphasize here that Y_1 is a hypothetical situation. If continuous changes in climatic state are taken into account, there will be another growth state in economic output, denoted as Y_2. It needs to be highlighted that Y_2 is an actual situation, that is, the economic state under the influence of continuous changes in both climatic and nonclimatic factors. Compared with the former, the latter will change. In short, the remaining state after Y_1 is removed from Y_2 is the influence caused by climatic factors. Thus, the goal of quantitatively distinguishing the influence caused by climatic factor is achieved. This change is the impact of climate change on economic output. We define this change as the yield impact of climatic change (YICC). In other words, the impact of climate change is the difference between Y_2 and Y_1, denoted as $\Delta = Y_2 - Y_1$. The schematic diagram is shown in **Figure 2**. What we want to study is the difference between economic output under a changing climatic state and that under a constant climatic state to indicate the impact of climate change on economic output.

Model Mechanism

Over time, climatic factors and nonclimatic factors change, so the actual economic outputs are the result of the comprehensive effect of these two changes. The C-D-C model reflects this situation. In the YICC, Y_1 is only a hypothetical value and has no actual data, so the results of climate model predictions can be used. Therefore, the C-D-C model cannot be used directly to predict the impact of climate change in the future, and further derivation is needed. First, four preconditions need to be made:

A. Assume that the mean states of economic output, nonclimatic and climatic factors are Y_0, N_1, and C_1 in the first n years (1, 2, 3..., n, $n \geq 15$), respectively. The climatic output elasticity is γ_1, as shown in **Eq. 4**.
B. Assuming that the climatic state does not undergone continuous changes during the next n years (still C_1) and the economic state does undergone continuous changes (N_2), then Y_1 is the amount of economic output that meets this condition, as shown in **Eq. 5**
C. Assuming that the climatic and economic states in the next n years ($n + 1$, $n + 2$..., $2n$) will undergone continuous changes, then the mean states of economic output, nonclimatic factors and climatic factors are Y_2, N_2, and C_2. The climate output elasticity is γ_2, as shown in **Eq. 6**.
D. Since statistical data on the future economy are not available, the climatic output elasticity γ_2 in the future cannot be calculated by the C-D-C model. We thus set $\gamma_2 = \gamma_1$, which is based on the historical climatic output elasticity, and assume that the future climate factors will continue to change in accordance with the elastic changes over historical time.

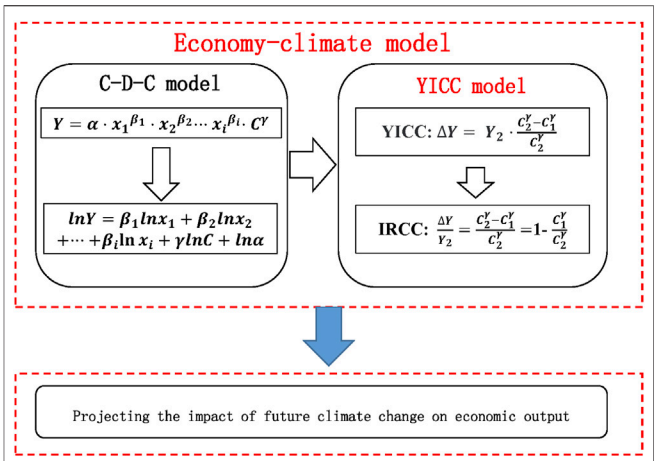

FIGURE 3 | A framework diagram of the economy-climate model for predicting the yield impact of climate change. Y is an economic output, x_i is an economic factor ($i \geq 3$), β_i is an output elasticity corresponding to the economic factor, C is a climatic factor, γ is an output elasticity corresponding to climatic factor (called "climatic output elasticity"), α represents the sum of the influence of factors other than economic and climatic factors. $\Delta Y/Y_2$ is the impact ratio of climate change (IRCC).

Finally, we define the difference (ΔY) between Y_2 and Y_1 as the "yield impact of climate change" in the next n years. The mathematical formula is shown in **Eq. 7**. It should be emphasized that the mean state values here are all multi-year averages for n years.

$$Y_0 = N_1 \times C_1^{\gamma_1} \tag{4}$$

$$Y_1 = N_2 \times C_1^{\gamma_1} \tag{5}$$

$$Y_2 = N_2 \times C_2^{\gamma_2} \tag{6}$$

$$\Delta Y = Y_2 - Y_1 = Y_2 \times \frac{C_2^{\gamma_1} - C_1^{\gamma_1}}{C_2^{\gamma_1}} \tag{7}$$

Indicator for the Impact Ratio of Climate Change

The yield impact of climate change (ΔY) is mainly determined by the future economic output (Y_2), the mean state of future climatic factor change (C_2), and the mean state of past climatic factor change (C_1). The inability to accurately know the future economic output (Y_2) and other socio-economic factor data make it difficult to directly calculate the impact of climate change. Y_1 is an imaginary value, and there are no actual data to use. Therefore, to project the impact of future climate change on economic output, ΔY needs to be further derived and transformed into **Eq. 8**. $\Delta Y/Y_2$ is called the impact ratio of climate change (IRCC).

$$IRCC = \frac{\Delta Y}{Y_2} = \frac{C_2^{\gamma_1} - C_1^{\gamma_1}}{C_2^{\gamma_1}} = 1 - \frac{C_1^{\gamma_1}}{C_2^{\gamma_1}} \tag{8}$$

The impact ratio of climate change is a benefit indicator that measures the impact of climate change on economic output and

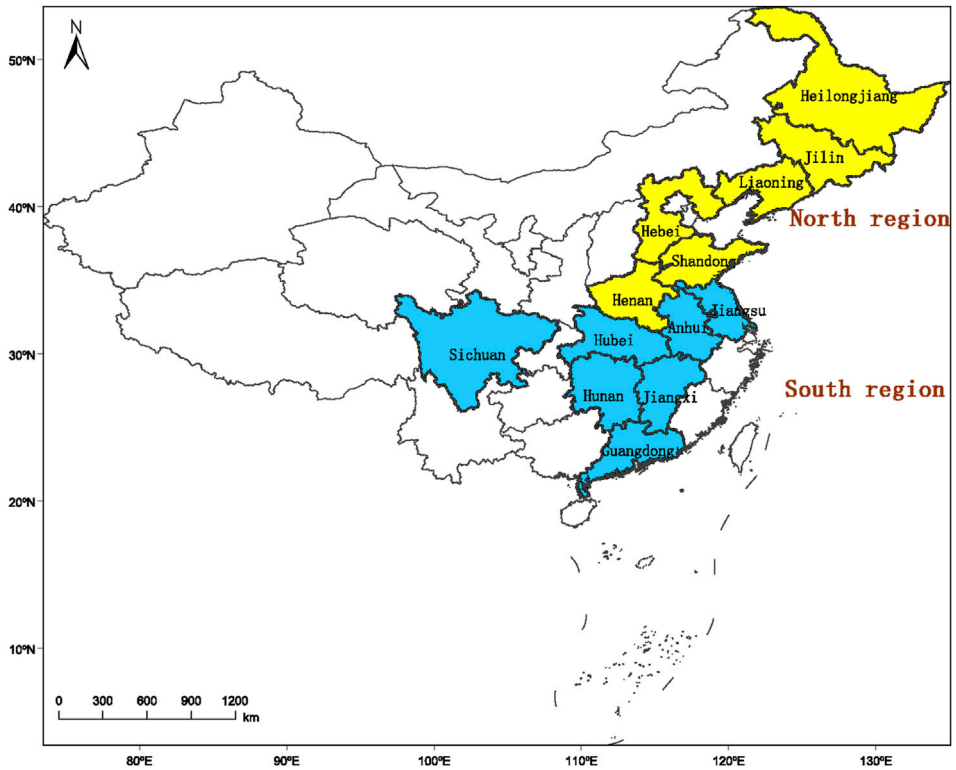

FIGURE 4 | The main grain-producing areas in China. The yellow area presents the North region, and the blue area shows the South region.

reflects the weight of the impact of climate factors on actual economic output. From an economic point of view, the greater the ratio is, the greater the proportion of the yield impact of climate change, in other words, the greater the impact of climate change on economic output. If the ratio is positive, it means that climate change has a positive effect on economic output. If the impact ratio of climate change is negative, it means that climate change has a negative impact on economic output. In addition, the forecast of the IRCC reflects that future economic output is the result of the nonlinear interaction of climatic factors and nonclimatic factors. We apply the IRCC model to the main grain-producing areas in China to project the impact of climate change on grain production in the next 15–30 years. The framework diagram of the economy-climate model is shown in **Figure 3.**

CASE STUDY

Study Area

The main grain-producing areas are important bases for grain production and an important contribution to food security. A total of 72.2% of the country's mean annual grain production comes from 13 main grain-producing areas in China (**Figure 4**), and their mean annual grain production concentration from 1981 to 2015 totaled 73.8% [29]. According to previous studies, the main grain-producing areas can be divided into the North and South regions [26]. The North region includes Heilongjiang (HeiLJ), Jilin (JiL), Liaoning (LiaoN), Hebei (HeB), Shandong (ShanD), and Henan (HeN) Provinces. The South region includes Anhui (AnH), Jiangsu (JiangS), Jiangxi (JiangX), Hubei (HuB), Hunan (HuN), Guangdong (GuangD), and Sichuan (SiC) Provinces.

Data

The climate model data include historical data and future scenario data of average temperature (unit: K), precipitation (unit: mm), surface downward shortwave radiation flux (unit: w/m^2) and CO_2 concentration (unit: mol/mol), which are derived from five global climate models tested in Coupled Model Intercomparison Project Phase 6 (CMIP6) (https://esgf-node.llnl.gov/search/cmip6/). The historical period is from April to September in 1981–2014, and the future period is from April to September in 2021–2050. The basic information of the five global climate model data is shown in **Table 1**. The future scenario data are predicted data under three different shared socio-economic paths (SSP1-2.6, SSP2-4.5, SSP5-8.5). The SSP-RCP scenario is an SSP scenario constructed based on the RCP scenario. This comprehensive scenario can better analyze the links and impacts of climate change and the social economy [35]. Among them, SSP1-RCP2.6 (SSP1-2.6) is the scenario with the lowest greenhouse gas emissions under sustainable development conditions. SSP2-RCP4.5 (SSP2-4.5) is described as a scenario with moderate greenhouse gas emissions under moderate development conditions. SSP5-RCP8.5 (SSP5-8.5) is described

TABLE 1 | Information regarding five CMIP6 climate models used in this study.

Model	Institution	Resolution (latitude × longitude)
BCC-CSM2-MR	Beijing Climate Center (BCC), China	1.1° × 1.125°
CESM2	National Center for Atmospheric Research (NCAR), USA	0.9° × 1.25°
GFDL-ESM4	National Oceanic and Atmospheric Administration, Geophysical Fluid Dynamics Laboratory (GFDL), USA	1.0° × 1.25°
NorESM2-LM	NorESM Climate modeling Consortium consisting of CICERO, Norway	1.9° × 2.5°
MRI-ESM2-0	Meteorological Research Institute (MRI), Japan	2.8° × 2.8°

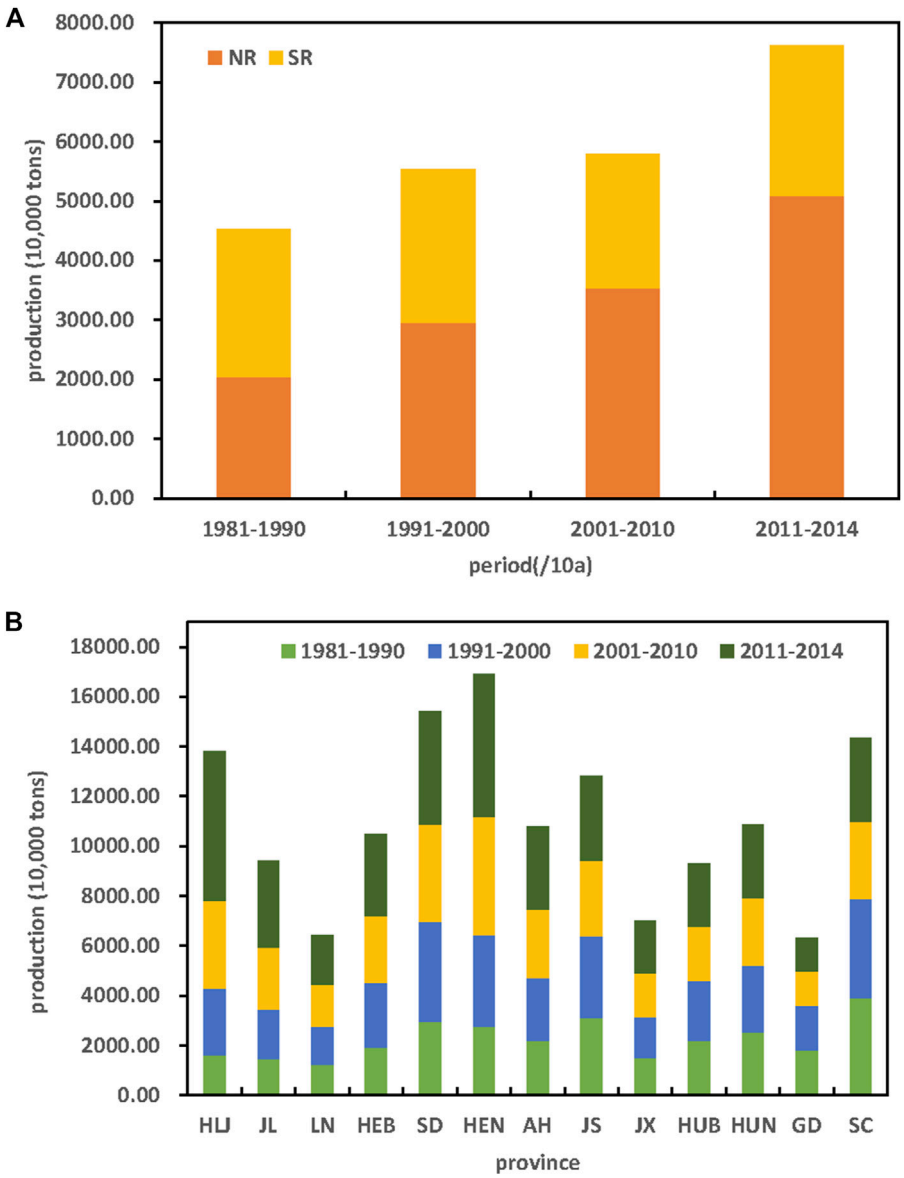

FIGURE 5 | The interdecadal changes in the grain production in the China's main grain-producing areas. **(A)**, the interdecadal grain production changes in the North and South regions from 1981 to 2014. **(B)**, the interdecadal changes in grain production in 13 provinces from 1981 to 2014, the first six provinces belong to the North region, and the last seven provinces belong to the South region. The North region (NR) includes Heilongjiang (HeiLJ), Jilin (JiL), Liaoning (LiaoN), Hebei (HeB), Shandong (ShanD) and Henan (HeN) Provinces. The South region (SR) includes Anhui (AnH), Jiangsu (JiangS), Jiangxi (JiangX), Hubei (HuB), Hunan (HuN), Guangdong (GuangD) and Sichuan (SiC) Provinces.

as the scenario with the highest greenhouse gas emissions under conventional development conditions. Since the resolution of each model is different, we need to first interpolate the model data to a grid station with a resolution of 0.5° × 0.5° through the bilinear interpolation method. Multi-model ensemble average (MME) is the equal-weight arithmetic average of multi-model simulation results. The climatic index (*C*) selected in this study is the comprehensive climate factor (CCF). It is constructed by the principal component analysis method from the average temperature, precipitation, radiation flux, and CO_2 concentration. The method description is shown in a previous study by Chou et al. [5].

The economic indices include the number of rural employed persons (unit: 10,000 persons), sown area of grain crops (unit: 1,000 ha), total power of agricultural machinery (unit: 10,000 kW), volume of effective component of chemical fertilizer (unit: 10,000 tons) and areas covered by natural disasters (unit: 1,000 ha). The economic output index is the output of grain crops (unit: 10,000 tons). The economic data come from the National Bureau of Statistics (http://www.bjstats.gov.cn) and the "Statistical Yearbook" of the provinces from 1981 to 2015. Since economic data are statistical data and cannot be used directly, they need to be preprocessed to enhance the credibility, rationality and consistency of the variable data used in the modeling. Both climatic data and economic data were preprocessed by the administrative area weight method and the three-point moving average method. The processed data can be found in **Supplementary Tables 1–4**.

The Current Situation of Grain Production in China

In the past 34 years (1981–2014), the interdecadal variation in total grain production in the North region has shown a clear increasing trend, while the interdecadal variation in production in the South region has shown a decreasing trend (**Figure 5A**). In particular, the total grain production in the North region has increased at a faster rate, reaching 9,669,300 tons/(10a). There have been obvious interdecadal differences in the grain production level of each province over the past 34 years (**Figure 5B**). In the North region, the total grain production of Heilongjiang and Henan Provinces has increased rapidly. In the South region, the production of Anhui Province has increased rapidly, but the interdecadal changes in the production of Guangdong and Sichuan Provinces have shown a downward trend.

Characteristics of Future Climate Change

Temperature, sunshine, and water are the most direct natural conditions for crops, and they are also important natural factors that affect crop production and sustainable development. In our previous research, we have found that changes in the climate elements in various provinces show complex, varying and regional characteristics of cold-warm and dry-wet cycles [29]. Different climatic conditions and regions have various possible impacts on grain production in China during the growth season. We thus chose average temperature, precipitation, radiant flux and CO_2 concentration as input factors for climate.

Driven by the complex and changeable climate system, the global climate model has become a powerful tool for studying future climate change and a vital tool for climate projection under different greenhouse gas emission scenarios [36]. With the increase in anthropogenic greenhouse gas emissions and changes in land use, the CMIP6 plan provides key data support for future climate change mechanism research and climate change mitigation and adaptation research based on various shared social and economic paths [37]. However, the climate models in the plan differ greatly in terms of mechanisms, climate forcing, model resolution, and scenario design, so they have different performances in simulating climate change. We first interpolate each model data to a grid with a resolution of 0.5° × 0.5° through the bilinear interpolation method, and then perform equal-weight arithmetic averages on the five model data. To visually observe the changing trend of future climate factors, we determine the difference between the average state of climate factors in the future time and the past time period.

The climate change in China's main grain-producing areas in the next 15 and 30 years will be similar under three different climate scenarios. Compared with the past 34 years (1981~2014), the climate change in the North region in the next 15 years (2021–2035) will present a trend of increasing temperature, slightly increasing precipitation and radiation flux, and a significant increase in CO_2 concentration. The trend of climate change in the South region is a slight increase in temperature, a slight decrease in precipitation, and a significant increase in radiant flux and CO_2 concentration (**Figure 6**). The temperature change in the North region is larger than that in the South region, and the radiant flux change in the South region is greater than that in the North region, mainly due to the latitude. The climate change in the next 30 years (2021~2050) is consistent with the change trend in 2021~2035, and climate change will be strengthened (**Figure 7**).

In fact, the growth and development of crops is not an independent impact of a single climatic factor but is an integrated effect of multiple climatic factors. This study constructed the main climatic factors (i.e., air temperature, precipitation, radiation flux and CO_2 concentration) into a Comprehensive Climate Factor (CCF) and quantitatively analyzed the impacts of integrated climate change in China's main grain-producing areas. This is a creative research method that combines complex factors in order to study main trends. The CCF is an important evaluation indicator that integrates information from climatic factors and provides a new perspective for research on regional responses to integrated climate change.

Projection of the Yield Impact of Future Climate Change

The year 2021 is the first year of China's "14th Five-Year Plan", and China has entered a new stage of accelerating the development of agricultural modernization and comprehensively promoting rural revitalization. The year 2035

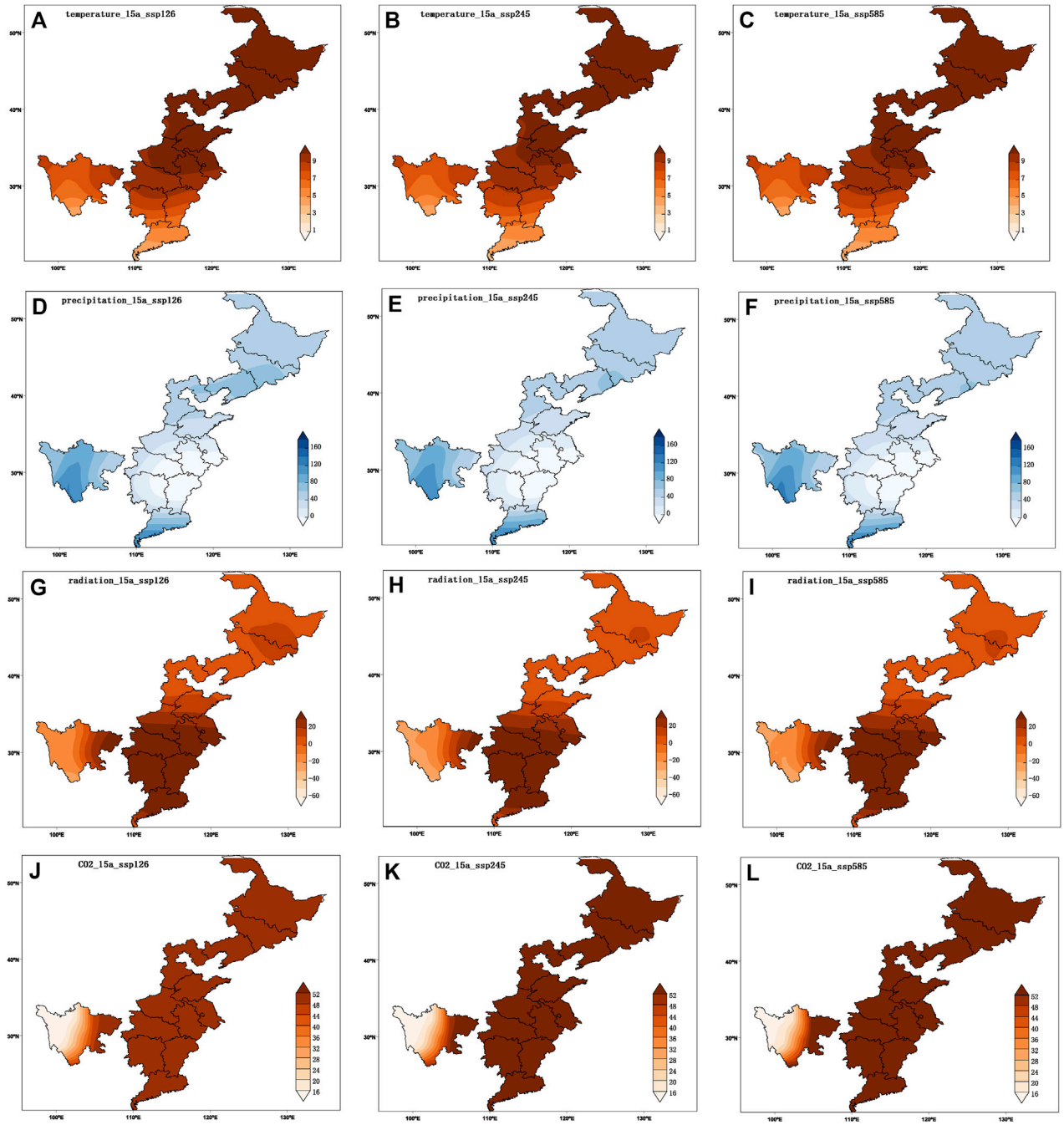

FIGURE 6 | Distribution of changes in climatic factors in China's main grain-producing areas in the next 15 years (2021–2035) under three future scenarios. **(A, B, C)** are the spatial distribution of mean temperature in SSP1-2.6, SSP2-4.5 and SSP5-8.5 scenarios, respectively. **(D, E, F)** are the spatial distribution of precipitation in SSP1-2.6, SSP2-4.5 and SSP5-8.5 scenarios, respectively. **(G, H, I)** are the spatial distribution of radiation in SSP1-2.6, SSP2-4.5 and SSP5-8.5 scenarios, respectively. **(J, K, L)** are the spatial distribution of CO_2 concentration in SSP1-2.6, SSP2-4.5 and SSP5-8.5 scenarios, respectively. The value is the difference between the mean annual value from 2021 to 2035 and the mean annual value from 1981 to 2014.

is the last year for China to basically realize socialist modernization, and the grain planting area will remain generally stable by 2035 [38]. The year 2050 is the last year for China to become a powerful modern socialist country. China's social and economic development trends and patterns will inevitably undergo great changes from 2021 to 2050. Moreover, 2035 and 2050 can reflect China's phased economic development and changes. Based on this, we use the years 1981~2014 as the base period to predict the average change in the next 15 years (2021~2035) and the next 30 years (2021~2050).

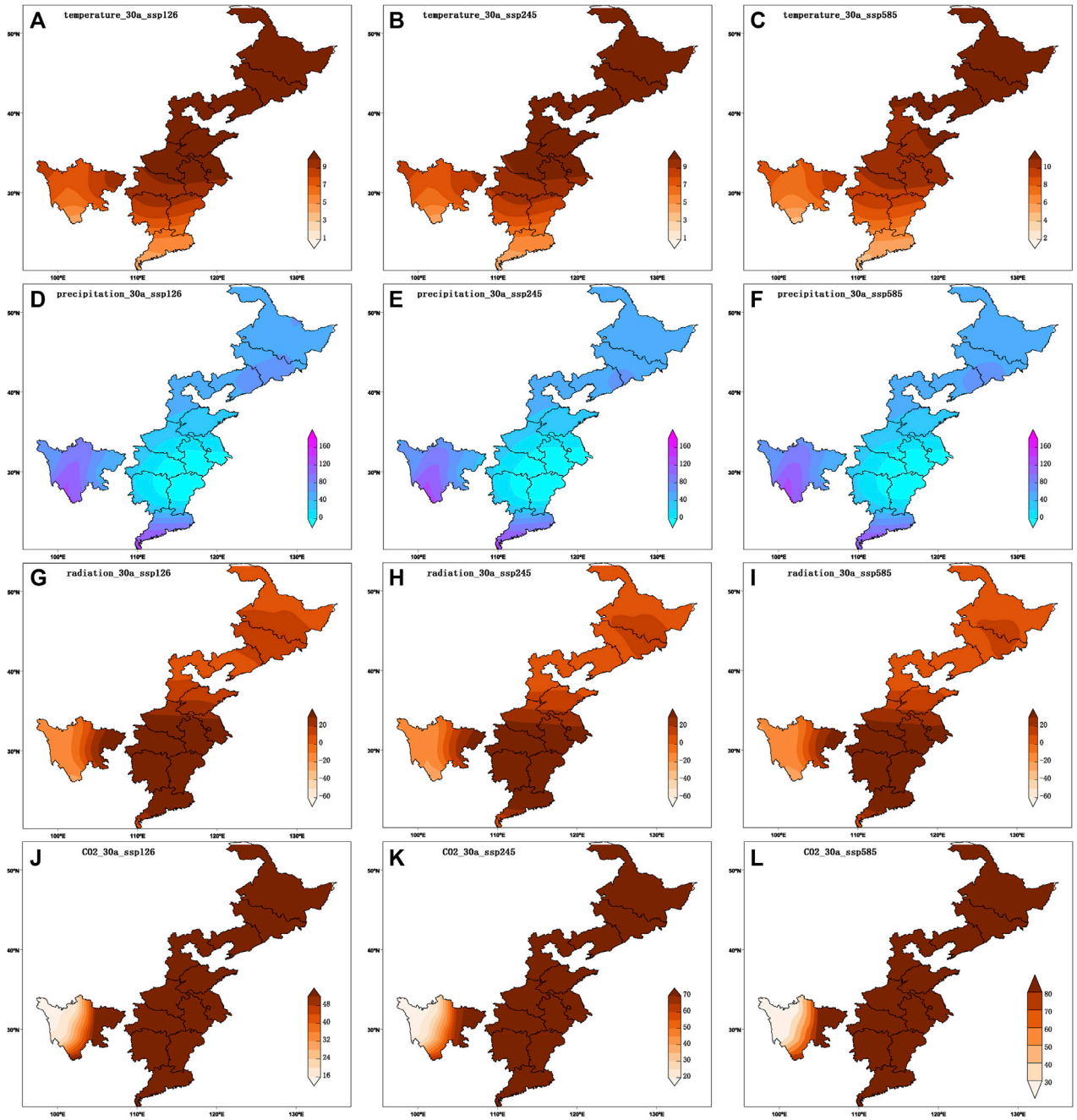

FIGURE 7 | Distribution of changes in climatic factors in China's main grain-producing areas in the next 30 years (2021–2050) under three future scenarios. **(A, B, C)** are the spatial distribution of mean temperature in SSP1-2.6, SSP2-4.5, and SSP5-8.5 scenarios, respectively. **(D, E, F)** are the spatial distribution of precipitation in SSP1-2.6, SSP2-4.5 and SSP5-8.5 scenarios, respectively. **(G, H, I)** are the spatial distribution of radiation in SSP1-2.6, SSP2-4.5 and SSP5-8.5 scenarios, respectively. **(J, K, L)** are the spatial distribution of CO_2 concentration in SSP1-2.6, SSP2-4.5 and SSP5-8.5 scenarios, respectively. The value in the figure is the difference between the mean annual value from 2021 to 2050 and the mean annual value from 1981 to 2014.

First, the climatic output elasticity of the North and South regions from 1981 to 2014 is calculated. According to **Eqs. 1**, **2** of the C-D-C model, the comprehensive climate factor and economic factor data are introduced into the C-D-C model to obtain the output elasticity of the comprehensive climate factor. Among them, the climatic output elasticity is 0.037 in the North region and -0.211 in the South region. The climatic output elasticity of the North region passes the 1% significance level, which shows that climate change in the past 34 years has promoted the total grain production. The climate output elasticity of the South region is negative, but the negative impact of climate change on the total grain output is not significant. Under the condition that other

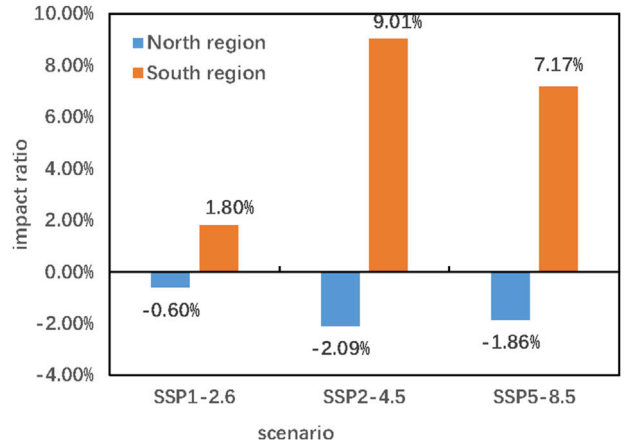

FIGURE 8 | The impact ratio of climate change in the main grain-producing areas from 2021 to 2035.

nonclimatic factors remain unchanged, for every 10% increase in the comprehensive climate factor, the production in the North region increases by 0.37%, and the production in the South region decreases by 2.11%. The main reason may be that: environment and climate in the North region are affected by global warming, which reduces the damage caused by natural disasters (e.g., low temperature and frost damage). Moreover, agricultural production conditions have improved significantly, such as gradual improvements in agricultural production, the strengthening of agricultural infrastructure construction, increase in agricultural subsidy support policies, and continued agricultural technological development, which has increased the enthusiasm of farmers to grow food production in the North region. Based on these findings, the total grain production in the North region has increased rapidly, particularly in Northeast China. However, the increases in temperature and precipitation in the South region might increase the impact of agricultural natural disasters, such as those caused by high temperature, heat damage, and summer drought. In addition, the rapid development of industry in the South region has reduced the crop planting area, and the rural labor force has been continuously diminishing, which has accelerated the decrease in grain prodution in the South region.

Finally, the impact ratio of climate change in the next 15– years is calculated. The impact ratio of climate change reflects the weight of the impact of CCF on actual grain output. Taking the climatic output elasticity from 1981 to 2014 as the benchmark, the climatic output elasticity and the mean annual of CCF under the three future scenarios of 2021–2035 and 2021–2050 are introduced into the YICC model to obtain the IRCC, according to **Eq. 8**.

From 2021 to 2035, the impact ratio of climate change in the North region is negative, and decreases with the increase of emission concentration. The ratio in the South region is positive, and increases with the increase of emission concentration (**Figure 8**). Under the SSP1-2.6 scenario, climate change will cause a 0.60% drop in grain output in the North region and an increase of 1.80% in grain output in the South region. Under the SSP2-4.5 scenario, climate change will cause a 2.09% drop in grain output in the North region and an increase of 9.01% in the South region. Under the SSP5-8.5 scenario, climate change will cause a 1.86% drop in grain output in the North region and an increase of 7.17% in the South region. The main reason may be that temperature and CO_2 concentration in the North region increase with the increase of the emission concentration, which leads to a warmer climate and is not conducive to the suitable growth of crops. The reduction in precipitation and radiation may cause damage to crops by natural disasters such as high temperature or drought, leading to a decline in grain output. The temperature in the South region may be suitable, the precipitation increases, and the radiation increases, which is conducive to the growth of crops. The future climate change in the South region will have a greater positive impact on food production than in the North region. The increase in CO_2 concentration is beneficial to alleviate or offset the negative effects caused by climate warming and increase grain production.

The change trend of the impact ratio of climate change from 2021 to 2050 is consistent with the change region from 2021 to 2035. Compared with the impact of climate change in the next 15 years (2021–2035), the negative impact of climate change on the grain production in the North region in the next 30 years will weaken as the emission concentration increases (**Figure 9**). Among them, the grain output affected by climate change in the North region is reduced by 0.52% under the SSP1-2.6 scenario, 1.99% under the SSP2-4.5 scenario, and 1.76% under the SSP5-8.5 scenario. The main reason may be that the temperature and precipitation in the next 30 years will be higher than the changes in the next 15 years, which may reduce the impact of natural disasters such as low temperature and cold damage and provide sufficient water resources for crop growth. As a result, the negative impact of climate change is reduced in the North region. For the South region, climate change still has a positive impact on grain production. Compared with the impact of climate change in the next 15 years, the climate impact in the next 30 years on grain production in the South region will be strengthened under the

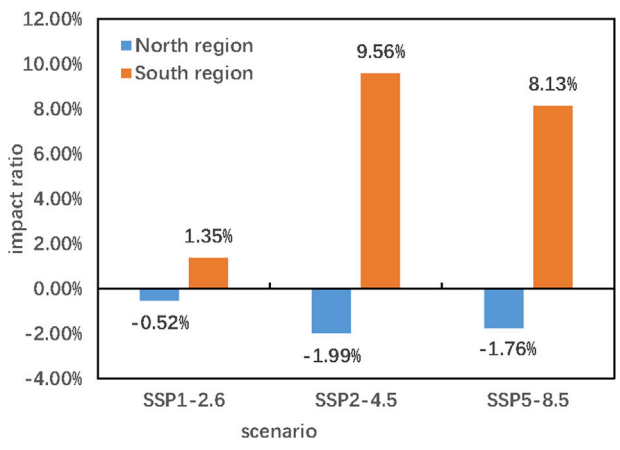

FIGURE 9 | The impact ratio of climate change in the main grain-producing areas from 2021 to 2050.

SSP2-4.5 and SSP5-8.5 scenarios, and weakened under the SSP1-2.6 scenario.

CONCLUSIONS AND DISCUSSIONS

1) Based on the traditional C-D-C model and the method for projecting the climate change impact, this paper introduces a comprehensive climate factor to improve the accuracy of the model and simplify the parameters. Combined with the new prediction achievements of the climate model of CMIP6, we further introduce the concept of the yield impact of climate change (YICC). The YICC represents the difference between economic output under a changing climatic state and a constant climatic state. It not only comprehensively considers the interaction between climate change and socio-economic factors but also takes into account the influence of the interdecadal climate change trend, thereby improving the accuracy of projecting the impact of future climate change.
2) To improve the impact assessment system of the economy-climate model, the yield impact of climate change (YICC) model is further introduced on the basis of the C-D-C model. The model can well project the impact of long-term climate change on economic output and reflect the sensitivity of economic output change to climate change by the impact ratio of climate change (IRCC) indicator in the model.
3) A case study of the yield impact of climate change model applied to the main grain-producing areas in China finds that the impact of climate change in the future 15– years on the grain output in the South region is beneficial under the three future scenarios, but it will have a negative impact on the grain output in the North region. From 2021 to 2035, the increase rate of grain production in the South region will range from 1.80 to 9.01% under the three future scenarios, and the rate of production reduction in the southern region will range from −2.09% to −0.60%. From 2021 to 2050, the production increase rate in the South region will be between 1.35% and 9.56%, and the production reduction rate in the North region will be between −1.99% and −0.52%. This modeling method has good prospects for application, and we will pay more attention to its application and promotion in future research.

To accurately and quantitatively project the impact of climate change on economic output in the next 15–30 years, this study combines the prediction achievements of the climatic model with econometrics and provides a new idea and method for studying the impact and adaptation of global change. It also provides a scientific basis for responding to climate change and preventing climate change risks in the socio-economic system. This study selects 5 GCMs in CMIP6, based on the shared socio-economic paths, and simulates the change range of future grain production in China and quantitatively gives the probability of increasing or decreasing grain production under the low-force scenario (SSP1-2.6), the medium-force scenario (SSP2-4.5), and the high-force scenario (SSP5-8.5). The application of the multi-model ensemble averaging method to the research of agricultural impact assessment can reduce the uncertainty of the impact of climate change on crop production. Grain production is affected by many factors, such as nature, economy and society. Among these factors, agricultural policies and government decisions play a leading role in China's agricultural production. For example, in 1998, China began to actively promote the strategic adjustment of agricultural and rural economic structures. In 2006, China exempted agriculture from taxes and other regulatory policies. Increasing grain production has been an important policy focus. In 2012, China has introduced a food security policy of "ensuring basic self-sufficiency of grain and absolute security of staple food" and established a national strategy on food security featuring self-sufficiency based on domestic grain production, guaranteed food production capacity, moderate imports, and technological support. Socioeconomic and climate change factors jointly affect China's grain production. Facing the changes in the spatial and temporal patterns of climate change in China's main grain-producing areas, humans can use real-time agricultural technology, combined with meteorological monitoring and forecasting techniques to monitor the real-time dynamics of climate factors such as temperature and precipitation and to prevent possible natural disasters.

Among previous studies, Ma et al. [39] found that climate change in northeast China from 2031 to 2040 would lead to a 5.3% reduction in maize production using the integral regression method. Li et al. [40], Li et al. [41], and Sun et al. [42] using crop models, found that the average production reduction of maize, rice, and wheat in China would be 3.7, 7.49, and 5.2%, respectively, under the background of a temperature increase of 1.5°C. Although the method in this study is not as strong as the mechanism of the crop model, it uses long-term economic and climatic data to project the impact of climate change for analysis. It analyzes the relationship between climatic factors and economic output under the interaction of climate factors and economic factors. When projecting the future, it still includes the interaction between climate and economy and the long-term change trend. Therefore, the results may be more consistent with the actual situation. Of course, this method has some issues to be improved, such as the limitations of the economic-climate model itself and the uncertainty of the scenario data predicted by the climate model. The existence of these problems will inevitably lead to uncertainty in the assessment results of the impact of climate change, which needs to be further explored in future work.

DATA AVAILABILITY STATEMENT

The original contributions presented in the study are included in the article/**Supplementary Material**, further inquiries can be directed to the corresponding author.

AUTHOR CONTRIBUTIONS

YX and JC: Methodology, conceptualization, writing—original draft preparation, writing—review and editing. JC: validation, resources, supervision, project administration, and funding

acquisition. YX and WZ: software, formal analysis. JL and YL: investigation, data curation. All authors have read and agreed to the published version of the manuscript.

FUNDING

This research was funded by the National Key Research and Development Program of China, grant number 2018YFC1509003; the National Natural Science Foundation of China, grant number 42075167.

SUPPLEMENTARY MATERIAL

The Supplementary Material for this article can be found online at: https://www.frontiersin.org/articles/10.3389/fphy.2021.723306/full#supplementary-material

REFERENCES

1. IPCC. *Climate Change 2014: Synthesis Report. Contribution of Working Groups I, II and III to the Fifth Assessment Report of the Intergovernmental Panel on Climate Change*. Intergovernmental Panel on Climate Change (IPCC) (2014). p. 151.
2. FAO. *The Future of Food and Agriculture: Alternative Pathways to 2050*. Food and Agriculture Organization of the United Nations (2018). p. 228.
3. Mbow C, Rosenzweig C, Barioni LG, Benton TG, Herrero M, Krishnapillai M, et al. Food Security in: Climate Change and Land: an IPCC Special Report on Climate Change. In: *Desertification, Land Degradation, Sustainable Land Management, Food Security, and Greenhouse Gas Fluxes in Terrestrial Ecosystems*. IPCC (2019).
4. Li JJ, Zhu JH, and Sun ZB. Larock Indole Synthesis. *Climatic Environ Res* (2002) 7:209. doi:10.1007/978-3-662-04835-1_161
5. Chou J, Xu Y, Dong W, Xian T, Xu H, and Wang Z. Comprehensive Climate Factor Characteristics and Quantitative Analysis of Their Impacts on Grain Yields in China's Grain-Producing Areas. *Heliyon* (2019) 5:e02846. doi:10.1016/j.heliyon.2019.e02846
6. Chou JM, Dong WJ, and Yan XD. The Impact of Climate Change on the Socioeconomic System: A Mechanistic Analysis. *Chin J Atmos Sci* (2016) 40: 191–200. doi:10.3878/j.issn.1006-9895.1507.15131
7. Ye DZ, and Lv JH. Adaptation and Sustainable Development to Future Impacts of Global Change. *Bull Chin Acad Sci* (2000) 3. doi:10.16418/j.issn.1000-3045.2000.03.007
8. Fu CB, Dong WJ, Wen G, and Ye DZ. Regional Response and Adaptation to Global Change. *Acta Meteorologica Sinica* (2003) 61:245–50.
9. Nicholls N. Increased Australian Wheat Yield Due to Recent Climate Trends. *Nature* (1997) 387:484–5. doi:10.1038/387484a0
10. Ray DK, West PC, Clark M, Gerber JS, Prishchepov AV, and Chatterjee S. Climate Change Has Likely Already Affected Global Food Production. *PLoS One* (2019) 14:e0217148. doi:10.1371/journal.pone.0217148
11. Wang Z, Hua QL, Kong XD, and Zhang YZ. Historical Reference of the Impact of Climate Warming on Agriculture in China. *Prog Nat Sci* (2005) 15:706–13. doi:10.1080/10020070512330018
12. Wang BH, Fu J, Xie YG, and Feng Y. A Review on Evaluation Method of Economic Loss of Flood in the World. *J Catastrophology* (2007) 22:95–9.
13. Wang FT. Advances in Climate Warming Impact Research in China in Recent Ten Years. *J Appl Meteorol Sci* (2002) 13.
14. Fang XQ, Wang Y, Xu T, and Yun YR. Contribution of Climate Warming to Rice Yield in Heilongjiang Province. *Acta Geographica Sinica* (2004) 59:820–8.
15. Tang XL, Jin XB, Sheng L, Zhou YK, and Sun T. Research on Response of Grain Output to Climate Change Based on Wavelet Analysis:A Case Study of Tibet. *Geogr Geo-information Sci* (2008) 24:88–92.
16. Tao F, Hayashi Y, Zhang Z, Sakamoto T, and Yokozawa M. Global Warming, rice Production, and Water Use in China: Developing a Probabilistic Assessment. *Agric For Meteorology* (2008) 148:94–110. doi:10.1016/j.agrformet.2007.09.012
17. Araya A, Hoogenboom G, Luedeling E, Hadgu KM, Kisekka I, and Martorano LG. Assessment of maize Growth and Yield Using Crop Models under Present and Future Climate in Southwestern Ethiopia. *Agric For Meteorology* (2015) 214-215:252–65. doi:10.1016/j.agrformet.2015.08.259
18. Mendelsohn R, Nordhaus W, and Shaw D. Climate Impacts on Aggregate Farm Value: Accounting for Adaptation. *Agric For Meteorology* (1996) 80: 55–66. doi:10.1016/0168-1923(95)02316-x
19. Chen Y, Wu Z, Okamoto K, Han X, Ma G, Chien H, et al. The Impacts of Climate Change on Crops in China: A Ricardian Analysis. *Glob Planet Change* (2013) 104:61–74. doi:10.1016/j.gloplacha.2013.01.005
20. Hossain MS, Arshad M, Qian L, Zhao M, Mehmood Y, and Kächele H. Economic Impact of Climate Change on Crop Farming in Bangladesh: An Application of Ricardian Method. *Ecol Econ* (2019) 164:106354. doi:10.1016/j.ecolecon.2019.106354
21. Kunimitsu Y. Regional Impacts of Long-Term Climate Change on Rice Production and Agricultural Income: Evidence from Computable General Equilibrium Analysis. *Jpn. Agric. Res. Q.* (2015) 49:173–85. doi:10.6090/jarq.49.173
22. Huang DL, Li XM, and Ju SP. Climate Change Affecting Grain Production, Consumption and Economic Growth in China: Based on the Agricultural CGE Model. *Chin Agric Sci Bull* (2016) 32.
23. Chou JM, and Ye DZ. Assessing the Effect of Climate Changes on Grains Yields with a New Economy-Climate Model. *Climatic Environ Res* (2006) 11: 347–53.
24. Chou J, Dong W, and Feng G. The Methodology of Quantitative Assess Economic Output of Climate Change. *Chin Sci Bull* (2011) 56:1333–5. doi:10.1007/s11434-011-4429-8
25. Chou J, Dong W, and Feng G. Application of an Economy-Climate Model to Assess the Impact of Climate Change. *Adv Atmos Sci* (2010) 27:957–65. doi:10.1007/s00376-009-8166-8
26. Xu Y, Chou J, Yang F, Sun M, Zhao W, and Li J. Assessing the Sensitivity of Main Crop Yields to Climate Change Impacts in China. *Atmosphere* (2021) 12: 172. doi:10.3390/atmos12020172
27. Zhou SD, and Zhu HG. Economic Analysis of Climate Change Impact on the Rice Yield in Southern China and its Adaptive Strategy. *China Popul Resour Environ* (2010) 20:152–7.
28. Lu S, Bai X, Li W, and Wang N. Impacts of Climate Change on Water Resources and Grain Production. *Technol Forecast Soc Change* (2019) 143: 76–84. doi:10.1016/j.techfore.2019.01.015
29. Chou J, Xu Y, Dong W, Xian T, and Wang Z. Research on the Variation Characteristics of Climatic Elements from April to September in China's Main Grain-Producing Areas. *Theor Appl Climatol* (2019) 137:3197–207. doi:10.1007/s00704-019-02795-y
30. Chou JM, Feng GL, Dong WJ, Ye DZ, and Chen HZ. A New Approach the Economy Evaluation of Influence on CHina Agriculture by Climate Change. *Climatic Environ Res* (2004) 9:361–8.
31. Zhou GS. Research Prospect on Impact of Climate Change on Agricultural Production in China. *Meteorol Environ Sci* (2015) 38. doi:10.3969/j.issn.1673-7148.2015.01.012
32. Wang J. The Economics of Climate Change: A Literature Review. *The J World Economy* (2008) 31.
33. Xu L, and Ma D. Parameter Estimation of C -- D Production Function. *Science-Technology Manage* (2001) 4. doi:10.16315/j.stm.2001.04.018
34. Fang SB. Exploration of Method for Discrimination between Trend Crop Yield and Climatic Fluctuant Yield. *J Nat Disasters* (2011) 20:13–8.
35. Cao LG, Fang YJ, and Luo Y. Advances in Shared Socio-Economic Pathways for Climate Change Research and Assessment. *Adv Clim Change Res* (2012) 8: 74–8. doi:10.3969/j.issn.1673-1719.2012.01.012
36. Yao Y, Luo Y, and Huang JB. Evaluation and Projection of Temperature Extremes over China Based on 8 Modeling Data from CMIP5. *Progressus Inquisitiones de Mutatione Climatis* (2012) 8:250–6.

37. Zhang LX, Chen XL, and Xin XG. Short Commentary on CMIP6 Scenario Model Intercomparison Project (ScenarioMIP). *Progressus Inquisitiones de Mutatione Climatis* (2019) 15:519–25.
38. The State Council Information Office of the People's Republic of China. *"China's Food Security" White Paper*. China: The State Council Information Office of the People's Republic of China (2019).
39. Ma YP, Sun LL, You-hao E, and Wu W. Predicting the Impact of Climate Change in the Next 40 Years on the Yield of maize in China. *Ying Yong Sheng Tai Xue Bao* (2015) 26:224–32.
40. Li K, Xiong W, Pan J, Lin ED, Li YC, and Han X. Trend Evaluation on Changes of Maize Yield in China under Global Warming by 1.5 and 2 ˚C .0 ˚C. *Chin J Agrometeorology* (2018) 39. doi:10.3969/j.issn.1000-6362.2018.12.001
41. Li M-Y, Gao X-N, Pan J, Xiong W, Guo L-P, Lin E-D, et al. Possible Trends of rice Yield in China under Global Warming by 1.5 ℃ and 2.0 ℃. *J Nat Resour* (2021) 36:567. doi:10.31497/zrzyxb.20210303
42. Sun R, Han X, Pan J, Xiong W, and Ju H. The Impact of 1.5˚C and 2.0˚C Global Warming on Wheat Production in China. *Progressus Inquisitiones de Mutatione Climatis* (2018) 14:573–82.
43. Masson-Delmotte V, Zhai P, Pörtner H-O, Roberts D, Skea J, Shukla PR, et al. Summary for Policymakers. In: *Global Warming of 1.5˚C an IPCC Special Report on the Impacts of Global Warming of 1.5˚C Above Pre-Industrial Levels and Related Global Greenhouse Gas Emission Pathways, in the Context of Strengthening the Global Response to the Threat of Climate Change*. IPCC (2018).

Conflict of Interest: The authors declare that the research was conducted in the absence of any commercial or financial relationships that could be construed as a potential conflict of interest.

Publisher's Note: All claims expressed in this article are solely those of the authors and do not necessarily represent those of their affiliated organizations, or those of the publisher, the editors and the reviewers. Any product that may be evaluated in this article, or claim that may be made by its manufacturer, is not guaranteed or endorsed by the publisher.

frontiers in Physics

ORIGINAL RESEARCH
published: 30 August 2021
doi: 10.3389/fphy.2021.718771

Trend, Seasonal, and Irregular Variations in Regional Actual Evapotranspiration Over China: A Multi-Dataset Analysis

Tao Su[1], Taichen Feng[2], Bicheng Huang[2], Zixuan Han[3], Zhonghua Qian[1], Guolin Feng[1,4,5] and Wei Hou[4]*

[1]College of Physical Science and Technology, Yangzhou University, Yangzhou, China, [2]Key Laboratory of Semi-Arid Climate Change, Ministry of Education, School of Atmospheric Sciences, Lanzhou University, Lanzhou, China, [3]College of Oceanography, Hohai University, Nanjing, China, [4]China Laboratory for Climate Studies, National Climate Center, China Meteorological Administration, Beijing, China, [5]Southern Ocean Science and Engineering Guangdong Laboratory, Zhuhai, China

Actual evapotranspiration (AE) is a crucial processes in terrestrial ecosystems. Global warming is expected to increase AE; however, various AE estimation methods or models give inconsistent trends. This study analyzed AE variability in China during 1982–2015 based on the Budyko framework (AE_Budyko), a complementary-relationship-based product (AE_CR), and the weighted average of six reanalyses (AE_WAR). Because the response of AE to driving factors and the performances of AE datasets are both scale-dependent, China has been categorized into six distinct climatic areas. From a regional perspective, the X-12-ARIMA method was used to decompose monthly AE into the trend, seasonal, and irregular components. We examined the main characteristics of these components and the relationships of climate factors with AE. The results indicate that the trend component of AE increased from the mid-1990s to the early 2000s and more recently in the hyper-arid and arid areas. Increasing AE was observed from 1982 to the early 1990s in the semi-arid and dry sub-humid areas. AE increased significantly and had substantial interannual variability for the entire period in the sub-humid and humid areas. Increased precipitation and water supply from terrestrial water storage contributed significantly to increasing AE in the drylands. The simultaneous occurrence of increasing precipitation and wet-day frequency caused increasing AE in the dry sub-humid area. Increased AE could be explained by the increased energy supply and precipitation in the sub-humid and humid areas. Precipitation had the strongest influence on the irregular component of AE in drylands. AE and potential evapotranspiration had a strong positive correlation in the sub-humid and humid areas. Regarding data availability, a discrepancy existed in the trend component of AE_CR because soil moisture was not explicitly considered, whereas the irregular component of AE_Budyko contained distinct variations in humid and sub-humid areas.

Keywords: actual evapotranspiration, X-12-ARIMA method, Budyko framework, reanalyses, potential evapotranspiration, China, Water supply

OPEN ACCESS

Edited by:
Yipeng Guo,
Nanjing University, China

Reviewed by:
Marija Mitrovic Dankulov,
University of Belgrade, Serbia
Ruolin Li,
Northwest Institute of Eco-Environment and Resources, CAS, China

****Correspondence:***
Guolin Feng
fenggl@cma.gov.cn

Specialty section:
This article was submitted to Interdisciplinary Physics, a section of the journal Frontiers in Physics

Received: *01 June 2021*
Accepted: *12 August 2021*
Published: *30 August 2021*

Citation:
Su T, Feng T, Huang B, Han Z, Qian Z, Feng G and Hou W (2021) Trend, Seasonal, and Irregular Variations in Regional Actual Evapotranspiration Over China: A Multi-Dataset Analysis. Front. Phys. 9:718771. doi: 10.3389/fphy.2021.718771

INTRODUCTION

Actual evapotranspiration (AE) is the process by which the Earth's surface water enters the atmosphere through evaporation or evapotranspiration [1]. Land AE plays an essential role in hydrology and climate change, as it links the water and energy cycles [1, 2] and affects water-energy balances significantly. On average, AE accounts for about 60% of the Earth's total land rainfall [3]. Meanwhile, AE as latent heat flux is a central component of the heat transfer. A drop in evaporative cooling generally causes higher surface air temperature [4]. Global warming is expected to increase AE rates, further accelerating warming via water vapor feedback, since water vapor is a potent greenhouse gas [5]. It should be noted that, however, AE is influenced by both local and global factors [1, 6]. The response of AE to global warming, if fully realized, can vary regionally across a continent [7].

AE is well known to be one of the most difficult variables to observe [8]. For now, only relatively few flux tower sites operate in China, and the period is concise [9]. The sparse observations are difficult to capture long-term variations in regional AE. Numerous theoretical and empirical methods have been proposed for estimating AE indirectly. For example [10], developed a data-oriented AE product by integrating a variety of data sources in a model tree ensemble approach, demonstrated that the majority of China (78%) showed an increasing trend in AE. [11], using a complementary relationship model, showed that annual AE increased significantly in western and northeastern parts of China. Recent improvements in retrospective analyses (or reanalyses) also enable AE estimates to be obtained at multiscale [12]. AE variability largely depends on local microclimatic conditions in a given region [13]. Various methods or models generally provide inconsistent AE estimates [11]. AE variability over China under global warming remains highly uncertain.

Due to the influence of the monsoon, the annual cycle is the major component of many climate variables in China [8]. Nevertheless, seasonality in time series can obscure movements of other parts that are operationally more important for climatological analysis. The annual cycle in most climate studies is assumed as a regular and recurring change with no interannual variation, whereas in reality climate change is reflected not only in the annual mean shift in climate variables, but also in their annual cycles [14]. Therefore, the seasonal, interannual, and interdecadal variations in AE and the associated drivers should be studied separately. Many deseasonalization methods and procedures have been proposed to deal with seasonal adjustment [14, 15]. The widely used X-12-ARIMA method allows for interannual variations in terms of seasonality [15] and has the advantage of diagnosing AE variability.

Various AE estimation methods or models give inconsistent trends, a single AE dataset is insufficient [12, 16]. Therefore, we examined AE variability over China derived from three sources, namely the Budyko framework, a complementary-relationship-based product [11], and a weighted average of six reanalyses. The X-12-ARIMA method was then used to comprehensively evaluate the performance of these three datasets in reproducing the trend, seasonal, and irregular variations in AE for China's six climatic areas. The six areas are divided according to the aridity index, and coincide roughly with China's climatic characteristics. Furthermore, the differences in the contributing factors to AE variations were determined. Our results mainly focused on the recent changes in and attributions of regional AE.

DATA AND METHODS

Actual Evapotranspiration Data

Reanalyses (or retrospective analyses) have been produced by various institutes. In this study, AE data from six different reanalyses are used—namely, ERA-Interim reanalysis (ERA-I) from ECMWF [17], MERRA and MERRA2 from the NASA Goddard Space Flight Center [18], the Japanese 55-years Reanalysis (JRA-55), NCEP/NCAR reanalysis I (NCEP-R1), and NCEP/DOE reanalysis II (NCEP-R2) (available online https://rda.ucar.edu/). These reanalyses were generated by various forecast models, assimilation systems, or input datasets. Different reanalyses provide a measure of uncertainty in estimating the AE variability. For detailed descriptions of the selected reanalyses, refer to [12, 13]; or the original dataset citations.

In China, many studies have attempted to estimate AE [8–10, 19]. For comparison, the calibration-free nonlinear complementary relationship modelled AE dataset (AE_CR) was also used [11].

Meteorological Data and NDVI Data

To clarify the primary cause for variations in AE, we analyzed the relation between AE and the climate variables, which include surface net solar radiation derived from ERA-I, mean temperature, maximum and minimum temperatures, diurnal temperature range, cloud cover, potential evapotranspiration, precipitation, wet-day frequency, and vapor pressure derived from the University of East Anglia CRU TS4.00 version dataset (available online https://crudata.uea.ac.uk/cru/data/hrg/cru_ts_4.00/; [20]. In addition, the 8 km Global Inventory Modeling and Mapping Studies (GIMMS) normalized difference vegetation index (NDVI) dataset was derived from the Advanced Very High Resolution Radiometer (AVHRR) sensor (available online https://www.ncei.noaa.gov/data/), and was used to estimate vegetation coverage [21]. Each dataset has a different time span, but all cover our analysis period of 1982–2015. For easy comparison and for computation purposes, all datasets were interpolated into a $0.5^{\circ} \times 0.5^{\circ}$ grid using bilinear interpolation.

Methods

The X-12 Seasonal Adjustment Procedure

Seasonal adjustment corresponds to an estimate of seasonal variation and its elimination from a time series [15, 22]. Seasonally adjusted data can be used to better visualize the long-term development of the data

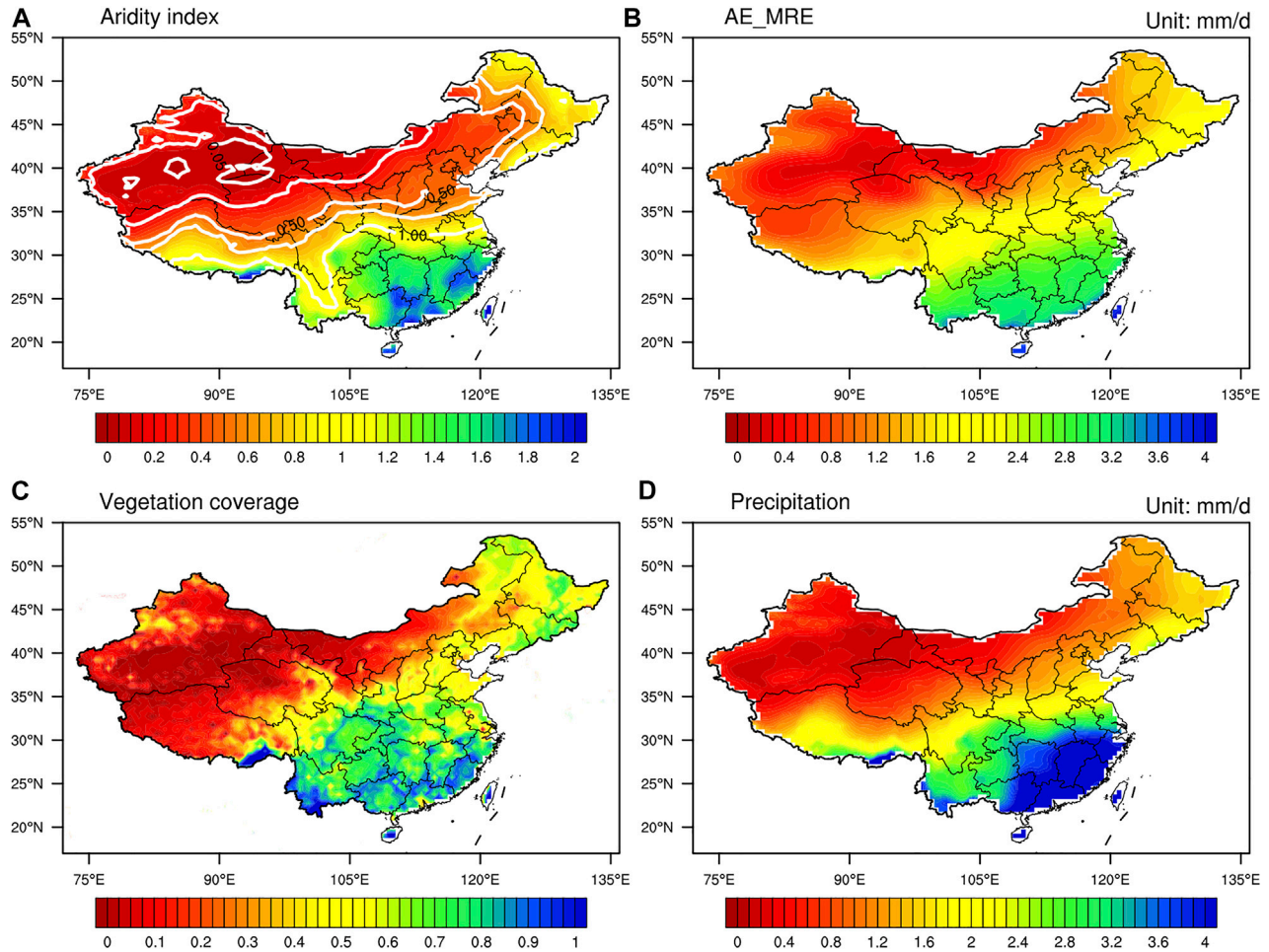

FIGURE 1 | The climatological distribution of **(A)** aridity index, **(B)** annual mean actual evapotranspiration (AE_MRE; mm d^{-1}) derived from the average of six reanalyses, **(C)** vegetation cover, and **(D)** annual mean precipitation (mm d^{-1}) for 1982–2015.

series. We adopted a widely-used seasonal adjustment method, which is known as the X-12-ARIMA-based filter, to give a richer diagnosis and clearer interpretation of climate variations in AE. To be more precise, the original series (X_t) can be decomposed into three components, as

$$X_t = T_t + S_t + I_t \tag{1}$$

where T_t, S_t, and I_t are defined as the trend, seasonal, and irregular components, respectively [22]. The trend component (T_t) captures the direction of the time series, thus the nonparametric Mann–Kendall test was applied to detect its linear trend. Irregular fluctuations were generally due to unpredictable and unexpected factors. For more sophisticated analyses, it was preferable to include both the seasonally adjusted data and its seasonal component to obtain maximum information from the data [15].

Weighted Average of AE From Six Reanalyses

Reanalysis AE is generally estimated from bulk flux formulas with inputs of surface temperature, wind, and surface air temperature and humidity [16]. Discrepancies in AE among reanalyses can be substantial [12, 13]. An intercomparison of different datasets is a key step in reducing uncertainties in AE estimates. After seasonal adjustment of AE, multiple linear regression, a sophisticated and quantitative analysis method, was used to analyze consistency across the six reanalyses.

For the X-12 trend, seasonal, and irregular components of AE from reanalysis X_1, a multiple linear regression was performed with the remaining five reanalyses (X_i, $i = 2, \ldots, 5$), respectively, that is,

$$X_1 = \beta_0 + \beta_1 X_2 + \beta_2 X_3 + \beta_3 X_4 + \beta_4 X_5 + \beta_5 X_6 \tag{2}$$

where β_i ($i = 0, \ldots, 5$) are the parameters generally estimated by least squares. Based on this, the corresponding squared multi-correlation coefficient (R_i^2) was used as the weight coefficient of each reanalysis. Then we calculated the weighted average of AE (AE_WAR) from the six reanalyses using **Eq. 3**,

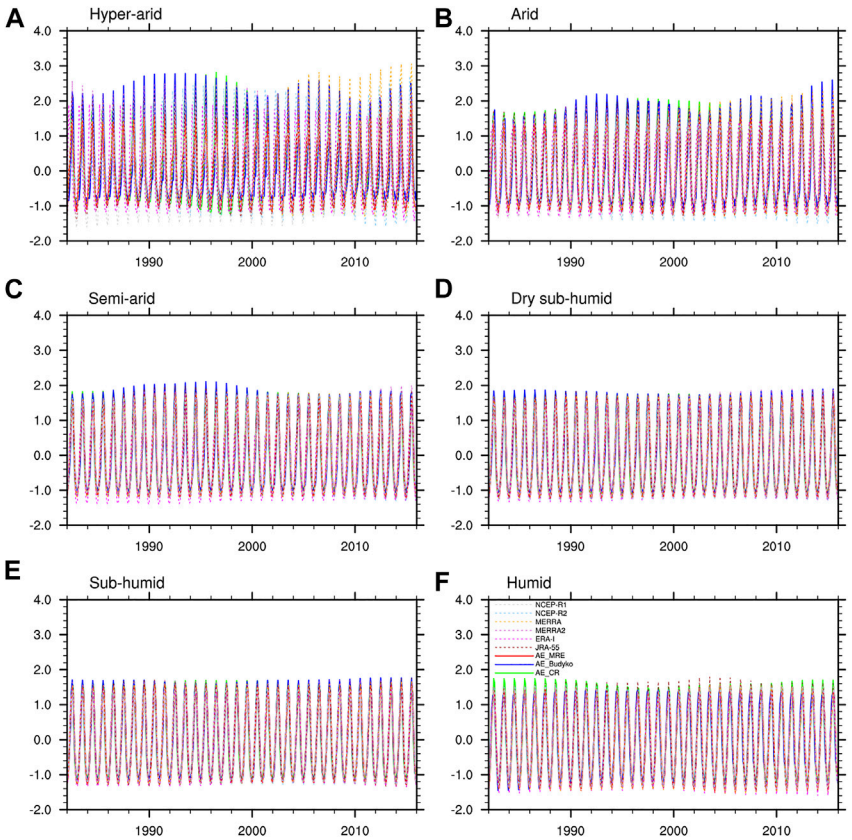

FIGURE 2 | X-12-ARIMA seasonal components (S_t) of actual evapotranspiration (AE) derived from AE_WAR, AE_CR, AE_Budyko, and reanalyses over the **(A)** hyper-arid, **(B)** arid, **(C)** semi-arid, **(D)** dry sub-humid, **(E)** sub-humid, and **(F)** humid regions.

$$AE\_WAR = \frac{X_1R_1^2 + X_2R_2^2 + X_3R_3^2 + X_4R_4^2 + X_5R_5^2 + X_6R_6^2}{\sum_1^6 R_i^2} \quad (3)$$

where the subscript i of R_i^2 represents different reanalysis data mentioned above.

AE Estimation Based on the Budyko Framework

In the Budyko framework, long-term AE (AE_Budyko) is largely controlled by the ratio of energy supply (potential evapotranspiration, PET) to water supply (precipitation, PRE). Several previous studies have developed various but somewhat similar coupled water–energy balance equations on the basis of the Budyko hypothesis [23]. Because of its strong theoretical basis and low data requirements, the Budyko equation has been widely used [24]. As pointed out by [25]; various types of Budyko-like equations have given broadly similar results. One of the most popular Budyko equation is expressed as [21]:

$$AE\_Budyko = \frac{PRE \cdot PET}{(PRE^n + PET^n)^{1/n}} \quad (4)$$

where n is a catchment-specific parameter that modifies the Budyko curve [24, 25]. China occupies a vast land territory, thus the parameter n shows a large spatial variation (ranging from 0.4 to 3.8) [25]. It should be noted that higher values of n denote a higher estimate of AE for a given PRE and PET in general [24]. To simplify the Budyko framework, the parameter n is traditionally set to be 1.8 [13, 23]. In the absence of better knowledge, we assume here that n remains constant over time.

RESULTS AND DISCUSSION

Climatic Characteristics of China

Climate variations in China are complicated because of the influence of various factors. Precipitation varied widely across space (**Figure 1D**). Generally, wetter environments had a higher vegetation cover (**Figure 1C**), indicating that long-term vegetation cover was sensitive to water availability. Considering geographical complexity, the response of regional AE to a warming climate should be investigated separately [13]. Meanwhile, the quality of the AE products may differ spatially as well. We thus differentiated the climatic areas in China and performed an attribution analysis on AE for each area.

According to the aridity index (AI) [26], the Budyko hypothesis generally separates catchments into energy-limited (AI < 1) and water-limited (AI > 1) areas [27]. As shown in

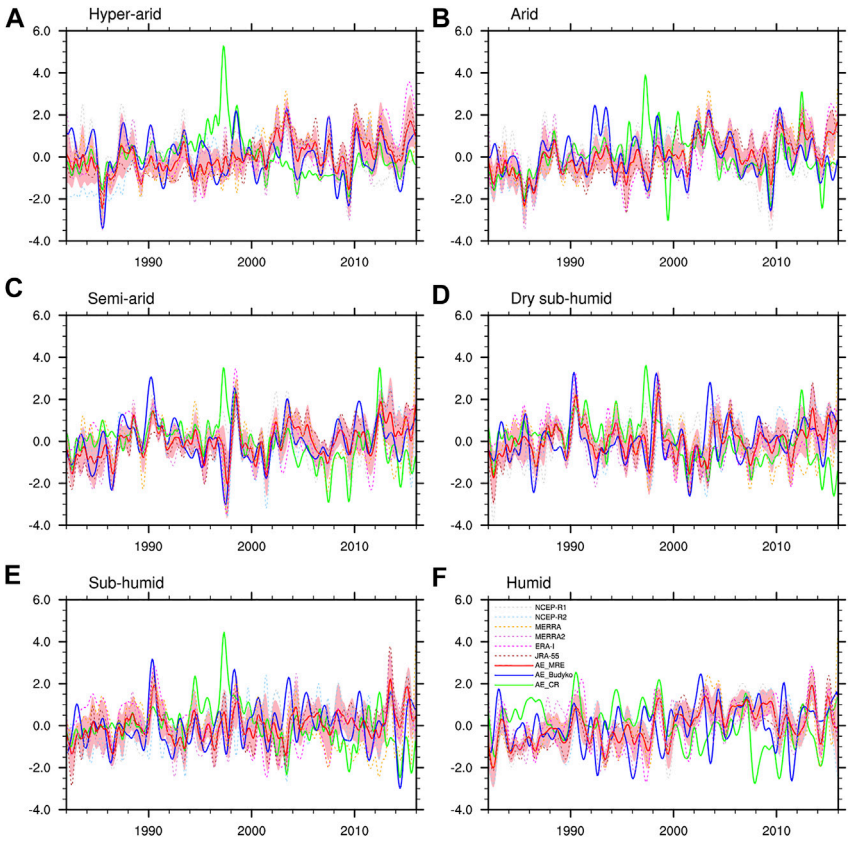

FIGURE 3 | X-12-ARIMA trend components (T_t) of actual evapotranspiration (AE) derived from AE_WAR, AE_CR, AE_Budyko, and reanalyses over the **(A)** hyper-arid, **(B)** arid, **(C)** semi-arid, **(D)** dry sub-humid, **(E)** sub-humid, and **(F)** humid regions.

Figure 1A, AI had a similar spatial distribution to precipitation (**Figure 1D**) and vegetation cover (**Figure 1C**). Consequently, the definition of AI was deemed reasonable and reliable. According to this index, China could be roughly divided into six climatic areas, namely, the hyper-arid (H-arid), arid, semi-arid (S-arid), dry sub-humid (DS-humid), sub-humid (S-humid), and humid areas [13].

Figure 1B shows the spatial distribution of climatological mean AE during 1982–2015, calculated from the average of six reanalyses. Generally, AE across China decreased from south to north and from east to west. For the mean annual water balance, the moisture supplied by precipitation was sufficient in most regions. In contrast, AE could be higher than precipitation in northwestern China, where glaciers have a direct impact on the water resource system [39]. Precipitation is used to measure water availability in the Budyko framework. It means that AE_Budyko may be biased low in some areas (discussed below).

Multi-Timescale Variability of AE

Figure 2 shows the seasonal component of AE for the six climatic areas. AE showed strong seasonality with different amplitudes over time. In comparison, seasonal variations in AE revealed by different datasets were generally consistent for most areas. The largest discrepancies were observed for the hyper-arid area (**Figure 2A**). Overall, AE_WAR agreed better with AE_CR (correlation 0.926) than with AE_Budyko (correlation 0.856). Modest differences also existed in the seasonal component for the arid area (**Figure 2B**). Seasonal variation is an essential aspect of climate change. As shown in **Figure 2**, seasonal components of AE in the hyper-arid and arid areas exhibited substantial interannual variations, which is a nonnegligible part of the original time series. It suggested that the conventional approach assuming fixed seasonality did not apply in these areas.

The trend components (T_t) of AE are shown in **Figure 3**. Compared to AE_CR, AE_WAR agrees better with AE_Budyko, as evidenced by the correlation coefficients shown in **Figure 4** (0.589, 0.623, 0.708, 0.540, 0.387, and 0.288 for the six areas, respectively). Despite the general similarity, disparities existed among the three datasets, partly owing to their differing linear trends (**Figure 5**). The statistical significance of the Mann–Kendall test for the increasing trend in AE_WAR exceeded the 99% confidence level in all areas (**Figure 5**). This was consistent with the traditional view that AE is likely to increase under global warming [7]. AE_Budyko also showed an increasing trend in most areas, whereas a significant negative trend was found for the hyper-arid area and no

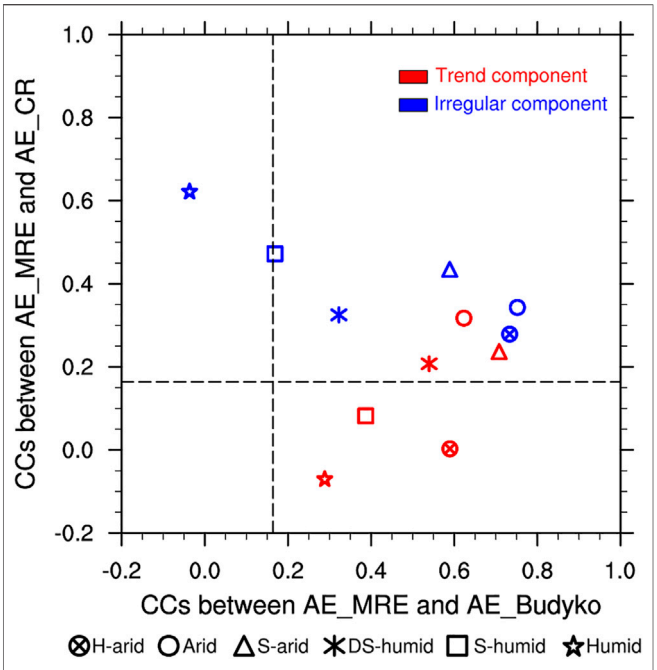

FIGURE 4 | Plot of correlation coefficients between AE_WAR and AE_CR vs correlation coefficients between AE_WAR and AE_Budyko in six climatic areas of China from 1982 to 2015 for the X-12-ARIMA trend and irregular components. The local 99.9% confidence levels are about ± 0.164 based on Student's *t*-test.

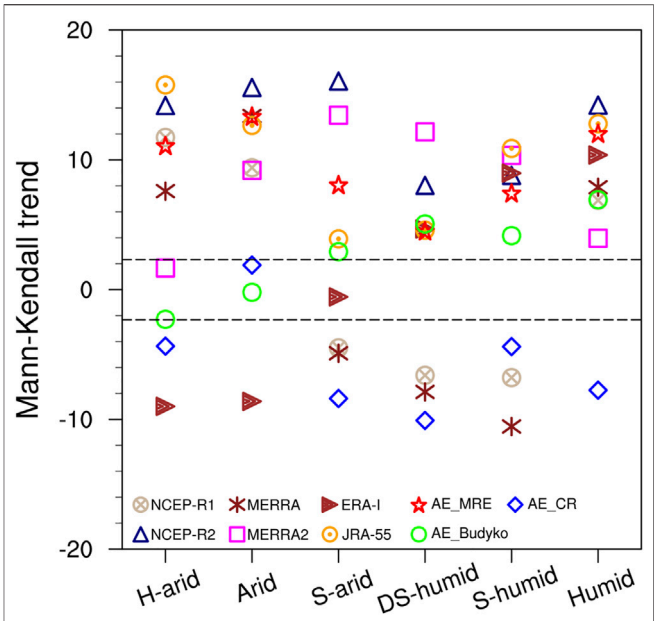

FIGURE 5 | Mann–Kendall trends for X-12-ARIMA trend component (T_t) of actual evapotranspiration (AE) derived from various datasets for six climatic areas of China from 1982 to 2015. The local 99% confidence levels are about ± 2.32.

significant trend existed for the arid area (**Figure 5**). AE_CR displayed a significantly decreasing trend in all areas, except for the arid area. The spatial patterns of the linear AE trends, and indeed the signs of the trends, differed between the datasets.

Compared to AE_WAR and AE_Budyko, AE_CR showed a significant discrepancy in the trend component (**Figure 4**). Specifically, AE_CR for many areas peaked in 1997 (**Figure 3**), increasing during 1982–1997 and declining after 1997. We suspected that the aforementioned weak correlation might have been caused by the effect of the spurious changes in AE_CR around 1997. A correlation analysis between AE_CR and AE_ WAR was performed for 1982–1995 and 1999–2015, respectively. Correlation coefficients were highly improved during 1982–1995. The correlations between AE_CR and AE_WAR were 0.500, 0.692, 0.702, 0.712, 0.519, and 0.413 ($p < 0.001$) for the six regions, respectively. The relationship between AE_CR and AE_Budyko showed roughly similar behavior. A comparison of various datasets revealed substantial uncertainties in the trend component of AE_CR, which was likely overestimated around 1997. It is therefore questionable whether a calibration-free AE estimation method without the use of precipitation or runoff rates could predict long-term changes in AE.

AE_WAR increased from the mid-1990s to the early 2000s and more recently in the hyper-arid area (**Figure 3A**); this was generally consistent with the AE_Budyko trend. Similar results were found for the arid area (**Figure 3B**), where AE_WAR also had an increasing trend in the late 1980s. At a regional scale, AE_WAR agreed better with AE_Budyko for the semi-arid area (**Figure 3C**), with both indicating a distinct increase in AE from 1982 to the early 1990s. During the same period, an increasing trend in AE_WAR was observed for the dry sub-humid area, whereas AE_Budyko showed no discernible trend (**Figure 3D**). Another significant shift in both AE_WAR and AE_Budyko occurred from the late 2010s onwards. Considerable differences in the trend components of AE among the three datasets were found in the sub-humid (**Figure 3E**) and humid (**Figure 3F**) areas. For these two areas, AE_WAR had a significantly increasing trend along with substantial interannual variability, which agreed with AE_Budyko. As noted above, both AE_WAR and AE_Budyko agreed well with AE_CR during 1982–1996. However, variations in AE obtained from the three datasets were not consistent and exhibited conflicting trends during 1997–2015.

At a regional level, multiple factors determined how much water evaporated from the land [1]. The irregular component of AE showed high variability (**Figure 6**). Considerable inconsistencies existed between the three datasets. Specifically, AE_WAR showed reasonable agreement with AE_Budyko for the drylands (i.e., hyper-arid, arid, and semi-arid areas). By contrast, only a weak negative correlation existed between AE_WAR and AE_Budyko for the humid area (**Figure 5F**). One possible reason for this was that changes in both rainfall and soil water storage significantly influenced the interannual variability of the hydrological responses [28]. For example, vegetation and the interactions between climate seasonality and soil water storage changes have also been

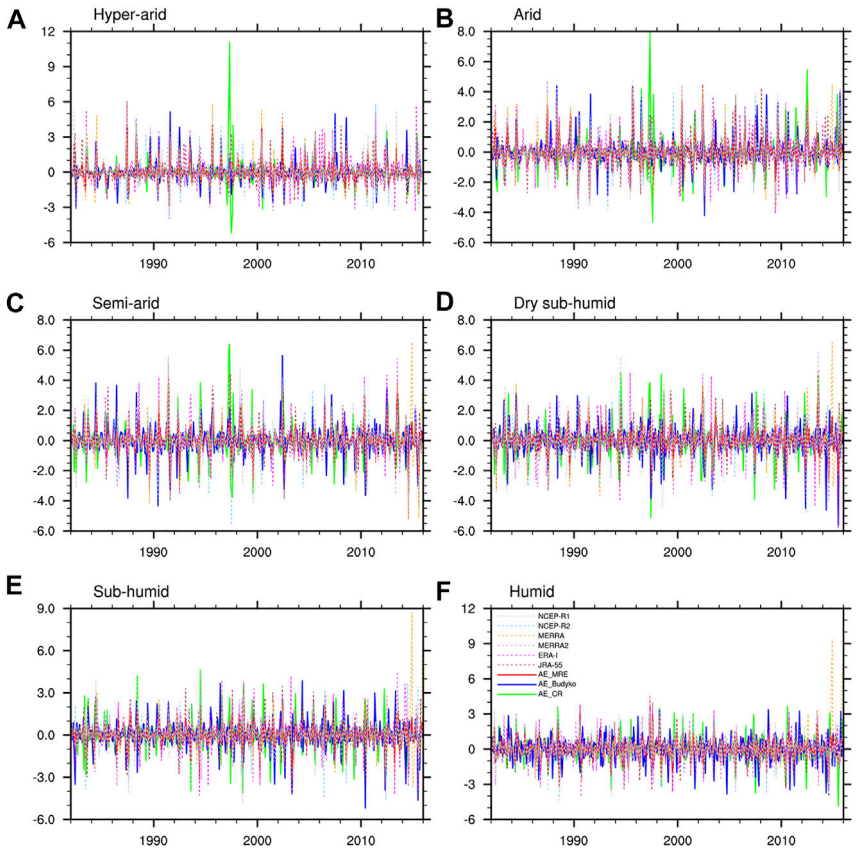

FIGURE 6 | X-12-ARIMA irregular components (I_t) of actual evapotranspiration (AE) derived from AE_WAR, AE_CR, AE_Budyko, and reanalyses over the **(A)** hyper-arid, **(B)** arid, **(C)** semi-arid, **(D)** dry sub-humid, **(E)** sub-humid, and **(F)** humid regions.

found to play important roles [25]. The magnitude of any change in the interannual variability of AE caused by variations in catchment vegetation was related to pre- and post-change vegetation types. Compared to the drylands, the vegetation cover in wetter environments tended to be denser (**Figure 1C**). Because of the mutual interactions among climate, hydrological processes, and land surface characteristics, AE had a nonlinear relationship with precipitation and potential evapotranspiration [24, 29], which led to deviations in the Budyko relationship [28]. As a result, the performance of AE_Budyko in reproducing the irregular component of AE remains doubtful for the humid area (**Figure 6F**).

Agreement between AE_WAR and AE_CR was observed for the humid and sub-humid areas (**Figure 4**). As the above mentioned, a calibration-free nonlinear complementary relationship model was utilized for monthly AE_CR taking air and dew-point temperature, wind speed, and net radiation as inputs [11, 30]. AE from surfaces with abundant moisture was mainly controlled by energy conditions [27, 31]. Atmospheric evaporative demand was primarily driven by two major components, namely radiative and aerodynamic components, both of which were associated with the AE_CR inputs. Therefore, the irregular component of AE_CR performed better than that of AE_Budyko for the humid and sub-humid areas (**Figure 4**).

Causes and Implications of Changes in AE

The response of AE to climate variables varies spatially (**Figure 7**). The causes of variations in AE are closely related to local climatic characteristics. The trend component of AE showed a strong positive correlation with precipitation, wet-day frequency, and vapor pressure ($p < 0.001$) (**Figure 7**) in the hyper-arid, arid, and semi-arid areas. This was consistent with the convention that AE is mainly controlled by water conditions in drylands. In water-limited environments, a substantial fraction of the variations in precipitation become variations in AE. Although precipitation was the dominant factor for the trend component of AE in the drylands, the increase in precipitation (**Figure 8**) was lower than that in AE (**Figure 4**) according to the Mann–Kendall test.

In fact, increased wet-day frequency could promote AE increase, even if there is no change in total precipitation. Besides, changes in runoff and water storage should be considered in the amount of moisture available for AE [31, 32], especially in drylands. Human activities and climate change have intensely influenced the ecohydrological pattern of many basins. For example, the Tarim River Basin is the most heavily glacierized watershed in arid northwestern China.

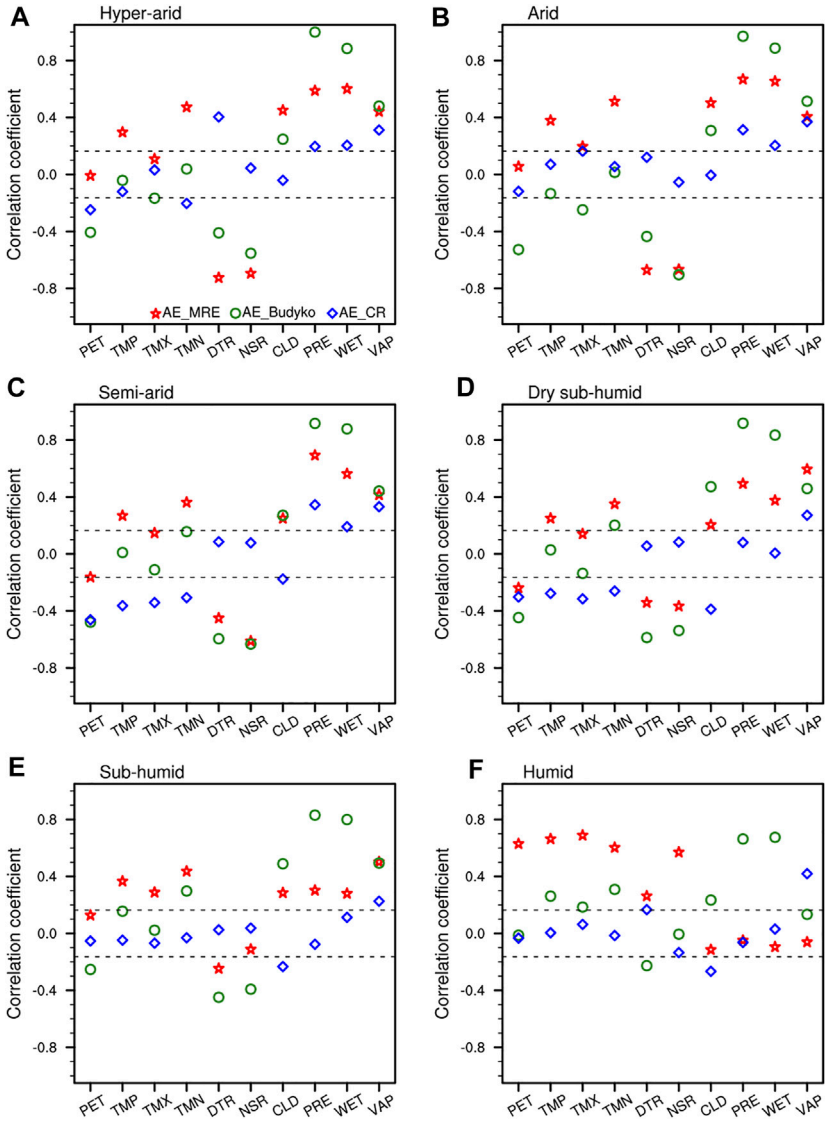

FIGURE 7 | Temporal correlation coefficients between X-12-ARIMA trend components of actual evapotranspiration and influencing factors, namely potential evapotranspiration (PET), mean temperature (TMP), maximum and minimum temperatures (TMX and TMN, respectively), diurnal temperature range (DTR), net solar radiation (NSR), cloud cover (CLD), precipitation (PRE), wet-day frequency (WET), and vapor pressure (VAP), over the **(A)** hyper-arid, **(B)** arid, **(C)** semi-arid, **(D)** dry sub-humid, **(E)** sub-humid, and **(F)** humid regions from 1982 to 2015. The local 99.9% confidence levels are about ± 0.164 based on Student's t-test.

The water supply from the mountains to the Tarim River Basin is favorable in recent decades; however, local human activities (such as irrigation and domestic water use) have reduced its runoff [33]. [34] also indicated that the influence of irrigation on AE variability became increasingly evident with the increase of irrigation in the Tarim River Basin. Accordingly, the increased water supply from catchment storage likely resulted in increased AE in the drylands.

AE_WAR and AE_Budyko were significantly correlated ($p < 0.001$) with diurnal temperature range, net solar radiation, and cloud cover in the drylands. The Mann–Kendall test indicated that diurnal temperature range decreased significantly in the drylands, mostly because of a more significant increase in minimum temperature relative to maximum temperature (**Figure 8**). This decrease in diurnal temperature range was mainly attributed to increased cloud cover, precipitation, and soil moisture [35]. Diurnal temperature range can represent the combined influence of these variables and hence has a strong relationship with AE [36].

Increased AE can modulate the climate by reducing the sensible heat flux, enhancing the air humidity, increasing the minimum temperature, and decreasing the maximum temperature [35]. It means that increased AE is a possible reason for the increase in minimum temperature has been higher than that in maximum temperature, that is, the decrease in diurnal temperature range might have resulted from the increased AE (**Figure 8**).

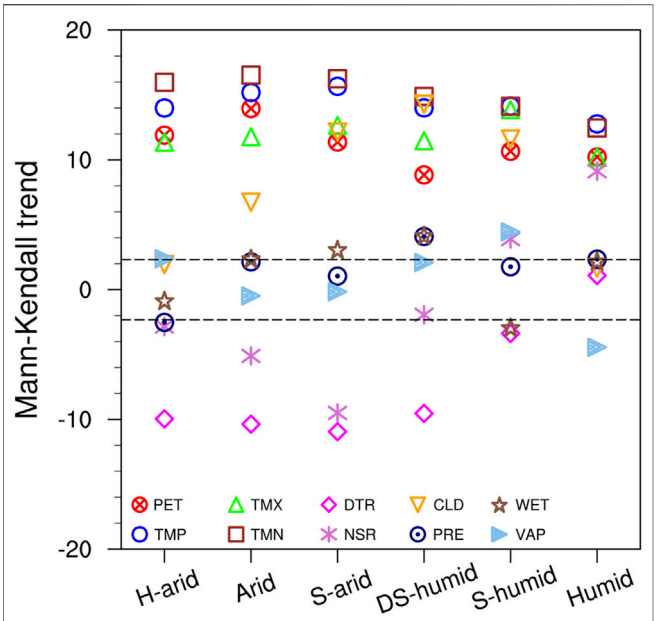

FIGURE 8 | Mann–Kendall trends in X-12-ARIMA trend components of influencing factors in six climatic areas of China from 1982 to 2015. The local 99% confidence levels are about ± 2.32.

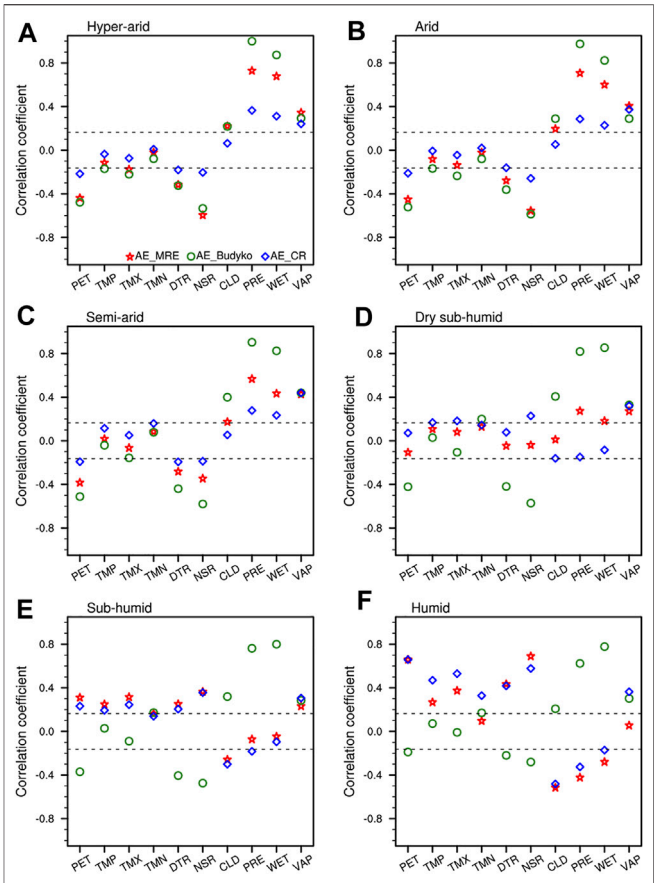

FIGURE 9 | Temporal correlation coefficients between X-12-ARIMA irregular component of actual evapotranspiration and influencing factors over the **(A)** hyper-arid, **(B)** arid, **(C)** semi-arid, **(D)** dry sub-humid, **(E)** sub-humid, and **(F)** humid regions from 1982 to 2015. The local 99.9% confidence levels are about ± 0.164 based on Student's *t*-test.

The correlations ranged more widely between the datasets in wetter areas. Vapor pressure was an essential factor influencing AE in the dry sub-humid area (**Figure 7D**). Increased AE led to increasing vapor pressure, thus increased vapor pressure could be interpreted as a sign of increasing AE [6]. Similar relationships were found in the sub-humid area (**Figure 7E**). Overall, the simultaneous increases in precipitation and wet-day frequency increased AE in the dry sub-humid area (**Figure 7D**). Increased minimum temperature was likely an essential cause of the increased AE in the sub-humid area (**Figure 7E**). For the humid area, the trend component of AE was less sensitive to precipitation than that in the drylands. AE increased under the integrated influence of potential evapotranspiration, mean temperature, and maximum and minimum temperatures (**Figure 7F**). Changes in AE were generally controlled by energy supply rather than precipitation.

In general, AE was driven mainly by climatic factors, regulated by land surface condition, and limited by water supply [19]. The trend component of AE_CR showed little correlation with climatic factors. An explanation is that AE_CR may fail in reproducing the long-term variation in AE. In contrast, AE_Budyko showed reasonable consistency with AE_WAR, demonstrating that AE_Budyko is more reliable in terms of long-term, large-scale changes in AE.

Figure 9 illustrates the influencing factors of the irregular component of AE at regional scales. As expected, precipitation had the strongest influence on AE in the hyper-arid, arid, and semi-arid areas. In the drylands, precipitation is temporarily stored in soil and then totally evaporates into the atmosphere [1]. In contrast, AE_WAR and AE_CR were significantly negatively correlated with precipitation in the humid area (**Figure 9F**), where AE was more sensitive to energy supply than water supply (**Figure 1A**). The irregular component of precipitation made a much smaller contribution to AE. Furthermore, precipitation usually coincides with an increase in cloud cover and a decrease in radiation, resulting in a reduction of energy supply to AE (**Figure 9F**). For this reason, precipitation had a negative effect on AE in the humid area. Similarly, positive correlations between AE and cloud cover dominated in drylands, but significantly negative associations existed between AE and surface net solar radiation.

AE was significantly negatively correlated with potential evapotranspiration in the drylands (**Figure 9**). [29] suggested that a complementary relationship between AE and potential evapotranspiration occurs in non-humid areas because these two factors are correlated *via* precipitation. In contrast, AE and potential evapotranspiration had a strong positive correlation in wet areas (**Figures 9E,F**). The inclusion of the regional dimension of AE drivers allows the scenarios both of increasing AE and potential evapotranspiration in water-rich areas and of increasing AE and decreasing potential evapotranspiration to be encompassed in the drylands (**Figure 9**).

In the humid area, surface net solar radiation was the most crucial variable regulating the irregular component of AE_WAR (**Figure 9F**), which was reasonable, as radiation is the energy source for AE. Overall, the result of AE_WAR matched that of AE_CR (**Figure 9F**). [37] also reported that in humid climates, such as northeast India, solar radiation supplied most of the energy required for water to change from a liquid to a vapor. Furthermore, AE was strongly correlated with diurnal temperature range. [1] pointed out that the variability in diurnal temperature was consistent with that in surface incident solar radiation at monthly to decadal timescales. Since surface incident solar radiation heats daytime air only, its variation was related to changes in diurnal temperature.

AE is a complex process that regulates land-atmosphere interactions. Increased water supply from catchment storage could be a primary contributor to increased AE. Nevertheless, accurate detection and attribution of complex variability in AE at multi-time scales remain challenging [33, 38]. The implications of variations in AE remain unclear.

CONCLUSION

According to the aridity index, China was divided into six climatic areas. This study analyzed regional AE variability across China using data from the weighted average of six reanalyses (AE_WAR), the Budyko framework (AE_Budyko), and a complementary-relationship-based AE product (AE_CR). Since seasonal variation complicates the detection of changes in AE, the X-12-ARIMA method was used to study the trend, seasonal, and irregular components of AE as well as the significant drivers.

According to the trend component, AE increased from the mid-1990s to the early 2000s and more recently in the hyper-arid and arid areas. An increasing trend in AE was also observed from 1982 to the early 1990s in the semi-arid and dry sub-humid areas. In the sub-humid and humid areas, AE had a significantly increasing trend along with substantial interannual variability. Increased precipitation and water supply from terrestrial water storage contributed significantly to increasing AE in drylands. The simultaneous occurrences of increased precipitation and wet-day frequency caused high AE in the dry sub-humid area. In contrast, increased AE in the sub-humid and humid areas could be explained by increased energy supply and precipitation.

Precipitation had the strongest influence on the irregular component of AE in the drylands. In contrast, AE_WAR and AE_CR were significantly negatively correlated with precipitation in the humid area. Negative correlations between AE and potential evapotranspiration occurred in the drylands, whereas positive relationships existed in the sub-humid and humid areas. The irregular component of AE was positively correlated with vapor pressure across China. Positive relationships between AE and cloud cover dominated in drylands, but significantly negative associations existed between AE and surface net solar radiation.

Considering data availability, the seasonal variations in AE revealed by the different datasets were generally consistent. The largest discrepancies occurred in the hyper-arid area. Compared to AE_WAR and AE_Budyko, the trend component of AE_CR showed inconsistent behavior across many areas, which was mainly caused by spurious changes around 1997. AE_CR did not consider soil moisture explicitly, which may have limited its ability to detect AE trends. The Budyko model is useful in large-scale hydrological research; however, the irregular component of AE_Budyko remains dubious for humid and sub-humid areas because of the complex interactions between climate, vegetation, and soil.

Water loss through AE is a major consideration in the design and management of water supply reservoirs. Efforts to evaluate AE in natural settings are made difficult by spatial heterogeneity in soil and unevenly distributed vegetation in addition to other biophysical processes. This study thoroughly compared different AE products for various climatic areas of China. Such knowledge is meaningful to hydrological, climatological, and ecological research.

DATA AVAILABILITY STATEMENT

The original contributions presented in the study are included in the article/Supplementary Material, further inquiries can be directed to the corresponding author. The GIMMS NDVI dataset, the Climate Research Unit datasets, and the six reanalyses used in this study can be freely accessed from the following websites: https://www.ncei.noaa.gov/data/, https://crudata.uea.ac.uk/cru/data/hrg/cru_ts_4.00/, and https://rda.ucar.edu/, respectively.

AUTHOR CONTRIBUTIONS

TS and GF conceived, and carried out the research, led the data analysis, and wrote the manuscript. TF and BH conceived the research, designed the analysis, and provided comments on the manuscript. ZH, ZQ, and WH provided comments on the manuscript.

FUNDING

This research was jointly funded by National Key Research and Development Program of China (Grant Nos. 2017YFC1502402 and 2017YFC1502303), National Natural Science Foundation of China (Grant Nos. 41975062, 41875097, 42175071, and 41705053), and China Postdoctoral Science Foundation (Grant Nos. 2017M611921).

ACKNOWLEDGMENTS

The authors thank Ning Ma (Institute of Tibetan Plateau Research) for providing the calibration-free nonlinear complementary relationship modelled evapotranspiration dataset used in this paper.

REFERENCES

1. Wang K, and Dickinson RE. A Review of Global Terrestrial Evapotranspiration: Observation, Modeling, Climatology, and Climatic Variability. *Rev Geophys* (2012) 50:RG2005. doi:10.1029/2011RG000373
2. Miralles DG, van den Berg MJ, Gash JH, Parinussa RM, de Jeu RAM, Beck HE, et al. El Niño-La Niña Cycle and Recent Trends in continental Evaporation. *Nat Clim Change* (2014) 4(2):122–6. doi:10.1038/nclimate2068
3. Teuling AJ, Hirschi M, Ohmura A, Wild M, Reichstein M, Ciais P, et al. A Regional Perspective on Trends in continental Evaporation. *Geophys Res Lett* (2009) 36:L02404. doi:10.1029/2008GL036584
4. Yin D, Roderick ML, Leech G, Sun F, and Huang Y. The Contribution of Reduction in Evaporative Cooling to Higher Surface Air Temperatures during Drought. *Geophys Res Lett* (2014) 41:7891–7. doi:10.1002/2014GL062039
5. Zhang Y, Leuning R, Chiew FHS, Wang E, Zhang L, Liu C, et al. Decadal Trends in Evaporation from Global Energy and Water Balances. *J Hydrometeorol* (2012) 13:379–91. doi:10.1175/jhm-d-11-012.1
6. van Heerwaarden CC, Vilà-Guerau de Arellano J, Gounou A, Guichard F, and Couvreux F. Understanding the Daily Cycle of Evapotranspiration: A Method to Quantify the Influence of Forcings and Feedbacks. *J Hydrometeorol* (2010) 11:1405–22. doi:10.1175/2010JHM1272.1
7. Douville H, Ribes A, Decharme B, Alkama R, and Sheffield J. Anthropogenic Influence on Multidecadal Changes in Reconstructed Global Evapotranspiration. *Nat Clim Change* (2013) 3:59–62. doi:10.1038/NCLIMATE1632
8. Wang Y, Liu B, Su B, Zhai J, and Gemmer M. Trends of Calculated and Simulated Actual Evaporation in the Yangtze River Basin. *J Clim* (2011) 24: 4494–507. doi:10.1175/2011JCLI3933.1
9. Ma N, Zhang Y, Xu CY, and Szilagyi J. Modeling Actual Evapotranspiration with Routine Meteorological Variables in the Data-scarce Region of the Tibetan Plateau: Comparisons and Implications. *J Geophys Res Biogeosci* (2015) 120:1638–57. doi:10.1002/2015JG003006
10. Li X, He Y, Zeng Z, Lian X, Wang X, Du M, et al. Spatiotemporal Pattern of Terrestrial Evapotranspiration in China during the Past Thirty Years. *Agric For Meteorology* (2018) 259:131–40. doi:10.1016/j.agrformet.2018.04.020
11. Ma N, Szilagyi J, Zhang Y, and Liu W. Complementary-relationship-based Modeling of Terrestrial Evapotranspiration across China during 1982-2012: Validations and Spatiotemporal Analyses. *J Geophys Res* (2019) 124: 4326–4351. doi:10.1029/2018JD02958010.1029/2018jd029850
12. Su T, Feng T, and Feng G. Evaporation Variability under Climate Warming in Five Reanalyses and its Association with pan Evaporation over China. *J Geophys Res Atmos* (2015) 120:8080–98. doi:10.1002/2014JD023040
13. Feng T, Su T, Ji F, Zhi R, and Han Z. Temporal Characteristics of Actual Evapotranspiration over China under Global Warming. *J Geophys Res Atmos* (2018) 123:5845–58. doi:10.1029/2017JD028227
14. Qian C, Fu C, and Wu Z. Changes in the Amplitude of the Temperature Annual Cycle in China and Their Implication for Climate Change Research. *J Clim* (2011) 24:5292–302. doi:10.1175/jcli-d-11-00006.1
15. Pezzulli S, Stephenson DB, and Hannachi A. The Variability of Seasonality. *J Clim* (2005) 18:71–88. doi:10.1175/jcli-3256.1
16. Trenberth KE, Fasullo JT, and Mackaro J. Atmospheric Moisture Transports from Ocean to Land and Global Energy Flows in Reanalyses. *J Clim* (2011) 24: 4907–24. doi:10.1175/2011jcli4171.1
17. Dee D, Uppala SM, Simmons AJ, Berrisford P, Poli P, Kobayashi S, et al. The ERA-Interim Reanalysis: Configuration and Performance of the Data Assimilation System. *Q J R Meteorol Soc* (2011) 137:553–97.
18. Gelaro R, McCarty W, Suárez MJ, Todling R, Molod A, Takacs L, et al. The Modern-Era Retrospective Analysis for Research and Applications, Version 2 (MERRA-2). *J Clim* (2017) 30:5419–54. doi:10.1175/jcli-d-16-0758.1
19. Gao G, Chen D, Xu C-y., and Simelton E. Trend of Estimated Actual Evapotranspiration over China during 1960-2002. *J Geophys Res* (2007) 112:D11120. doi:10.1029/2006JD008010
20. Harris I, Jones PD, Osborn TJ, and Lister DH. Updated High-Resolution Grids of Monthly Climatic Observations - the CRU TS3.10 Dataset. *Int J Climatol* (2014) 34:623–42. doi:10.1002/joc.3711
21. Yang H, Yang D, Lei Z, and Sun F. New Analytical Derivation of the Mean Annual Water-Energy Balance Equation. *Water Resour Res* (2008) 44:W03410. doi:10.1029/2007WR006135
22. Yaya OS, and Fashae OA. Seasonal Fractional Integrated Time Series Models for Rainfall Data in Nigeria. *Theor Appl Climatol* (2015) 120:99–108. doi:10.1007/s00704-014-1153-8
23. Choudhury B. Evaluation of an Empirical Equation for Annual Evaporation Using Field Observations and Results from a Biophysical Model. *J Hydrol* (1999) 216:99–110. doi:10.1016/s0022-1694(98)00293-5
24. Roderick ML, and Farquhar GD. A Simple Framework for Relating Variations in Runoff to Variations in Climatic Conditions and Catchment Properties. *Water Resour Res* (2011) 47:W00G07. doi:10.1029/2010WR009826
25. Yang H, Qi J, Xu X, Yang D, and Lv H. The Regional Variation in Climate Elasticity and Climate Contribution to Runoff across China. *J Hydrol* (2014) 517(1):607–16. doi:10.1016/j.jhydrol.2014.05.062
26. Feng S, and Fu Q. Expansion of Global Drylands under a Warming Climate. *Atmos Chem Phys* (2013) 13:10081–94. doi:10.5194/acp-13-10081-2013
27. McVicar TR, Roderick ML, Donohue RJ, Li LT, Van Niel TG, Thomas A, et al. Global Review and Synthesis of Trends in Observed Terrestrial Near-Surface Wind Speeds: Implications for Evaporation. *J Hydrol* (2012) 416-417:182–205. doi:10.1016/j.jhydrol.2011.10.024
28. Zhang Q, Singh VP, Sun P, Chen X, Zhang Z, and Li J. Precipitation and Streamflow Changes in China: Changing Patterns, Causes and Implications. *J Hydrol* (2011) 410:204–16. doi:10.1016/j.jhydrol.2011.09.017
29. Yang D, Sun F, Liu Z, Cong Z, and Lei Z. Interpreting the Complementary Relationship in Non-humid Environments Based on the Budyko and Penman Hypotheses. *Geophys Res Lett* (2006) 33:L18402. doi:10.1029/2006GL027657
30. Szilagyi J, Crago R, and Qualls R. A Calibration-free Formulation of the Complementary Relationship of Evaporation for continental-scale Hydrology. *J Geophys Res Atmos* (2017) 122:264–78. doi:10.1002/2016jd025611
31. Lawrimore JH, and Peterson TC. Pan Evaporation Trends in Dry and Humid Regions of the United States. *J Hydrometeor* (2000) 1(6):543–6. doi:10.1175/1525-7541(2000)001<0543:petida>2.0.co;2
32. Budyko MI. *Climate and Life, Translated from Russian by: Miller, D. H.* San Diego, CA, USA: Academic (1974). p. 321–30.
33. Tao H, Gemmer M, Bai Y, Su B, and Mao W. Trends of Streamflow in the Tarim River Basin during the Past 50 years: Human Impact or Climate Change? *J Hydrol* (2011) 400(1-2):1–9. doi:10.1016/j.jhydrol.2011.01.016
34. Han S, Hu H, Yang D, and Liu Q. Irrigation Impact on Annual Water Balance of the Oases in Tarim Basin, Northwest China. *Hydrol Process* (2011) 25: 167–74. doi:10.1002/hyp.7830
35. Dai A, Trenberth KE, and Karl TR. Effects of Clouds, Soil Moisture, Precipitation, and Water Vapor on Diurnal Temperature Range. *J Clim* (1999) 12:2451–73. doi:10.1175/1520-0442(1999)012<2451:eocsmp>2.0.co;2
36. Liu B, Xu M, Henderson M, and Gong W. A Spatial Analysis of pan Evaporation Trends in China, 1955-2000. *J Geophys Res* (2004) 109:D15102. doi:10.1029/2004JD004511
37. Jhajharia D, Shrivastava SK, Sarkar D, and Sarkar S. Temporal Characteristics of pan Evaporation Trends under the Humid Conditions of Northeast India. *Agric For Meteorology* (2009) 149:763–70. doi:10.1016/j.agrformet.2008.10.024
38. Xie P, Wu Z, Sang Y-F, Gu H, Zhao Y, and Singh VP. Evaluation of the Significance of Abrupt Changes in Precipitation and Runoff Process in China. *J Hydrol* (2018) 560:451–60. doi:10.1016/j.jhydrol.2018.02.036
39. Sorg A, Bolch T, Stoffel MO, Solomina O, and Beniston M. Climate Change Impacts on Glaciers and Runoff in Tien Shan (Central Asia). *Nat Clim Change* (2012) 2:725–31. doi:10.1038/nclimate1592

Conflict of Interest: The authors declare that the research was conducted in the absence of any commercial or financial relationships that could be construed as a potential conflict of interest.

frontiers in Physics

ORIGINAL RESEARCH
published: 30 August 2021
doi: 10.3389/fphy.2021.718968

Simulated Variation Characteristics of Oceanic CO_2 Uptake, Surface Temperature, and Acidification in Zhejiang Province, China

Kuo Wang[1], *Han Zhang*[1], *Gao-Feng Fan*[1]*, *Zheng-Quan Li*[1], *Zhen-Yan Yu*[1] *and Pei-Pei Liu*[2]

[1]Zhejiang Climate Center, Meteorological Bureau of Zhejiang Province, Hangzhou, China, [2]Ankang Meteorological Bureau of Shaanxi Province, Ankang, China

Since preindustrial times, atmospheric CO_2 content increased continuously, leading to global warming through the greenhouse effect. Oceanic carbon sequestration mitigates global warming; on the other hand, oceanic CO_2 uptake would reduce seawater pH, which is termed ocean acidification. We perform Earth system model simulations to assess oceanic CO_2 uptake, surface temperature, and acidification for Zhejiang offshore, one of the most vulnerable areas to marine disasters. In the last 40 years, atmospheric CO_2 concentration increased by 71 ppm, and sea surface temperature (SST) in Zhejiang offshore increased at a rate of 0.16°C/10a. Cumulative oceanic CO_2 uptake in Zhejiang offshore is 0.3 Pg C, resulting in an increase of 20% in sea surface hydrogen ion concentration, and the acidification rate becomes faster in the last decade. During 2020–2040, under four RCP scenarios, SST in Zhejiang offshore increases by 0.3–0.5°C, whereas cumulative ocean carbon sequestration is 0.150–0.165 Pg C. Relative to RCP2.6, the decrease of surface pH in Zhejiang offshore is doubled under RCP8.5. Furthermore, simulated results show that the relationship between CO_2 scenario and oceanic carbon cycle is nonlinear, which hints that deeper reduction of anthropogenic CO_2 emission may be needed if we aim to mitigate ocean acidification in Zhejiang offshore under a higher CO_2 concentration scenario. Our study quantifies the variation characteristics of oceanic climate and carbon cycle fields in Zhejiang offshore, and provides new insight into the responses of oceanic carbon cycle and the climate system to oceanic carbon sequestration.

Keywords: oceanic carbon sequestration, climate change, ocean acidification, UVic model, Zhejiang province

OPEN ACCESS

Edited by:
Yipeng Guo,
Nanjing University, China

Reviewed by:
Xuanze Zhang,
Institute of Geographic Sciences and Natural Resources Research (CAS), China
Tao Su,
Yangzhou University, China

***Correspondence:**
Gao-Feng Fan
fangaofengcn@163.com

Specialty section:
This article was submitted to Interdisciplinary Physics, a section of the journal Frontiers in Physics

Received: *01 June 2021*
Accepted: *19 July 2021*
Published: *30 August 2021*

Citation:
Wang K, Zhang H, Fan G-F, Li Z-Q, Yu Z-Y and Liu P-P (2021) Simulated Variation Characteristics of Oceanic CO_2 Uptake, Surface Temperature, and Acidification in Zhejiang Province, China. Front. Phys. 9:718968. doi: 10.3389/fphy.2021.718968

INTRODUCTION

Atmospheric CO_2 concentration has reached 410.07 ± 0.10 ppm (parts per million) by 2019, and increased by 46% since preindustrial time, which is primarily resulting from human activities of fossil fuel burning and land use changes [1]. Observational-based estimates showed that during 1750–2019, total anthropogenic CO_2 emissions were 700 ± 75 Pg C (1 Pg C = 10^{15} g of carbon) [1]. About 41% of these emissions stayed in the atmosphere, whereas about 24% of these emissions were absorbed by the ocean, which is considered as a main sink of atmospheric CO_2 [1]. Besides, the ocean also plays an important role in regulating climate by key air–sea interaction processes [2–6].

Increased atmospheric CO_2 causes global warming (GW) through the greenhouse effect. Global warming has become one of the most challenging global issues and the core issue of global change

[7–11]. Carbon capture and sequestration is a major player in reducing atmospheric CO_2 concentrations and the resultant global warming. However, the absorption of anthropogenic CO_2 by the ocean would also decrease seawater pH, causing ocean acidification and having important effects on the oceanic carbon cycle and ecosystem [12]. Therefore, it is important to investigate the response mechanisms of oceanic carbon cycle and climate system to oceanic CO_2 sequestration. In addition, owing to the inhomogeneous physical and biogeochemical features in different oceanic basins or areas, vulnerability assessment of different oceanic areas under the impacts of climate change has become a forefront topic of international scientific research [13–16].

Besides GW, ocean acidification is another significant impact induced by greenhouse gas emissions [12, 17, 18]. With the increased annual CO_2 emissions, ocean acidification has been exacerbated in recent years [19]. The main concern of ocean acidification originates from its potentially adverse effects of $CaCO_3$ saturation state (Ω) reductions on marine calcifying organisms. Reduced Ω would decrease the calcification rate and increase the $CaCO_3$ dissolution rate of calcifying organisms, making their skeletons or shells vulnerable [20–23]. For instance, aragonite is the main constituent of corals' calcareous endoskeleton; therefore, corals surrounded by seawater which is undersaturated with respect to aragonite ($\Omega_A < 1$) could encounter adverse effects. There are intriguing evidences that $CaCO_3$ could also dissolve even in supersaturated seawater [24, 25].

Marine organisms in the China seas are ecologically and economically important. China is known as one of the most important countries of ocean aquaculture industry, where more than 70% of the major cities and 50% of the populations are concentrated in the eastern and southern coastal regions. Maintaining sustainable development of resources and environment in offshore and coastal regions is an urgent strategic requirement for the future development of the country [26, 27]. Zhejiang is a highly developed province in East China, which takes a leading position in the national marine economic development strategy. Therefore, it is necessary to assess the variation characteristics of oceanic climate, carbon cycle, and acidification in Zhejiang offshore. However, due to the lack of historical observational data in oceanic physical and chemical fields, uncertainties exist in assessing changes in oceanic climate, acidification, and biogeochemical processes in regional areas.

In this study, the variation characteristics of oceanic CO_2 uptake, SST, and ocean acidification in historical times and future trends in Zhejiang offshore are quantified. In order to acquire reasonable assessments, reanalysis data and numerical simulated results are used. The data and model used are introduced in Data and Method section, changes in oceanic carbon cycle and climate system are analyzed in Results section, and the summary and advice for adapting to climate change and ocean acidification are in Conclusion and Discussion section.

DATA AND MODELING

Data and Method

The historical SST data used in this article are from ERA-Interim high-precision reanalysis data published by the ECMWF (European Center for Medium-Range Weather Forecasts) [28]. The time span is 1980–2019, and the resolution is $0.125^\circ \times 0.125^\circ$.

Seawater pH is a measurement to quantify the degree of ocean acidification [29]. The increased hydrogen ion concentration tended to reduce carbonate ion concentration ($[CO_3^{2-}]$) *via* the following:

$$H^+ + CO_3^{2-} \rightarrow HCO_3^- \tag{1}$$

Model and Simulations

The University of Victoria Earth System Climate Model (UVic ESCM) version 2.9 used in this study is an intermediate complexity Earth system model [30]. The UVic model is composed of an energy–moisture balance atmospheric model, a 3-D ocean general circulation model, a thermodynamic/dynamic sea ice model, and land and ocean carbon cycle models [31–34]. The model's horizontal resolution is 1.8° (latitude)×3.6° (longitude), which is similar to most coupled atmosphere–ocean general circulation models (AOGCMs). The ocean model of UVic is the modular ocean model (MOM) version 2.2 developed by the Geophysical Fluid Dynamics Laboratory (GFDL), which has a vertical resolution of 19 levels [35].

First, the UVic model was spun up for 10,000 model years with a fixed preindustrial CO_2 concentration of 280 ppm to reach a quasi-equilibrium state of carbon cycle and the climate system. Then, this preindustrial state was used as an initial condition for the calendar year of 1800, 300-years transient simulations were performed (i.e., from 1800 to 2100) [36, 37]. From 1800 to 2019, atmospheric CO_2 concentration data were taken from observation-based estimates [38], and after 2019, CO_2 concentrations were taken from the Representation Concentration Pathway scenarios (RCPs) and their extensions up to 2100. The four scenarios used are RCP2.6, RCP4.5, RCP6.0, and RCP8.5, based on different mitigation policies for greenhouse gases [39, 40]. The numbers after "RCP" represent that by 2100, the radiative forcing reaches 2.6, 4.5, 6.0, and 8.5 W m^{-2}, respectively.

Analysis of Marine Chemistry Fields

In this study, we calculate ocean carbonate chemistry fields, such as pH, based on equations in the Ocean Carbon-Cycle Model Intercomparison Project phase 3 (OCMIP-3, http://ocmip5.ipsl.jussieu.fr/OCMIP/). UVic-simulated ocean temperature, salinity, DIC (dissolved inorganic carbon), ALK (alkalinity), and data-based estimates of ocean silicate and phosphate concentrations from the GLODAP (Global Ocean Data Analysis Project) [41] are used. The calculations are shown as follows [42].

Thermodynamic carbonate chemistry fields generally include the following six variables: DIC, ALK, $[H^+]$, $[CO_2]$, $[CO_3^{2-}]$, and $[HCO_3^-]$. Here, $[CO_2]$ represents the sum of aqueous carbon dioxide concentrations and H_2CO_3 (carbonate acid); $[HCO_3^-]$ denotes bicarbonate ion concentration. Equilibrium expressions for H_2CO_3 dissociation are as follows:

$$K_1^* = \frac{[HCO_3^-][H^+]}{[CO_2]} \tag{2}$$

$$K_2^* = \frac{[CO_3^{2-}][H^+]}{[HCO_3^-]} \tag{3}$$

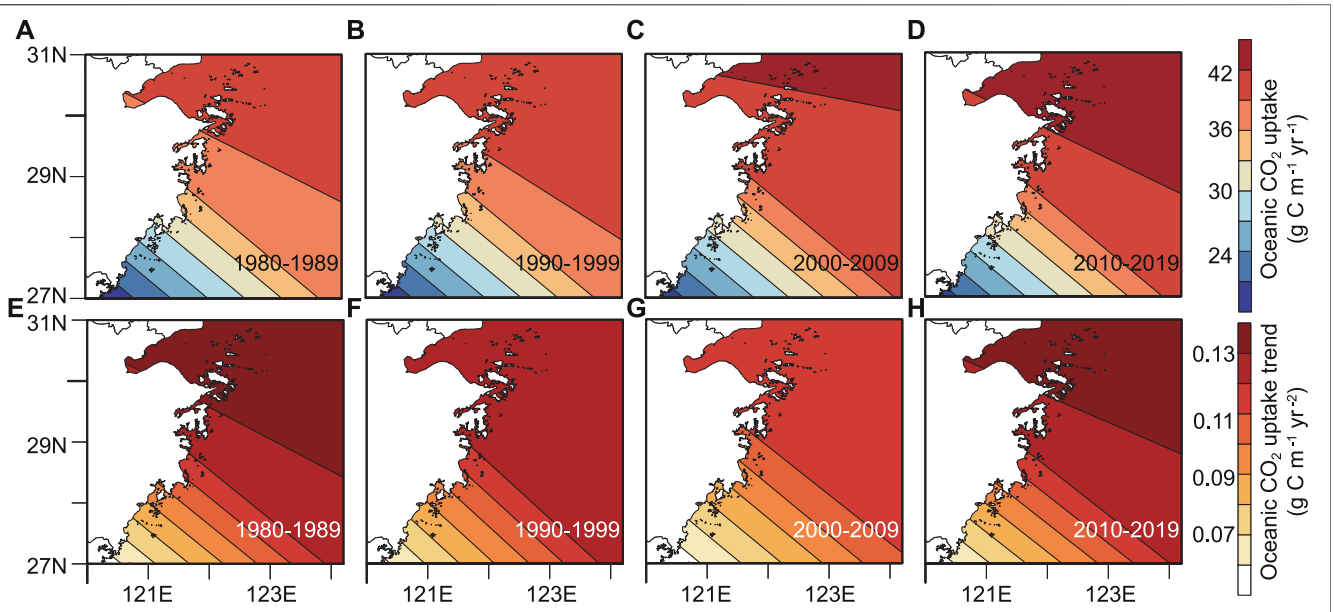

FIGURE 1 | Spatial distributions of simulated decadal mean **(A–D)** oceanic CO_2 uptake and **(E–H)** trends of oceanic CO_2 uptake in Zhejiang offshore. Results are shown for **(A,E)** 1980–1989, **(B,F)** 1990–1999, **(C,G)** 2000–2009, and **(D,H)** 2010–2019.

Expressions for DIC and ALK are as follows:

$$DIC = [CO_2] + [HCO_3^-] + [CO_3^{2-}] \quad (4)$$

$$ALK \approx [HCO_3^-] + 2[CO_3^{2-}] + [OH^-] - [H^+] \quad (5)$$

Based on the above six variables (DIC, ALK, $[H^+]$, $[CO_2]$, $[CO_3^{2-}]$, and $[HCO_3^-]$) and four equations (**Eqs 2–5**), and given two known variables, we can calculate the rest of the four variables [43].

Regions of Interest

This study investigates historical and future variation characteristics of oceanic CO_2 uptake, SST, and ocean acidification in Zhejiang offshore, China. Our regions of interest include the oceanic area of 27.0°–31.0° latitude and 120.0°–124.2° longitude (**Figure 1**). Zhejiang offshore locates in North West of the East China Sea, the subtropical humid climate zone [44]. In addition to the atmospheric circulation system, including East Asian monsoon, the climate system in Zhejiang offshore could also be affected by the continental climate system and oceanic currents, such as the Kuroshio and coastal upwelling currents [45]. Zhejiang is a highly developed province in East China, which takes a leading position in national marine economic development strategy. Changes in oceanic carbon cycle and climate system in Zhejiang offshore could have drastic effects on millions of people who depend on marine resources.

RESULTS

Model-simulated historical oceanic CO_2 uptake for the global ocean is consistent with observation-based estimates reported by IPCC AR5 (Intergovernmental Panel on Climate Change Fifth Assessment Report) [46]. For example, UVic-simulated cumulative oceanic CO_2 uptake during preindustrial time to 2011 was 147 Pg C, which compares well with the observational range of 155 ± 30 Pg C reported by IPCC AR5 (**Table 1**). Model-simulated averaged oceanic CO_2 uptake during 2002 to 2011 was 2.4 Pg C yr^{-1}, within the observed value of 2.4 ± 0.7 Pg C yr^{-1} (**Table 1**).

TABLE 1 | Model-simulated global oceanic CO_2 uptake compared with observation-based estimates reported by IPCC AR5, which show uncertainties as 90% confidence intervals [46].

	IPCC AR5	UVic ESCM
Preindustrial-2011 cumulative	155 ± 30	147
1980–1989 average (Pg C yr^{-1})	2.0 ± 0.7	1.8
1990–1999 average (Pg C yr^{-1})	2.2 ± 0.7	2.0
2000–2009 average (Pg C yr^{-1})	2.3 ± 0.7	2.3
2002–2011 average (Pg C yr^{-1})	2.4 ± 0.7	2.4

Model-simulated key carbon-related tracers are also compared with observation-based estimates from the GLODAP [46]. As shown in **Figure 2**, simulated vertical profiles of DIC and ALK for Zhejiang offshore largely agree with observed estimates. In addition, UVic-simulated large-scale distributions of key variables in the oceanic carbon cycle [45–47], climate [48–50], and historical oceanic uptake of carbon and its isotopes [42] also compare well with observation-based estimates.

SST and Ocean Acidity of Zhejiang Offshore in the Last 40 Years

Zhejiang offshore SST ranges from 19 to 22°C, with higher SST farther offshore at the same latitude. From 1980 to 2019, the hottest

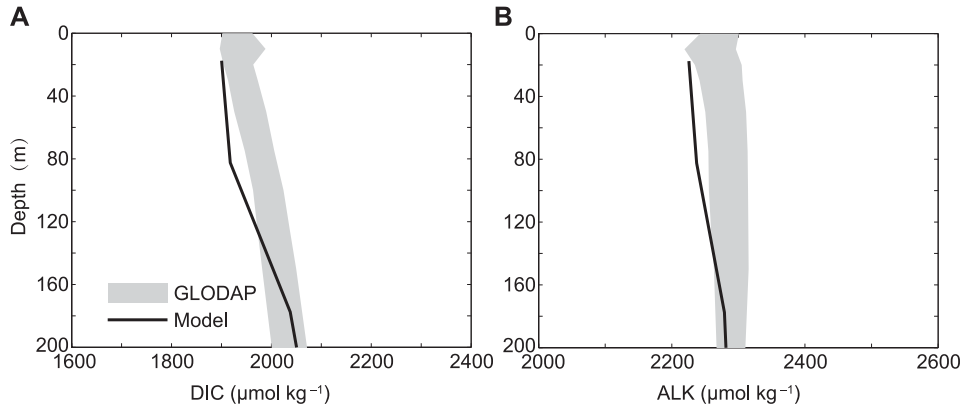

FIGURE 2 | Modeled mean vertical profiles for Zhejiang offshore of **(A)** dissolved inorganic carbon (DIC) and **(B)** alkalinity (ALK) (1990–1999 average) compared with observed estimates from GLODAP data (gray shaded areas denote estimated uncertainties) [41].

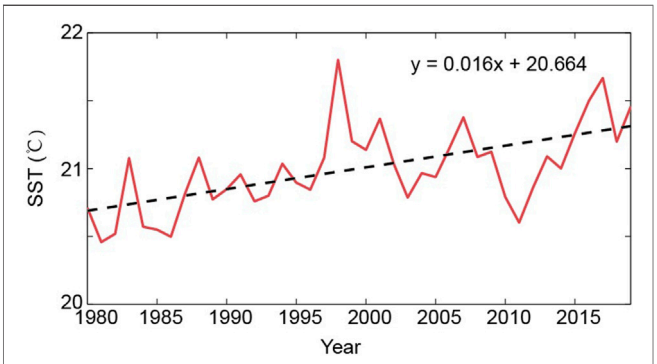

FIGURE 3 | Annual mean variation and linear trend of SST in Zhejiang offshore from 1980 to 2019.

season in Zhejiang offshore sea surface is summer, with SST mainly in the range of 25–28°C, whereas the coldest season is winter, with SST in the 13–17°C range. Across the four seasons, SST spatial gradient is larger in spring and winter, and the smallest in summer.

Observation-based estimates show that during 1980–2019, atmospheric CO_2 concentration increased from 339 to 410 ppm. The increment of atmospheric CO_2 concentration led to rising SST through the enhanced greenhouse effect (**Figure 3**). During 1980–2019, SST of Zhejiang offshore increased at a rate of 0.16°C/10a, which reached its highest level in 1998 (21.8°C), and the lowest in 1981 (20.5°C) (**Figure 3**). From the perspective of interdecadal change, SST of Zhejiang offshore mainly increased from 1980s to late 1990s, decreased at the beginning of the 21st century, and increased again in the 2010s. Annual mean SST of Zhejiang offshore reached 21.5°C in 2019.

In addition to rising seawater temperatures, another important impact of CO_2 emissions on marine environment is ocean acidification. With the increasing of atmospheric CO_2 concentration, the ocean, as an important carbon sink, continuously absorbs anthropogenic CO_2 from the atmosphere (**Figures 1**, **4**). For instance, simulated results show that during 1980–2019, cumulative oceanic CO_2 uptake in Zhejiang offshore is 0.3 Pg C. The increase of annual oceanic CO_2 uptake in Zhejiang offshore is largely related to the rise of atmospheric CO_2 concentration. Continuous oceanic CO_2 uptake would lead to ocean acidification, resulting in the rise of seawater hydrogen ion concentration, reducing the calcification rate of marine organisms, making their skeletons or shells vulnerable, and consequently, having adverse impacts on the marine ecosystem.

In the last 40 years, atmospheric CO_2 concentration increased by 21%. Simulated results show that the decrease rate of pH in Zhejiang sea surface is closely related to the increasing rate of atmospheric CO_2 concentration and oceanic CO_2 uptake. With the increase of atmospheric CO_2, the ocean's continuous absorption of CO_2 leads to the exacerbation of ocean acidification in Zhejiang offshore (**Figures 1**, **4-6**).

Compared with low- and high-latitude sea surface, sea surface of Zhejiang offshore, which is located in the mid-latitude, suffered greater acidification. During 1980–2019, sea surface pH at low and high latitudes decreased by 0.06 units, while that at Zhejiang offshore decreased by 0.08 units, 23% greater than the decrease rate of sea surface pH in the global ocean. As atmospheric CO_2 increases, the acidification rate of seawater also accelerates. For the past 20 years, especially the last 10 years (2010–2019), the reduction rate of Zhejiang offshore sea surface pH significantly accelerated compared to 1980–1999. The pH reduction rate increased from 0.017/10a in 1980–1989 to 0.023/10a in 2010–2019 (accelerated by 35%, **Figure 6**).

Zhejiang offshore is the habitat of a large number of marine organisms, where fisheries amount to about 220,000 km^2. The main fishery products include fish, shrimp, crab, shellfish, and other calcified organisms. The total allowable catch in Zhejiang offshore ranks the first in China, and in recent years, the annual production all reached three million tons. By conducting pCO_2/pH perturbation experiments, Wu and Gao concluded that, the effects of ocean acidification and solar UV changes would also suppress photosynthesis in the China seas [51]. Physiology, morphology, and behavior of some marine organisms (e.g., cnidarians and molluscs) would also be influenced by seawater

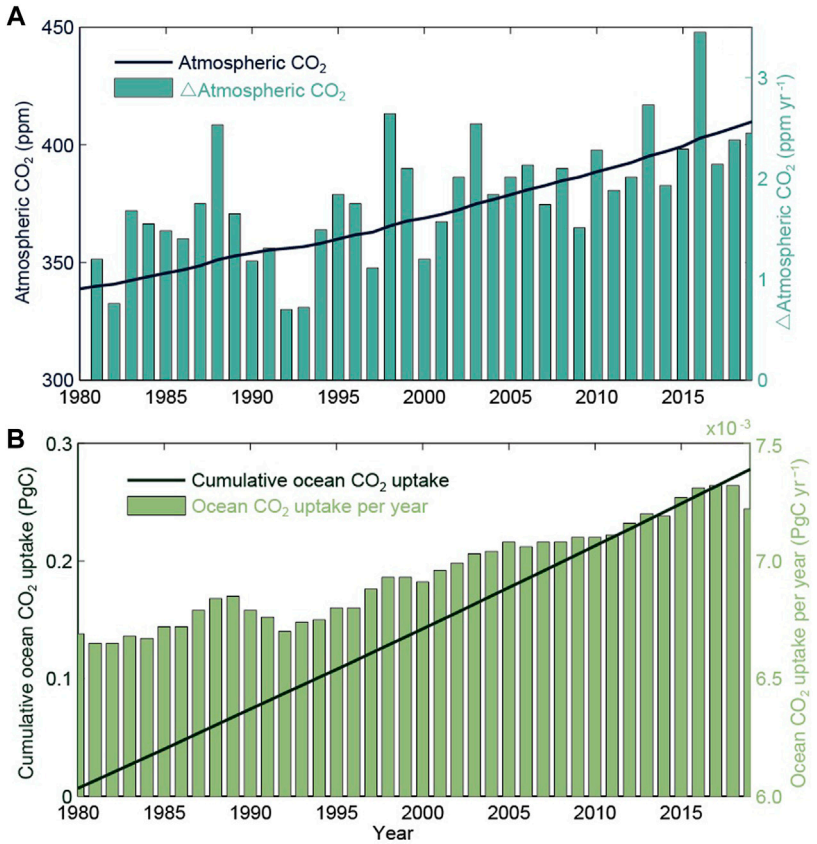

FIGURE 4 | (A) Prescribed atmospheric CO_2 concentration and **(B)** model-simulated time series of annual cumulative oceanic CO_2 uptake in Zhejiang offshore (lines). Changes of atmospheric CO_2 concentration relative to the previous year and oceanic CO_2 uptake per year are also shown by the boxes.

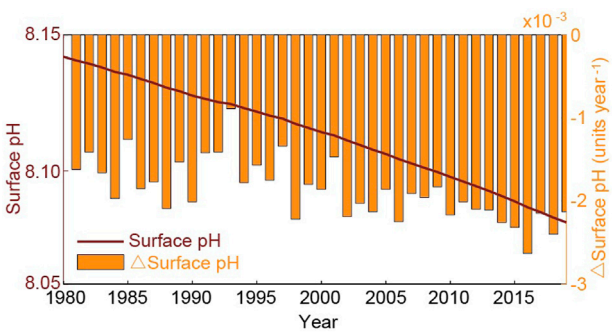

FIGURE 5 | Model-simulated time series of annual mean sea surface pH in Zhejiang offshore (line). Changes of surface pH relative to the previous year are also shown by the boxes.

acidification [52]. Therefore, ocean acidification would have important effects on the basic biochemical processes and ecosystem in Zhejiang offshore, leading to reductions in fisheries and aquaculture production, resulting in economic losses and important impacts on millions of people depending on seafood and other marine resources. Meanwhile, acidified seawater could accelerate the corrosion of building materials, having adverse impacts on the quality of marine constructions, causing economic losses.

SST Changes and Ocean Acidification of Zhejiang Offshore in the Next 20 Years

The UVic model was used to quantify changes in SST and ocean acidification in Zhejiang offshore from 2020 to 2040, under different greenhouse gas emission scenarios (RCP2.6, RCP4.5, RCP6.0, and RCP8.5). Under four RCP scenarios, atmospheric CO_2 concentration would increase by 28–74 ppm in the next 20 years, resulting in a rise of 0.3–0.5°C in Zhejiang offshore SST (**Figures 7A,C**).

With the continuing increases in atmospheric CO_2 content, Zhejiang offshore keeps absorbing atmospheric CO_2, resulting in continuous acidification of seawater. During 2020–2040, under different RCP scenarios, simulated cumulative CO_2 uptakes of Zhejiang offshore are 0.150–0.165 Pg C (**Figure 7B**). Under RCP8.5, from 2020 to 2040, Zhejiang sea surface pH decreases by 0.07, corresponding to an increase of 17% in hydrogen ion concentration, while under the RCP2.6 scenario, Zhejiang sea surface pH decreases by 0.03, corresponding to an increase of 7% in hydrogen ion concentration (**Figure 7D**). Therefore, in the next 20 years,

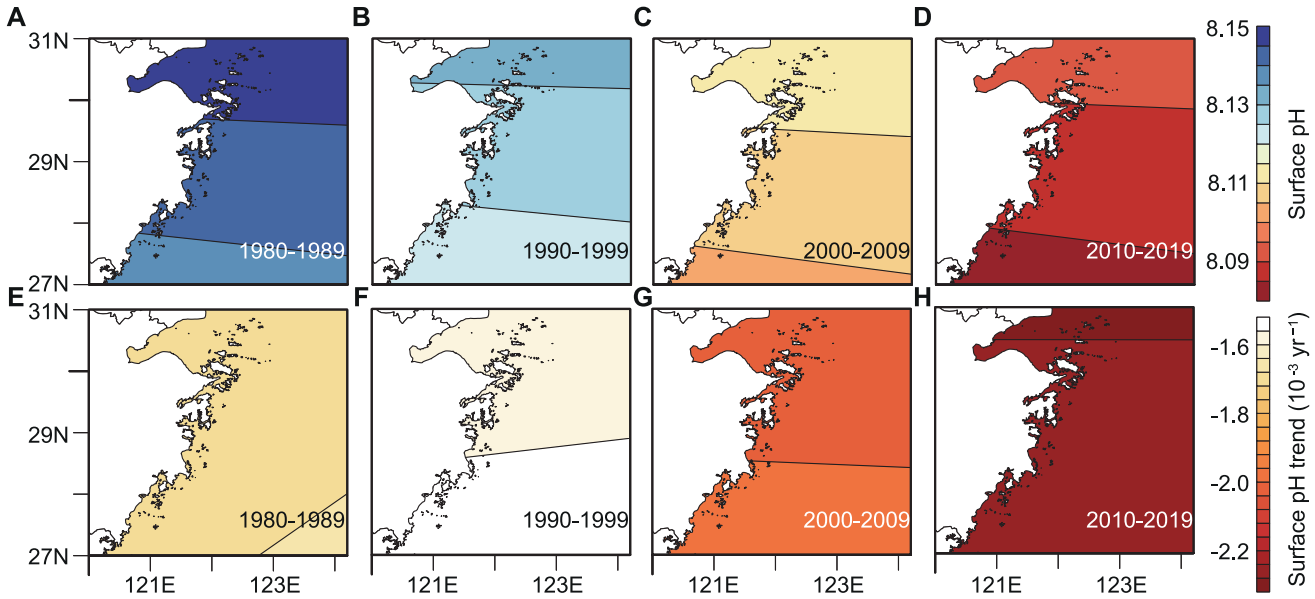

FIGURE 6 | Spatial distributions of simulated decadal mean **(A–D)** sea surface pH and **(E–H)** trends of sea surface pH in Zhejiang offshore. Results are shown for **(A,E)** 1980–1989, **(B,F)** 1990–1999, **(C,G)** 2000–2009, and **(D,H)** 2010–2019.

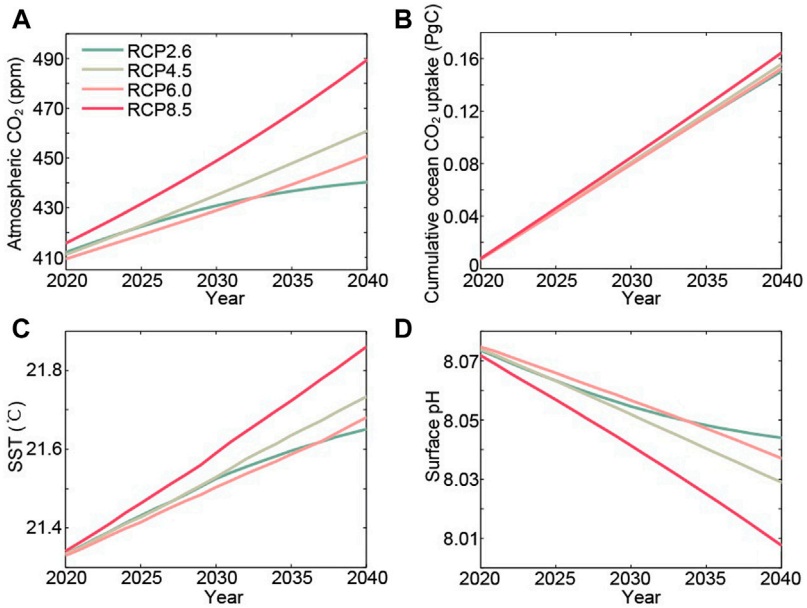

FIGURE 7 | (A) Prescribed atmospheric CO_2 concentration and model-simulated time series of annual mean **(B)** cumulative oceanic CO_2 uptake, sea surface **(C)** temperature, and **(D)** pH in Zhejiang offshore. Results are shown for the four simulations using the four RCP scenarios depicted in the Data and Modeling section.

resulting from the rises in atmospheric CO_2 concentration, Zhejiang offshore SST would rise continuously, and risks of ocean acidification would further increase. Consequently, further studies would be needed to develop a better understanding of the effects of climate change on the marine ecosystem; meanwhile, the capacity of climate change adaptation in Zhejiang should be improved.

The Nonlinear Relationship Between Atmospheric CO_2 Scenario and Oceanic Carbon Cycle

Simulated results under different scenarios show that the relationships among the atmospheric CO_2 scenario used, oceanic climate, and carbon cycle fields in Zhejiang offshore

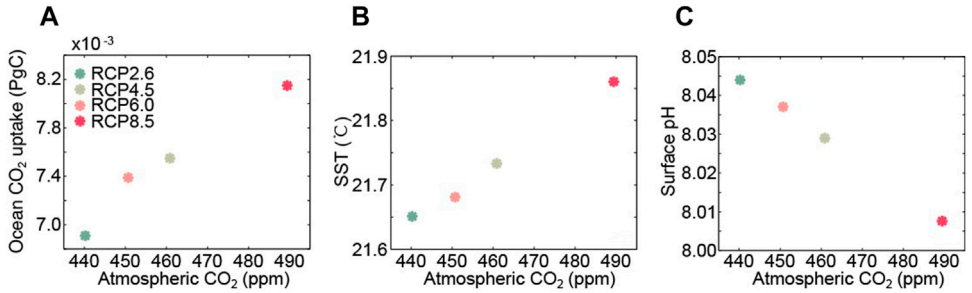

FIGURE 8 | Prescribed atmospheric CO_2 concentration against model-simulated **(A)** oceanic CO_2 uptake, **(B)** sea surface temperature, and **(C)** sea surface pH in Zhejiang offshore at 2040. Results are shown for the four simulations using the four RCP scenarios depicted in the Data and Modeling section, revealing the nonlinearity relationships among the atmospheric CO_2 scenario used, oceanic climate, and carbon cycle fields.

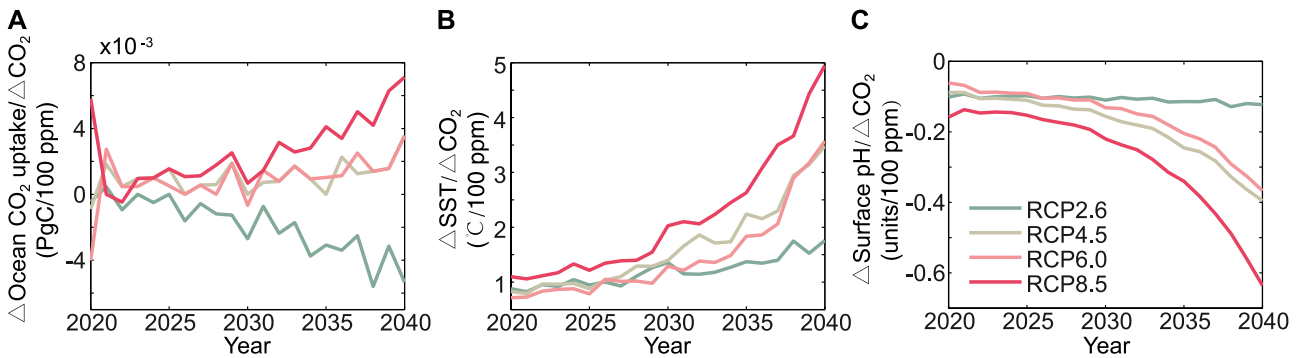

FIGURE 9 | Model-simulated time series of **(A)** Δoceanic CO_2 uptake/ΔCO_2, **(B)** Δsea surface temperature/ΔCO_2, and **(C)** Δsea surface pH/ΔCO_2 in Zhejiang offshore. Results are shown for the four simulations using the four RCP scenarios depicted in the Data and Modeling section.

are nonlinear (**Figure 8**). First, the RCP scenario of high CO_2 emissions does not necessarily correspond to high atmospheric CO_2 concentration. For example, during 2020–2040, atmospheric CO_2 concentration of RCP4.5 is higher than that of RCP6.0. Therefore, the RCP scenario of higher CO_2 emissions does not necessarily lead to larger oceanic CO_2 uptake, higher SST, or lower surface pH. For instance, at 2040, simulated oceanic CO_2 uptake in Zhejiang offshore is larger under RCP4.5 than that under RCP6.0 (0.0076 Pg C in RCP4.5 and 0.0074 Pg C in RCP6.0, respectively). In 2040, Zhejiang offshore seawater would experience greater warming and acidification under RCP4.5 than under RCP6.0 (**Figures 8B,C**). In addition, the RCP scenario of higher CO_2 emissions not necessarily leads to faster change of oceanic CO_2 uptake, SST, or surface pH. For example, at 2040, Δsurface pH/ΔCO_2 is faster under RCP4.5 than that under RCP6.0 (−0.40 units/100 ppm in RCP4.5 *versus* −0.37 units/100 ppm in RCP6.0, **Figure 9**).

Second, the relationship among atmospheric CO_2 concentration, ocean climate, and carbon cycle fields in Zhejiang offshore is nonlinear. For instance, at 2040, for Zhejiang offshore sea surface pH, $\Delta pH_{RCP8.5\text{-}RCP4.5}/\Delta CO_{2\ RCP8.5\text{-}RCP4.5}$ = -0.0749 units/100 ppm, $\Delta pH_{RCP4.5\text{-}RCP6.0}/\Delta CO_{2\ RCP4.5\text{-}RCP6.0}$ = -0.0796 units/100 ppm, while $\Delta pH_{RCP6.0\text{-}RCP2.6}/\Delta CO_{2\ RCP6.0\text{-}RCP2.6}$ = -0.0803 × 10^{-4} units/100 ppm, indicating faster acidification rates under scenarios of lower atmospheric CO_2 concentration. In comparison, the relationships among atmospheric CO_2 concentration, oceanic CO_2 uptake, and SST are far more nonlinear (**Figures 8A,B**). For example, at 2040, for SST in Zhejiang offshore, $\Delta SST_{RCP8.5\text{-}RCP4.5}/\Delta CO_{2\ RCP8.5\text{-}RCP4.5}$ = -0.44°C/100 ppm, $\Delta SST_{RCP4.5\text{-}RCP6.0}/\Delta CO_{2\ RCP4.5\text{-}RCP6.0}$ = -0.52°C/100 ppm, while $\Delta SST_{RCP6.0\text{-}RCP2.6}/\Delta CO_{2\ RCP6.0\text{-}RCP2.6}$ = -0.35°C/100 ppm. The nonlinearity between atmospheric CO_2 concentration and ocean acidification is noteworthy because it hints that if we aim to mitigate ocean acidification in Zhejiang offshore under a high emission scenario, deeper reductions of anthropogenic CO_2 emission may be needed.

CONCLUSION AND DISCUSSION

Under the background of greenhouse gas emissions and GW, it is an important issue to analyze the variation characteristics in ocean climate and carbon cycle fields, which determines the capacity of the ocean to capture atmospheric CO_2 [53–55]. In this article, changes of oceanic CO_2 uptake, SST, and acidification in Zhejiang offshore in last 40 years are assessed. Future changes in the next 20 years are also simulated by the UVic Earth system model. In addition, we also quantify the differences of oceanic carbon cycle under different RCP

scenarios, which contributes to develop a better understanding of oceanic carbon capture and climate adaptation.

Our results show that over the past 40 years, with the increasing atmospheric CO_2 content, SST in Zhejiang offshore increased at a rate of 0.16°C/10a. Meanwhile, the increase of annual oceanic CO_2 uptake in Zhejiang offshore is also closely related to the rise of atmospheric CO_2 concentration, which results in an increase of 20% in sea surface hydrogen ion concentration over the past 40 years, and accelerated acidification over the past 10 years.

Previous projects and studies also reported data-based estimates of changes in oceanic climate and seawater acidity. For instance, Kennedy et al. announced an increase in global SST of 0.124 ± 0.030°C/10a in 1979–2012 by using observation-based HadSST3 data [56]. Smith et al. reported an increase in global SST of 0.105 ± 0.031°C/10a in 1979–2012 by using ERSSTv3b data [57]. These assessed SST growth rates are relatively slower than our result of 0.16°C/10a for Zhejiang offshore. Ishii et al. analyzed observations in the coast of western North Pacific, reporting a decrease rate of 0.020 ± 0.007 units/10a in surface pH during 1994–2008 [58], consistent with our simulated results, faster than central Pacific of 0.014 ± 0.002 units/10a in 1998–2007 [59] and Eastern North Atlantic Ocean of 0.015 ± 0.002 units/10a in 1995–2004 [60]. Therefore, Zhejiang offshore is one of the most vulnerable areas to climate change and ocean acidification.

Four CO_2 emission scenarios are used to simulate oceanic CO_2 uptake, SST, and pH in Zhejiang offshore during 2020–2040. By 2040, with the rise of atmospheric CO_2 concentration under four RCP scenarios, SST in Zhejiang offshore increases by 0.3–0.5°C, whereas cumulative oceanic CO_2 uptake is 0.150–0.165 Pg C, leading to a decrease of sea surface pH by 0.03–0.07. Compared to RCP2.6, the decrease of surface pH in Zhejiang offshore is doubled under RCP8.5. In addition, the relationship between the CO_2 scenario used and oceanic carbon cycle is nonlinear, which is important because if we want to mitigate ocean acidification in Zhejiang offshore under a higher CO_2 concentration scenario, more effective anthropogenic CO_2 emission reductions may be needed.

This study has investigated the variation characteristics of oceanic climate and carbon cycle fields in Zhejiang offshore on timescales of decades by using an Earth system model. Some processes or feedbacks that are not considered in this study may also have impacts on the ocean carbon cycle and climate system. For instance, ocean acidification tends to decrease the calcification rate of some ocean calcifying organisms, increasing sea surface alkalinity, promoting oceanic CO_2 sequestration, and mitigating ocean acidification. Moreover, this study has not included the interactive effects between ocean acidification and $CaCO_3$ in the sediments, which is considered to mitigate the chemistry change in the deep ocean on millennia timescales.

Until now, although Zhejiang has taken steps to develop climate change adaptation and emission reduction policies, more meteorological and climatological measures still need to be adopted to reduce the impacts of extreme climate events on coastal regions, for example, 1) strengthening the monitoring and early warning system for marine disasters in Zhejiang province; 2) paying more attention to the adverse impacts of future climate change on marine fisheries, aquaculture, ecosystems, major infrastructure constructions, and city planning in coastal regions; and 3) investigating innovations to cope with the adverse effects of marine disasters, which is crucial for the sustainable development of the oceans. In addition, further observational and modeling studies would be required to develop a better understanding of the response of oceanic carbon cycle and the climate system to oceanic carbon sequestration, which is vital for more reliable projections of future climate and marine ecosystem changes.

DATA AVAILABILITY STATEMENT

The original contributions presented in the study are included in the article/Supplementary Material; further inquiries can be directed to the corresponding author.

AUTHOR CONTRIBUTIONS

All authors contributed to this research in collaboration. KW and HZ wrote the manuscript, GF proposed the conceptualization, ZL, ZY, and PL provided substantial help with the paper schedule and gave advice on the experiment and supervised. All authors have read and agreed to the published version of the manuscript.

FUNDING

This study was supported by the Natural Science Foundation of Zhejiang Province (LQ20D050003), the Natural Science Foundation of China (42005027 and 41605049), the Key R&D Program of Zhejiang Province (2021C02036), Fund for Meteorological Science and Technology of Zhejiang Province, China (2019YB03 and 2020YB04), the Natural Science Basic Research Program of Shaanxi (2021JQ-957), and the Talent Cultivation Project of Zhejiang Association for Science and Technology in 2020 (CTZB-2020080127).

REFERENCES

1. Friedlingstein P, O'Sullivan M, Jones MW, Andrew RM, Hauck J, Olsen A, et al. Global Carbon Budget 2020. *Earth Syst Sci Data* (2020) 12(4):3269–340. doi:10.5194/essd-12-3269-2020
2. Cai W, Ng B, Geng T, Wu L, Santoso A, and McPhaden MJ. Butterfly Effect and a Self-Modulating El Niño Response to Global Warming. *Nature* (2020) 585(7823):68–73. doi:10.1038/s41586-020-2641-x
3. Yin Z, Wang H, and Ma X. Possible Relationship between the Chukchi Sea Ice in the Early Winter and the February Haze Pollution in the North China Plain. *J Clim* (2019) 32(16):5179–90. doi:10.1175/jcli-d-18-0634.1
4. Wang K, Feng G, Zeng Y, Li Z, and Wang Y. Extraction of 10-30-day Stable Components from a Boreal Atmosphere during ENSO Phases. *Discrete Dyn Nat Soc* (2015) 2015:1–6. doi:10.1155/2015/919286
5. Guo Y, and Tan Z. On the Sensitivity of the Relationship between Hadley Circulation Asymmetry and ENSO in CMIP5 Models. *Geophys Res Lett* (2018) 45(17):9253–9. doi:10.1029/2018gl079515

6. Hu D, Guan Z, Guo Y, Lu C, and Jin D. Dynamical Connection between the Stratospheric Arctic Vortex and Sea Surface Temperatures in the North Atlantic. *Clim Dyn* (2019) 53(11):6979–93. doi:10.1007/s00382-019-04971-2
7. Hoegh-Guldberg O, Hughes L, McIntyre S, Lindenmayer DB, Parmesan C, Possingham HP, et al. ECOLOGY: Assisted Colonization and Rapid Climate Change. *Science* (2008) 321(5887):345–6. doi:10.1126/science.1157897
8. Dai A. Increasing Drought under Global Warming in Observations and Models. *Nat Clim Change* (2013) 3(1):52–8. doi:10.1038/nclimate1633
9. Huang J, Yu H, Guan X, Wang G, and Guo R. Accelerated Dryland Expansion under Climate Change. *Nat Clim Change* (2016) 6(2):166–71. doi:10.1038/nclimate2837
10. Wang K, Feng G, Ye T, Wang X, and Liu P. The Variation Characteristics of Asian Surface Temperature and Precipitation in the Early 21st century. *Discrete Dyn Nat Soc* (2016) 7929647. doi:10.1155/2016/7929647
11. Su T, Feng T, and Feng G. Evaporation Variability under Climate Warming in Five Reanalyses and its Association with pan Evaporation over China. *J Geophys Res Atmos* (2015) 120(16):8080–98. doi:10.1002/2014jd023040
12. Caldeira K, and Wickett ME. Anthropogenic Carbon and Ocean pH. *Nature* (2003) 425(6956):365. doi:10.1038/425365a
13. Yan P, Hou W, and Feng G. Transition Process of Abrupt Climate Change Based on Global Sea Surface Temperature over the Past century. *Nonlin Process. Geophys* (2016) 23(3):115–26. doi:10.5194/npg-23-115-2016
14. Wang K, Feng G, Zhang H, Li Z, Fan G, and Yu Z. Climate Change Characteristics and Adaptation in the Offshore East China Sea from 1979 to 2017. *J Coastal Res* (2020) 99(SI):54–9. doi:10.2112/si99-008.1
15. Cai R, Tan H, and Kontoyiannis H. Robust Surface Warming in Offshore China Seas and its Relationship to the East Asian Monsoon Wind Field and Ocean Forcing on Interdecadal Time Scales. *J Clim* (2017) 30(22):8987–9005. doi:10.1175/jcli-d-16-0016.1
16. Guo Y, and Tan Z. Westward Migration of Tropical Cyclone Rapid-Intensification over the Northwestern Pacific during Short Duration El Niño. *Nat Commun* (2018) 9(1). doi:10.1038/s41467-018-03945-y
17. McCulloch M, Falter J, Trotter J, and Montagna P. Coral Resilience to Ocean Acidification and Global Warming through pH Up-Regulation. *Nat Clim Change* (2012) 2(8):623–7. doi:10.1038/nclimate1473
18. Zhai W. Exploring Seasonal Acidification in the Yellow Sea. *Sci China Earth Sci* (2018) 61(6):647–58. doi:10.1007/s11430-017-9151-4
19. Kwiatkowski L, and Orr JC. Diverging Seasonal Extremes for Ocean Acidification during the Twenty-First century. *Nat Clim Change* (2018) 8(2):141–5. doi:10.1038/s41558-017-0054-0
20. Keir RS. The Dissolution Kinetics of Biogenic Calcium Carbonates in Seawater. *Geochimica et Cosmochimica Acta* (1980) 44(2):241–52. doi:10.1016/0016-7037(80)90135-0
21. Iglesias-Rodriguez MD, Halloran PR, Rickaby REM, Hall IR, Colmenero-Hidalgo E, Gittins JR, et al. Phytoplankton Calcification in a High-CO_2 World. *Science* (2008) 320(5874):336–40. doi:10.1126/science.1154122
22. Lombard F, Da Rocha RE, Bijma J, and Gattuso J. Effect of Carbonate Ion Concentration and Irradiance on Calcification in Planktonic Foraminifera. *Biogeosciences* (2010) 7(1):247–55. doi:10.5194/bg-7-247-2010
23. Subhas AV, Adkins JF, Rollins NE, Naviaux J, Erez J, and Berelson WM. Catalysis and Chemical Mechanisms of Calcite Dissolution in Seawater. *Proc Natl Acad Sci USA* (2017) 114(31):8175–80. doi:10.1073/pnas.1703604114
24. Ning W, Liquan Z, Lin Y, and Bing CH. Research into Vulnerability Assessment for Coastal Zones in the Context of Climate Change. *Acta Ecologica Sinica* (2012) 32(7):2248–58. doi:10.5846/stxb201109291437
25. Sarmiento JL, and Gruber N. *Ocean Biogeochemical Dynamics*. Princeton University Press (2006). p. 73–394.
26. Gazeau F, Quiblier C, Jansen JM, Gattuso J, Middelburg JJ, and Heip CHR. Impact of Elevated CO_2 on Shellfish Calcification. *Geophys Res Lett* (2007) 34(7):L07603. doi:10.1029/2006gl028554
27. Wu T, Hou X, and Xu X. Spatio-temporal Characteristics of the mainland Coastline Utilization Degree over the Last 70 Years in China. *Ocean Coastal Manag* (2014) 98:150–7. doi:10.1016/j.ocecoaman.2014.06.016
28. Dee D. The Climate Data Guide: ERA-Interim (2020). Available from: https://climatedata guide.ucar.edu/climate-data/era-interim.
29. Zhang H, and Cao L. Simulated Effect of Calcification Feedback on Atmospheric CO_2 and Ocean Acidification. *Sci Rep* (2016), United Kingdom 6:20284. doi:10.1038/srep20284
30. Schmittner A, Oschlies A, Matthews HD, and Galbraith ED. Future Changes in Climate, Ocean Circulation, Ecosystems, and Biogeochemical Cycling Simulated for a Business-As-Usual CO_2 emission Scenario until Year 4000 AD. *Glob Biogeochem. Cycles* (2008) 22(1):GB1013. doi:10.1029/2007gb002953
31. Hunke EC, and Dukowicz JK. An Elastic-Viscous-Plastic Model for Sea Ice Dynamics. *J Phys Oceanogr* (1997) 27(9):1849–67. doi:10.1175/1520-0485(1997)027<1849:aevpmf>2.0.co;2
32. Bitz CM, Holland MM, Weaver AJ, and Eby M. Simulating the Ice-Thickness Distribution in a Coupled Climate Model. *J Geophys Res* (2001) 106(C2):2441–63. doi:10.1029/1999jc000113
33. Fanning AF, and Weaver AJ. An Atmospheric Energy-Moisture Balance Model: Climatology, Interpentadal Climate Change, and Coupling to an Ocean General Circulation Model. *J Geophys Res* (1996) 101(D10):15111–28. doi:10.1029/96jd01017
34. Meissner KJ, Weaver AJ, Matthews HD, and Cox PM. The Role of Land Surface Dynamics in Glacial Inception: a Study with the UVic Earth System Model. *Clim Dynam* (2003) 21(7-8):515–37. doi:10.1007/s00382-003-0352-2
35. Pacanowski R. MOM 2 Documentation User's Guide and Reference Manual. In: *GFDL Ocean Group Technical Report 3.2*. Princeton: NOAA, GFDL (1995).
36. Cao L, and Zhang H. The Role of Biological Rates in the Simulated Warming Effect on Oceanic CO_2 Uptake. *J Geophys Res Biogeosci* (2017) 122(5):1098–106. doi:10.1002/2016jg003756
37. Zhang H, and Wang K. Simulated CO_2-induced Ocean Acidification for Ocean in the East China: Historical Conditions since Preindustrial Time and Future Scenarios. *Sci Rep* United Kingdom (2019) 9:18559. doi:10.1038/s41598-019-54861-0
38. Dlugokencky E, and Tans P. Trends in atmospheric carbon dioxide. *National Oceanic & Atmospheric Administration*. USA: Earth System Research Laboratory (NOAA/ESRL) (2020). Available from: http://www.esrl.noaa.gov/gmd/ccgg/trends/global.html. [Accessed December 2, 2020].
39. Meinshausen M, Smith SJ, Calvin K, Daniel JS, Kainuma MLT, Lamarque J, et al. The RCP Greenhouse Gas Concentrations and Their Extensions from 1765 to 2300. *Climatic Change* (2011) 109(1-2):213–41. doi:10.1007/s10584-011-0156-z
40. Huang J, Yu H, Dai A, Wei Y, and Kang L. Drylands Face Potential Threat under 2 °C Global Warming Target. *Nat Clim Change* (2017) 7(6):417–22. doi:10.1038/nclimate3275
41. Key RM, Kozyr A, Sabine CL, Lee K, Wanninkhof R, Bullister JL, et al. A Global Ocean Carbon Climatology: Results from Global Data Analysis Project (GLODAP). *Glob Biogeochem Cy* (2004) 18(4). doi:10.1029/2004gb002247
42. Zeebe RE, and Wolf-Gladrow D. *CO_2 in Seawater: Equilibrium, Kinetics, Isotopes*. Bremerhaven: Gulf Professional Publishing (2001).
43. Zeebe RE. History of Seawater Carbonate Chemistry, Atmospheric CO_2, and Ocean Acidification. In: R Jeanloz, editor. *Annual Review of Earth and Planetary Sciences*, 40 (2012). p. 141–65. doi:10.1146/annurev-earth-042711-105521
44. Wei R, Zheng Y, Wu R, Xu X, and Chen Y. Vertical Change of Simulated Wind Speed in Offshore Area of Zhejiang Province by Assimilating QuikSCAT Ocean Surface Winds. *Sci Tech Eng* (2016) 16(01):17–23+52. doi:10.1175/MWR-2861.1
45. Shen J, Zhou S, Dong Y, and Cui X. Analysis on the winter Warm Currents in the East China Sea in the winter of 2003. *J. Shanghai Fish. Univ.* (2005). (1):51–4.
46. Ciais P, Sabine C, Bala G, Bopp L, Brovkin V, Canadell J, et al. Carbon and Other Biogeochemical Cycles. In: D Stocker TF, GK Qin, M Plattner, SK Tignor, J Allen, A Boschung, et al.,editors. *Climate Change 2013: The Physical Science Basis. Contribution of Working Group I to the Fifth Assessment Report of the Intergovernmental Panel on Climate Change*. Cambridge, United Kingdom and New York, NY, USA: Cambridge University Press (2013). p. 486.
47. Cao L, Wang S, Zheng M, and Zhang H. Sensitivity of Ocean Acidification and Oxygen to the Uncertainty in Climate Change. *Environ Res Lett* (2014) 9(6):064005. doi:10.1088/1748-9326/9/6/064005
48. Zhang H, and Cao L. Simulated Effects of Interactions between Ocean Acidification, marine Organism Calcification, and Organic Carbon export on Ocean Carbon and Oxygen Cycles. *Sci China Earth Sci* (2018) 61(6):804–22. doi:10.1007/s11430-017-9173-y

49. Schmittner A, Oschlies A, Giraud X, Eby M, and Simmons HL. A Global Model of the marine Ecosystem for Long-Term Simulations: Sensitivity to Ocean Mixing, Buoyancy Forcing, Particle Sinking, and Dissolved Organic Matter Cycling. *Glob Biogeochem Cycles* (2005) 19(3):GB3004. doi:10.1029/2004gb002283
50. Weaver AJ, Eby M, Wiebe EC, Bitz CM, Duffy PB, Ewen TL, et al. The UVic Earth System Climate Model: Model Description, Climatology, and Applications to Past, Present and Future Climates. *Atmosphere-Ocean* (2001) 39(4):361–428. doi:10.1080/07055900.2001.9649686
51. Wu Y, and Gao K. Combined Effects of Solar UV Radiation and CO_2-induced Seawater Acidification on Photosynthetic Carbon Fixation of Phytoplankton Assemblages in the South China Sea. *Chin Sci Bull* (2010) 55(32):3680–6. doi:10.1007/s11434-010-4119-y
52. Ishimatsu A, and Dissanayake A. Life Threatened in Acidic Coastal Waters. In: A Ishimatsu and H Lie, editors. *Coastal Environmental and Ecosystem Issues of the East China Sea*. Tokyo: TERRAPUB and Nagasaki University (2010). p. 283–303.
53. Wei T, Yang S, Moore JC, Shi P, Cui X, Duan Q, et al. Developed and Developing World Responsibilities for Historical Climate Change and CO_2 Mitigation. *Proc Natl Acad Sci* (2012) 109(32):12911–5. doi:10.1073/pnas.1203282109
54. Huang B, Su T, Wu Y, and Feng G. The Interdecadal Reverse of the Relationship and Feedback Mechanism between Sea Surface Temperature and Evaporation over the Indian Ocean during Boreal Autumn. *J Clim* (2020) 33(23):10205–19. doi:10.1175/jcli-d-20-0009.1
55. Han Z, Su T, Zhang Q, Wen Q, and Feng G. Thermodynamic and Dynamic Effects of Increased Moisture Sources over the Tropical Indian Ocean in Recent Decades. *Clim Dyn* (2019) 53(11):7081–96. doi:10.1007/s00382-019-04977-w
56. Kennedy JJ, Rayner NA, Smith RO, Parker DE, and Saunby M. Reassessing Biases and Other Uncertainties in Sea Surface Temperature Observations Measured *In Situ* since 1850: 2. Biases and Homogenization. *J Geophys Res* (2011) 116(D14):D14104. doi:10.1029/2010jd015220
57. Smith TM, Reynolds RW, Peterson TC, and Lawrimore J. Improvements to NOAA's Historical Merged Land-Ocean Surface Temperature Analysis (1880-2006). *J Clim* (2008) 21(10):2283–96. doi:10.1175/2007jcli2100.1
58. Ishii M, Kosugi N, Sasano D, Saito S, Midorikawa T, and Inoue HY. Ocean Acidification off the South Coast of Japan: A Result from Time Series Observations of CO_2 parameters from 1994 to 2008. *J Geophys Res* (2011) 116(C6):C06022. doi:10.1029/2010jc006831
59. Dore JE, Lukas R, Sadler DW, and Karl DM. Climate-driven Changes to the Atmospheric CO_2 Sink in the Subtropical North Pacific Ocean. *Nature* (2009) 424(6950):754–7. doi:10.1038/nature01885
60. González-Dávila M, Santana-Casiano JM, Rueda MJ, and Llinás O. The Water Column Distribution of Carbonate System Variables at the ESTOC Site from 1995 to 2004. *Biogeosciences* (2010) 7(10):3067–81. doi:10.5194/bg-7-3067-2010

Conflict of Interest: The authors declare that the research was conducted in the absence of any commercial or financial relationships that could be construed as a potential conflict of interest.

Publisher's Note: All claims expressed in this article are solely those of the authors and do not necessarily represent those of their affiliated organizations, or those of the publisher, the editors, and the reviewers. Any product that may be evaluated in this article, or claim that may be made by its manufacturer, is not guaranteed or endorsed by the publisher.

frontiers in Physics

ORIGINAL RESEARCH
published: 30 August 2021
doi: 10.3389/fphy.2021.721115

Pattern Dynamics of Vegetation Growth With Saturated Water Absorption

Li Li[1,2]*, *Jia-Hui Cao*[3] *and Xin-Yue Bao*[4]

[1]School of Computer and Information Technology, Shanxi University, Taiyuan, China, [2]Science and Technology on Electronic Test and Measurement Laboratory, North University of China, Taiyuan, China, [3]Complex Systems Research Center, Shanxi University, Taiyuan, China, [4]Yangzhou Shuren School, Yangzhou, China

Regular pattern is a typical feature of vegetation distribution and thus it is important to study the law of vegetation evolution in the fields of desertification and environment conservation. The saturated water absorption effect between the soil water and vegetation plays an crucial role in the vegetation patterns in semi-arid regions, yet its influence on vegetation dynamics is largely ignored. In this paper, we pose a vegetation-water model with saturated water absorption effect of vegetation. Our results show that the parameter $1/P$, which is conversion coefficient of water absorption, has a great impact on pattern formation of vegetation: with the increase of P, the density of vegetation decrease, and meanwhile it can induce the transition of different patterns structures. In addition, we find that the increase of appropriate precipitation can postpone the time on the phase transition of the vegetation pattern. The obtained results systematically reveal the effect of saturated water absorption on vegetation systems which well enrich the findings in vegetation dynamics and thus may provide some new insights for vegetation protection.

Keywords: vegetation pattern, saturated water absorption, pattern transition, dynamical model, desertification

OPEN ACCESS

Edited by:
Yipeng Guo,
Nanjing University, China

Reviewed by:
Zhiqiang Gong,
Beijing Climate Center (BCC), China
Sanling Yuan,
University of Shanghai for Science and Technology, China

***Correspondence:**
Li Li
lili831113@sxu.edu.cn

Specialty section:
This article was submitted to Interdisciplinary Physics, a section of the journal Frontiers in Physics

Received: *06 June 2021*
Accepted: *14 July 2021*
Published: *30 August 2021*

Citation:
Li L, Cao J-H and Bao X-Y (2021) Pattern Dynamics of Vegetation Growth With Saturated Water Absorption. Front. Phys. 9:721115. doi: 10.3389/fphy.2021.721115

1 INTRODUCTION

In nature, vegetation is very widely distributed in different places all over the world. At the same time, vegetation, as a producer in nature, converts carbon dioxide into carbohydrates through photosynthesis, which ensures the food source for humans and animals and keeps the content of carbon dioxide and oxygen in the environment relatively stable [1, 2]. Moreover, the soil and water conservation function of vegetation is also very significant. For example, vegetation can reduce the loss of rainwater on the surface and the erosion of the surface soil, and protect the sloping land. Vegetation stems and leaves release water vapor into the atmosphere by transpiration, so that water vapor emitted into the atmosphere and condensed water alleviates drought. Based on the above functions of vegetation, it is particularly necessary to study vegetation dynamics [3–6].

In recent years, duo to the impact of the greenhouse effect on human life and climate, vegetation plays an indispensable role in climate regulation [7, 8]. As for vegetation, people are always concerned about its growth and distribution. There are many factors affecting vegetation distribution, among which climate, geographical conditions and human factors are the most important. Moreover, different conditions will form different vegetation structure, and inhomogeneous distribution of vegetation is called vegetation pattern [9]. Pattern is a kind of non-uniform macroscopic structure with some regularity in space or time, which is ubiquitous in

nature, such as stripes of clouds in the sky, waves on the water, figures on the animals and regular spatial pattern which observed in spatiotemporal systems far from equilibrium states [10, 11].

Patterns have been extensively studied and a wide range of patterns are found including vegetation patterns [12], infectious disease patterns [13], and patterns on predator-prey systems [14–16]. They are induced by different mechanisms and it is vital to understand these mechanisms. Mathematical modeling has become one of the most useful tools in exploring the mechanisms on vegetation dynamics including pattern formation and ecological functions [17]. There are many studies on vegetation pattern. In 1997, Lefever and Lejeune established a single-variable model, which revealed a resource competition mechanism among vegetation communities, namely promotion at short distance and inhibition at long distance [18]. In 1999, Klausmeier firstly proposed the classical vegetated-water model, explaining the regular stripes on the slopes and irregular mosaics on the ground, and pointed out that nonlinear mechanisms play a major role in determining the spatial structure of plant communities [19]. In 2013, Sun et al. revealed the relationship between precipitation and pattern formation: when rainfall is small, the vegetation will form spot pattern; when precipitation increases, the density of the spot pattern will increase, and vegetation appears as spot-stripes mixed pattern with low density [20]. In 2018, Liu et al. proposed a cross-diffusion vegetation system, in which the phenomenon of spot pattern transition was found [17]. In addition, cross-diffusion increased the vegetation density. In 2017, Zhang et al. proposed a vegetation-soil model and explained that wind can induce the generation of vegetation spot pattern. These models do not take into account that vegetation water absorption is not immoderate [21]. When vegetation water absorption reaches a certain degree, vegetation water absorption rate will decrease, which is called the saturation effect of vegetation water absorption. Yuval revealed that high water absorption and rapid diffusion of water in perennial herbs [22]. Of particular interest, this work showed that the pattern transition between multi-steady states is not necessarily catastrophic, yet it can be gradually phase-changed. Based on the observation data of mathematical model, the cause of fairy circles vegetation patch is explained as intra specific competition and the scale dependent effect of vegetation between animals that capture from plants [23]. There are also some work on the early warning signal of desertification [24–26].

Water absorption by vegetation is an important process of vegetation growth. The existed work assumed that water absorption is a linear function of vegetation biomass [6, 9, 19]. However, many types of vegetation have a saturation effect when absorbing water [27–30], which is generally not well studied by scientists. In fact, this saturated water absorption may have great influences of the vegetation pattern. In this sense, we will show the effect of saturation on the dynamical behavior of vegetation system.

The paper is organized as follows. In **Section 2**, we pose a vegetation-water model with saturated water absorption of vegetation and mathematical analysis on the emergence of Turing patterns is presented. In **Section 3**, we reveal the influences of saturated water absorption of vegetation on the patterns and persistence of vegetation system. In the last section, we give some discussion and conclusion.

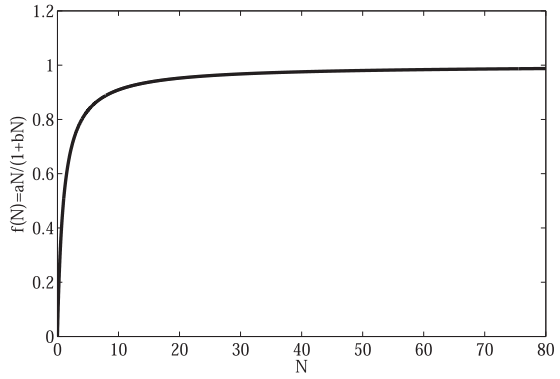

FIGURE 1 | Saturated water absorption on vegetation. When the water concentration is small, the water absorption of vegetation will increase with the increase of water concentration. However, as the water concentration continues to increase, the water absorption of vegetation tends to be constant.

2 MATHEMATICAL ANALYSIS

In this section, we will introduce two-dimensional model to descrbe the interactions of vegetation and water, which is posed by Klausmeier [19]:

$$\begin{cases} \dfrac{\partial W}{\partial T} = A - LW - RWN^2 + V\dfrac{\partial W}{\partial X}, \\ \dfrac{\partial N}{\partial T} = RJWN^2 - MN + D\Delta N. \end{cases} \tag{1}$$

In the above model, there are seven parameters, which are used to depict vegetation physiological phenomena and the change of water. They are all positive depend on what the parameters mean. The first equation of the model (1) represents the change of water. A represents precipitation and water is reduced by evaporation at rate LW. Vegetation absorbs water at rate $RG(W)F(N)N$, where $G(W) = W$ is saturated water absorption on vegetation, and take $F(N) = N$. The second equation of the model (1) is used to simulate the growth process of vegetation, where J is the conversion rate of vegetation into biomass through water absorption and M is lost through mortality. Water flow downhill at speed V and vegetation dispersal is modeled by a diffusion term with diffusion coefficient D.

In this work, we introduce a model contains two variables with saturated vegetation water absorption. This model is more reasonable compare with that model, in which the saturation of vegetation in absorbing water is not taken into account. It is because that the physiological process by which vegetation absorbs water from the soil and forms vegetation biomass is not inordinate, instead, as water increases, it is absorbed by

TABLE 1 | Description of the parameters in the model (2).

Parameter	Units	Description
A	kg/m^2yr^{-1}	Precipitation rate
L	yr^{-1}	Water evaporation rate
R	$(kg/m^2)^{-1}yr^{-1}$	Water consumption rate
J	$(kg/m^2)^{-1}yr^{-1}$	Conversion coefficient of plant water absorption into biomass
A	–	Water absorption rate
B	–	Saturated rate
M	yr^{-1}	Mortality rate
D_1	m^2/yr^{-1}	Diffusion coefficient of seed
D_2	m^2/yr^{-1}	Diffusion coefficient of soil-water

vegetation to a state of saturation. Therefore, we take $F(N) = \frac{aN}{1+bN}$ to model the saturated water absorption of vegetation (**Figure 1**).

At the same time, due to the diffusion of water, we will add $D_1\Delta\bar{W}$ to our system, namely:

$$\begin{cases} \frac{\partial \bar{W}}{\partial \bar{T}} = A - L\bar{W} - R\bar{W}\frac{a\bar{N}^2}{1+b\bar{N}} + D_1\triangle\bar{W}, \\ \frac{\partial \bar{N}}{\partial \bar{T}} = RJ\bar{W}\frac{a\bar{N}^2}{1+b\bar{N}} - M\bar{N} + D_2\Delta\bar{N}, \end{cases} \tag{2}$$

where the biological meanings and units of the parameters in system (2) can be found in **Table 1**.

Let

$$t = L\bar{T}, \quad N = b\bar{N}, \quad B = \frac{M}{L}, \quad S = \frac{RJaA}{L^2b}, \quad P = \frac{Ra}{Lb^2},$$
$$W = \frac{RJa}{Lb}\bar{W}, \quad x = \sqrt{\frac{bD_2}{L}}X, \quad y = \sqrt{\frac{bD_2}{L}}Y, \quad D = \frac{D_1RJa}{D_2Lb^2}.$$

After the original system (2) is dimensionless, the following system is obtained:

$$\begin{cases} \frac{\partial W}{\partial t} = S - W - P\frac{WN^2}{1+N} + D\triangle W, \\ \frac{\partial N}{\partial t} = \frac{WN^2}{1+N} - BN + \triangle N. \end{cases} \tag{3}$$

The initial conditions and boundary conditions are as follows:

$$W(x,y,0) > 0, \ N(x,y,0) > 0, \ (x,y) \in \Omega = [0, L_x] \times [0, L_y], \tag{4}$$
$$\frac{\partial W}{\partial \vec{n}} = \frac{\partial N}{\partial \vec{n}} = 0, \ (x,y) \in \partial\Omega,$$

where L_x and L_y give region size in the directions of x and y respectively, $\vec{n}$ is the outward unit normal vector of the boundary $\partial\Omega$, here we consider the boundary $\partial\Omega$ with no flux, namely, Neumann boundary [31–33].

In the absence of diffusion, we consider the following system:

$$\begin{cases} \frac{dW}{dt} = S - W - P\frac{WN^2}{1+N} \triangleq f(W,N), \\ \frac{dN}{dt} = \frac{WN^2}{1+N} - BN \triangleq g(W,N). \end{cases} \tag{5}$$

It is easy to gain that system (3) has a boundary equilibrium $E_0 = (S, 0)$ and two positive equilibriums

$$E_1 = (W_1, N_1) = \left(B + \frac{2PB^2}{S - B + \sqrt{(B-S)^2 - 4PB^2}}, \frac{S - B + \sqrt{(B-S)^2 - 4PB^2}}{2PB} \right),$$

$$E_2 = (W_2, N_2) = \left(B + \frac{2PB^2}{S - B - \sqrt{(B-S)^2 - 4PB^2}}, \frac{S - B - \sqrt{(B-S)^2 - 4PB^2}}{2PB} \right).$$

provided that

$$(1) S > B; \ \ (2)(B-S)^2 - 4PB^2 > 0; \ \ (3)\sqrt{(B-S)^2 - 4PB^2} < S - B.$$

Under conditions (1), (2), (3), we focus on the stability of three equilibriums E_0, E_1, and E_2. The Jacobian matrix corresponding to equilibrium (W^*, N^*) as follows:

$$J = \begin{pmatrix} a_{11} & a_{12} \\ a_{21} & a_{22} \end{pmatrix},$$

where $a_{11} = -1 - \frac{PN^2}{1+N}$, $a_{12} = \frac{-2PWN}{1+N} + \frac{PWN^2}{(1+N)^2}$, $a_{21} = \frac{N^2}{1+N}$, $a_{22} = \frac{2WN}{1+N} - \frac{WN^2}{(1+N)^2}$.

Then we can gain the linearized system:

$$\begin{cases} \frac{dW}{dt} = a_{11}W + a_{12}N, \\ \frac{dN}{dt} = a_{21}W + a_{22}N. \end{cases} \tag{6}$$

And characteristic equation is:

$$\lambda^2 - (a_{11} + a_{22})\lambda + a_{11}a_{22} - a_{12}a_{21} = 0, \tag{7}$$

where

$$-(a_{11} + a_{22}) = b_1,$$
$$a_{11}a_{22} - a_{12}a_{21} = b_2.$$

i) When we consider $E_0(S, 0)$, one can obtain

$$|\lambda E - J|_{E_0} = (\lambda + B)(\lambda + 1),$$

and thus it is clear that $E_0(S, 0)$ is stable.

ii) When we consider $E_1 = (W_1, N_1)$, then one can obtain the Jacobian matrix of system (5) at equilibrium E_1:

$$J|_{E_1} = \begin{pmatrix} -1 - \dfrac{PN_1^2}{1+N_1} & -\dfrac{PB(N_1+2)}{1+N_1} \\ \dfrac{N_1^2}{1+N_1} & \dfrac{B}{1+N_1} \end{pmatrix},$$

$$F(\lambda)|_{E_1} = |\lambda E - J\|_{E_1} = \lambda^2 + b_{11}\lambda + b_{12},$$

where

$$b_{11} = 1 + \frac{PN_1^2 - B}{1+N_1}, b_{12} = \frac{B\left(PN_1^2 - 1\right)}{1+N_1}.$$

Therefore the necessary and sufficient conditions for the equilibrium E_1 being stable is $b_{11} > 0$ and $b_{12} > 0$.

Now combining biological significance of each parameter, $S > B$ holds. Then

$$b_{12} = \frac{\triangle + (S-B)\sqrt{\triangle}}{S - B + \sqrt{\triangle} + 2PB} > 0,$$

where $\triangle = (B–S)^2 – 4PB^2$. In the following, we consider the sign of b_{11},

$$\begin{aligned} b_{11} &= 1 + \frac{(S - B + \sqrt{\triangle})^2 - 4PB^3}{2B(S - B + \sqrt{\triangle} + 2PB)} \\ &= 1 + \frac{\triangle + (S-B)\sqrt{\triangle} + 2PB^2(1-B)}{B(S - B + \sqrt{\triangle} + 2PB)}. \end{aligned}$$

When $S(S-B) + S\sqrt{\Delta} > 2PB^3$, $b_{11} > 0$ holds.

iii) Next, we investigate the stability of $E_2 = (W_2, N_2)$. Similarly, we note the above equation as:

$$F_2(\lambda) = \lambda^2 + b_{21}\lambda + b_{22},$$

$$b_{21} = 1 + \frac{PN_2^2 - B}{1+N_2},\ b_{22} = \frac{B\left(PN_2^2 - 1\right)}{1+N_2}.$$

Substituting N_2 for b_{21} and b_{22}, then we can obtain:

$$b_{21} = \frac{\Delta - (S-B)\sqrt{\Delta} + 2PB(1-B)}{B(S - B - \sqrt{\Delta} + 2PB)} + 1,\ b_{22} = \frac{\Delta - (S-B)\sqrt{\Delta}}{S - B - \sqrt{\Delta} + 2PB}.$$

Then analyzing the sign of b_{21} and b_{22}. Because

$$\sqrt{\Delta} = \sqrt{(S-B)^2 - 4PB^2} < S - B,$$

therefore $b_{22} < 0$. So the equilibrium E_2 is unstable.

Therefore the system has only one stable positive equilibrium E_1. From biological perspective, we are interested in studying the stability behavior of E_1. The Jacobian matrix corresponding to E_1 is as follows:

$$J = \begin{pmatrix} a_{111} & a_{112} \\ a_{121} & a_{122} \end{pmatrix},$$

where

$$a_{11}^* = -1 - \frac{(S - B + \sqrt{\Delta})^2}{2B(S - B + \sqrt{\Delta} + 2PB)} < 0,$$

$$a_{12}^* = -PB\left(1 + \frac{2PB}{S - B + \sqrt{\Delta} + 2PB}\right) < 0,$$

$$a_{21}^* = -\frac{(S - B + \sqrt{\Delta})^2}{2PB(S - B + \sqrt{\Delta} + 2PB)} < 0,$$

$$a_{22}^* = \frac{2PB^2}{S - B + \sqrt{\Delta} + 2PB} > 0.$$

In the absence of diffusion, E_1 is stable, whereas become unstable when diffusion is added, which is called Turing instability.

$$\begin{cases} \dfrac{\partial W}{\partial t} = a_{11}W + a_{12}N + D\Delta W, \\ \dfrac{\partial N}{\partial t} = a_{21}W + a_{22}N + \Delta N. \end{cases} \tag{8}$$

Nonuniform perturbation near the equilibrium point E_1:

$$\begin{pmatrix} w \\ n \end{pmatrix} = \begin{pmatrix} w^* \\ n^* \end{pmatrix} + \varepsilon \begin{pmatrix} w_k \\ n_k \end{pmatrix} e^{\lambda t + ik\vec{n}} + c \cdot c \cdot + O(\varepsilon^2), \tag{9}$$

where λ is the growth rate of perturbations in time t, and i is the imaginary unit, k is the wave number, $r = (x, y)$ is the spatial vector in two dimensional space and *c. c.* stands for the complex conjugate. Substituting (**Eq. 9**) into (**Eq. 8**), we obtain characteristic equation:

$$\lambda^2 - tr(k)\lambda + \triangle_k = 0,$$

where

$$tr_k = a_{11} + a_{22} - (1+D)k^2 = tr_0 - k^2(1+D), \tag{10a}$$

$$\Delta_k = a_{11}a_{22} - a_{12}a_{21} - k^2(a_{11} + a_{22}D) + k^4 D = \Delta_0 - k^2(a_{11} + a_{22}D) + k^4 D. \tag{10b}$$

It is easy to get $tr_k < 0$ for any k due to that $tr_0 < 0$, while the sign of $\triangle k$ is indeterminate. Hopf bifurcation occurs when Im $(\lambda_0) \neq 0$, Re $(\lambda_0) = 0$, that is $a_{11} + a_{22} = 0$, $a_{11}a_{22} - a_{12}a_{21} > 0$, then we obtain critical Hopf bifurcation curve $a_{11} + a_{22} = 0$. Then choosing S as Hopf bifurcation parameter, then

$$S_H = \frac{B^2}{B-2}, \tag{11}$$

$Im(\lambda_k) = Re(\lambda_k) = 0$ at $k = k_T \neq 0$, that is $\Delta_{k_T} = 0$. And critical wave number satisfies

$$k_T^2 = \frac{(a_{11} + a_{22}D)}{(2D)}.$$

We take S as Turing bifurcation parameter, and its critical value S_T satisfies the following equation:

$$\begin{aligned} &\left((B^2D^2 + 2BD + 1)S^4\right. \\ &+ P^2D^4B^4 + 16B^3P^2D^3 - 20B^3PD^3 + 4B^3D^3 + 64B^2P^2D^2 - 16B^2PD^2 \\ &+ \left(26B^3PD^3 - 12B^3D^3 + 64B^2PD^2 - 8B^2D^2\right)S \\ &+ \left(-6B^3PD^3 + 12B^3D^3 - 14B^2PD^2 + 17B^2D^2 - 16BPD + 4BD\right)S^2 \\ &+ \left.\left(-4B^3D^3 - 10B^2D^2 - 6BD\right)S^3\right)B = 0. \end{aligned}$$

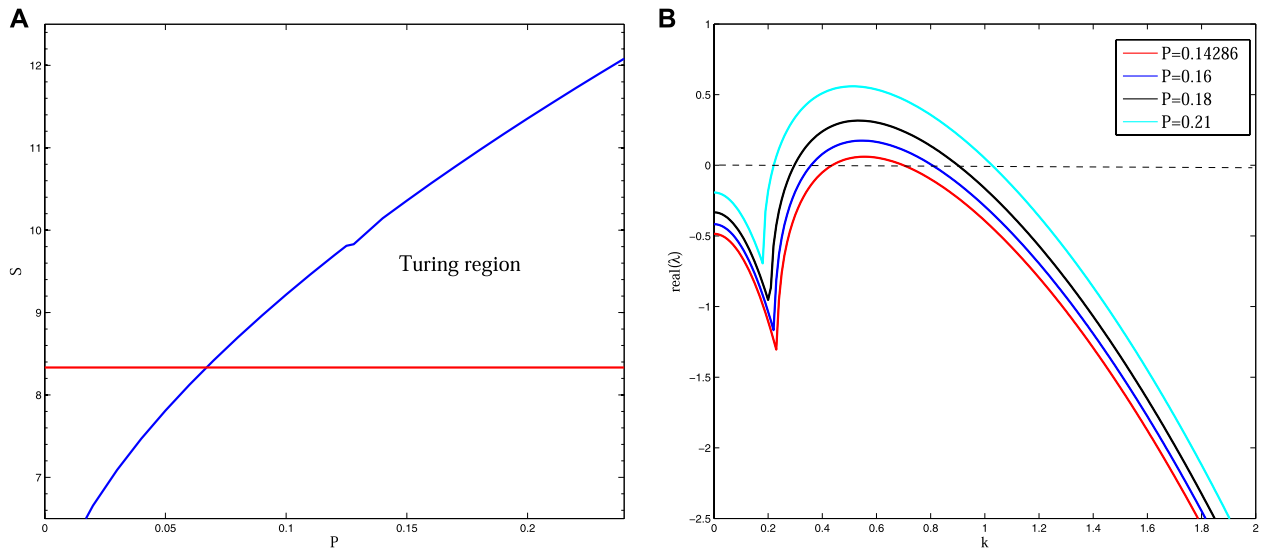

FIGURE 2 | (Color online) **(A)** The bifurcation diagram for system (3) in $P-S$ plane. In Turing region, Turing pattern will form. **(B)** Dispersion relation of system (3) with different P, other parameter values are taken as: $S = 10$, $B = 5$, $D = 30$, which reveals that the real-part of eigenvalues $\Re(\lambda)$ increases with P increasing.

In this paper, taking $D = 30$, $B = 5$, we gain the Turing region of system (3). In this region, stationary patterns can be observed (**Figure 2**). In addition, we obtain the dispersion relation, and find that the real part of the eigenvalue $\Re(\lambda)$ increases as the value of P increases. Moreover, Turing pattern will appear within the appropriate parameter range. Dispersion relation shows that when there is no space, the equilibrium point E_1 is stable. When combined with space, loss of stability occurs in relation to the wave numbers. These curves reveal that saturated water absorption induces the instability of system (3).

3 MULTIPLE SCALE ANALYSIS FOR TURING PATTERNS

The standard multiple-scale analysis yields the well-known amplitude equations. Close to the onset $S = S_T$, the eigenvalues associated to the critical modes are close to zero, and they are slowly varying modes, whereas the off-critical mode relax quickly [15, 34]. Consequently, the whole dynamical behaviors can be mainly determined by the dynamics of the active slow modes. The stability and the selection of the different patterns close to onset can be derived from the amplitude equations that govern the dynamics of these active modes. Turing patterns (e.g., hexxagon and stripe patterns) are thus well described by a system of three active resonant pair of modes $(k_j,-k_j)$ $(j = 1, 2, 3)$ making angles of $\frac{2\pi}{3}$ and $|k_j = k_T|$. We obtain the linearized form of model (3) at the equilibrium point E_1 as follows:

$$\begin{cases} \frac{\partial x}{\partial t} = a_{11}x + a_{12}y - \frac{PN^*(N^*+2)}{(1+N^*)^2}xy - \frac{PW^*}{(1+N^*)^3}y^2 - \frac{P}{(1+N^*)^3}xy^2 + \frac{PW^*}{(1+N^*)^4}y^3 + D\Delta x, \\ \frac{\partial y}{\partial t} = a_{21}x + a_{22}y + \frac{N^*(N^*+2)}{(1+N^*)^2}xy + \frac{W^*}{(1+N^*)^3}y^2 + \frac{1}{(1+N^*)^3}xy^2 - \frac{W^*}{(1+N^*)^4}y^3 + \Delta y. \end{cases} \tag{12}$$

We note

$$a_{13} = -\frac{PN^*(N^*+2)}{(1+N^*)^2}; a_{14} = -\frac{PW^*}{(1+N^*)^3}; a_{15} = -\frac{P}{(1+N^*)^3};$$
$$a_{16} = \frac{PW^*}{(1+N^*)^4};$$
$$a_{23} = \frac{N^*(N^*+2)}{(1+N^*)^2}; a_{24} = \frac{W^*}{(1+N^*)^3}; a_{25} = \frac{1}{(1+N^*)^3};$$
$$a_{26} = -\frac{W^*}{(1+N^*)^4};$$

and we will gain:

$$\begin{cases} \frac{\partial x}{\partial t} = a_{11}x + a_{12}y + a_{13}xy + a_{14}y^2 + a_{15}xy^2 + a_{16}y^3 + D\Delta x, \\ \frac{\partial y}{\partial t} = a_{21}x + a_{22}y + a_{23}xy + a_{24}y^2 + a_{25}xy^2 + a_{26}y^3 + \Delta y. \end{cases} \tag{13}$$

Close to onset $S = S_T$, the solutions of model (5*a*) (5*b*) can be expanded as

$$U = U_S + \Sigma_{j=1}^{3} U_0\left[A_j exp\left(ik_j \cdot \vec{r}\right) + \overline{A_j} exp\left(-ik_j \cdot \vec{r}\right)\right]. \tag{14}$$

At the same time, the solution of model (12) can be expanded as

$$U^0 = \Sigma_{j=1}^{3} U_0\left[A_j exp\left(ik_j \cdot \vec{r}\right) + \overline{A_j} exp\left(-ik_j \cdot \vec{r}\right)\right], \tag{15}$$

where U_S represents the uniform steady state. A_j and the conjugate $\overline{A_j}$ are the amplitudes associated with the modes k_j and $-k_j$, respectively. The amplitude equations are described through the equations:

$$\begin{cases} \tau_0 \dfrac{\partial A_1}{dt} = \mu A_1 + h\overline{A}_2\overline{A}_3 - \left(g_1|A_1|^2 + g_2\left(|A_2|^2 + |A_3|^2\right)\right)A_1, \\ \tau_0 \dfrac{\partial A_2}{dt} = \mu A_2 + h\overline{A}_1\overline{A}_3 - \left(g_1|A_2|^2 + g_2\left(|A_1|^2 + |A_3|^2\right)\right)A_2, \\ \tau_0 \dfrac{\partial A_3}{dt} = \mu A_3 + h\overline{A}_1\overline{A}_2 - \left(g_1|A_3|^2 + g_2\left(|A_1|^2 + |A_2|^2\right)\right)A_3. \end{cases} \quad (16)$$

where $\mu = (S_T - S)/S_T$ is a normalized distance to onset, τ_0 is a typical relaxation time. In the following, we will give the exact expressions of the coefficient τ_0, h, g_1 and g_2. Setting $X = (x, y)^T$, $N = (N_1, N_2)$, model (12) can be converted to the following system:

$$\frac{\partial X}{\partial t} = LX + N, \quad (17)$$

where

$$L = \begin{pmatrix} a_{11} + D\Delta & a_{12} \\ a_{21} & a_{22} + \Delta \end{pmatrix},$$

$$\begin{pmatrix} N_1 \\ N_2 \end{pmatrix} \begin{pmatrix} -\dfrac{PN^*(N^*+2)}{(1+N^*)^2}xy - \dfrac{PW^*}{(1+N^*)^3}y^2 - \dfrac{P}{(1+N^*)^3}xy^2 + \dfrac{PW^*}{(1+N^*)^4}y^3 \\ \dfrac{N^*(N^*+2)}{(1+N^*)^2}xy + \dfrac{W^*}{(1+N^*)^3}y^2 + \dfrac{1}{(1+N^*)^3}xy^2 - \dfrac{W^*}{(1+N^*)^4}y^3 \end{pmatrix}.$$

During the calculation, we just analysis the behavior of the parameter close to onset $S = S_T$. With this method, we can expanded S in the following term:

$$S_T - S = \varepsilon S_1 + \varepsilon^2 S_2 + \varepsilon^3 S_3 + O(\varepsilon^4), \quad (18)$$

where ε is a small parameter. Expanding the variable X and the nonlinear term N according to this small parameter, we have the following results:

$$X = \begin{pmatrix} x \\ y \end{pmatrix} = \varepsilon \begin{pmatrix} x_1 \\ y_1 \end{pmatrix} + \varepsilon^2 \begin{pmatrix} x_2 \\ y_2 \end{pmatrix} + O(\varepsilon^3), \quad (19)$$

$$N = \varepsilon^2 h^2 + \varepsilon^3 h^3 + O(\varepsilon^4). \quad (20)$$

where h^2 and h^3 are corresponding to the second and the third order of ε in the expansion of the nonlinear term N. At the same time, the linear operator L can be expanded as follows:

$$L = L_T + (S_T - S)M, \quad (21)$$

where

$$L_T = \begin{pmatrix} a_{11}^* + D\Delta & a_{12}^* \\ a_{21}^* & a_{22}^* + \Delta \end{pmatrix},$$

$$M = \begin{pmatrix} \dfrac{a_{11} - a_{11}^*}{S_T - S} & \dfrac{a_{12} - a_{12}^*}{S_T - S} \\ \dfrac{a_{21} - a_{21}^*}{S_T - S} & \dfrac{a_{22} - a_{22}^*}{S_T - S} \end{pmatrix} = \begin{pmatrix} m_{11} & m_{12} \\ m_{21} & m_{22} \end{pmatrix}.$$

Here one can have the expression of a_{ij}^* by substituting A_T for A in a_{ij} and b_{ij} is easy to be obtained. As for multiple-scale analysis, what really pivotal is that we can separate the dynamic behavior according to different time or spatial scale. We only need to separate the time scale for model (16) (*i.e.*, $T_0 = t$, $T_1 = \varepsilon t$, $T_2 = \varepsilon^2 t$). Each time scale T_i can be considered as independent variable. The derivative with respect to time becomes the following form:

$$\frac{\partial}{\partial t} = \frac{\partial}{\partial T_0} + \varepsilon \frac{\partial}{\partial T_1} + \varepsilon^2 \frac{\partial}{\partial T_2} + O(\varepsilon^3). \quad (22)$$

Since that amplitude A is a variable that changes slowly, the derivative with respect to time $\frac{\partial}{\partial T_0}$, which changes fast does not effect on the amplitude A. As a result, we have the following result:

$$\frac{\partial A}{\partial t} = \varepsilon \frac{\partial A}{\partial T_1} + \varepsilon^2 \frac{\partial A}{\partial T_2} + O(\varepsilon^3). \quad (23)$$

By using the **Eq. 19**, **Eq. 20**, **Eq. 21**, **Eq. 22**, and expanding **Eq. 15**. according to different orders of ε, we can obtain three equations as follows: The first order of ε:

$$L_T \begin{pmatrix} x_1 \\ y_1 \end{pmatrix} = 0;$$

The second order of ε:

$$L_T \begin{pmatrix} x_2 \\ y_2 \end{pmatrix} = \frac{\partial}{\partial T_1} \begin{pmatrix} x_1 \\ y_1 \end{pmatrix} - S_1 M \begin{pmatrix} x_1 \\ y_1 \end{pmatrix} - \begin{pmatrix} \dfrac{-PN^*(N^*+2)}{(1+N^*)^2}xy - \dfrac{PW^*}{(1+N^*)^3}y^2 \\ \dfrac{N^*(N^*+2)}{(1+N^*)^2}xy + \dfrac{W^*}{(1+N^*)^3}y^2 \end{pmatrix};$$

The third order of ε:

$$L_T \begin{pmatrix} x_3 \\ y_3 \end{pmatrix} = \frac{\partial}{\partial T_1} \begin{pmatrix} x_2 \\ y_2 \end{pmatrix} + \frac{\partial}{\partial T_2} \begin{pmatrix} x_1 \\ y_1 \end{pmatrix} - S_1 M \begin{pmatrix} x_2 \\ y_2 \end{pmatrix} - S_2 M \begin{pmatrix} x_1 \\ y_1 \end{pmatrix} - Z,$$

$$Z = \begin{pmatrix} \dfrac{-PN^*(N^*+2)}{(1+N^*)^2}(x_1y_2 + x_2y_1) - \dfrac{2PW^*}{(1+N^*)^3}y_1y_2 - \dfrac{P}{(1+N^*)^3}x_1y_1^2 + \dfrac{PW^*}{(1+N^*)^4}y_1^3 \\ \dfrac{N^*(N^*+2)}{(1+N^*)^2}(x_1y_2 + x_2y_1) + \dfrac{2W^*}{(1+N^*)^3}y_1y_2 + \dfrac{1}{(1+N^*)^3}x_1y_1^2 - \dfrac{W^*}{(1+N^*)^4}y_1^3 \end{pmatrix}.$$

As for the first order of ε:

$$L_T \begin{pmatrix} x_1 \\ y_1 \end{pmatrix} = 0, \quad (24)$$

as L_T is the linear operator of the system close to the onset, $(x_1, y_1)^T$ is the linear combination of the eigenvectors that corresponding to the eigenvalue 0. Solving the first order of ε, we can obtain:

$$\begin{pmatrix} x_1 \\ y_1 \end{pmatrix} = \begin{pmatrix} l \\ 1 \end{pmatrix} \left(W_1 e^{ik_1\vec{r}} + W_2 e^{ik_2\vec{r}} + W_3 e^{ik_3\vec{r}}\right) + c.c., \quad (25)$$

where $|k_j| = k_T^*$, $l = \frac{a_{11}^* - a_{22}^* D}{2a_{12}^* D}$. W_j is the amplitude of the mode $e^{ik_j\vec{r}}$ when the system is under the first order perturbation.

For the second order of ε, we can obtain:

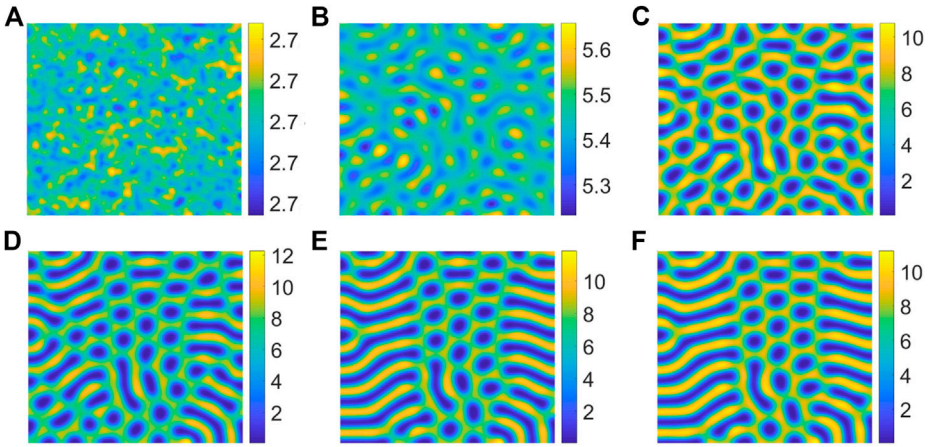

FIGURE 3 | Snapshots of contour pictures of the time evolution of vegetation at different instants with $p = 0.15$, $S = 10$, $D = 30$ and $B = 5$. **(A)** 0 iteration; **(B)** 1,000 iterations; **(C)** 2000 iterations; **(D)** 4,000 iterations; **(E)** 10,000 iterations; **(F)** 20,000 iterations.

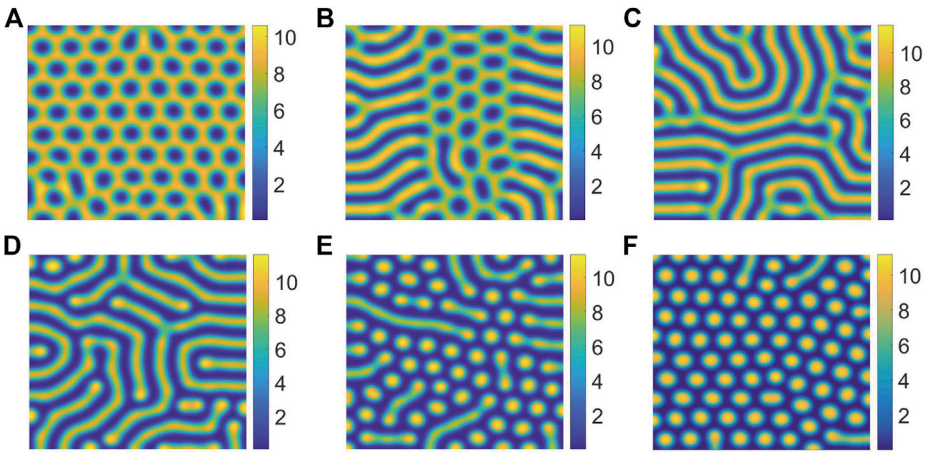

FIGURE 4 | Snapshots of the countour pictures of evolution of vegetation with different values of P, **(A)** $p = 0.14286$; **(B)** $p = 0.15$; **(C)** $p = 0.16$; **(D)** $p = 0.18$; **(E)** $p = 0.21$; **(F)** $p = 0.22$. The other parameters are taken as $S = 10$, $B = 5$, and $D = 30$.

$$L_T\begin{pmatrix} x_2 \\ y_2 \end{pmatrix} = \frac{\partial}{\partial T_1}\begin{pmatrix} x_1 \\ y_1 \end{pmatrix} - S_1 M\begin{pmatrix} x_1 \\ y_1 \end{pmatrix} - \begin{pmatrix} \frac{-PN^*(N^*+2)}{(1+N^*)^2}xy - \frac{PW^*}{(1+N^*)^3}y^2 \\ \frac{N^*(N^*+2)}{(1+N^*)^2}xy + \frac{W^*}{(1+N^*)^3}y^2 \end{pmatrix} = \begin{pmatrix} F_x \\ F_y \end{pmatrix}. \tag{26}$$

According to the Fredholm solubility condition, the vector function of the right hand of **Eq. 25**. must be orthogonal with the zero eigenvectors of operator L_c^+, where L_c^+ is the adjoint operator of L_c^+. In this system, the zero eigenvectors of operator L_c^+ are

$$\begin{pmatrix} 1 \\ -lD \end{pmatrix} e^{-ik_j\vec{r}} + c.c.\,(j = 1, 2, 3) \tag{27}$$

The orthogonality condition is

$$(1, -lD)\begin{pmatrix} F_x^i \\ F_y^i \end{pmatrix} = 0, \tag{28}$$

where F_x^i and F_y^i, separately, represent the coefficients corresponding to $e^{ik_j\vec{r}}$ in F_x and F_y. Taking $e^{ik_1\vec{r}}$ for instance, we will gain

$$l(1-D)\frac{\partial W_1}{\partial T_1} = S_1[(m_{11}l + m_{12}) - lD(m_{21}l + m_{22})]W_1 + 2[(a_{13}l + a_{14}) - lD(a_{23}l + a_{24})]\bar{W}_2\bar{W}_3. \tag{29}$$

The coefficient in **Eq. 30**. are obtained by solving the sets of the linear equations about $exp\ (0)$, $exp(ik_j\vec{r})$, $exp(i2k_j\vec{r})$, $exp(i(k_j - k_k)\vec{r})$.

With this method, we have

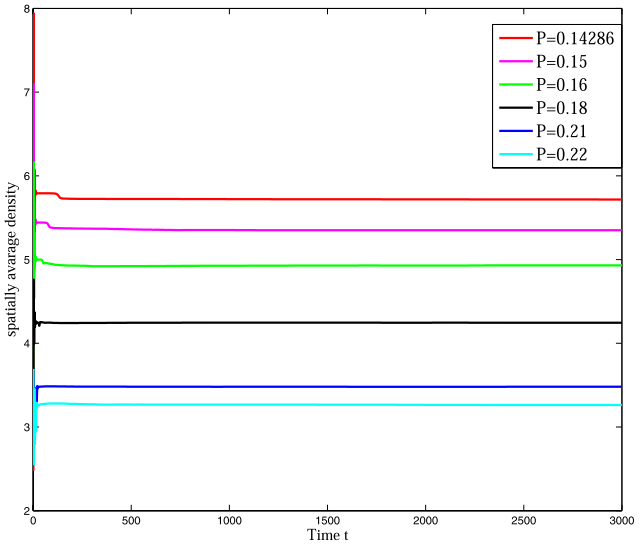

FIGURE 5 | (Color online) The time series of vegetation with P taking different values.

$$\begin{pmatrix} X_0 \\ Y_0 \end{pmatrix} = \begin{pmatrix} f_0 \\ g_0 \end{pmatrix} (|W_1|^2 + |W_2|^2 + |W_3|^2),$$

$$X_i = lY_i,$$

$$\begin{pmatrix} X_{jj} \\ Y_{jj} \end{pmatrix} = \begin{pmatrix} s \\ t \end{pmatrix} W_j^2,$$

$$\begin{pmatrix} X_{jk} \\ Y_{jk} \end{pmatrix} = \begin{pmatrix} p \\ q \end{pmatrix} W_j \bar{W}_k,$$

For the third order, we can gain

$$L_T \begin{pmatrix} x_3 \\ y_3 \end{pmatrix} = \frac{\partial}{\partial T_1} \begin{pmatrix} x_2 \\ y_2 \end{pmatrix} + \frac{\partial}{\partial T_2} \begin{pmatrix} x_1 \\ y_1 \end{pmatrix} - S_1 M \begin{pmatrix} x_2 \\ y_2 \end{pmatrix} - S_2 M \begin{pmatrix} x_1 \\ y_1 \end{pmatrix} - Z. \quad (30)$$

Using the Fredholm solubility condition again, we can obtain

$$\begin{aligned} & l(1-D)\left[\frac{\partial W_1}{\partial T_2} + \frac{\partial Y_1}{\partial T_1}\right] \\ & = S_1[(m_{11}l + m_{12}) - lD(m_{21}l + m_{22})]Y_1 + S_2[(m_{11}l + m_{12}) - lD(m_{21}l + m_{22})]W_1 \\ & + 2[(a_{13}l + a_{14}) - lD(a_{23}l + a_{24})](\bar{Y}_2\bar{W}_3 + \bar{Y}_3\bar{W}_2) \\ & - (G_1|W_1|^2 + G_2(|W_2|^2 + |W_3|^2))W_1, \end{aligned}$$

where

$$G_1 = (a_{13} - lDa_{23})(lg_0 + f_0) + 6[(a_{15}l + a_{16}) - lD(a_{25}l + a_{26})]$$
$$G_2 = (a_{13} - lDa_{23})(lg_0 + f_0) + 9[(a_{15}l + a_{16}) - lD(a_{25}l + a_{26})]$$

By transformation of W, the other two equations can be obtained and the amplitude A_i can be expanded as

$$A_i = \varepsilon W_i + \varepsilon^2 Y_i + O(\varepsilon^3). \quad (31)$$

For the order ε^2 and ε^3, we can obtain the amplitude equation corresponding to A_1 as follows:

$$\tau_0 \frac{\partial A_1}{\partial t} = \mu A_1 + h\bar{A}_2\bar{A}_3 - (g_1|A_1|^2 + g_2(|A_2|^2 + |A_3|^2))A_1, \quad (32)$$

where

$$\tau_0 = \frac{l}{H} S_T(1-D), \mu = \frac{S_T - S}{S_T}, h = \frac{2C}{lHS_T},$$
$$g_1 = \frac{G_1 S_T}{Hl^2}, g_2 = \frac{G_2 S_T}{Hl^2}.$$

with $H = [(m_{11}l + m_{12}) - lD(m_{21}l + m_{22})]$, $C = 2[(a_{13}l + a_{14}) - lD(a_{23}l + a_{24})]$.

The other two equations we can gain by transforming the subscript of A. Based on Ref. [10], one can calculate the values of μ_i $(i = 1, 2, 3, 4)$. When the controlled parameter μ increase to the critical point $\mu_2 = 0$, the stationary state of the system begins to lose stability. If $\mu_1 < \mu < \mu_2$, then the system exists a bistable region in the range of the controlled parameter. The emergence of Stripe patterns derives from supercritical bifurcation which are unstable

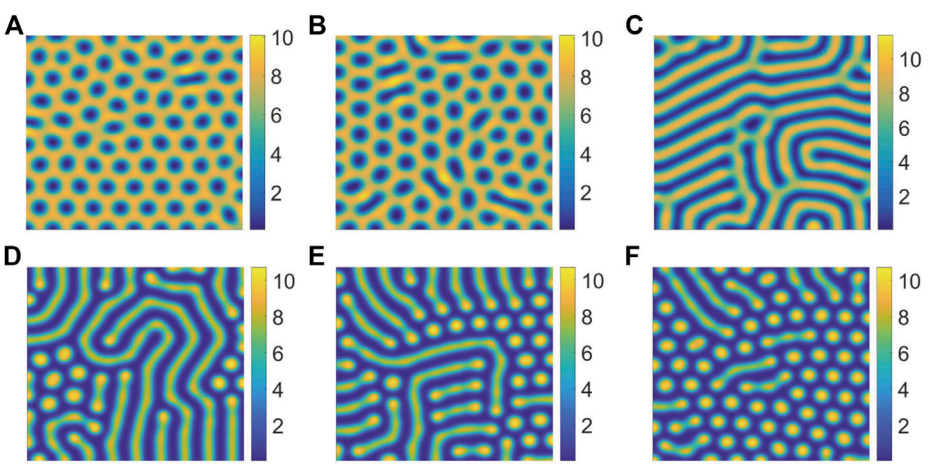

FIGURE 6 | Snapshots of the countour pictures of evolution of vegetation with different values of P, **(A)** $p = 0.16$; **(B)** $p = 0.17$; **(C)** $p = 0.18$; **(D)** $p = 0.23$; **(E)** $p = 0.238$; **(F)** $p = 0.25$. The other parameters are taken as $S = 10.5$, $B = 5$, and $D = 30$.

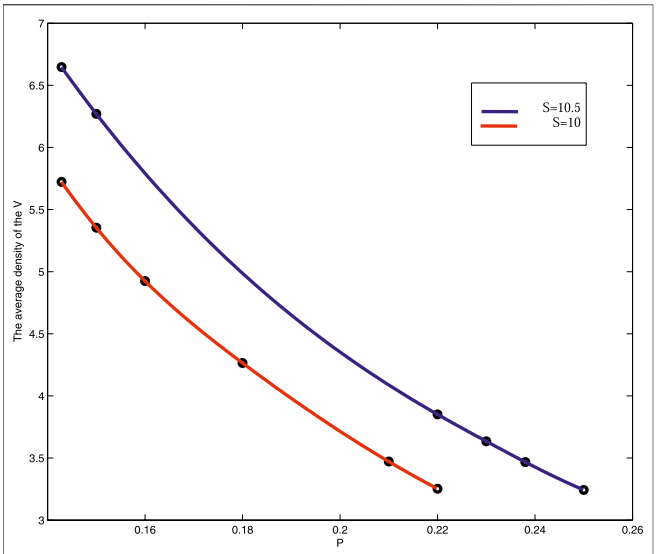

FIGURE 7 | (Color online) The average density map of vegetation is compared when precipitation is taken S = 10 and S = 10.5 respectively.

for $\mu < \mu_3$ and stable for $\mu > \mu_3$. When the controlled parameter μ exceed μ_4, there is coexistence of hexagon and stripe pattern.

4 MAIN RESULTS

In order to verify the above theoretical results, we carry out numerical simulation by taking B = 5, D = 30, and S = 10. This paper focuses on the spatial distribution of vegetation with the change of parameter P.

Currently, the desertification phenomenon is particularly austere, so it is the fundamental way for people to understand the cause of desertification correctly to master the law of vegetation evolution [35, 36].

Figure 3 shows the evolution of the spatial pattern of vegetation at 0, 1,000, 2000, 4,000, 10,000 and 20,000 iterations with p = 0.15. In (A), the vegetation distribution presents an irregular uniform mixing state, and the vegetation is uniformly distributed in the two-dimensional space. Then in (B), the vegetation can be observed to begin to gather into spot and stripe, but the density is not high. With time going by, in (C), the vegetation density increased. In (D), the spatial distribution of vegetation changes, forming a low-density stripe state. However, in (E), the structure of vegetation changes from low density stripe to higher stripe state gradually. At last, in (F), the density of the mixed pattern increases to form a clearer mixed pattern, and it doesn't change for a long time. The above figures show the change and evolution of vegetation structure over time. It can be concluded from this figure that random distribution can result in mixed patterns.

In **Figure 4**, we can find that the pattern is self-organizing. When the parameter(P) describing the saturated water absorption of vegetation changes, self-organizing patterns of different states can be obtained. **Figure 4** shows the transition of the vegetation pattern with p = 0.14286, 0.15, 0.16, 0.18, 0.21 and 0.22, where B = 5, D = 30, S = 10. From the simulation results of **Figure 5**, we can conclude that vegetation density get smaller and smaller with P increasing, which is consistent with the fact that $1/P$ is proportional to the rate at which vegetation absorbs water to generate vegetation. Meanwhile, we can find that the pattern changes from honeycomb pattern to mixed pattern, then changes from mixed pattern to labyrinth pattern, at last pattern changes from labyrinth pattern to spot pattern. As a result, we can conclude that the change of P induces pattern phase transition. Many researchers have proposed that spot pattern is the early warning of desertification [31, 37, 38], therefore we can get that P is of great significance in indicating desertification. Moreover, from the tendency of pattern phase transition, it can be found that P also has a vital influence on the ecosystem robustness. The larger P is, the more unstable the system tends to be. In general, the bigger vegetation density corresponds to a more robust ecosystem.

It is well known that precipitation plays a very significant role in vegetation growth. However, the relationship between precipitation and saturated water absorption of vegetation is still unclear. To reveal the relationship between them, we take S = 10.5, B = 5 and D = 30 and perform simulations. Then we gain the effect of P on the pattern phase transition and find several types of typical patterns in **Figure 6**.

On the circumstance of the increase of S, the pattern phase transition is insensitive to P. That is to say, when P changes from 0.1428 to 0.15 with S = 10, the pattern structure changes from honeycomb pattern to mixed pattern, however, when S = 10.5, the same transition tendency of which pattern structure from honeycomb pattern to mixed pattern will need a change of P from 0.16 to 0.23. Of course, the increase of the value of precipitation also increases the density of vegetation (**Figure 7**).

5 CONCLUSION

In this work, we show the effect of saturated water absorption on the vegetation dynamics based on a mathematical model in the form of reaction-diffusion equations. We gain rich pattern structures including spotted, mixed, stripe, honeycomb, and labyrinth patterns. It is revealed that there is a negative correlation between P and vegetation density. That is to say, the vegetation biomass decreases as the increase of P, and saturated water absorption can induces the pattern transition of vegetation structures in two-dimensional space. In addition, we also conclude that appropriate precipitation increase can postpone the pattern phase transition.

In this work, we focused our attention on the influences of parameter change on the dynamical behaviors. The results showed that small change may induce the behavior shift between different dynamical regions [39]. The findings can also be applied in other related fields, such as ecosystems, disease transmission, evolutions and so on.

It needs to point out that climatic factors are important impact factors for vegetation dynamics [40, 41]. In this sense, we need to combine these factors including temperature, illumination and wind to the mathematical models. Furthermore, big data analysis is useful to explore the inherent law of vegetation evolution in both space and time [42, 43]. These topics will be well addressed in the further study.

DATA AVAILABILITY STATEMENT

The original contributions presented in the study are included in the article/Supplementary Material, further inquiries can be directed to the corresponding author.

AUTHOR CONTRIBUTIONS

All authors have made great contributions to the writing of study and approved the submitted version. LL, J-HC, and X-YB established dynamical modeling. LL and J-HC participated in the program design. LL and X-YB mainly wrote the manuscript.

FUNDING

The project is funded by the National Natural Science Foundation of China under Grant No. 42075029, Program for the Outstanding Innovative Teams (OIT) of Higher Learning Institutions of Shanxi, and China Postdoctoral Science Foundation under Grant Nos. 2017M621110 and 2019T120199.

REFERENCES

1. Porporato A, D'Odorico P, Laio F, Ridolfi L, and Rodriguez-Iturbe I. Ecohydrology of Water-Controlled Ecosystems. *Adv Water Resour* (2002) 25:1335–48. doi:10.1016/S0309-1708(02)00058-1
2. Morgan RPC, and Duzant JH. Modified MMF (Morgan-Morgan-Finney) Model for Evaluating Effects of Crops and Vegetation Cover on Soil Erosion. *Earth Surf Process Landforms* (2008) 33:90–106. doi:10.1002/esp.1530
3. Balke T, Herman PMJ, and Bouma TJ. Critical Transitions in Disturbance-Driven Ecosystems: Identifying Windows of Opportunity for Recovery. *J Ecol* (2014) 102:700–8. doi:10.1111/1365-2745.12241
4. Claussen M, Bathiany S, Brovkin V, and Kleinen T. Simulated Climate-Vegetation Interaction in Semi-arid Regions Affected by Plant Diversity. *Nat Geosci* (2013) 6:954–8. doi:10.1038/ngeo1962
5. Juergens N. The Biological Underpinnings of Namib Desert Fairy Circles. *Science* (2013) 339:1618–21. doi:10.1126/science.1222999
6. Getzin S, Yizhaq H, Bell B, Erickson TE, Postle AC, Katra I, et al. Discovery of Fairy Circles in Australia Supports Self-Organization Theory. *Proc Natl Acad Sci USA* (2016) 113:3551–6. doi:10.1073/pnas.1522130113
7. Anselmo C, Thomas B, Miffre A, Francis M, Cariou JP, and Rairoux P. Remote Sensing of Greenhouse Gases by Combining Lidar and Optical Correlation Spectroscopy. *EPJ Web of Conferences* (2016) 119:05007. doi:10.1051/epjconf/201611905007
8. Giorgi F. Uncertainties in Climate Change Projections, from the Global to the Regional Scale. *EPJ Web of Conferences* (2010) 9:115–29. doi:10.1051/epjconf/201009009
9. Sun G-Q, Wang C-H, Chang L-L, Wu Y-P, Li L, and Jin Z. Effects of Feedback Regulation on Vegetation Patterns in Semi-arid Environments. *Appl Math Model* (2018) 61:200–15. doi:10.1016/j.apm.2018.04.010
10. Ou-Yang Q. *Introduction to Nonlinear Science and Speckle Pattern Dynamice*. Beijing: Peking university press (2010). p. 7.
11. Ma J, Xu Y, Wang C, and Jin W. Pattern Selection and Self-Organization Induced by Random Boundary Initial Values in a Neuronal Network. *Physica A: Stat Mech its Appl* (2016) 461:586–94. doi:10.1016/j.physa.2016.06.075
12. Sun G-Q, Wang C-H, and Wu Z-Y. Pattern Dynamics of a Gierer-Meinhardt Model With Spatial Effects. *Nonlinear Dyn* (2017) 88:1385–96. doi:10.1007/s11071-016-3317-9
13. Guo Z-G, Sun G-Q, Wang Z, Jin Z, Li L, and Li C. Spatial Dynamics of an Epidemic Model With Nonlocal Infection. *Appl Mathematics Comput* (2020) 377:125158. doi:10.1016/j.amc.2020.125158
14. Yang J, and Yuan S. Dynamics of a Toxic Producing Phytoplankton-Zooplankton Model With Three-Dimensional Patch. *Appl Mathematics Lett* (2021) 118:107146. doi:10.1016/j.aml.2021.107146
15. Jia D, Zhang T, and Yuan S. Pattern Dynamics of a Diffusive Toxin Producing Phytoplankton-Zooplankton Model With Three-Dimensional Patch. *Int J Bifurcation Chaos* (2019) 29:1930011. doi:10.1142/s0218127419300118
16. Xu C, Yuan S, and Zhang T. Competitive Exclusion in a General Multi-Species Chemostat Model With Stochastic Perturbations. *Bull Math Biol* (2021) 83:4. doi:10.1007/s11538-020-00843-7
17. Yin H-M, Chen X, and Wang L. On a Cross-Diffusion System Modeling Vegetation Spots and Strips in a Semi-arid or Arid Landscape. *Nonlinear Anal* (2017) 159:482–91. doi:10.1016/j.na.2017.02.022
18. Lefever R, and Lejeune O. On the Origin of Tiger bush. *Bltn Mathcal Biol* (1997) 59:263–94. doi:10.1007/bf02462004
19. Klausmeier CA. Regular and Irregular Patterns in Semiarid Vegetation. *Science* (1999) 284:1826–8. doi:10.1126/science.284.5421.1826
20. Sun G-Q, Zhang H-T, Wang J-S, Li J, Wang Y, Li L, et al. Mathematical Modeling and Mechanisms of Pattern Formation in Ecological Systems: a Review. *Nonlinear Dyn* (2021) 104:1677–96. doi:10.1007/s11071-021-06314-5
21. Zhang F, zhang H, Evans MR, and Huang T. Vegetation Patterns Generated by a Wind Driven Sand-Vegetation System in Arid and Semi-arid Areas. *Ecol Complexity* (2017) 31:21–33. doi:10.1016/j.ecocom.2017.02.005
22. Zelnik YR, Meron E, and Bel G. Gradual Regime Shifts in Fairy Circles. *Proc Natl Acad Sci USA* (2015) 112:12327–31. doi:10.1073/pnas.1504289112
23. Tarnita CE, Bonachela JA, Sheffer E, Guyton JA, Coverdale TC, Long RA, et al. A Theoretical Foundation for Multi-Scale Regular Vegetation Patterns. *Nature* (2017) 541:398–401. doi:10.1038/nature20801
24. HilleRisLambers R, Rietkerk M, van den Bosch F, Prins HHT, and de Kroon H. Vegetation Pattern Formation in Semi-Arid Grazing Systems. *Ecology* (2001) 82:50–61. doi:10.1890/0012-9658(2001)082[0050:vpfisa]2.0.co;2
25. Kéfi S, Rietkerk M, Alados CL, Pueyo Y, Papanastasis VP, ElAich A, et al. Spatial Vegetation Patterns and Imminent Desertification in Mediterranean Arid Ecosystems. *Nature* (2007) 449:213–7. doi:10.1038/nature06111
26. Scheffer M, Bascompte J, Brock WA, Brovkin V, Carpenter SR, Dakos V, et al. Early-Warning Signals for Critical Transitions. *Nature* (2009) 461:53–9. doi:10.1038/nature08227
27. Braud I, Biron P, Bariac T, Richard P, Canale L, Gaudet JP, et al. Isotopic Composition of Bare Soil Evaporated Water Vapor. Part I: RUBIC IV Experimental Setup and Results. *J Hydrol* (2009) 369:1–16. doi:10.1016/j.jhydrol.2009.01.034
28. Liu Z, Yu X, and Jia G. Water Utilization Characteristics of Typical Vegetation in the Rocky Mountain Area of Beijing, China. *Ecol Indicators* (2018) 91:249–58. doi:10.1016/j.ecolind.2018.03.083
29. Chang E, Li P, Li Z, Xiao L, Zhao B, Su Y, et al. Using Water Isotopes to Analyze Water Uptake during Vegetation Succession on Abandoned Cropland on the Loess Plateau, China. *Catena* (2019) 181:104095. doi:10.1016/j.catena.2019.104095
30. Xue Q, Liu C, Li L, Sun G-Q, and Wang Z. Interactions of Diffusion and Nonlocal Delay Give Rise to Vegetation Patterns in Semi-Arid Environments. *Appl Mathematics Comput* (2021) 399:126038. doi:10.1016/j.amc.2021.126038
31. Dufiet V, and Boissonade J. Dynamics of Turing Pattern Monolayers Close to Onset. *Phys Rev E* (1996) 53:4883–92. doi:10.1103/physreve.53.4883
32. Fasani S, and Rinaldi S. Remarks on Cannibalism and Pattern Formation in Spatially Extended Prey-Predator Systems. *Nonlinear Dyn* (2012) 67:2543–8. doi:10.1007/s11071-011-0166-4
33. Ma J, Ja Y, Tang J, and Chen Y. Parameter Fluctuation-Induced Pattern Transition in the Complex Ginzburg-Landau Equation. *Int J Mod Phys B* (2010) 24:4481–500. doi:10.1142/s0217979210056530
34. Zhang S, Zhang T, and Yuan S. Dynamics of a Stochastic Predator-Prey Model With Habitat Complexity and Prey Aggregation. *Ecol Complexity* (2021) 45:100889. doi:10.1016/j.ecocom.2020.100889
35. Man DQ, Liu SZ, Wei ZH, Liu HJ, Li YK, and Liu SJ. The Vegetation Evolution in the Middle and Lower Reaches of the Shiyanghe River Basin, Gansu, China. *J Desert Res* (2013) 33:613–8. doi:10.7522/j.issn.1000-694X.2013.00084

36. Nie HG, Yue LP, Yang W, Li ZP, and Yang XK. Present Situation, Evolution Trend and Causes of Sandy Desertification in Hulunbuir Steppe. *J Desert Res* (2005) 25:635–9.
37. Sherratt JA. An Analysis of Vegetation Stripe Formation in Semi-arid Landscapes. *J Math Biol* (2005) 51:183–97. doi:10.1007/s00285-005-0319-5
38. Sherratt JA, and Lord GJ. Nonlinear Dynamics and Pattern Bifurcations in a Model for Vegetation Stripes in Semi-arid Environments. *Theor Popul Biol* (2007) 71:1–11. doi:10.1016/j.tpb.2006.07.009
39. Wei Y, Song B, and Yuan S. Dynamics of a Ratio-Dependent Population Model for Green Sea Turtle With Age Structure. *J Theor Biol* (2021) 516:110614. doi:10.1016/j.jtbi.2021.110614
40. Kefi S, Rietkerk M, and Katul GG. Vegetation Pattern Shift as a Result of Rising Atmospheric CO2 in Arid Ecosystems. *Theor Popul Biol* (2008) 74:332–44. doi:10.1016/j.tpb.2008.09.004
41. Chen Z, Wu Y-P, Feng G-L, Qian Z-H, and Sun G-Q. Effects of Global Warming on Pattern Dynamics of Vegetation: Wuwei in China as a Case. *Appl Mathematics Comput* (2021) 390:125666. doi:10.1016/j.amc.2020.125666
42. Kamilaris A, Kartakoullis A, and Prenafeta-Boldú FX. A Review on the Practice of Big Data Analysis in Agriculture. *Comput Electronics Agric* (2017) 143:23–37. doi:10.1016/j.compag.2017.09.037
43. Angela L, Olaf B, Stefan K, Pedro JL, Andras J, Duccio R, et al. Understanding and Assessing Vegetation Health by *In Situ*. *J Methods Ecol Evol* (2018) 9:1799–809. doi:10.1111/2041-210X.13025

Conflict of Interest: The authors declare that the research was conducted in the absence of any commercial or financial relationships that could be construed as a potential conflict of interest.

Publisher's Note: All claims expressed in this article are solely those of the authors and do not necessarily represent those of their affiliated organizations, or those of the publisher, the editors and the reviewers. Any product that may be evaluated in this article, or claim that may be made by its manufacturer, is not guaranteed or endorsed by the publisher.

frontiers in Physics

ORIGINAL RESEARCH
published: 23 September 2021
doi: 10.3389/fphy.2021.736085

The Effect of the Arctic Oscillation on the Predictability of Mid-High Latitude Circulation in December

Zhihai Zheng[1], *Jin Ban*[2]* *and Yongsheng Li*[2]

[1]National Climate Center, Laboratory for Climate Studies, China Meteorological Administration, Beijing, China, [2]Heilongjiang Meteorological Bureau, Harbin, China

The impact of the Arctic Oscillation (AO) on the predictability of mid-high latitude circulation in December is analysed using a full set of hindcasts generated form the Beijing Climate Center Atmospheric General Circulation Model version 2.2 (BCC_AGCM2.2). The results showed that there is a relationship between the predictability of the model on the Eurasian mid-high latitude circulation and the phase of AO, with the highest predictability in the negative AO phase and the lowest predictability in the normal AO phase. Moreover, the difference of predictability exists at different lead times. The potential sources of the high predictability in the negative AO phase in the BCC_AGCM2.2 model were further diagnosed. It was found that the differences of predictability on the Eurasian mid-high latitude circulation also exist in different Arctic sea ice anomalies, and the model performs well in reproducing the response of Arctic sea ice on the AO. The predictability is higher when sudden stratospheric warming (SSW) events occur, and strong SSW events tend to form a negative AO phase distribution in the Eurasian mid-high latitudes both in the observation and model. In addition, the model captured the blocking over the mid-high latitudes well, it may be related to the relatively long duration of the blocking. Changes in the AO will affect the blocking circulations over the mid-high latitudes, which partly explains the high predictability of the model in negative AO phases from the aspect of the internal atmospheric dynamics.

Keywords: The Arctic Oscillation, predictability, prediction skill, blocking, Arctic sea ice, interaction between stratosphere and troposphere

OPEN ACCESS

Edited by:
Gui-Quan Sun,
North University of China, China

Reviewed by:
Feng Juan,
Beijing Normal University, China
Xuelei Feng,
University Corporation for Atmospheric Research (UCAR), United States

***Correspondence:**
Jin Ban
banjincy@163.com

Specialty section:
This article was submitted to Interdisciplinary Physics, a section of the journal Frontiers in Physics

Received: *04 July 2021*
Accepted: *08 September 2021*
Published: *23 September 2021*

Citation:
Zheng Z, Ban J and Li Y (2021) The Effect of the Arctic Oscillation on the Predictability of Mid-High Latitude Circulation in December. Front. Phys. 9:736085. doi: 10.3389/fphy.2021.736085

INTRODUCTION

The Arctic Oscillation (AO) is the dominant mode of the interannual variability in the extratropical regions of the Northern Hemisphere in winter. Its typical feature is the opposite change in pressure between the polar regions and the mid-high latitudes in the Northern Hemisphere [1, 2]. The AO exerts a strong impact on the climate of North America, Eurasia, and North Africa through the zonal variation in the North Atlantic storm track and the related temperature, precipitation, and cyclone activities in winter [3–9]. Changes in the East Asian winter monsoon (EAWM) and winter surface climate that have a great social impact on East Asia are closely related to the interannual and interdecadal changes in the AO. The atmospheric circulation anomaly corresponding to the negative AO phase tends to be a strong EAWM and cold surface air temperature (SAT) anomaly in East Asia in winter and often brings strong cold wave events [10, 11], and vice versa [12–14].

The AO is most common in winter and occurs on time scales ranging from intraseasonal to interdecadal [15]. On subseasonal to interannual time scales, the predictability of the AO is mainly affected by the chaotic characteristics of the air-sea system and the nonlinear dynamics of the extratropical atmosphere [16, 17]. Many studies have focused on the forecast skill of the AO on the scale of the winter average [18–21]. Recent studies have shown that advanced seasonal forecast models have significantly improved the forecast skill of the AO in winter [22, 23]. In terms of predictable sources on the seasonal scale, in addition to the internal atmospheric dynamics, the predictability of the AO in winter is related to underlying surface anomalies, such as the North Atlantic sea surface temperature and the snow cover anomalies in the Northern Hemisphere [24–26].

However, the forecast skill of the AO is more challenging on the subseasonal scale. Currently, there are relatively few assessments on this time scale. The forecast skills of some operational dynamical forecast systems, such as the National Centers for Environmental Prediction (NCEP), the European Centre for Medium-Range Weather Forecasts (ECMWF) and the Beijing Climate Center, were evaluated, the results showed that the forecast skills were low at the subseasonal scale [20, 27, 28]. The low forecast skill of the AO on the subseasonal scale is related to a lack of understanding of its predictable sources. The variability in the stratospheric polar vortex may also provide an important source for the predictability of the subseasonal AO. Studies have shown that the stratospheric polar vortex can propagate downward through westerly and easterly wind anomalies. Sudden stratospheric warming (SSW) can dramatically weaken the stratospheric polar vortex, and the weakened Northern Hemispheric stratospheric polar vortex is beneficial for the turning of the tropospheric and near-surface AO to the negative phase in winter [29, 30]. In addition, the recent accelerated reduction in Arctic sea ice is also considered to be a possible factor in the changes in the mid-high latitude circulation in winter, and the response characteristics of circulation are often similar to AO modes, especially in some numerical models [31, 32]. However, the relatively short observational record and the low mid-latitude signal-to-noise ratio (SNR) lead to difficulties when explaining the physical connection between Arctic sea ice and the AO mode, so this connection is still controversial.

Existing studies have shown that the ability of a model to forecast the AO differs in different months, including winter months. At the same time, the relationship between the AO and the East Asian climate shows intraseasonal variability, and the impact of the AO on the temperature in southern China in December is different from that in January-February [8]. Meanwhile, the circulation anomalies affected by the December AO for December and for the following January are primarily confined to the Euro-Atlantic sector while they extend to East Asia during the following February [33]. In addition, the standard deviation of the AO has increased significantly in December since the 1990s, while this phenomenon has not been observed in November and January [34]. Therefore, this study aims to evaluate the predictability of mid-high latitude circulation in BCC_AGCM2.2, with a focus on December. More importantly, we investigate the differences of predictability in different AO phases and the possible causes for the differences are also further analysed.

Data

The BCC_AGCM2.2 has a horizontal resolution of T106 and includes 26 vertical levels [35]. The top of the model is at 2.3 hPa. The model is initialized using the atmospheric conditions from the NCEP Reanalysis dataset [36] and sea-surface conditions from NOAA Optimum Interpolation Sea Surface Temperature V2 [37]. Four model runs (00Z, 06Z, 12Z, and 18Z) are initialized every day starting on January 1, 1983 and run for 55 days each. The lagged average forecasting (LAF) technique is used to produce the ensemble mean. The LAF ensemble includes the latest 5 days (A total of 20 members) operational forecasts, and also forecasts for the same verification time stated one or more days earlier than the latest one. The model output is interpolated to a 2.5 × 2.5 horizontal resolution prior to analysis. To verify the model hindcast, we use the daily and monthly NCEP-NCAR reanalysis dataset for the period 1983–2015. The NCEP-NCAR reanalysis data are gridded at 2.5 × 2.5 resolution. The SST data gridded at 2 × 2 resolution used in this study are taken from the National Oceanic and Atmospheric Administration extended reconstructed SST version 4 (ERSST V4) [38]. The optimal interpolated global sea ice density data from December 1981 to December 2015 are provided by NOAA, with a horizontal resolution of 1.0 ×1.0. The observed monthly AO index derive from the Climate Prediction Center of NOAA (https://www.cpc.ncep.noaa.gov/products/precip/CWlink/pna/nao.shtml), which is defined as the first leading mode of empirical orthogonal function (EOF) analysis of area-weighted monthly mean 1000 mb anomalies north of 20°N. The predicted index is calculated using the 1000 mb anomalies of ensemble mean.

Methods

The Signal-to-noise ratio (SNR) is used to account for the predictability of mid-high latitude circulation, which is estimated by the ratio of the variances of ensemble mean (the signal) to the deviations or spreads among the ensemble members (the noise) [39, 40]. At a given location, the prediction of a single ensemble member is denoted by F_{ij}, where j is the year index that goes from 1 to 33 and i is the case number of the ensemble that goes from 1 to 20. For year j, the climate signal F_j is estimated as the mean of all 20 members, that is

$$F_j = \frac{1}{20}\sum_{i=1}^{20} F_{i,j}, \tag{1}$$

The yearly mean climatology $\overline{F}$ could be recalculated as

$$\overline{F} = \frac{1}{33}\sum_{j=1}^{33} F_j, \tag{2}$$

The variance of ensemble mean represents the climate signal as

$$\sigma_s = \frac{1}{33-1}\sum_{j=1}^{33}\left(F_j - \overline{F}\right)^2, \tag{3}$$

Note that the denominator is 32 instead of 33 because the degrees of freedom are one less than the total number for a second moment. Similarly, the deviations or spreads among the ensemble members represents the noise as

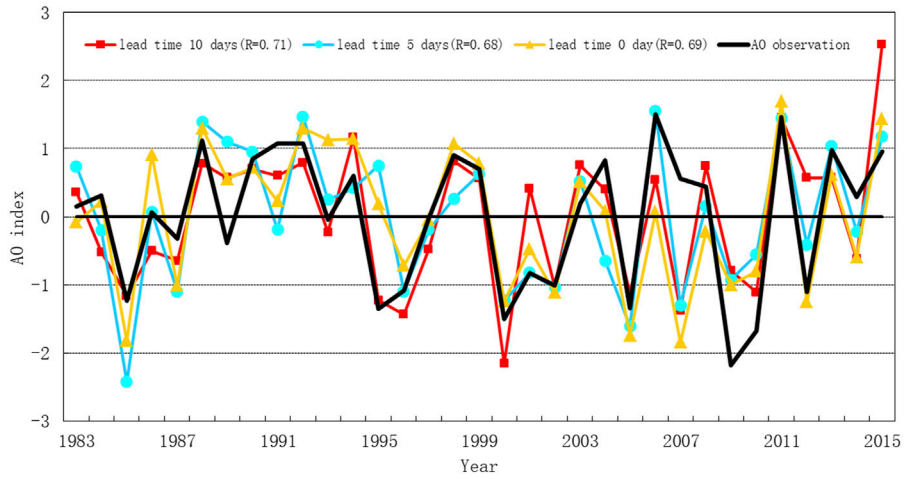

FIGURE 1 | Temporal evolution of December AO index hindcast by BCC_AGCM2.2 at 0-days (yellow), 5-days (Cyan), and 10-days (red) lead times for the ensemble mean, and the observations (black).

$$\sigma_n = \frac{1}{33 \times (20-1)} \sum_{j=1}^{33} \sum_{i=1}^{20} \left(F_{i,j} - F\right)_j^2, \tag{4}$$

The Signal-to-noise ratio is recalculated as

$$R = \frac{\sigma_s}{\sigma_n}. \tag{5}$$

The anomaly correlation coefficient (ACC) is also chosen as a measure to gauge the predictability that we are interested in. The ACC is defined as:

$$\mathrm{ACC} = \frac{\sum_{i=1}^{N}\left(\Delta R_f - \overline{\Delta R}_f\right)\left(\Delta R_0 - \overline{\Delta R}_0\right)}{\sqrt{\sum_{i=1}^{N}\left(\Delta R_f - \overline{\Delta R}_f\right)^2 \sum_{i=1}^{N}\left(\Delta R_0 - \overline{\Delta R}_0\right)^2}}, \tag{6}$$

Where ΔR_f and ΔR_0 denote the predicted and observed anomaly fields, respectively, and their averages are $\Delta\bar{R}_f$ and $\Delta\bar{R}_0$. N is the number of points.

The composite is employed to compare prediction skill in different AO phases. The wave activity flux is used to provide information about the large-scale wave source and sink [41].

Prediction Skill and Predictability of AO and Mid-high Latitude Circulation

To test the forecast skill of AO, we first decomposed the 1,000 hPa extratropical height in the Northern Hemisphere (0–360°E, 20°N-90°N) using the empirical orthogonal function (EOF) and then projected the result onto the observed first mode to obtain the AO index series predicted by the model. **Figure 1** shows the temporal evolution of December AO index hindcast by BCC_AGCM2.2 at 0-days, 5-days, and 10-days lead times for the ensemble mean from 1983 to 2015. The results showed that the temporal evolution of AO index predicted at different lead times were relatively consistent with the observation. The correlation coefficients between the AO indexes predicted at 0-days, 5-days, and 10-days lead times and the observed AO indexes were 0.71, 0.68, and 0.69, respectively, which all exceed 99.9% confidence, indicating that the dynamic model can well capture the AO interannual variability in December. In addition, in the typical positive and negative phase years, the AO index predicted by the model were also very close to the observed AO index.

The AO is the dominant mode of the interannual variability in atmospheric circulation in the mid-high latitude regions of the Northern Hemisphere. **Figure 2** shows the ACC of the 500 hPa geopotential height over the Eurasian region (20°-80°N, 50°-180°E) predicted by the model at 0-days, 5-days, and 10-days lead times. According to the AO index and its standard deviations, the 33 years for 1983–2015 were divided into negative AO phase, normal AO phase and positive AO phase. Negative AO years include 1985, 1995, 2000, 2005, 2009, 2010, and 2012, and the index is greater than 1 standard deviation. Positive AO years include 1988, 1991, 1992, 1998, 2006, 2011, 2013, and 2015, and the index is greater than 1 standard deviation. The remaining 18 years are the normal AO years. In terms of the average over all years, the forecast skill decreased rapidly with the extension of the lead time, the ACCs predicted at 0-days, 5-days, and 10-days lead times were approximately 0.5, 0.4, and 0.27, respectively. Additionally, the ACC predicted at 0-days lead time was 0.76 in the negative AO phase, 0.48 in the positive AO phase, and 0.4 in the normal AO phase. Although the forecast skills at 5-days and 10-days lead times were both lower than those at 0-days lead time, the ACC was still highest in the negative AO phase, followed by the positive AO phase, and lowest in the normal AO phase. Interestingly, when the AO phase was positive, the forecast skill decreased the slowest with the extension of the lead time.

To further examine the prediction skill in the lower troposphere, **Figure 3** displays the composites of 1,000 hPa geopotential height for different AO phases in the model and

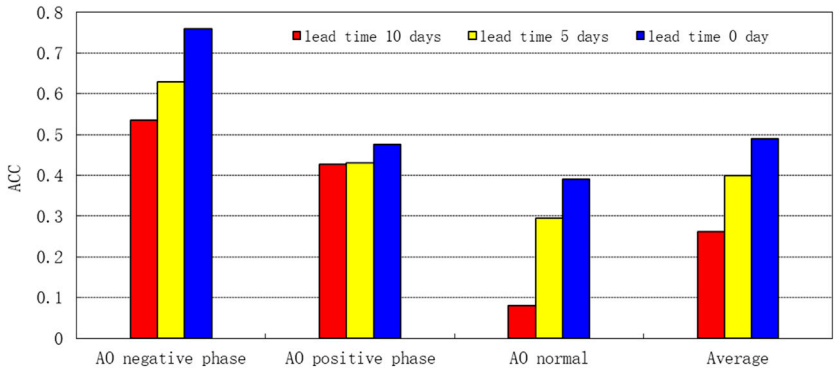

FIGURE 2 | ACC of the 500 hPa geopotential height in the Eurasian region predicted by BCC_AGCM2.2 in negative, positive, and normal AO phases.

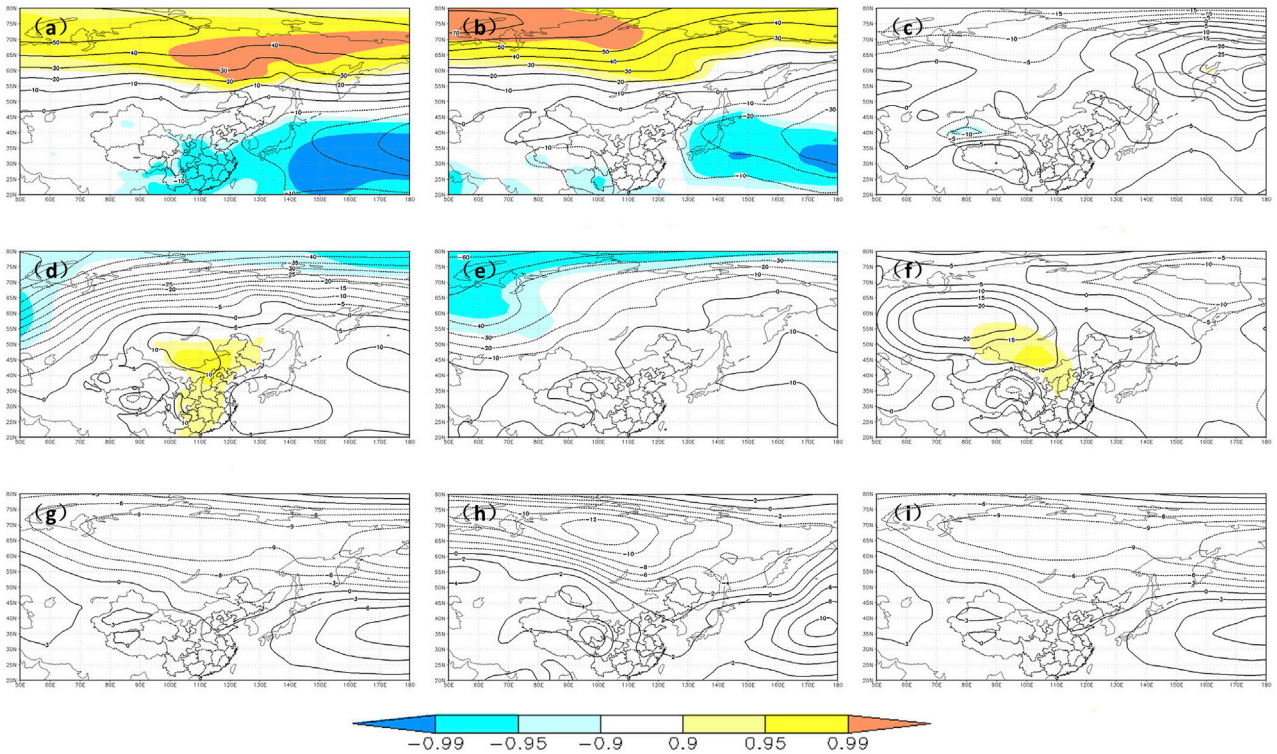

FIGURE 3 | Composites of 1,000 hPa geopotential height for the negative AO phase in **(A)** model **(B)** observations **(C)** The difference between prediction and observation **(D–F)** As in **(A–C)**, but for the positive AO phase **(G–I)** As in **(A–C)**, but for the normal AO phase. Light, middle, and dark shading indicate the 90, 95, and 99% confidence levels based on a Student's t-test, respectively.

observations. Due to different lead times the skill changes are similar, we only chose the prediction at 0-days lead time. In the negative AO phase, a huge positive anomaly occupies the entire northern Eurasia continent, and a negative anomaly is seen over the Northwest Pacific. The large zonal gradient between the anomalous Eurasia continent high and the subtropical North Pacific low implies strong EAWM. The distributions in the model and observation were very similar, including the significant positive and negative anomaly region. The anomalous distributions in positive AO phase were also quite similar, with a major trough extending southward along the Ural Mountain and a ridge extending northward along the Mongolia. However, the intensity of the trough and ridge in the model prediction is obviously weak, and the significant positive anomaly in Eastern China and Mongolia is not seen in prediction. The anomalous center in prediction and observation are not significant in the normal AO Phase.

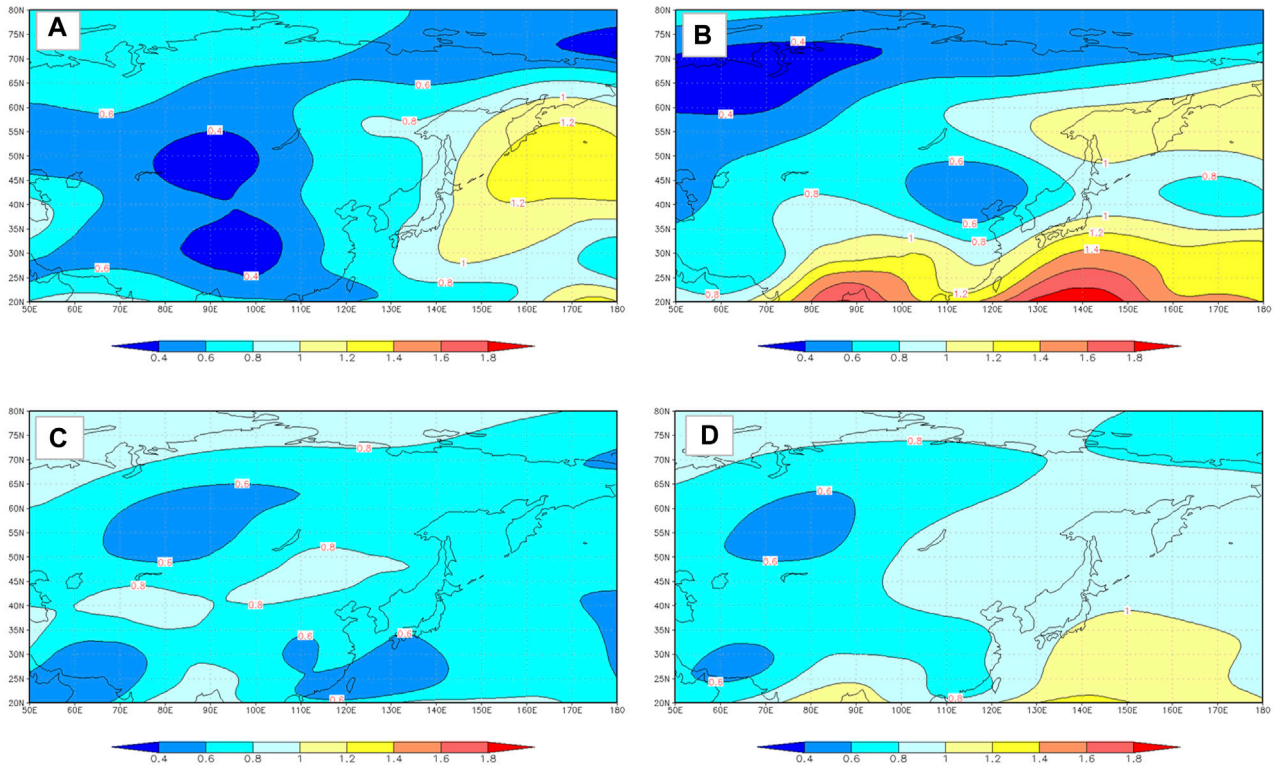

FIGURE 4 | The signal-to-noise ratio distributions for the AO in the **(A)** negative phase, **(B)** positive phase, **(C)** normal phase, and **(D)** all years.

Based on the above analysis, the model has a high predictability for the geopotential height in the Eurasian region in the negative AO phase. On this basis, the SNR method was applied to further analyse the predictability of the model over the Eurasian region in different AO phases (**Figure 4**). In the case of a negative AO phase, the SNR of the model was greater than 1 from east of Japan to the northwest Pacific, indicating that the model can generally well capture the strength and location of the East Asian trough in the negative AO phase. The model predicted a high SNR in the Sea of Okhotsk region and West Pacific in positive AO phase. Additionally, The SNR in the normal AO phase was the lowest.

Causes for the Different Predictability

The above results show that the prediction skill of the negative AO phase is higher than that of the positive and normal AO phases. To explain the origins of the potential predictable sources of the high forecast skill of the negative AO phase in the BCC_AGCM2.2 model, the possible causes were analysed from the aspects of the Arctic sea ice, sudden stratospheric warming (SSW), and the internal atmospheric dynamics.

As a component of the Earth's climate system, Arctic sea ice plays an important role in the surface energy budget of the high latitudes in the Northern Hemisphere by regulating the surface albedo and the turbulent heat and momentum fluxes at the ocean-atmosphere interface. The atmospheric response to reductions in Arctic sea ice is often associated with changes in the AO [31, 32]. **Figure 5** shows the composite Arctic sea ice anomalies in the negative and positive AO phases. The figure shows that when the AO is in the negative phase, the Arctic sea ice has a significantly negative anomaly centre in the Kara Sea region, which exceeds the 95% confidence level. When the AO is in the positive phase, the positive Arctic sea ice anomaly only exceeds the 95% confidence level in the vicinity of the Kara Sea, and the region that passes the 95% confidence level is significantly smaller than that in the negative AO phase.

We define the sea ice in the Barents Sea-Kara Sea region (60°-90°E, 70°-80°N) in October as the Arctic sea ice index, they are area weighted and linearly detrended before the analysis. The correlation coefficient between the December AO index and the autumn Arctic sea ice index is 0.40 (**Figure 6B**), which exceeds the 95% confidence. Then, 5 years with less sea ice (1984, 1985, 1995, 2009, and 2012) and 5 years with more sea ice (1992, 1996, 1998, 1999, and 2002) were selected for comparing the prediction skill. The ACC of the 500 hPa geopotential height in the Eurasian region predicted by BCC_AGCM2.2 in less Arctic sea ice years at 0-days and 5-days lead times were 0.63 and 0.62, respectively, which were significantly higher than those (0.4 and 0.35) in years with more ice (**Figure 6A**). This finding is consistent with the observed and model-predicted negative feedback between the sea ice and the atmosphere, indicating that less Arctic sea ice is one of the predictable sources of the Eurasian mid-high latitude circulation. The composites of the 500 hPa geopotential height in years with less and more sea ice was further analysed in

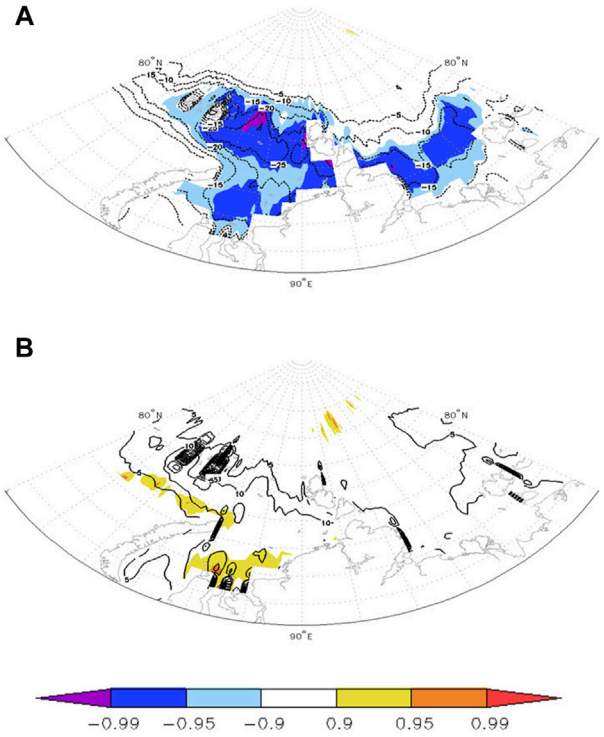

FIGURE 5 | Composite of autumn Arctic sea ice in the **(A)** negative AO phase and **(B)** positive AO phase years. Light, middle, and dark shading indicate the 90, 95, and 99% confidence levels based on a Student's *t*-test, respectively.

Figure 7. There are significant negative anomalies over most areas of China in years with less Arctic sea ice, while the anomalies are not clearly significant in years with more Arctic sea ice, indicating that the response to less Arctic sea ice forcing over the Eurasian mid-high latitudes is much obvious than more Arctic sea ice.

The influence of the stratospheric polar vortex can last for several weeks or even several months, and SSW can dramatically weaken the stratospheric polar vortex. The zonal geopotential height anomalies of 90°N and 60°N at 10 hPa were averaged separately, and then the mean zonal geopotential height anomaly of 60°N was subtracted from the mean zonal geopotential height anomaly of 90°N to obtain the index [29]. The specific formula is $\Delta H = [H']_{90°N} - [H']_{60°N}$, where $[H']$ represents the mean value of the zonal geopotential height anomalies, and ΔH represents the SSW index. **Figure 8** shows the SSW index in November and the AO index in December. The correlation coefficient between the two was -0.51, which exceed the 99% confidence. It is indicated that when a strong SSW event occurs, the 500 hPa height field in the troposphere rapidly adjusts, forming a negative AO phase distribution in the Eurasian mid-high latitudes. Based on the above definition, 4 years (1987, 1996, 2000, and 2009) with an SSW index greater than 200 were selected to compare the prediction skill. **Figure 9** shows the average ACC in Eurasia predicted by the years with strong SSW events. The ACC at 0-days and 10-days lead times in SSW events was higher than the average of all years, indicating that strong SSW has a certain contribution for predictability in negative AO years.

Some studies pointed out that the blocking high over the Ural Mountains in winter occurs more frequently in years with a weak AO and less frequently in years with a strong AO [42]. The composite of the observed 500 hPa geopotential high is computed based on the mean of years with the positive AO minus that with the negative AO (**Figure 10A**). The strong high pressure anomaly is located at the Ural Mountains and the Sea of Okhotsk, and the low pressure anomaly is located at the Northern China and Mongolia. The anomalous high over Ural Mountains and the Sea of Okhotsk are conductive to the activity of blocking. The similar distribution is also seen in model (**Figure 10B**), which implies good prediction of blocking in extreme years of AO. To further explain that the predictability of the model under different AO phases is related to the blocking high situation over the mid-high latitudes, the average of 500 hPa geopotential high over the Ural Mountains (40°N-50°N, 40°E-80°E), the Lake Baikal (60°N-70°N, 80°E-120°E), and the Sea of Okhotsk (60°N-70°N, 120°E-160°E) were defined as the blocking indices, and their normalized indices were shown in **Figure 11**. Blocking activity in the three regions were obvious for 6 out of 7 negative AO years. However, there were only 4 years with active blocking in 8 positive AO phase years. Therefore, the probability of the occurrence of a blocking high over the mid-high latitudes is higher in the negative AO phase and lower in the positive AO phase. The model can capture most of the blocking, but all three blocking in 2000,

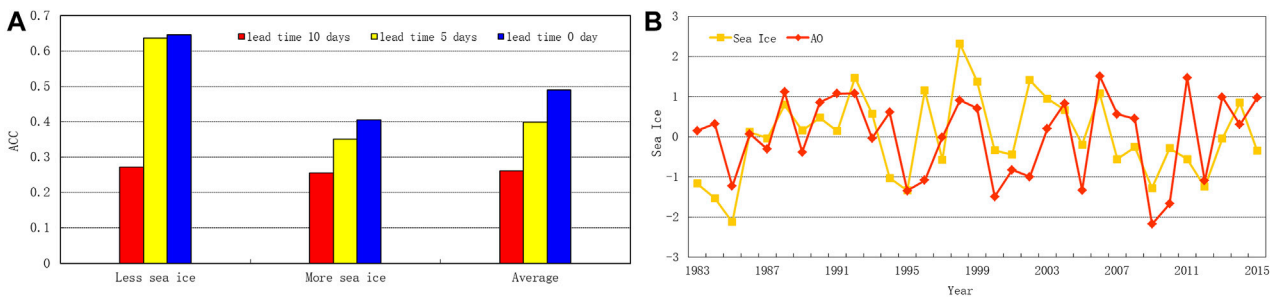

FIGURE 6 | (A) ACC of the 500 hPa geopotential height in the Eurasian region predicted by BCC_AGCM2.2 in less, more, and average Arctic sea ice, **(B)** temporal evolution of December AO index and Arctic sea ice.

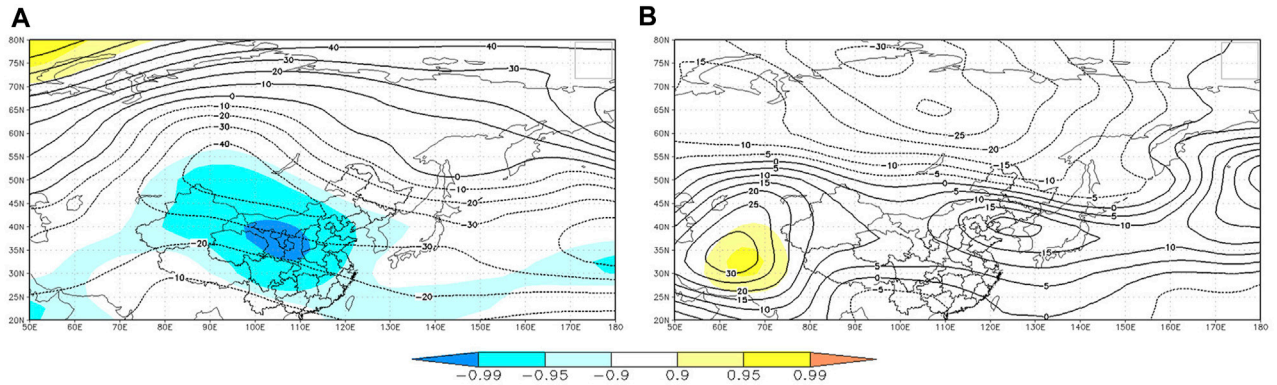

FIGURE 7 | Composite of the 500 hPa geopotential height in years with **(A)** less and **(B)** more Arctic sea ice. Light, middle, and dark shading indicate the 90, 95, and 99% confidence levels based on a Student's *t*-test, respectively.

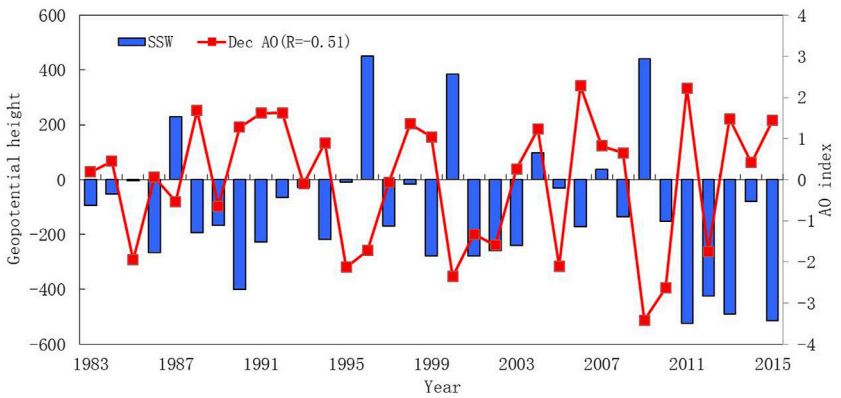

FIGURE 8 | The SSW index in November and the AO index in December.

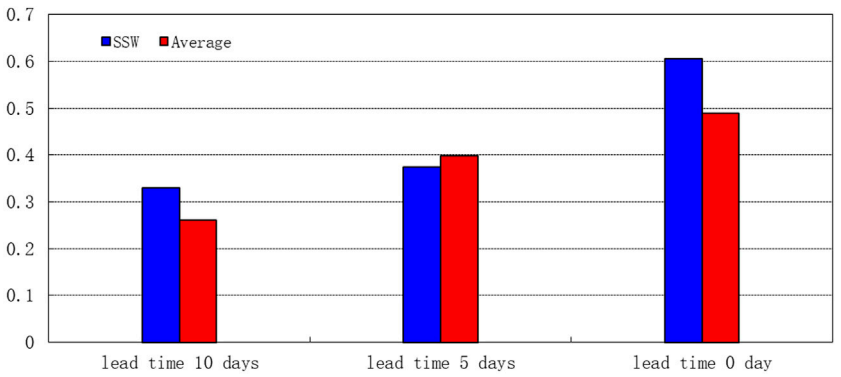

FIGURE 9 | ACC of the 500 hPa geopotential height in the Eurasian region predicted by BCC_AGCM2.2 in SSW events and all years.

blocking of the Sea of Okhotsk in 2009 and the blocking of the Ural Mountains in 2010. In summary, changes in the AO will affect the blocking circulations over the mid-high latitudes, and the model can well capture the blocking over the mid-high latitudes, it may be related to the long duration and persistence of blocking [43]. It partly explains the high predictability of the model in negative AO phases from the aspect of the internal atmospheric dynamics.

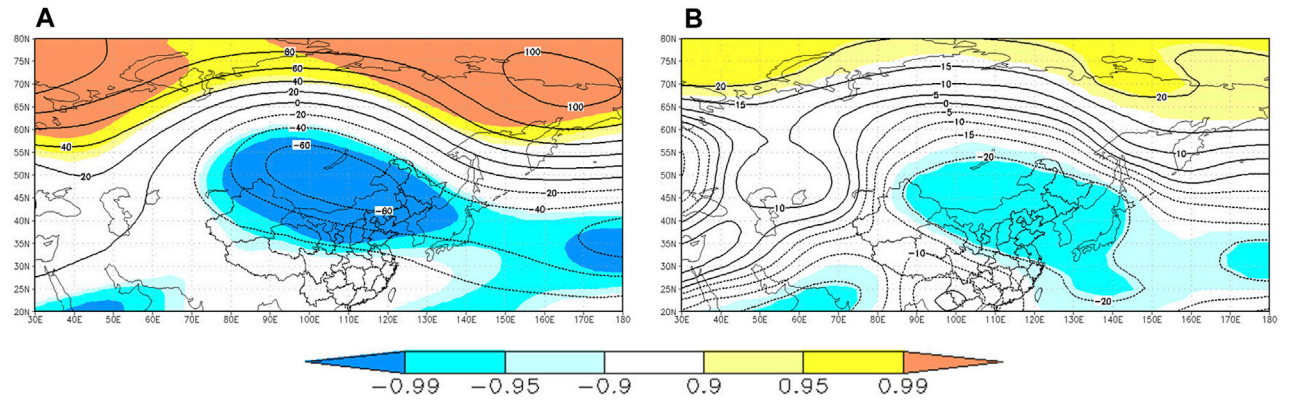

FIGURE 10 | The composite of the 500 hPa geopotential height in **(A)** observation and **(B)** model, which are defined as the mean of years with the positive AO minus that with the negative AO. Light, middle, and dark shading indicate the 90, 95, and 99% confidence levels based on a Student's *t*-test, respectively.

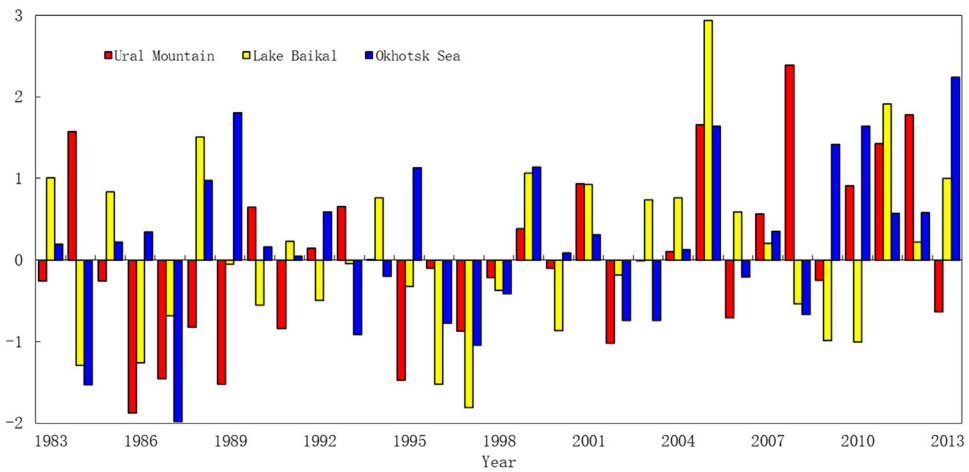

FIGURE 11 | Blocking high indexes of the Ural Mountains, Lake Baikal, and the Sea of Okhotsk.

The wave source is in the North Atlantic Ocean and gradually propagates along Europe to the mid-high latitudes of Asia in the negative AO phase (**Figure 12**). The model also predicts a westward propagating wave source in the North Atlantic Ocean, which also moves towards the mid-high latitudes of Asia, but there are differences in magnitude and propagation phase. However, the wave activity center over Tibetan Plateau is underestimated by BCC_AGCM2.2. In general, the internal atmospheric dynamics of the model in the negative AO phase are better than those in positive AO phase.

DISCUSSION AND CONCLUSIONS

The Arctic Oscillation (AO) is the dominant mode of the interannual variability in atmospheric circulation in the extratropical regions of the Northern Hemisphere in winter. The impact of the AO on the predictability of mid-high latitude circulation in December was analysed using a full set of hindcasts generated form the Beijing Climate Center Atmospheric General Circulation Model version 2.2 (BCC_AGCM2.2). The results showed that there is a relationship between the predictability of the model on the Eurasian mid-high latitude circulation and the phase of AO, with the highest predictability in negative AO phase and lowest predictability in normal AO phase. Moreover, the difference of predictability exists in different lead times.

To explain the origins of the potential predictable sources of the high forecast skill of the negative AO phase in the BCC_AGCM2.2 model, the possible causes of these conditions were diagnosed. We found that the differences of predictability on the Eurasian mid-high latitude circulation also exist in different Arctic sea ice anomalies. When Arctic sea ice decreases, the AO response is likely to be in a negative phase. The model also performs well in reproducing the response of Arctic sea ice on the AO. Sudden stratospheric warming is another potential source of

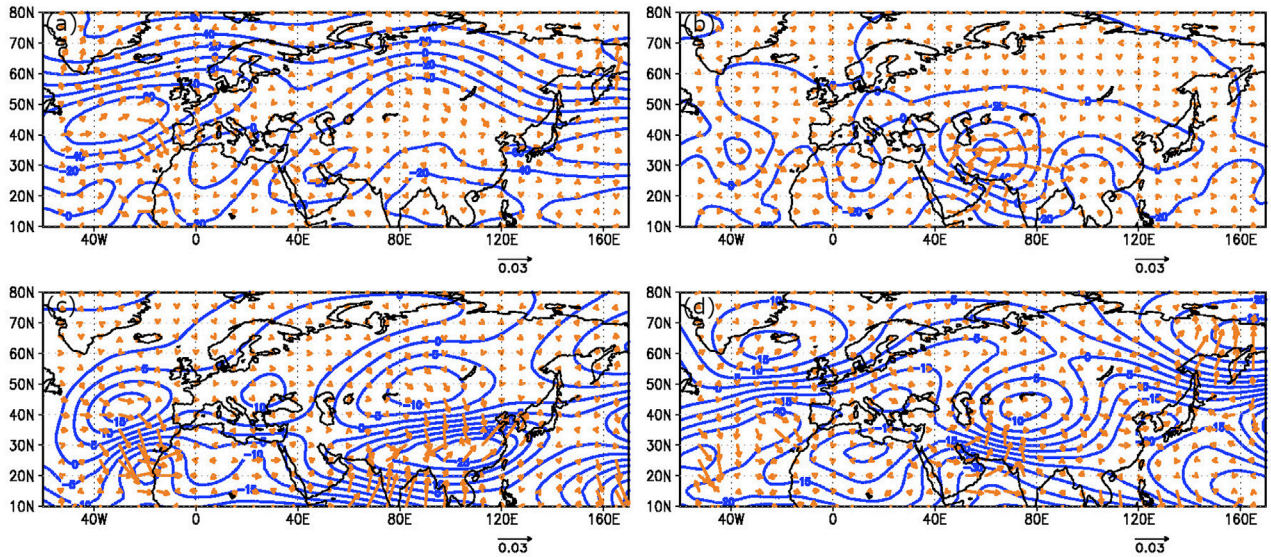

FIGURE 12 | Composites of wave activity flux for the **(A)** negative and **(B)** positive AO phase in observations, **(C–D)** As in **(A–B)**, but for model.

higher predictability on the Eurasian mid-high latitude circulation in negative AO phase. The ACC at 0-days and 10-days lead time in SSW events was higher than the average of other years, and strong SSW events tend to form a negative AO phase distribution in the Eurasian mid-high latitudes. In addition, the model captures the blocking over the mid-high latitudes well, which may be related to the relatively long duration of the blocking. Further, changes in the AO will affect the blocking circulations over the mid-high latitudes, which explains the high predictability of the model under negative AO phases from the aspect of the internal atmospheric dynamics.

Although BCC_AGCM2.2 has relatively high predictability of mid-high latitude circulation in December in negative AO phase, the predictability is still much lower in other conditions and other months. Apart from the AO, other factors such as Madde–Julian Oscillation (MJO) and the sea surface temperature over the North Atlantic Ocean and Indian Ocean are also important for the predictability of Eurasian mid-high latitude circulation [44, 45]; meanwhile, the predictability of models are different; these would be worthwhile to address in further works.

DATA AVAILABILITY STATEMENT

The original contributions presented in the study are included in the article/supplementary material, further inquiries can be directed to the corresponding author.

AUTHOR CONTRIBUTIONS

ZZ initiated the project. JB performed the data analysis. ZZ and JB wrote the initial draft of the paper. All authors contributed to interpreting results and improvement of this paper.

FUNDING

This work was supported by the National Natural Science Foundation of China (41875101), the National Key Research and Development Program of China (2017YFC1502303) and the National Natural Science Foundation of China (41805060).

REFERENCES

1. Thompson D. W. J., and Wallace J. M., Annular Modes in the Extratropical Circulation. Part I: Month-To-Month Variability. *J Clim* (2000) 13:1000–16. doi:10.1175/1520-0442(2000)013<1000:amitec>2.0.co;2
2. Thompson D. W. J., and Wallace J. M., The Arctic Oscillation Signature in the Wintertime Geopotential Height and Temperature fields. *Geophys Res Lett* (1998) 25:1297–300. doi:10.1029/98gl00950
3. Hurrell J. W., Decadal Trends in the North Atlantic Oscillation: Regional Temperatures and Precipitation. *Science* (1995) 269:676–9. doi:10.1126/science.269.5224.676
4. Li J., Zheng F., Sun C., Feng J., and Wang J., Pathways of Influence of the Northern Hemisphere Mid-high Latitudes on East Asian Climate: A Review. *Adv Atmos Sci* (2019) 36:902–21. doi:10.1007/s00376-019-8236-5
5. Huang J., Ji M., Higuchi K., and Shabbar A., Temporal Structures of the North Atlantic Oscillation and its Impact on the Regional Climate Variability. *Adv Atmos Sci* (2006) 23:23–32. doi:10.1007/s00376-006-0003-8
6. Sun C., Li J., Feng J., and Xie F., A Decadal-Scale Teleconnection between the North Atlantic Oscillation and Subtropical Eastern Australian Rainfall. *J Clim* (2015) 28:1074–92. doi:10.1175/jcli-d-14-00372.1
7. Feng J., Zhu J., Li J., and Liao H. Aerosol Concentrations Variability over China: Two Distinct Leading Modes. *Atmos Chem Phys* (2020) 20:9883–9893. doi:10.5194/acp-20-9883-2020
8. Zuo J., Ren H-L., and Li W., Contrasting Impacts of the Arctic Oscillation on Surface Air Temperature Anomalies in Southern China between Early and Middle-To-Late Winter. *J Clim* (2015) 28:4015–26. doi:10.1175/jcli-d-14-00687.1
9. Feng J., Li J., Liao H., and Zhu J., Simulated Coordinated Impacts of the Previous Autumn North Atlantic Oscillation (NAO) and winter El Niño on

winter Aerosol Concentrations over Eastern China. *Atmos Chem Phys* (2019) 19:10787–800. doi:10.5194/acp-19-10787-2019
10. Jeong J. H., and Ho C. H., Changes in Occurrence of Cold Surges over East Asia in Association with Arctic Oscillation. *Geophys Res Lett* (2005) 32:L14704. doi:10.1029/2005gl023024
11. Hong C. C., Hsu H. H., Chia H. H., and Wu C. Y., Decadal Relationship between the North Atlantic Oscillation and Cold Surge Frequency in Taiwan. *Geophys Res Lett* (2008) 35:L24707. doi:10.1029/2008gl034766
12. Gong D. Y., Wang S. W., and Zhu J. H., East Asian winter Monsoon and Arctic Oscillation. *Geophys Res Lett* (2001) 28:2073–6. doi:10.1029/2000gl012311
13. Wu B., and Wang J., Winter Arctic Oscillation, Siberian High and East Asian winter Monsoon. *Geophys Res Lett* (2002) 29:1897. doi:10.1029/2002gl015373
14. Gong D., and Wang S., Influence of Arctic Oscillation on winter Cclimate over China. *J Geogr Sci* (2003) 13:208–16. doi:10.1007/bf02837460
15. Gong G., Entekhabi D., and Cohen J., A Large-Ensemble Model Study of the Wintertime AO-NAO and the Role of Interannual Snow Perturbations. *J Clim* (2002) 15:3488–99. doi:10.1175/1520-0442(2002)015<3488:alemso>2.0.co;2
16. Feldstein S. B., The Dynamics of NAO Teleconnection Pattern Growth and Decay. *Q.J.R Meteorol Soc* (2003) 129:901–24. doi:10.1256/qj.02.76
17. Robertson A. W., Influence of Ocean-Atmosphere Interaction on the Arctic Oscillation in Two General Circulation Models. *J Clim* (2001) 14:3240–54. doi:10.1175/1520-0442(2001)014<3240:iooaio>2.0.co;2
18. Baker L. H., Shaffrey L. C., Sutton R. T., Weisheimer A., and Scaife A. A., An Intercomparison of Skill and Overconfidence/Underconfidence of the Wintertime North Atlantic Oscillation in Multimodel Seasonal Forecasts. *Geophys Res Lett* (2018) 45:7808–17. doi:10.1029/2018gl078838
19. Müller WA., Appenzeller C., and Schär C., Probabilistic Seasonal Prediction of the winter North Atlantic Oscillation and its Impact on Near Surface Temperature. *Clim Dyn* (2005) 24:213–26. doi:10.1007/s00382-004-0492-z
20. Johansson Å., Prediction Skill of the NAO and PNA from Daily to Seasonal Time Scales. *J Clim* (2007) 20:1957–75. doi:10.1175/jcli4072.1
21. Kim H. M., Webster P. J., and Curry J. A., Seasonal Prediction Skill of ECMWF System 4 and NCEP CFSv2 Retrospective Forecast for the Northern Hemisphere Winter. *Clim Dyn* (2012) 39:2957–73. doi:10.1007/s00382-012-1364-6
22. Kang D., Lee M. I., Im J., Kim D., Kim H. M., Kang H. S, et al. Prediction of the Arctic Oscillation in Boreal winter by Dynamical Seasonal Forecasting Systems. *Geophys Res Lett* (2014) 41:3577–85. doi:10.1002/2014gl060011
23. Sun J., and Ahn J. B., Dynamical Seasonal Predictability of the Arctic Oscillation Using a CGCM. *Int J Climatol* (2015) 35:1342–53. doi:10.1002/joc.4060
24. Rodwell M. J., Rowell D. P., and Folland C. K., Oceanic Forcing of the Wintertime North Atlantic Oscillation and European Climate. *Nature* (1999) 398:320–3. doi:10.1038/18648
25. Robertson A. W., Mechoso C. R., and Kim Y. J., The Influence of Atlantic Sea Surface Temperature Anomalies on the North Atlantic Oscillation. *J Clim* (2000) 13:122–38. doi:10.1175/1520-0442(2000)013<0122:tioass>2.0.co;2
26. Cohen J., and Fletcher C., Improved Skill of Northern Hemisphere Winter Surface Temperature Predictions Based on Land-Atmosphere Fall Anomalies. *J Clim* (2007) 20:4118–32. doi:10.1175/jcli4241.1
27. Vitart F., Evolution of ECMWF Sub-seasonal Forecast Skill Scores. *Q.J.R Meteorol Soc* (2014) 140:1889–99. doi:10.1002/qj.2256
28. Zuo J., Ren H-L., Wu J., Nie Y., and Li Q., Subseasonal Variability and Predictability of the Arctic Oscillation/North Atlantic Oscillation in BCC_AGCM2.2. *Dyn Atmospheres Oceans* (2016) 75:33–45. doi:10.1016/j.dynatmoce.2016.05.002
29. Baldwin M. P., and Dunkerton T. J., Stratospheric Harbingers of Anomalous Weather Regimes. *Science* (2001) 80-294:581–4. doi:10.1126/science.1063315
30. Baldwin M. P., Stephenson D. B., Thompson D. W. J., Dunkerton T. J., Charlton A. J., and O'Neill A., Stratospheric Memory and Skill of Extended-Range Weather Forecasts. *Science* (2003) 301:636–40. doi:10.1126/science.1087143
31. Ding S., Wu B., and Chen W., Dominant Characteristics of Early Autumn Arctic Sea Ice Variability and its Impact on Winter Eurasian Climate. *J Clim* (2021) 34:1825–46. doi:10.1175/jcli-d-19-0834.1
32. Alexander M. A., Bhatt U. S., Walsh J. E., Timlin M. S., Miller J. S., and Scott J. D., The Atmospheric Response to Realistic Arctic Sea Ice Anomalies in an AGCM during Winter. *J Clim* (2004) 17:890–905. doi:10.1175/1520-0442(2004)017<0890:tartra>2.0.co;2
33. Qiao S., and Feng G., Impact of the December North Atlantic Oscillation on the Following February East Asian Trough. *J Geophys Res Atmos* (2016) 121:10,074–10.doi:10.1002/2016jd025007
34. Overland J. E., and Wang M., Increased Variability in the Early Winter Subarctic North American Atmospheric Circulation*. *J Clim* (2015) 28:7297–305. doi:10.1175/jcli-d-15-0395.1
35. Wu T., Song L., Li W., Wang Z., Zhang H., Xin X., et al. An Overview of BCC Climate System Model Development and Application for Climate Change Studies. *Acta Meteorol Sin* (2014) 28:34–56. doi:10.1007/s13351-014-3041-7
36. Kalnay E., Kanamitsu M., Kistler R., Collins W., Deaven D., Gandin L., et al. The NCEP/NCAR 40-Year Reanalysis Project. *Bull Amer Meteorol Soc.* (1996) 77:437–71. doi:10.1175/1520-0477(1996)077<0437:tnyrp>2.0.co;2
37. Reynolds R. W., Rayner N. A., Smith T. M., Stokes D. C., and Wang W., An Improved *In Situ* and Satellite SST Analysis for Climate. *J Clim* (2002) 15:1609–25. doi:10.1175/1520-0442(2002)015<1609:aiisas>2.0.co;2
38. Huang B., Banzon VF., Freeman E., Lawrimore J., Liu W., Peterson T. C, et al. Extended Reconstructed Sea Surface Temperature Version 4 (ERSST.V4). Part I: Upgrades and Intercomparisons. *J Clim* (2015) 28:911–30. doi:10.1175/jcli-d-14-00006.1
39. Kumar A., and Hoerling M. P., Prospects and Limitations of Seasonal Atmospheric GCM Predictions. *Bull Amer Meteorol Soc.* (1995) 76:335–45. doi:10.1175/1520-0477(1995)076<0335:palosa>2.0.co;2
40. Zheng Z., Hu Z. Z., and L'Heureux M., Predictable Components of ENSO Evolution in Real-Time Multi-Model Predictions. *Sci Rep* (2016) 6:35909. doi:10.1038/srep35909
41. Takaya K., and Nakamura H., A Formulation of a Wave-Activity Flux for Stationary Rossby Waves on a Zonally Varying Basic Flow. *Geophys Res Lett* (1997) 24:2985–8. doi:10.1029/97gl03094
42. Cheung H. N., Zhou W., Mok H. Y., and Wu M. C., Relationship between Ural-Siberian Blocking and the East Asian Winter Monsoon in Relation to the Arctic Oscillation and the El Niño-Southern Oscillation. *J Clim* (2012) 25:4242–57. doi:10.1175/jcli-d-11-00225.1
43. Miyakoda K., Gordon T., Caverly R., Stern W., Sirutis J., and Bourke W., Simulation of a Blocking Event in January 1977. *Mon Weather Rev* (1983). 111, p. 846–69. doi:10.1175/1520-0493(1983)111<0846:soabei>2.0.co;2
44. Zhou S., and Miller A. J., The Interaction of the Madden-Julian Oscillation and the Arctic Oscillation. *J Clim* (2005) 18:143–59. doi:10.1175/jcli3251.1
45. Wang B., Wu Z., Chang C. P., Liu J., Li J., and Zhou T., Another Look at Interannual-To-Interdecadal Variations of the East Asian Winter Monsoon: The Northern and Southern Temperature Modes. *J Clim* (2010) 23:1495–512. doi:10.1175/2009jcli3243.1

Conflict of Interest: The authors declare that the research was conducted in the absence of any commercial or financial relationships that could be construed as a potential conflict of interest.

frontiers in Climate

ORIGINAL RESEARCH
published: 29 September 2021
doi: 10.3389/fclim.2021.694384

Remote Effects of IOD and ENSO on Motivating the Atmospheric Pattern Favorable for Snowfall Over the Tibetan Plateau in Early Winter

Hongyan Shen[1,2,3], *Zhiqiang Gong*[3,4], *Boqi Liu*[5], *Yipeng Guo*[6], *Xiaoli Feng*[2], *Tingting Wen*[2], *Xiaojuan Wang*[3]* and *Guolin Feng*[1,4,7]

[1] College of Atmospheric Sciences, Lanzhou University, Lanzhou, China, [2] Qinghai Climate Center, Qinghai Meteorological Administration, Xining, China, [3] College of Physics and Electronic Engineering, Changshu Institute of Technology, Suzhou, China, [4] National Climate Center, China Meteorological Administration, Beijing, China, [5] State Key Laboratory of Severe Weather and Institute of Climate System, Chinese Academy of Meteorological Sciences, Beijing, China, [6] College of Atmospheric Sciences, Nanjing University, Nanjing, China, [7] Southern Marine Science and Engineering Guangdong Laboratory, Zhuhai, China

The interannual variation of snowfall over the Tibetan Plateau (TP) in early winter (November–December) and its related atmospheric attribution are clarified. Meanwhile, the influence of tropical sea surface temperatures (SSTs) on TP snowfall is investigated by diagnostic analyses and Community Atmosphere Model (CAM5) simulations. The leading mode of TP snowfall in early winter features a spatially uniform pattern with remarkable interannual variability. It is found that the Indian Ocean Dipole (IOD) and El Niño Southern Oscillation (ENSO) are main external forcing factors for TP snowfall. Positive IOD with positive ENSO and positive IOD with neutral ENSO cases both have remote impact on motivating Southern Eurasia (SEA) pattern, which can induce an anomalous cyclone around the TP. The corresponding anomalous ascending motion and cold air in the mid-upper troposphere provide the dynamical and thermal conditions for heavy snowfall. The low-level southwesterly winds are enhanced over the Arabian Sea and Bay of Bengal, bringing abundant water vapor into the TP for excessive snowfall. Furthermore, CAM5 simulation experiments forced by IOD- and ENSO-related SST anomalies are performed to verify their combined and independent effects on TP snowfall in early winter. It is confirmed that either positive IOD or El Niño has certain impacts on motivating circulation anomalies favorable for snowfall over the TP. However, IOD plays a leading role in producing the excessive snowfall-related atmospheric conditions, and there is an asymmetric influence of ENSO and IOD on the TP snowfall.

Keywords: snowfall, Indian Ocean Dipole, El Niño-Southern Oscillation, remote effects, early winter

OPEN ACCESS

Edited by:
Shangfeng Chen,
Institute of Atmospheric Physics, Chinese Academy of Sciences (CAS), China

Reviewed by:
Ruowen Yang,
Yunnan University, China
Chujie Gao,
Hohai University, China

***Correspondence:**
Xiaojuan Wang
mouse0903@126.com

Specialty section:
This article was submitted to Climate Services, a section of the journal Frontiers in Climate

Received: *13 April 2021*
Accepted: *28 July 2021*
Published: *29 September 2021*

Citation:
Shen H, Gong Z, Liu B, Guo Y, Feng X, Wen T, Wang X and Feng G (2021) Remote Effects of IOD and ENSO on Motivating the Atmospheric Pattern Favorable for Snowfall Over the Tibetan Plateau in Early Winter. Front. Clim. 3:694384. doi: 10.3389/fclim.2021.694384

INTRODUCTION

Although winter precipitation accounts for a relatively small fraction of total annual rainfall comparing to summer season, it experiences obvious annual variability over some regions such as the Tibetan Plateau (TP). Snowfall is solid precipitation formed by condensation of moisture in the air. Heavy snowfall may be a natural hazard to life and property. Severe cold surges accompanied with heavy snowfall during winter can significantly impact agriculture, transportation, livestock

production, and water resources, resulting in serious economic losses. In the context of climate warming, intense snowfall has hit China more frequently in recent winters and caused severe damages to the sustainability of the society. For instance, a severe snowfall event that occurred in later winter 2008 over southern China led to an economic loss of above 20 billion US dollars and affected more than 100 million people (Zhou et al., 2009, 2011).

The Tibetan Plateau (TP), known as the third pole and Asia's water tower, frequently suffers from severe snowfall events due to the combined effects of its steep topography, the East Asian winter monsoon (Webster, 1998; Wu et al., 2011, 2012), and the westerly circulation (Schieman et al., 2009). Entering early winter, the TP ground becomes frozen, and snow is the main form of precipitation over the TP. Snowfall is an important element of the hydrological cycle, replenishing soil moisture, and contributing runoff to river basins through spring melt (Lettenmaier and Gan, 1990; Groisman et al., 2001). Therefore, understanding the mechanism of TP snowfall can provide insights on better prediction of winter climate.

The El Niño-Southern Oscillation (ENSO), which is the strongest atmosphere-ocean coupled mode on the interannual scale, is one of the most important factors that can influence winter climate variability in Eurasia (Wang et al., 2000; Sun and Wang, 2010; Zhou and Wu, 2010; Jia and Lin, 2011; Wang and Feng, 2011; Gong et al., 2014, 2017; Wang and Chen, 2014; Ge et al., 2016). Yang (1996) found that the Eurasian winter snow cover increased during El Niño winters (and decreased during La Niña winters). Using a global atmospheric general circulation model (GCM), Meehl (1997) proposed a hypothesis that the tropical sea surface temperature (SST) has crucial impact on the south Asian monsoon, which can further affect the mid-latitude snow, especially over the Eurasia. Dong and Valdes (1998) also found evidence that El Niño conditions lead to increased snow in Eurasia. Wang and Chen (2010) point out that the western Pacific subtropical high can act as a bridge for ENSO's influence on the East Asian climate. During El Niño events, this system can enhance the moisture transport to China and cause abnormally wet conditions. El Niño might excite the stationary Rossby waves extending along the North African-Asian jet, resulting in anomalous increase of potential vorticity and snow depth over the TP in winter, based on the Nimbus-7 Scanning Multichannel Microwave Radiometer (SMMR) satellite estimates of snow depth (Shaman and Tziperman, 2005). This mechanism was confirmed by Wang and Xu (2018), who used snow water equivalent data from 1987 to 2007.

On the other hand, based on satellite data, Yuan et al. (2009, 2014) reported that the interannual variability of the winter TP snow cover is linked to Indian Ocean dipole (IOD) rather than ENSO, and emphasized that in the pure ENSO years with no co-occurrences of IOD, the influence of ENSO on TP snow cover is negligible (Yuan et al., 2009). Using the ERA-Interim reanalysis data, Zhang et al. (2019) also found the IOD forcing on snow depth over the TP. Jiang et al. (2013, 2019) claimed that anomalous convection over the western Indian Ocean related to the positive IOD could generate a wave train propagating northeastward and induce an anomalous cyclonic circulation over the central western TP, then transport extra moisture from the tropics to the central western TP, causing deep snow depth there. The above studies concentrated on TP snow cover/depth affected by IOD or ENSO through the low-latitude circulations, but less has been investigated in the mid- and high-latitude circulation pattern.

In addition, it is interesting why these studies have obtained different conclusions regarding the impacts of ENSO and IOD on snow over the TP. It is confusing whether the ENSO can affect snow over the TP or not. Of note is that two satellite-based or reanalysis-based snow parameters have been investigated in these studies: snow cover and snow depth (Shaman and Tziperman, 2005; Yuan et al., 2009, 2014; Wang and Xu, 2018; Zhang et al., 2019). The snow depth derived from satellites shows considerable biases (Frei et al., 2012). Thus, it is necessary to use *in situ* snowfall data to re-investigate the relationship of TP snowfall with ENSO and IOD. Direct observations of snowfall *in situ* have a certain length of record and spatial coverage. They are issued after strict quality control, which can promote the study reliability about TP snow. On the other hand, snowfall is the major precipitation event over the TP in winter. Heavy snowfall and freezing temperature lead to snow cover/depth on the ground for a long time. Therefore, snowfall is the leading and direct factor that produces and maintains snow cover/depth. As a result, the changes in TP snowfall have yet to be systematically addressed, and what processes decides the severe TP snowfall is still not fully understood. Given the serious impacts of snowfall events, investigating the possible causes in snowfall is an urgent necessity for disaster prevention and mitigation. Furthermore, most previous studies investigating the contributions of ENSO and/or IOD to the precipitation variation over China only considered a single index for ENSO or IOD. Results obtained without considering the interdependence of ENSO and IOD might include the impacts of both factors. Since ENSO and IOD sometimes co-occur, it is also necessary to identify their respective and combined influences on TP snowfall. Moreover, it is important to explore the influences of IOD and ENSO on the snowfall over TP in early winter utilizing the statistic and simulation approaches.

This paper examines the interannual variability of the early winter snowfall over the TP and the underlying physical mechanisms, especially focusing on independent and joint roles of IOD and ENSO on influencing the TP early winter snowfall. The paper is organized as follows. Section Data, Method, and Model introduces the data and methodology. Section Spatial-Temporal Features of TP Early Winter Snowfall presents the characteristics of snowfall over the TP in early winter. Section SSTAs Associated With Early Winter TP Snowfall discusses the SSTAs associated with early winter snowfall over the TP. Section Numerical Experiments analyzes IOD and ENSO associated with TP early winter snowfall by statistics, and then validates the observed and statistical results utilizing the Community Atmosphere Model version 5 (CAM5) model. Section Conclusion and Discussion provides a brief conclusion and discussion of this study.

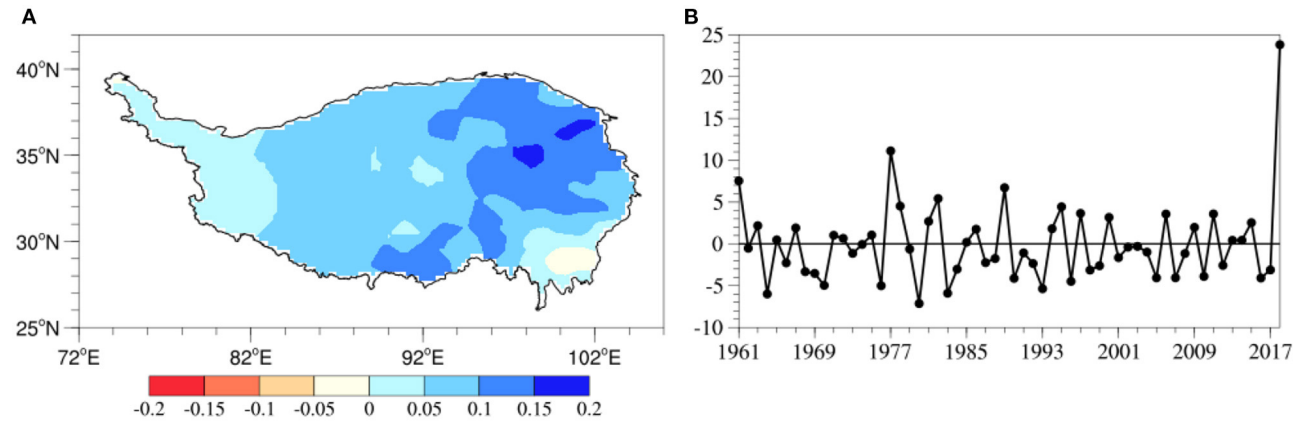

FIGURE 1 | The EOF-1 **(A)** mode and detrended PC1 **(B)** of early winter snowfall on TP.

DATA, METHOD, AND MODEL

In this paper, snowfall data are collected from 85 observation stations over the TP, which are released by the National Meteorological Information Center of China Meteorological Administration. These stations are located in Qinghai (45 stations), Xizang (19 stations), Gansu (4 stations), and Sichuan (17 stations) Provinces, respectively. The monthly snowfall during early winter (November–December) was derived from the daily observation records during 1961–2018. The large-scale atmospheric state is obtained from the NCEP/NCAR reanalysis data (Kalney et al., 1996). The variables include geopotential height, horizontal wind, humidity, and vertical velocity, with a horizontal resolution of 2.5° × 2.5°. Monthly mean sea surface temperature (SST) data were based on the Extended Reconstruction SST version 5 (ERSST5) dataset, which is provided by the NOAA/Oceanic and Atmospheric Research (OAR)/Earth System Research Laboratory of Physical Science (Huang and Cai, 2017). The period of the dataset is from 1961 to 2018, and early winter in this article refers to November–December.

A wave-activity flux (WAF) derived by Takaya and Nakamura (2001) is used to diagnose the mid–high-latitude wave train (Equation 1).

$$W = \frac{p\cos\varphi}{2\left|\vec{U}\right|}\begin{Bmatrix} \frac{U}{a^2\cos^2\varphi}[((\frac{\partial\psi}{\partial\lambda})^2 - \psi\frac{\partial^2\psi}{\partial\lambda^2})] + \frac{V}{a^2\cos\varphi}[\frac{\partial\psi}{\partial\lambda}\frac{\partial\psi}{\partial\varphi} - \psi\frac{\partial^2\psi}{\partial\lambda\partial\varphi}] \\ \frac{U}{a^2\cos\varphi}[\frac{\partial\psi}{\partial\lambda}\frac{\partial\psi}{\partial\varphi} - \psi\frac{\partial^2\psi}{\partial\lambda\partial\varphi}] + \frac{V}{a^2}[(\frac{\partial\psi}{\partial\varphi})^2 - \psi\frac{\partial^2\psi}{\partial\varphi^2}] \\ \frac{f_0^2}{N^2}[\frac{U}{a\cos\varphi}(\frac{\partial\psi}{\partial\lambda}\frac{\partial\psi}{\partial z} - \psi\frac{\partial^2\psi}{\partial\lambda\partial z}) + \frac{V}{a}(\frac{\partial\psi}{\partial\varphi}\frac{\partial\psi}{\partial z} - \psi\frac{\partial^2\psi}{\partial\varphi\partial z})] \end{Bmatrix} \quad (1)$$

In which (U, V) are the climatological winds in the zonal and meridional directions;(λ, φ) are longitude and latitude, a is the earth's radius; $z = -Hlnp$; $p = pressure/1000$ hPa; H is the constant scale height; ψ is the perturbation of geostrophic stream function; $\left|\vec{U}\right|$ is the magnitude of the wind; f_0 is the Coriolis parameter; and N^2 is the buoyancy frequency.

The moisture flux $(\vec{Q})$ and its divergence $(\vec{D})$ are calculated as:

$$\vec{Q} = -\frac{1}{g}\int_{p_u}^{p_s} q\vec{V}\,dp, Q_\lambda = -\frac{1}{g}\int_{p_u}^{p_s} qudp, Q_\varphi = -\frac{1}{g}\int_{p_u}^{p_s} qvdp \quad (2)$$

$$\vec{D} = -\nabla\cdot\vec{Q} = -\frac{1}{a\cos\varphi}(\frac{\partial Q_\lambda}{\partial\lambda} + \frac{\partial Q_\varphi\cos\varphi}{\partial\varphi}), \quad (3)$$

where p_s is the surface pressure; p_u is the pressure of the top moisture layer (300 hPa); p is pressure; q is the specific humidity; and (u, v) are horizontal velocity components. a is earth radius, λ is longitude, φ is latitude.

The present study also used the statistical analysis to show the features and circulation associated with the early winter snowfall over the TP, including the empirical orthogonal function (EOF) analysis, correlation and partial correlation analysis, and composite analysis methods.

The Community Atmosphere Model version 5 (CAM5) model is utilized for validating the observed and statistical results. As stated in the introduction, it is derived from the model used in Khairoutdinov and Randall (2001) and is a component of Community Earth System Model developed at NCAR with many external collaborators. This model uses a default finite-volume dynamical core with a hybrid pressure-sigma vertical coordinate (Simmons and Burridge, 1981) that has 30 levels with a top at 2.255 hPa. The CAM5 has the same land, ocean, and sea ice components as in CCSM4, with the biggest change occurring in the atmosphere. The CAM5 is essentially new atmospheric model with improved and more realistic formulations of radiation, boundary layer, and aerosols. CAM5 features (1) a new shallow convection scheme and a new moist turbulence scheme developed by the University of Washington, (2) a two-moment cloud microphysics scheme, and a cloud macrophysics scheme from the parameterizations of clouds.

The model code can be downloaded from the NCAR code repository online and was run locally at the National Meteorological Information Center (NMIC) of the China Metrological Administration (CMA). This model has been widely used to investigate the effects of the underlying condition on the winter climate. Four sets of numerical experiments are designed with CAM5 driven by the global SST data of Hadley Center. One is a control experiment forced by the global SST climatology of observational monthly SST data in early winter, and the other three are sensitivity experiments forced by combined IOD and ENSO, independent IOD with no co-occurrence of El Niño, and independent El Niño with no co-occurrence of IOD. The first principal component (PC1) of TP snowfall in early winter by using the Empirical Orthogonal Function (EOF) expansion is defined as the TP snowfall index. We add the regression SST value against this index to the climatology as SST external forcing signal. The three sensitivity experiments represent the single IOD and ENSO forcing, respectively, and IOD-ENSO joint forcing. Each experiment includes 10 members with different initial states in order to verify the sensitivity to different atmospheric initial values, and the 10-member average results will be used for analysis. The differences between the sensitivity and control runs show the influences of SSTAs on the early winter snowfall over the TP.

SPATIAL-TEMPORAL FEATURES OF TP EARLY WINTER SNOWFALL

Interannual Variation of TP Snowfall

Interannual variability of the early winter snowfall over the TP is revealed by using the Empirical Orthogonal Function (EOF) expansion (**Figure 1**) based on solid precipitation observations over the TP from 85 stations. The first EOF mode (EOF-1) explains about 32.2% of the total variance and exhibits a regional consistency of snowfall anomaly (**Figure 1A**). The higher loading value lies in the Northeast and center of TP, which is the frequent location of snow disaster. The corresponding first principal component (PC1) shows a remarkable interannual variability (**Figure 1B**). For example, in winter 2018, heavy snowfall occurred in the northeast of the Tibetan Plateau. Such an extreme snowfall is enhanced as a possible response to climate warming. Sun and Wang (2010) claimed that heavy snow events of more than 5 mm/day increased in the eastern of TP since the 1960s. At the same time, the snow days have increased (Zhou et al., 2017). Danco et al. (2016) used phase 5 of the Coupled Model Inter-comparison Project (CMIP5) to reveal that snow rate and heavy snowfall frequency will increase during 2021–2050 and 2070–2100 over the TP. Therefore, TP snow disaster may become a severe challenge in the future.

Atmospheric Circulation

Now we discuss the atmospheric circulation affecting the TP early winter snowfall. Firstly, simultaneous regressions of 200- and 500-hPa geopotential height (GPH) against PC1 of TP snowfall in early winter show a wave train with barotropic structure

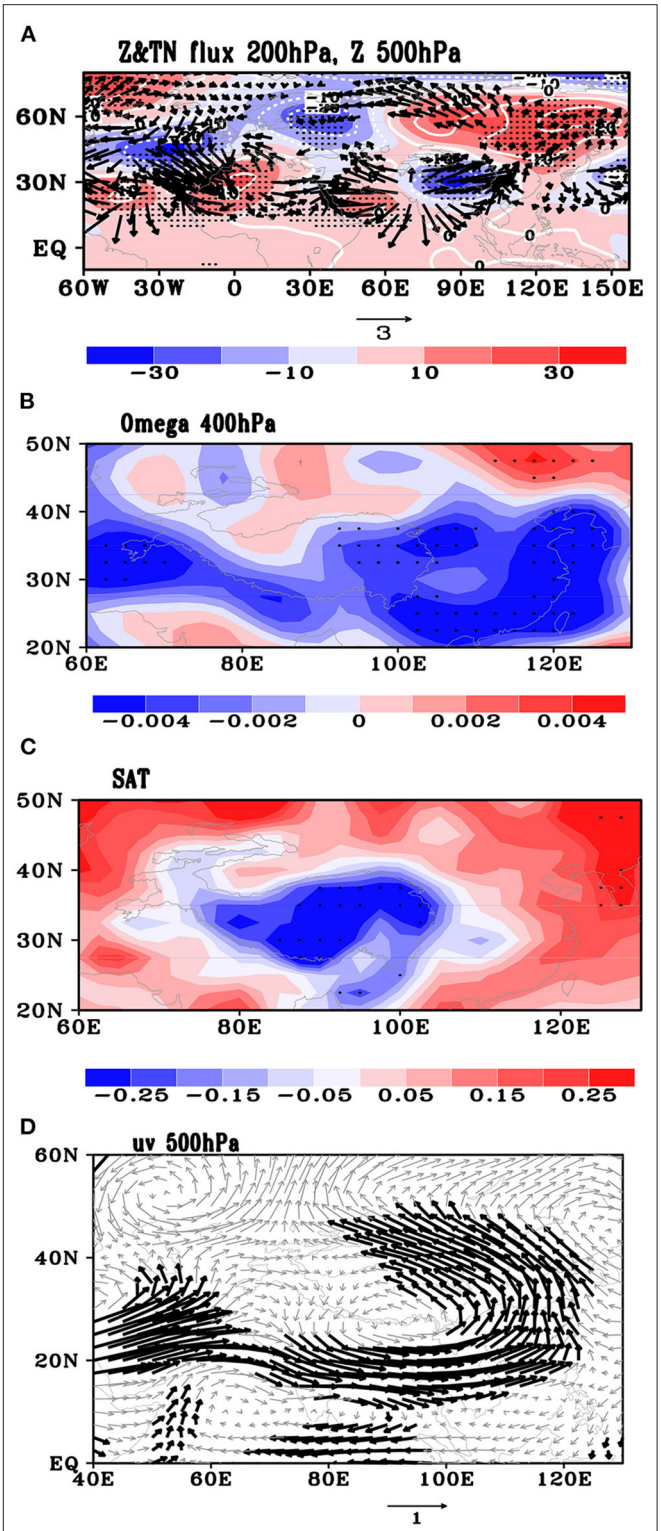

FIGURE 2 | (A) 200-hPa Geopotential height (shadings, gpm) and wave activity fluxes (vectors, $m^2\ s^{-2}$) and 500-hPa geopotential height (contours, gpm), **(B)** 400 hPa vertical velocity (Pa s^{-1}) and **(C)** surface temperature (°C), **(D)** 500-hPa horizontal wind (m s^{-1}) regressed against PC1 of TP snowfall in early winter. Black dots in **(A–C)** and the bold vector in **(D)** indicate the values exceeding the 95% confidence level.

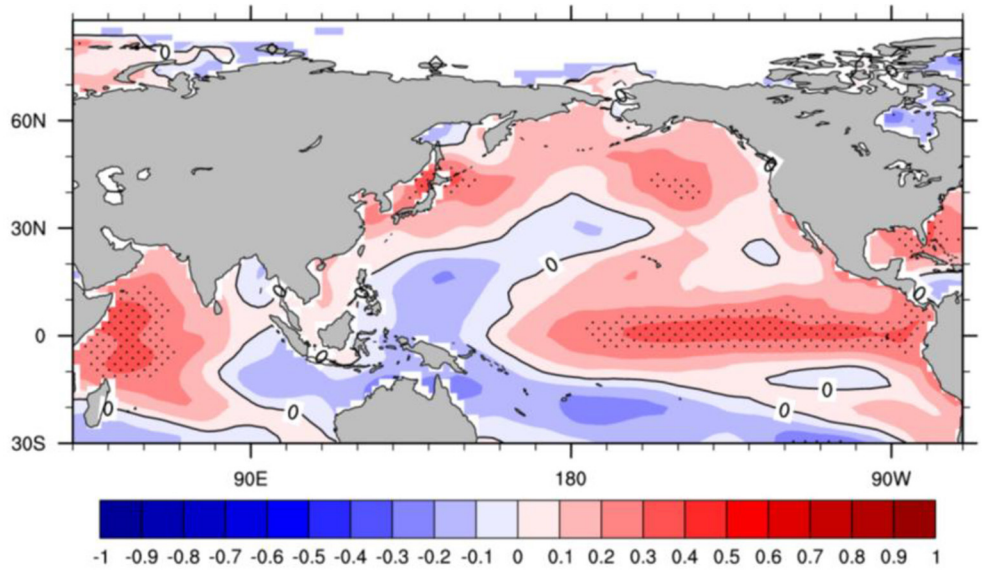

FIGURE 3 | Regression of global sea surface temperature (unit: °C) in early winter against PC1 of TP snowfall in early winter (black dots indicate the values exceeding the 95% confidence level).

from Southwest Europe-Northwest Africa to East Asian at mid-high latitude (**Figure 2A**). The WAF suggests that the wave train originates from Greenland and then extends to Northeast Asia with two propagating pathways (**Figure 2A**). One is from Greenland to North Atlantic and Sahara as the North path, and the other one stems from the Arabian Peninsula and propagates northeastward to TP and Northeast Asia. We defined two indices to describe the two pathways of the wave train (Equation 4). The South index (SI) is based on averaged anomalous geopotential height at level 500 hPa over the TP, Arabian Peninsula, and Northeast Asia as formula (4). The North index (NI) also includes three centers over Greenland, North Africa, and North Atlantic, respectively. These two indices properly reflect features of remote connections across the Eurasia continent, which can be used to identify whether the northern or southern wave train has more significant impact on the atmospheric circulations over the TP region.

$$SI = H_{TP}(80-105^{\circ}E,\ 25-32^{\circ}N) - H_{AP}(32-60^{\circ}E, 10-20^{\circ}N) - H_{NEA}(100-140^{\circ}E,\ 45-60^{\circ}N)$$
$$NI = H_{GL}(58-32^{\circ}W,\ 60-70^{\circ}N) + H_{NA}(15W-15^{\circ}E, 25-40^{\circ}N) - H_{NAT}(50-20^{\circ}W,\ 40-50^{\circ}N) \quad (4)$$

The SI and NI are two indices, respectively. The H_{TP} is the Tibetan Plateau region (100–140°E, 45–60°N) geopotential height departure; similarly, H_{AP}refers to Arabian Peninsula (32–60°E, 10–20°N), H_{NEA} Northeast Asian (100–140°E, 45–60°N), H_{GL} Greenland (58–32°W, 60–70°N), H_{NA} North Atlantic (50–20°W, 40–50°N), and H_{NAT} North Atlantic (50–20°W, 40–50°N).

TABLE 1 | Temporal correlation coefficients (TCC) between PC1 and IOD/ENSO indices.

	IOD	ENSO
Correlation	0.50	0.31
Partial correlation	0.45	0.10

The SI and NI present significant negative correlation with −0.48 temporal correlation coefficient (TCC). The TCC between PC1 and SI (NI) is −0.52 (0.39), respectively. All the TCCs have exceeded the 99.9% confidence level. This results implicate more the important role of the southern path on early winter snowfall over TP. Actually, the southern path of this wave train is similar to the Southern Eurasian (SEA) teleconnection (Xu et al., 2012; Li, 2016). It is one of the Eurasian (EU) patterns (Wallace and Gutzler, 1981). In boreal winter, the SEA teleconnection pattern is an important intermediate track linking the NAO and weather climate over East Asia (Xu et al., 2012; Li, 2016). Five main centers of action lie in the following regions: Southwest Europe, the Middle East, the Arabian Sea, the Tibetan Plateau/Southwest China, and Northeast Asia (Li et al., 2019).

In **Figure 2A**, the prominent positive geopotential height anomalies embedded in the wave train exist in the Southwest of Europe, Northwest of Africa, TP, and Northeast Asia. This anomalous center at 500 hPa level is in agreement with the characteristic of the SEA pattern. The positive (negative) SEA pattern in boreal winter indicates positive (negative) geopotential height anomalies over Southwest Europe and the Arabian Sea, as well as Northeast Asia (the Middle East and Tibetan Plateau/Southwest China), and more (less) precipitation in

TABLE 2 | Frequency (number of years) corresponding to IOD and ENSO combinations during 1961–2018.

	I^+	I^0	I^-	Total
P^+	6	8	1	15
P^0	4	21	5	31
P^-	1	5	7	12
Total	11	35	12	58

I^+, I^0, and I^- represent the strong positive (IOD index value higher than 0.7 standard deviations), neutral (IOD index value between −0.7 and 0.7 standard deviations), and negative (IOD index value lower than −0.7 standard deviations) cases, respectively. P^+, P^0, and P^- represent the same meaning but for ENSO index.

TABLE 3 | Years of IOD and ENSO combinations.

Categories	I^+P^+	I^+P^0	P^+I^0	I^-P^-	I^-P^0	P^-I^0
Frequency	6	4	8	7	5	5
Years	1963	1961	1965	1974	1966	1983
	1972	1967	1969	1984	1971	1988
	1997	1977	1982	1998	1973	1995
	2006	2012	1986	2005	1993	1999
	2015		1991	2007	1996	2011
	2018		1994	2010		
			2002	2016		
			2009			

*The meaning of I^+, I^0, I^-, P^+, P^0, and P^- are the same as that in **Table 2**.*

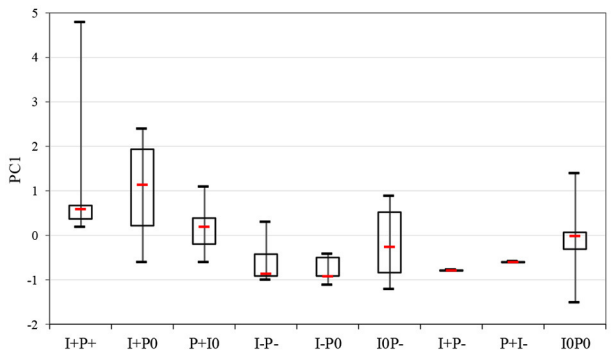

FIGURE 4 | Boxplot of PC1 anomaly of TP snowfall in case of IOD and ENSO combinations. Red shorts line denote the median, black short lines are minimum and maximum value, the top and bottom of the box are the 25th and 75th percentile, respectively.

Southwest China (Li et al., 2019). Therefore, the SEA pattern may have a close connection to TP snowfall. The significant negative center is also observed at 200 hPa over the TP. They accompany the 500 hPa anticyclonic anomalies over the Arabian Sea at lower latitude and anomalous cyclone around the TP at mid–high latitude from North Africa to East Asia (**Figure 2D**). The southerly wind gets enhanced around the TP, which can transport more water vapor from the Bay of Bengal into the TP. In the meantime, an anomalous ascending branch occurs over the TP and Southeastern China (**Figure 2B**), along with the land surface cooling surrounding the TP with above-normal snowfall in early winter (**Figure 2C**).

SSTAS ASSOCIATED WITH EARLY WINTER TP SNOWFALL

Previous studies (Yuan et al., 2014; Jiang et al., 2019) implied that the anomalies of TP snow cover/depth and circulation in early winter can be ascribed to the heat forcing of low-latitude SSTAs. **Figure 3** indicates that the significant positive SSTAs regressed against PC1 of early winter TP snowfall appear in the western Indian Ocean, while weak negative SSTAs emerge in the eastern Indian Ocean, constituting a positive Indian Ocean Dipole (IOD) pattern (Saji et al., 1999). Additionally, IOD can also preserve its footprints on the Tibetan Plateau via the Tibetan snow anomalies and influence the subsequent spring and summer climate even after its disappearance (Kripalani and Kulkarni, 1999). It is also found that another positive SSTA exists in the eastern equatorial Pacific, corresponding to an El Niño event (**Figure 3**). At the same time, wintertime air temperature over southeastern TP is related to convection anomaly over the western North Pacific, which is significantly affected by ENSO (Jiang et al., 2013). Is it possible that ENSO can affect snowfall over the TP?

Statistical Analysis

In general, IOD and ENSO peak in autumn and winter, respectively. Both of them have strong climate effects on the cold season of the Northern Hemisphere. The monthly Niño 3.4 and IOD indices used to measure the ENSO and IOD events are obtained from https://www.cpc.ncep.noaa.gov/data/indices. An intimate TCC exists between IOD and ENSO with a significant correlation coefficient of 0.47 during 1961–2018. As to the early winter snowfall over TP, the significant TCCs between PC1 and IOD and ENSO reach 0.50 and 0.31, respectively. The partial TCC between PC1 and ENSO dramatically decreases to 0.10 after removing the IOD signal (**Table 1**). In contrast, the partial TCC between PC1 and IOD is 0.45 and remains remarkable while excluding the effect of ENSO. Therefore, IOD not only exerts a direct influence on the early winter snowfall over the TP but is also crucial for maintaining the linkage between PC1 and the ENSO event.

As a consequence, ENSO impacts on TP snowfall by depending on IOD; meanwhile, ENSO has contributed to the relationship between IOD and PC1. It is assumed that the early winter IOD and ENSO may affect the Tibetan Plateau snowfall both independently and concurrently. Yamagata et al. (2004) found that one-third of IOD events are connected with ENSO. Behera and Yamagata (2003) also verified that a significant fraction of IOD events were correlated with tropical Pacific variability, including ENSO. The influence of ENSO on Indian Ocean SSTs is characterized by taking the complex development of ENSO into account: the spatiotemporally varying impact of both canonical and non-canonical ENSO variability is estimated

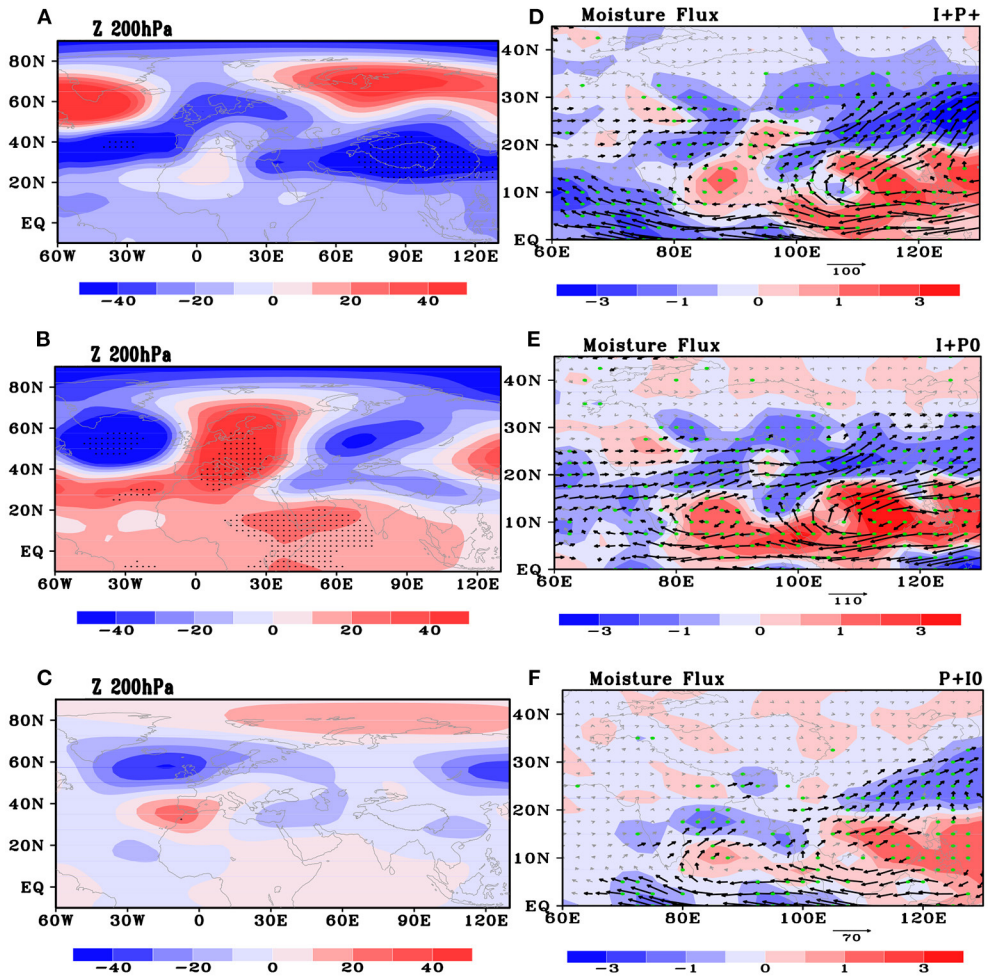

FIGURE 5 | The early winter circulation at positive IOD and ENSO combinations **(A–C)**. For 200 hPa geopotential height (gpm), **(D–F)**. For moisture flux (kg m^{-1} s^{-1}). **(A,D)** refer to the positive IOD and El Niño combination case, **(B,E)** refer to the case of positive IOD and neutral ENSO, **(C,F)** refer to the case of positive El Niño and neutral IOD.

and filtered prior to the search for recurrent modes of SST variability in the Indian Ocean (Yamagata et al., 2004).

For further examination of the effects of IOD and ENSO, we divide the 58 years (during 1961–2018) into some categories based on the combinations of IOD and ENSO indices (**Table 2**). In this study, the strong IOD (ENSO) events are defined as the absolute value of the IOD (Nino 3.4) index above 0.7 standard deviation, whereas the other cases are in the neutral conditions. During 1961–2018, there are 6 (7) years with a strong positive (negative) IOD–ENSO combination, and 21 years with a normal IOD–ENSO combination (**Tables 2**, **3**). Other years with either strong IOD or ENSO mainly represent the individual influence of strong IOD or ENSO.

As shown in **Figure 4**, the variation of early winter snowfall over the TP is quite different with IOD and ENSO combinations. The medium values of snowfall anomaly are above normal in the combinations of strong positive IOD events (I^+) with positive (P^+) or normal (P^0) ENSO events, while the snowfall is below normal in the combinations if the IOD presents the strong negative values (I^-). It is also noted that the medium PC1 of TP snowfall is positive when both IOD and ENSO are positive (I^+P^+) but lower than the combination with positive IOD and normal ENSO (I^+P^0), indicating the positive ENSO won't further enhance the IOD's effect on producing more snowfall over the TP in early winter. Besides, the uncertainty of the PC1 of TP snowfall is large in the years with only a strong ENSO event (P^+), which is consistent with the insignificant partial TCC between ENSO and PC1 without an IOD event (**Table 1**). The early winter snowfall anomaly is quite close to zero with large uncertainty in the neutral IOD–ENSO combinations (I^0P^0). Accordingly, the individual strong positive IOD or ENSO has a remote effect on motivating the early winter snowfall over the TP, but IOD plays a more important role than ENSO. It has also been verified in the study of the respective influences of IOD and ENSO on the TP snow cover in early winter (Yuan et al., 2009).

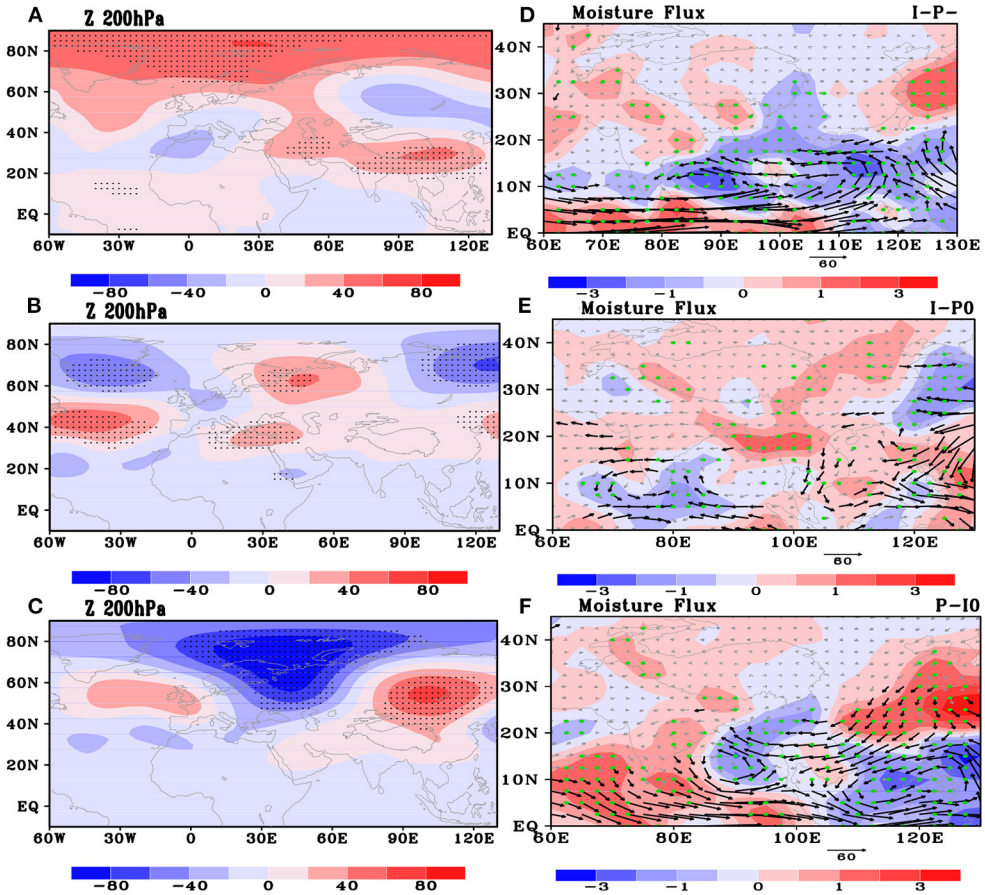

FIGURE 6 | As in **Figure 5**, but for the negative phases of IOD and ENSO.

Composite Results

We further investigate the combined effect of IOD and ENSO on TP snowfall in early winter by means of composite analysis for each category. In case of positive IOD and ENSO (I^+P^+), the circulation anomaly is similar to the SEA-like pattern at 200-hPa level from western Europe to East Asia. Especially, the anomaly centers including Greenland, western Europe, and Northwest Africa just lie in the North pathway. That is consistent with the circulation facilitating the above-normal TP snowfall in early winter (**Figures 2A, 5A**). It is worth noting that the most remarkable negative anomaly occurs in the TP and its neighboring regions, which is in agreement with **Figure 2A**. These circulation anomalies are associated with warm and humid southwesterly anomalies to enter the TP and cause moisture convergence that dominates the whole TP region (**Figure 5D**). A strong ascending motion may imply an unstable atmospheric condition.

Figures 5B,E illustrate the circulation anomalies in positive IOD and neutral ENSO (I^+P^0) case. A zonal wave train pattern across North Atlantic to Asia is observed at 200-hPa level. It is a Eurasian-like pattern and TP has been covered by negative anomaly, thus weaker than in **Figures 5A,B**. The maximum moisture convergence occurs in south of TP affected by air flow from the northwest Pacific and Arabian sea via the India Peninsula (**Figure 5E**), leading to above-normal snowfall *in situ*. It is dynamically consistent with the regression of geopotential height and wind anomalies against the PC1 of TP snowfall (**Figure 2**). It reflects that the positive IOD is conducive to motivating the atmospheric condition of TP snowfall in early winter. As demonstrated by Yamagata et al. (2004), positive IOD can cause convergence anomalies over the Mediterranean/Sahara region at the upper troposphere. With positive ENSO and neutral IOD (P^+I^0) (**Figures 5C,F**), the circulation anomaly and water vapor transfer from the low-latitude region become more weaker than in I^+P^0 case.

Figure 6 gives the circulation anomalies based on the opposite combination including negative IOD and ENSO (I^-P^-), negative IOD and neutral ENSO (I^-P^0), and negative ENSO and neutral IOD (P^-I^0). It presents almost opposite characteristics to I^+P^+, I^+P^0, and P^-I^0 cases, which illustrates that IOD avails for the North pathway wave train development and negative anomalies on the TP.

In conclusion, the individual IOD can stimulate the SEA-like pattern from the Arabian sea via the TP to Northeast Asia; thus, the effect of the individual effect became weaker. Yuan et al. (2009) also revealed that the Eurasia waves can be generated by

TABLE 4 | Schemes of the four CAM5 simulations.

Experiment name	Schemes	Integral times
Control experiment (E0)	CAM5 is forced by global SST climatology	10
Sensitivity experiment in both Indian and Pacific Ocean (E1)	CAM5 is forced by SST anomaly within both tropical Indian and Pacific Ocean	10
Sensitivity experiment in Indian Ocean (E2)	CAM5 is forced by SST anomaly within the tropical Indian Ocean related to the independent IOD with no co-occurrence of El Niño	10
Sensitivity experiment in Pacific Ocean (E3)	CAM5 is forced by SST anomaly within the tropical Pacific Ocean related to the independent El Niño with no co-occurrence of IOD	10

the IOD-related convection anomalies over the western/central Indian Ocean. The anomalies of moisture supply and surface temperature over the TP are significant. All of which suggested the crucial influences of IOD on early winter TP snowfall, while the influences of ENSO is weaker.

NUMERICAL EXPERIMENTS

In order to further verify the effects of IOD and ENSO, one control experiment and three sensitivity experiments by CAM5 are implemented, respectively. The experiment schemes are listed in **Table 4**. As described in section Data, Method, and Model, the differences between the sensitivity and control runs show the influences of SSTA on TP early winter snowfall. In the first sensitivity experiment (E1), we prescribe the positive SST anomaly in the tropical western Indian and Pacific Ocean featured with positive IOD and ENSO phase (**Figure 7A**). The second experiment (E2) denotes an IOD-like pattern with the positive–negative anomaly seesaw in the western and eastern Indian Ocean (**Figure 7B**). The third experiment (E3) is referred to as El Niño condition in the tropical Pacific (**Figure 7C**). Based on these simulation experiments, we may able to further verify the individual or joint roles of IOD and ENSO on motivating the early winter snowfall-related atmospheric patterns over the TP and its surrounding regions.

Figure 8 shows the circulation response in the above three SST external forcing conditions. Compared with **Figure 6**, simulation results reproduce the circulation pattern, i.e., SEA-like pattern can be reproduced by forces of the positive IOD and ENSO (I^+P^+) (**Figure 8A**) or force of positive IOD (I^+) (**Figure 8B**). Maybe due to model uncertainty, the I^+ corresponding pattern is a little bit weaker than I^+P^+.

Compared with the observations (**Figure 5**), the simulated anomaly phase and the location of anomaly centers are very similar to each other. Although the center of TP cannot be simulated exactly in the condition of positive IOD, it is still covered by the negative geopotential height anomalies south of the TP and the mid-low latitude, which is consistent with the above analysis. Besides, it is also presented that the simulated geopotential height anomalies for the P^+I^0 are quite weak over the TP region, which is consistent with the feature of **Figure 6C**. Therefore, individual positive ENSO has limited effect on motivating the SEA-like pattern and circulation anomalies around the TP region. Therefore, CAM5 simulation further confirmed that I^+P^+ and I^+P^0 cases have remote effects on motivating the SEA-like pattern across Euro-Asia continent then cause geopotential height anomaly over the TP. Noteworthily, the anomaly of horizontal wind field have consistent in I^+P^+ (**Figure 9A**) and P^+ cases (**Figure 9C**), the northwesterly prevailed over TP and an anticyclone occur in the southeastern TP, which can hinder the warm moisture entering into the TP. On the contrary, in **Figure 9B**, the I^+P^0 force can produce an anticyclone at the southeastern TP, transporting more water vapor into the TP, providing the moisture condition for snowfall.

Besides, in **Figures 10A–C**, a 400-hPa vertical velocity field shows an anomalous ascending motion in I^+P^+ and I^+P^0 cases, which avails for more snowfall over the TP region. Therefore, the I^+P^+ or I^+P^0 corresponding wind field and vertical motion in the middle troposphere can lead to heavy snowfall over the TP in early winter, while the function of I^0P^+ is quite weak. Jiang et al. (2019) also revealed that anomalous convection over the western Indian Ocean related to the positive IOD could generate a wave train propagating northeastward and induce an anomalous cyclonic circulation over the central western of TP. The associated anomalous circulation transports extra moisture from the tropics to the central western TP, providing favorable conditions for more snowfall over the central western of TP.

CONCLUSION AND DISCUSSION

In this paper, we examine the interannual variability of TP snowfall in early winter and its underlying physical mechanisms based on observational and NCEP reanalysis data, and the mechanisms of respective and combined IOD and ENSO effects on TP snowfall are investigated using the CAM5 model.

The interannual oscillation indicated by the first EOF mode of TP snowfall in early winter shows good uniformity regionally, which is closely related to the SEA-like pattern from the North Atlantic to East Asian at mid and high latitudes. The TP region is characterized by negative geopotential height anomalies at 200 hPa, the vertical ascending motion at 400 hPa, and the negative temperature anomalies. Cyclonic circulation anomalies around the TP region intensified southwesterly moisture flow into the TP from the Arabians Sea and Bay of Bengal. All these circulation anomalies provide the favorable thermal and dynamical conditions for more snowfall over the TP.

Either the respective effect of IOD and ENSO, or their combined effect can motivate negative geopotential anomalies and cyclone water vapor flow in the surrounding area of TP. We note that the positive IOD could excite the obvious SEA-like

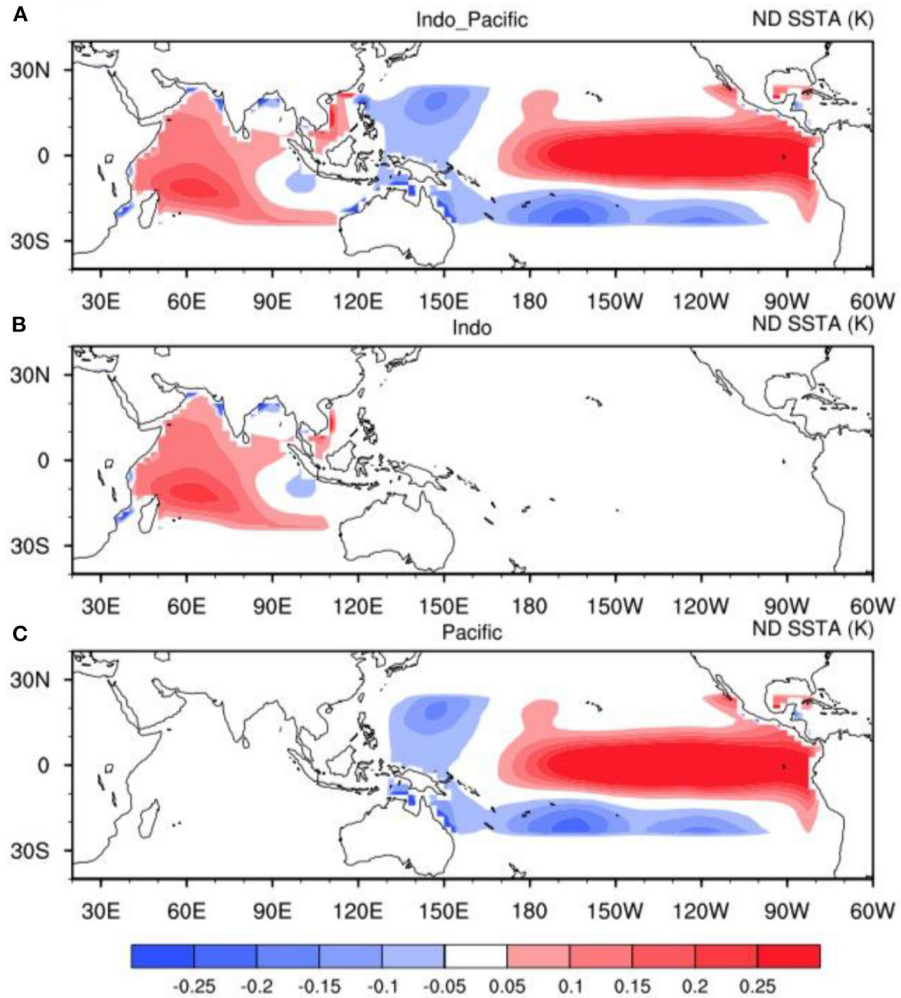

FIGURE 7 | The SST anomalous forcing scheme in model experiments. **(A)** SST forcing added in both western Indian ocean and tropical Pacific ocean, **(B)** SST forcing added only in the western Indian ocean, **(C)** SST forcing added only in the tropical Pacific ocean.

pattern, southerly moisture supply and vertical ascending motion over the TP. Therefore, IOD plays a leading role in producing uniform pattern of TP snowfall. While the respective effect of positive ENSO is weak and wouldn't enhance the IOD's effect on the early winter snowfall related atmospheric pattern over the TP and its surrounding region.

We have utilized the CAM5 model (the Community Atmosphere Model version 5) to reproduce the observed circulation anomalies related to the positive IOD and ENSO, which can explain their combined and respective effects on the TP snowfall in early winter. One control experiment and three sensitivity experiments by the CAM5 model were implemented to further verify the different roles of IOD and ENSO in motivating the SEA-like pattern and uniformed snowfall pattern over the TP. The differences in the influence of SSTA on the early winter snowfall over the TP are shown in the control and sensitivity runs. The simulated results further confirmed that the CAM5 model can depict the positive IOD and the remote effect of ENSO in motivating the SEA-like circulation pattern, especially verifying that positive IOD can significantly enhance the moisture supply from the low-latitude region and cause sufficient snowfall over the TP. As demonstrated by Jiang et al. (2019), convection anomalies over the western Indian Ocean associated with IOD could generate a barotropic Rossby wave that propagates northeastward along the South Asian wave guide. This Rossby wave induces an anomalous cyclonic circulation across the northern India, which transports more moisture to the TP from the tropics, providing a favorable condition for heavy snowfall and deepening of snow depth over the TP region. Sardeshmukh and Hoskins (1988), using a vorticity model, demonstrated that a divergence center over the tropical western Indian Ocean can directly generate the mid-latitude stationary Rossby waves with negative geopotential height anomalies north of India. More recently, Barlow et al. (2007) put an additional deep diabatic heating over the eastern Indian Ocean around the eastern pole of

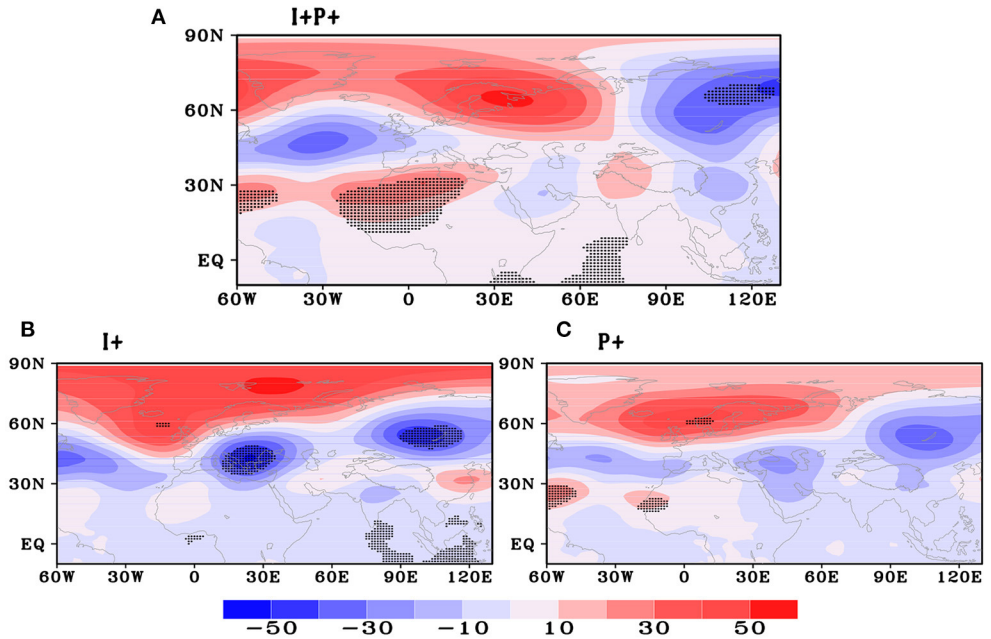

FIGURE 8 | A 200-hPa geopotential height anomaly (gpm) of the CAM5 simulation experiments forced by **(A)** positive IOD and ENSO simultaneously, **(B)** individual positive IOD, and **(C)** individual El Niño, respectively. Black dots indicate that the values exceeding the 95% confidence level.

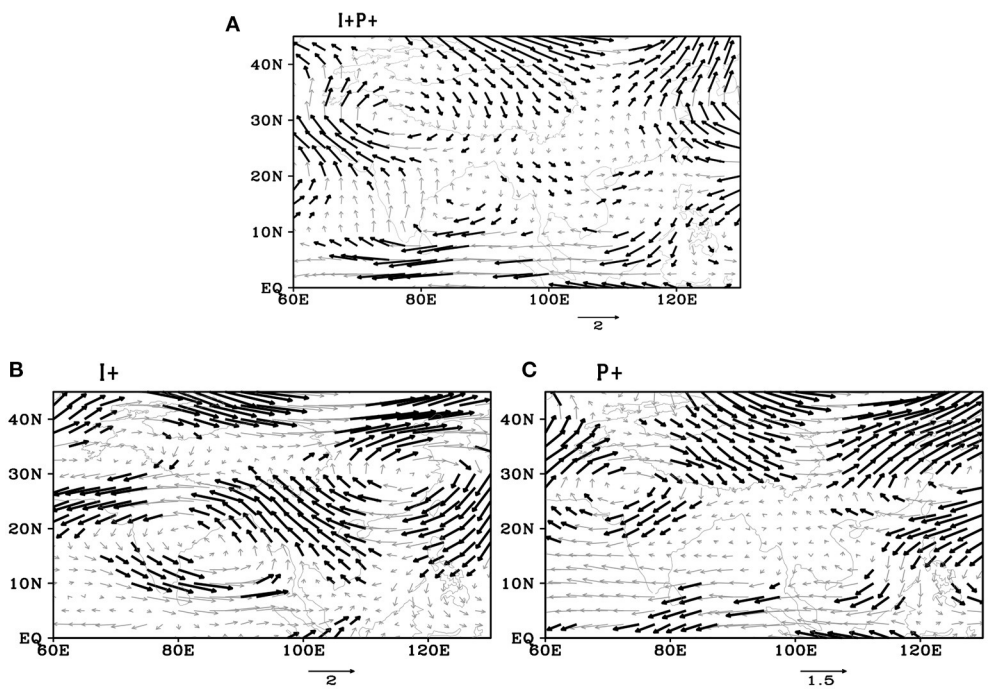

FIGURE 9 | As in **Figure 8**, but for 500-hPa horizontal wind anomaly field (m s^{-1}). Bold vectors indicate that the values exceeding the 95% confidence level.

IOD in winter. Therefore, the Rossby waves along the wave guide in the early winter of pure IOD years may be caused by the IOD-related convection anomalies over the tropical Indian Ocean.

It is also noted that there is an uncertainty in the CAM5 model in climate simulation, especially for the middle- and high-latitude regions, which may lead to a certain bias in the simulated results presented in this study relative to the observation.

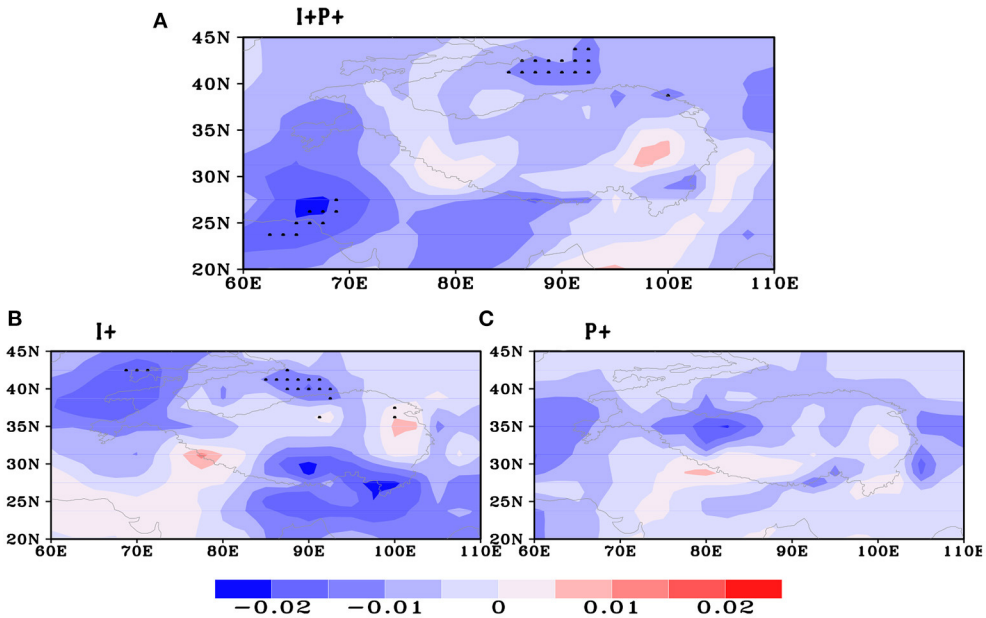

FIGURE 10 | As in **Figure 8**, but for the 400-hPa vertical velocity anomaly field (m s^{-1}). Black dots indicate that the values exceeding the 95% confidence level.

DATA AVAILABILITY STATEMENT

The raw data supporting the conclusions of this article will be made available by the authors, without undue reservation.

AUTHOR CONTRIBUTIONS

ZG was responsible for writing the manuscript. BL was responsible for the numerical simulation. YG helped with the writing of the manuscript. XF and TW helped revise the manuscript. XW designed the thesis framework and helped with the writing of the manuscript. GF helped the writing of the manuscript.

FUNDING

This work was supported by the National Key Research and Development Program of China (2018YFC1507702) and the National Natural Science Foundation of China Project (42065003, 42075057, and 41875100), Qinghai Science and Technology Department Project (2021-ZJ-757), and Opening Fund of Key Laboratory of Land Surface Process and Climate Change in Cold and Arid Regions, CAS (LPCC2019009).

REFERENCES

Barlow, M., Hoell, A., and Colby, F. (2007). Examining the wintertime response to tropical convection over the Indian Ocean by modifying convective heating in a full atmospheric model. *Geophys. Res. Lett.* 34:L19702. doi: 10.1029/2007GL030043

Behera, S. K., and Yamagata, T. (2003). Influence of the Indian Ocean on the Southern Oscillation. *J. Meteorol. Soc. Jpn.* 81, 169–177. doi: 10.2151/jmsj.81.169

Danco, J. F., Deangelis, A. M., Raney, B. K., and Broccoli, A. J. (2016). Effects of a warming climate on daily snowfall events in the Northern Hemisphere. *J. Clim.* 29, 6295–6318. doi: 10.1175/JCLI-D-15-0687.1

Dong, B., and Valdes, P. J. (1998). Simulations of the Last Glacial Maximum climates using a general circulation model: prescribed versus computed sea surface temperatures. *Clim. Dyn.* 14, 571–591. doi: 10.1007/s003820050242

Frei, A., Tedesco, M., Lee, S., Foste, J., Hall, D. K., Kelly, R., et al. (2012). A review of global satellite-derived snow products. *Adv. Space Res.* 50, 1007–1029. doi: 10.1016/j.asr.2011.12.021

Ge, J. W., Jia, X. J., and Lin, H. (2016). The interdecadal change of the leading mode of the winter precipitation over China. *Clim. Dyn.* 47, 2397–2411. doi: 10.1007/s00382-015-2970-x

Gong, Z. Q., Feng, G., Dogar, M. M., and Huang, G. (2017). The possible physical mechanism for the EAP-SR co-action. *Clim. Dyn.* 132, 1156–1163. doi: 10.1007/s00382-017-3967-4

Gong, Z. Q., Feng, G. L., Ren, F. M., and Li, J. (2014). A regional extreme low temperature event and its main atmospheric contributing factors. *Theor. Apply Climatol.* 117, 195–206. doi: 10.1007/s00704-013-0997-7

Groisman, P. Y., Knight, R. W., Karl, T. R., and Karl, T. R. (2001). Heavy precipitation and high streamflow in the contiguous United States: trends in the twentieth century. *Bull. Amer. Meteorol. Soc.* 82, 219–246. doi: 10.1175/1520-0477(2001)082<0219:HPAHSI>2.3.CO;2

Huang, W. J., and Cai, W. J. (2017). Eutrophication-induced acidification of coastal waters in the northern Gulf of Mexico: insights into origin and processes from a coupled physical-biogeochemical model. *Geohys. Res Lett.* 12:L19801. doi: 10.1002/2016GL071881

Jia, X. J., and Lin, H. (2011). Influence of forced large-scale atmo-spheric patterns on surface air temperature in China. *Mon. Wea. Rev.* 139, 830–852. doi: 10.1175/2010MWR3348.1

Jiang, X., Li, Y., Yang, S., Ke, Z., Li, J., and Hu, H. (2013). Dominant modes of wintertime upper-tropospheric temperature variations over Asia and links to surface climate. *J. Clim.* 26, 9043–9060. doi: 10.1175/JCLI-D-12-00774.1

Jiang, X. W., Zhang, T. T., Tam, C. Y., Chen, J., Lau, N. C., Yang, S., et al. (2019). Impacts of ENSO and IOD on snow depth over the Tibetan Plateau: roles of convections over the western North Pacific and Indian Ocean. *J. Geophys Res. Atmos*. 124, 11961–11975. doi: 10.1029/2019JD031384

Kalney, E., Kanamitsu, M., Kistler, R., Collins, W., Deaven, D., Gandin, L., et al. (1996). The NCEP/NCAR 40-year reanalysis project. *Bull. Am. Meteorol. Soc.* 74, 789–799. doi: 10.1175/1520-0477(1996)077<0437:TNYRP>2.0.CO;2

Khairoutdinov, M. F., and Randall, D. A. (2001). A cloud resolving model as a cloud parameterization in the NCAR Community Climate System Model: preliminary results. *Geophys. Res. Lett,* 28, 3617–3620. doi: 10.1029/2001GL013552

Kripalani, R. H., and Kulkarni, A. (1999). Climatology and variability of historical Soviet snow depth data: Some new perspectives in snow-Indian monsoon teleconnections. *Clim. Dyn*. 15, 475–489. doi: 10.1007/s003820050294

Lettenmaier, D., and Gan, T. (1990). Hydrologic sensitivities of the Sacramento–San Joaquin River basin, California, to global warming. *Water Resour. Res.* 26, 69–86. doi: 10.1029/WR026i001p00069

Li, J. P. (2016). "Impacts of annular modes on extreme climate events over the East Asian monsoon region," in *Dynamics and Predictability of Large-scale High-Impact Weather and Climate Events* (Beijing: Cambridge University Press), 343–353. doi: 10.1017/CBO9781107775541.028

Li, J. P., Zheng, F., Sun, C., Feng, J., and Wang, J. (2019). Pathways of influence of the Northern Hemisphere mid-high latitudes on East Asian climate: a review. *Adv. Atmos. Sci.* 36, 902–921. doi: 10.1007/s00376-019-8236-5

Meehl, G. A. (1997). The south Asian monsoon and the tropospheric biennial oscillation. *J. Clim.* 10, 1921–1943. doi: 10.1175/1520-0442(1997)010<1921:TSAMAT>2.0.CO;2

Saji, N. H., Goswami, B. N., Vinayachandran, P. N., and Yamagata, T. (1999). A dipole mode in the tropical Indian Ocean. *Nature* 401, 360–363. doi: 10.1038/43854

Sardeshmukh, P., and Hoskins, B. (1988). The generation of global rotational flow by steady idealized tropical divergence. *J. Atmos. Sci.* 45, 1228–1251. doi: 10.1175/1520-0469(1988)045<1228:TGOGRF>2.0.CO;2

Schieman, R. D., Luethi, P. L., and Schaer, C. (2009). Seasonality and interannual variability of the westerly jet in the Tibetan Plateau region. *J. Clim.* 22, 2940–2957. doi: 10.1175/2008JCLI2625.1

Shaman, J., and Tziperman, E. (2005). The effect of ENSO on Tibetan Plateau snow depth: a stationary wave teleconnection mechanism and implications for the South Asian monsoons. *J. Clim.* 18, 2067–2078. doi: 10.1175/JCLI3391.1

Simmons, A. J., and Burridge, D. M. (1981). An energy and angular-momentum conserving vertical finite-difference scheme and hybrid vertical coordinates. *Mon. Wea. Rev*. 109, 758–766. doi: 10.1175/1520-0493(1981)109<0758:AEAAMC>2.0.CO;2

Sun, J. H., and Wang, W. Y. (2010). Spatial-temporal features of intense snowfall events in China and their possible change. *J. Geophys. Res.* 115, 136–149. doi: 10.1029/2009JD013541

Takaya, K., and Nakamura, H. (2001). A formulation of a phase-independent wave-activity flux for stationary and migratory quasi geostrophic eddies on a zonally varying basic flow. *J. Atmos. Sci.* 58, 608–627. doi: 10.1175/1520-0469(2001)058<0608:AFOAPI>2.0.CO;2

Wallace, J. M., and Gutzler, D. S. (1981). Teleconnections in the geopotential height field during the Northern Hemisphere winter. *Mon. Wea. Rev*. 109, 784–812. doi: 10.1175/1520-0493(1981)109<0784:TITGHF>2.0.CO;2

Wang, B., Wu, R. G., and Fu, X. H. (2000). Pacific-East Asian teleconnection: how does ENSO affect Asian climate? *J. Clim.* 13, 1517–1536. doi: 10.1175/1520-0442(2000)013<1517:PEATHD>2.0.CO;2

Wang, L., and Chen, W. (2010). How well do existing indices mea-sure the strength of the East Asian winter monsoon? *Adv. Atmos. Sci.* 27, 855–870. doi: 10.1007/s00376-009-9094-3

Wang, L., and Chen, W. (2014). The East Asian winter monsoon: reamplification in the mid-2000s. *Chin. Sci. Bull*. 59, 430–436. doi: 10.1007/s11434-013-0029-0

Wang, L., and Feng, J. (2011). Two major modes of the wintertime precipitation over China. *Chin. J. Atmos. Sci*. 35, 1105–1116. (in Chinese). doi: 10.3878/j.issn.1006-9895.2011.06.10

Wang, Y., and Xu, X. (2018). Impact of ENSO on the thermal condition over the Tibetan Plateau. *J. Meteorol. Soc. Jpn*. 96, 269–281. doi: 10.2151/jmsj.2018-032

Webster, P. J. (1998). Monsoons: processes, predictability, and the prospects for prediction. *J. Geophys. Res.* 103, 14451–14510. doi: 10.1029/97JC02719

Wu, Z., Li, J., Jiang, Z., and Ma, T. (2012). Modulation of the Tibetan Plateau snow cover on the ENSO teleconnections: from the East Asian summer monsoon perspective. *J. Clim.* 25, 2481–2489. doi: 10.1175/JCLI-D-11-00135.1

Wu, Z. W., Li, J. P., Jiang, Z. H., and He, J. (2011). Predictable climate dynamics of abnormal East Asian winter monsoon: once-in-a-century snowstorms in 2007/2008 winter. *Clim. Dyn.* 37, 1661–1669. doi: 10.1007/s00382-010-0938-4

Xu, H., Li, J., Feng, J., and Mao, J. (2012). The asymmetric relationship between the winter NAO and the precipitation in Southwest China. *Acta Meteorol. Sin.* 70, 1276–1291. doi: 10.11676/qxxb2012.107 (in Chinese).

Yamagata, T., Behera, S. K., Luo, J. J., Masson, S., Jury, M. R., and Rao, S. A. (2004). Coupled Ocean-Atmosphere variability in the tropical Indian Ocean. *Geophy. Monogr*. 147, 189–211. doi: 10.1029/147GM12

Yang, S. (1996). ENSO–snow–monsoon associations and seasonal interannual predictions. *Clim. Dyn*. 16, 125–134. doi: 10.1002/(SICI)1097-0088(199602)16:2<125::AID-JOC999>3.0.CO;2-V

Yuan, C. X., Tozuka, T., Luo, J. J., and Yamagat, T. (2014). Predictability of the subtropical dipole modes in a coupled ocean-atmosphere model. *Climate Dyn*. 42, 1291–1308. doi: 10.1007/s00382-013-1704-1

Yuan, C. X., Tozuka. T., Miyasaka, T., and Yamagata, T. (2009). Respective influences of IOD and ENSO on the Tibetan snow cover in early winter. *Climate Dyn*. 33, 509–520. doi: 10.1007/s00382-008-0495-2

Zhang, Y., Zhou, W., Chow, E. C., and Leung, M. Y. T. (2019). Delayed impacts of the IOD: cross-seasonal relationships between the IOD, Tibetan Plateau snow, and summer precipitation over the Yangtze-Huaihe River region. *Clim. Dyn.* 53, 4077–4093. doi: 10.1007/s00382-019-04774-5

Zhou, B., Gu, L., Ding, Y., Shao, L., Wu, Z., Yang, X., et al. (2011). The great 2008 Chinese ice storm: its socioeconomic–ecological impact and sustainability lessons learned. *Bull. Amer. Meteorol. Soc.* 92, 47–60. doi: 10.1175/2010BAMS2857.1

Zhou, B., Wang, Z., and Shi, Y. (2017). Possible role of hadley circulation strengthening in interdecadal intensification of snowfalls over northeastern China under climate change. *J. Geophys. Res.* 122:265–283. doi: 10.1002/2017JD027574

Zhou, L., and Wu, R. (2010). Respective impacts of the East Asian winter monsoon and ENSO on winter rainfall in China. *J. Geophys. Res.* 115:D02107. doi: 10.1029/2009JD012502

Zhou, W., Chan, J. C. L., Chen, W., Ling, J., Pinto, J. G., and Shao, Y. (2009). Synoptic-scale controls of persistent low temperature and icy weather over Southern China in January 2008. *Mon. Wea. Rev*. 137, 3978–3991. doi: 10.1175/2009MWR2952.1

Conflict of Interest: The authors declare that the research was conducted in the absence of any commercial or financial relationships that could be construed as a potential conflict of interest.

Publisher's Note: All claims expressed in this article are solely those of the authors and do not necessarily represent those of their affiliated organizations, or those of the publisher, the editors and the reviewers. Any product that may be evaluated in this article, or claim that may be made by its manufacturer, is not guaranteed or endorsed by the publisher.

frontiers in Climate

PERSPECTIVE
published: 15 November 2021
doi: 10.3389/fclim.2021.716507

Unprecedented Climate Change in India and a Three-Pronged Method for Reliable Weather and Climate Prediction

Vadlamudi Brahmananda Rao[1,2]*, *Karumuri Ashok*[3] and *Dandu Govardhan*[3]

[1] National Institute for Space Research, São José dos Campos, Brazil, [2] Department of Meteorology and Oceanography, Andhra University, Visakhapatnam, India, [3] Centre for Earth, Ocean and Atmospheric Sciences, University of Hyderabad, Hyderabad, India

India, one of the most disaster-prone countries in the world, has suffered severe economic losses as well as life losses as per the World Focus report.[1] More than 80% of its land and more than 50 million of its people are affected by weather disasters. Disaster mitigation necessitates reliable future predictions, which need focused climate change research. From the climate change perspective, the summer monsoon, the main lifeline of India, is predicted to change very adversely. The duration of the rainy season is going to shrink, and pre-monsoon drying can also occur. These future changes can impact the increase of vector-borne diseases, such as malaria, dengue, and others. In another recent study, 29 world experts from various institutions found that the largest exposure to disasters, such as tropical cyclones (TCs), river floods, droughts, and heat waves, is over India. For improved and skillful prediction, we suggest a three-stage cumulative method, namely, K is for observational analysis, U is for knowledge and understanding, and M is for modeling and prediction. In this brief note, we report our perspective of imminent weather disasters to India, namely, monsoons and TCs, and how the weather and climate forecasting can be improved, leading to better climate change adaptation.

Keywords: KUM method, extreme weather, human suffering, tropical cyclone, monsoon, Indian summer monsoon (ISM)

OPEN ACCESS

Edited by:
Bai-Lian Li,
University of California, Riverside, United States

Reviewed by:
Ladislaus Benedict Chang'A, Tanzania Meteorological Agency, Tanzania
Zablon W. Shilenje, Charles University, Czechia

***Correspondence:**
Vadlamudi Brahmananda Rao
raovadlamud@gmail.com
orcid.org/0000-0001-5905-9806

Specialty section:
This article was submitted to Climate Services, a section of the journal Frontiers in Climate

Received: *28 May 2021*
Accepted: *04 October 2021*
Published: *15 November 2021*

Citation:
Brahmananda Rao V, Ashok K and Govardhan D (2021) Unprecedented Climate Change in India and a Three-Pronged Method for Reliable Weather and Climate Prediction. Front. Clim. 3:716507. doi: 10.3389/fclim.2021.716507

INTRODUCTION

The Indian economy still significantly depends on agriculture, which, in turn, depends on the summer monsoon rains occurring from June to September. In the present scenario of climate change, it is essential to know how the Indian summer monsoon rainfall is going to change in the future. In a recent detailed study with regional climate model projections, Ashfaq et al. (2020) suggest that an important adverse signal of future climate change over the Indian monsoon region in the RCP8.5 scenario (Krishnan et al., 2020; Jyoteeshkumar Reddy et al., 2021) can occur. The sinking of the Indian monsoon rainy season onset is projected to delay by five to eight pentads and a shrinking of the monsoon rainy season. India can experience pre-monsoon drying as well.

[1] World focus-special issue July 2014, editorial (peer-reviewed, refereed research journal).

In a recent innovative study, 29 world experts (Lange et al., 2020) from different institutions and different countries, reached some important conclusions. These inferences deserve urgent attention and action plans by policymakers. They considered six categories of extreme climate impact events, namely, river floods, cyclones, crop failures, wildfires, heat waves, and droughts. These authors (Lange et al., 2020) quantified the pure effect of climate change on the exposure of the global population to the events mentioned. One important conclusion, which is of grave concern to India, is that the largest increase in exposure is projected here. Thus, to avoid huge damages due to these disasters, such as deaths and loss of property, urgent and more reliable predictions are needed. We, however, must clarify that there has been tremendous improvement in numerical prediction of tropical cyclones (TCs) in the last few decades in India [e.g., Pattanaik and Mohapatra, 2021; Saranya Ganesh et al., 2021; Sarkar et al., 2021, and all other papers in January 2021 of Mausam, a special issue on the state of the art on TC prediction in the North Indian Ocean (NIO)], but what we claim is that applying theory can enhance the skills from the current day model outputs substantially more as discussed in the following section. To provide an analogy, in a recent study, Rao et al. (2021) attempted to connect observations, theory, and a prediction plan for heat waves. This prediction method can be applied to a numerical weather prediction model to predict deadly heat waves; thus, Rao et al. (2021) used a K, U, and M approach for the prediction of deadly heat waves over India.

From the context of the three-pronged K, U, and M method (hereafter, KUM), there are sufficient observational studies, or K, and also some attempts have been made using highly sophisticated, state-of-the-art (atmosphere and ocean) coupled models for predictions, M. What is most lacking, however, are theoretical studies (U) aiming to find out the causes for disastrous TCs or the highly complex regional monsoons.

According to a recent 2021 overview of current research results by the Geophysical Fluid Dynamics Laboratory of Global Warming and Hurricanes[2], the severity and frequency of TCs are increasing globally. A recent study (Balaguru et al., 2015) also suggests an increase of TCs globally even over the NIO. Essentially, the increase in the strong TCs has far-reaching implications for society because these include the most harmful aspects, namely, storm surges and heavy rains with intense wind speeds. Indeed, TC rainfall rates will possibly increase in the future due to various anthropogenic effects and accompanying increases in atmospheric moisture. Rapid intensification of TCs poses forecast challenges and increased risks for coastal communities (Emanuel, 2017). Recent modeling studies (Emanuel, 2020) show an increase of 10–15% for precipitation rates averaged within about 100 km of the cyclone for a 2°C global warming scenario. As per IPCC AR5, higher levels of coastal flooding due to TCs are expected to occur, all else assumed to be constant due to rising sea levels. In this situation, together with the rise in sea level, the impact due to the strong TCs deteriorates the conditions of the increasing coastal population across India and the neighborhood. As the NIO is one of the typical regions with a population of 1.353 billion (2018), about 18% of the global population by 2020, it is highly susceptible to strong TCs causing adverse living conditions, and the implication is that stronger TCs will be worse.

According to reports from a respected BBC newspaper[3,4], and a potential report[5] from the Indian Meteorological Department, Amphan is a very severe cyclone that transited the west coast of India in 2020 and also caused a lot of damage. The super cyclonic storm Amphan is the costliest case in the recorded history of TCs with damage of US$15.78 billion and also total fatalities of 269. Similarly, in the year 2019, a loss of US$11 billion occurred due to TCs. In the year 2020, there was a record-breaking occurrence of eight TCs over the NIO: five cyclones and three major cyclones compared to the climatology of 4.9, 1.5, and 0.7. We note a drastic increase in category 3 and beyond hurricanes occurring in the NIO and also a significant increase in the Northern and Southern hemispheres (**Figure 1**). Also, there is a substantial increase in accumulated cyclone energy (ACE) in the last two decades in the NIO and Northern and Southern hemispheres (**Figure 2**). In 2019, record-breaking ACE of 85×10^4 knots^2, occurred in the NIO, nearly twice the previous record (Singh et al., 2021; Wang et al., 2021, BAMS). The decrease in the projected number of TCs found in some studies (Sugi et al., 2017) is overcompensated by the huge increase in intensity similar to that found over the NIO in 2019 and 2020. Furthermore, as if to worsen the situation in a colloquial sense, Wang and Murakami (2020) show that the general atmospheric and ocean parameters, which show a high global correlation with the number of TCs, nevertheless show only a very low correlation with TCs of the NIO. Thus, urgent research should be carried out to understand the causes of the occurrence of TCs over the NIO. Even globally, in the last 39 years (1980–2018), weather disasters caused about 23,000 fatalities and US$100 billion in damages worldwide. Each year, weather events displace huge populations, drive people into poverty, and dampen economic growth globally (Kousky, 2014; Munich, 2020; Hoegh-Guldberg et al., in press). The underlying causes show a marked signal of anthropogenic roots and global warming (e.g., Sobel et al., 2016; Im et al., 2017).

Henceforth, we focus on the TCs as well as summer monsoons, which are the two most relevant weather and climate phenomena for the Indian region.

A THREE-STAGE METHOD TO STUDY AND PLAN RELIABLE PREDICTION

Because India is rigorously prone to natural disasters as well as impacts due to anticipated changes in the summer monsoon in the future, there is indeed a serious question as to how to study the causal mechanisms of these disasters and plan to mitigate them. In this context, the late Gill (1985), an accomplished geosciences expert, suggested almost 35 years ago the KUM method, namely, knowledge, understanding, and modeling, a three-pronged approach. The first step (K) is to improve

[2]https://www.gfdl.noaa.gov/global-warming-and-hurricanes/

[3]https://www.bbc.com/news/world-asia-india-52749935

[4]https://en.wikipedia.org/wiki/2020_North_Indian_Ocean_cyclone_season

[5]https://mausam.imd.gov.in/Forecast/marquee_data/indian111.pdf

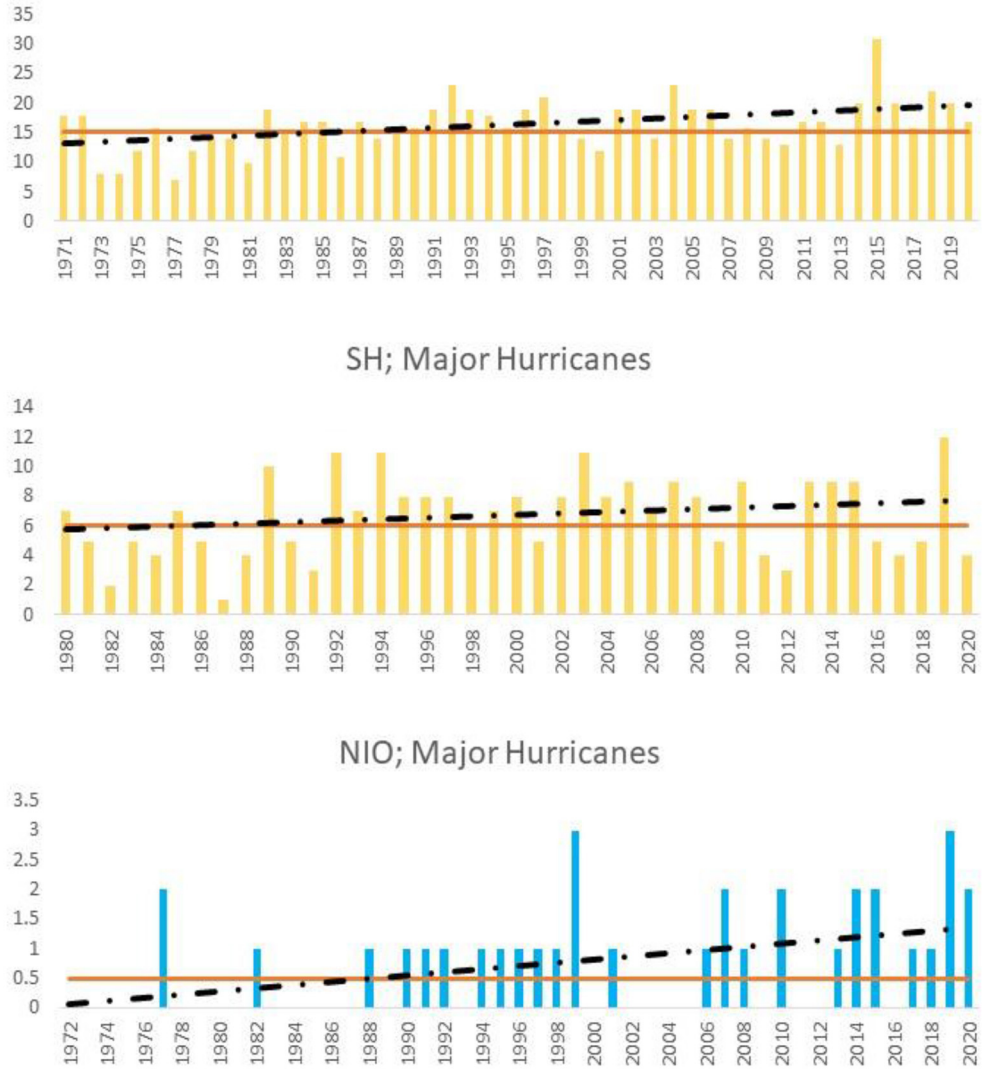

FIGURE 1 | The number of category 3+ hurricanes that occurred in the Northern and Southern hemispheres and the NIO (black dotted line indicates a linear trend, and orange line indicates significance at the 95% confidence level) (http://tropical.atmos.colostate.edu/Realtime/index.php?archandloc=northindian).

observational knowledge of calamity-causing weather events and next a theoretical understanding to find out the cause of a specific effect, probably utilizing linear analytical mathematical solutions (U). Finally, the third one (M), using the presently available highly complex coupled (atmosphere and ocean) models giving numerical solutions to non-linear equations, pioneered by Phillips (1956), predicting future occurrences. The order of KUM seems to be important. Although relatively substantial observational results are available in the Indian context for meteorological and oceanographic events, very few theoretical studies have been made delineating the causal mechanisms. Thus, this aspect should be given priority. In a recent comment, Emanuel (2020) also stressed the need for theoretical studies. Finally, only after acquiring the observational, knowledge, and cause-and-effect relationships in theoretical studies, *only then*, should one embark on numerical or climate modeling to successfully predict the future.

In this context, it is illuminating to recall the comments of Phillips (1970), one of the founding fathers of theoretical meteorology and numerical weather prediction: "in making a numerical forecast, one takes a set of numbers...regardless of...synoptic structures...by another set of numbers, representing the forecast. The computation of a set of numbers depicting the formation of a front, is of course, not a theory of fronts (unless one is content to point to the equation of motion as theory!!!!!)" Thus, one should be very careful using numerical models to develop a theory of TCs, and in the Indian context, *monsoon depressions* (MDs) are crucial for monsoon

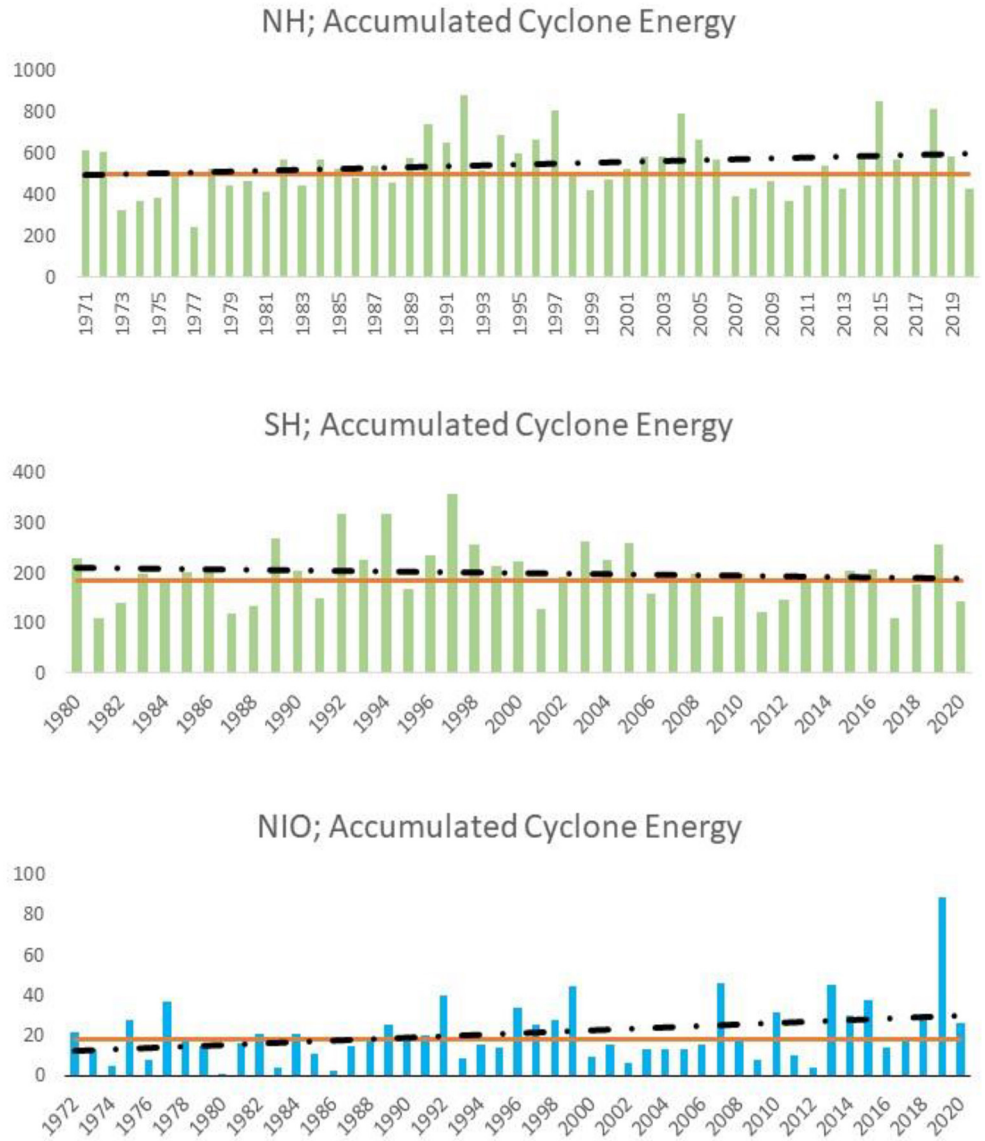

FIGURE 2 | ACE (in 10^4 Knots^2) in the Northern and Southern hemispheres and the NIO (black dotted line indicates a linear trend, and orange line indicates significance at 95% confidence level) (http://tropical.atmos.colostate.edu/Realtime/index.php?archandloc=northindian).

rainfall. Today, many students and scientists worldwide spend most of their valuable time dealing with huge data sets and running numerical models to simulate rather than to develop a theory. Tellingly, Emanuel (2020), mentions that presently there is "computing too much and thinking too little." Indeed, there is an urgent need for curiosity-driven theoretical research even in the Indian context. One interesting example to stress the importance of theory is, today, that the best numerical weather prediction is in mid and high latitudes in winter. This is because the basic theory behind the mechanism of winter weather changes, the baroclinic instability, was discovered more than 70 years ago by Charney (1947), and models and observations evolved accordingly. Thus, it is important to realize, without the correct understanding of the causal mechanisms through theory, one will never be able to predict correctly and completely the required weather or climate or its changes with just the brute force of computers available today!!!

TCS OVER THE NIO

Regarding the theory of the generation mechanisms of TCs, there are two well-known hypotheses, namely, (a) the conditional instability of the second kind (CISK) and (b) wind-induced surface heat exchange (WISHE) (please refer to Tomassini, 2020 for a comprehensive discussion of these two processes). A detailed discussion of these two is beyond the scope of the

present short article. However, the authors quickly discuss these two mechanisms in the context of TCs over NIO.

In the case of TCs, the pre-synoptic disturbances get their energy by the complex interaction of two different horizontal scales, namely, cumulus convection of about 1 km and synoptic systems of about 500 km. How this interaction happens is a topic of debate, though, and most of the research in the published literature is about TCs in tropical ocean basins other than the NIO region.

Briefly, we discuss the basic characteristics of CISK and quasi-equilibrium (or WISHE). In the process of CISK, the buoyant convection can occur only when *low-level stability* is weakened (see **Figure 2**; Ooyama, 1969), and in the other, moist convection is governed by the *vertically integrated measure* of instability. As noted by Tomassini (2020), meteorological conditions vary greatly from one region to the other in the tropics and also in the same region from one season to another (see Ashok et al., 2000; Rao et al., 2000; Raymond et al., 2015). Raymond mentions two tropical places, Sahel and the Western Pacific, where conditions are very different. Now, how do the conditions vary, during (i) pre-monsoon, (ii) MDs, and (iii) post-monsoon TCs? Similar to Bony et al. (2017), we suggest that more detailed observations of both satellite measurements and data developed in field programs should be used to understand the convection and circulation coupling of TCs over NIO. For example, the INCOMPASS IOP field program, which collects data from strategically installed ground-based instruments in India, is one such program (Fletcher et al., 2018).

Another, synoptic disturbance of importance is a MD. Despite several observational and theoretical studies by many authors (for example, Sikka, 1977; Mishra and Salvekar, 1979; Aravequia et al., 1995; Boos et al., 2017) trying to understand the basic mechanism of origin, some fundamental questions remain unanswered. Similar to TCs, the lack of understanding of how convection and MD circulation couple hinders the prediction. For both TCs and MDs, we suggest analyzing time vertical sections of potential temperature, equivalent potential temperature, and saturated equivalent potential temperature such that one can get an idea of the relative importance of CISK or the quasi-equilibrium hypothesis discussed briefly above.

Another method for elucidating the study is to examine the system's energetics, i.e., TCs or MDs. Lorenz (1960) mentions, "one enlightening method of studying the behaviour of the atmosphere, or a portion of it, consists of examining the behaviour of the energy involved." Earlier Mishra and Rao (2001) used limited area energetics to infer the mechanism of generation of Northeast Brazil's upper tropospheric vortices. Also, Rao and Rajamani (1972) examined the energetics of MDs. These methods of energy analysis, for example, can be used to isolate or single out the basic mechanism of generation of TCs or MDs, using more recent well-covered data, such as the INCOMPASS IOP program (Turner et al., 2019). Later, targeted numerical model studies should be used to not only verify the process/processes identified in energetic and diagnostic studies, but to design dynamics-based indices related to TC formation that are relatively easier to predict. For example, a CISK parameter may be easier to predict with a longer lead as compared with the TC rainfall. These methods are again akin to the KUM approach. Such carefully verified and designed indices, when operationalized, will substantially help in extending the lead prediction time. Probabilistic dynamical-statistical downscaling tools can also be developed to relate local rainfall with these indices. This will also potentially enhance the lead time of the TC-related deluge. Similarly, a better understanding of model ability in capturing the conversions between different forms of energy.

MONSOONS

Again, several aspects of monsoons, particularly, the Indian Monsoon are still not completely clear and hinder the mechanisms of prediction. In a recent exhaustive study, Geen et al. (2020), discussed several aspects, primarily from a theoretical standpoint even though this study was developed based on the concept of a global monsoon, Figure 2 of Geen et al. (2020) shows only a very low correlation in interannual variations of rainfall, the main meteorological element that must be predicted. However, the different regions of monsoons with different geographical boundaries raise serious objections about the global monsoon concept.

Several studies exist in the literature regarding the observed aspects of the Indian summer monsoon (the K part of the three-pronged method), and modern numerical models are employed to improve prediction skills (Sahai et al., 2016; Rao et al., 2019; Mohanty et al., 2020). From an almost zero skill, we have reached a stage at which the skills for predicting the area-averaged Indian summer monsoon are found to be statistically significant. This is great progress. Having said that, there is a great scope for further improvement. Although the broad regionally averaged skills are statistically significant, they are modest. Further, improving the skills such that they are locally useful is the obvious goal but still a long way ahead. Although the prediction skill improved through better methods of, for example, data assimilation and parametrization schemes, to improve the predictions further, we need to diagnose the improved representation (e.g., Halder et al., 2016; Saha et al., 2019; Hazra et al., 2020), better replication of physical processes and scale interactions.

Notwithstanding all these technical improvements, the large-scale physical causal mechanisms are not clear yet. This can only be done with the studies aiming to understand the cause-and-effect relation or the U in the three-pronged method. As mentioned earlier, with more observational studies aiming to identify the correct interaction mechanism over NIO between convection and large-scale monsoon circulation (either CISK or WHISE), then this mechanism can be included in the numerical models. Also, controlled experiments using simple models, such as the one by Rao et al. (2000), can be used to identify relative roles of mountains and thermal contrast in generating the Indian summer monsoon. In the state-of-the-art coupled models, because of extremely complex non-linear interactions among various physical mechanisms, it is almost impossible to isolate the cause of a specific effect.

Again, the diagnostic study based on energetics, such as the generation of available potential energy (PE) by latent heat and the baroclinic conversions, for example, may reveal relative roles of some physical processes, such as convection in the Indian monsoon. In a recent companion study (Rao et al., under review), comparing the South American and Indian monsoons, we found that, in the Indian monsoon, the baroclinic conversions P (mean available PE) to P' (eddy PE) to kinetic energy (KE) is non-existent, and the KE of monsoon is mainly furnished by the generation of perturbation PE by latent heating (rainfall) and subsequent conversion to KE. In contrast, over the South American monsoon, both the baroclinic conversions and generation terms are equally important. This is probably because the Himalayas extend from East to West across the cardinal northern border of the country, which does not allow mid-latitude baroclinic waves to penetrate at lower levels while the Andes mountains in South America extend along North to South, permit these waves to penetrate even as low latitude as Manaus, where even austral summer cold waves (FRAIAGENS) are noted. Furthermore, studies are necessary to verify how energetics vary between wet and dry monsoons in these two regions.

In a review article by Geen et al. (2020), the authors discuss attempts to understand fundamental dynamics (U in our three-pronged method). Geen et al. (2020) mention a very similar KUM approach for monsoons (their section 3). Such efforts are urgently needed from the context of the Indian monsoon. They even discuss the south Asian monsoon (their section 3.1.2). Although they tried to reconcile between global and regional monsoon features, the differences are more striking as we mentioned earlier, regarding the Indian and South American monsoons. In the case of the East Asian monsoon, at least one author (Molnar et al., 2010) mentions, "'monsoon' is somewhat of a misnomer."

Although there are some uncertainties in the methods used by Lange et al. (2020), the importance of their conclusion is unambiguous. They mention that "anthropogenic" climate change has already substantially increased the exposure to extreme global climatic impacts, and anthropogenic warming is projected to exacerbate the pattern of climate change that we are already noticing nowadays. Thus, it is urgent to restrain the increase in global average temperature well below 2°C, which would significantly reduce the risks and impacts of climate change[6] (Benitez, 2009; Dash et al., 2013). All this, therefore, underscores the urgency for climate action expressed in the Paris agreement of 2015. Even in a climate change context, using the KUM approach will help in a better diagnosis of the changes in regional implications for large-scale instabilities to diabatic processes. These can help in design model-based indices that can inform the stakeholders working on climate change mitigation and adaptation.

[6]https://unfccc.int/process-and-meetings/the-paris-agreement/the-paris-agreement

RECOMMENDATIONS

We are in an era in which observational data availability in the tropics has improved significantly and is going to be further improved. In this context, it is recommended that the forecasters and researchers of Indian weather and climate use this excellent opportunity to build theoretical knowledge unique to the regional weather and climate. The knowledge gained should be translated to identify tangible, large-scale dynamical process indices. Such indices will be very useful to extend the lead prediction skills of important weather and climate phenomenon, such as TCs, MDs, etc. Similarly, (i) evaluating the model capacity in predicting and calibration of association between hindcast perturbation PE, latent heating, and subsequent conversion to KE, and (ii) comparing the observations will potentially provide us with indices that can be directly used to predict subseasonal monsoonal rainfall with longer leads. The above recommendations are just examples. In summary, identifying the key dynamics behind important weather and climate processes at discernible time scales and designing useful dynamical indices that can be used to extend the lead forecast envelope will be the way forward.

DATA AVAILABILITY STATEMENT

The datasets presented in this study can be found in online repositories. The names of the repository/repositories and accession number(s) can be found below: http://tropical.atmos.colostate.edu.

AUTHOR CONTRIBUTIONS

VB conceived the idea. VB wrote the manuscript with inputs from KA and using the results from DG analysis. KA comprehensively revised the article. All authors contributed to the article and approved the submitted version.

FUNDING

The publication charge of this article is fully funded by the Frontiers in Climate Journal.

ACKNOWLEDGMENTS

The authors thank Prof. Matthew Collins, Specialty Chief Editor, Frontiers in Climate Journal, and reviewers for their helpful feedback and recommendations in improving the manuscript quality. The authors are grateful to the Frontiers in Climate Journal Committee for waiving the article's publishing fees. We thank the reviewers for their critical comments, which helped to improve the quality of the article.

REFERENCES

Aravequia, J. A., Brahmananda Rao, V., and Bonatti, J. P. (1995). The role of moist baroclinic instability in the growth and structure of monsoon depressions. *J. Atmos. Sci.* 52, 4393–4409. doi: 10.1175/1520-0469(1995)052<4393:TROMBI>2.0.CO;2

Ashfaq, M., Cavazos, T., Reboita, M. S., Torres-Alavez, J. A., Im, E.-S., Olusegun, F. M., et al. (2020). Robust late twenty-first century shift in the regional

monsoons in RegCM-CORDEX simulations. *Clim. Dyn*. 57, 1463–1488. doi: 10.1007/s00382-020-05306-2

Ashok, K., Soman, M., and Satyan, V. (2000). Simulation of monsoon disturbances in a GCM. *Pure Appl. Geophys*. 157, 1509–1539. doi: 10.1007/PL00001131

Balaguru, K., Foltz, G. R., Leung, L. R., D'Asaro,E., Emanuel, K. A., Liu, H., et al. (2015). Dynamic potential intensity: an improved representation of the ocean's impact on tropical cyclones. *Geophys. Res. Lett*. 42, 6739–6746. doi: 10.1002/2015GL064822

Benitez, M. A. (2009). Climate change could affect mosquito - borne diseases in Asia. *Lancet*. 373, 1070. doi: 10.1016/S0140-6736(09)60634-6

Bony, S., Stevens, B., Ament, F., Bigorre, S., Chazette, P., Crewell, S., et al. (2017). EUREC4A: a field campaign to elucidate the couplings between clouds convection and circulation. *Surv. Geophys.* 38, 1529–1568. doi: 10.1007/s10712-017-9428-0

Boos, W. R., Mapes, B. E., and Murthy, V. S. (2017). Potential vorticity structure and propagation mechanism of Indian monsoon depressions. *Glob Monsoon Syst Res Forecast* 2017, 187–199. doi: 10.1142/9789813200913_0015

Charney, J. G. (1947). The dynamics of long waves in a baroclinic westerly current. *J. Meteor*. 4, 135–162. doi: 10.1175/1520-0469(1947)004<0136:TDOLWI>2.0.CO

Dash, A. P., Bhatia, R., Suyoto, T., and Mourya, D. T. (2013). Emerging and re-emerging arbovorial diseases in South-east Asia. *J. Vector. Borne Dis.* 50,77–84.

Emanuel, K. (2017). Assessing the present and future probability of Hurricane Harvey's rainfall. *Proc. Natl. Acad. Sci. U.S.A*. 114, 12681–12684. doi: 10.1073/pnas.1716222114

Emanuel, K. (2020). The relevance of theory for contemporary research in atmospheres, oceans, and climate. *AGU Adv*. 1, e2019AV000129. doi: 10.1029/2019AV000129

Fletcher, J. K., Parker, D. J., Turner, A. G., Menon, A., and Martin, G. M., et al. (2018). The dynamic and thermodynamic structure of the monsoon over southern India: new observations from the INCOMPASS IOP. *Q. J. R. Meteorol. Soc*. 146, 2876–2890. doi: 10.1002/qj.3439

Geen, R., Bordoni, S., Battisti, D. S., and Hui, K. (2020). Monsoons, ITCZs, and the concept of the global monsoon. *Rev. Geophys.* 58, e2020RG000700. doi: 10.1029/2020RG000700

Gill, A. E. (1985). "An overview of the dynamics of the tropical oceans and global atmosphere," in *International Conference on TOGA*. WCRP. NO 4 WMO/TD-5 (Paris).

Halder, S., Saha, S. K., Dirmeyer, P. A., Chase, T. N., and Goswami, B. N. (2016). Investigating the impact of land-use land-cover change on Indian summer monsoon daily rainfall and temperature during 1951–2005 using a regional climate model. *Hydrol. Earth Syst. Sci*. 20, 1765–1784. doi: 10.5194/hess-20-1765-2016

Hazra, A., Chaudhari, H. S., Saha, S. K., Pokhrel, S., Dutta, U., Goswami, B. N., et al. (2020). Role of cloud microphysics in improved simulation of the Asian monsoon quasi-biweekly mode (QBM). *Clim. Dyn. (2020)* 54, 599–614. doi: 10.1007/s00382-019-05015-5

Hoegh-Guldberg, O., Jacob, D., Taylor, M., Bindi, M., Brown, S., Camilloni, I., et al. (in press). "Impacts of 1.5°C Global Warming on Natural and Human Systems," in *Global Warming of 1.5°C. An IPCC Special Report on the Impacts of Global Warming of 1.5°C Above Pre-industrial Levels and Related Global Greenhouse Gas Emission Pathways, in the Context of Strengthening the Global Response to the Threat of Climate Change, Sustainable Development, and Efforts to Eradicate Poverty*, eds V. Masson-Delmotte, P. Zhai, H.-O. Pörtner, D. Roberts, J. Skea, P. R. Shukla, A. Pirani, W. Moufouma-Okia, C. Péan, R. Pidcock, S. Connors, J. B. R. Matthews, Y. Chen, X. Zhou, M. I. Gomis, E. Lonnoy, T. Maycock, M. Tignor, and T. Waterfield. Available online at: https://www.ipcc.ch/sr15/chapter/chapter-3/

Im, E. S., Pal, J. S., and Eltahir, E. A. B. (2017). Deadly heat waves projected in the densely populated agricultural regions of South Asia. *Sci. Adv*. 3, e1603322. doi: 10.1126/sciadv.1603322

Jyoteeshkumar Reddy, P., Sriram, D., Gunthe, S. S., and Balaji, C. (2021). Impact of climate change on intense Bay of Bengal tropical cyclones of the post-monsoon season: a pseudo global warming approach. *Clim. Dyn.* 56, 2855–2879. doi: 10.1007/s00382-020-05618-3

Kousky, C. (2014). Informing climate adaptation: a review of the economic costs of natural disasters. *Energy Econ.* 46, 576–592. doi: 10.1016/j.eneco.2013.09.029

Krishnan, R., Sanjay, J., Gnanaseelan, C., Mujumdar, M., Kulkarni, A., and Chakraborty, S. (2020). *Assessment of Climate Change Over the Indian Region: A Report of the Ministry of Earth Sciences (MoES), Government of India*. Singapore: Springer. doi: 10.1007/978-981-15-4327-2

Lange, S., Volkholz, J., Geiger, T., Zhao, F., Vega, I., and Veldkamp, T. (2020). Projecting exposure to extreme climate impact events across six event categories and three spatial scales. *Earth Fut*. 8, e2020EF001616. doi: 10.1029/2020EF001616

Lorenz, E. N. (1960). Energy and numerical weather prediction. *Tellus* 12, 364–373. doi: 10.1111/j.2153-3490.1960.tb01323.x

Mishra, S. K., and Rao,. V. B. (2001). The energetics of an upper tropospheric cyclonic vortex over north-east Brazil. *Q. J. R. Meterol. Soc.* 127, 2329–2351. doi: 10.1002/qj.49712757707

Mishra, S. K., and Salvekar, P. S. (1979). Role of baroclinic instability in the development of the monsoon disturbances. *J. Atmos. Sci*. 37, 383–394. doi: 10.1175/1520-0469(1980)037<0383:ROBIIT>2.0.CO;2

Mohanty, U. C., Mohapatra, M., Ashok, K., and Raghavan, K. (2020). Indian monsoons variability and extreme weather events: recent improvements in observations and modelling. *Proc. Ind. Natl. Sci. Acad.* 86, 503–524. doi: 10.16943/ptinsa/2020/49817

Molnar, P., Boos, W. R., and Battisti, D. S. (2010). Orographic controls on climate and paleoclimate of Asia. Thermal and mechanical roles of the Tibetan Plateau. *Annu. Rev. Earth Planet. Sci.* 38, 77–102. doi: 10.1146/annurev-earth-040809-152456

Munich, R. E. (2020). *NatCatSERVICE Analysis Tool*. Available online at: https://natcatservice.munichre.com/

Ooyama, K. (1969). Numerical simulation of the life cycle of tropical cyclones. *J. Atmos. Sci.* 26, 3–40. doi: 10.1175/1520-0469(1969)026<0003:NSOTLC>2.0.CO

Pattanaik, D. R., and Mohapatra, M. (2021). Evolution of IMD's operational extended range forecast system of tropical cyclogenesis over North Indian Ocean during 2010–2020. *Mausam* 72, 35–56. doi: 10.54302/mausam.v72i1.124

Phillips, A. (1956). The general circulatin of the atmosphere: a numerical experiment. *Q. J. R. Meterol. Soc*. 82, 123–164. doi: 10.1002/qj.49708235202

Phillips, N. A. (1970). Models for weather prediction. *Ann. Rev. Fluid Mech.* 2, 251–290.

Rao, K. V., and Rajamani, S. (1972). Study of heat sources and sinks and the generation of available potential energy in the Indian region during the southwest monsoon season. *Mon. Weath. Rev.* 100, 383–388. doi: 10.1175/1520-0493(1972)100<0383:SOHSAS>2.3.CO

Rao, S. A., Goswami, B. N., Sahai, A. K., Rajagopal, E. N., Mukhopadhyay, P., Rajeevan, M., et al. (2019). Monsoon mission: a targeted activity to improve monsoon prediction across scales. *Bull. Amer. Meteorol. Soc.* 100, 2509–2532. doi: 10.1175/BAMS-D-17-0330.1

Rao, V. B., Rao, K. K., Mahendranath, B., Lakshmi Kumar, T. V., and Govardhan, D. (2021). Large-scale connection to deadly Indian heatwaves. *Q. J. R. Meterol. Soc.* 147, 1419–1430. doi: 10.1002/qj.3985

Rao, V. B., Reyes Fernandez, J. P., and Franchito, S. H. (2000). Monsoonlike circulations in a zonally averaged numerical model with topography. *Month. Weath. Rev.* 128, 779–794. doi: 10.1175/1520-0493(2000)128<0779:MCIAZA>2.0.CO;2

Raymond, D., Fuchs, Z., Gjorgjievska, S., and Sessions, S. (2015). Balanced dynamics and convection in the tropical atmosphere. *J. Adv. Model. Earth Syst.* 7, 1093–1116. doi: 10.1002/2015MS000467

Saha, S. K., Hazra, A., Pokhrel, S., Chaudhari, H. S., Sujith, K., Rai, A., et al. (2019). Unraveling the mystery of Indian summer monsoon prediction: improved estimate of predictability limit. *J. Geophys. Res. Atmos*. 124, 1962–1974. doi: 10.1029/2018JD030082

Sahai, A. K., Chattopadhyay, R., Joseph, S., Phani, R., and Abhilash, S. (2016). Extended range prediction system and its application. *Vayu Mandal* 42, 75–96. Available online at: http://imetsociety.org/wpcontent/pdf/vayumandal/2016422/2016422_3.pdf

Saranya Ganesh, S., Abhilash, S., Joseph, S., Kaur, M., Dey, A., Mandal, R., et al. (2021). A review of the development and implementation of tropical cyclone prediction system for North Indian Ocean in a multi-model ensemble framework. *Mausam* 72, 57–76. doi: 10.54302/mausam.v72i1.126

Sarkar, A., Kumar, S., Dube, A., Prasad, S. K., Mamgain, A., Chakraborty, P., et al. (2021). Forecasting of tropical cyclone using global and reginal

ensemble prediction systems of NCMRWF: a review *Mausam* 72, 77–86. doi: 10.54302/mausam.v72i1.131

Sikka, D. R. (1977). Some aspects of the life history, structure and movement of monsoon depressions. *Pageoph* 115, 1501–1529. doi: 10.1007/BF00874421

Singh, V. K., Roxy, M. K., and Deshpande, M. (2021). Role of warm ocean conditions and the MJO in the genesis and intensification of extremely severe cyclone Fani. *Sci. Rep*. 11:3607. doi: 10.1038/s41598-021-82680-9

Sobel, A. H., Camargo, S. J., Hall, T. M., Lee, C.-Y., Tippett, M. K., and Wing, A. A. (2016). Human influence on tropical cyclone intensity. *Science* 353, 242–246. doi: 10.1126/science.aaf6574

Sugi, M., Murakami, H., and Yoshida, K. (2017). Projection of future changes in the frequency of intense tropical cyclones. *Clim. Dyn.* 49, 619–632 doi: 10.1007/s00382-016-3361-7

Tomassini, L. (2020). The interaction between moist convection and the atmospheric circulation in the tropics. *Bull. Amer. Meteorol. Soc.* 101, E1378–E1396. doi: 10.1175/BAMS-D-19-0180.1

Turner, A. G., Bhat, G. S., Martin, G. M., Parker, D. J., Taylor, C. M., Mitra, A. K., et al. (2019). Interaction of convective organization with monsoon precipitation, atmosphere, surface and sea: the 2016 INCOMPASS field campaign in India. *Q. J. R. Meteorol. Soc.* 146, 2828–2852. doi: 10.1002/qj.3633

Wang, B., Biasutti, M., Byrne, M. P., Castro, C., Chang, C., Cook, K., et al. (2021). Monsoons climate change assessment. *Bull. Am. Meteorol. Soc*. 102, E1–E19. doi: 10.1175/BAMS-D-19-0335.1

Wang, B., and Murakami, H. (2020). Dynamic genesis potential index for diagnosing present-day and future global tropical cyclone genesis. *Environ. Res. Lett*. 15, 114008. doi: 10.1088/1748-9326/abbb01

Conflict of Interest: The authors declare that the research was conducted in the absence of any commercial or financial relationships that could be construed as a potential conflict of interest.

Publisher's Note: All claims expressed in this article are solely those of the authors and do not necessarily represent those of their affiliated organizations, or those of the publisher, the editors and the reviewers. Any product that may be evaluated in this article, or claim that may be made by its manufacturer, is not guaranteed or endorsed by the publisher.

frontiers in Physics

ORIGINAL RESEARCH
published: 02 December 2021
doi: 10.3389/fphy.2021.720533

Climate Change Characteristics of Coastal Wind Energy Resources in Zhejiang Province Based on ERA-Interim Data

Nan Wang[1], Kai-Peng Zhou[2], Kuo Wang[3], Tao Feng[3], Yu-Hui Zhang[3] and Chao-Hui Song[3,4]*

[1]Hangzhou Meteorological Bureau, Hangzhou, China, [2]Jiuquan Satellite Launch Center, Kuerle, China, [3]Zhejiang Climate Center, Meteorological Bureau of Zhejiang Province, Hangzhou, China, [4]Chun'an Meteorological Bureau, Hangzhou, China

The reanalysis of sea surface wind speed is compared with the measured wind speed of five offshore wind towers in Zhejiang, China. The applicability of reanalysis data in the Zhejiang coastal sea surface and the climatic characteristics of sea surface wind power density is analyzed. Results show that the reanalysis of wind field data at the height of 10 m can well capture the wind field characteristics of the actual sea surface wind field. The sea surface wind power density effective hours increases from west to east and north to south. Then Empirical orthogonal function (EOF) is used to analyze the sea surface wind power density anomaly field, and the first mode is a consistent pattern, the second mode is a North-South dipole pattern, the third mode is an East-West dipole pattern respectively. The stability of wind energy resources grows more stable with increasing distance from the coast, and the northern sea area which is far away from the coastal sea is more stable than that of the southern sea area. The yearly linear trend of sea surface wind power density is in an East-West dipole pattern respectively. The wind energy resources are more stable farther from the coast, and the wind energy resources in the northern sea are more stable than that of the southern sea. The yearly linear trend of sea surface wind power density is the East-West dipole type, the seasonal linear trend is a significant downward trend from West to East in spring, and on the contrary in summer, a non-significant trend in autumn and winter. The monthly change index shows that the linear trend near the entrance of Hangzhou Bay in Northern Zhejiang is of weak increase or decrease, which is good for wind energy development. When the wind power density is between 0 and 150 $W{\cdot}m^{-2}$, its frequency mainly shows the distribution trend of high in the West and low in the East, but the wind power density is between 150 and 600 $W{\cdot}m^{-2}$, its distribution is the opposite.

Keywords: wind tower, empirical orthogonal function, wind power density, linear trend, zhejiang province

OPEN ACCESS

Edited by:
Gui-Quan Sun,
North University of China, China

Reviewed by:
Aixia Feng,
Kyoto University, Japan
Xiaofeng Luo,
North University of China, China

****Correspondence:***
Kuo Wang
wangkuo.climate@qq.com

Specialty section:
This article was submitted to Interdisciplinary Physics, a section of the journal Frontiers in Physics

Received: *04 June 2021*
Accepted: *05 November 2021*
Published: *02 December 2021*

Citation:
Wang N, Zhou K-P, Wang K, Feng T, Zhang Y-H and Song C-H (2021) Climate Change Characteristics of Coastal Wind Energy Resources in Zhejiang Province Based on ERA-Interim Data. Front. Phys. 9:720533. doi: 10.3389/fphy.2021.720533

INTRODUCTION

With the rapid development of human society, all kinds of fossil fuels have been overdeveloped and used, and further causing a dramatic increase in greenhouse gases [1–3]. As renewable and clean energy resources, wind and wave energy resources are of great significance for environmental protection and greenhouse effect mitigation. In recent decades, wind energy, especially offshore wind energy, has developed rapidly all over the world [4–7]. In 2015, the total installed capacity of wind energy in the world surpassed that of nuclear power, becoming the mainstream form of clean energy development [8]. China, as

a developing country with large energy consumption, actively encourages and guides the development and utilization of renewable energy [9]. In 2011, the China Meteorological Administration completed and released the detailed investigation and assessment results of national wind energy resources. Based on the annual average wind power density of 70 m high layer greater than 300 W/m^2, the technical development volume of wind energy resources within the water depth of 5–50 m is 500 million KW [10]. According to the scale and total amount of wind energy resources that can be developed in China, maturity of development technology and economy, and so on, all indicators are in line with the basic principles in the field of renewable energy development in China. It is expected that the development of near sea wind fields will be a key direction of wind power development after 2020, and the technologies of wind power complementation and energy storage will be actively developed to increase the utilization rate of wind energy [11]. A study by the Global Wind Energy Council (GWEC) shows that the global installed capacity of offshore wind reached a record of 6.1 GW in 2019, accounting for 10% of new installed capacity; 2020 is expected to be a new record year for wind energy, and China's offshore wind project development and investors will commission their offshore wind projects before 2021 in order to make good use of relevant subsidies [12]. Wind energy resource observation is an essential way for assessment [13, 14]. The conventional offshore observation is mainly point observation [15], that is, through the on-site real-time observation methods such as island meteorological stations [16], buoy station, lidars, wind measuring tower, etc., to obtain the wind speed of the nearby sea area and evaluate the local wind energy resources. In addition, satellite remote sensing [17, 18], numerical simulation [19], reanalysis data [20, 21] and other methods can also obtain the offshore wind speed.

Zhejiang Province is located on the southeast coast. The coastline is 6,696 km long, the longest of any Chinese province. The development and utilization of wind energy resources have a very broad prospect. There are relatively few studies on the trend of sea surface wind energy changes, which is closely related to the medium and long-term planning of wind energy resources development. At present, the observation and evaluation of wind energy resources in Zhejiang coastal areas are mostly scattered observation models of offshore wind towers. The observation time of wind towers is short and the distribution is uneven [22]. At the same time, typhoons and tropical cyclones attack Zhejiang every year, which makes the observation results less representative for the adjacent sea areas [23]. To better analyze the characteristics of wind energy resources in the Zhejiang area, this paper uses the reanalysis data from the European Center of Medium-Range Weather Forecast (ECMWF) to analyze the climate change characteristics of sea surface wind energy in the coastal areas of Zhejiang, and the data of five local wind towers are selected to calibrate the reanalysis data. In addition, wind energy resource development and utilization in Zhejiang coastal areas are discussed against the background of climate change.

DATA SELECTION AND CALCULATION METHOD

According to the suggestion of relevant literature [24], the data used in this paper mainly include: 1) the real-time observation data of Zhejiang coastal wind towers, with a time resolution of 10min, and the observation data and location information are shown in **Table 1** and **Figure 1**; 2) The reanalysis data of ERA-Interim is published by ECMWF, including the sea surface 10 m wind speed, sea surface temperature, sea surface pressure. The spatial resolution is 0.125° × 0.125°, the spatial range is 120° E-125° E, 27.125° N-30.75° N. The time resolution is four times every day (UTC: 00, 06, 12, 18) from 1979 to 2018, the reanalysis data can be obtained from https://apps.ecmwf.int/datasets/data/interim-full-daily/levtype=sfc/ [25, 26].

The amount of wind energy resources in a place is usually characterized by density of wind power (Dwp), which refers to the power per unit area perpendicular to the wind direction. The calculation method is as follows:

$$D_{WP} = \frac{1}{2n}\bar{\rho}\sum_{i=1}^{n} v_i^3 \tag{1}$$

in the formula, D_{WP} is the average wind power density (w/m^2), n is the number of records in the set time period, v_i is the wind speed value of the ith record, and $\bar{\rho}$ is the air density (kg/m^3), the calculation method is as follows:

$$\bar{\rho} = \frac{\bar{P}}{R\bar{T}} \tag{2}$$

Among them, $\bar{P}$ is the mean sea level pressure of the Zhejiang coastal sea surface for years, R is the air gas constant, $\bar{T}$ is the mean absolute temperature of the Zhejiang coastal sea surface for many years, and the mean air density of the Zhejiang sea surface for years is 1.212 kg/m^3.

EOF is a common way for atmospheric study to get the distribution characteristics [27, 28]. EOF analysis of the wind power density anomaly field for a total of 40 years from 1979 to 2018 was carried out. First, we calculate the output of its standardized eigenvector and time series, i.e., solve the covariance matrix of sea surface wind energy resource anomaly, and then calculate its eigenvalues and eigenvectors. Then the main spatial distribution modes of the wind power density anomaly field are obtained.

To obtain the variation coefficient analysis of the wind power density near the Zhejiang coast for the most recent 40 years [29], we first calculated the standard deviation of the wind power density, and the average wind power density across the 40 years. Then, the variation coefficient which the standard deviation is divided by the average value could be carried out.

COMPARISON OF WIND SPEEDS BETWEEN REANALYSIS DATA AND WIND TOWER

The most effective way to evaluate the reliability of reanalysis data is to compare it with observation data. As shown in **Figure 2**, the daily wind speed correlation between a wind tower and the ERA-Interim of the adjacent grid is close, and the correlation coefficients are above 0.8, passing the t-test of significance level $\alpha = 0.001$. The ERA-Interim data can capture the wind speed better in the north sea area than the south sea area of Zhejiang. Due to the high correlation, their trends are generally consistent, so the reanalysis of wind speed data at the height of 10 m is credible.

TABLE 1 | Information of Zhejiang coastal wind towers.

Wind tower number	Start time of wind speed observation	Altitude of anemometer (m)	Average wind speed (m/s)	The standard deviation (m/s)
1#	2014.1.1~2014.12.31	22	6.25	2.17
2#	2013.1.1~2014.12.31	20	6.72	2.57
3#	2008.1.1~2009.12.31	20	6.27	2.25
4#	2013.1.1~2013.12.31	38	6.54	2.76
5#	2010.11.7~2011.11.6	20	6.52	2.97

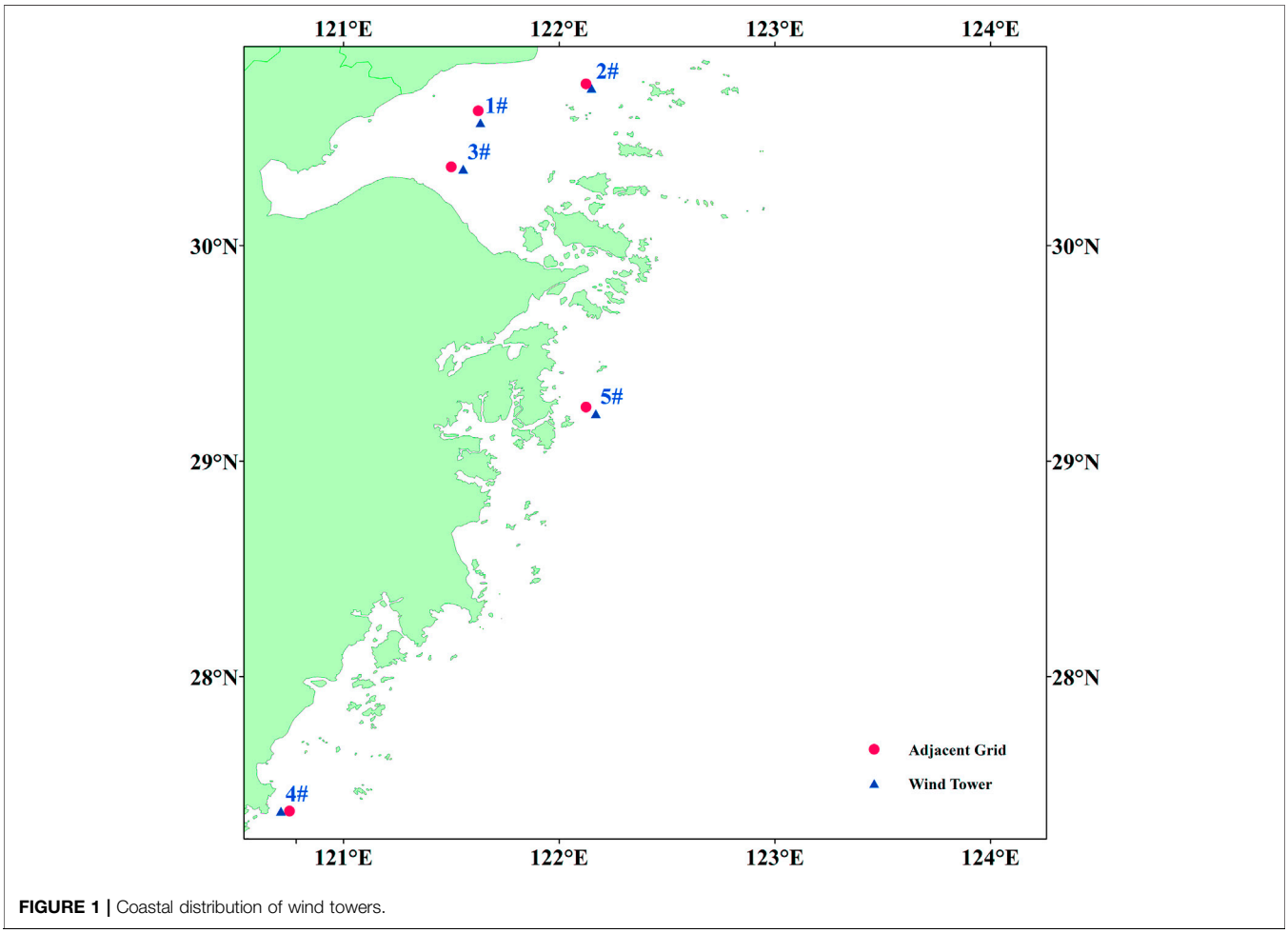

FIGURE 1 | Coastal distribution of wind towers.

In the following parts, the climate characteristics of sea surface wind energy are estimated by reanalysis data.

WIND ENERGY DISTRIBUTION CHARACTERISTICS OF ZHEJIANG SEA SURFACE

Climatic Pattern of Zhejiang Sea Surface Wind Energy

Generally, a wind speed of 3 to 25 m/s is the most efficient for the collection and conversion of wind energy resources, which is called effective wind speed [30, 31]. Wind towers #1 and #2 have more hours of effective wind speed, as shown in **Table 2**. The effective wind energy hours near the wind tower are all more than 80%, and the percentage of effective wind energy hours in Hangzhou Bay is over 86%. The percentage of effective wind energy hours near wind tower #2 is 90%, which indicates that effective wind energy hours are positively correlated with the coastal distance. The percentage of effective wind energy hours near wind towers #4 and #5 is 83%. As shown in **Figure 3**, the percentage of offshore effective wind energy hours increases with latitudinal offshore distance, and decreases southward with longitudinal distance.

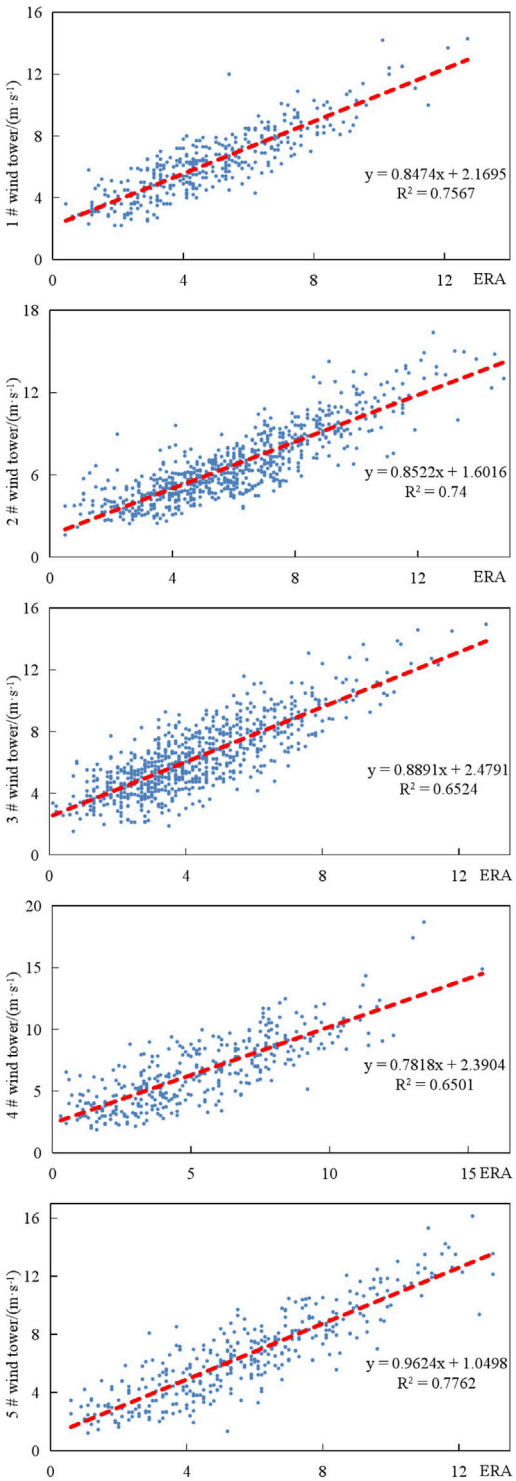

FIGURE 2 | The relevant information between measured wind speed and reanalysis data of ERA-Interim (units:m·s^{-1}). The blue point represents the wind speed, the red dotted line represents the linear trend.

In order to provide a reference for the development and utilization of offshore wind energy resources, the spatial and temporal distribution characteristics of coastal wind energy

TABLE 2 | Wind energy effective hours percentage of Zhejiang coastal.

Station no.	Effective wind hours (h)	Effective wind hours percentage (%)	Observation time
1#	7,797	89	1 year
2#	15,525	90	2 years
3#	15,129	86	2 years
4#	7,243	83	1 year
5#	7,273	83	1 year

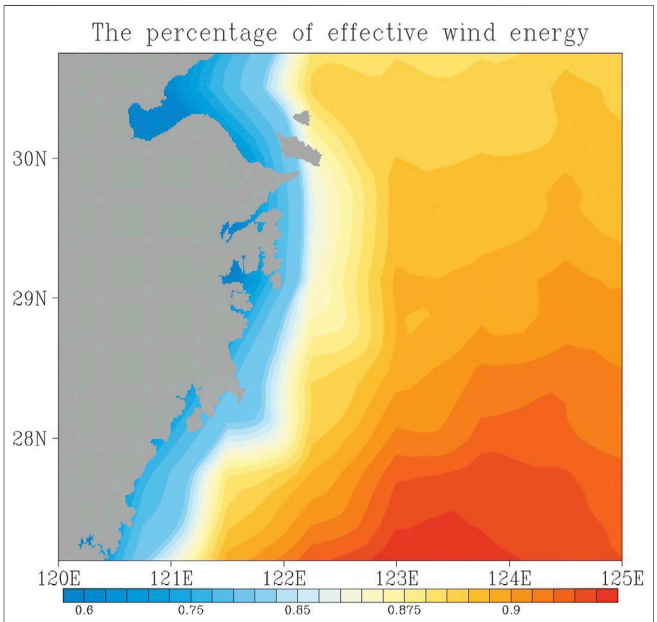

FIGURE 3 | The percentage of effective wind energy of the Zhejiang coastal area (units:w·m^{-2}).

resources in Zhejiang are analyzed. As shown in **Figure 4**, the spatial distribution of the climate mean value of wind energy resources on the Zhejiang sea surface across 1979–2018 is calculated, and the mean value of sea surface wind power density near Hangzhou Bay is lower than other coastal areas. The climatic mean value of sea surface wind power density increases with distance from the coastline, and decreases from south to north with the same offshore distance in different latitudes. From the perspective of wind power density, the location of offshore wind fields should be toward to the south, yielding higher benefits. However, moving south leads to greater risk of typhoon disasters being undertaken, meaning the necessary wind resistance design standard becomes higher and so does the cost.

The amount of offshore wind energy resources is affected by wind speed, which changes with the seasons, especially in winter and summer when the sea surface wind speed is more sensitive to the influence of sea-land temperature difference. The spatial distribution of climate average wind power density on the Zhejiang sea surface in each season from 1979 to 2018 is calculated, as shown in **Figure 5**. In terms of season, the surface wind power density near the Hangzhou bay estuary

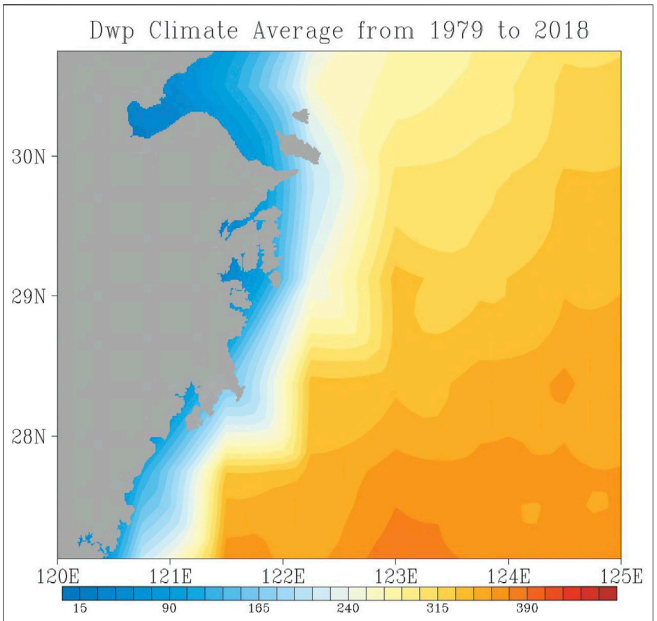

FIGURE 4 | The climate average of Zhejiang coastal wind energy resource in 1979–2018 (units:w·m^{-2}).

and the Zhejiang coastal sea does not change significantly with seasons. In other areas of the sea surface wind power density is the highest in winter, followed by autumn, and the lowest in spring and summer. In terms of space, the seasonal variation range of sea surface wind power density increases with the increase of offshore distance.

In order to further clarify the distribution of sea surface wind energy resources in various time periods, the spatial distribution of climatic average wind power density of Zhejiang in each month from 1979 to 2018 is calculated, as shown in **Figure 6**, the Zhejiang coastal wind power density generally shows a "V" change trend as the month goes on, the variation of the wind power density near the coast of Zhejiang is not obvious, on the contrary, the variation of the sea surface wind power density far from the coast of Zhejiang with the month is obvious, which is similar to the seasonal variation. The evolution speed of sea surface wind power density from high to low is faster than that from low to high. The reason may be that the strong southward cold air of the north in winter causes the obvious increasement of the sea surface wind speed, and then the power density of the sea surface wind is greater than that in other seasons.

Spatial-Temporal Distribution Characteristics of Zhejiang Surface Wind Energy

The sea area of Zhejiang is vast and the sea surface wind speed has much differences, which directly leads to the strong locality of the spatial distribution of sea surface wind energy. In order to further

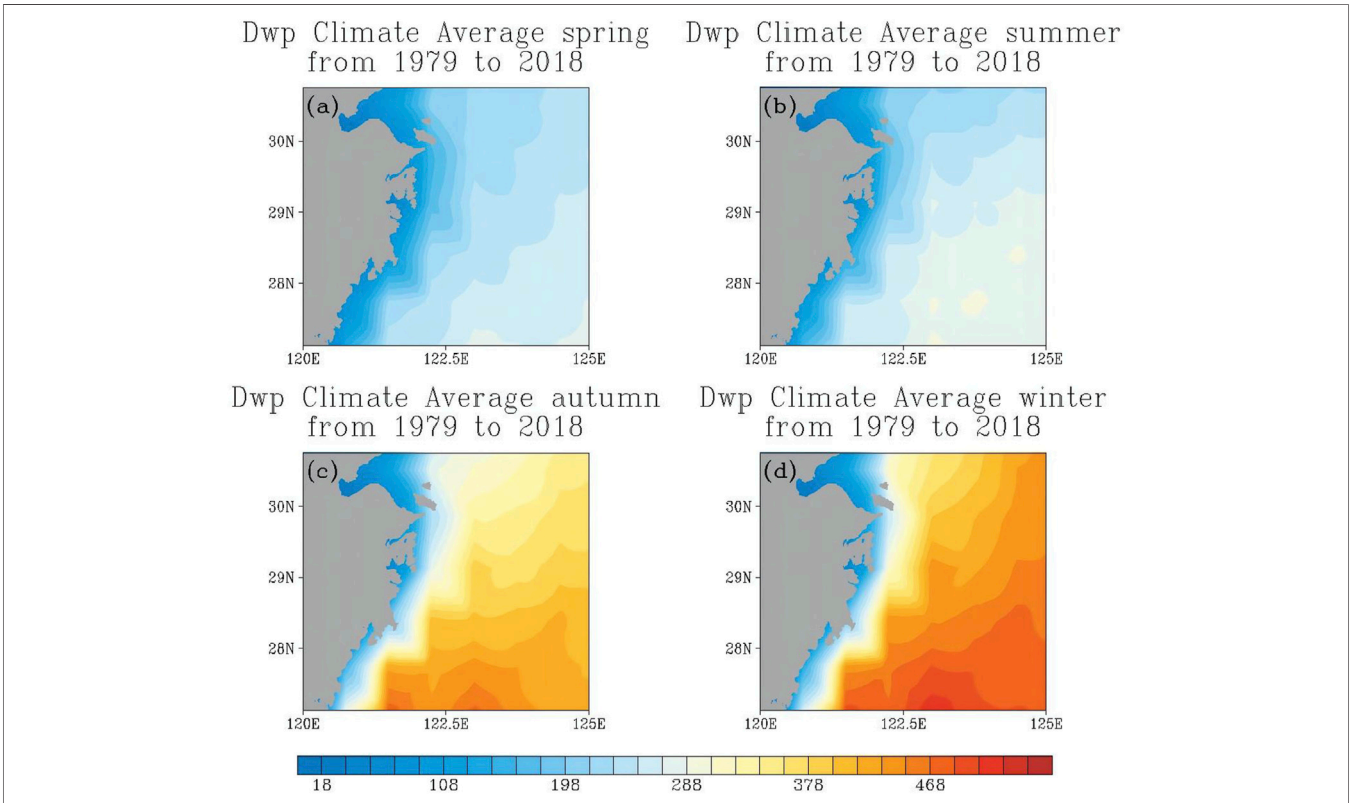

FIGURE 5 | The seasonal climate average of Zhejiang coastal wind energy resource (units:w·m^{-2}):(a) the spring Dwp; (b) the summer Dwp; (c) the autumn Dwp; (d) the winter Dwp.

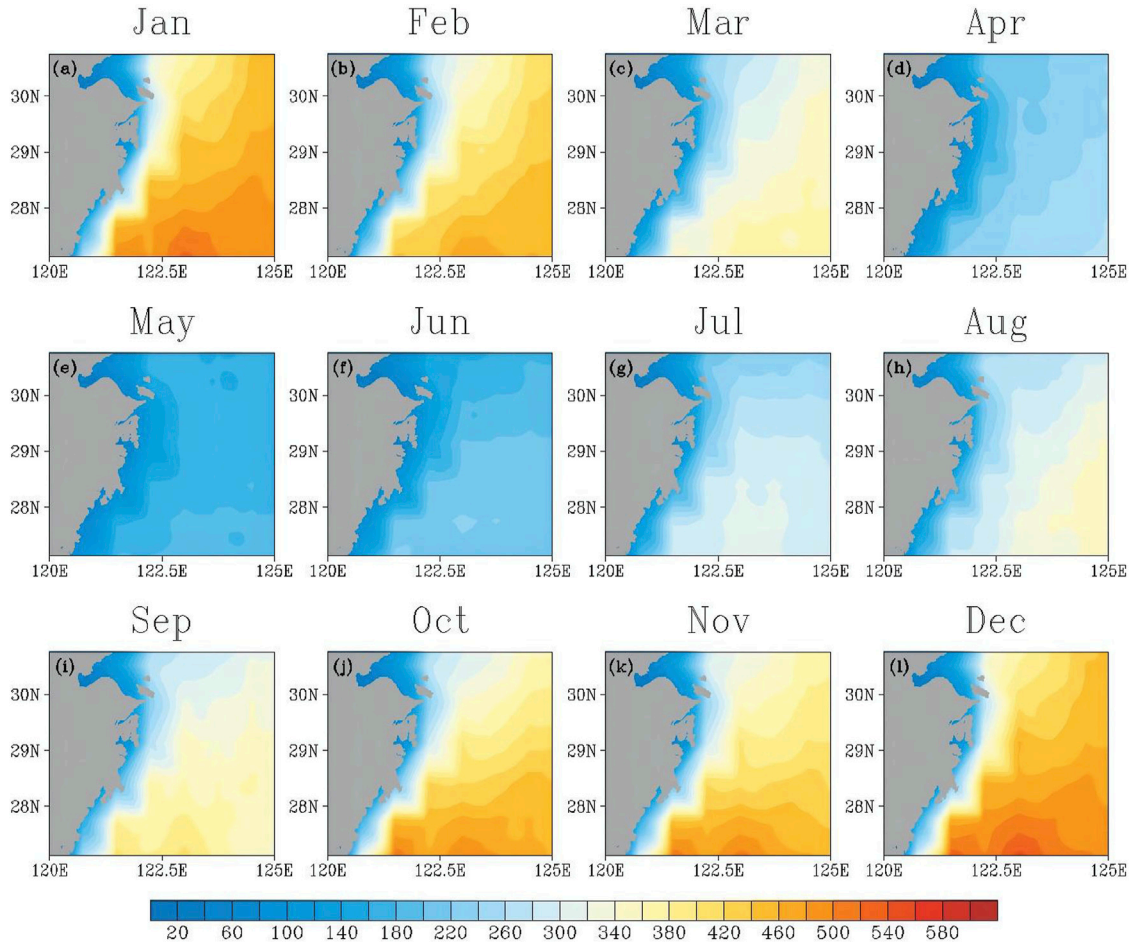

FIGURE 6 | The monthly climate average of Zhejiang coastal wind energy resource (units:w·m^{-2}). (a-l) represent January to December respectively.

analyze the spatial and temporal variation characteristics of sea surface wind energy, EOF analyzed the annual average power density anomaly field of sea surface wind energy in 40 years, as shown in **Figure 7**, the variance contribution rate of the first three modes reached 87.3% and passed the North significance test. The spatial and temporal fields of the first three modes can basically reflect the variation characteristics of the sea surface wind power density in the Zhejiang coastal area.

The variance contribution rate of the first mode has reached 61.1%, which is much higher than the other modes. As shown in **Figure 7A**, the first mode mainly reflects a consistency increasing or decreasing trend of sea surface wind power density in Zhejiang coastal sea area. The center is in the southeast of Zhejiang coastal sea area, the value of space field contours near Zhejiang coastal is small, which indicates that the inter-annual variation of the wind power density in the Zhejiang coastal area is smaller than that in the eastern sea area, the time coefficient in **Figure 7D** shows an obvious upward trend, and it mainly presents positive anomaly value in recent years.

As shown in **Figure 7B**, the second mode mainly reflects that the sea surface wind power density along the coast of Zhejiang presents a North-South dipole type change trend with north latitude of 28°N as the boundary, the variation range of time coefficient in **Figure 7E** is small, so the trend of inter-annual variation can be ignored.

As shown in **Figure 7C**, the third mode mainly reflects that the wind power density in the Zhejiang coastal region shows the trend of East-West dipole type change trend, and the change range on the west side is larger than that on the east side, and the center on the west side is in the southwest coastal Zhejiang. The variation range of time coefficient in **Figure 7F** shows an upward trend with the change of time, and in recent years it has shown a weak positive anomaly.

The Stability of Wind Energy in Zhejiang Sea Surface

For wind power development enterprises and the State Grid, the stability of offshore wind energy directly affects the development potential of wind energy resources and the rational planning of power generation into the grid. In the energy assessment of wave energy, tidal energy, the coefficient of variation has been widely used [32]. The smaller the coefficient of variation, the better the stability of energy. In this paper, the coefficient of variation is introduced to measure the stability of wind energy resources.

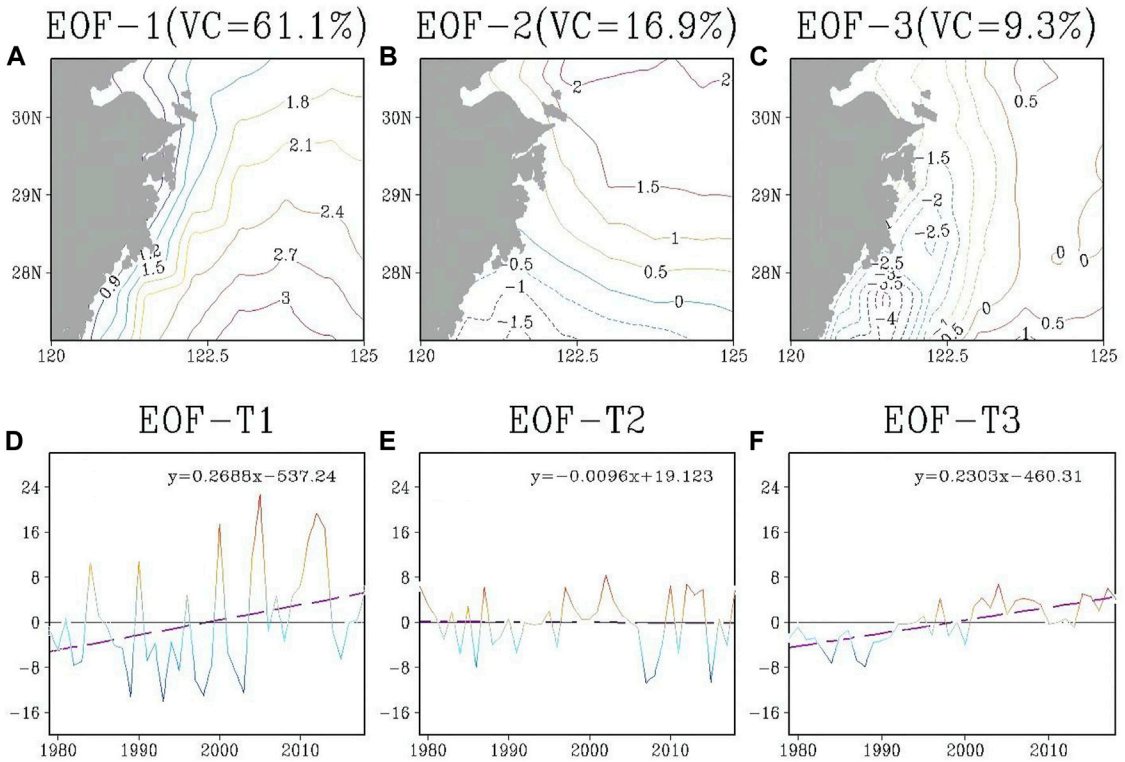

FIGURE 7 | (A–C) Distribution patterns and **(D–F)** time coefficients of the first three modes of sea surface wind power density anomaly field in Zhejiang coastal area: **(A,D)** the first mode; **(B,E)** the second mode; **(C,F)** the third mode.

The formula of variation coefficient is: $C_v = \frac{S}{\bar{x}}$, C_v is the coefficient of variation, S is the standard deviation, and $\bar{x}$ is the 40 years average value.

The coefficient of variation was calculated for the annual average wind power density. As shown in **Figure 8**, the variation coefficient is inversely related to the distance from the coast. The variation coefficient is the smallest in the sea area of Taizhou, which means that the interannual variation of the annual average wind power density near the coast is greater than that of the other areas of Zhejiang. The interannual variation of the annual average wind power density reached the maximum in Hangzhou bay, the variation coefficient is the smallest in the offshore sea surface of Taizhou, then followed by Wenzhou. The interannual variation of the northern part of the distant sea is smaller than that of the southern part.

The reason for the great difference in the interannual variation of the sea surface wind power density near the coast of Zhejiang may be that the urbanization process is too fast, which is affected by the change of the topography and geomorphology onshore.

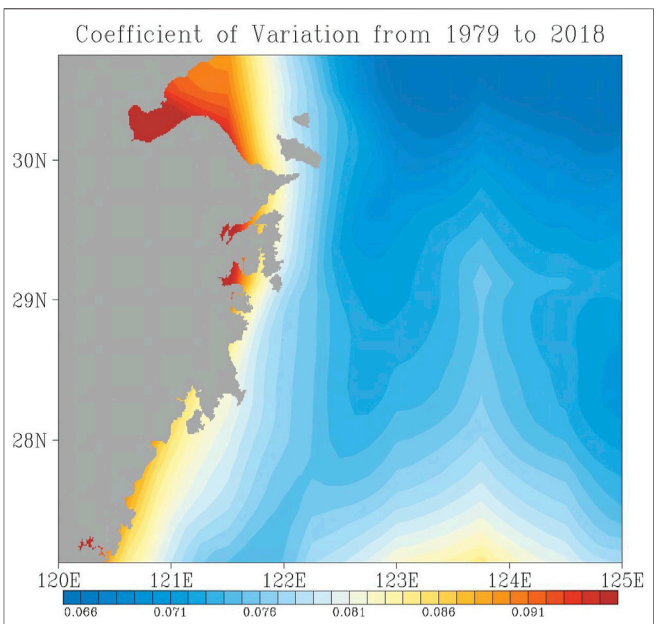

FIGURE 8 | Multi-year averaged coefficient of variation of the wind power density.

The Trend of Sea Surface Wind Energy in Zhejiang

Under the influence of human activities and air-sea interaction, there are large differences in the tendency of interannual change of sea surface wind energy in different regions. In this section, the tendency coefficient of one-dimensional linear regression is used to estimate the interannual trend of wind power density over the past 40 years.

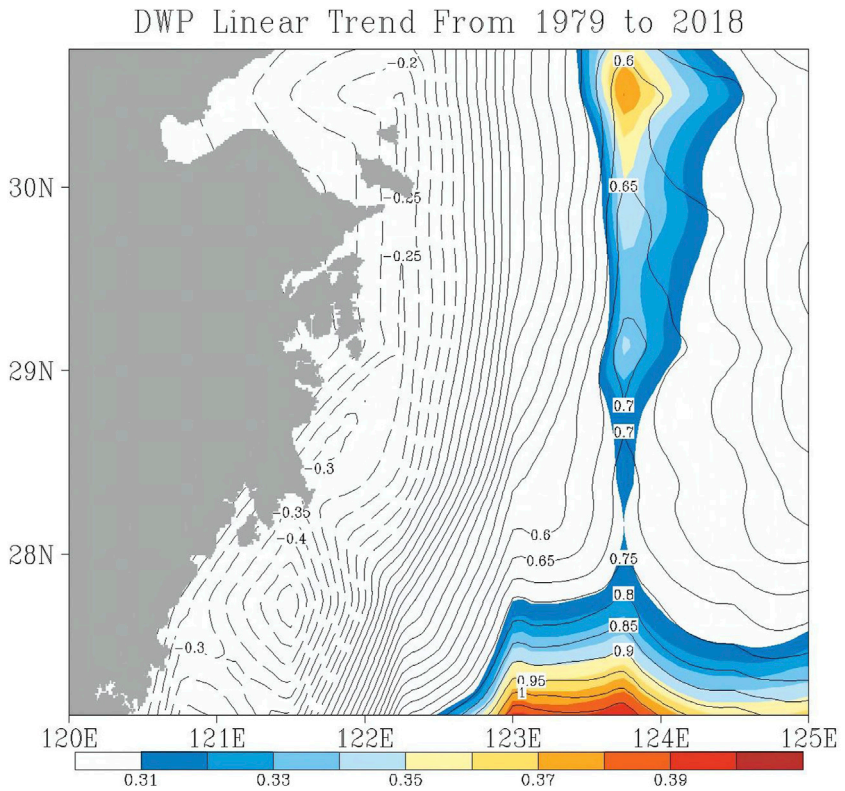

FIGURE 9 | Interannual trend of wind power density (the contour line is the tendency value, the shaded part is the area put through the significance test).

Taking time as the independent variable and interannual wind power density as the dependent variable, linear regression statistics were performed, as shown in **Figure 9**, where the dotted line indicates the downward trend and the solid line indicates the upward trend. The interannual variation of wind power density in coastal areas of Zhejiang shows an obvious East-West pattern, the wind power density in the whole coastal area of Zhejiang shows a downward trend, and the downward trend is most obvious in the coastal area of Taizhou, the tendency estimate is about $-0.5\ W{\cdot}m^{-2}{\cdot}a^{-1}$. The downward trend in the offshore area of Hangzhou Bay is not obvious, the tendency estimate is about $-0.1\ W{\cdot}m^{-2}{\cdot}a^{-1}$, the corresponding correlation coefficient does not pass a 95% reliability test. Therefore, the overall wind power density on the west side of the offshore area tends to decline, which is consistent with the observation results of the actual meteorological station, but the trend is not obvious. On the contrary, the significance of the correlation coefficient passes the 95% reliability test in the east side of the offshore shaded area, the wind power density shows an obvious upward trend, and there are two centers in the North and South. The northern upward trend center estimate is more than $0.7\ W{\cdot}m^{-2}{\cdot}a^{-1}$, the southern upward trend center is more than $1.0\ W{\cdot}m^{-2}{\cdot}a^{-1}$, so the trend of interannual change is larger in the South. Generally speaking, the rate of rising in the east sea area is faster than the rate of decline in the west sea area.

The interannual variation trend of wind power density in each season is statistically analyzed. As shown in **Figure 10**, the spring interannual variation trend in the whole coastal area of Zhejiang shows a significant downward trend which passes the 95% reliability test. The trend is -0.75~$-2.0\ W{\cdot}m^{-2}{\cdot}a^{-1}$ near the coast and -4.5~$-6.0\ W{\cdot}m^{-2}{\cdot}a^{-1}$ in the east sea area, and the downward trend increases from west to east. The summer interannual variation trend in the whole coastal area of Zhejiang shows a significant upward trend which passes the 95% reliability test. The trend is 1.0~$2.0\ W{\cdot}m^{-2}{\cdot}a^{-1}$ near the coast and 3.5~$4.5\ W{\cdot}m^{-2}{\cdot}a^{-1}$ in the east sea area, and the upward trend increases from west to east. The autumn interannual variation trend shows an insignificant slight upward trend in the near coast, the trend is 0~$1.0\ W{\cdot}m^{-2}{\cdot}a^{-1}$, but there is a significant upward trend in the east sea area, the trend is 2.0~$3.0\ W{\cdot}m^{-2}{\cdot}a^{-1}$, and the upward trend increases from west to east. The winter interannual variation trend shows an insignificant slight upward trend in the whole sea area, the trend estimation value is 0~$1.0\ W{\cdot}m^{-2}{\cdot}a^{-1}$, and the upward trend increases from north to south.

The monthly variation range of wind energy resources has a great influence on the collection of wind energy, the life of wind turbines, and the utilization ratio of power grid connection. In the evaluation of wave energy, the monthly variability index can better reflect the change of wave energy [33], the smaller the index, the better the energy stability in each month. Here, the

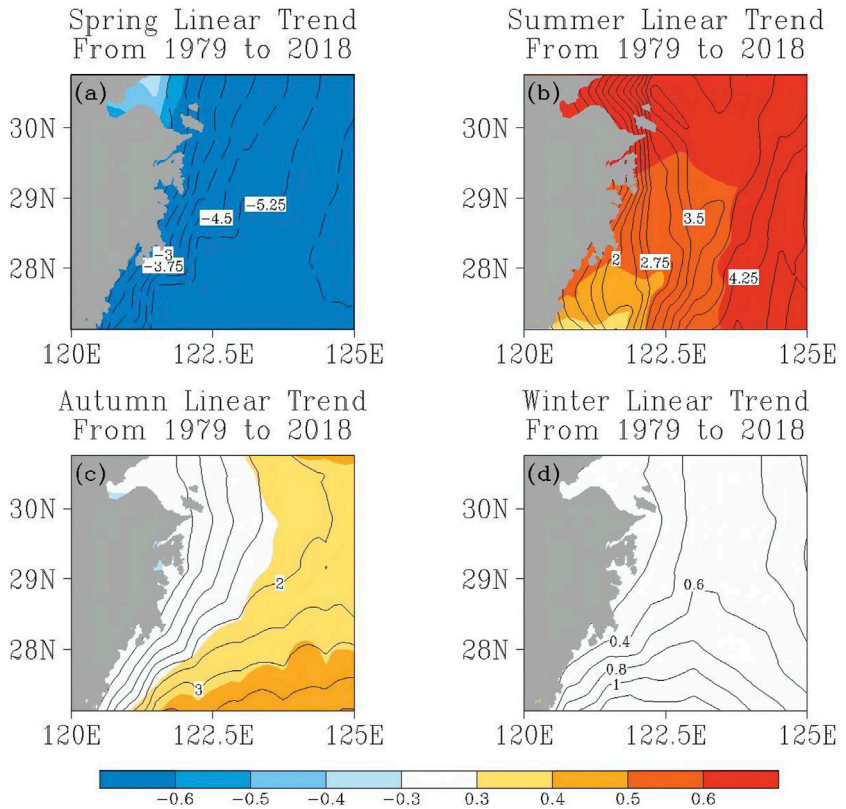

FIGURE 10 | Seasonal trend of wind power density (the contour line is the tendency value, the shaded part is the area put through the significance test): (a) the spring linear trend; (b) the summer linear trend; (c) the autumn linear trend; (d) the winter linear trend.

monthly variability index is introduced to measure the monthly variation trend of wind energy resources.

The formula of the monthly variability index is: $M_v = \frac{d_{\max} - d_{\min}}{d_{ave}}$, M_v is the monthly variability index, $d_{\max}$ is the maximum average monthly wind power density in the year, d_{min} is the minimum average monthly wind power density in the year, d_{ave} is the average monthly wind power density in the year.

According to the calculation method of the monthly variability index, we calculated the index every year, and then calculated the annual variation trend of the index in the past 40 years, as shown in **Figure 11**. The positive trend of the index means the monthly energy differential increases. On the contrary, the negative trend of the index means the differential narrows, which is conducive to wind energy development. The shaded part in the figure passes the 95% reliability test. The sea area passing the test has two centers of positive annual variation trends, the interannual variation trend value of the index in the east sea reaches 0.012 and near Taizhou to Wenzhou reaches 0.011, which means that the monthly differential increases. The interannual variation trend of the monthly variability index near the Hangzhou bay is insignificantly weak growth or decrease. Compared with the shaded area, the interannual variation of the index changes little, which is beneficial to the development of wind energy.

Frequency Distribution of Sea Surface Wind Power Density in Zhejiang

The wind power density frequency of 0–600w·m^{-2} at the sea surface in the last 40 years in Zhejiang is analyzed, and the results are shown in **Figure 12**. When the wind power density is between 0–150 W·m^{-2}, the frequency in the coastal area of Zhejiang shows a trend of gradual decline from west to east, with a large gradient. The frequency near Hangzhou bay reaches a maximum of 80%, and in the eastern sea, the area is between 40% and 50%. When the wind power density is between 150–300 W·m^{-2}, the frequency in the coastal area of Zhejiang shows a trend of gradual increase from west to east, with a small gradient. The wind power density frequency near Hangzhou bay reaches about 10%, in the area south of Hangzhou Bay is about 16–18%, and in the eastern sea area is about 20%. When the wind power density is between 300–450 W·m^{-2}, the frequency also shows a trend of gradual increase from west to east, with a small gradient. The wind power density frequency near the Hangzhou bay reaches about 6%, in the south of Hangzhou Bay is about 10%, and in the eastern sea area is about 12%. When the wind power density is between 450–600 W·m^{-2}, the frequency shows a trend of gradual increase from northwest to southeast, with a small gradient also. The frequency near the Hangzhou bay reaches about 4%, in the area

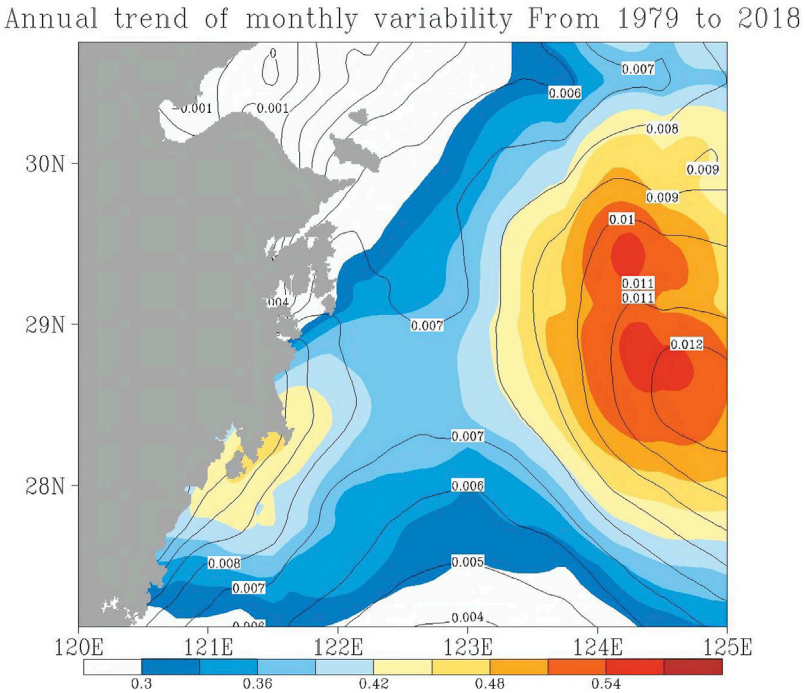

FIGURE 11 | Longterm annual trend of monthly variability index for the period 1979 to 2018.

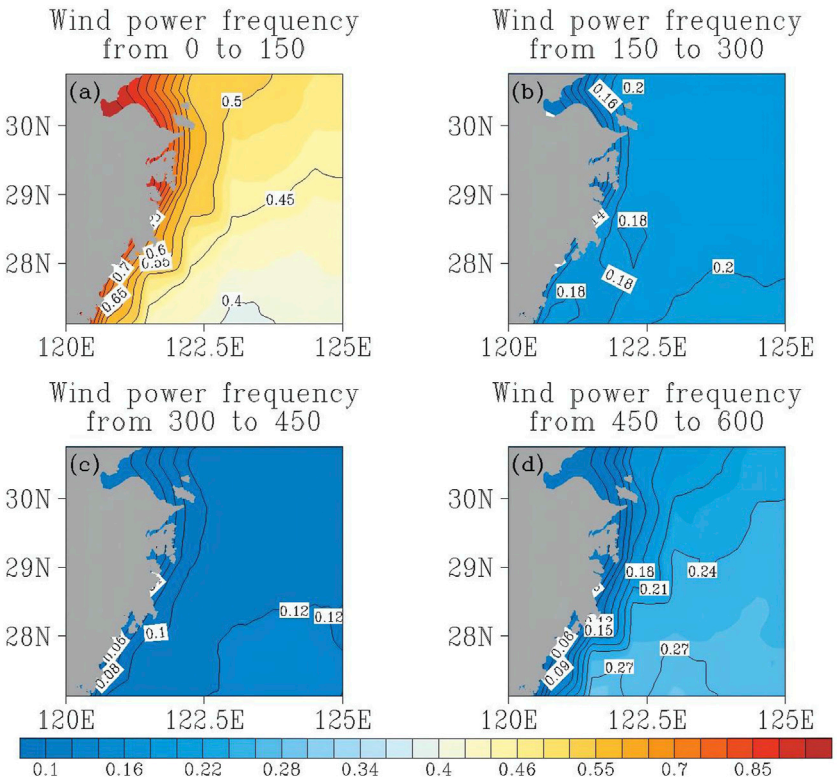

FIGURE 12 | Frequency distribution of wind energy resources on the coastal sea surface: (a) the frequency of Dwp from 0 to 150; (b) the frequency of Dwp from 150 to 300; (c) the frequency of Dwp from 300 to 450; (d) the frequency of Dwp from 450 to 600.

south of Hangzhou Bay is about 6–15%, and in the eastern sea area is about 27%.

In general, when the wind power density is between 0–150 $W{\cdot}m^{-2}$, the frequency mainly shows the distribution trend of high in the west and low in the east, when the wind power density is between 150–600 $W{\cdot}m^{-2}$, the frequency mainly shows the distribution trend of high in the east and low in the west.

CONCLUSION AND DISCUSSION

The applicability of ERA-interim data in the Zhejiang sea area was analyzed by comparing the reanalysis data of wind speed at the height of 10 m in a fixed year with the wind speed measured by the wind tower. Furthermore, the climate change characteristics of sea surface wind power were analyzed based on the ERA-interim data.

1) We compared the measured wind speed data of the five offshore wind towers with the reanalysis wind speed data of the adjacent grid of the same period. The correlation coefficient reached more than 0.8 which passes the significance level test of α= 0.001. The reanalysis of the sea surface wind at the height of 10 m can well represent the actual sea surface wind speed characteristics, and sea surface wind speed increases as latitude decreases.
2) Zhejiang is rich in sea surface wind energy resources: according to the effective wind energy hours, the actual effective wind energy hours measured by the offshore wind tower exceed 80%. In the east-west direction, the percentage of effective wind energy hours increases with longitude; in the north-south direction, it increases as latitude decreases. From the perspective of the spatial distribution of the average wind power density over many years, the mean value of sea surface wind power density near Hangzhou Bay is lower than other coastal areas. The climatic mean value of sea surface wind power density increases with the distance from the coast, on the contrary, the gradient of mean surface wind power density increases as distance from coast decreases. From the perspective of the spatial distribution of multi-year seasonal average wind power density, the wind power density is the highest in winter, followed by autumn, and the lowest in spring and summer. From the spatial distribution of multi-year monthly average wind power density, the wind power density along the coast of Zhejiang generally shows a v-shaped change trend, among them, it does not change significantly near the Zhejiang coast, while it changes significantly far away from the coastal waters of Zhejiang.
3) EOF decomposition of the Zhejiang sea surface wind power density anomaly field was carried out, the variance contribution rate of the first mode reached 61.1%, the spatial field was consistency type, and the time coefficient showed an obvious upward trend; the variance contribution rate of the second mode was 16.9%, and the spatial field was of north-south dipole type, with a small range of time coefficient; the variance contribution rate of the third mode was 9.3%, and the spatial field was of west-east dipole type, and the time coefficient showed an obvious upward trend.
4) The stability of wind energy in the coastal sea surface of Zhejiang is one of the factors considered by wind power generation. Due to the rapid urbanization, the change of shore topography, geomorphology, and other factors, the stability of wind energy resources near the coast is low, and wind energy stability away from the coast gradually increases from south to north.
5) The linear trend of interannual, seasonal, and monthly variation coefficients of the sea surface wind power density was calculated: the coastal areas of Zhejiang show an obvious interannual variation trend of east-west dipole type. Spring is a significant downward trend from west to east, summer is a significant upward trend from west to east, autumn and winter are an insignificant weak upward trend. The linear trend of the monthly variability index in the Hangzhou bay estuary in northern Zhejiang is insignificant weak growth or weak decrease. Compared with the south coastal area and the eastern sea area, the interannual change of the index is not significant, which is beneficial to the development of wind energy.
6) When the wind power density is between 0–150 $W{\cdot}m^{-2}$, the frequency mainly shows the distribution trend of high in the west and low in the east, and the wind power density is between 150–600 $W{\cdot}m^{-2}$, the frequency mainly shows the distribution trend of high in the east and low in the west.

It should be pointed out that there is a certain deviation between the reanalyzed wind speed and the measured wind speed. This article makes a macro analysis of the trend of wind energy resources in the Zhejiang marine economic demonstration area. Subsequent work can be combined with higher resolution SAR satellite data to carry out a refined evaluation of wind energy resources in the region [34, 35].

Until now, the green development concept of peak carbon dioxide emissions and carbon neutrality is deeply rooted in people's hearts, and Zhejiang have also taken relevant measures to save energy and reduce emissions. However, as one of the developing coastal provinces in eastern China, the demand for and consumption of energy, especially electric energy, is increasing day by day, which requires our province to take more energy supply measures to deal with it, and the rational use of offshore wind energy will alleviate the problem of electric energy supply to a certain extent. For example, by 1) strengthening the analysis of high-resolution meteorological data, and excavating the sea area which is rich in wind energy resources and suitable for developing wind power along the coast of Zhejiang; and 2) paying more attention to the long-term changes of offshore wind speed, accurately estimating the wind power generation capacity in different time periods and reasonably integrate it into the power grid to promote the efficient use of energy. In addition, it is necessary to further study the future trend of sea-surface wind energy resources in the context of global climate change, which is of forward-looking significance for guiding the future development of sea-surface wind energy in the Zhejiang Province.

DATA AVAILABILITY STATEMENT

The raw data supporting the conclusion of this article will be made available by the authors, without undue reservation.

AUTHOR CONTRIBUTIONS

All authors contributed to this research in collaboration. NW and CH-S wrote manuscript, KW proposed the conceptualization, KP-Z, TF, and YH-Z provided substantial help with the paper schedule and gave advice on the experiment and supervised. All authors have read and agreed to the published version of the manuscript.

FUNDING

This work was supported by the Key R&D Program of Zhejiang Province (2021C02036), the Natural Science Foundation of China (42005027), Fund for Meteorological Science and Technology of Zhejiang Province, China (2021ZD08, 2020YB04).

REFERENCES

1. Mitchell JFB, Johns TC, Gregory JM, Tett SFB. Climate Response to Increasing Levels of Greenhouse Gases and Sulphate Aerosols. *Nature* (1995) 376:501–4. doi:10.1038/376501a0
2. Zhang H, Wang K. Simulated CO2-induced Ocean Acidification for Ocean in the East China: Historical Conditions since Preindustrial Time and Future Scenarios. *Sci Rep* (2019) 9(9):18559. doi:10.1038/s41598-019-54861-0
3. Wang K, Zhang H, Fan G-F, Li Z-Q, Yu Z-Y, Liu P-P. Simulated Variation Characteristics of Oceanic CO2 Uptake, Surface Temperature, and Acidification in Zhejiang Province, China. *Front Phys* (2021) 9:718968. doi:10.3389/fphy.2021.718968
4. Zheng CW. Wave Energy and Other Renewable Energy Resources in South China Sea: Advantages and Disadvantages. *J. Subtropical Res. Environ.* (2011) 6(3):76. (in Chinese). doi:10.19687/j.cnki.1673-7105.2011.03.011
5. Liang B, Shao Z, Wu G, Shao M, Sun J. New Equations of Wave Energy Assessment Accounting for the Water Depth. *Appl Energ* (2017) 188:130–9. doi:10.1016/j.apenergy.2016.11.127
6. Li Z-q., Chen S-j., Ma H, Feng T. Design Defect of Wind Turbine Operating in Typhoon Activity Zone. *Eng Fail Anal* (2013) 27:165–72. doi:10.1016/j.engfailanal.2012.08.013
7. Sara P, Esparza DM, Munters W, Beeck JV, Lipzig NV. Impact of Ocean Waves on Offshore Wind Farm Power Production. *Renew Energ* (2021) 180:1179–93. doi:10.1016/j.renene.2021.08.111
8. Sawyer S, Rave K. *Global Wind Report-2015*. Brussels: Global Wind Energy Council (2016). p. 8.
9. Dong W, Yuan W, Liu S, Moore J, Shi P, Feng S. China-Russia Gas deal for a Cleaner China. *Nat Clim Change* (2014) 4:940–2. doi:10.1038/nclimate2382
10. Song LL, Zhou RW, Yang ZB, Zhu R. Meteorological Technology Application and Development in Wind Energy Resources Utilization. *Eng Sci* (2012) 14(9): 96, 2012. (in Chinese) doi:10.3969/j.issn.1009-1742.2012.09.012
11. Bilgili M, Yasar A, Simsek E. Offshore Wind Power Development in Europe and its Comparison with Onshore Counterpart. *Renew Sustain Energ Rev* (2011) 15(2):905–15. doi:10.1016/j.rser.2010.11.006
12. Sawyer S, Rave K. *Global Wind Report-2019*. Brussels: Global Wind Energy Council (2020). p. 61.
13. Ajayi OO, Fagbenle RO, Katende J, Okeniyi JO. Availability of Wind Energy Resource Potential for Power Generation at Jos, Nigeria. *Front Energ* (2011) 5: 376–85. doi:10.1007/s11708-011-0167-5
14. Li ZC, Zhu R, He XF, Zhang D. Study on the Assessment Technology of Wind Energy Resource. *Acta Meteorologica Sinica* (2007) 65(5):708, 2007. (in Chinese) doi:10.3321/j.issn:0577-6619.2007.05.006
15. Zheng CW, Li CY, Pan J, Liu MY, Xia LL. An Overview of Global Ocean Wind Energy Resource Evaluations. *Renew Sustain Energ Rev* (2016) 53:1240–51. doi:10.1016/j.rser.2015.09.063
16. Wang K, Feng G, Zhang H, Li Z, Fan G, Yu Z. Climate Change Characteristics and Adaptation in the Offshore East China Sea from 1979 to 2017. *J Coastal Res* (2020) 99:54. doi:10.2112/si99-008.1
17. Fang H, Perrie W, Fan GF, Xie T, Yang JS. Ocean Surface Wind Speed Retrieval from C-Band Quad-Polarized SAR Measurements at Optimal Spatial Resolution. *Remote Sensing Lett* (2021) 12(2):155. doi:10.1080/2150704x.2020.1846220
18. Liu S, Wei E, Jin X, Lv A, Dang H. The Performance of Dual-Frequency Polarimetric Scatterometer in Sea Surface Wind Retrieval. *J Ocean Univ China* (2019) 18(5):1051–60. doi:10.1007/s11802-019-4018-z
19. Fang H, Perrie W, Zhang G, Xie T, Khurshid S, Warner K. Ocean Surface Wind Speed Retrieval Using Simulated RADARSAT Constellation Mission Compact Polarimetry SAR Data. *Remote Sensing* (2019) 11(16):1876. doi:10.3390/rs11161876
20. Song CH, Wang N, Wang K, Fan GF, Feng T, Li ZQ. Variation and Cause of Sea Surface Wind Speed in Zhejiang Coastal Area Based on CCMP Data from 1988 to 2017. *Trans Atmos Sci* (2019) 42(4):562. (in Chinese). doi:10.13878/j.cnki.dqkxxb.20180816001
21. Gao QJ. *Data Intercomparison Among Reanalyses and Observations in Perspective of Multi-Scale Variations of Summer Climate in east China*. PhD thesis. Nanjing: Nanjing University of Information Science & Technology (2013). (in Chinese with English abstract).
22. Hughes BR, Calautit JK, Ghani SA. The Development of Commercial Wind Towers for Natural Ventilation: a Review. *Appl Energ* (2012) 92:606–27. doi:10.1016/j.apenergy.2011.11.066
23. Chan JCL. Tropical Cyclone Activity in the Northwest Pacific in Relation to the El Niño/Southern Oscillation Phenomenon. *Mon Wea Rev* (1985) 113(4): 599–606. doi:10.1175/1520-0493(1985)113<0599:tcaitn>2.0.co;2
24. Vitor P, Milton K, Rosio C, Angeles GM. Comparison of Multiple Surface Ocean Wind Products with Buoy Data over Blue Amazon (Brazilian Continental Margin). *Adv Meteorology* (2021) 2021:1–19. doi:10.1155/2021/6680626
25. Dee DP, Uppala SM, Simmons AJ. The ERA-Interim Reanalysis: Configuration and Performance of the Data Assimilation System. *Q J R Meteorol Soc* (2011) 137(656):553–97. doi:10.1002/qj.828
26. Sun PJ, Wang BB, Cheng ZH, Zhang XT, Xu Y, Meng D. Analysis of the Influence of Wind Speed Interpolation on Wind Power Density Error from Wind Tower Data. *Adv Meteorol Sci Technol* (2019) 9(2):63.
27. Ye T, Shen Q, Wang K, Zhang Z, Zhao J. Interdecadal Change of the Northward Jump Time of the Western Pacific Subtropical High in Association with the Pacific Decadal Oscillation. *J Meteorol Res* (2015) 29(1):59–71. doi:10.1007/s13351-014-4040-4
28. Wang K, Ma H, Li J, Gu BH, Wu H. Assessment of the POEM2 Model for Simulating Tropical Intraseasonal Oscillation. *J Trop Meteorology* (2018) 24(3):323. doi:10.16555/j.1006-8775.2018.03.006
29. Wang K, Feng G-L, Zeng Y-X, Wang X-J. Analysis of Stable Components in the Extended-Range Forecast for the Coming 10-30 Days in winter 2010 and 2011. *Chin Phys. B* (2013) 22(12):129202. doi:10.1088/1674-1056/22/12/129202
30. Zheng CW, Pan J, Li JX. Assessing the China Sea Wind Energy and Wave Energy Resources from 1988 to 2009. *Ocean Eng* (2013) 65:39–48. doi:10.1016/j.oceaneng.2013.03.006
31. Shi J, Guo J, Zheng S. Evaluation of Hybrid Forecasting Approaches for Wind Speed and Power Generation Time Series. *Renew Sustain Energ Rev* (2012) 16(5):3471–80. doi:10.1016/j.rser.2012.02.044
32. Zheng CW, Li CY. Propagation Characteristic and Intraseasonal Oscillation of the Swell Energy of the Indian Ocean. *Appl Energ* (2017) 197:342–53. doi:10.1016/j.apenergy.2017.04.052
33. Cornett AM. A Global Wave Energy Resource Assessment. In: Proceedings of the Eighteenth (2008) International Offshore and Polar Engineering

Conference; July 2008; Ontario, Canada. Berlin: Canadian Hydraulics Centre, National Research Council Ottawa (2008). p. 318.
34. Shao W, Sun J, Guan C, Sun Z. A Method for Sea Surface Wind Field Retrieval from SAR Image Mode Data. *J Ocean Univ China* (2014) 13(2):198–204. doi:10.1007/s11802-014-1999-5
35. Shao W, Zhu S, Sun J, Yuan X, Sheng Y, Zhang Q. Evaluation of Wind Retrieval from Co-polarization Gaofen-3 SAR Imagery Around China Seas. *J Ocean Univ China* (2019) 18(1):80–92. doi:10.1007/s11802-019-3779-8

Conflict of Interest: The authors declare that the research was conducted in the absence of any commercial or financial relationships that could be construed as a potential conflict of interest.

Publisher's Note: All claims expressed in this article are solely those of the authors and do not necessarily represent those of their affiliated organizations, or those of the publisher, the editors and the reviewers. Any product that may be evaluated in this article, or claim that may be made by its manufacturer, is not guaranteed or endorsed by the publisher.

frontiers in Climate

ORIGINAL RESEARCH
published: 08 December 2021
doi: 10.3389/fclim.2021.735988

Assessment of CMIP6 Model Performance for Wind Speed in China

Lijun Zhao [1,2†], Shuanglong Jin [1,2*†], Xiaolin Liu [1,2], Bo Wang [1,2], Zongpeng Song [1,2], Ju Hu [1,2] and Yuyang Guo [1,2]*

[1] State Key Laboratory of Operation and Control of Renewable Energy and Storage Systems, China Electric Power Research Institute Co., Ltd., Beijing, China, [2] Electric Power Meteorology State Grid Corporation Joint Laboratory, Beijing, China

OPEN ACCESS

Edited by:
Yipeng Guo,
Nanjing University, China

Reviewed by:
Zablon W. Shilenje,
Charles University, Czechia
Guangwei Li,
Northwest Institute of Eco-Environment and Resources, Chinese Academy of Sciences (CAS), China

***Correspondence:**
Lijun Zhao
lijunz_mail@163.com
Shuanglong Jin
ceprijinsl@163.com

† These authors have contributed equally to this work and share first authorship

Specialty section:
This article was submitted to Climate Services, a section of the journal Frontiers in Climate

Received: *04 July 2021*
Accepted: *02 November 2021*
Published: *08 December 2021*

Citation:
Zhao L, Jin S, Liu X, Wang B, Song Z, Hu J and Guo Y (2021) Assessment of CMIP6 Model Performance for Wind Speed in China. Front. Clim. 3:735988. doi: 10.3389/fclim.2021.735988

As the major renewable energy, wind can greatly reduce carbon emissions. Following the "carbon neutral" strategy, wind power could help to achieve the realization of energy transformation and green development. Based on ERA5 reanalysis data and the multi-ensemble historical and scenario simulations of the Coupled Model Intercomparison Project Phase 6 (CMIP6), a variety of statistical analyses are used to evaluate the performance of CMIP6 simulating the wind speed in China. The conclusions are as follows: spatial patterns of the nine CMIP6 models are similar with ERA5, but BCC-CSM2-MR and MRI-ESM2-0 highly overestimate the wind speed in northwest China. CESM2-WACCM, NorESM2-MM, and HadGEM3-GC31-MM behave better than the other six CMIP6 models in four specific regions are chosen for detailed study. CESM2-WACCM, NorESM2-MM, and HadGEM3-GC31-MM tend to simulate a larger wind speed than ERA5 except the yearly averaged wind speed in region II and region IV. CESM2-WACCM and NorESM2-MM simulate a large monthly mean wind speed, but the value is relatively close with ERA5 in the summer. HadGEM3-GC31-MM overestimates wind speed in region I and region II from April to October, but gets closer with ERA during winter. CESM2-WACCM, NorESM2-MM, and HadGEM3-GC31-MM simulate an increasing trend in Tibetan Plateau and Xinjiang in the next 100 years, while NorESM2-MM projects rising wind speed in the eastern part of Inner Mongolia, and HadGEM3-GC31-MM simulates increasing wind speed in the northeast and central China. The future wind speed in three models is projected to decline in region I, and the value of HadGEM3-GC31-MM is much larger. In region II, wind speed simulated by three models is projected to decrease, but the wind speed from HadGEM3-GC31-MM in region III and modeled wind speed in region IV from NorESM2-MM would climb with the slope equal to 0.0001 and 0.0012, respectively. This study indicates that the CMIP6 models have certain limitations to perform realistic wind changes, but CMIP6 could provide available reference for the projection of wind in specific areas.

Keywords: model assessment, carbon neutral, renewable energy, wind, CMIP6

INTRODUCTION

Renewable energy, energy efficiency, and electrification are three drivers of deep de-carbonization, and developing renewable energy is an important measure for global climate governance and achieving the goal of carbon neutrality. It is estimated that by 2050, the proportion of renewable energy supply will exceed 50% (IRENA, 2018). As one of the primary carbon-free resources, wind energy meets the electricity demand dramatically. However, a significant decreasing trend of wind speed is reported in numerous studies. Near-surface wind speed over the globe is dropping at 5–15% since 1960, which is called as global stilling (Pryor et al., 2009). The global average wind speed trend is −0.014 m/s/a, while the wind speed over the low- to middle-latitude areas is declining and the wind speed of high-latitude areas is rising (McVicar et al., 2012). There was a decreasing wind speed trend with −0.005 m/s/a in the USA (Hobbins, 2004). The declining wind speed trend across the Australia has reached 0.009 m/s/a since 2006 (McVicar et al., 2008). A significant declining wind speed of −0.017 m/s/a is showed in western Canada (Tuller, 2004; Wan et al., 2010). The downward change of wind speed in Italy is −0.013 m/s/a, while the falling trend is −0.026 m/s/a before 1975 and decreased to −0.002 m/s/s after 1975 (Pirazzoli and Tomasin, 2003).

As one of the countries with abundant wind resource, China has a large amount of wind power capacities and plays a dominant role in developing renewable energy. The annual mean wind speed in China is 4.09 m/s, while the wind power density is 164.1 W/m^2. Northeast China is the most potential area with an annual mean wind speed 4.64 m/s while the wind power density is 204 W/m^2, and coastal areas in east China have wind power density larger than 500 W/m^2 (Liu et al., 2019). The annual mean wind speed and maximum wind speed in China were decreasing since 1956 (Jiang et al., 2013), and reanalysis datasets and station observational data showed the near-surface wind speed had been decreasing by −0.109 m/s per decade from 1958 to 2015 (Zhang et al., 2019). In the catchment of Yangtze River, the downward trend of wind speed was −0.008 m/s/a between 1960 and 2000 (Xu et al., 2006). The near-surface wind speed in the Loess Plateau of China had declined by −0.01 m/s/a (McVicar et al., 2005). Previous researches have been done to evaluate the possible factors related with the surface wind speed decrease in China. The land-use and cover change over the Eastern China Plain could lead a 0.17-m/s wind speed decrease every decade in China. The primary cause is the pressure-gradient force, and the surface drag force also has a significant effect on the declining wind speed (Wu et al., 2017). The weakening of the East Asian monsoons mainly causes the decreasing average and maximum wind speed, and the relatively less land-falling typhoons and cold waves lead to the reduced maximum wind speed in southeast coastal China (Jiang et al., 2013).

As for now, the climate models cannot well-quantify the effect from climate change (IPCC, 2007). The World Climate Research Program's (WCRP) Coupled Model Intercomparison Project (CMIP) has been operated since 1990s, aiming to understand the past, the present, and the future of climate. The new Coupled Model Intercomparison Project Phase 6 (CMIP6) is designed to better estimate the climate (Eyring et al., 2016). To better know the future of wind energy, the simulations of updated climate models could be helpful to predict the change of wind speed.

DATA AND METHODOLOGY

ERA5

ERA5 is a fifth-generation European Centre for Medium-Range Weather Forecasts (ECMWF) atmospheric reanalysis of the global climate and is doing well in depicting the

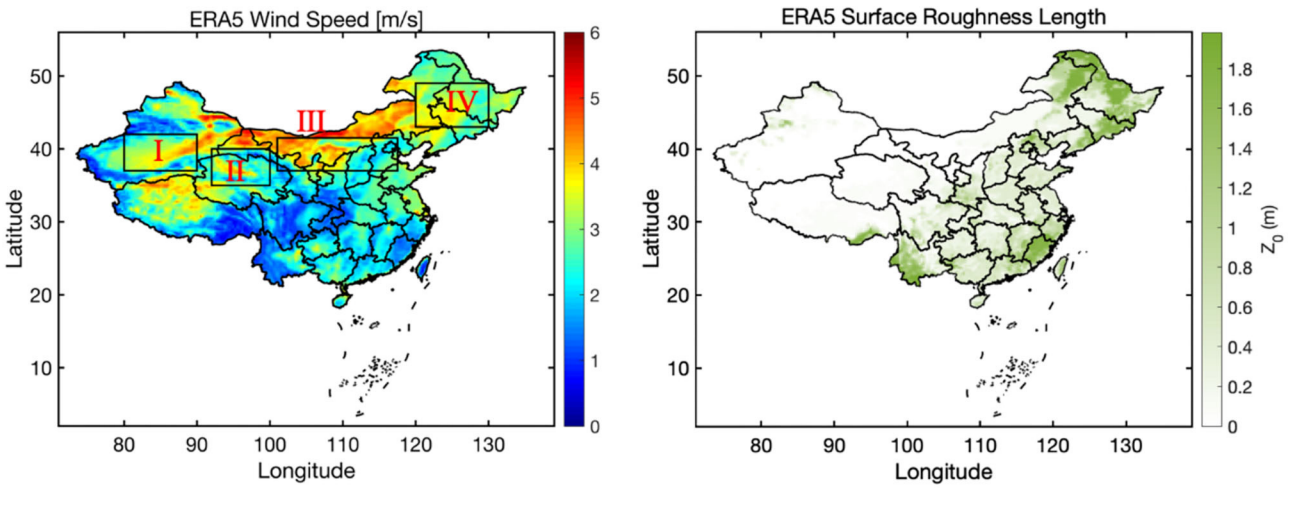

FIGURE 1 | The spatial distribution of multi-year (1986–2014) mean 10-m wind speed (left) and surface roughness length (right) over China. The four specific regions are shown as black rectangles.

TABLE 1 | CMIP6 models used in this study.

Model name	Modeling center	Resolution
BCC-CSM2-MR	Beijing Climate Center, China	320 × 160
CESM2	National Center for Atmospheric Research, USA	288 × 192
CESM2-WACCM	National Center for Atmospheric Research, USA	288 × 192
CESM2-WACCM-FV2	National Center for Atmospheric Research, USA	144 × 96
HadGEM3-GC31-MM	Met Office Hadley Centre, UK	432 × 324
MRI-ESM2-0	Meteorological Research Institute, Japan	320 × 160
NorESM2-MM	NorESM Climate Modeling Consortium, Norway	288 × 192
SAM0-UNICON	Seoul National University, South Korea	288 × 192
TaiESM1	Research Center for Environmental Changes, Taiwan, China	288 × 192

atmospheric circulation. ERA5 is produced by 4D-Var data assimilation in CY41R2 of the Integrated Forecasting System (IFS), providing global atmospheric, land-surface, and sea-state parameters. The dataset is on regular latitude–longitude grids at 0.25° × 0.25° resolution with 37 pressure levels vertically and covers the period from 1950 to the present. In this study, the near-surface wind speed from 1986 to 2014 over China is used to evaluate the CMIP6 models. Since the north China is abundant with wind resources, four specific regions from I to IV shown in **Figure 1** are chosen for further study: region I (80°∼90°E, 37°∼42°N), region II (92°∼100°E, 35°∼40°N), region III (101°∼117.5°E, 37°∼41.5°N), and region IV (120°∼130°E, 43°∼49°N).

CMIP6

CMIP6 historical simulations take the natural causes and human factors into consideration and reproduce the historical variability of climate from 1850 to 2014. The historical simulations could be used for assessing model performance in climate and weather (Eyring et al., 2016). Moreover, the Scenario Model Intercomparison Project (ScenarioMIP) could provide a new set of emissions and land-use scenarios, which, along with the Shared Socioeconomic Pathways (SSPs), allows twenty-first century projections to be assessed from the new future forcing experiments. SSP585 used in our study is the updated scenario of RCP8.5 using the rapid fossil energy evolution with SSP5 following the high greenhouse emissions (O'Neill et al., 2014, 2017). Multi-ensembles are averaged to maintain the quality of evaluation, and the group of nine newest CMIP6 global climate models from China, USA, UK, Japan, Norway, and South Korea is used in this study. Model name, modeling centers, and resolution of models are described in **Table 1**.

Methodology

Based on the different latitude-longitude grids between CMIP6 and ERA5, the ERA5 is interpolated to the grid of corresponding CMIP6 models before comparison. The metrics of bias, spatial correlation coefficient (R), and root mean square error (RMSE) are used to evaluate the models' performance, and the equations of calculating are shown in following. W_{m} is the wind speed of CMIP6, W_{E} represents the ERA5 wind speed, and i is the pixel where CMIP6 and ERA5 coincide.

$$Bias = \frac{\sum_{i=1}^{N}(W_{mi} - W_{Ei})}{N} \quad (1)$$

$$R = \frac{\sum_{i=1}^{N}\left(W_{mi} - \overline{W}_m\right)\left(W_{Ei} - \overline{W}_E\right)}{\sqrt{\sum_{i=1}^{N}\left(W_{mi} - \overline{W}_m\right)^2}\sqrt{\sum_{i=1}^{N}\left(W_{Ei} - \overline{W}_E\right)^2}} \quad (2)$$

$$RMSE = \sqrt{\frac{(W_{m1} - W_{E1})^2 + (W_{m2} - W_{E2})^2 + \cdots + (W_{mn} - W_{En})^2}{N}} \quad (3)$$

RESULTS

Spatial Pattern of ERA5

Figure 1 shows the spatial distribution of multi-year mean 10-m wind speed and surface roughness length over China. Larger values of wind speed are shown in north China and Tibetan Plateau, and relatively smaller wind speed is shown in southwest China and southeast China. Comparing with the surface roughness length, the spatial distribution of wind speed is negatively related with the spatial pattern of surface roughness length. Wind speed tends to be smaller while the surface roughness length is larger, which is similar with the finding of a previous study (Vautard et al., 2010).

Spatial Pattern of CMIP6 Models

The multi-year mean 10-m wind speed (1986–2014) of the nine CMIP6 models is shown in **Figure 2**. Spatial patterns of the nine CMIP6 models are similar with ERA5 shown in **Figure 1**, but the wind speed in north China is larger and the wind speed in the Sichuan Basin is much smaller. However, the values of wind speed in north China and northeast China are highly overestimated by BCC-CSM2-MR and MRI-ESM2-0, and the maximum of simulated wind speed tends to be over 8.78 m/s, which is far higher than ERA5.

Metrics of Spatial Distributions

The metrics of comparison are shown in **Figure 3**; higher R and lower RMSE represent that the corresponding model has better consistency with ERA5. CESM2-WACCM, HadGEM3-GC31-MM, and NorESM2-MM behave better than the other six CMIP6 models; the RMSE ranges from 0.48 to 2.41, and the R is between 0.52 and 0.90. From the results above, the spatial difference between BCC-CSM2-MR and MRI-ESM2-0 is much larger, and in **Figure 3**, the RMSE of these two models over the four regions is still large and the R tends to be negative, which means that in either the whole country or the specific regions, the simulation of wind speed of BCC-CSM2-MR and MRI-ESM2-0 tends to result

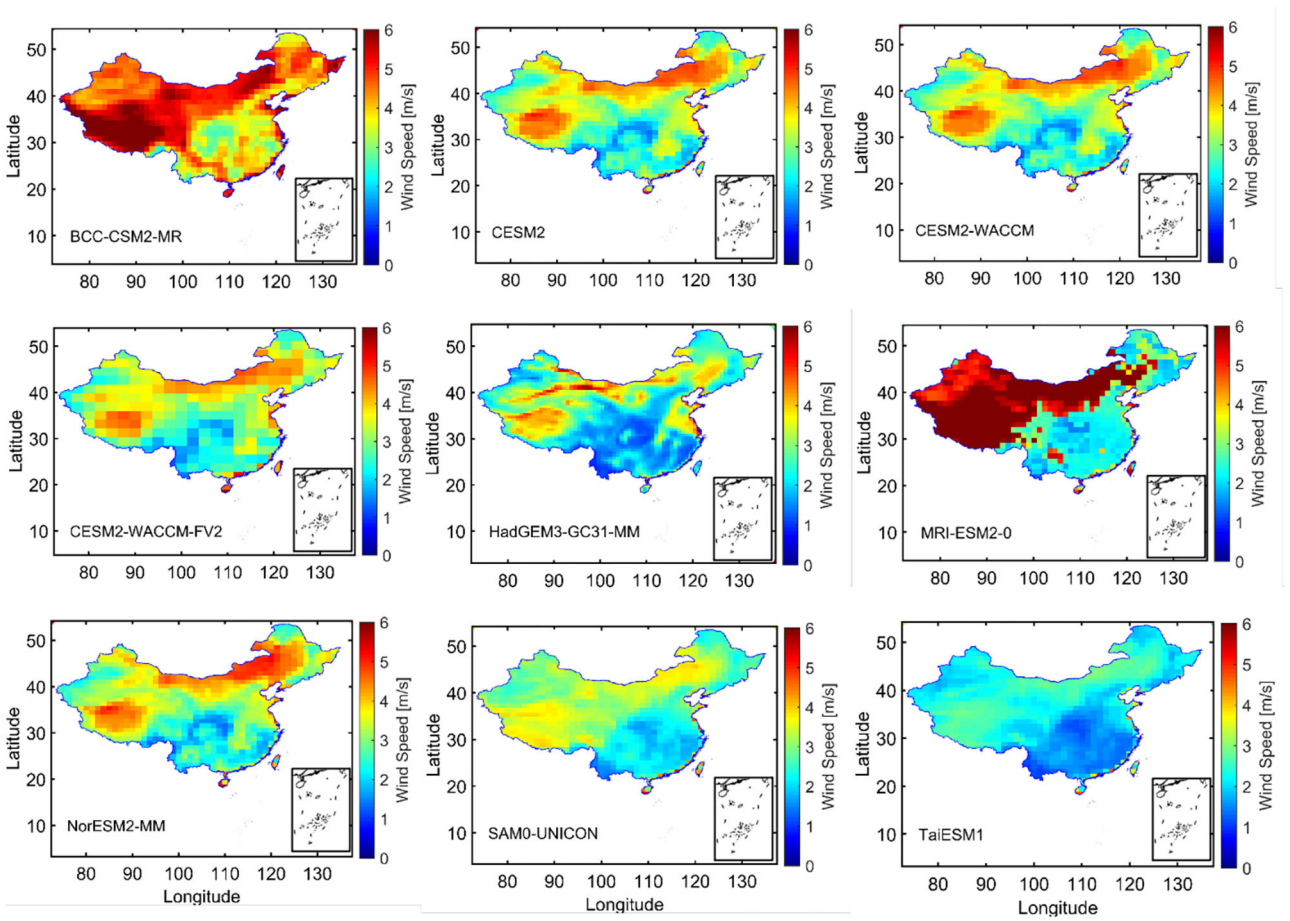

FIGURE 2 | Spatial distribution of mean 10-m wind speed (1986–2014) in CMIP6 historical simulations.

in large bias and uncertainty. Based on the performance of these three CMIP6 models, the temporal variability of wind speed over the four specific regions is also analyzed for further study.

Temporal Variability of the Four Regions

To quantitatively measure the performances of three CMIP6 models, the temporal correlation coefficients of near-surface wind speeds during 1979 to 2014 over the four regions between ERA5 and three CMIP6 models are shown in **Table 2**. The temporal correlation coefficients in region I are higher than the other regions, and the CESM2-WACCM and HadGEM3-GC31-MM are 0.84 and 0.86 with $p < 0.05$, respectively, which indicate the better correlation with the ERA5 in region I. In the other three regions, HadGEM3-GC31-MM simulates the wind speed in region II better and CESM2-WACCM does relatively better in region III and region IV.

Figures 4A–D shows the yearly mean 10-m wind speed of CMIP6 and ERA5 over the four specific regions (black line represents ERA5, and the blue, red, and green lines represent the CESM2-WACCM, NorESM2-MM, and HadGEM3-GC31-MM, respectively). In region I and region II, three CMIP6 models overestimate the wind speed largely, and in region III and region IV, comparing with ERA5, the wind speed of HadGEM3-GC31-MM is underestimated, while the wind speed simulated by NorESM2-MM and HadGEM3-GC31-MM are much larger.

Figure 5 shows the monthly mean 10-m wind speed of CMIP6 and ERA5 over the four specific regions (the black line represents ERA5, and the blue, red, and green lines represent the CESM2-WACCM, NorESM2-MM, and HadGEM3-GC31-MM, respectively). In the four regions, the 10-m wind speed of ERA5 gets larger from January and reaches peak at April (region II, region III, and region IV) or May (region I). In region II and region IV, the wind speed tends to increase again after August. The seasonal cycles of near-surface wind speed in HadGEM3-GC31-MM, CESM2-WACCM, and NorESM2-MM are similar with ERA5, but different in the values of monthly mean 10-m wind speed. CESM2-WACCM and NorESM2-MM tend to overestimate the wind speed from January to May and October to December, and the value is closer with ERA5 between June and September. For HadGEM3-GC31-MM, the simulated wind speed could be closer or smaller than ERA5 from January to May and October to December, and the wind speed tends to be overestimated from June to September.

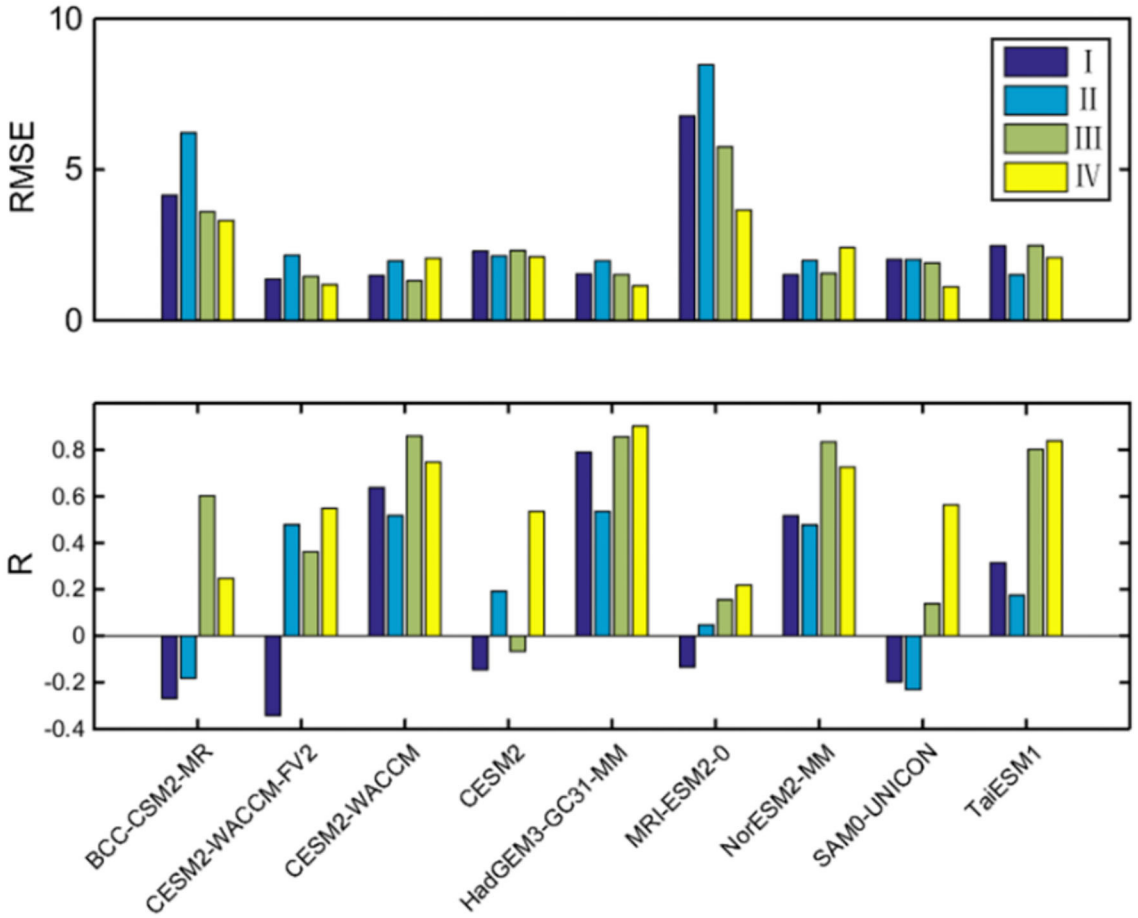

FIGURE 3 | The bar plots of metrics root mean square error (RMSE) and spatial correlation coefficient (*R*). Four different colors represent the four specific regions.

TABLE 2 | The temporal correlation coefficients of near-surface wind speeds during 1979 to 2014 over the four regions between ERA5 and three CMIP6 historical simulations.

Model	Region I	Region II	Region III	Region IV
CESM2-WACCM	0.84	0.46	0.55	0.63
HadGEM3-GC31-MM	0.86	0.57	0.48	0.37
NorESM2-MM	0.79	0.37	0.42	0.61

Future Spatial and Temporal Variability of the Four Specific Regions

The spatial bias between the historical and ssp585 simulations from CESM2-WACCM, NorESM2-MM, and HadGEM3-GC31-MM in China is shown in **Figure 6**. The wind speed projected by the three models shows an upward trend of wind speed in western China in the future, especially over the Tibetan Plateau and Xinjiang. From the simulation of NorESM2-MM, the wind speed in the eastern part of Inner Mongolia tends to increase in the next 100 years. Different with CESM2-WACCM and NorESM2-MM, the wind speed simulated by the HadGEM3-GC31-MM tends to slightly increase over a relatively wider range in China.

The wind speed of ssp585 simulation in the four specific regions from CESM2-WACCM, NorESM2-MM, and HadGEM3-GC31-MM is shown in **Figure 7**. In region I, the linear regression shows that all three CMIP6 models show a downward trend in the future 100 years, especially during the 2050 to 2083, there is an obvious jump of wind speed. The wind speed of HadGEM3-GC31-MM in region I is much higher than the other two models, which is distinct comparing with the other three regions. Different with region I, the simulated wind speed of HadGEM3-GC31-MM falls behind CESM2-WACCM and NorESM2-MM in the other three regions. In region II, the linear regression shows that the wind speed simulated by the three models is projected to decrease with the slope of −0.004, −0.003, and −0.001, respectively. HadGEM3-GC31-MM simulates a slight climb of wind speed in region III, which is distinct from the other two models, CESM2-WACCM and NorESM2-MM represent a similar fluctuation from 2015 to 2050 while the HadGEM3-GC31-MM shows an adverse change. NorESM2-MM simulates a relatively strong increasing trend of wind speed with

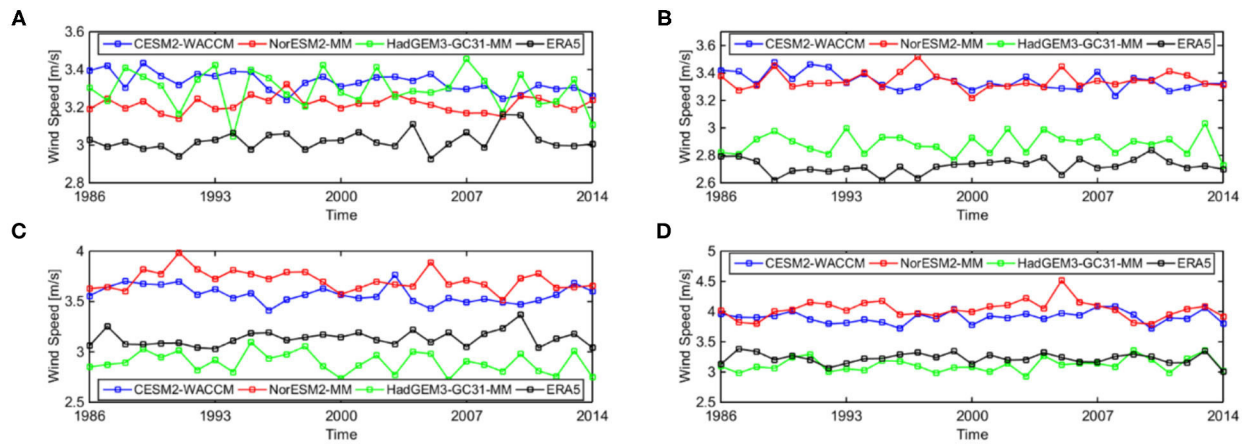

FIGURE 4 | Yearly mean 10-m wind speed (1986–2014) of CMIP6 and ERA5 (black line represents ERA5, and the blue, red, and green lines represent CESM2-WACCM, NorESM2-MM, and HadGEM3-GC31-MM, respectively). **(A–D)** Region I, region II, region III, and region IV, respectively.

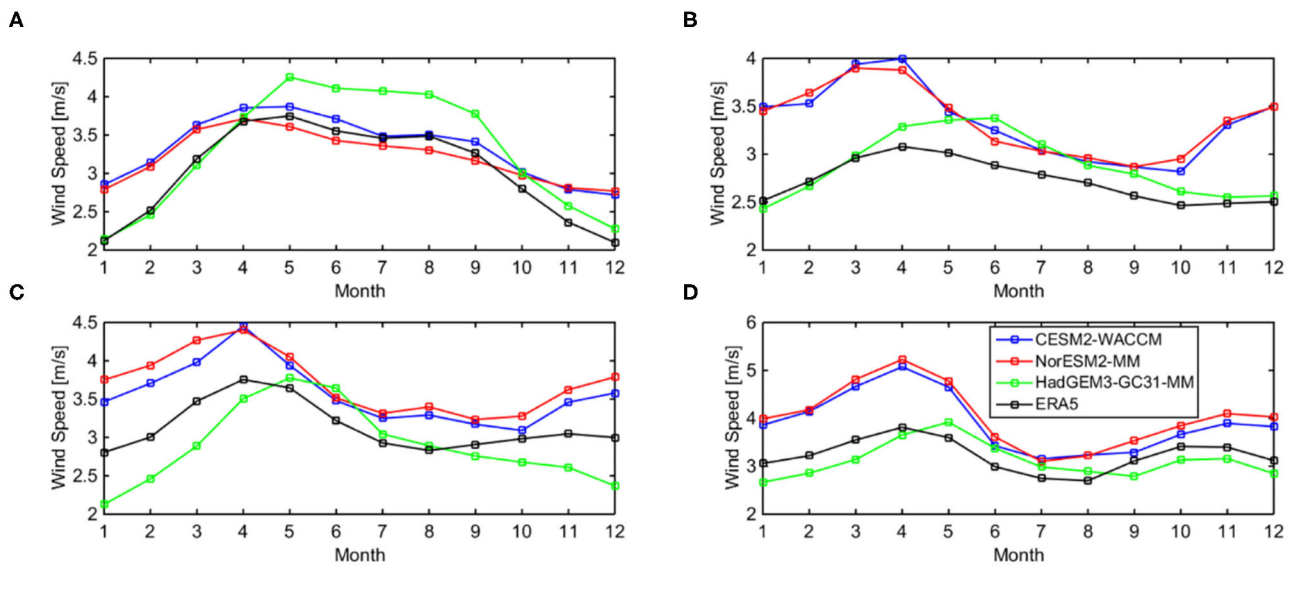

FIGURE 5 | Monthly mean 10-m wind speed (1986–2014) in CMIP6 and ERA5 (black line represents ERA5, and the blue, red, and green lines are the CESM2-WACCM, NorESM2-MM, and HadGEM3-GC31-MM, respectively). **(A–D)** Region I, region II, region III, and region IV, respectively.

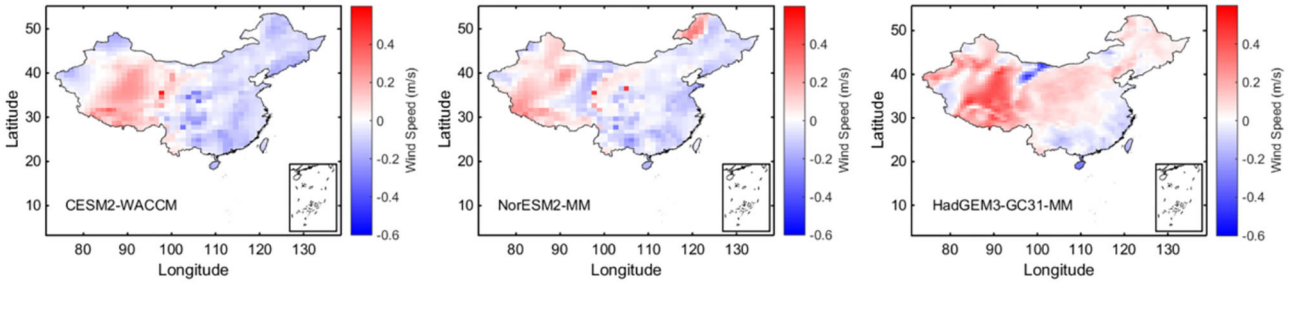

FIGURE 6 | The spatial distribution of wind speed bias (ssp5-8.5 minus historical) from CESM2-WACCM, NorESM2-MM, and HadGEM3-GC31-MM.

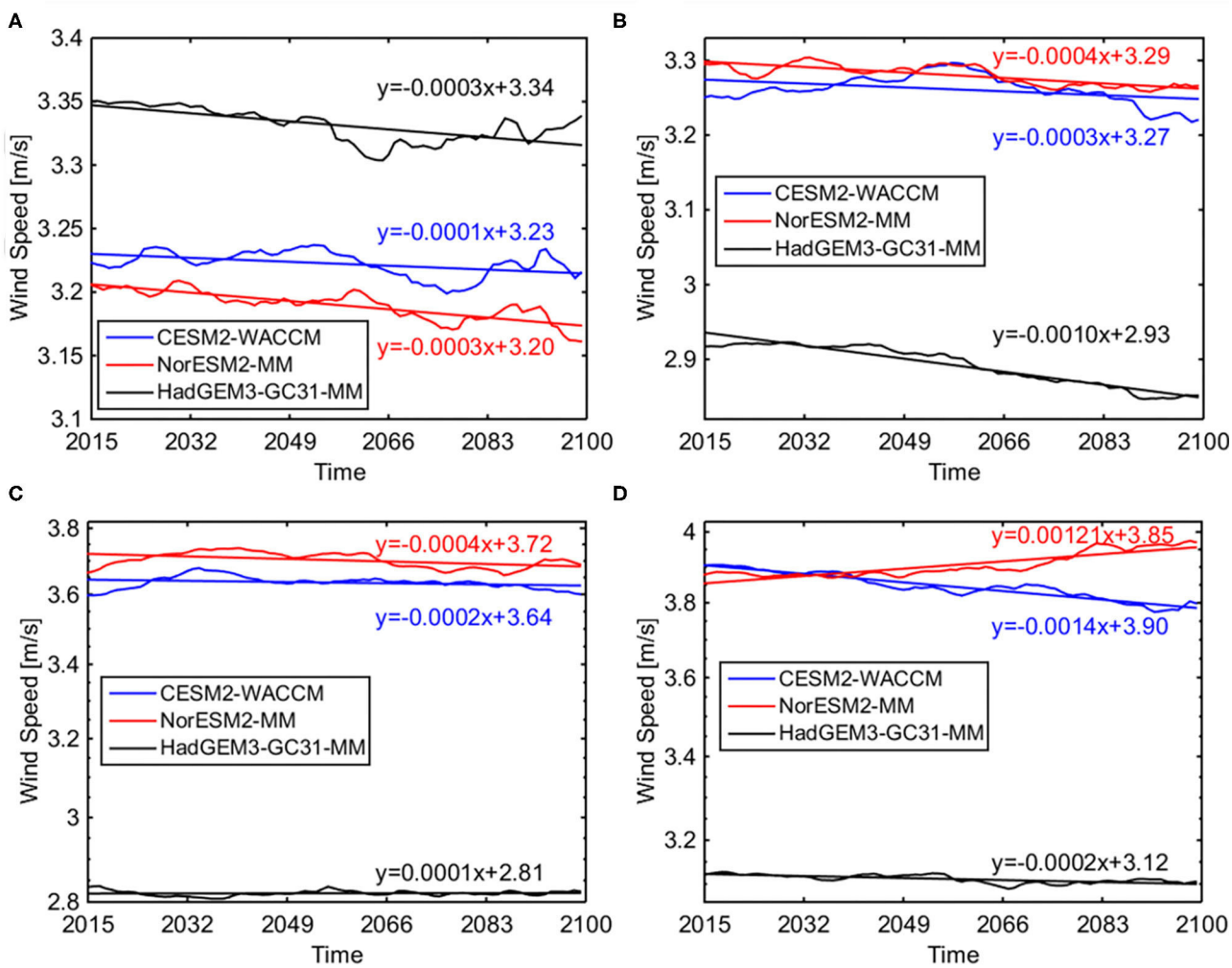

FIGURE 7 | The wind speed of ssp585 simulation in the four specific regions from CESM2-WACCM, NorESM2-MM, and HadGEM3-GC31-MM. **(A–D)** Region I, region II, region III, and region IV, respectively.

the slope of 0.0012 in region IV, which is totally different from HadGEM3-GC31-MM and CESM2-WACCM.

DISCUSSION

This study uses the ERA5 reanalysis data to evaluate the near-surface wind speed of nine global climate models in China. Spatial patterns of the nine CMIP6 models are similar with ERA5, but BCC-CSM2-MR and MRI-ESM2-0 highly overestimate the wind speed in northwest China. Focusing on four specific regions in China, nine CMIP6 models are assessed by using correlation coefficient *R* and RMSE, and CESM2-WACCM, NorESM2-MM, and HadGEM3-GC31-MM behave better than the other six CMIP6 models, which are chosen for further study. Except the yearly averaged wind speed in region II and region IV underestimated by HadGEM3-GC31-MM, three CMIP6 models tend to simulate a larger wind speed. As for the monthly change, CESM2-WACCM and NorESM2-MM simulate a large wind speed, and the value is relatively close with ERA5 in the summer. HadGEM3-GC31-MM overestimates wind speed in region I and region II from April to October, but gets closer with ERA5 during winter.

In the future, CESM2-WACCM, NorESM2-MM, and HadGEM3-GC31-MM simulate an increasing trend in the Tibetan Plateau and Xinjiang, while NorESM2-MM projects rising wind speed in the eastern part of Inner Mongolia and HadGEM3-GC31-MM simulates increasing wind speed in the northeast and central China. In region I, the future wind speed in the three models is projected to decline and the value of HadGEM3-GC31-MM is much larger. Except region I, the wind speed simulated by HadGEM3-GC31-MM is the lowest. In region II, wind speed modeled by the three models is projected to decrease, but the wind speed from HadGEM3-GC31-MM in region III and modeled wind speed in region IV from NorESM2-MM would climb with the slope equal to 0.0001 and 0.0012, respectively.

DATA AVAILABILITY STATEMENT

The CMIP6 data used in this study are archived on the website https://esgf-node.llnl.gov/projects/cmip6/ and ERA5 data can be downloaded from the website https://www.ecmwf.int/en/forecasts/datasets/reanalysis-datasets/era5.

AUTHOR CONTRIBUTIONS

LZ and SJ contributed in the visualization, methodology, writing original draft preparation. XL and BW contributed in the methodology and writing original draft preparation. ZS, JH, and YG downloaded the datasets. All authors contributed to the article and approved the submitted version.

FUNDING

The authors declare that this study received funding from Science and Technology Foundation of State Grid Corporation of China (Grant No. 5200-202016243A-0-0-00) and (Grant No. 5200-201955490A-0-0-00). The funder was not involved in the study design, collection, analysis, interpretation of data, the writing of this article, or the decision to submit it for publication.

REFERENCES

Eyring, V., Bony, S., Meehl, G., Senior, C., Stevens, B., Ronald, S., et al. (2016). Overview of the coupled model intercomparison project phase 6 (CMIP6) experimental design and organization. *Geosci. Model Dev.* 9, 1937–1958. doi: 10.5194/gmd-9-1937-2016

Hobbins, M. T. (2004). *Regional Evapotranspiration and Pan Evaporation: Complementary Interactions and Long-Term Trends Across the Conterminous United States*. [Ph.D. thesis]. Colorado State University.

IPCC (2007). "Climate Change 2007: Synthesis Report," in *Contribution of Working Groups I, II and III to the Fourth Assessment Report of the Intergovernmental Panel on Climate Change [Core Writing Team*, eds R. K, Pachauri and A. Reisinger (Geneva: IPCC). p. 104.

IRENA (2018). *Global Energy Transformation: A Roadmap to 2050*. International Renewable Energy Agency. Abu Dhabi.

Jiang, Y., Luo, Y., and Zhao, Z. (2013). Maximum wind speed changes over China. *Acta Meteorol. Sinica* 27, 63–74. doi: 10.1007/s13351-013-0107-x

Liu, F., Sun, F. B., Liu, W. B., Wang, T. T., Wang, H., Wang, X. M., et al. (2019). On wind speed pattern and energy potential in China. *Appl. Energy*. 236, 867–876. doi: 10.1016/j.apenergy.2018.12.056

McVicar, T. R., Li, L. T., Van Niel, T. G., Hutchinson, M. F., Mu, X. M., and Liu, Z. H. (2005). *Spatially Distributing 21 Years of Monthly Hydrometeorological Data in China: Spatio-Temporal Analysis of FAO 56 Crop Reference Evapotranspiration and Pan Evaporation in the Context of Climate Change*. CSIRO Land and Water Technical Report 8/05, Canberra 316.

McVicar, T. R., Roderick, M. L., Donohue, R. J., Li, L. T., Van, N. T. G., Thomas, A. G. J., et al. (2012). Global review and synthesis of trends in observed terrestrial near-surface wind speeds: implications for evaporation. *J. Hydrol.* 416–417, 182–205. doi: 10.1016/j.jhydrol.2011.10.024

McVicar, T. R., Van Niel, T. G., Li, L. T., Roderick, M. L., Rayner, D. P., Ricciardulli, L., et al. (2008). Wind speed climatology and trends for Australia, 1975-2006: capturing the stilling phenomenon and comparison with near-surface reanalysis output. *Geophys. Res. Lett.* 35:L20403. doi: 10.1029/2008GL035627

O'Neill, B. C., Kriegler, E., Ebi, K. L., Kemp-Benedict, E., Riahi, K., Rothman, D. S., et al. (2017). The roads ahead: narratives for shared socioeconomic pathways describing world futures in the 21st century. *Global Environ. Change* 42, 169–180. doi: 10.1016/j.gloenvcha.2015.01.004

O'Neill, B. C., Kriegler, E., Riahi, K., Ebi, K. L., Hallegatte, S., Carter, T. R., et al. (2014). A new scenario framework for climate change research: the concept of shared socioeconomic pathways. *Climatic Change* 122, 387–400. doi: 10.1007/s10584-013-0905-2

Pirazzoli, P. A., and Tomasin, A. (2003). Recent near-surface wind changes in the central Mediterranean and Adriatic areas. *Int. J. Climatol.* 23, 963–973. doi: 10.1002/joc.925

Pryor, S. C., Barthelmie, R. J., Young, D. T., Takle, E. S., Arritt, R. W., Flory, D., et al. (2009). Wind speed trends over the contiguous United States. *J. Geophys. Res.* 114:D14105. doi: 10.1029/2008JD011416

Tuller, S. E. (2004). Measured wind speed trends on the west coast of Canada. *Int. J. Climatol.* 24, 1359–1374. doi: 10.1002/joc.1073

Vautard, R., Cattiaux, J., Yiou, P., Thépaut, J., and Ciais, P. (2010). Northern Hemisphere atmospheric stilling partly attributed to an increase in surface roughness. *Nat. Geosci.* 3, 756–761. doi: 10.1038/ngeo979

Wan, H., Wang, X. L., and Swail, V. R. (2010). Homogenization and trend analysis of canadian near-surface wind speeds. *J. Climate* 23, 1209–1225. doi: 10.1175/2009JCLI3200.1

Wu, J., Zha, J. L., and Zhao, D. M. (2017). Evaluating the effects of land use and cover change on the decrease of surface wind speed over China in recent 30 years using a statistical downscaling method. *Climate Dynamics* 48, 131–149. doi: 10.1007/s00382-016-3065-z

Xu, C. Y., Gong, L. B., Tong, J., Chen, D. L., and Singh, V. P. (2006). Analysis of spatial distribution and temporal trend of reference ET in Changjiang catchments. *J. Hydrol.* 327, 81–93. doi: 10.1016/j.jhydrol.2005.11.029

Zhang, R. H., Zhang, S. Y., Luo, J. L., Han, Y. Y., and Zhang, J. X. (2019). Analysis of near-surface wind speed change in China during 1958-2015. *Theoretical Appl. Climatol.* 137, 2785–2801. doi: 10.1007/s00704-019-02769-0

Conflict of Interest: LZ, SJ, XL, BW, ZS, JH, and YG were employed by the China Electric Power Research Institute Co., Ltd.

Publisher's Note: All claims expressed in this article are solely those of the authors and do not necessarily represent those of their affiliated organizations, or those of the publisher, the editors and the reviewers. Any product that may be evaluated in this article, or claim that may be made by its manufacturer, is not guaranteed or endorsed by the publisher.

frontiers in Physics

ORIGINAL RESEARCH
published: 03 January 2022
doi: 10.3389/fphy.2021.665828

A Dynamic Statistical Subseasonal Forecast Model for OLR Over Tropical Pacific Region

Kuo Wang[1,2], *Gao-Feng Fan*[1] *and Guo-Lin Feng*[3]*

[1]Zhejiang Climate Center, Meteorological Bureau of Zhejiang Province, Hangzhou, China, [2]College of Atmospheric Sciences, Lanzhou University, Lanzhou, China, [3]College of Physical Science and Technology, Yangzhou University, Yangzhou, China

How to improve the subseasonal forecast skills of dynamic models has always been an important issue in atmospheric science and service. This study proposes a new dynamical-statistical forecast method and a stable components dynamic statistical forecast (STsDSF) for subseasonal outgoing long-wave radiation (OLR) over the tropical Pacific region in January-February from 2004 to 2008. Compared with 11 advanced multi-model ensemble (MME) daily forecasts, the STsDSF model was able to capture the change characteristics of OLR better when the lead time was beyond 30 days in 2005 and 2006. The average pattern correlation coefficients (PCC) of STsDSF are 0.24 and 0.16 in 2005 and 2006, while MME is 0.10 and 0.05, respectively. In addition, the average value of PCC of the STsDSF model in five years is higher than MME in 7–11 pentads. Although both the STsDSF model and MME show a similar temporal correlation coefficient (TCC) pattern over the tropical Pacific region, the STsDSF model error grows more slowly than the MME error during 8–12 pentads in January 2005. This phenomenon demonstrates that STsDSF can reduce dynamical model error in some situations. According to the comparison of subseasonal forecasts between STsDSF and MME in five years, STsDSF model skill depends strictly on the predictability of the dynamical model. The STsDSF model shows some advantages when the dynamical model could not forecast well above a certain level. In this study, the STsDSF model can be used as an effective reference for subseasonal forecast and could feasibly be used in real-time forecast business in the future.

Keywords: subseasonal forecast, dynamic-statistical method, STsDSF model, stable components, multi-model ensemble

OPEN ACCESS

Edited by:
Bai-Lian Li,
University of California, Riverside, United States

Reviewed by:
Boris Podobnik,
University of Zagreb, Croatia
Allbens Picardi Faria Atman,
Federal Center for Technological Education of Minas Gerais, Brazil

***Correspondence:**
Guo-Lin Feng
fenggl@cma.gov.cn

Specialty section:
This article was submitted to Interdisciplinary Physics, a section of the journal Frontiers in Physics

Received: *09 February 2021*
Accepted: *25 November 2021*
Published: *03 January 2022*

Citation:
Wang K, Fan G-F and Feng G-L (2022) A Dynamic Statistical Subseasonal Forecast Model for OLR Over Tropical Pacific Region. Front. Phys. 9:665828. doi: 10.3389/fphy.2021.665828

INTRODUCTION

The atmosphere is a complex nonlinear giant system with external forcings and internal dissipations. Under the impact of external forcing factors, such as the sun, ocean, land, and human activities, a series of physical and chemical changes and interactions occur in the atmosphere, which brings great difficulties to weather and climate prediction [1–3]. A small error can be dramatically amplified over time, which allows for a predictable limit on the weather forecast. Moreover, some studies suggest that the chaotic effects could prove the predictable limits of weather systems in theoretical ways [4, 5]. It is now accepted that the upper limit on the predictability of actual weather systems is approximately 2 weeks [6, 7]. However, studies have shown that the predictability of some large-scale components is significantly higher than that of small-scale components, which could be more

than 2 weeks [8, 9]. At the same time, some low frequency weather systems with a duration of more than 2 weeks were found in the observations.

Based on the theory of predictability, the prediction error of dynamic models mainly results from the following aspects: the initial error of observation data, the error caused by the set scheme in the dynamic model simulation, and the systematic error of the model in the single variable simulation [10]. The initial error of the observation data is mainly caused by the inaccuracy of the observation value and the uneven distribution of observation stations. The error of set scheme in dynamic mode simulations is mainly caused by the numerical set in order to deduct the random error. The systematic error of the single variable simulation is mainly caused by the performance of the model itself, such as the model resolution, parameterization scheme for the physical processes, and the calculations of the discrete numerical difference scheme [11–13]. The reasons described above limit the forecast accuracy of dynamic models and are the main obstacles to the further improvement of the subseasonal forecast.

Given the shortcomings of error growth theory based on the linear framework, Chen *et al.* and Ding *et al.* developed a new theory of nonlinear error growth to measure the predictability of atmosphere and the nonlinear local Lyapunov exponent (NLLE), revealing the temporal and spatial distribution of the predictable duration in different weather and climate variables [14, 15]. Theoretical studies show that climate variables are composed of climate signals and noises, and climate signal is mainly affected by the external boundary conditions of the climate system [16, 17]. For example, the heat capacity of subsurface water during an El Niño event can significantly enhance the East Pacific tropical cyclone [18]. When the proportion of climate signals in variables is large enough to overcome the destructive effects of noises, climate anomalies may show a certain degree of predictability [19]. Observational studies show that there are some slow changing processes in atmospheric evolution above the level of weather noises, these slow changing processes are associated with large-scale atmospheric motions and a timescale of several weeks, which is much longer than that estimated by nonlinear hydrodynamics [20–22]. There are still some predictable meteorological characteristics in the subseasonal time scale, and the atmospheric stable component can be robustly predicted [23, 24].

Although the development of extended period forecast skills is remarkable, its technical difficulty can not be covered up. On the one hand, it is difficult to use commonly used methods to predict the intensity and duration of the weather process objectively. On the other hand, the ability of the daily weather forecast depends on the increase of initial error by chaotic motion in the atmosphere [25, 26]. According to the chaotic characteristics of the atmospheric system, Chou *et al.* expounded the extraction method of the predictable components in the 10–30 days extended period, and further suggest that different strategies and methods should be adopted for predictable components and random components [27]. However, if each time step needs to be checked in the actual forecast process, the computation expenses will be very large. Ren *et al.* proposed a similar evolution method, assuming that similar initial conditions have similar prediction errors in the allowable time range [28]. By synthesizing and analyzing the prediction errors of historical similar initial conditions, the current prediction errors are estimated. The calculations are greatly simplified and more easily incorporated into numerical prediction models. Zheng *et al.* discussed the properties of predictable components in the extension period and their application in numerical models [29].

Based on predictable components theory, the model subseasonal forecasts can be divided into two parts: the predictable component and the random component. The numerical model error can also be reduced in the process of integration by using historical observation data. Therefore, it is obvious that the method exists on model dependence. For different numerical models, the model performance is different, and the definition and extraction of predictable components are different too. Focusing on the prediction of weather or climate at different time and spatial scales, the stable components should be especially investigated. To improve subseasonal process diagnosis and prediction skills, it is important to grasp the main characteristics of the subseasonal stable component [30, 31]. Under the same initial and exogenous forcing characteristics, the atmospheric system with a large-space time scale is more predictable. Therefore, it is necessary to distinguish the stable components from atmospheric circulation on a subseasonal scale and analyze the properties and improve subseasonal prediction skills by using stable components [32, 33]. Moreover, because the extraction method of stable components is based on historical observation data instead of model data, it can overcome the shortcoming of model dependence.

Subseasonal precipitation prediction is one of the most important aspects of weather forecasting [34, 35]. The tropical area accounts for about half of the total global area, of which the ocean accounts for about 3/4. The solar radiation energy received in the tropical area is much more than that be reflected into space, which makes the tropical ocean a vital energy source for global atmospheric circulation movement [36, 37]. In addition, the tropical ocean is one of the most important water vapor sources for the global atmosphere [38, 39]. Due to the abundant water vapor contents in tropical marine areas, precipitation generation is closely related to atmospheric vertical convection intensity. The intensity of precipitation can be characterized by OLR in the tropics. If the subseasonal variability of OLR can be forecasted well, the tropical precipitation forecast skills will be robust [40, 41]. Therefore, this study mainly uses a dynamic statistical forecast model (STsDSF) to improve the subseasonal forecast skills of 11 advanced multi-model ensembles for OLR over the tropical Pacific region (140°E-100°W, 30°S-30°N) and discusses the predictability of STsDSF in January and February from 2004 to 2008. It proposes a new application of the dynamic-statistical method in subseasonal forecast.

DATA AND METHODOLOGY

The daily OLR data was published by the National Oceanic and Atmospheric Administration (NOAA) over the period from 1979

to 2008 with a horizontal resolution of 2.5° × 2.5° [42]. The external boundary conditional forcing of sea surface temperature (SST) is represented by Oceanic Niño Index (Niño 3.4), which is also published by NOAA.

The hindcast data of the dynamical model is from Intraseasonal Variability Hindcast Experiment (ISVHE), which is jointly supported by the Asian Pacific Climate Center (APCC), NOAA, Climate Variability and Predictability (CLIVAR) Asian-Australian Monsoon Panel, and some other organizations [43]. The model products of ISVHE have been studied at the predictability of intraseasonal variability as a whole [44, 45]. In total, ten one-tier hindcasts and one two-tier hindcast from ISVHE were used in this study, including the Australian Bureau of Meteorology (AOBM) coupled model, the coupled model of Euro-Mediterranean Center on Climate Change (CMCC), the European Centre for Medium-Range Weather Forecasts (ECMWF) model, the Geophysical Fluid Dynamics Laboratory (GFDL) model, the Japan Meteorological Agency (JMA) coupled model, the Japan Agency for Marine-Earth Science and Technology (JAMSTEC) model, the NCEP/Climate Prediction Center (CPC) coupled model, the Pusan National University (PNU) model, the Seoul National University (SNU) coupled model, University of Hawaii (UH)/International Pacific Research Center (IPRC) model, and the European Centre (EC) model [46–51]. The details of the model data and operation scheme are briefly shown in **Table 1**. Because the skill of MME is better than that of any single model in seasonal forecasting [52, 53], the improvement of STsDSF is mainly based on the MME forecast. In this study, five daily OLR forecast cases were selected. The start time of each was January 1 every year from 2004 to 2008.

STsDSF is a hybrid dynamical-statistical method for subseasonal prediction, which consists of four steps 1) distinguish the stable components from climatic state vector by training daily contribution rate of variance and persist time 2) divide the dynamical model output into predictable components and random components by projection 3) forecast predictable components in dynamical simulation and forecast random components in statistical estimation 4) make ensemble predictands for dynamical simulation and statistical estimation. **Figure 1** is the schematic diagram of the STsDSF model, and the details of the STsDSF model have been introduced in [32, 33]. In this study, the Niño 3.4 index is considered as a similarity criterion that represents the external boundary conditions of tropical SST, and three similar years chosen for statistical estimation in the STsDSF model from 1979 to 2003.

In this study, the subseasonal forecast skill of OLR is measured by PCC and TCC. The PCC formula is expressed as follows:

$$PCC = \frac{\sum_{i=1}^{n}\left(X_f - X_c - M_{f,c}\right)_i \left(X_v - X_c - M_{v,c}\right)_i \cos\phi_i}{\sqrt{\sum_{i=1}^{n}\left(X_f - X_c - M_{f,c}\right)_i^2 \cos\phi_i} \bullet \sqrt{\sum_{i=1}^{n}\left(X_v - X_c - M_{v,c}\right)_i^2 \cos\phi_i}} \quad (1)$$

where X_f, X_v, and X_c are the predicted value, observed value, and climate mean, respectively; $M_{f,c}$ and $M_{v,c}$ represent the deviation means of X_f and X_v from X_c, respectively; n represents the number of grids in the chosen area, and $\cos\varphi_i$ is the latitude of grid i.

The TCC formula is expressed as follows:

$$TCC = \frac{\sum_{t=1}^{n}\left(X_f - \bar{X}_f\right)_t \left(X_v - \bar{X}_v\right)_t}{\sqrt{\sum_{t=1}^{n}\left(X_f - \bar{X}_f\right)_t^2} \bullet \sum_{t=1}^{n}\left(X_v - \bar{X}_v\right)_t^2} \quad (2)$$

where X_f and X_v are the predicted value and observed value; $\bar{X}_f$ and $\bar{X}_v$ represent the means of X_f and X_v, respectively; and n represents the number of times. Every grid TCC is calculated by **formula (2)**.

SUBSEASONAL FORECAST SKILL OF MME AND STSDSF MODEL

For subseasonal forecast products, the development trend is more reliable than daily outputs [54, 55]. In this study, five-day mean PCCs for both MME and STsDSF are calculated as 12 pentads. The comparison between MME PCC and STsDSF PCC shows that the trend of STsDSF is similar to MME. However, the variance of MME PCC is greater than STsDSF PCC. For example, MME PCC ranges from 0.80 to -0.18, while STsDSF PCC ranges from 0.36 to -0.15 in 2004 (**Figure 2A**). The reason

TABLE 1 | One-Tier and Two-Tier System description of models and experiments.

	Model	Control	ISO hindcast		
		Run	Period	Ens No	Initial condition
ABOM	POAMA 1.5 & 2.4 (ACOM2+BAM3)	CMIP (100years)	2004–2008	10	The first day of every month
CMCC	CMCC (ECHAM5+OPA8.2)	CMIP (20years)	2004–2008	5	Every 10 days
ECMWF	ECMWF (IFS + HOPE)	CMIP (11yeaear)	2004–2008	15	Every 15 days
GFDL	CM2 (AM2/LM2+MOM4)	CMIP (50years)	2004–2008	10	The first day of every month
JMA	JMA CGCM	CMIP (20years)	2004–2008	6	Every 15 days
JAMSTEC	SINTEX-F	CMIP (20years)	2004–2008	9	The first day of every month
NCEP/CPC	CFS v1 (GFS + MOM3) and v2	CMIP (100years)	2004–2008	5	Every 10 days
PNU	CFS with RAS scheme	CMIP (13years)	2004–2008	3	The first day of each month
SNU	SNU CM (SNUAGCM + MOM3)	CMIP (20years)	2004–2008	1	Every 10 days
UH/IPRC	UH HCM	CMIP (20years)	2004–2008	6	Every 10 days
EC	GEM	AMIP (21years)	2004–2008	10	Every 10 days

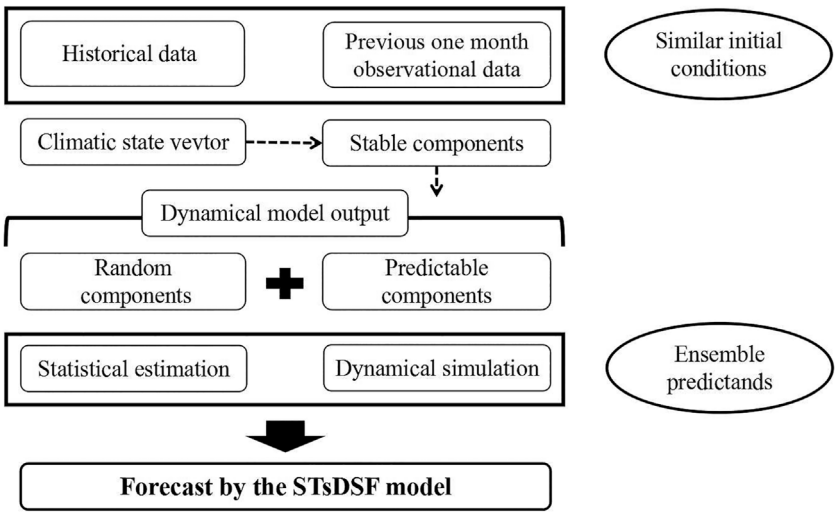

FIGURE 1 | Schematic diagram of the STsDSF model.

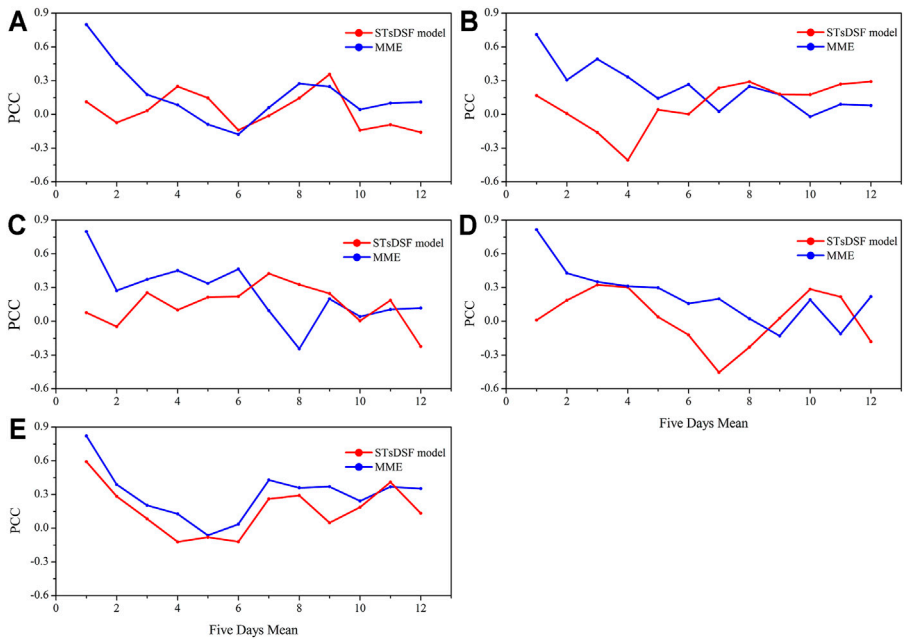

FIGURE 2 | PCC of STsDSF model and MME for OLR subseasonal forecasting over the tropical Pacific region during 2004–2008: **(A)** 2004; **(B)** 2005; **(C)** 2006; **(D)** 2007; **(E)** 2008. Red line is STsDSF model and blue line is MME.

for this is that MME is effective at simulating OLR at the start time, but the accuracy drops quickly over time. According to five OLR subseasonal forecasting cases from 2004 to 2008 (**Figure 2**), the PCC of STsDSF was higher than that of MME when the lead time was beyond 6 pentads.

During 7–12 pentads, the average value PCC of STsDSF is 0.24 and 0.16 in 2005 and 2006, verses 0.10 and 0.05 from MME, respectively. For instance, the PCC of STsDSF is higher than that of MME during 7–12 pentads in 2005 and 7–11 pentads in 2006 (**Figures 2B,C**). In 2007, the PCC of STsDSF is higher than that of MME in 9–11 pentads (**Figure 2D**), while the forecasting skill of STsDSF is worse than MME in 2008 (**Figure 2E**). The possible reason may be attributed to the PCC of the MME forecast being very accurate compared to other cases, which means MME PCC drop slowly over time, and there is no capacity for improvement by STsDSF in 2008. The OLR forecast skill of STsDSF depends on the performance of the model simulation. If the model can reasonably capture the

climatic patterns on a subseasonal scale, the forecast skill of STsDSF will be reduced.

Different from 1–6, the STsDSF model shows some advantages in 7–12 pentads. The five-year mean PCC of the STsDSF model is compared with MME for OLR in 7–12 pentads in **Figure 3**. The PCC of the STsDSF model ranges from -0.03 to 0.20, and the PCC of MME ranges from 0.10 to 0.18. Besides 12 pentads, the STsDSF model is more skillful than MME in 7–11 pentads. Therefore, the numerical simulation for the five consecutive year average also agrees with the conclusion above. Only when the skill of MME reduces to a certain level, the improvement of MME by STsDSF can show some advantages.

The standard deviation of STsDSF PCC is less than that of MME PCC (**Figure 3**), which indicates that the STsDSF model is more stable. The reason is that the principle of the STsDSF model is to distinguish model predictable information based on climate state and to replace random information with climate analogue. For the subseasonal OLR forecast over tropical Pacific region after 30 days, statistical methods still have the potential to surpass the dynamic model. To further investigate the STsDSF model performance in subseasonal time scale pentad by pentad, in the next section of the article, a case study from 2005 is presented to analyze the characteristics of OLR forecast error over the Pacific region.

SUBSEASONAL FORECAST OF STSDSF MODEL AND MME IN 2005

In this section, a forecast case covering January-February 2005 is selected as an example for specific analysis. TCC is a common way to investigate the predictability distribution. The TCC of the STsDSF model and MME is shown in **Figure 4**. The red area indicates that the forecasting skill is high, and the blue area indicates that the forecasting skill is low. As shown in **Figure 4B**, MME forecasts well in most tropical regions, with TCC exceeding 0.993. Only in two meridional zonal regions (180° and 120°W), the TCC is lower than 0.989 and the distribution patterns of the two regions are very similar. The corresponding TCC of the STsDSF model in **Figure 4A** shows that the overall distribution pattern is the same as that of MME, and the values are close. However, the TCC of the STsDSF model is more complete and more continuous in the blue areas, and the TCC of MME is more dispersed. Comparing **Figure 4A** with **Figure 4B**, the overall forecast skill pattern has no great change in the subseasonal period, and the distribution characteristics of MME are retained in the STsDSF model.

The variation of MME forecast error for OLR in January-February 2005 is exhibited pentad by pentad (**Figure 5**). MME can capture the movement of OLR very well in pentad 1 (**Figure 5A**). During pentad two to five, the forecast error increases to 60 W/m^2, and the discrete anomaly is mainly distributed in the southwest and northeast of the tropical Pacific (**Figures 5A–E**). During pentads 8–12, the forecast error increases to 80 W/m^2, and the error region are complete and continuous. Overall, MME forecast error is mainly negative anomalous, and the skill is poor over southwest and northeast of the tropical Pacific. MME can capture the patterns of OLR over the tropical Pacific in the beginning, and the error grows gradually over time, which is consistent with the PCC changes in the above analysis (**Figure 2**).

Different from the error distribution of MME for OLR subseasonal forecasts, the forecast error of the STsDSF model shows larger negative anomalies in 1–4 pentads (**Figures 6A–D**).

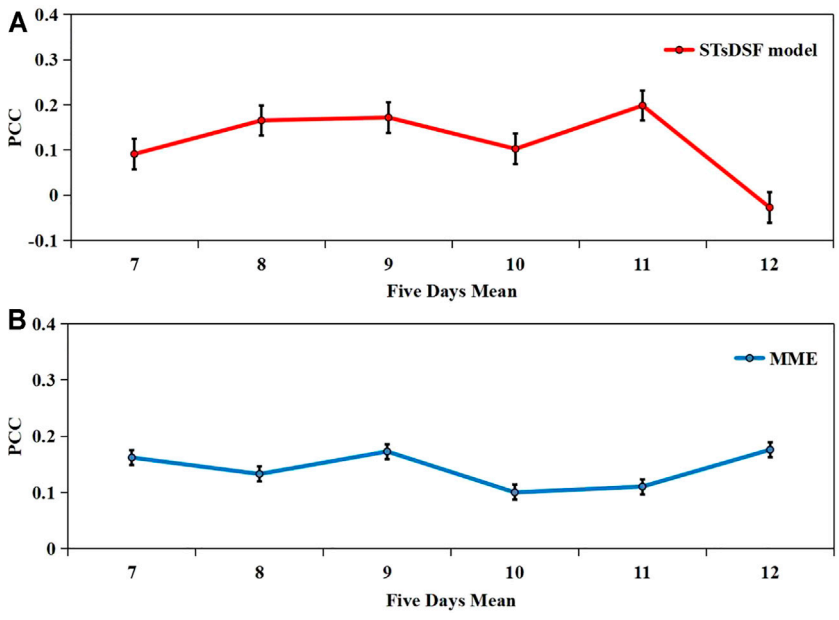

FIGURE 3 | Five-year mean PCC of **(A)** STsDSF model and **(B)** MME for OLR subseasonal forecasting over the tropical Pacific region in 7–12 pentads. The standard deviation is marked as a vertical black line.

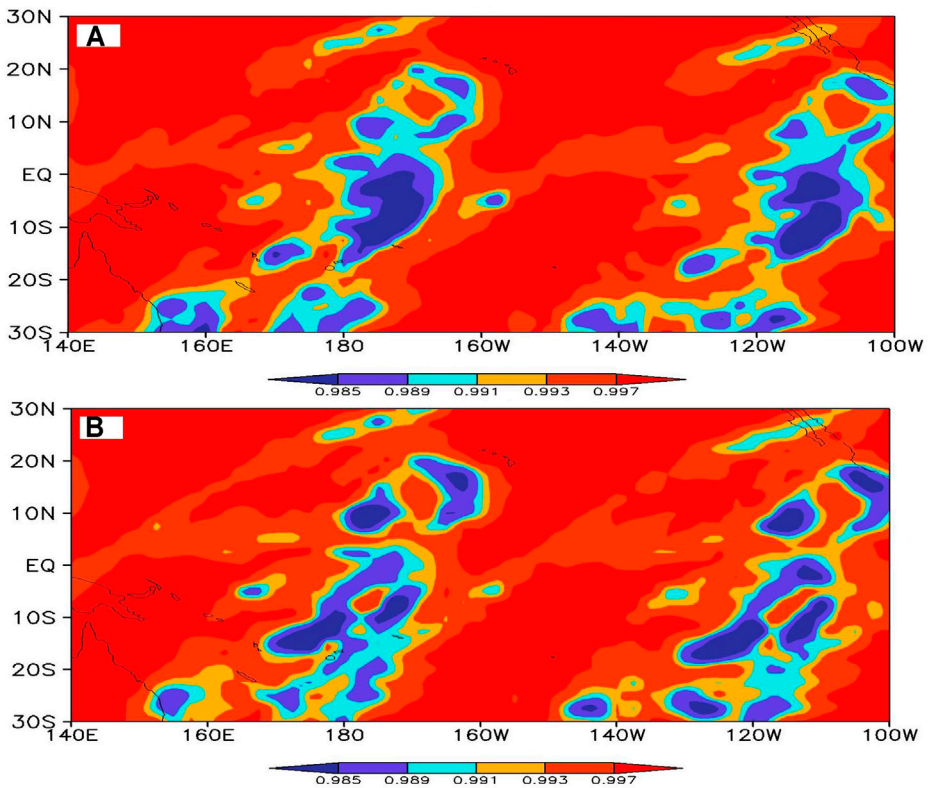

FIGURE 4 | TCC of **(A)** STsDSF model and **(B)** MME for OLR subseasonal forecasting over tropical Pacific region.

The error is smaller in equatorial and larger in the higher latitudes over the Pacific. In addition, the pattern and intensity of STsDSF model error change little during 5–12 pentads (**Figure 6E–l**). Based on the diagnosis of OLR subseasonal forecast skill of STsDSF model and MME in January-February 2005, although STsDSF model error is larger than MME at the beginning, it grows slowly and shows some advantages in 8–12 pentad (**Figure 6H–l**).

DISCUSSION AND SUMMARY

The predictability of atmospheric stable component mainly comes from three aspects: outer boundary condition forcing, a continuous component of low frequency wave, and atmospheric periodic component. Furthermore, these atmospheric components are statistically regular [56, 57]. In this study, a new method called the STsDSF model is proposed, to improve the subseasonal dynamic model for OLR over the tropical Pacific region in January-February from 2004 to 2008. We compare subseasonal forecast skills of the STsDSF model and MME of 11 advanced models and analyze the growth characteristics of subseasonal forecast error.

The conclusions of this study reveal that the performance of the STsDSF model is largely determined by the forecasting skill of the dynamical model. The STsDSF model only provides additional improvement information when the dynamical model output incredible data. According to five OLR subseasonal forecasting cases from 2004 to 2008, the PCC of STsDSF will be higher than that of MME when the lead time is beyond 6 pentads. These results demonstrate that the STsDSF model can be used as an important reference for subseasonal forecasting after 30 days. The numerically simulated results for five consecutive years on average have a good agreement with the above discussion.

Moreover, the overall OLR TCC pattern of the STsDSF model is similar to that of MME, and the TCC values are close over the tropical Pacific. The change characteristics of MME are retained in the STsDSF model in time scale, as well as in the space scale. In addition, by comparing the subseasonal forecast error pentad by pentad, the error of the STsDSF model grows more slowly than that of the MME model in 12 pentads.

The STsDSF model only uses the initial condition and historical observation data to improve the subseasonal dynamical model and could feasibly be incorporated into existing business real-time forecast products. However, further studies are still needed. For example, we focus on the subseasonal forecast over tropical Pacific OLR in January-February 2004–2008. Further investigations of the STsDSF model, considering different meteorological elements, periods, and regions, needs more modeling studies. In this study, the similarity criterion of selecting historical data is Niño 3.4, considered as an important external boundary forcing signal.

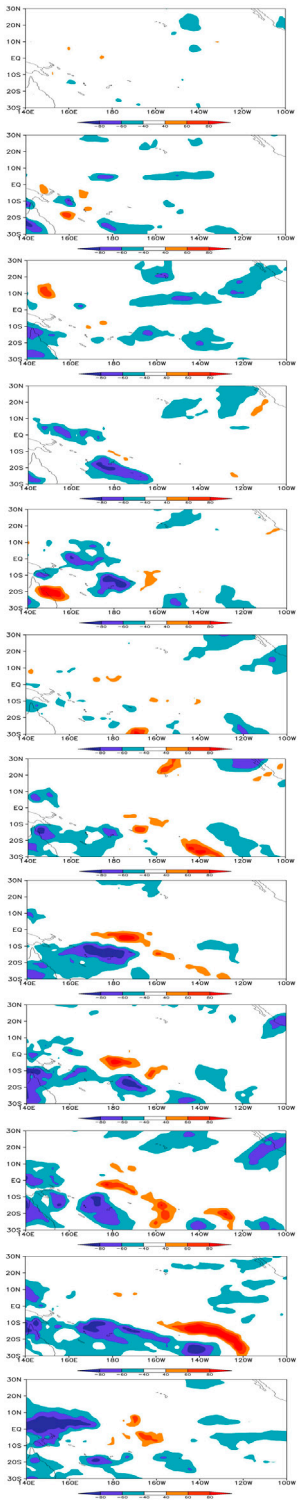

FIGURE 5 | The error distribution of MME for OLR subseasonal forecasts over the tropical Pacific region in 1**(A)**–12**(L)** pentad. (Unit: W/m^2).

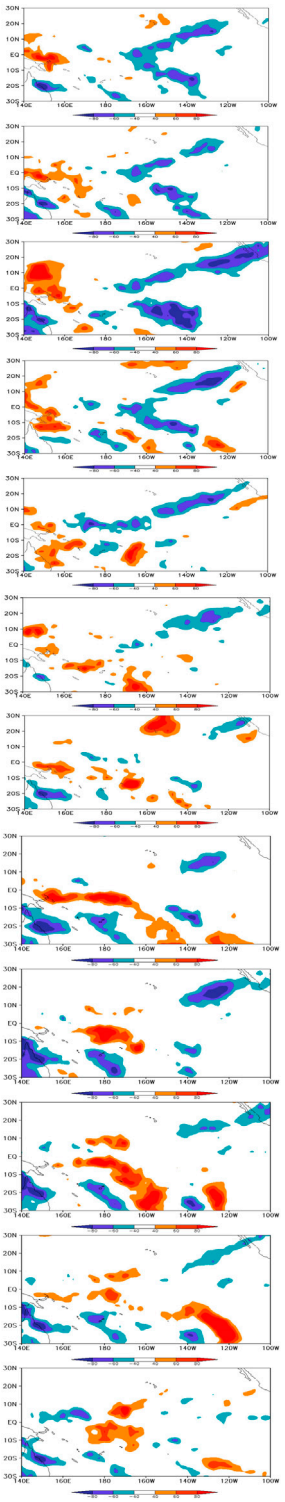

FIGURE 6 | The error distribution of STsDSF model for OLR subseasonal forecasts over tropical Pacific region in 1**(A)**–12**(L)** pentad. (Unit: W/m^2).

However, Niño 3.4 is a Pacific index and can not stand for all SST forcings [58, 59]. Therefore, a more comprehensive index considering different weights for different ocean forcings could be developed. In addition, when we analyze the subseasonal forecast skill of the STsDSF model, considering El Niño-Southern Oscillation (ENSO) cycle in interannual timescale, the relationship between subseasonal forecast skill and ENSO cycle is intriguing, a new story which could be further discussed in the future.

The hindcast skill of ISVHE performs better than the business model, so it needs to be further verified whether the improvement effect of the STsDSF model is different for the dynamical model forecasts with different forecasting skills. Moreover, due to the limitation of the time span of dynamical model data, we only select cases of five consecutive years for comparative analysis. Therefore, more simulation experiments are needed in further studies.

DATA AVAILABILITY STATEMENT

The raw data supporting the conclusions of this article will be made available by the authors, without undue reservation.

AUTHOR CONTRIBUTIONS

KW and G-LF designed the research. KW performed analysis. Both KW, G-FF and G-LF contributed to the writing of the paper.

FUNDING

This work was supported by the National Key R&D Program of China (2017YFC1502303), the Basic Public Welfare Project of Zhejiang Province (LGF22D050001), the Natural Science Foundation of China (41605049, 42005027), the Key R&D Program of Zhejiang Province (2021C02036), the Natural Science Foundation of Zhejiang Province (LQ20D050003), the Fund for Meteorological Science and Technology of Zhejiang Province, China (2021ZD08, 2019ZD07), and the Hangzhou Agricultural and Social Development Scientific Research Project (20201203B155).

ACKNOWLEDGMENTS

The ISVHE model data was sorted out by Dr. Song-Sun Lee in International Pacific Research Center (IPRC).

REFERENCES

1. Charney JG, Fleagle RG, Lally VE, Riehl H, Wark DQ. The Feasibility of a Global Observation and Analysis experiment. *Bull Amer Meteorol Soc.* (1966) 47:200. doi:10.1175/1520-0477-47.3.200
2. Simmons AJ, Hollingsworth A. Some Aspects of the Improvement in Skill of Numerical Weather Prediction. *Q J R Meteorol Soc* (2002) 128:647–77. doi:10.1256/003590002321042135
3. Kalnay E, Lord SJ, Mcpherson RD. Maturity of Operational Numerical Weather Prediction: Medium Range. *Bull Amer Meteorol Soc.* (1998) 79: 2753–69. doi:10.1175/1520-0477(1998)079<2753:moonwp>2.0.co;2
4. Lorenz EN. A Study of the Predictability of a 28-variable Atmospheric Model. *Tellus* (1965) 17:321–33. doi:10.3402/tellusa.v17i3.9076
5. Lorenz EN. Atmospheric Predictability as Revealed by Naturally Occurring Analogues. *J Atmos Sci* (1969) 26:636–46. doi:10.1175/1520-0469(1969)26<636:aparbn>2.0.co;2
6. Dalcher A, Kalnay E. Error Growth and Predictability in Operational ECMWF Forecasts. *Tellus* (1987) 39A:474–91. doi:10.1111/j.1600-0870.1987.tb00322.x
7. Li J, Ding R. Temporal-Spatial Distribution of Atmospheric Predictability Limit by Local Dynamical Analogs. *Mon Wea Rev* (2011) 139:3265–83. doi:10.1175/mwr-d-10-05020.1
8. Shukla J. Dynamical Predictability of Monthly Means. *J Atmos Sci* (1981) 38: 2547–72. doi:10.1175/1520-0469(1981)038<2547:dpomm>2.0.co;2
9. Shukla J. Predictability in the Midst of Chaos: A Scientific Basis for Climate Forecasting. *Science* (1998) 282:728–31. doi:10.1126/science.282.5389.728
10. Kumar A, Jha B, Zhang Q, Bounoua L. A New Methodology for Estimating the Unpredictable Component of Seasonal Atmospheric Variability. *J Clim* (2007) 20(15):3888–901. doi:10.1175/jcli4216.1
11. Huang JP, Yi YH, Wang SW, Chou JF. An Analogue-Dynamical Long-Range Numerical Weather Prediction System Incorporating Historical Evolution. *Quart J Roy Meteorol Soc.* (1993) 119(511):547. doi:10.1002/qj.49711951111
12. Wang B, Lee J-Y, Kang I-S, Shukla J, Park C-K, Kumar A, et al. Advance and Prospectus of Seasonal Prediction: Assessment of the APCC/CliPAS 14-model Ensemble Retrospective Seasonal Prediction (1980-2004). *Clim Dyn* (2009) 33(1):93–117. doi:10.1007/s00382-008-0460-0
13. Xue H-L, Shen X-S, Chou J-F. A Forecast Error Correction Method in Numerical Weather Prediction by Using Recent Multiple-Time Evolution Data. *Adv Atmos Sci* (2013) 30(5):1249–59. doi:10.1007/s00376-013-2274-1
14. Chen B, Li J, Ding R. Nonlinear Local Lyapunov Exponent and Atmospheric Predictability Research. *Sci China Ser D* (2006) 49(10):1111–20. doi:10.1007/s11430-006-1111-0
15. Ding R, Li J. Nonlinear Finite-Time Lyapunov Exponent and Predictability. *Phys Lett A* (2007) 364(5):396–400. doi:10.1016/j.physleta.2006.11.094
16. Horel JD, Wallace JM. Planetary-Scale Atmospheric Phenomena Associated with the Southern Oscillation. *Mon Wea Rev* (1981) 109(4):813–29. doi:10.1175/1520-0493(1981)109<0813:psapaw>2.0.co;2
17. Hoskins BJ, Karoly DJ. The Steady Linear Response of a Spherical Atmosphere to thermal and Orographic Forcing. *J Atmos Sci* (1981) 38(6):1179–96. doi:10.1175/1520-0469(1981)038<1179:tslroa>2.0.co;2
18. Jin F-F, Boucharel J, Lin I-I. Eastern Pacific Tropical Cyclones Intensified by El Niño Delivery of Subsurface Ocean Heat. *Nature* (2014) 516(7529):82–5. doi:10.1038/nature13958
19. Chen WY, Van den Dool HM. Atmospheric Predictability of Seasonal, Annual, and Decadal Climate Means and the Role of the ENSO Cycle: A Model Study. *J Clim* (1996) 10(6):1236. doi:10.1175/1520-0442(1997)010<1236:aposaa>2.0.co;2
20. Li C, Pan J. Atmospheric Circulation Characteristics Associated with the Onset of Asian Summer Monsoon. *Adv Atmos Sci* (2006) 23(6):925–39. doi:10.1007/s00376-006-0925-1
21. Li T. Recent advance in Understanding the Dynamics of the Madden-Julian Oscillation. *Acta Meteorol Sin* (2014) 28(1):1–33. doi:10.1007/s13351-014-3087-6
22. Wang K, Ma H, Li J, Gu BH, Wu H. Assessment of the POEM2 Model for Simulating Tropical Intraseasonal Oscillation. *J Trop Meteorol* (2018) 24(3): 323. doi:10.16555/j.1006-8775.2018.03.006
23. Blackmon ML, Geisler JE, Pitcher EJ. A General Circulation Model Study of January Climate Anomaly Patterns Associated with Interannual Variation of Equatorial Pacific Sea Surface Temperatures. *J Atmos Sci* (1983) 40(6): 1410–25. doi:10.1175/1520-0469(1983)040<1410:agcmso>2.0.co;2
24. DelSole T, Tippett MK. Predictable Components and Singular Vectors. *J Atmos Sci* (2008) 65(5):1666–78. doi:10.1175/2007jas2401.1

25. Weber NJ, Mass CF. Subseasonal Weather Prediction in a Global Convection-Permitting Model. *Bull Amer Meteorol Soc.* (2019) 100(6):1079–89. doi:10.1175/bams-d-18-0210.1
26. Zhou T, Zou L. Understanding the Predictability of East Asian Summer Monsoon from the Reproduction of Land-Sea Thermal Contrast Change in AMIP-type Simulation. *J Clim* (2010) 23(22):6009–26. doi:10.1175/2010jcli3546.1
27. Chou JF, Zheng ZH, Sun SP. The Think about 10~30 D Extendedrange Numerical Weather Prediction Strategy-Facing the Atmosphere Chaos. *Scientia Meteorologica Sinica (Qixiang Kexue)* (2010) 30(5):569, 2010 . (in Chinese).
28. Ren H, Chou J, Huang J, Zhang P. Theoretical Basis and Application of an Analogue-Dynamical Model in the Lorenz System. *Adv Atmos Sci* (2009) 26(1):67–77. doi:10.1007/s00376-009-0067-3
29. Zheng Z, Huang J, Feng G, Chou J. Forecast Scheme and Strategy for Extended-Range Predictable Components. *Sci China Earth Sci* (2012) 56: 878–89. doi:10.1007/s11430-012-4513-1
30. Ren F, Ding C, Zhang D-L, Chen D, Ren H-l., Qiu W. A Dynamical-Statistical-Analog Ensemble Forecast Model: Theory and an Application to Heavy Rainfall Forecasts of Landfalling Tropical Cyclones. *Mon Wea Rev* (2020) 148:1503–17. doi:10.1175/mwr-d-19-0174.1
31. Wang K, Feng G-L, Zeng Y-X, Wang X-J. Analysis of Stable Components in the Extended-Range Forecast for the Coming 10-30 Days in winter 2010 and 2011. *Chin Phys. B* (2013) 22:129202. doi:10.1088/1674-1056/22/12/129202
32. Feng G, Sun S, Zhao J, Zheng Z. Analysis of Stable Components for Extended-Range (10-30 Days) Weather Forecast: A Case Study of Continuous Overcast-Rainy Process in Early 2009 over the Mid-lower Reaches of the Yangtze River. *Sci China Earth Sci* (2013) 56:1576–87. doi:10.1007/s11430-012-4527-8
33. Wang K, Feng GL, Zeng YX, Li ZQ. Extraction of 10-30-day Stable Components from a Boreal Atmosphere during ENSO Phases. *Discrete Dyn Nat Soc* (2015) 2015 919286. doi:10.1155/2015/919286
34. Vitart F, Ardilouze C, Bonet A, Brookshaw A, Chen M, Codorean C, et al. The Subseasonal to Seasonal (S2S) Prediction Project Database. *Bull Amer Meteorol Soc.* (2017) 98(1):163–73. doi:10.1175/bams-d-16-0017.1
35. Zhu ZW, Li T. Extended-range Forecasting of Chinese Summer Surface Air Temperature and Heat Waves. *Clim Dyn* (2017) 50:1. doi:10.1007/s00382-017-3733-7
36. Zheng Z, Hu Z-Z, L'Heureux M. Predictable Components of ENSO Evolution in Real-Time Multi-Model Predictions. *Sci Rep* (2016) 6:35909. doi:10.1038/srep35909
37. Wang K, Zhang H, Fan G-F, Li Z-Q, Yu Z-Y, Liu P-P. Simulated Variation Characteristics of Oceanic CO2 Uptake, Surface Temperature, and Acidification in Zhejiang Province, China. *Front Phys* (2021) 9:718968. doi:10.3389/fphy.2021.718968
38. Wu Y-P, Shen Y-P, Larry Li B. Possible Physical Mechanism of Water Vapor Transport over Tarim River Basin. *Ecol Complexity* (2012) 9:63–70. doi:10.1016/j.ecocom.2011.12.002
39. Han ZX, Su T, Zhang Q, Wen Q, Feng GL. Thermodynamic and Dynamic Effects of Increased Moisture Sources over the Tropical Indian Ocean in Recent Decades. *Clim Dyn* (2019) 53(9):7081. doi:10.1007/s00382-019-04977-w
40. Weaver SJ, Wang W, Chen M, Kumar A. Representation of MJO Variability in the NCEP Climate Forecast System. *J Clim* (2011) 24:4676–94. doi:10.1175/2011jcli4188.1
41. Liu F, Wang B. A Frictional Skeleton Model for the Madden-Julian Oscillation*. *J Atmos Sci* (2012) 69:2749–58. doi:10.1175/jas-d-12-020.1
42. Chelliah M, Arkin P. Large-Scale Interannual Variability of Monthly Outgoing Longwave Radiation Anomalies over the Global Tropics. *J. Clim.* (1992) 5(4): 371–89. doi:10.1175/1520-0442(1992)005<0371:LSIVOM>2.0.CO;2
43. Neena JM, Lee JY, Waliser D, Wang B, Jiang X. Predictability of the Madden-Julian Oscillation in the Intraseasonal Variability Hindcast Experiment (ISVHE)*. *J Clim* (2014) 27(12):4531–43. doi:10.1175/jcli-d-13-00624.1
44. Neena JM, Jiang X, Waliser D, Lee J-Y, Wang B. Eastern Pacific Intraseasonal Variability: a Predictability Perspective. *J Clim* (2014) 27(23):8869–83. doi:10.1175/jcli-d-14-00336.1
45. Lee SS, Wang B. Regional Boreal Summer Intraseasonal Oscillation over Indian Ocean and Western Pacific: Comparison and Predictability Study. *Clim Dyn* (2016) 46(7-8):2213. doi:10.1007/s00382-015-2698-7
46. Cottrill A, Hendon HH, Lim E-P, Langford S, Shelton K, Charles A, et al. Seasonal Forecasting in the Pacific Using the Coupled Model POAMA-2. *Wea Forecast* (2013) 28:668–80. doi:10.1175/waf-d-12-00072.1
47. Scoccimarro E, Gualdi S, Bellucci A, Sanna A, Giuseppe Fogli P, Manzini E, et al. Effects of Tropical Cyclones on Ocean Heat Transport in a High-Resolution Coupled General Circulation Model. *J Clim* (2011) 24:4368–84. doi:10.1175/2011jcli4104.1
48. Alves O, Balmaseda MA, Anderson D, Stockdale T. Sensitivity of Dynamical Seasonal Forecasts to Ocean Initial Conditions. *Q J R Meteorol Soc* (2004) 130: 647–67. doi:10.1256/qj.03.25
49. Theja PK, Sreejith OP, Pai DS. Monsoon Teleconnections over Indian and Pacific Oceans in Japan Meteorological Agency Model Simulation. *Int J Climatol* (2015) 35:4728–37. doi:10.1002/joc.4319
50. Saha S, Nadiga S, Thiaw C, Wang J, Wang W, Zhang Q, et al. The NCEP Climate Forecast System. *J Clim* (2006) 19:3483–517. doi:10.1175/jcli3812.1
51. Kug J-S, Kang I-S, Choi D-H. Seasonal Climate Predictability with Tier-One and Tier-Two Prediction Systems. *Clim Dyn* (2008) 31:403–16. doi:10.1007/s00382-007-0264-7
52. Thomson MC, Doblas-Reyes FJ, Mason SJ, Hagedorn R, Connor SJ, Phindela T, et al. Malaria Early Warnings Based on Seasonal Climate Forecasts from Multi-Model Ensembles. *Nature* (2006) 439:576–9. doi:10.1038/nature04503
53. Feng G-L, Yang J, Zhi R, Zhao J-H, Gong Z-Q, Zheng Z-H, et al. Improved Prediction Model for Flood-Season Rainfall Based on a Nonlinear Dynamics-Statistic Combined Method. *Chaos, Solitons & Fractals* (2020) 140:110160. doi:10.1016/j.chaos.2020.110160
54. Vitart F, Robertson AW. The Sub-seasonal to Seasonal Prediction Project (S2S) and the Prediction of Extreme Events. *Npj Clim Atmos. Sci.* (2018) 1:1. doi:10.1038/s41612-018-0013-0
55. Zhang T, Yang S, Jiang X, Dong S. Sub-Seasonal Prediction of the Maritime Continent Rainfall of Wet-Dry Transitional Seasons in the NCEP Climate Forecast Version 2. *Atmosphere* (2016) 7:28. doi:10.3390/atmos7020028
56. Lo F, Hendon HH. Empirical Extended-Range Prediction of the Madden-Julian Oscillation. *Mon Wea Rev* (2000) 128(7):2528–43. doi:10.1175/1520-0493(2000)128<2528:eerpot>2.0.co;2
57. Jones C, Waliser DE, Lau KM, Stern W. The Madden-Julian Oscillation and its Impact on Northern Hemisphere Weather Predictability. *Mon Wea Rev* (2004) 132(6):1462–71. doi:10.1175/1520-0493(2004)132<1462:tmoaii>2.0.co;2
58. Walter K, Graf H-F. Life Cycles of North Atlantic Teleconnections under strong and Weak Polar Vortex Conditions. *Q J R Meteorol Soc* (2006) 132(615): 467–83. doi:10.1256/qj.05.25
59. Zhao Y, Feng G, Zheng Z, Zhang D, Jia Z. Evolution of Tropical Interannual Sea Surface Temperature Variability and its Connection with Boreal Summer Atmospheric Circulations. *Int J Climatol* (2020) 40:2702–16. doi:10.1002/joc.6361

Conflict of Interest: The authors declare that the research was conducted in the absence of any commercial or financial relationships that could be construed as a potential conflict of interest.

frontiers in Physics

BRIEF RESEARCH REPORT
published: 04 February 2022
doi: 10.3389/fphy.2022.713087

Dominant Role of Meridional Circulation in Regulating the Anomalous Subsidence of the Western Pacific Subtropical High in Early Summer 2020

Yuheng Zhao[1], Jianbo Cheng[2,3], Guolin Feng[2,4]*, Zhihai Zheng[1], Rong Zhi[1], Zengping Zhang[2], Jinlong Yan[3] and Dongdong Zuo[5]*

[1]Laboratory for Climate Studies, National Climate Center, China Meteorological Administration, Beijing, China, [2]College of Physical Science and Technology, Yangzhou University, Yangzhou, China, [3]School of Environmental Science and Engineering, Yancheng Institute of Technology, Yancheng, China, [4]Southern Marine Science and Engineering Guangdong Laboratory (Zhuhai), Zhuhai, China, [5]School of Mathematics and Physics, Yancheng Institute of Technology, Yancheng, China

OPEN ACCESS

Edited by:
Eric Josef Ribeiro Parteli, University of Duisburg-Essen, Germany

Reviewed by:
Xiaolong Zheng, Chinese Academy of Sciences (CAS), China
Mark Reyers, University of Cologne, Germany

***Correspondence:**
Jianbo Cheng
chengjb1992@163.com
Guolin Feng
Fenggl@cma.gov.cn

Specialty section:
This article was submitted to Interdisciplinary Physics, a section of the journal Frontiers in Physics

Received: *21 May 2021*
Accepted: *17 January 2022*
Published: *04 February 2022*

Citation:
Zhao Y, Cheng J, Feng G, Zheng Z, Zhi R, Zhang Z, Yan J and Zuo D (2022) Dominant Role of Meridional Circulation in Regulating the Anomalous Subsidence of the Western Pacific Subtropical High in Early Summer 2020. Front. Phys. 10:713087. doi: 10.3389/fphy.2022.713087

Anomalous subsidence over the western part of the western Pacific subtropical high (WPSH) caused record-breaking precipitation anomalies over the Yangtze-Huaihe River catchment in early summer 2020 (June–July 2020). The meridional circulation (MC) made a positive contribution to this anomalous subsidence, while the zonal circulation (ZC) made a negative contribution. The quantitative contributions of the MC and ZC to this anomalous subsidence were approximately 110% and –10% in June, 130% and –30% in July, and 120% and –20% for the mean of June and July, respectively, suggesting that the MC played a dominant role in the anomalous subsidence of the western part of the WPSH. The anomalous MC, with a rising branch located at the Maritime Continent and a descending branch located over South China, was forced by the warming of the northern tropical Indian Ocean and the rapidly developed La Niña event, which further resulted in the intensification and southwestward expansion of the WPSH and thus in heavy rainfall over the Yangtze River region.

Keywords: anomalous subsidence, western pacific subtropical high, meridional circulation, meiyu rain, early summer 2020

1 INTRODUCTION

The Meiyu in China or the Baiu in Japan and Changma in Korea is the major rainy season over the East Asian with duration from early-June to mid-July, which can have vital importance on the economic development and human society of East Asian regions [1–7]. The Meiyu rain season in 2020 started early (began on June 1, 7 days earlier than usual) and ended late (ended on August 2, 15 days later than usual), lasting for 62 days, which was the longest since 1961 (**Figure 1A**) [1–7]. The amount of precipitation averaged over the Yangtze and Huaihe Rivers during this season reached 759.2 mm, recording a precipitation anomaly that was higher than the precipitation anomaly in the second year of a strong El Niño, ranking the highest amount since 1961. In early summer 2020 (June–July), the mid–lower reaches of the Yangtze River catchment experienced more than 10 heavy rainfall events, leading to direct economic losses of approximately 116 billion Chinese yuan [3].

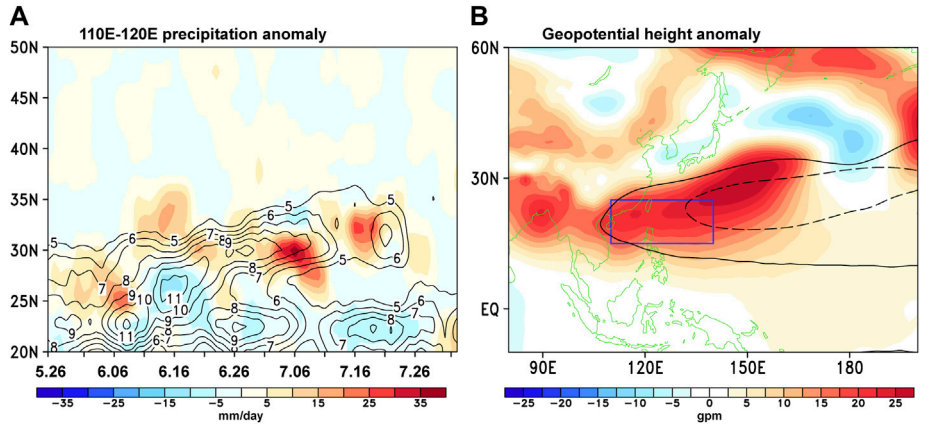

FIGURE 1 | (A) Time-latitude cross-section of the climatological precipitation (1981–2010, contour interval: 1 mm day^{-1}) and precipitation anomaly in 2020 (shading, mm day^{-1}) averaged over 110°E–120°E from 26 May to 2 August. **(B)** Horizontal distribution of the geopotential height anomaly at 850 hPa in early summer 2020 (1 June–31 July 2020, shading, gpm). Dashed and solid black lines in **(B)** represent the 5,880 gpm contour of the 500 hPa geopotential height in climatology and 2020, respectively. The blue box in **(B)** (110°E–140°E, 15°N–25°N) indicates the region of the western part of the western Pacific subtropical high (WPSH). Anomalies were computed based on the climatology of 1981–2010.

To investigate the underlying causes of the Meiyu in summer 2020, many efforts have been made. Takaya et al. [2] and Zhou et al. [7] proposed that the extraordinary rainfall was originated from the tropical Indian Ocean warming, and this warming was possibly resulted from the enhanced western Pacific subtropical high (WPSH) [5]. Zheng and Wang [6] suggested that all three oceans of the Pacific, Indian, and Atlantic Oceans contributed to the Meiyu, and the Atlantic Ocean made the dominate contribution. Liu et al. [1] and Qiao et al. [5] investigated the causes of the Meiyu from the subseasonal time scale. Liu et al. [1] divided the duration of Meiyu into two periods and claimed that the sequential warm and cold Meiyu front regulated by the North Atlantic Oscillation was responsible for this unexpected extreme Meiyu event. Qiao et al. [5] divided the duration of Meiyu into three stages: advanced-onset, strong-persisting, and delayed-withdrawal, and suggested different causes in different periods. Although these studies suggested different causes of the extraordinary Meiyu in summer 2020, they consistently emphasized the role of the anomalous WPSH.

Climatologically, the WPSH can transport the water vapor from the western Pacific toward mainland China by the low-level southwesterly jet along the edge of the WPSH, which can influence the rainfall over the Yangtze River catchment [8–15]. The above-normal (subnormal) precipitation over the Yangtze River catchment in early summer is commonly accompanied by an intensification and westward shift (a weakening and eastward shift) of the WPSH [11–15]. Thus, the location, intensity, and variability of the WPSH are vitally important to the precipitation anomaly over the Yangtze River catchment in early summer [8–10]. In June and July of 2020, the area of exceptionally strong WPSH showed a strong anomalous subsidence, especially in the western part of the WPSH (**Figures 2A,D,G**), which caused record-breaking precipitation anomalies over the Yangtze River catchment in early summer 2020. Therefore, it is necessary to investigate the source of the anomalous subsidence in the western part of the WPSH.

Recently, to achieve a uniform description of the general circulation of the atmosphere from a global perspective and to reveal the mechanism of the complicated interactions and connections of the circulations between the low latitudes and mid–high latitudes, a novel three-pattern decomposition of global atmospheric circulation (3P-DGAC) method was proposed [16–21]. Hu et al. [17] suggested that tropical overturning circulations consist of a couple of orthogonal overturning circulations, i.e., meridional circulation (MC) and zonal circulation (ZC). Climatologically, the MC averaged over 135°E–160°E is characterized as the anticlockwise circulation in both hemispheres, while the ZC averaged over 15°N–25°N is characterized as the anticlockwise circulation in Indian Ocean and the clockwise circulation in the Pacific and Atlantic Ocean (**Supplementary Figure S1**). The sinking motion of the MC between 15°N and 25°N makes positive contribution to the WPSH, while the rising motion of the ZC between 135°E–160°E makes the negative contribution (**Supplementary Figure S1**). Since the tropical overturning circulation can be decomposed into the MC and ZC, the vertical wind contains two components, i.e., the vertical winds of the MC and ZC (**Supplementary Figure S2**). **Supplementary Figure S2** shows that when analyzing the MC (ZC), the vertical velocity of the MC (ZC) should be used, and the vertical velocity of the ZC (MC) is regarded as the deviation if the total vertical velocity is used. Thus, there may be a bias in studying the MC and ZC in some previous studies because the total vertical velocity has commonly been used. Additionally, the anomalous subsidence in the western part of the WPSH in early summer 2020 could be decomposed into two parts that corresponded to anomalous MC and anomalous ZC (**Figure 2**), and thus the quantitative contribution of the MC and ZC to the anomalous WPSH can be clarified, which is not investigated in previous studies. Therefore, we would like to address the question: what were the effects of the MC and the ZC on the anomalous subsidence of the western part of the

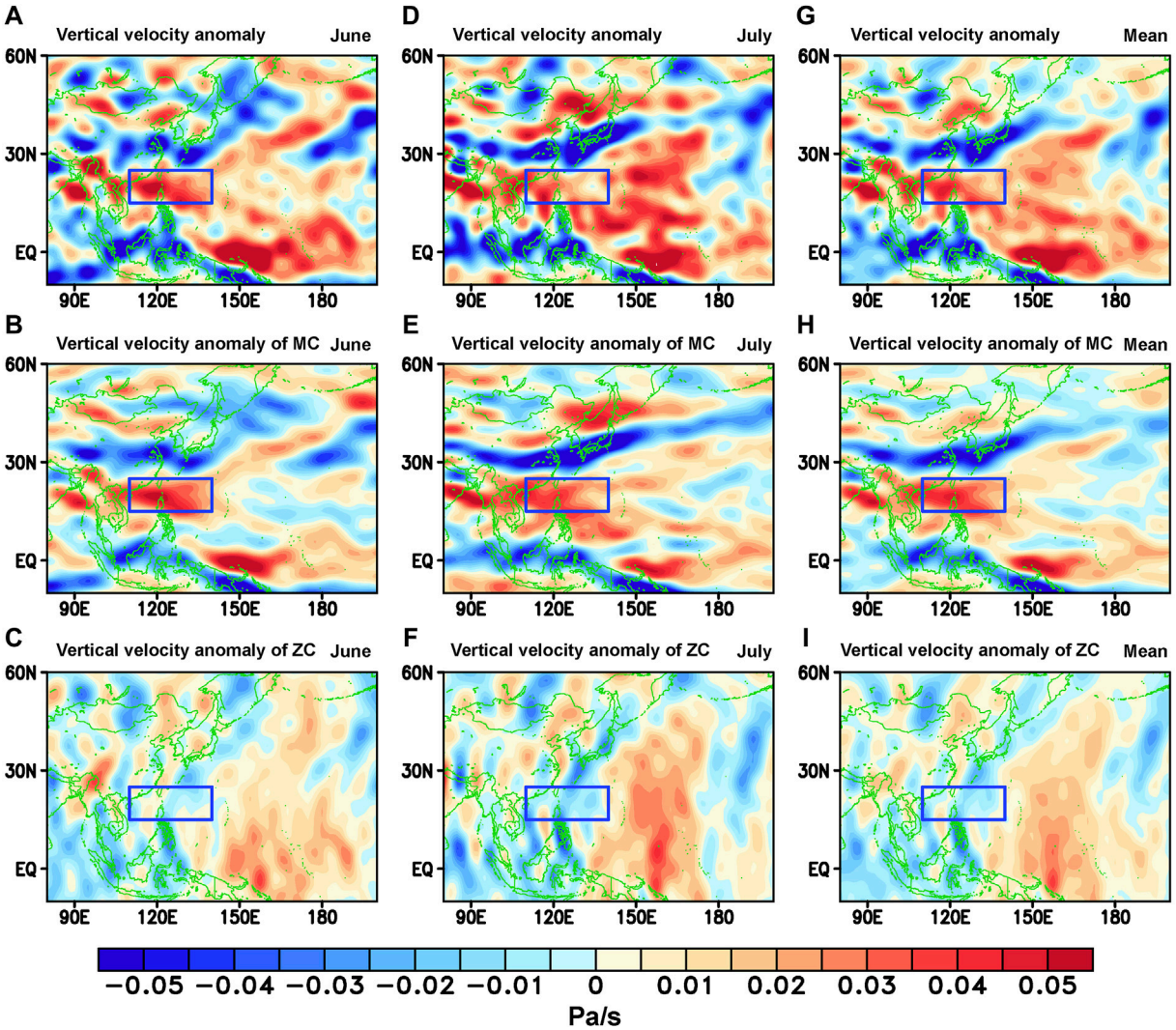

FIGURE 2 | (A) Horizontal distribution of the vertical velocity anomaly at 500 hPa in June 2020 derived from the ensemble means of five reanalysis data sets (shading, Pa s^{-1}). **(B)** and **(C)** Same as **(A)** but for the vertical velocity anomalies of meridional circulation (MC) and zonal circulation (ZC), respectively. **(D–F)** and **(G–I)** Same as **(A–C)** but for the results in July and the mean of June and July, respectively. The blue box in each plot indicates the region of the western part of the WPSH. Anomalies were computed based on the climatology of 1981–2010. The decomposition of the vertical velocity anomaly was based on the three-pattern decomposition of the global atmospheric circulation (3P-DGAC) method.

WPSH in early summer 2020? This issue was investigated by using the 3P-DGAC method in this study.

DATA AND METHODS

Data

In this study, we employed monthly horizontal winds and vertical velocity data from five reanalysis datasets as follows: the Climate Forecast System Reanalysis Version 1 and Version 2 (hereafter CSFR) [22, 23], the fifth generation of European Centre for Medium-Range Weather Forecast (ECMWF) atmospheric reanalysis of the global climate (hereafter ERA5) [24], the Japanese Meteorological Agency 55-years reanalysis (hereafter JRA-55) [25], the National Centers for Environmental Prediction (NCEP)/National Center for Atmospheric Research (NCAR) reanalysis (hereafter NCEP1) [26], and the NCEP/Department of Energy (DOE) reanalysis (hereafter NCEP2) [27]. The daily precipitation data were obtained from the Climate Prediction Center (CPC) Global Daily Unified Gauge-Based Analysis of Precipitation [28], and the monthly precipitation data were obtained from the Global Precipitation Climatology Project monthly precipitation dataset [29]. The monthly geopotential height data were obtained from ERA5 reanalysis datasets. The monthly sea surface temperature (SST) data were taken from the Extended Reconstructed SST version 5 (ERSST5) dataset [30]. For consistency, all datasets used in this study were interpolated to a 2.5°× 2.5° horizontal resolution. The time period analyzed in

this study was early summer 2020 (i.e., June–July 2020), and the climatology of variables was defined as the climatological mean from 1981 to 2010.

Three-Pattern Decomposition of Global Atmospheric Circulation

A simple introduction of the 3P-DGAC method is offered in this section. To solve the unit discrepancy in calculating the three-dimensional (3D) vorticity vector in the pressure coordinates, the spherical σ-coordinate system was adopted [17], namely:

$$u' = \frac{u}{a}, v' = \frac{v}{a}, \dot{\sigma} = \frac{\omega}{P_s}, \sigma = \frac{p}{P_s} \tag{1}$$

where a is the Earth's radius, p is the pressure, and P_s = 1000 hPa is the pressure at the Earth's surface. $(u', v', \dot{\sigma})$ and (u, v, ω) represent the three velocity components in the spherical σ-coordinate system and spherical p-coordinate system, respectively. Thus, the 3D velocity field in the spherical σ-coordinate system can be represented as follows:

$$\vec{V}'(\lambda, \theta, \sigma) = u'(\lambda, \theta, \sigma)\vec{i} + v'(\lambda, \theta, \sigma)\vec{j} + \dot{\sigma}(\lambda, \theta, \sigma)\vec{k} \tag{2}$$

which satisfies the following continuity equation:

$$\frac{1}{\sin\theta}\frac{\partial u'}{\partial \lambda} + \frac{1}{\sin\theta}\frac{\partial\left(\sin\theta v'\right)}{\partial\theta} + \frac{\partial\dot{\sigma}}{\partial\sigma} = 0 \tag{3}$$

Based on the features of the Rossby wave in the middle–high latitudes and the Hadley and Walker circulations in the low latitudes, Hu et al. [17] defined the 3D horizontal circulation $\vec{V}'_R$, MC $\vec{V}'_H$, and ZC $\vec{V}'_W$ as follows:

$$\begin{cases} \vec{V}_R'(\lambda, \theta, \sigma) = u_R'(\lambda, \theta, \sigma)\vec{i} + v_R'(\lambda, \theta, \sigma)\vec{j}, \\ \vec{V}_H'(\lambda, \theta, \sigma) = v_H'(\lambda, \theta, \sigma)\vec{j} + \dot{\sigma}_H(\lambda, \theta, \sigma)\vec{k}, \\ \vec{V}_W'(\lambda, \theta, \sigma) = u_W'(\lambda, \theta, \sigma)\vec{i} + \dot{\sigma}_W(\lambda, \theta, \sigma)\vec{k}, \end{cases} \tag{4}$$

and the following continuity equations were satisfied:

$$\begin{cases} \frac{1}{\sin\theta}\frac{\partial u_R'}{\partial\lambda} + \frac{1}{\sin\theta}\frac{\partial\left(\sin\theta v_R'\right)}{\partial\theta} = 0, \\ \frac{1}{\sin\theta}\frac{\partial\left(\sin\theta v_H'\right)}{\partial\theta} + \frac{\partial\dot{\sigma}_H}{\partial\sigma} = 0, \\ \frac{1}{\sin\theta}\frac{\partial u_W'}{\partial\lambda} + \frac{\partial\dot{\sigma}_W}{\partial\sigma} = 0. \end{cases} \tag{5}$$

Eq. 5 is the sufficient condition that the components of $\vec{V}'_R$, $\vec{V}'_H$, and $\vec{V}'_W$ can be represented by the stream functions $R(\lambda, \theta, \sigma)$, $H(\lambda, \theta, \sigma)$, and $W(\lambda, \theta, \sigma)$, respectively, as follows:

$$\begin{cases} u_R' = -\frac{\partial R}{\partial\theta}, v_R' = \frac{1}{\sin\theta}\frac{\partial R}{\partial\lambda}, \\ v_H' = -\frac{\partial H}{\partial\sigma}, \dot{\sigma}_H = \frac{1}{\sin\theta}\frac{\partial(\sin\theta H)}{\partial\theta}, \\ u_W' = \frac{\partial W}{\partial\sigma}, \dot{\sigma}_W = -\frac{1}{\sin\theta}\frac{\partial W}{\partial\lambda}. \end{cases} \tag{6}$$

Because three-pattern circulations (horizontal circulation, MC, and ZC) exist in both the low and the middle–high latitudes, the global atmospheric circulation can be expressed as the superposition of the horizontal circulation, MC, and ZC, as follows:

$$\vec{V}' = \vec{V}_H' + \vec{V}_W' + \vec{V}_R' \tag{7}$$

with the following components:

$$\begin{cases} u' = u_W' + u_R' = \frac{\partial W}{\partial\sigma} - \frac{\partial R}{\partial\theta}, \\ v' = v_R' + v_H' = \frac{1}{\sin\theta}\frac{\partial R}{\partial\lambda} - \frac{\partial H}{\partial\sigma}, \\ \dot{\sigma} = \dot{\sigma}_H + \dot{\sigma}_W = \frac{1}{\sin\theta}\frac{\partial(\sin\theta H)}{\partial\theta} - \frac{1}{\sin\theta}\frac{\partial W}{\partial\lambda}. \end{cases} \tag{8}$$

The following restriction condition is needed to pick up the correct decomposition:

$$\frac{1}{\sin\theta}\frac{\partial H}{\partial\lambda} + \frac{1}{\sin\theta}\frac{\partial(W\sin\theta)}{\partial\theta} + \frac{\partial R}{\partial\sigma} = 0. \tag{9}$$

Eq. 9 guarantees the uniqueness of the stream functions R, H, and W.

By combining **Eqs. 8**, **9**, the following equations were obtained:

$$\begin{cases} \Delta_3 R = \zeta, \\ \frac{\partial H}{\partial\sigma} = \frac{1}{\sin\theta}\frac{\partial R}{\partial\lambda} - v', \\ \frac{\partial W}{\partial\sigma} = \frac{\partial R}{\partial\theta} + u', \end{cases} \tag{10}$$

where $\Delta_3 = \frac{1}{\sin^2\theta}\frac{\partial^2}{\partial\lambda^2} + \frac{1}{\sin\theta}\frac{\partial}{\partial\theta}(\sin\theta\frac{\partial}{\partial\theta}) + \frac{\partial^2}{\partial\sigma^2}$ is the 3D Laplacian in the spherical σ-coordinates, and $\zeta = \frac{1}{\sin\theta}\frac{\partial v'}{\partial\lambda} - \frac{1}{\sin\theta}\frac{\partial(u'\sin\theta)}{\partial\theta}$ is the vertical vorticity of the entire atmospheric layer. The stream functions R, H, and W can be obtained by using **Eq. 10**. The global atmospheric circulation $\vec{V}'$ is then decomposed into the three-pattern circulations $\vec{V}_R$, $\vec{V}_H$, and $\vec{V}_W$ by using **Eq. 6**.

Since the MC and ZC can be effectively separated from the tropical atmospheric circulation by using the 3P-DGAC method (**Eq. 8**, **Supplementary Figure S2**), the 3P-DGAC method is potentially useful for analyzing the relative contributions of the MC and the ZC to the anomalous sinking motion of the western part of the WPSH. Therefore, in this study, the 3P-DGAC method was used to investigate the effects of the MC and the ZC on the anomalous subsidence of the western part of the WPSH.

In addition to the 3P-DGAC method, by using the traditional two-dimensional (2D) decomposition method of the vortex and divergent circulations [31, 32], the vertical velocity could also be decomposed into two parts, i.e., the vertical velocity of the regional Hadley circulation (RHC) and regional Walker circulation (RWC) (**Supplementary Figure S3**, **Supplementary Figure S4**). Thus, the traditional 2D method was also adopted in this study. However, the results derived from the traditional 2D method were displayed in the **Supplementary Materials**. More

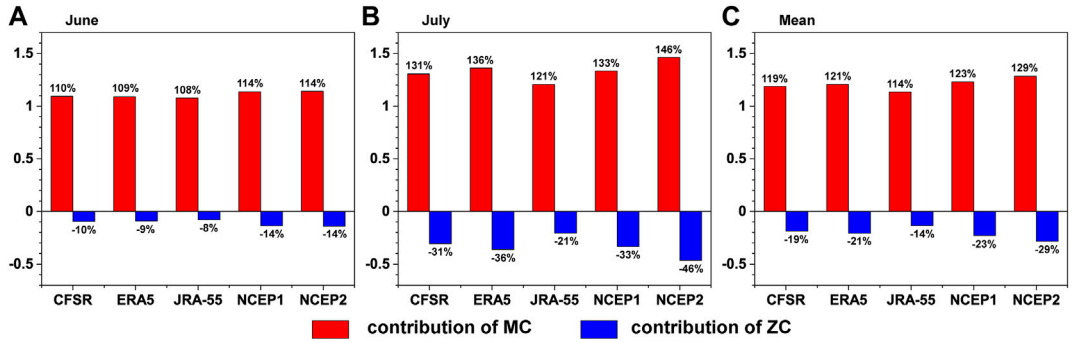

FIGURE 3 | Contributions of the MC (red bars) and ZC (blue bars) to the anomalous vertical velocity of the western part of the WPSH at 500 hPa in **(A)** June, **(B)** July, and **(C)** the mean of June and July 2020 based on the 3P-DGAC method derived from the CFSR, ERA5, JRA-55, NCEP1, and NCEP2 reanalysis data sets. The quantitative contributions are shown at the top of each bar.

information of the traditional 2D method and 3P-DGAC method can be found in [17–19].

RESULTS

Figure 2 displays the horizontal distribution of the vertical velocity anomaly at 500 hPa in early summer 2020. The anomalous subsidence of the western part of the WPSH can be decomposed into two parts that correspond to the anomalous MC and ZC by using the 3P-DGAC method, and the vertical velocity anomaly of MC was positive, while the vertical velocity anomaly of ZC was negative in the region of the western part of the WPSH from June to July, implying that the MC (ZC) made a positive (negative) contribution to the anomalous subsidence of the western part of the WPSH (**Figure 2**). Additionally, by comparing the first and second rows of **Figure 2** (i.e., comparing **Figures 2A,D,G** and **Figures 2B,E,H**), it was found that the original vertical velocity anomaly and the vertical velocity anomaly of MC were quite similar, suggesting that the MC played a dominating role in the anomalous subsidence of the western part of the WPSH. Although **Figure 2** displays the qualitative contributions of the MC and the ZC to the anomalous subsidence, further quantitative analysis is needed.

Figure 3 displays the quantitative contributions of the MC and the ZC to the anomalous subsidence of the western part of the WPSH at 500 hPa in early summer 2020 based on the 3P-DGAC method derived from five reanalysis datasets. The quantitative contributions of the MC and the ZC to the anomalous subsidence of the western part of the WPSH were approximately 110% and −10% in June, 130% and −30% in July, and 120% and −20% for the mean of June and July, respectively (**Figure 3**). Specifically, the quantitative contributions of the MC (ZC) were 110, 109, 108, 114, and 114% (−10%, −9%, −8%, −14%, and −14%) in June for the CFSR, ERA5, JRA-55, NCEP1, and NCEP2 reanalysis datasets, respectively. In July, the quantitative contributions of the MC (ZC) were 131, 136, 121, 133, and 146% (−31%, −36%, −21%, −33%, and −46%) for the five reanalysis datasets. For the mean of June and July, the quantitative contributions of the MC (ZC) were 119, 121, 114, 123, and 129% (−19%, −21%, −14%, −23%, and −29%) for the five reanalysis datasets. Although discrepancies existed in the quantitative contributions of the MC and the ZC to the anomalous subsidence based on the five different reanalysis datasets, the main results obtained from all five reanalysis datasets indicated that the MC played a dominant role in the anomalous subsidence of the western part of WPSH in early summer 2020. Additionally, although the quantitative contributions of the RHC and the RWC to the anomalous subsidence of the western part of the WPSH based on the traditional 2D decomposition method were different from those based on the 3P-DGAC method, the results derived from the two methods both supported the conclusion that meridional circulation played a dominant role in the anomalous subsidence of the western part of the WPSH in early summer 2020 (**Figure 3**, **Supplementary Figure S5**).

Since the MC played a dominating role in the anomalous subsidence of the western part of the WPSH in early summer 2020, we then wondered how the MC caused this anomalous subsidence. **Figures 4A–D** display the correlation between the regionally averaged vertical velocity anomaly of the MC over the region of the western part of the WPSH in June–July and the SST anomaly (SSTA) from December–January to June–July based on the seasonal means for the period 1979–2020. The correlation maps show that the correlated SSTA in the tropics is characterized by the persistent warming of the northern tropical Indian Ocean and the La Niña developing phase (**Figures 4A–D**), which was also observed from the actual SSTA (**Supplementary Figures S6A–D**). The warming of the northern tropical Indian Ocean is strengthened from December–January to June–July, and the northern tropical Indian Ocean warming can heat the troposphere and force the equatorial Kelvin wave to propagate eastward [33, 34], which triggers a positive Pacific–Japan (PJ) pattern (**Figure 4E**) and strengthens the northwest Pacific anomalous anticyclone (vectors in **Figure 4D**). Additionally, an enhanced zonal SST gradient is caused by the rapidly developed La Niña event, forcing anomalous easterly winds in the equatorial western Pacific (vectors in **Figure 4D**), which generates anomalous convection and precipitation anomalies over the Maritime Continent (**Figures 4F**, **Supplementary Figure S6F**) [5]. These two processes can lead to anomalous MC with a rising branch located on the Maritime Continent and a descending branch located over South China

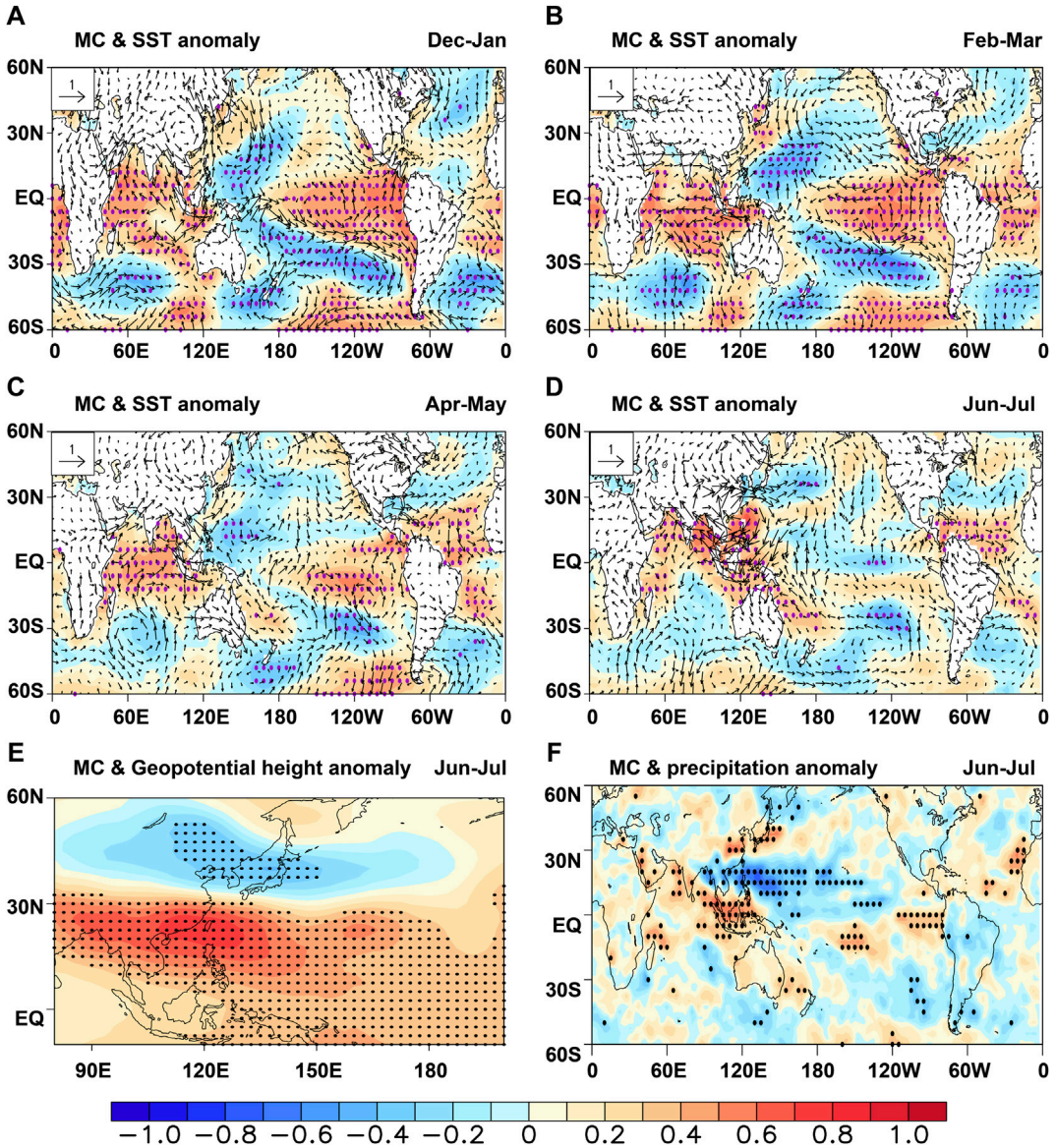

FIGURE 4 | Correlation between the regionally averaged vertical velocity anomaly of the MC over the region of the western part of the WPSH (110°E–140°E, 15°N–25°N) in June–July derived from the ensemble means of five reanalysis data sets and the sea surface temperature (SST) anomaly (shading) and horizontal wind anomaly (vector) in **(A)** December–January, **(B)** February–March, **(C)** April–May, and **(D)** June–July from 1979 to 2020 based on the seasonal means. **(E)** Same as **(D)** but for the correlation between the regionally averaged vertical velocity anomaly of the MC and the geopotential height anomaly at 500 hPa in June–July. **(F)** Same as **(D)** but for the correlation between the regionally averaged vertical velocity anomaly of the MC and the precipitation anomaly in June–July. Stippling over the shading indicates that these correlation coefficients are significant above the 95% confidence level based on Student's *t*-test.

(**Figures 2B,E,H**), which can enhance the subsidence of the western part of the WPSH and lead to the southwestward expansion of the WPSH (**Figure 4E**, **Supplementary Figure S6E**) [33, 34].

DISCUSSION

The results in this study show that the anomalous subsidence over the western part of the WPSH is vitally important because the WPSH was stronger and inclined more toward the west, which caused record-breaking precipitation anomalies over the Yangtze River catchment in early summer 2020. The MC made a positive contribution to the anomalous subsidence of the western part of the WPSH, while the ZC made a negative contribution. This finding is also obtained by previous studies [1–7]. However, in this study, the quantitative contribution of the MC and ZC to the anomalous WPSH is obtained by using the 3P-DGAC method, which is not investigated in previous studies. The quantitative contributions of the MC and the ZC to the anomalous subsidence of the western part of the WPSH were approximately 110% and −10% in June, 130%

and −30% in July, and 120% and −20% for the mean of June and July, respectively, suggesting that the MC played a dominant role in the anomalous subsidence of the western part of the WPSH. It should be noted that these results are obtained from the seasonal time scale and results may not the same in different periods from the subseasonal time scale, as Liu et al. [1] and Qiao et al. [5] suggested that the causes of the extraordinary Meiyu rain vary in different periods. Thus, the relative contribution of the MC and ZC to the extraordinary Meiyu rain from the subseasonal time scale should be investigated in the future. Chen et al. [35] proposed that the regional MC over the 110°E–160°E has intensified from 1979 to 2010, and the intensification of the regional MC is maintained under global warming [36]. Whether the rainfall over the Yangtze River catchment has intensified accompanied by the enhancement of the MC under global warming should also be explored.

The warming of the northern tropical Indian Ocean and the rapidly developed La Niña event forced anomalous MC with a rising branch located on the Maritime Continent and a descending branch located over South China, which further resulted in the intensification and southwestward expansion of the WPSH and anomalous precipitation over the Yangtze and Huaihe River catchment. The relative role of the warming of the northern tropical Indian Ocean and the rapidly developed La Niña events in forcing anomalous MC is not clear and should be investigated in the future.

According to Hu et al. [19], the dynamical equations of the three-pattern circulations have been established by combining the primitive equations and the 3P-DGAC method. The novel dynamical equations can be used to diagnose and predict the changes of the horizontal, meridional, and zonal circulations. Thus, the novel dynamical equations are potentially useful for prediction of the anomalous WPSH since the anomalous WPSH is closely related to the anomalous MC.

DATA AVAILABILITY STATEMENT

The original contributions presented in the study are included in the article/**Supplementary Material**, further inquiries can be directed to the corresponding authors.

AUTHOR CONTRIBUTIONS

YZ and JC: methodology. YZ and JC: writing original draft preparation. GF, ZZ(4th author), RZ, JY and DZ: writing review and editing. YZ and JC: visualization. All authors contributed to the article and approved the submitted version.

FUNDING

This work was funded by National Natural Science Foundation of China (Grant Nos 42130610, 42005012, 41975088), National Key Research and Development Program of China (Grant No. 2017YFC1502303), Natural Science Foundation of Jiangsu Province (Grant No. BK20201058), and School-level research projects of Yancheng Institute of Technology (Grant No. xjr2020022).

SUPPLEMENTARY MATERIAL

The Supplementary Material for this article can be found online at: https://www.frontiersin.org/articles/10.3389/fphy.2022.713087/full#supplementary-material

REFERENCES

1. Liu B, Yan Y, Zhu C, Ma S, Li J. Record-Breaking Meiyu Rainfall Around the Yangtze River in 2020 Regulated by the Subseasonal Phase Transition of the North Atlantic Oscillation. *Geophys Res Lett* (2020) 47(22):e2020GL090342. doi:10.1029/2020GL090342
2. Takaya Y, Ishikawa I, Kobayashi C, Endo H, Ose T. Enhanced Meiyu-Baiu Rainfall in Early Summer 2020: Aftermath of the 2019 Super IOD Event. *Geophys Res Lett* (2020) 47(22):e2020GL090671. doi:10.1029/2020GL090671
3. Wei K, Ouyang C, Duan H, Li Y, Chen M, Ma J, et al. Reflections on the Catastrophic 2020 Yangtze River Basin Flooding in Southern China. *The Innovation* (2020) 1(2):100038. doi:10.1016/j.xinn.2020.100038
4. Ding Y, Liu Y, Hu Z-Z. The Record-Breaking Mei-Yu in 2020 and Associated Atmospheric Circulation and Tropical SST Anomalies. *Adv Atmos Sci* (2021) 38:1980–93. doi:10.1007/s00376-021-0361-2
5. Qiao S, Chen D, Wang B, Cheung HN, Liu F, Cheng J, et al. The Longest 2020 Meiyu Season over the Past 60 years: Subseasonal Perspective and its Predictions. *Geophys Res Lett* (2021) 48(9):e2021GL093596. doi:10.1029/2021GL093596
6. Zheng J, Wang C. Influences of Three Oceans on Record-Breaking Rainfall over the Yangtze River Valley in June 2020. *Sci China Earth Sci* (2021) 64:1607–18. doi:10.1007/s11430-020-9758-9
7. Zhou Z-Q, Xie S-P, Zhang R. Historic Yangtze Flooding of 2020 Tied to Extreme Indian Ocean Conditions. *Proc Natl Acad Sci USA* (2021) 118(12):e2022255118. doi:10.1073/pnas.2022255118
8. Wang B, LinHo. Rainy Season of the Asian-Pacific Summer Monsoon. *J Clim* (2002) 15(4):386–98. doi:10.1175/1520-0442(2002)015<0386:rsotap>2.0.co;2
9. Ding Y, Chan JCL. The East Asian Summer Monsoon: An Overview. *Meteorol Atmos Phys* (2005) 89(1):117–42. doi:10.1007/s00703-005-0125-z
10. Ye H, Lu R. Subseasonal Variation in ENSO-Related East Asian Rainfall Anomalies during Summer and its Role in Weakening the Relationship between the ENSO and Summer Rainfall in Eastern China since the Late 1970s. *J Clim* (2011) 24(9):2271–84. doi:10.1175/2010JCLI3747.1
11. Huang R, Wu Y. The Influence of ENSO on the Summer Climate Change in China and its Mechanismfluence of ENSO on the Summer Climate Change in China and its Mechanism. *Adv Atmos Sci* (1989) 6:21–32. doi:10.1007/BF02656915
12. Zhang R, Sumi A, Kimoto M. Impact of El Niño on the East Asian Monsoon. *J Meteorol Soc Jpn* (1996) 74(1):49–62. doi:10.2151/jmsj1965.74.1_49
13. Wang B, Wu R, Fu X. Pacific-east Asian Teleconnection: How Does ENSO Affect East Asian Climate? *J Clim* (2000) 13(9):1517–36. doi:10.1175/1520-0442(2000)013<1517:peathd>2.0.co;2
14. Yang J, Liu Q, Xie S-P, Liu Z, Wu L. Impact of the Indian Ocean SST basin Mode on the Asian Summer Monsoon. *Geophys Res Lett* (2007) 34(2):L02708. doi:10.1029/2006GL028571
15. Xie S-P, Hu K, Hafner J, Tokinaga H, Du Y, Huang G, et al. Indian Ocean Capacitor Effect on Indo-Western Pacific Climate during the Summer Following El Niño. *J Clim* (2009) 22(3):730–47. doi:10.1175/2008JCLI2544.1
16. Liu H, Hu S, Xu M, Chou J. Three-dimensional Decomposition Method of Global Atmospheric Circulation. *Sci China Ser D-earth Sci* (2008) 51:386–402. doi:10.1007/s11430-008-0020-9
17. Hu S, Cheng J, Chou J. Novel Three-Pattern Decomposition of Global Atmospheric Circulation: Generalization of Traditional Two-Dimensional Decomposition. *Clim Dyn* (2017) 49:3573–86. doi:10.1007/s00382-017-3530-3

18. Hu S, Chou J, Cheng J. Three-pattern Decomposition of Global Atmospheric Circulation: Part I-Decomposition Model and Theorems. *Clim Dyn* (2018) 50: 2355–68. doi:10.1007/s00382-015-2818-4
19. Hu S, Cheng J, Xu M, Chou J. Three-pattern Decomposition of Global Atmospheric Circulation: Part II-Dynamical Equations of Horizontal, Meridional and Zonal Circulations. *Clim Dyn* (2018) 50:2673–86. doi:10.1007/s00382-017-3763-1
20. Hu S, Zhou B, Gao C, Xu Z, Wang Q, Chou J. Theory of Three-Pattern Decomposition of Global Atmospheric Circulation. *Sci China Earth Sci* (2020) 63:1248–67. doi:10.1007/s11430-019-9614-y
21. Cheng J, Gao C, Hu S, Feng G. High-stability Algorithm for the Three-Pattern Decomposition of Global Atmospheric Circulation. *Theor Appl Climatol* (2018) 133:851–66. doi:10.1007/s00704-017-2226-2
22. Saha S, Moorthi S, Pan H-L, Wu X, Wang J, Nadiga S, et al. The NCEP Climate Forecast System Reanalysis. *Bull Amer Meteorol Soc.* (2010) 91(8):1015–58. doi:10.1175/2010BAMS3001.1
23. Saha S, Moorthi S, Wu X, Wang J, Nadiga S, Tripp P, et al. The NCEP Climate Forecast System Version 2. *J Clim* (2014) 27(6):2185–208. doi:10.1175/JCLI-D-12-00823.1
24. Hersbach H, Dee D. ERA5 Reanalysis Is in Production. *ECMWF Newsl* (2016) 147:7.
25. Kobayashi S, Ota Y, Harada Y, Ebita A, Moriya M, Onoda H, et al. The JRA-55 Reanalysis: General Specifications and Basic Characteristics. *J Meteorol Soc Jpn* (2015) 93:5–48. doi:10.2151/jmsj.2015-001
26. Kalnay E, Kanamitsu M, Kistler R, Collins W, Deaven D, Gandin L, et al. The NCEP/NCAR 40-Year Reanalysis Project. *Bull Amer Meteorol Soc.* (1996) 77(3):437–71. doi:10.1175/1520-0477(1996)077<0437:tnyrp>2.0.co;2
27. Kanamitsu M, Ebisuzaki W, Woollen J, Yang S-K, Hnilo JJ, Fiorino M, et al. NCEP-DOE AMIP-II Reanalysis (R-2). *Bull Amer Meteorol Soc.* (2002) 83(11): 1631–44. doi:10.1175/BAMS-83-11-1631
28. Xie P, Chen M, Yang S, Yatagai A, Hayasaka T, Fukushima Y, et al. A Gauge-Based Analysis of Daily Precipitation over East Asia. *J Hydrometeorol* (2007) 8(3):607–26. doi:10.1175/JHM583.1
29. Adler RF, Huffman GJ, Chang A, Ferraro R, Xie P-P, Janowiak J, et al. The Version-2 Global Precipitation Climatology Project (GPCP) Monthly Precipitation Analysis (1979-Present). *J Hydrometeor* (2003) 4(6):1147–67. doi:10.1175/1525-7541(2003)004<1147:tvgpcp>2.0.co;2
30. Huang B, Thorne PW, Banzon VF, Boyer T, Chepurin G, Lawrimore JH, et al. Extended Reconstructed Sea Surface Temperature, Version 5 (ERSSTv5): Upgrades, Validations, and Intercomparisons. *J Clim* (2017) 30(20): 8179–205. doi:10.1175/JCLI-D-16-0836.1
31. Schwendike J, Govekar P, Reeder MJ, Wardle R, Berry GJ, Jakob C. Local Partitioning of the Overturning Circulation in the Tropics and the Connection to the Hadley and Walker Circulations. *J Geophys Res Atmos* (2014) 119(3): 1322–39. doi:10.1002/2013JD020742
32. Schwendike J, Berry GJ, Reeder MJ, Jakob C, Govekar P, Wardle R. Trends in the Local Hadley and Local Walker Circulations. *J Geophys Res Atmos* (2015) 120(15):7599–618. doi:10.1002/2014JD022652
33. Xie S-P, Kosaka Y, Du Y, Hu K, Chowdary JS, Huang G. Indo-western Pacific Ocean Capacitor and Coherent Climate Anomalies in post-ENSO Summer: A Review. *Adv Atmos Sci* (2016) 33(4):411–32. doi:10.1007/s00376-015-5192-6
34. Kosaka Y, Xie S-P, Nakamura H. Dynamics of Interannual Variability in Summer Precipitation over East Asia*. *J Clim* (2011) 24:5435–53. doi:10.1175/2011JCLI4099.1
35. Chen S, Wei K, Chen W, Song L. Regional Changes in the Annual Mean Hadley Circulation in Recent Decades. *J Geophys Res Atmos* (2014) 119: 7815–32. doi:10.1002/2014JD021540
36. Cheng J, Hu S, Gao C, Hou X, Xu Z, Feng G. On the Discrepancies in the Changes in the Annual Mean Hadley Circulation Among Different Regions and between CMIP5 Models and Reanalyses. *Theor Appl Climatol* (2020) 141(3–4):1475–91. doi:10.1007/s00704-020-03292-3

Conflict of Interest: The authors declare that the research was conducted in the absence of any commercial or financial relationships that could be construed as a potential conflict of interest.

Publisher's Note: All claims expressed in this article are solely those of the authors and do not necessarily represent those of their affiliated organizations, or those of the publisher, the editors, and the reviewers. Any product that may be evaluated in this article, or claim that may be made by its manufacturer, is not guaranteed or endorsed by the publisher.

frontiers in Climate

ORIGINAL RESEARCH
published: 15 February 2022
doi: 10.3389/fclim.2021.736459

Response of Temperature-Related Rice Disaster to Different Warming Levels Under an RCP8.5 Emission Scenario in a Major Rice Production Region of China

Shuangyi Luo[1], Zhihong Jiang[1], Jieming Chou[2], Gang Tu[3] and Shuyu Wang[4]**

[1] School of Atmospheric Sciences, Nanjing University of Information Science and Technology, Nanjing, China, [2] State Key Laboratory of Earth Surface Processes and Resource Ecology, Beijing Normal University, Beijing, China, [3] Jilin Provincial Key Laboratory of Changbai Mountain Meteorology & Climate Change, Institute of Meteorological Sciences of Jilin Province, Changchun, China, [4] School of Atmospheric Sciences, Nanjing University, Nanjing, China

OPEN ACCESS

Edited by:
Bai-Lian Li,
University of California, Riverside, United States

Reviewed by:
Chujie Gao,
Hohai University, China
Xiong Zhe,
Institute of Atmospheric Physics (CAS), China
Laurent Li,
UMR8539 Laboratoire de Météorologie Dynamique (LMD), France

***Correspondence:**
Gang Tu
shenxintu@aliyun.com
Shuyu Wang
wsy@nju.edu.cn

Specialty section:
This article was submitted to Climate Services, a section of the journal Frontiers in Climate

Received: *05 July 2021*
Accepted: *17 December 2021*
Published: *15 February 2022*

Citation:
Luo S, Jiang Z, Chou J, Tu G and Wang S (2022) Response of Temperature-Related Rice Disaster to Different Warming Levels Under an RCP8.5 Emission Scenario in a Major Rice Production Region of China. Front. Clim. 3:736459. doi: 10.3389/fclim.2021.736459

Rice is the basic food for about 50% of the global population, and feeds two-thirds of the Chinese population. Under the influence of global change, extreme weather, and climate events increase in frequency, duration, and intensity, which affect food production substantially. In the medium-to-long term in the future, the impacts of climate change on food availability are likely to grow. In this work, we first define the rice damage indices and then use surface observation and regional climate downscaling results from the variable resolution model LMDZ4 driven by the six Coupled Model Intercomparison Project phase 5 (CMIP5) global climate models (GCMs) to describe the temporal-spatial characteristics and the future changes of the temperature-related rice damages in Northeast China and Central and East China, the major commercial rice production regions in China. Compared with the observation, LMDZ4 demonstrates its ability to reproduce the regional characteristics of both heat and chilling rice damages. Based on the future regional projections under the RCP8.5 pathway, future changes of rice damage under four temperature-rising categories of 1.5, 2, 3, and 4°C are estimated. In the two rice production regions, the future extent of heat-related damage for Northeast China is mostly limited to the western area, and the occurrence of heat damage generally increases with global warming levels, particularly when it is higher than 2°C. For Central and East China, the heat-related rice damage increases in both coverage and intensity. The region is also likely to have a faster increasing rate of heat damage than in Northeast China. When global warming reaches 3 and 4°C, the median heat-related damage spreads over almost the whole region of Central and East China. Moreover, the probability of regional-scale heavy level heat damage would be over 50% by the end of twenty-first century. On the other hand, the disastrous impact of a cold event affecting rice yield is reduced in both coverage and duration although the model projections over Northeast China show larger intermodel variability and uncertainty.

Keywords: heat and chilling damage, damage index, global warming, regional climate, rice production

INTRODUCTION

Rice is the basic food for about 50% of the global population, providing 20% of global food energy. In Asia, more than 2 billion people depend on rice for more than 60–70% of their daily diet (FAO, 2017; Sekhar, 2018). Economically, rice cultivation is the main source of income for approximately 300 million people globally and an important contribution to national GDP in Asian agricultural countries. Rice production in Asia accounts for more than 90% of the global rice yield and about 70% of global exports. The largest Asian rice-producing countries are China, India, Indonesia, Bangladesh, Vietnam, and Thailand, and 40% of the harvested area is from rain-fed lowland, deep water/intertidal wetland, and some highland. Consequently, the Asian rice industry is fragile to water demand and regional hydrological cycles, which are associated strongly with the accelerated warming climate and related natural disasters, including storms, floods, and droughts.

Due to the combined effects of natural variability of the Asian monsoon system and anthropogenic forcings, the observed changes in the Asian regional climate for the past few decades are evident and significant. Studies demonstrate that the regional warming trend continues in China and other Asian countries, and the extreme climate events have increased in intensity, frequency, and duration (IPCC, 2013; CMA Climate Change Centre, 2019). At the regional level, the impacts of multiple factors, such as rising temperature, higher evaporation, and changing rainfall variability, show substantial impact on water resources and affect the regional food production and national GDP (IFPRI, 2016). The natural variability of the hydrological cycle, the exuberant human consumption, and increased intensity of agricultural water management put further stress on the already scarce water resources in some Asian agriculture regions, and consequently, the increasing water shortage damaged the major important food crops, including rice, corn, and wheat, in many parts of Asia (Wijeratne, 1996; Aggarwal et al., 2000; Fischer et al., 2002; Tao et al., 2003, 2004).

Temperature is one of the main environmental factors that affects the growth and development of crops. Studies indicate that current temperature change has a negative impact on global and regional crop yields. Without taking the effects of CO_2 fertilization, effective adaptation measurement, and genetic improvement of plants into consideration, the major global food yields will suffer a reduction of 6.0% for wheat, 3.2% for rice, 7.4% for maize, and 3.1% for soybean per 1°C global warming (Zhao et al., 2017). The rice yield and quality are also constrained by the temperature. When the temperature exceeds or falls below the critical value that favors rice growth, it damages the growth and development of rice, resulting in a decline in yield or poor quality. Therefore, the temperature-related agri-meteorological disasters can be divided into two categories: high temperature heat damage and low temperature chilling damage of rice.

Rice is extremely sensitive to temperature. For rice production, the high-temperature hazard occurring in the booting-flowering and grain-filling stages is one of the major factors that limits the crop yield and quality (Yang et al., 2020). It is agreed by observational analysis and future climate projection that, with global warming, high temperature stress occurs more frequently. Regionally, the occurrence of rice heat damage in East China is consistent with the temporal evolution of the surface air temperature, and consequently, global warming is a major factor that caused the reduction of rice yield (Bao et al., 2012).

In the meantime, a low-temperature event that damaged rice production in the high latitude region of Northeast China was observed in the 1960s and 1970s, and chilling damage can lead to a yield loss of more than 10%—up to 20% if the damages are serious ones. However, the frequency and intensity of large-scale sterile-type rice chilling damage have decreased due to intensified warming in recent years. Even so, the obstacle-type chilling damage tended to be more frequent, affecting the rice growth especially in northern Heilongjiang and eastern Northeast China.

Regional climate projection shows that the magnitude of warming in Asia is likely to be higher than the global average, and the annual precipitation increases in high latitudes and decreases in subtropical latitudes, leading to the continuation of the current dry pattern in some areas (Bates et al., 2008; Huang et al., 2013; Hui et al., 2018a,b). Compared to 1960–1990 averages, the temperatures are projected to increase by up to 4.5°C in the north and west and by up to around 3°C in the southeast by 2100. In the medium term, annual mean temperature is likely to increase by 1.5–2.4°C from 2031 to 2040 and by 2.3–3.0°C from 2051 to 2060. These findings are comparable to those reported in the IPCC's AR5. The effect of climate change on crops varies with the crop and land types (IFPRI, 2016). For example, with the higher variability of rainfall pattern at the regional level, global warming would damage the rainfed farms while benefiting irrigated cropland (Wang et al., 2010). The wide application of agriculture irrigation and water management systems further implicates assessing the climate change impact on food production.

Rice is the leading cereal in Chinese food consumption, and it is mainly produced in Central and East China, South and Southwest China, and Northeast China (Mei et al., 1988; Li et al., 2015). In China, food production was greatly affected by regional climate change. According to the 2019 Blue Book on Climate Change in China (CMA Climate Change Centre, 2019), the increase of the national averaged surface air temperature warming rate of China is significantly higher than the global average. With the warming conditions during the past 50 years, the frequency of extreme high temperature events demonstrated a clear interdecadal variability, and the frequency of extreme daily precipitation events showed an increasing tendency. Since the late 1990s, extreme weather and climate events, such as drought, heavy rainfall, floods, and heatwaves have been widely observed and show extensive socioeconomic impacts. Climate change in China shows a negative impact on agriculture and food production as it affects the major crops, livestock, and fisheries production adversely (Bates et al., 2008; IPCC, 2013). In the near to far future, the negative impacts of regional climate change on food security in China are expected to grow with time.

As hydrological factors are major constraints of China food production (Tao et al., 2003), higher temperature-related heat hazards also damage the growth and maturation of various crops. Study shows that the global rice yield decreases by 3.2% on

TABLE 1 | Basic information of models.

Driving GCM	Research Institutions	Resolution
BCC-csm1-1m	China, BCC	1.125° × 1.12°
FGOALS-g2	China, IAP	2.8° × 2.8°
IPSL-CM5A-MR	France, IPSL	2.5° × 1.26°
CNRM-CM5	France, CNRM	1.4° × 1.4°
MPI-ESM-MR	Germany, MPI	1.875° × 1.875°
MPI-ESM-LR	Germany, MPI	1.875° × 1.875°

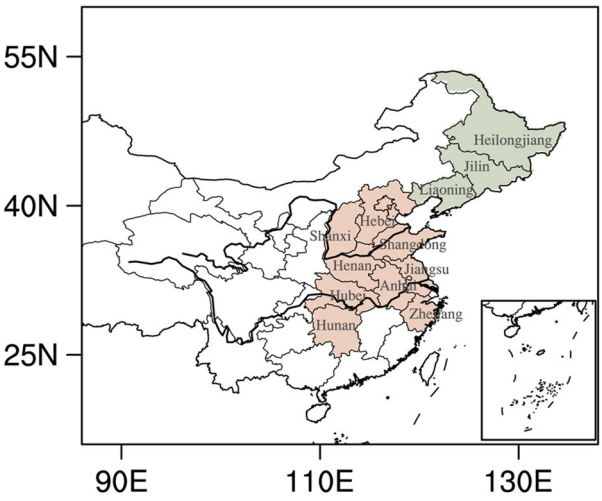

FIGURE 1 | The research domain. The region with green color denotes the northeast China, and the region with red color is Central and East China.

average for every 1°C increases in global average temperature (Yang et al., 2020). The regional response of rice heat damage to different and higher global warming levels over the Chinese rice production region were evaluated in previous work (Xiong et al., 2016; Wang et al., 2020). However, the uncertainty in chilling/hot rice damage from climate models are not well-addressed. Meanwhile, though the high-latitude region, such as northeastern China, has experienced the most significant warming during a few decades in the past, low temperature events and chilling damage occur from time to time (Ma et al., 2011; Shi et al., 2020). Under such circumstances, the accurate projection and evaluation of occurrence of future low- and high-temperature events as well as the heat and cold rice damage will contribute to the regional effective adaptation and to prevention of the rice yield loss.

In this paper, we use a high-resolution observation data set over China (CN05.1) and simulations of the regional climate model LMDZ4 driven by six Coupled Model Intercomparison Project phase 5 (CMIP5) models to study the changes in frequency and intensity of future rice-related heat and chilling damages in the near and far future under different warming levels. The regional temperature changes that threaten the already fragile carrying capacity of rice fields was assessed.

The paper is organized as follows: the observational data, model, and definition of extreme temperature-related rice damage indexes are introduced in section Data and Methods. In section Results, the projected changes of the above indexes under various global warming levels in China are presented, and section Conclusion gives a summary of the main conclusions of this study.

DATA AND METHODS

Model Information and Data

The dynamic downscaling in this study is performed with LMDZ4, a variable resolution stretched grid atmospheric general circulation model developed at the Laboratoire de Météorologie Dynamique (Li, 1999; Frédéric et al., 2006). In this study, LMDZ4 was used as a limited area model and integrated with enhanced and fine resolution of 60 km over East Asia, covering the region of 5.52–54.87 N in latitude, 85.98–134.53 E in longitude. In vertical, there are 19 sigma-pressure hybrid layers. The LMDZ4 model physics and parameterization schemes can be found described in Frédéric et al. (2006) and Dufresne et al. (2013) for more details.

Driven by six CMIP5 global models in the lateral and lower boundaries (**Table 1**), LMDZ4 was integrated from 1961 to 2005. We selected 1986 to 2005 as the reference climate, and 2006–2100 for future climate under RCP8.5 emission scenario. The equal-weighted ensemble average of six downscaling results, referred to as LMDZ MME in the following text, was used for extreme temperature and rice disaster analysis for both reference and future climate.

The analysis region is centered at 30°N/110°E, covering 5°–55°N in latitude and 85°–135°E in longitude. The region is further divided into northeast China and Central and East China, according to rice cultivation in China (**Figure 1**, Mei et al., 1988).

LMDZ4 can generally well-simulate the regional climate of East Asia (Yang et al., 2016; Gao et al., 2017; Guo et al., 2018). Yang et al. (2016) compare differences between model simulation results before and after downscaling by LMDZ, showing that LMDZ can evidently improve depiction of regional terrain. Gao et al. (2017) suggest that LMDZ4 can reproduce the spatial pattern of extreme temperature in Central and East China better compared with forcing global climate models (GCMs). Guo et al. (2018) project the response of three extreme temperature indices to 1.5 and 2°C global warming in Central and East China by a corrected LMDZ daily temperature data set under RCP4.5 scenario.

For the purposes of model assessment, the 0.25° × 0.25° resolution data sets, CN05.1, which are based on the interpolation form more than 2,400 observing stations in China, are used as observations (Wu and Gao, 2013). We further interpolate model data to the same resolution of observation by Earth System Modeling Framework (ESMF) software, a regridding function incorporated into NCL.

TABLE 2 | Definitions of heat and chilling damage indices.

Index	Definition	Rank		
		Light	Medium	Heavy
H_a	Hazardous accumulated temperature (unit: °C·day)	$0 < H_a \leq 15$	$15 < H_a \leq 30$	
T_{MX}	Maximum temperature during heat damage (unit: °C)	$35 \leq T_{MX} < 38$	$38 \leq T_{MX} < 40$	
SDHD	Duration of single heat damage event (unit: day)	$3 \leq D < 5$	$5 \leq D < 10$	$D \geq 10$
MDHD	Duration of multiple heat damage events (unit: day)	$6 \leq D < 12$	$12 \leq D < 24$	$D \geq 24$
DCD	Consecutive days with daily average temperature lower than 17/19°C (To the South/North of Yangtze River Reaches, unit: day)	2	3–4	5

Time Windows of Reaching 1.5, 2, 3, and 4°C Global Warming Threshold

To evaluate the impacts of various warming levels to rice production in China, we choose 1986–2005 as the reference time period, during which the climate is 0.61°C warmer than the preindustrial level of 1850–1900 (IPCC, 2013; Chen et al., 2017). According to the method of Chen et al. (2017), the ensemble mean of driving GCMs reach the 1.5, 2, 3, and 4°C global warming levels above the preindustrial period by the time windows of 2019–2039, 2033–2053, 2055–2075, and 2076–2096, respectively. Here, the time series of global mean temperature were smoothed by the 21-year moving average first, and the time window of reaching the warming threshold was defined as the first year when temperature reaching the corresponding threshold with 10 years before and after it. Correspondingly, the warming in the individual time windows are 0.89, 1.39, 2.39, and 3.39°C above mean temperature of 1986–2005.

Definitions of Heat and Chilling Damage Indices

In this study, we mainly consider the changes of extreme high and low temperatures and their impacts to rice during the key time periods of grain-filling and heading periods. Therefore, for the heat damage that affects Northeast China, a time slice of July 15–August 31 is selected, and for Central and East China, a time slice of August 1–September 10 is selected. Correspondingly, the low temperature events damage the physiological function of the rice during its booting and heading periods, forming empty grains and reducing yield. The heat and chilling damage indices to rice used in this study are generated with the ensemble mean of LMDZ downscaled daily maximum and minimal temperatures.

To describe the damage quantitatively, we define several indices (**Table 2**). Their calculations are based on the Chinese National Standards for Grade of Chilling damage for rice and maize (People Republic of China Meteorological Industry Standard, 2009) and Meteorological grades of heat damage to rice (People Republic of China National Standard, 2020).

For heat damage, we firstly identify the days with daily maximum temperature higher than 35°C (referred to as heatday in the following figure and text) and then calculate the index of H_a to describe the heat damage to rice:

(1) H_a: Hazardous accumulated temperature. When consecutive heatdays with daily maximum temperature Tmax higher than 35°C are 3 days or longer, H_a is calculated as the accumulation of difference between daily maximum temperature Tmax to 35°C. H_a is then used to calculate the single point heat damage intensity *HDI*.

(2) T_{MX}: Maximum temperature during heat damage.

In addition to the magnitude of heat damage, we also consider the length of heat damage to rice by calculating following indices:

1. Duration of high temperature during heat damage (*DHD*): Here, high temperature event are divided into two types: single and multiple events. The former is for the case when only one heat damage occurs during the entire growing season of rice for a particular year, recording its duration as DHD. Duration of multiple events is the accumulation amount of days when more than one heat damage event happens in 1 year;
2. Duration of low temperature event (*DCD*): For the chilling damage index, we only consider damages that affect the rice productivity, that is, the low temperature events during the rice reproductive period that physiologically destroy the rice plant and cause empty grains. The chilling damage is estimated by the duration of low temperature event (*DCD*) and can be categorized into three levels, that is, light damage with *DCD* equaling 2 days, middle damage with *DCD* lasting for 3–4 days, and heavy damage with *DCD* longer than 5 days.

The threshold to define *DCD* varies with regions. For the area to the south of the Yangtze River, daily temperatures lower than 17°C are considered to cause chilling damage to rice production and used to calculate *DCD*, and for the region to the south of the Yangtze River, the threshold of daily temperature lower than 19°C is used to calculate the *DCD*.

(3) The regional impact of heat/cold events to rice production is estimated by defining SH/SC index:

$$SH(SC) = \frac{Number\ of\ grid\ points\ Seffering\ from\ Heat\ (Cold)\ damagages}{total\ grid\ points\ of\ analysis\ region}$$

We then use SH_i and SC_i to estimate the regional coverage of heat and cold events with different intensity. Here, i stands for the intensity levels.

$$SH1/SH2/SH3(SC1/SC2/SC3) = \frac{Number\ of\ grid\ points\ witH\ LigHt/middle/HigH\ Heat/Cold\ Events}{Number\ of\ grid\ points\ with\ Heat/Cold\ Events\ in\ the\ region}$$

RESULTS

Evaluation of Model's Ability to Simulate Current Temperature Related Damages

Heat Damage

As a major single-cropping rice production region of China, Northeast China experiences little heat-related damages in observation (figure not shown) with the observed heat days <1 day, H_a smaller than 4°C·day, and T_{MX} no more than 36°C. There are no multiple heat events, and the single heat event is limited to the small area of northern Heilongjiang province. The LMDZ MME well-reproduce the observed distributions of H_a, T_{MX}, SDHD, and MDHD, suggesting that LMDZ has the ability to describe the intensity and duration of heat damage in Northeast China.

In contrast to Northeast China, the rice production region in the lower latitude of Central and East China is greatly affected by heat damage represented by T_{MX}, H_a, SDHD, and MDHD. In observation, the H_a and T_{MX} show south–north gradients with higher H_a of more than 12°C·day in eastern Hunan and north Zhejiang provinces. Most of Hunan, Hubei, Henan, Anhui, and Zhejiang observe T_{MX} over 36°C during the filling and heading seasons. The LMDZ MME is unable to reproduce the south–north gradients of H_a and T_{MX}. Instead, the high H_a is limited to the narrow band across the center of Henan and Hubei, and T_{MX} is evidently underestimated, especially for the area south of 30 N. Consequently, the index for a single heat event SDHD ranges between 5 and 10 days. The index for multiple events MDHD lasts between 6 and 12 days in most parts of Central and East China, but Zhejiang province has enduring multiple events with MDHD of 24 days. LMDZ MME can reasonably produce the distributions of the heat damage of Henan, Anhui, and Shandong provinces, but it greatly underestimates the magnitude of all indices for the area lower than 32 N and shows overestimation for the area higher than 34 N. For example, LMDZ MME has a negative bias for Hunan, Zhejiang, Anhui, and the southern part of Jiangsu provinces. The model's cold bias in maximum temperature in Zhejiang and Hunan provinces induces large underestimation in both SDHD and MDHD in Zhejiang and Hunan provinces by 5 and 6–20 days, respectively. On the other hand, LMDZ MME has overestimation of SDHD due to its overestimation of maximum temperature at southern Hebei and northern Henan provinces. The LMDZ MME also overestimates SDHD for Anhui by almost 5 days (**Figure 2**).

Chilling Damage

Compared with the heat damage, Northeast China experiences frequent chilling damage during 1986–2005 (**Figure 3B**) with the least damage of 2 days. The heaviest damage that lasts longer than days mainly happens along the range of the Xiaoxing'an and Changbai Mountains, displaying the possible impact of terrain. Damage with medium intensity that lasts for 3–4 days distributes on both sides of the mountain range, located in the Sanjiang and Songnen plains. The southern part of northeast China has the relatively small-scale light damage of 2 days. The rice production area of Northeast China is mainly in the plains, such as the Sanjiang and Songnen plains around the south slope of the Xiaoxing'an Mountains and is definitely affected by chilling damage with various intensity.

Compared with the observation, LMDZ reproduces well the pattern of chilling damage (**Figure 3A**). The simulated heaviest chilling damage is along the mountains, which well-agrees with the observation. However, LMDZ shows a warm bias in the west of the mountain range and reduces the length of regional chilling damage by 1 day. The extent of damage with medium intensity decreases largely and location of light damage shifts to north of the Songnen plain. Similarly, in LMDZ simulations, the southern and central part of Northeast China has chilling damage <2 days in the historical period due to the model's warm bias.

Chilling damage in Central and East China is mainly observed in northern and part of the western area (figure not shown). Shandong, Anhui, Hunan, and Zhejiang provinces also have scattered distributions. The damage of the highest intensity in Central and East China distributes along the mountainous terrain, i.e., the Yanshan and Taihang Mountains, similar to the case in Northeast China. A medium-level event spreads around the mountains and in the western part of Central China. The extent of the damage with light intensity is slightly larger than that of the medium level. The main rice production area of Central and East China is in the lower latitude provinces of Anhui, Jiangsu, Hunan, southern Hubei, and Zhejiang. Scattered rice fields are located on the south bank of the Yellow River and northern provinces of Shanxi and Hebei. Therefore, though north of Hebei, Shanxi provinces and the west part of Henan, Hubei provinces have light-to-heavy cold events, the overall loss of rice from chilling damage in Central and East China is manageable.

LMDZ can basically represent the characteristic of the heaviest chilling damage, but large bias exists for damage with medium and light intensities as the model's cold event concentrates along the mountain range and surrounding areas.

Above all, LMDZ is able to reproduce the pattern of chilling damage in the rice production region of China; it especially well-represents the distribution of the heaviest chilling damage in Northeast China.

Future Projection of Extreme Temperature-Related Damage to Rice Under Different Warming Levels

Heat Damage

Spatial Distribution

As shown in **Figure 4**, in Northeast China, the maximum temperature T_{MX}, the accumulated hazardous Ha, and the duration of both single and multiple events increases in magnitudes with increasing warming levels. Meanwhile, they all spatially spread eastward and reach 120E. If the warming limited to 1.5°C, the Ha, T_{MX}, and SDHD is confined to the west corner of Jilin province, and a multiple heat event would not happen as that of the reference time period. When the warming level reaches more than 3°C, both intensity and duration of heat damage in the east part of Northeast China are intensified (**Figure 4**). Compared with the reference time, the SDHD and MDHD can increase by more than 20 and 18 days at most, and the heat damage could spread eastward and cover northwest Liaoning,

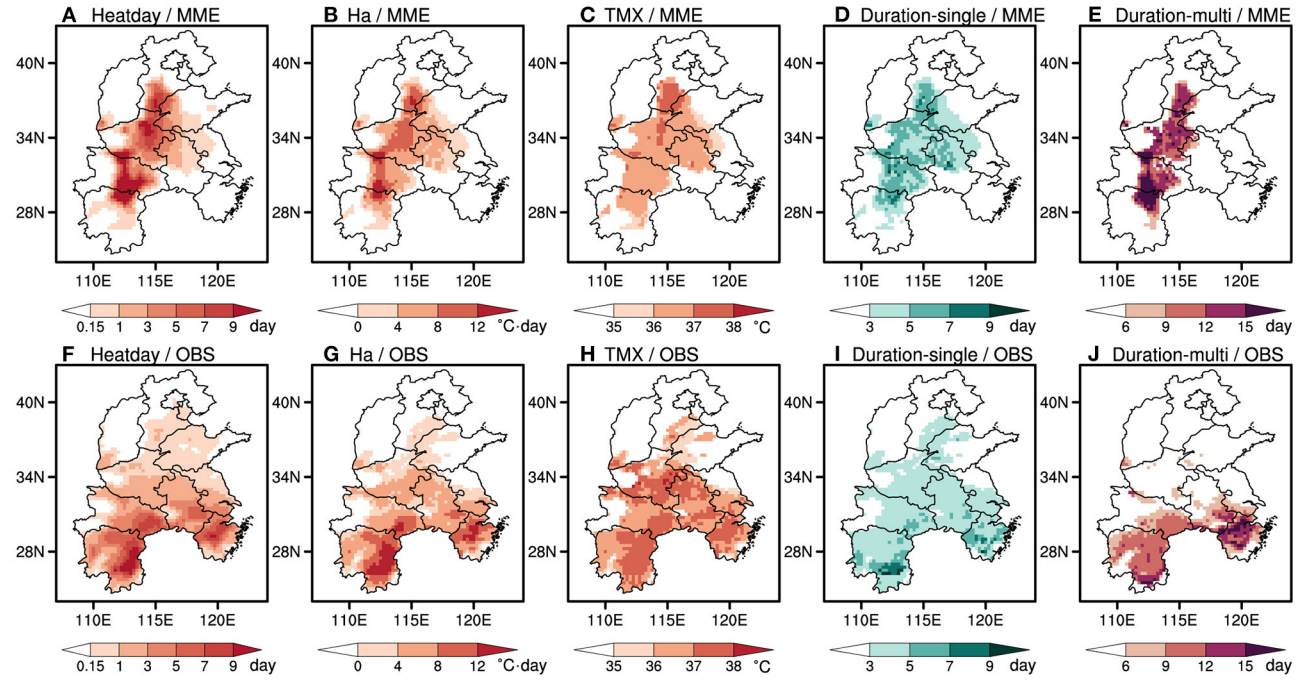

FIGURE 2 | Spatial distributions of observed and multimodel averaged heat damage indexes in Central and East China during 1986–2005. **(A,F)** The number of high-temperature days (unit: day), **(B,G)** hazardous heat accumulation temperature (unit: °C·day), **(C,H)** maximum temperature in the process of heat damage (unit: °C), **(D,I)** single-process duration of heat damage (unit: day), and **(E,J)** multiple-process duration of heat damage process (unit: day).

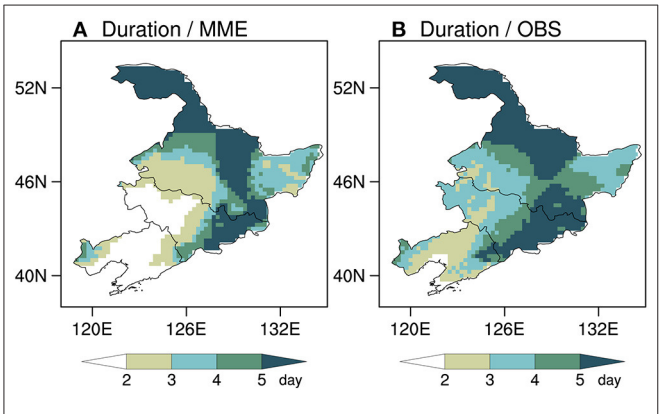

FIGURE 3 | Spatial patterns of chilling damage duration (unit: day) for **(A)** LMDZ-MME and **(B)** observation in Northeast China during 1986–2005.

western Jilin, and southwest Heilongjiang. The intensity indices share the similar distributions to those of duration indices, and the magnitudes of T_{MX} and Ha increase with warming levels until reaching more than 38 and 12°C day when 4°C warming occurs. Both tensity (i.e., Ha and TMX) and duration heat damage (e.g., Heatday, SDHD and MDHD) indices show increasing trends with time (**Figure 5**). The trend from the temporal evolution of MDHD shows that it increases by 0.91 d/10a, and for the duration of single event by 0.19 d/10a (**Figure 5D**).

In Central and East China, which produces more than 45% of rice yield in the last 20 years, higher warming levels are inevitably accompanied by the wider spread of heat damage from the center of the rice-production region to the whole center-east China (**Figure 6**). For the reference time, the highest TM is 38.1°C located at 37.75 N, 116.25 E (boundary region of Hubei and Hunan provinces). Associated with strengthening warming, the T_{MX} increase from 38.9°C at 1.5°C to 41.5°C at 4°C warming. The high T_{MX} area with value higher than 38°C extends southward from southern Hebei province to cover most of Hebei, Hubei, and Hunan provinces, and regional averaged T_{MX} for the whole rice production region can be more than 35°C for 4°C warming. The hazardous accumulation temperature H_a is projected to have similar spatial distributions to that of T_{MX} for different warming levels. Comparing the distributions under 2°C warming, it can be seen that H_a is reduced by about 20°C·day in Hebei, Hubei, and Hunan provinces under the 1.5°C warming scenario, greatly lowering the dangers of heat damage to the rice.

For each individual warming level, the duration indices of heat damage, SDHD and MDHD, in Central and East China have the similar spatial distributions (**Figure 6**), that is, the most hit area from heat damage gradually enlarges southwestward until it finally covers the whole region below 36 N. Compared with the reference time, the regional average of single heat event duration increases by 2.06, 4.25, 7.05, and 11.05 days for 1.5, 2, 3, and 4°C warming; and for multiple events, the changes will be 2.02, 4.46, 6.09, and 8.95 days. If the 4°C warming occurs, even if the yearly heat damage comes from a single event, it is likely to last for more than 15 days regionally in the whole 41-day grain-filling periods. Moreover, it is likely that more than 90% of the Central and East China's rice production region will be hit by either single or multiple heat events, and the total lasting time

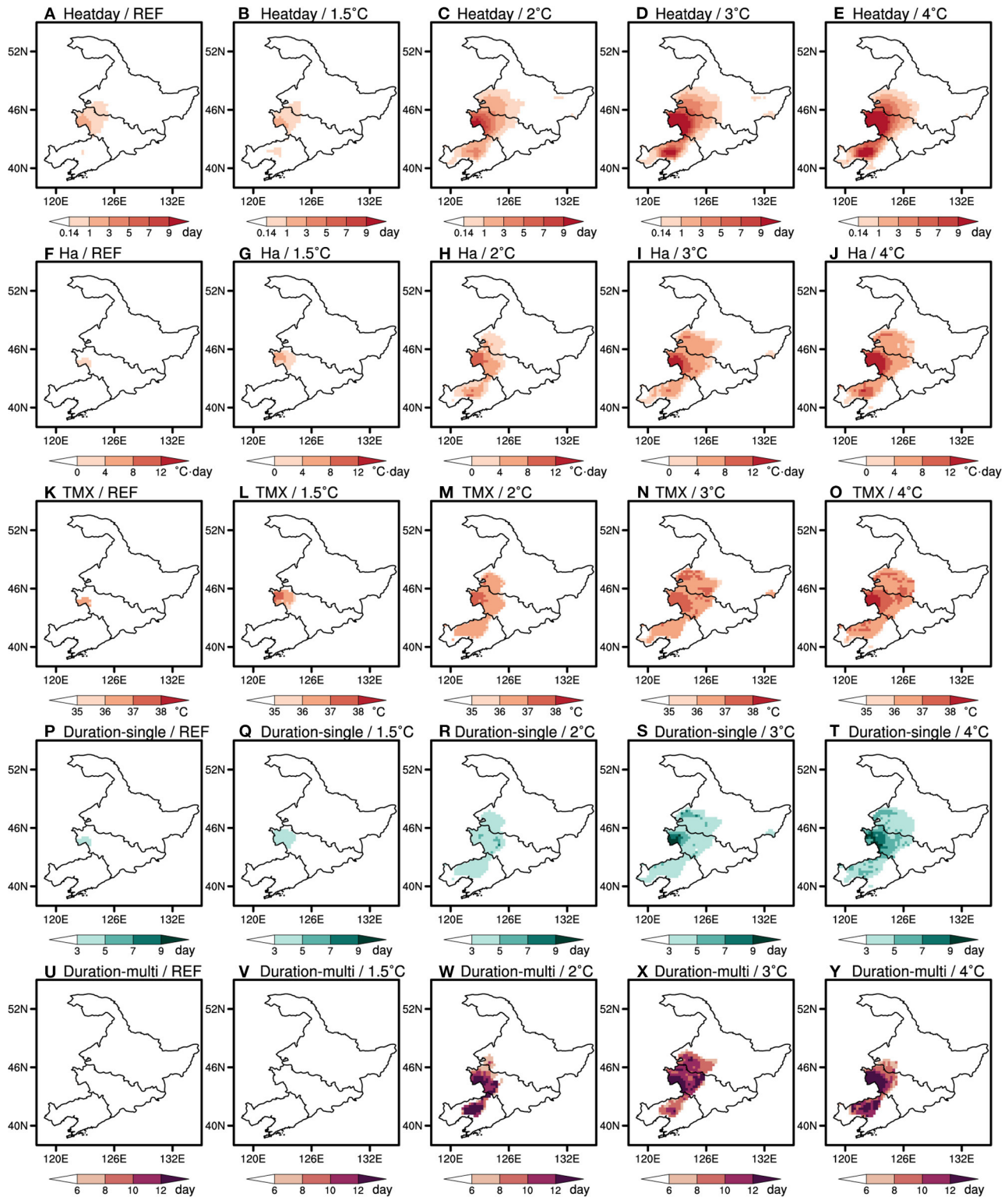

FIGURE 4 | Spatial distribution of **(A–E)** the number of high-temperature days (unit: day), **(F–J)** hazardous heat accumulation temperature (unit: °C·day), **(K–O)** maximum temperature in the process of heat damage (unit: °C), **(P–T)** single-process duration of heat damage (unit: day), and **(U–Y)** multiple-process duration of heat damage (unit: day) simulated (the first column) and projected by LMDZ-MME (the second to fifth columns) in Northeast China. The reference time period is 1986–2005. For future projection, the warming levels of 1.5, 2, 3, and 4°C are presented under the emission pathway of RCP8.5.

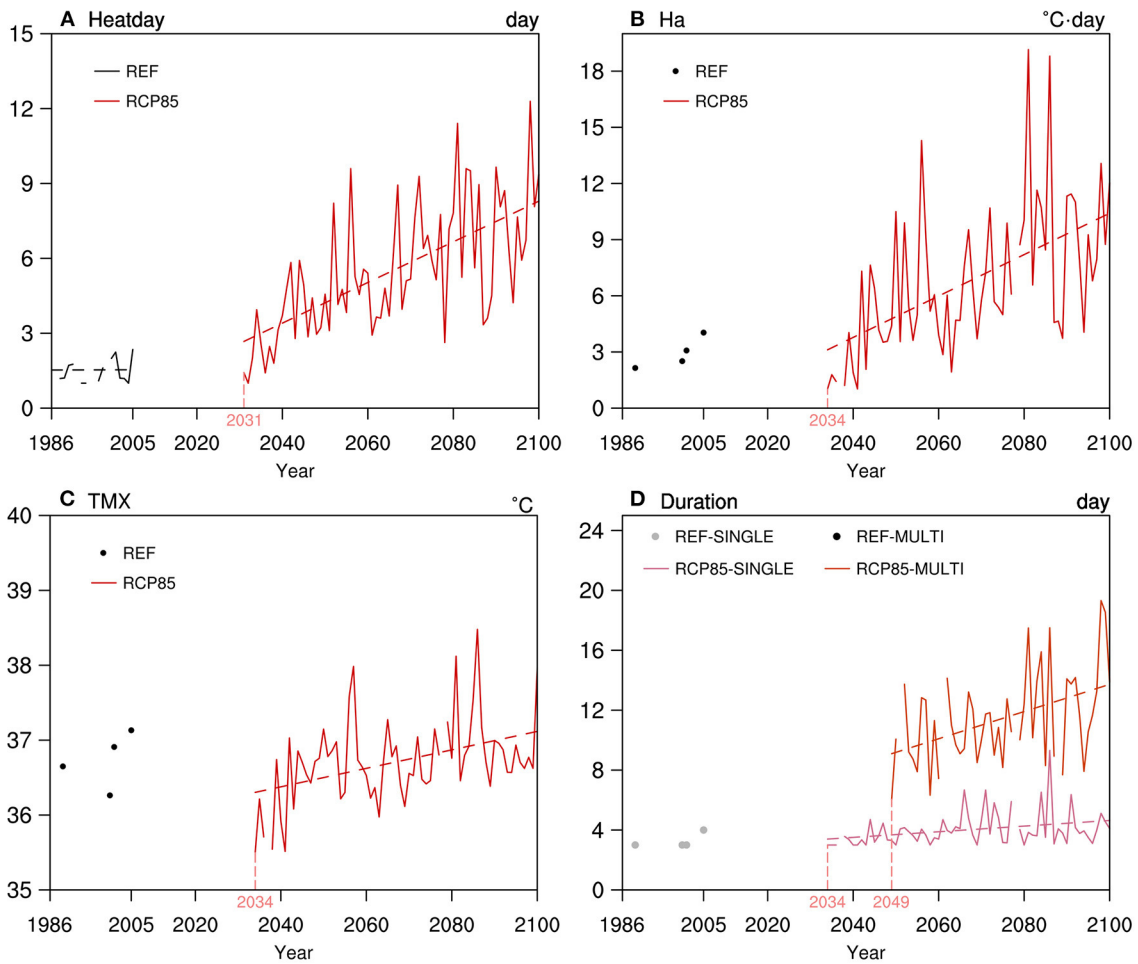

FIGURE 5 | Time series of **(A)** the number of high-temperature days (unit: day), **(B)** hazardous heat accumulation temperature (unit: °C·day), **(C)** maximum temperature in the process of heat damage (unit: °C), **(D)** single- and multiple process durations of heat damage (unit: day) simulated and projected by LMDZ-MME averaged over Northeast China. The reference time period is 1986–2005, and for future projection, the time period of 2006–2100 is taken under the emission pathway of RCP8.5. The black and gray dots, and gray dotted line denote the historical simulation results. The red and magenta solid lines denote the multimodel projections under RCP8.5 pathway. In the plot, all the long dashed lines are for the linear regressions of different indexes with the vertical magenta short lines and corresponding years indicating the first occurrence times of individual hot extreme indexes.

of such heat damage will be longer than 35 days, which accounts for more than half of the grain-filling season. Combining the damage intensity and duration, we can see that the severest heat-related disaster coincides with the major rice production area of Henan, Hubei, and Anhui provinces and leads to massive rice production cuts.

The temporal evolution of intensity and duration of heat damage in Central and East China is shown in **Figure 7**. Under the RCP8.5 emission scenario, the heat damage would endure as indicators of heat duration of SDHD increased by 1.68 d/10a, and MDHD by 1.89d/10a. Meanwhile, the T_{MX} increases by the rate of 0.22°C/10a. All the above changes are statically significant and pass the 95% confidence level.

Changes of Intensity, Duration, Danger Level, and Coverage

The danger level of rice heat damage grows with increasing global warming levels in both intensity and duration. It is evident that the uncertainty ranges of projected indices that are induced by various driving GCMs enlarge with warming level, especially for H_a and MDHD (**Figure 8**). We further divide T_{MX} and H_a into three categories to describe the risk level of heat damage to better describe the severity of potential risk. As shown in **Figure 8A**, rice-producing Northeast China is a region that is seldom troubled by heat-related damage in the current climate. In the future, the intense heat damage affecting the rice production can be avoided in Northeast China with global warming limited below 3°C; otherwise, the region will have "light" level heat damage with H_a increasing up to 6°C·day. On the other hand, the risk level measured by T_{MX} is categorized as light for all four warming levels (**Figure 8A**). To identify risk arising from an enduring heat event, the indices of MDHD and SDHD are categorized into "short," "medium," and "long" according to their lasting days. Over Northeast China, the impact level from the single heat event remains short for all four warming levels. In

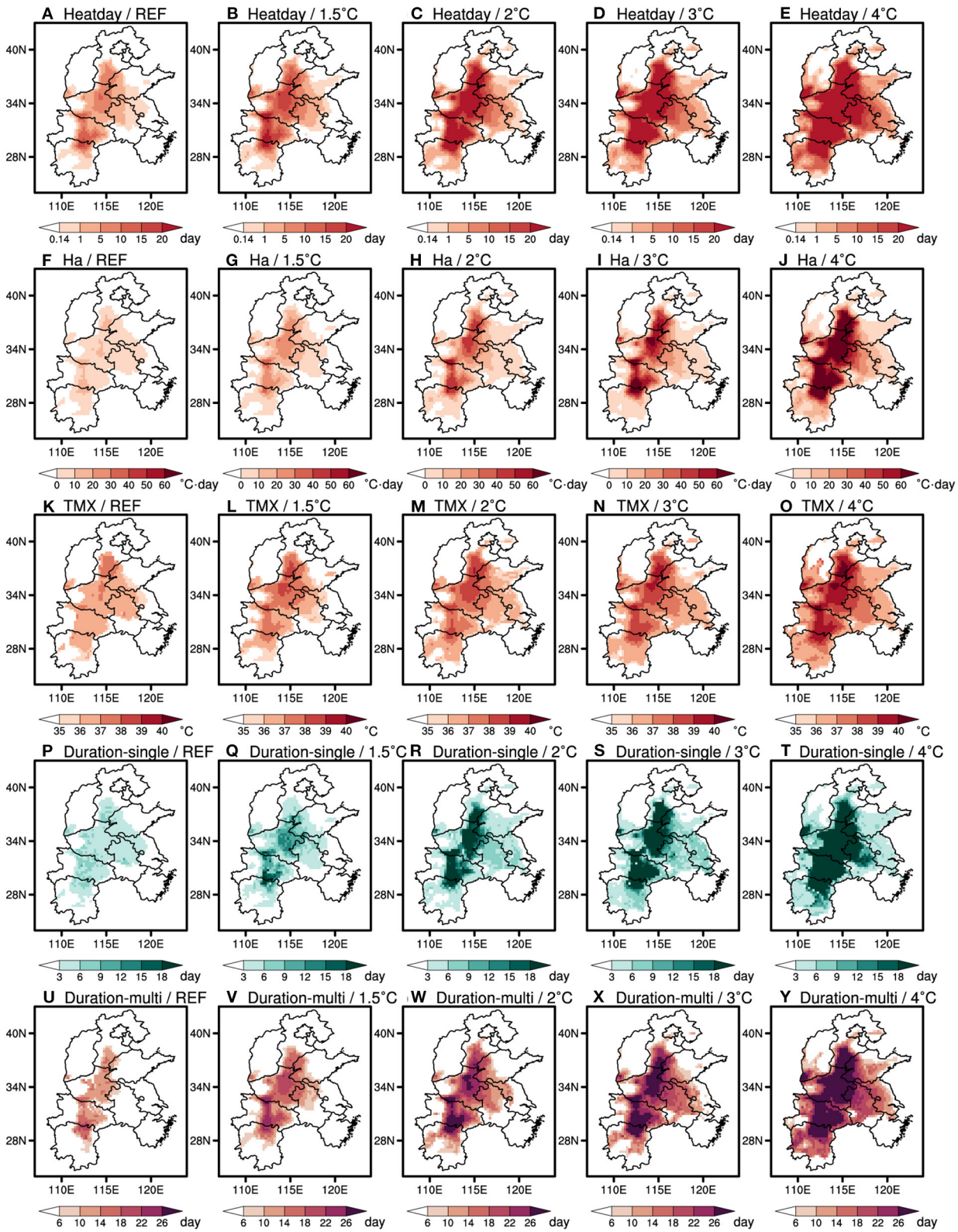

FIGURE 6 | Same as **Figure 4** but for Central and East China.

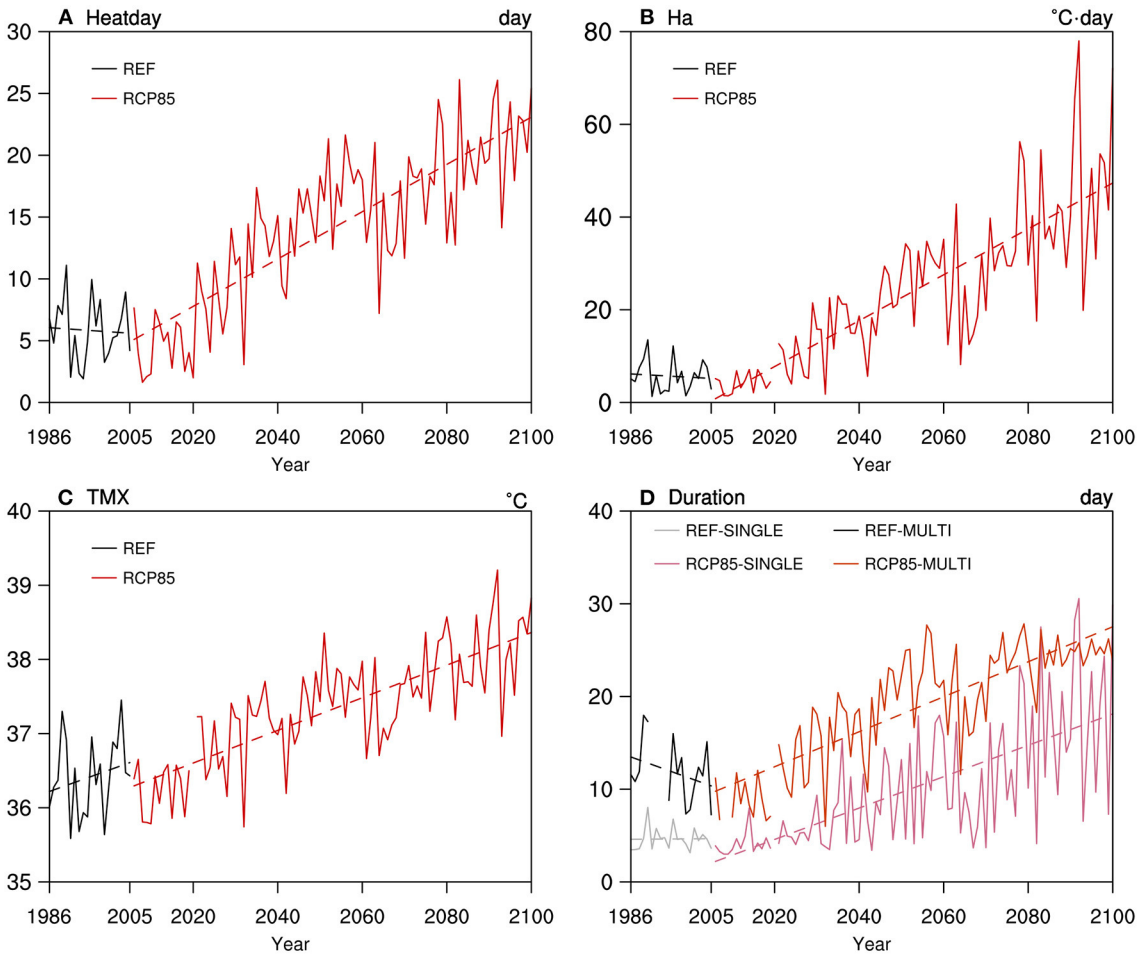

FIGURE 7 | Same as **Figure 5** but averaged over Central and East China.

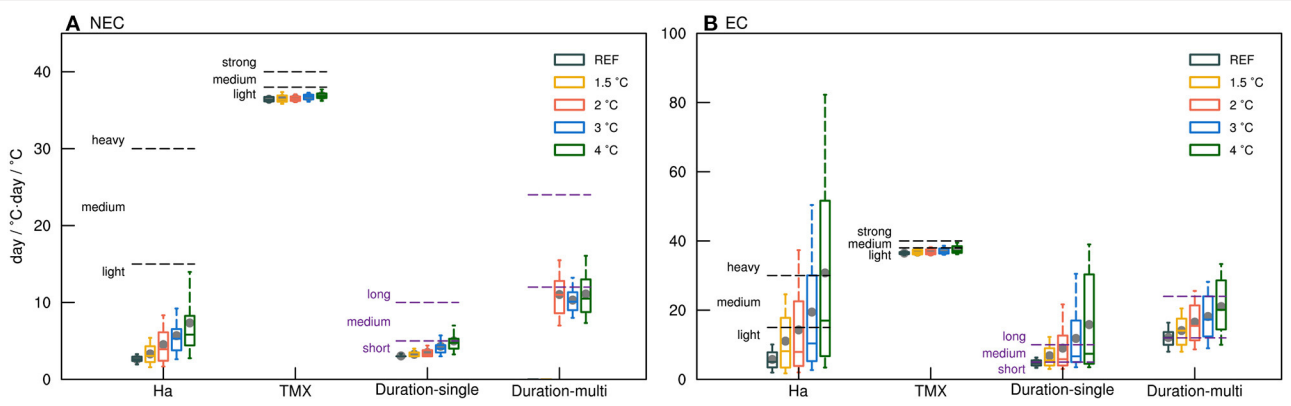

FIGURE 8 | Boxplots of the number of high-temperature days (unit: day), hazardous heat accumulation temperature (unit: °C·day), maximum temperature in the process of heat damage (unit: °C), durations of single- and multiple-process of heat damage (unit: day) of control (1986–2005), and projected climate (2006–2100) by LMDZ-MME averaged over the **(A)** Northeast China and **(B)** Central and East China. For future climate projection, warming levels of 1.5, 2, 3, and 4°C under emission pathway of RCP8.5 are considered. The top and bottom whiskers are the 10th and 90th percentiles. The black and purple dotted lines indicate the corresponding rank of each event.

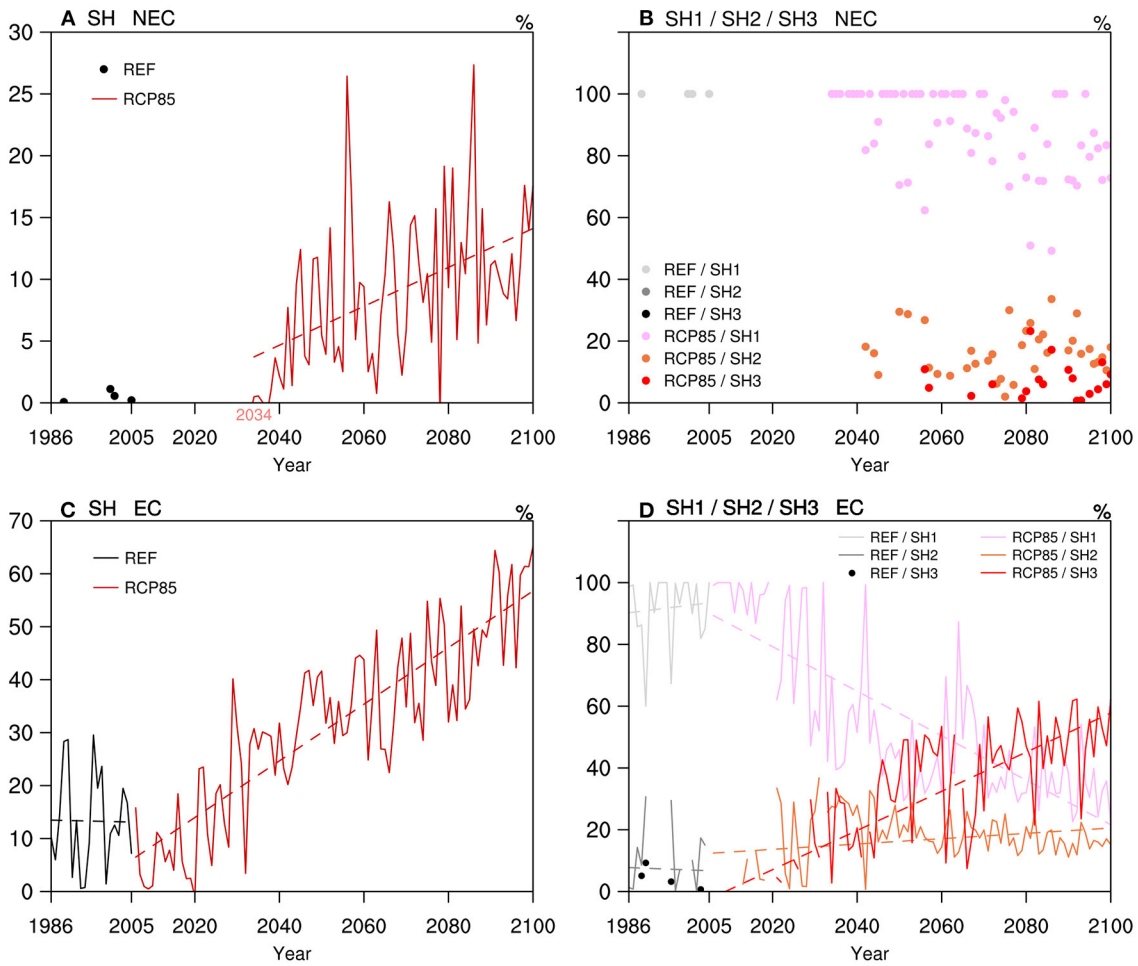

FIGURE 9 | Time series of indexes of regional impact of heat damage (SH, unit: %) and regional coverage of heat damage with different intensity (SH1/SH2/SH3, unit: %) for reference (years 1986–2005) and projected (years 2006–2100 under the RCP8.5 pathway) climate by LMDZ-MME. **(A,B)** are for regional average of Northeast China, and **(C,D)** for Central and East China. The light gray, dark gray, and black solid lines denote the historical temporal variations of indexes and magenta, orange, and red solid lines for projection results under RCP8.5 scenario. The corresponding long dashed lines indicate the linear trends of individual index.

Northeast China, the occurrence of multiple heat events increases with the warming levels. In the last 40 years of the twenty-first century, all enduring heat events can be categorized as multiple type. In conclusion, the risk of having multiple heat events cannot be avoided if the warming is over 1.5°C, and Northeast China will have short multiple heat events under 2, 3, and 4°C warming.

For Central and East China, the risk level for intensified heat is measured by the variation of the T_{MX}, and the damage level is below light when warming is <3°C and strong when it is 4°C warming. H_a can also be used to describe the severity of heat damage from intensified high temperature. From variation of Ha, it can be seen that the *HDI* would keep being light with the global warming below 2°C. With the warming reaching 4°C globally, the *HDI* in Central and East China would develop into the stage of heavy with H_a up to 37°C by LMDZ MME (**Figure 8B**). Examining the endangerment of enduring high temperatures to rice production, the danger level for a single heat event is medium for 1.5 and 2°C in Central and East China, but extends to long when the warming level is 3°C and above. Meanwhile, the risk level of multiple heat events varies between short and medium levels according to the variations of MDHD under different warming levels.

During the 20-year reference time, the percentages of area affected by hot weather are <3% in Northeast China. Global warming increases the risks of heat damage as the highest percentage of area that suffered from heat damage reaches 25% with the linear tendency of 1.57%/10a during 2034–2100 (**Figure 9A**). In contrast to the reference time when there are no medium and heavy types of heat damage, Northeast China has a large chance to witness a drastic increase in light-type heat events with the percentage of the affected area more than 50% for year of 2040–2100. Scattered cases of heavy heat damage are projected for Northeast China though the affected area may be <10–20%. The area affected by medium type events ranges from 5 to 40% (**Figure 9B**). As shown in **Figure 9C**, the overall coverage of the heat-damaged area, indicated by the index of SH, in Central and East China has a clear annual variability for reference time periods and a linear increasing tendency by 5.35%/10a for

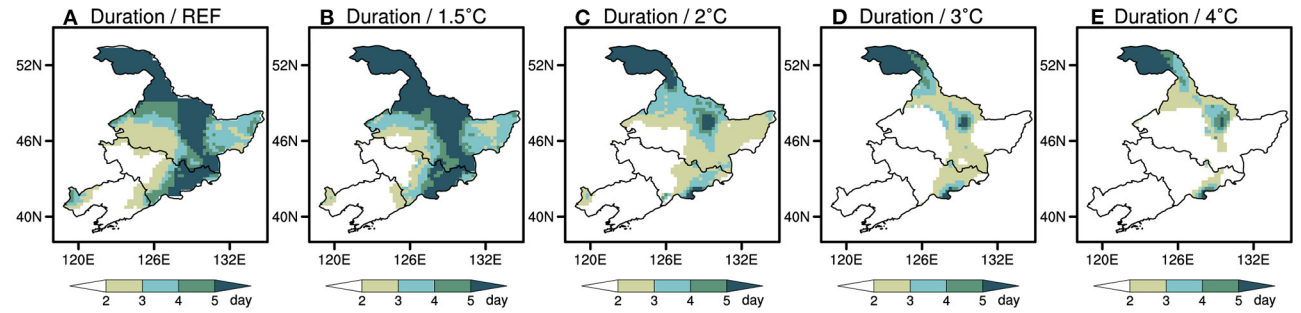

FIGURE 10 | Spatial distributions of chilling damage duration (unit: day) for **(A)** reference (1986–2005) and **(B–E)** future projection by LMDZ-MME in Northeast China.

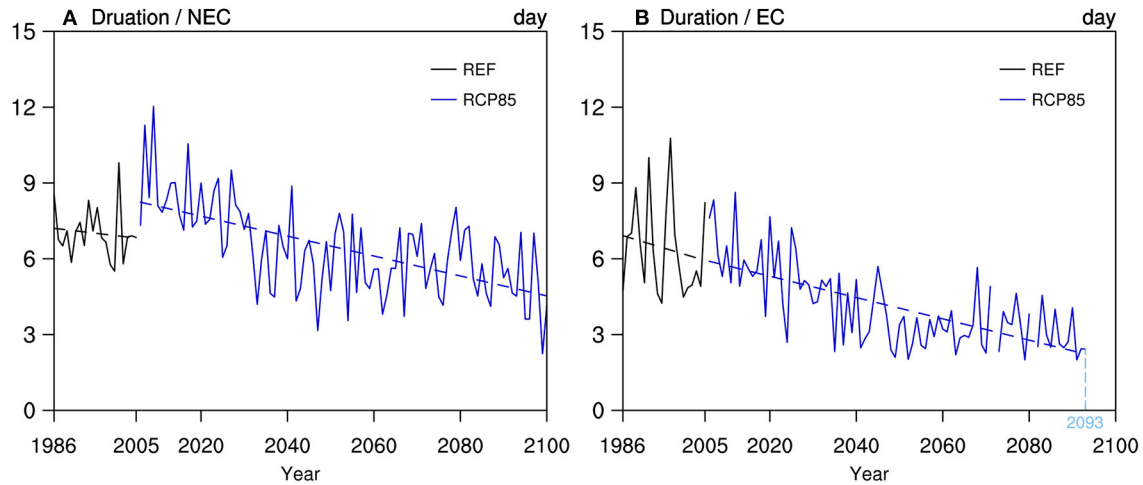

FIGURE 11 | Time series of chilling damage duration (unit: day) for reference (1986–2005) and future projection (2006–2100) by LMDZ-MME averaged over **(A)** Northeast China and **(B)** Central and East China. The black solid line indicates the historical simulation, and the blue solid line indicates the projection results under the RCP8.5 scenario; the dotted line indicates the linear regressions. The vertical light blue line and corresponding year represents the last time of event occurrence.

warming future. By the time of 2090–2100, the area hit by heat damage would be five times the reference value of 5% during 1986–2005. Examining the three risk levels of severity from heat damage, the heavy type shows the most conspicuous increasing tendency, whereas the medium type shows slight increasing during 2006–2100, and the light type decreases drastically by −11.5%/10a (**Figure 9D**).

Chilling Damage

Spatial Distribution

Under the emission scenario of RCP8.5, both intensity and extent of chilling damage in Northeast China decrease gradually (**Figure 10**). Pattern of DCD under 1.5°C global warming is similar with that in reference period except extent of light damage narrows northward slightly. When global warming reaches 2°C, the range of the heaviest chilling damage in the Xiaoxing'an Mountains decreases rapidly and almost diminishes in the Changbai Mountains. The area that might be hit with medium-intensity damage (3–4 days) shrinks further toward the north mountains. A light event with duration of 2 days widely spreads in the east Songnen plain. When global warming continues to rise to 3°C, the heaviest chilling damage remains largely the same in the area to the north 50 N, but coverage of the two other levels of DCD contracts and is limited in the plains between the Xing'anling and Changbai mountains. For 4°C global warming, the extent of light chilling damage further decreases, and there would be no more chilling damage in the Changbai Mountains.

The temporal variation of chilling damage of Northeast China during reference and projection time periods is shown in **Figure 11A**. During the reference time, the duration decreases at a rate of −0.20 d/10a, and the longest one exceeds 9 days. For 2006–2100, the duration of cold days decreases significantly at a rate of −0.39 d/10a with a significance level of 0.05. In addition, projected DCD shows a decadal variability, as Northeast China has longer low temperature days during 2006–2030 than the current climate by about 1.3 days. With regard to the effects of chilling damage on rice, both the extent and duration of a cold event in Northeast China decrease significantly with time, which indicates that rice is unlikely to be affected by severe chilling damage under the RCP8.5 emission scenario.

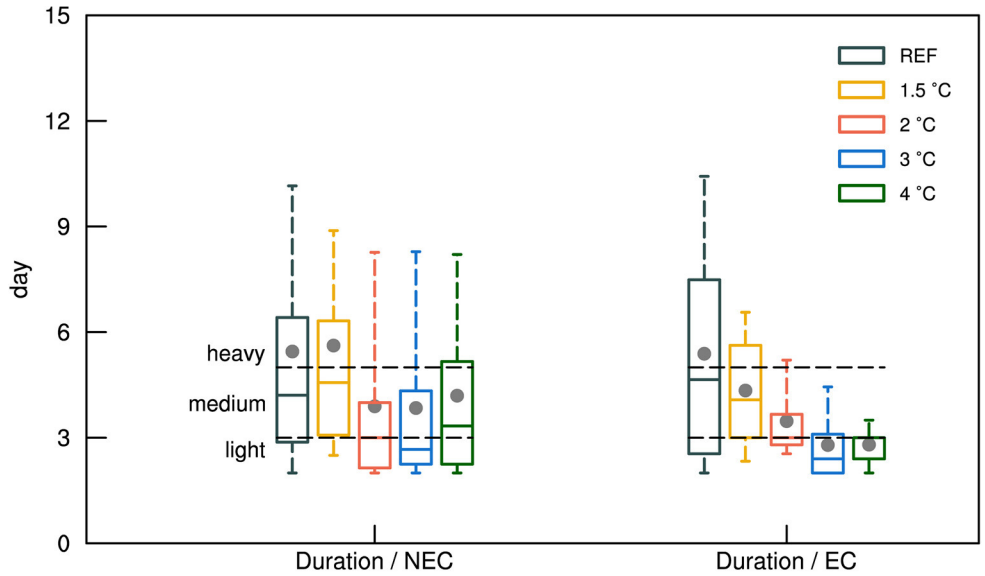

FIGURE 12 | Boxplots of chilling damage duration (unit: day) during the reference time period (1986–2005) and for 1.5, 2, 3, and 4°C warming levels in the future by LMDZ-MME over Northeast China and Central and East China. The top and bottom whiskers are the 10th and 90th percentiles. The black dotted lines indicate the corresponding rank of durations.

With global warming intensifying, a decrease of DCD also occurs in Central and East China (figure not shown). Similar to the pattern in the reference period, chilling damage mainly concentrates in the mountainous area under 1.5°C global warming. The heaviest damage in the Taihang Mountains reduces slightly, and two other level events basically maintain. With global warming reaching 2°C, the range of the heaviest chilling damage further reduces. If the global average warming reaches 3°C, cold events with duration longer than 5 days would not exist in Central and East China. Meanwhile, the extent of medium and light damage decreases gradually. With the global warming reaching 4°C, only the moderate and light chilling damage can be detected in Hebei and Shanxi provinces. Similar to those in Northeast China, chilling damage would greatly reduce in coverage, scattering over a few rice-producing areas in the north of Central and East China.

The DCD in Central and East China also has a decreasing tendency during both historical and projection time periods (**Figure 11B**). During the reference period, the duration has large interannual variability and linearly decreases with time at a rate of −0.52 d/10a. For 2006–2100, the DCD decreases at a rate of −0.42 d/10a with a significant level of 0.05. Notably, few chilling damages exist in Central and East China after 2093 under RCP8.5.

Changes of Impact Intensity and Coverage

As shown in **Figure 12**, DCD decreases gradually in both Northeast China and Central and East China though the discrepancies among different global warming thresholds are evident.

For Northeast China, light level chilling damage occurs over 25% of the area during the reference period. Under 1.5°C global warming, the median and mean are even greater than that in the reference period although the range of duration between 10th and 90th percentiles decreases by comparison. When global warming reaches 2°C, the median and mean reduces rapidly from 4.57 to 3.00 and 5.62 to 3.89 days, respectively (the former is the corresponding value under 1.5°C warming). Projection under 2°C warming associates with a much smaller interquartile model spread compared with that under 1.5°C warming, showing a larger proportion of light cold events and smaller of the heaviest one among cold events. However, a range between the 10th and 90th percentiles reduces slightly, which indicates that there is larger uncertainty in model projection under the warmer case. The response of DCD to 3°C global warming is similar to that of 2°C warming with a little bit lower median (2.67 days) and close mean (3.84 days). With the global warming rising to 4°C, the median, mean, and interquartile spread increase again. Proportion of medium-level chilling damage becomes greater.

Compared with Northeast China, the spread and intermodel variability of DCD differ among four global warming thresholds more obviously in Central and East China. During the reference period, although the heaviest chilling damage exists only at the north of Hebei and Shanxi province, it takes nearly half of the extent of cold events when a medium level event takes another. Under 1.5°C global warming, the range of duration decreases rapidly, particularly the 90th percentile end. The median and mean values reduce from 4.65 to 4.08 days and 5.39 to 4.34 days, respectively. When global warming is 2°C, the interquartile model spread further reduces evidently with median and mean decreasing by nearly 1 day. Medium chilling damage predominates the area. After global warming reaching 3 and 4°C, significantly, there is hardly any existence of the heaviest chilling damage. Light-intensity events become the main trend of damage.

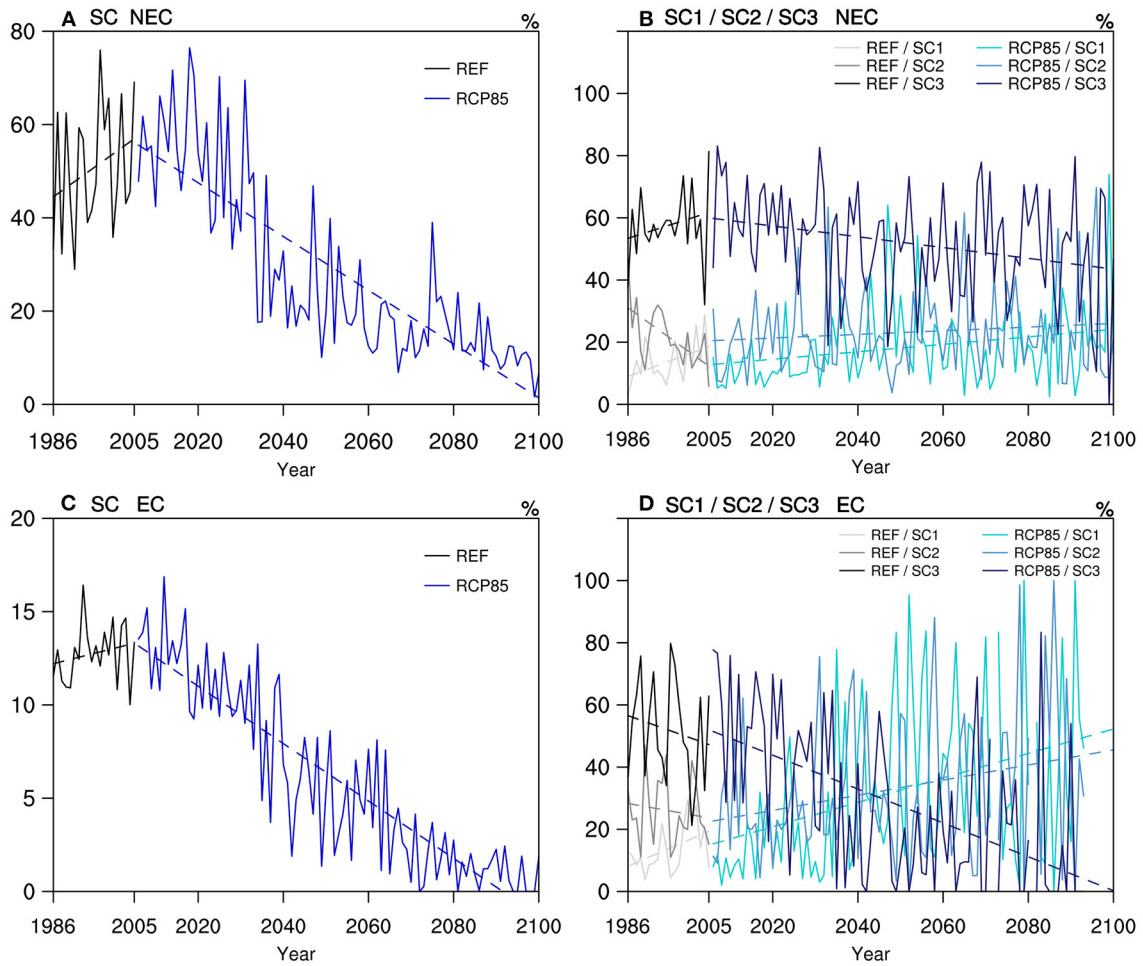

FIGURE 13 | Time series of control and projected indexes of regional impact of chilling damage (SC, unit: %) and of regional coverage of chilling damage with different intensity (SC1/SC2/SC3, unit: %) averaged over the **(A,B)** Northeast China and **(C,D)** Central and East China during 1986–2100. The light gray, dark gray, and black solid lines are for the historical simulation, and the light, bright, and dark blue lines represent the projection results under RCP8.5 scenario. The corresponding dotted lines indicate the linear regressions.

To examine the response of regional coverage of cold events from various severity to different warming levels, we define SC and SCi (i stands for the intensity levels) indices to focus on this part through investigating their temporal variation (**Figure 13**).

In Northeast China, the range of cold events (SC) increases at a rate of 6.55%/10a with a maximum percentage close to 80% during the reference period (**Figure 13A**). Among these events, the proportion of the heaviest (SC1) and light (SC3) damage continue to increase with time at rate of 5.05% and 4.39% per decade, respectively. Instead, the percentage of damage with medium intensity (SC2) decreases at rate of −9.89%/10a, and the trend passes the significant test at the 0.05 significance level.

However, SC decreases sharply at a significant rate of −5.76%/10a in 2006–2100 under the RCP8.5 scenario, especially after 2040s. By the end of the twenty-first century, the extent of occurrence of chilling damage is almost zero. On the other hand, different from the simulation, projected SC1 and SC2 both show the slow rise tendency at rate of 1.20 and 0.59% per decade with the former passing the significant test. On the contrary, projected SC3 declines at a significant rate of −1.73%/10a, which is faster than two other level events. These results indicate that, in the warming future, the range and intensity of chilling damage in Northeast China decrease constantly.

Events in Central and East China are similar to those in Northeast China with much slower trends at a rate of 0.58%/10a (**Figure 13C**). Because of wider domains and lower latitude, SC of Central and East China has a smaller value and the maximum is about 16%. Considering the different intensity level of the event, both SC2 and SC3 reduce at a rate of −2.43 and −4.89% per decade. SC1 has the opposite trend and increases at a significant rate of 5.89%/10a. What is more, in common with events in Northeast China, SC declines rapidly at a rate of −1.54%/10a under RCP8.5 scenario. Particularly, the range of chilling damage reaches zero first around the 2070s. Besides this, SCi in Central and East China has the same tendency as in Northeast China, i.e., SC1 and SC2 increase at rate of 3.93% and 2.43% per decade, and

SC3 declines at a rate of −5.44%/10a. All tendencies in Central and East China under the RCP8.5 scenario pass the significance test at the 0.05 significance level. Note that the amplitude of SCi in Central and East China is much larger that in Northeast China, SC1 even varying from 0 to 100% in the late twenty-first century.

In summary, chilling damage in Northeast China and Central and East China have similar characteristics of variation under global warming; that is, the spatial scale and duration of chilling damage reduces continuously with time. Events in Central and East China change at faster and more dramatic rates in comparison. The rice production area affected by cold events is also reducing gradually with global warming, particularly for areas in Northeast China.

CONCLUSION

Most of the rice yield of China is produced in the east, northeast, and central parts of the country, where the regional climate is dominated by the large-scale atmospheric circulations, such as the East Asia summer monsoon as well as regional scale climate processes. The regional climate change, including the occurrence of high temperatures and heavy rainfall events, can greatly affect regional crop production under future warming scenarios. Globally, the potential crop reduction in the future warming and increased extreme climate would enlarge the undernourished population and obscure the opportunities to fight poverty. Therefore, accurate evaluation of changes in rice-production related climate extremes can reduce the uncertainty in estimation of global food yields, improving the strategies and actions to secure regional food availability, guaranteeing the future sustainable agricultural development. In this study, we apply a stretch grid global model LMDZ4 to downscale six CMIP5 GCMs for historical and future regional climate under the emission pathway of RCP8.5. The temperature-related rice damage indexes were then generated using an ensemble average of six LMDZ4 downscaling runs (LMDZ MME). Our analysis shows that LMDZ can well-reproduce the spatial characteristics of both heat and chilling damage in Northeast China and Central and East China, especially in terms of presenting the heaviest chilling damage. LMDZ MME underestimates the magnitude of heat damage indexes for the area south of 32N when it shows an overestimation for the area north of 34N.

As temperatures are rising under the RCP8.5 emission pathway globally, significant changes in heat damage in the future are projected. For Northeast China, the extent of heat events continuously spread eastward with rapid increasing intensity, particularly under the 2°C threshold of global warming and above. For Central and East China, the rice heat damage spreads from a narrow band in Central China to the surrounding areas. When global warming reaches 4°C, almost the whole region is under the influence of a rice heat event of various intensities.

In the next 95 years, all of the heat indexes increase at a significant rate. Among the indices, H_a has the fastest increasing rate, followed by SDHD and MDHD, and finally T_{MX} in both regions. In terms of coverage of heat damage, the proportion of medium and heavy events gradually increases and light events decrease dramatically with the whole damage extent spreading, especially in Central and East China. Meanwhile, DCD and its spatial range in Northeast China and Central and East China both decrease with time for different global warming thresholds. It can be concluded that the rice production in the future will be less affected by the chilling events. Regionally, the chilling damage in Central and East China drops faster in coverage, whereas in Northeast China, relatively larger uncertainty is observed in model projected chilling events.

Chou et al. (2021) also show that H_a in North and Central China increased by 3.4–4.3°C/day and low-temperature damage decreased steadily in Northeast China when the global temperature rises from 1.5 to 2°C under SSP245 scenario. Similar results here confirm that Northeast China and Central and East China will experience a significant rise in risk of extreme heat disasters, significantly increasing the negative impact on rice production. With the growing population, unbalanced geographic distribution of wealth and resources, meeting the requirement/need for basic food and nutrition is a task in many regions and countries. At the same time, the urbanization in the major rice production countries of East and South Asia continues to expand, accelerating the transfer of precious paddy fields and other cropland into urban areas. In the future, the shortage of land and intensified natural disasters related to warmer climates would damage the already fragile rice production, adding an extra dimension of challenges and uncertainties in assessing the future food security. This paper is committed to estimate the responses of extreme temperature and related rice disasters to various warming thresholds in a major rice production area of China. So far, the influence of rice varieties, prices, planting techniques, and other socioeconomic factors is not considered in our study though we believe they all play important roles on rice security at various spatial and temporal scales. In the future, by applying the Earth System Model that contains the socioeconomic module, more thorough assessment can be performed.

DATA AVAILABILITY STATEMENT

The original contributions presented in the study are included in the article/supplementary material, further inquiries can be directed to the corresponding author/s.

AUTHOR CONTRIBUTIONS

SL was responsible for data analysis, plotting, and drafting the manuscript. SW and GT contributed to the experimental design, providing analysis plan, and drafting the manuscript. ZJ and JC contributed to this work by providing data, related references, information, and proofreading of the manuscript. All authors contributed to the article and approved the submitted version.

FUNDING

This research was supported by the National Key Research Development Program of China (2017YFA0603803) and Science and Technology Development Plan in Jilin Province of China (Grant 20180101016JC).

REFERENCES

Aggarwal, P. K., Bandyopadhyay, S. K., Pathak, H., Kalra, N., Chander, S., and Kumar, S. (2000). Analysis of yield trends of the rice-wheat system in north-western India. *Outlook Agric*. 29, 259–268. doi: 10.5367/000000000101293329

Bao, Y.-X., Liu, W., and Gao, P., Shen, S.-H. (2012). Study on characteristics of rice heat damages in Jiangsu province under the background of climate warming and its influence on the rice yield. *Chin. J. Agrometeorol*. 33, 289–296. doi: 10.3969/j.issn.1000-6362.2012.02.022

Bates, B.C., Kundzewicz, Z. W., Wu, S., and Palutikof, J. P., (eds.). (2008). *Climate Change and Water. Technical Paper of the Intergovernmental Panel on Climate Change*. Geneva: IPCC Secretariat. p. 210.

Chen, J., Gao, C., Zeng, X., Xiong, M., Wang, Y., Jing, C., et al. (2017). Assessing changes of river discharge under global warming of 1.5 °C and 2 °C in the upper reaches of the Yangtze River Basin: approach by using multiple- GCMs and hydrological models. *Quat. Int*. 453, 63–73. doi: 10.1016/j.quaint.2017.01.017

Chou, J., Zhao, W., Li, J., Xu, Y., Yang, F., Sun, M., et al. (2021). Changes in extreme climate events in rice-growing regions under different warming scenarios in China. *Front. Earth Sci*. 9, 655128. doi: 10.3389/feart.2021.655128

CMA Climate Change Centre (2019). *Blue Book on Climate Change in China*. Beijing: Science Press.

Dufresne, J. L., Foujols, M. A., Denvil, S., Caubel, A., Marti, O., Aumont, O., et al. (2013). Climate change projections using the IPSL-CM5 earth system model: from CMIP3 to CMIP5. *Clim. Dyn*. 40, 2123–2165. doi: 10.1007/s00382-012-1636-1

FAO (2017). *The Future of Food and Agriculture – Trends and Challenges*. Rome: FAO.

Fischer, G., Shah, M., and van Velthuizen, H. (2002). *Climate Change and Agriculture Vulnerability. Special Report as Contribution to the World Summit on Sustainable Development, Johannesburg 2002.* Laxenburg: International Institute for Applied Systems Analysis. p. 150–152.

Frédéric, H., Ionela, M., Sandrine, B., Pascale, B., Francis, C., and Jean-Louis, D. (2006). The LMDZ4 general circulation model: climate performance and sensitivity to parametrized physics with emphasis on tropical convection. *Clim. Dyn*. 27, 787–813. doi: 10.1007/s00382-006-0158-0

Gao, Q., Jiang, Z., and Li, Z. (2017). Simulation and evaluation of multi-model dynamical downscaling of temperature extreme indices over the Middle and East China. *Acta Meteorol. Sin*. 75, 917–933. doi: 10.11676/qxxb2017.067

Guo, L., Gao, Q., Jiang, Z., and Laurent, L. (2018). Bias correction and projection of surface air temperature in LMDZ multiple simulation over central and eastern China. *Adv. Clim. Change Res.* 9, 81–92. doi: 10.1016/j.accre.2018.02.003

Huang, J., Ji, M., Liu, Y., Zhang, L., and Gong, D. (2013). An overview of arid and semi-arid climate change. *Adv. Clim. Change Res.* 9, 9–14. doi: 10.3969/j.issn.1673-1719.2013.01.002

Hui, P., Tang, J., Wang, S., Niu, X., Zong, P., and Dong, X. (2018a). Climate change projections over China using regional climate models forced by two CMIP5 global models. Part I: evaluation of historical simulations. *Int. J. Climatol*. 38, e57–e77. doi: 10.1002/joc.5351

Hui, P., Tang, J., Wang, S., Niu, X., Zong, P., and Dong, X. (2018b). Climate change projections over China using regional climate models forced by two CMIP5 global models. Part II: projections of future climate. *Int. J. Climatol*. 38, e78–e94. doi: 10.1002/joc.5409

IFPRI (2016). *2016 Global Food Policy Report*. Washington, DC: International Food Policy Research Institute.

IPCC (2013). Climate Change 2013: *The Physical Science Basis. Contribution of Working Group I to the Fifth Assessment Report of the Intergovernmental Panel on Climate Change.* [T.F. Stocker, D. Qin, G.-K. Plattner, M. Tignor, S.K. Allen, J. Boschung, A. Nauels, Y. Xia, V. Bex and P. M. Midgley, (eds.)]. Cambridge, UK; New York, NY: Cambridge University Press. p. 1535.

Li, Z. (1999). Ensemble atmospheric GCM simulation of climate interannual variability from 1979 to 1994. *J. Clim*. 12, 986–1001. doi: 10.1175/1520-0442(1999)012<0986:EAGSOC>2.0.CO;2

Li, Z., Liu, Z., Anderson, W., Yang, P., Wu, W., Tang, H., et al. (2015). Chinese rice production area adaptations to climate changes, 1949–2010. *Environ. Sci. Technol*. 49, 2032–2037. doi: 10.1021/es505624x

Ma, S., Wang, Q., Wang, C., and Huo, Z. (2011). Climate risk and economy vulnerability of rice chilling damage and division in Northeast China. *Geograph. Res*. 30, 931–938. doi: 10.11821/yj2011050017

Mei, F. Q., Wu, X. Z., Yao, C. X., Li, L. P., Wang, L., and Chen, Q. Y. (1988). Rice cropping regionalization in China. *Chin. Rice Sci. J*. 2, 97–110. doi: 10.16819/j.1001-7216.1988.03.001

People Republic of China Meteorological Industry Standard (2009). *Grade of Chilling damage for rice and maize, the People Republic of China Meteorological Industry Standard QX/T 101-2009*. Available online at: www.csres.com/ (accessed Jan, 18, 2022).

People Republic of China National Standard (2020). *Meteorological Grades of Hot Damage to Rice, the People Republic of China National Standard GB/T 37744-2019*. Available online at: www.cma.gov.cn (accessed Jan, 18, 2022).

Sekhar, C.S. C. (2018). *Climate Change and Rice Economy in Asia: Implications for Trade Policy*. Rome: FAO. p. 62.

Shi, Y., Guo, E., Zhang, Z., Zhu, X., and Yang, X. (2020). Spatial-temporal characteristics of agricultural climate resources and sterile-type chilling injury in rice growing season in three provinces of Northeast China. *Chin. J. Appl. Ecol*. 31, 1625–1635. doi: 10.13287/j.1001-9332.202005.030

Tao, F., Yokozawa, M., Hayashi, Y., and Lin, E. (2003). Changes in agricultural water demands and soil moisture in China over the last half-century and their effects on agricultural production. *Agric. For. Meteorol*. 118, 251–261. doi: 10.1016/S0168-1923(03)00107-2

Tao, F., Yokozawa, M., Zhang, Z., Hayashi, Y., Grassl, H., and Fu, C. (2004). Variability in climatology and agriculture production in China in association with the East Asian summer monsoon and El Nino Southern Oscillation. *Clim. Res*. 28, 23–30. doi: 10.3354/cr028023

Wang, J., Huang, J., and Rozelle, S. (2010). *Climate Change and China's Agricultural Sector: An Overview of Impacts, Adaptation and Mitigation, ICTSD–IPC Platform on Climate Change, Agriculture and Trade, Issue Brief No.5*. International Centre for Trade and Sustainable Development. Geneva, Switzerland and International Food and Agricultural Trade Policy Council, Washington DC, USA.

Wang, P., Wei, X., Zhang, Z., Chen, Y., Song, X., Shi, P., et al. (2020). A review of cold injury and heat damage to rice growth under global warming. *Resour. Sci*. 36, 2316–2326.

Wijeratne, M. A. (1996). Vulnerability of Sri Lanka tea production to global climate change. *Water Air Soil Pollut*. 92, 87–94. doi: 10.1007/978-94-017-1053-4_8

Wu, J., and Gao, X. (2013). A gridded daily observation dataset over China region and comparison with the other datasets. *Chin. Geophys. J*. 56, 1102–1111. doi: 10.6038/cjg20130406

Xiong, W., Feng, L., Ju, H., and Yang, D. (2016). Possible impacts of high temperatures on China's rice yield under climate change. *Adv. Earth Sci*. 31, 515–528. doi: 10.11867/j.issn.1001-8166.2016.05.0515

Yang, H., Jiang, Z., and Laurent, L. (2016). Biases and improvements in three dynamical downscaling climate simulations over China. *Clim. Dyn*. 47, 3235–3251. doi: 10.1007/s00382-016-3023-9

Yang, J., Zhang, Y. Z., He, H. H., Li, Y. C., Chen, X. R., Bian, J. M., et al. (2020). Current status and research advances of high-temperature hazards in rice. *Ying Yong Sheng Tai Xue Bao*. 31, 2817–2830. doi: 10.13287/j.1001-9332.202008.027

Zhao, C., Liu, B., Piao, S., Wang, X., Lobell, D. B., Huang, Y., et al. (2017). Temperature increase reduces global yields of major crops in four independents estimates. *Proc. Natl. Acad. Sci. USA*. 114, 9326–9331. doi: 10.1073/pnas.1701762114

Conflict of Interest: The authors declare that the research was conducted in the absence of any commercial or financial relationships that could be construed as a potential conflict of interest.

Publisher's Note: All claims expressed in this article are solely those of the authors and do not necessarily represent those of their affiliated organizations, or those of the publisher, the editors and the reviewers. Any product that may be evaluated in this article, or claim that may be made by its manufacturer, is not guaranteed or endorsed by the publisher.

frontiers in Physics

ORIGINAL RESEARCH
published: 21 February 2022
doi: 10.3389/fphy.2021.687900

An Attempt to Appreciate Climate Change Impacts From a Rank-Size Rule Perspective

*Kazuya Hayata**

Department of Economics, Sapporo Gakuin University, Ebetsu, Japan

For representative observational stations on the globe, rank-size analyses are made for vectors arising from sequences of the monthly distributions of temperatures and precipitations. The ranking method has been shown to be useful for revealing a statistical rule inherent in complex systems such as texts of natural languages. Climate change is detectable through the rotation angle between two 12-dimensional vectors. The rankings of the angle data for the entire station are obtained and compared between the former (from 1931 to 1980) and the latter (from 1951 to 2010) period. Independently of the period, the variation of the angles is found to show a long tail decay as a function of their ranks being aligned in descending order. Furthermore, it is shown that for the temperatures, nonlinearities in the angle-rank plane get stronger in the latter period, confirming that the so-called snow/ice-albedo feedback no doubt arises. In contrast to the temperatures, no sign of a feedback is found for the precipitations. Computed results for Japan show that the effect is consistent with the global counterpart.

Keywords: global warming, climate crisis, climate emergency, snow/ice-albedo feedback, vectorial rotation method, rank-size rule, long tail phenomena

OPEN ACCESS

Edited by:
Yongping Wu,
Yangzhou University, China

Reviewed by:
Abraão Nascimento,
Federal University of Pernambuco, Brazil
Federico Musciotto,
Central European University, Hungary

***Correspondence:**
Kazuya Hayata
hayata@sgu.ac.jp

Specialty section:
This article was submitted to Interdisciplinary Physics, a section of the journal Frontiers in Physics

Received: *30 March 2021*
Accepted: *17 December 2021*
Published: *21 February 2022*

Citation:
Hayata K (2022) An Attempt to Appreciate Climate Change Impacts From a Rank-Size Rule Perspective. Front. Phys. 9:687900. doi: 10.3389/fphy.2021.687900

INTRODUCTION

All the governments in the world are currently confronted with the difficult problem of both mitigating climate change and maintaining sustainable development. Of the climate change impacts [1–3], in particular, global warming has become the most serious problem necessary to be dealt with urgently in cooperation with the developed and developing countries. In recent years, research articles of climate change have grown substantially in number, even if we restrict our attention within interdisciplinary physics [4–19]. For the analytical methods, besides conventional techniques that have been adopted in statistical physics, novel approaches have been attempted such as wavelet transformation methods [9–13], multiscale entropy analysis [10], convergent cross mapping (CCM) [12], a method using Minkowski distance functions [18], and the vectorial rotation method [19]. In this paper, for representative observational stations in the world as dotted on the map in **Figure 1** [19], rank-size analyses are made for vectors that reflect sequential variations of the monthly temperatures and precipitations. The ranking method has been applied principally to revealing a statistical rule or law hidden in texts of natural languages; the most typical example is no doubt the Zipf's law, being known as a power law relation in the word occurrence versus its rank that is aligned in descending order [20–26]. To our knowledge, however, no attempt has been made to apply the rank-size methodology to the study of climate change impacts. Through specific numerical results we can examine whether, along with conventional applications to complex systems, the rank-size approach is useful for revealing climate change impacts both in the global and in the regional scale.

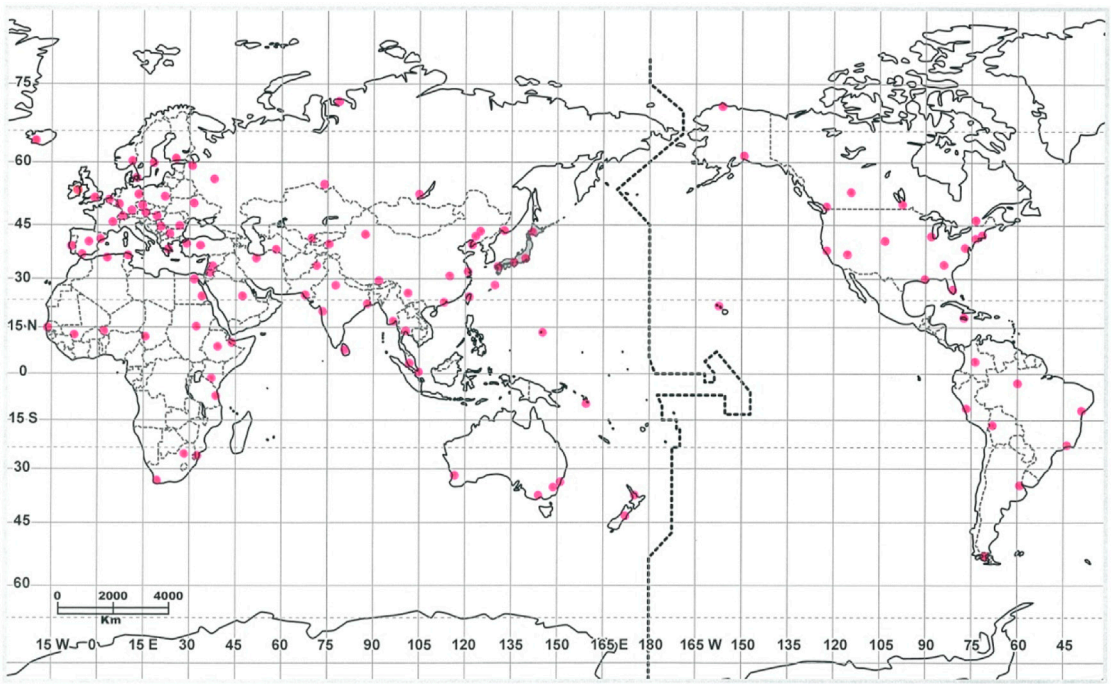

FIGURE 1 | The plots of observational stations (pink dots) in the world [19].

METHODOLOGY

Generating Angle Data

From the original data of the monthly temperatures and precipitations [27–29], the angle data can be obtained according to the procedure detailed in Ref. [19]. The cross angle θ between two twelve-dimensional vectors, $\boldsymbol{p}$ and $\boldsymbol{q}$, of the subsequent periods can be obtained by

$$\theta = \arccos[(\boldsymbol{p}\cdot\boldsymbol{q})/(|\boldsymbol{p}||\boldsymbol{q}|)], \tag{1}$$

which corresponds to climate change from the former to the latter periods. Here $\boldsymbol{p}\cdot\boldsymbol{q}$ indicates the scalar product between $\boldsymbol{p}$ and $\boldsymbol{q}$. For instance, for the temperatures, the magnitude of the angle at a certain station with relatively high latitude increases substantially because of the snow/ice-albedo feedback [30–32].

Rank-Size Analysis

The intersecting angles θ_i ($0 \le \theta_i \le 180^\circ$; $i = 1, 2, \ldots, n$; n being the size of samples, i.e. the number of stations) will be analyzed statistically. Specifically, as regressions on the angles versus the ranks, three modellings are possible:

$$\text{Linear}: \theta = a - b\chi, \tag{2}$$

$$\text{Exponential}: \log\theta = a - b\chi, \tag{3}$$

$$\text{Logarithmic}: \theta = a - b\log\chi, \tag{4}$$

where log abbreviates the common logarithm; χ represents the rank variable in descending order; a and b are positive constants to be determined with the least squares fit. The accuracy of the respective model can be examined by the degree of fit, $|r|$, namely with the Pearson's coefficient ($0 < |r| < 1$), and with the Durbin-Watson ratio, d ($0 < d < 4$) [33–35]. In what follows, to exclude unnecessary meanderings of dots in the $\theta\chi$-plane we shall restrict our attention to n less than the Dunbar's number, i.e., $n \lesssim 150$. Provided that the best logarithmic fit is established, **Eq. 4** will subsequently be modified with introducing a positive parameter q [36–38]

$$\theta^q = a - b\log\chi. \tag{5}$$

Note that with the additional parameter the optimal values for (a, b) are renewed. Although, mathematically, extending a domain of q to the complex number might be interesting, we confine the domain within the real number. It should be noted here that because the relative angle is confined within [0, 180°], no problem arises in making regression of an angular response variate on a set of linear explanatory variables [39, 40]. In order to analytically examine the behavior of the regression curve, the first derivative of θ is given

$$\theta'/\theta = -b/(q\chi\theta^q) \propto -1/(q\theta^q), \tag{6}$$

where $\theta' = \mathrm{d}\theta/\mathrm{d}\chi$. **Eq. 6** shows that for $\theta > 1$, $|\theta'/\theta|$ gets larger with decreasing q.

Finally, to comprehend the link with the power law (i.e., log-log) relation, with the use of the Box-Cox transformation [41], **Eq. 5** will be rewritten as

$$(\log e)(\theta^q - 1)/q = a' - b'\log\chi, \tag{7}$$

$$a' = (\log e)(a-1)/q,\ b' = (\log e)b/q, \tag{8}$$

where e is the Napier's constant. In the derivation of **Eq. 7** the formula [41]

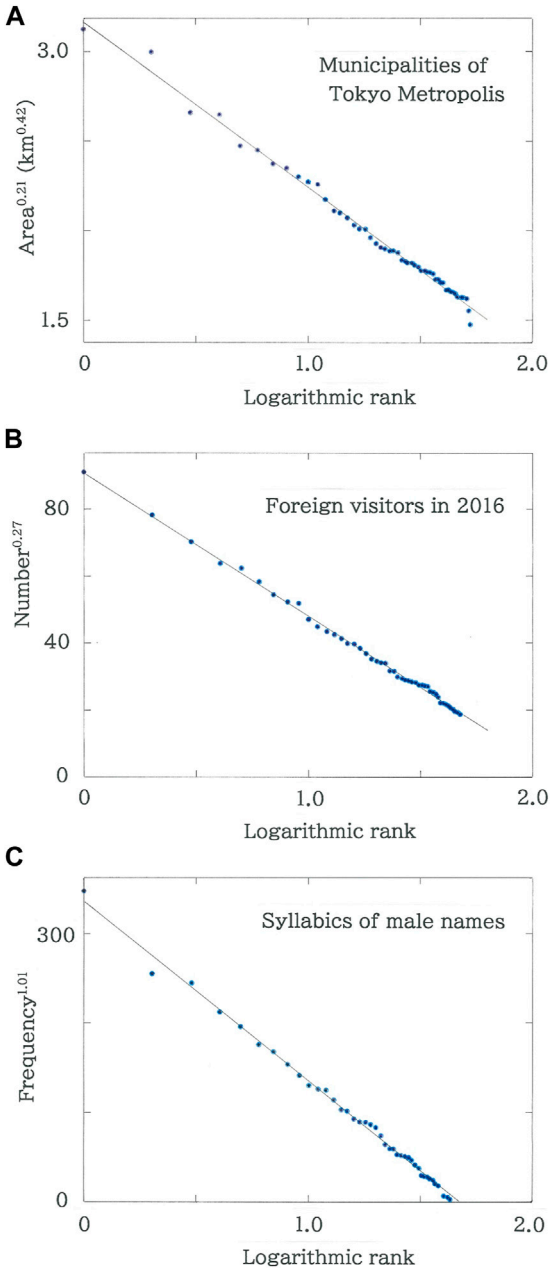

FIGURE 2 | Examples of rank-size rules. **(A)** Rank dependence of the areas of municipalities in the Metropolis of Tokyo. The line indicates the optimized fit ($|r| = 0.9961$ with $d = 1.861$ for $q = 0.21$ and $n = 53$). **(B)** Rank dependence of the numbers of foreign visitors in the 47 Japanese prefectures (data from January to December, 2016). The line indicates the optimized fit ($|r| = 0.9988$ with $d = 1.160$ for $q = 0.27$ and $n = 47$). **(C)** Rank dependence of the frequencies of Japanese syllabics in 1,000 male given names. The line indicates the optimized fit ($|r| = 0.9977$ with $d = 2.041$ for $q = 1.01$ and $n = 41$).

$$(\log e)(\theta^q - 1)/q \to \log\theta \; as \; q \to 0, \tag{9}$$

has been implied. The smaller the magnitude of q, the stronger the kurtosis (i.e., nonlinearities with the positive curvature) in the plane on the rotation angle versus the rank. Thus, along with ΔT (K) and ΔH (mm), by tracing the change of the key parameter q, one can appreciate a sign of a global-scale positive feedback. Here ΔT (K) (ΔH (mm)) stands for the increment of the mean temperature (the mean annual precipitation) from the former to the latter period.

Examples of Rank-Size Rules

To date, sustained efforts have been made to find nontrivial rules in the ranking of a variety of complex systems, not only in linguistics but in geometry, geography, demography, and sciences on social phenomena [20–26, 36–38]. More recently has ranking been regarded as a tool useful for condensing large-scale data that have been accumulating in contemporary sciences such as, e.g., computational metallurgy [42] and gravitational wave astronomy [43], though the results are not yet ready for finding a rule. Below, to illustrate the rank-size rule, three examples of the preceding analysis are selected in **Figure 2**:

1) The Metropolis of Tokyo with the entire area 2,187 km^2 consists of 62 municipalities, nine of which are located off the main land [44]. **Figure 2A** shows the rank dependence of the areas of municipalities (excluding those on islands) in the Metropolis of Tokyo. The line in the figure indicates the optimal fit to **Eq. 5** ($|r| = 0.9961$ with $d = 1.861$ for $q = 0.21$ and $n = 53$). The rank-size rule has been preserved at least for several decades because this prefecture has not experienced a large-scale municipal consolidation. The magnitude of q was found to be smallest among all the prefectures in Japan. Indeed, the value tends to be larger as the number density of municipalities of a prefecture gets lower [36, 37]. In computational geometry, an analog with such an extremely squeezed configuration as seen for Tokyo Metropolis can be found in squared squares [36]. For instance, for the Willcocks' square [45], $q = 0.78$ with $|r| = 0.9945$ and $d = 1.450$, while for the Duijvestijin's square [46], $q = 0.84$ with $|r| = 0.9977$ and $d = 1.521$.
2) Japan is divided into 47 prefectures, each of which has been playing a battle to increase its share of the market for the foreign visitors from East Asian countries as well as the United States, Europe, and Australia. **Figure 2B** plots the rank dependence of the numbers of foreign visitors in the 47 Japanese prefectures (data from January to December, 2016 [47]). The line in the figure indicates the optimal fit ($|r| = 0.9988$ with $d = 1.160$ for $q = 0.27$ and $n = 47$). With the extremely high degree of fit to the function of **Eq. 5** a series of 47 dots align in an exquisite harmony. The top three on the ranking are Tokyo Metropolis, Osaka Prefecture, and Hokkaido. The arrangement of dots on the line bears the strong nonlinearity ($q = 0.27$), which reminds one of the so-called Matthew effect [48–51] that implies 'rich-get-richer.'
3) Japanese texts can be written with 45 syllabaries. **Figure 2C** depicts the dependence of the frequencies of Japanese syllabics in 1,000 male given names [52]. The line in the figure indicates the optimal fit to **Eq. 5** ($|r| = 0.9977$ with $d = 2.041$ for $q = 1.01$ and $n = 41$). It is surprising to note that without interactions among godparents the distribution of the syllabics exhibits

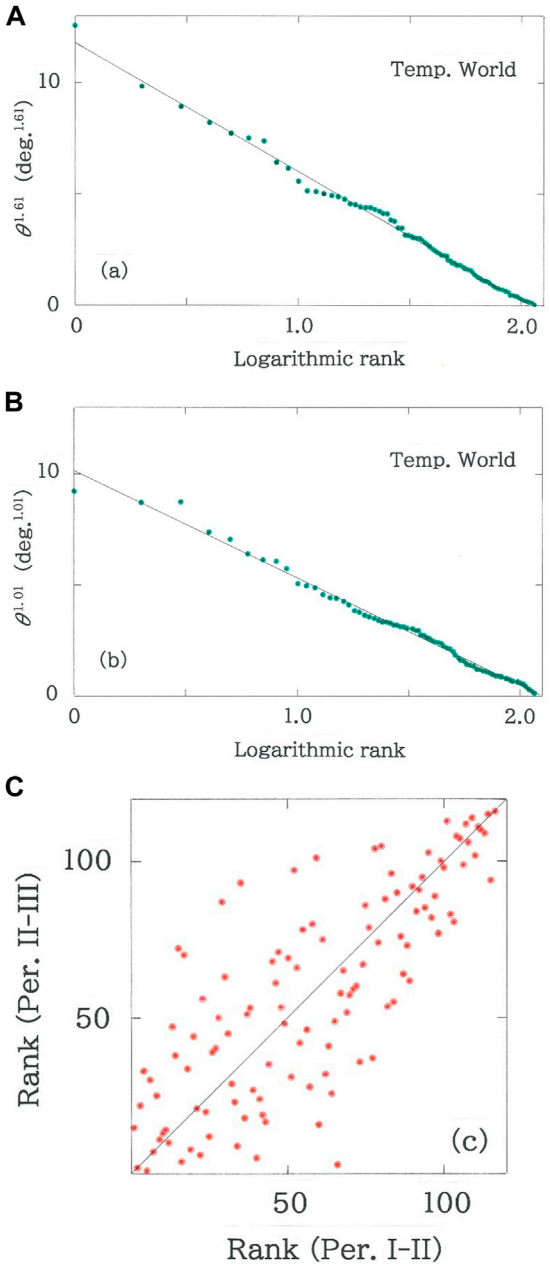

FIGURE 3 | Rank dependence of the cross angles of the monthly temperatures on the World stations (**Supplementary Tables S1,S2** in Supplementary Material). **(A)** From Period I (from 1931 to 1960) to Period II (from 1951 to 1980). The line indicates the optimized fit ($|r|$ = 0.9974 with d = 0.594 for q = 1.61 and n = 115). **(B)** From Period II (from 1951 to 1980) to Period III (from 1981 to 2010). The line in the plots indicates the optimized fit ($|r|$ = 0.9961 with d = 0.784 for q = 1.01 and n = 116). **(C)** Scattergram of rank data of Period II to III versus the data of Period I to II (r_S = 0.7907 with d = 2.021 for n = 116).

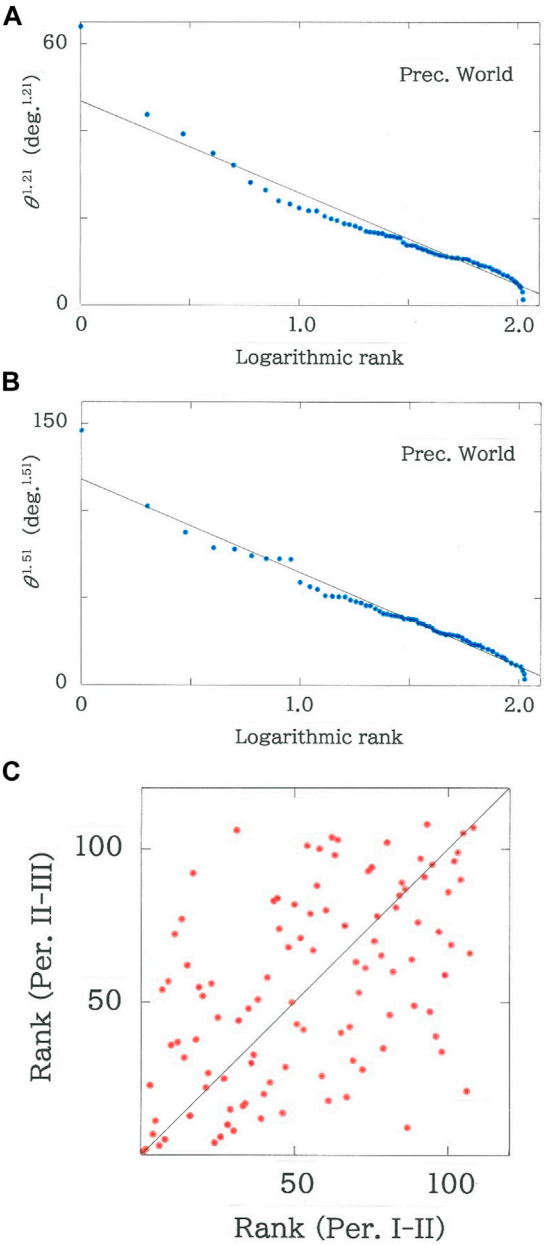

FIGURE 4 | Rank dependence of the cross angles of the monthly precipitations on the World stations. **(A)** From Period I (from 1931 to 1960) to Period II (from 1951 to 1980). The line indicates the optimized fit ($|r|$ = 0.9675 with d = 0.409 for q = 1.21 and n = 106). **(B)** From Period II (from 1951 to 1980) to Period III (from 1981 to 2010). The line indicates the optimized fit ($|r|$ = 0.9863 with d = 0.709 for q = 1.51 and n = 107). **(C)** Scattergram of rank data of Period II to III versus the data of Period I to II (r_S = 0.5183 with d = 1.994 for n = 108).

such a simple rule. Incidentally it should be remembered here that instead of the power law (Zipf's law) for the word occurrence, alphabetical frequencies in English texts obey the logarithmic law with q = 1 [20].

RESULTS

Global Analysis

Computed results of the temperatures and precipitations, respectively, are given in **Figures 3**, **4**. In both cases, of the

TABLE 1A | Top-twenty World stations in the intersecting angle of the monthly temperatures from Period I (from 1931 to 1960) to Period II (from 1951 to 1980).

Rank	Station	Lat. (°′)		θ (°)	Δ T (K)
01	Urumchi	43	47 N	10.93	+2.9
02	Oslo	60	12 N	4.81	−0.6
03	Reykjavik	64	08 N	4.14	−0.4
04	Ostrov Dikson	73	30 N	3.90	−1.4
05	Edmonton	53	34 N	3.70	+0.4
06	Sofia	42	39 N	3.57	−0.2
07	Omsk	55	01 N	3.50	+0.4
08	Luxembourg	49	37 N	3.47	−0.5
09	Helsinki	60	19 N	3.17	+0.3
10	Vladivostok	43	07 N	2.98	−0.1
11	Warszawa	52	09 N	2.91	−0.1
12	Stockholm	59	21 N	2.77	−0.4
13	Atlanta	33	39 N	2.75	−0.5
14	Kashgar	39	28 N	2.73	0.0
15	Damascus	33	25 N	2.70	−1.5
16	Moskva	55	50 N	2.68	+0.2
17	Ankara	39	57 N	2.64	0.0
18	Tashkent	41	20 N	2.57	+0.4
19	Winnipeg	49	55 N	2.56	−0.3
20	Addis Ababa	09	02 N	2.52	+1.1

ΔT stands for the increment of the mean temperature from the former to the latter period.

TABLE 1B | Top-twenty World stations in the intersecting angle of the monthly temperatures from Period II (from 1951 to 1980) to Period III (from 1981 to 2010).

Rank	Station	Lat. (°′)		θ (°)	Δ T (K)
01	Edmonton	53	34 N	9.05	+1.2
02	Oslo	60	12 N	8.57	+1.1
03	Anchorage	61	09 N	8.56	+1.0
04	Moskva	55	50 N	7.26	+1.2
05	St. Petersburg	59	58 N	6.93	+1.2
06	Irkutsk	52	16 N	6.31	+1.3
07	Omsk	55	01 N	6.05	+1.3
08	Winnipeg	49	55 N	5.98	+0.7
09	Chang-chun	43	54 N	5.63	+0.8
10	Stockholm	59	21 N	5.00	+0.5
11	Helsinki	60	19 N	4.90	+0.6
12	Kiev	50	24 N	4.80	+0.8
13	Vladivostok	43	07 N	4.52	+0.7
14	Warszawa	52	09 N	4.35	+0.7
15	Urumchi	43	47 N	4.34	+0.1
16	Muenchen	48	21 N	4.21	+1.3
17	Dalian	38	54 N	4.05	+0.2
18	London	51	28 N	3.82	+2.3
19	Koebenhavn	55	41 N	3.75	+0.6
20	Sapporo	43	03 N	3.62	+0.9

four modellings (**Eqs. 2–5**) the best fit to the logarithmic function, **Eq. 5**, has been confirmed. Specifically, for the temperatures, over Period I (from 1931 to 1960) to Period II (from 1951 to 1980), $|r| = 0.9974$ with $d = 0.594$ for $q = 1.61$ ($n = 115$), while over Period II (from 1951 to 1980) to Period III (from 1981 to 2010), $|r| = 0.9961$ with $d = 0.784$ for $q = 1.01$ ($n = 116$). For the precipitations, over Period I to II, $|r| = 0.9675$ with $d = 0.409$ for $q = 1.21$ ($n = 106$), while over Period II to III, $|r| = 0.9863$ with $d = 0.709$ for $q = 1.51$ ($n = 107$). The reason why the number of dots fluctuates within $106 \leq n \leq 116$ will be mentioned below. The top-twenty rankings of the rotation angle are listed, respectively, in **Tables 1A**, **1B**, and in **Tables 2A**, **2B**. With these results we comment as follows:

1) For Period I (from 1931 to 1960) to Period II (from 1951 to 1980), rank dependence of the rotation angles of the monthly distributions of temperatures on the World stations is shown in **Figure 3A**. The line in the figure indicates the optimized fit to **Eq. 5** ($|r| = 0.9974$ with $d = 0.594$ for $q = 1.61$ and $n = 115$), where an exceptional datum on the top ranking, Urumchi, is excluded. It can be seen that the dots are regularly arranged according to the rank-size rule, but there exist three clusters in the dots' aggregations. The magnitude of q considerably larger than unity ($q = 1.61$) indicates that the effect due to the snow/ice-albedo feedback is not yet so critical in this period (**Table 1A**).
2) For Period II (from 1951 to 1980) to Period III (from 1981 to 2010) the rank dependence of the cross angles is given in **Figure 3B**. The line in the figure indicates the optimal fit with **Eq. 5** ($|r| = 0.9961$ with $d = 0.784$ for $q = 1.01$ and $n = 116$). It is found that although the rank-size rule is preserved, the magnitude of q decreases substantially in comparison with the former period, suggesting that the snow/ice-albedo feedback becomes critical in particular on the highly latitudinal stations in the Northern Hemisphere (for specific numeric, **Table 1B**).
3) In **Figure 3C**, scattergram is plotted for rank data of Period II to III versus those of Period I to II ($r_S = 0.7907$ with $d = 2.021$ for $n = 116$). Here r_S denotes the Spearman's coefficient of rank correlation

$$r_S = 1 - k_n \sum_i (\chi_i - \Psi_i)^2,\ k_n = 6/[n(n^2 - 1)] \qquad (10)$$

with the summation Σ_i for $i = 1$ to n; χ_i and ψ_i are the rank data along the axis of abscissas and ordinates, respectively. It is evident from the plots that, like a stomach bounded by the bottom of an esophagus and the top of a duodenum, the envelope of the intermediate dots swells out, indicating that the ranks exhibit higher mobilities in comparison with those aggregated in the vicinity of the top and bottom.

4) For Period I (from 1931 to 1960) to Period II (from 1951 to 1980), rank dependence of the rotation angles of the monthly distributions of precipitations on the World stations is shown in **Figure 4A**. The line in the figure indicates the optimized fit with **Eq. 5** ($|r| = 0.9675$ with $d = 0.409$ for $q = 1.21$ and $n = 106$), wherein two exceptional data on the top ranking, Asswan and Kashgar, are foreclosed. First, it is found in the plots that in sharp contrast to the temperature counterpart ($|r| = 0.9974$ in **Figure 3A**) the degree of fit, $|r|$, reduces substantially. Indeed, the arrangement of the dots creates a sigmoid curve rather than a straight line.
5) For Period II (from 1951 to 1980) to Period III (from 1981 to 2010) the rank dependence of the precipitations is given in **Figure 4B**. The line in the figure indicates the optimal fit to **Eq. 5** ($|r| = 0.9863$ with $d = 0.709$ for $q = 1.51$ and $n = 107$).

TABLE 2A | Top-twenty World stations in the intersecting angle of the monthly precipitations from Period I (from 1931 to 1960) to Period II (from 1951 to 1980).

Rank	Station	Lat. (°′)		θ (°)	Δ H (mm)
01	Asswan	23	57 N	90.00	−1.5
02	Kashgar	39	28 N	48.06	−33.9
03	Riyadh	24	42 N	31.06	+21.4
04	Cairo	30	06 N	22.73	−3.6
05	Urumchi	43	47 N	20.80	−97.4
06	Amman	31	59 N	18.83	+8.5
07	Damascus	33	25 N	17.59	−82.6
08	Kingston	17	56 N	15.75	+5.4
09	Ostrov Dikson	73	30 N	14.97	+77.4
10	Wuhang	30	36 N	13.78	−53.9
11	Taipei	25	02 N	13.43	−96.1
12	Buenos Aires	34	35 S	13.06	+122.9
13	Dalian	38	54 N	12.73	+52.0
14	Peshawar	34	01 N	12.72	−5.0
15	Luxembourg	49	37 N	12.15	+40.0
16	Tunis	36	50 N	11.82	+27.7
17	Dar Es Salaam	06	52 S	11.65	+87.5
18	Istanbul	40	54 N	11.32	−102.7
19	New Delhi	28	35 N	11.25	+71.9
20	Barcelona	41	17 N	11.01	+55.6

ΔH stands for the increment of the mean annual precipitation from the former to the latter period. Without their precipitation data available, Tehran, Khartoum, Djibouti, Bogota, La Paz, Lima, Maputo, and Honiara are excluded.

TABLE 2B | Top-twenty World stations in the intersecting angle of the monthly precipitations from Period II (from 1951 to 1980) to Period III (from 1981 to 2010).

Rank	Station	Lat. (°′)		θ (°)	Δ H (mm)
01	Asswan	23	57 N	52.52	+2.6
02	Kashgar	39	28 N	27.12	+19.4
03	Amman	31	59 N	21.46	−13.0
04	Karachi	24	54 N	19.37	−57.6
05	Kingston	17	56 N	18.00	+12.7
06	Las Vegas	36	05 N	17.88	+1.9
07	Cairo	30	06 N	17.33	+13.2
08	Melbourne	37	39 S	17.08	−239.7
09	Lyon	45	43 N	17.05	+24.4
10	Sydney	33	56 S	17.00	−212.9
11	Urumchi	43	47 N	14.85	+110.6
12	Shanghai	31	25 N	14.50	+36.5
13	Tunis	36	50 N	14.28	−26.8
14	Athinai	37	44 N	13.58	−12.8
15	Dar-El-Beida	36	41 N	13.57	−148.4
16	Madrid	40	24 N	13.43	−41.8
17	Lisboa	38	43 N	13.39	−39.0
18	Sofia	42	39 N	13.20	−67.0
19	Gibraltar	36	09 N	12.98	+23.2
20	Nairobi	01	19 S	12.81	−260.5

Without their precipitation data available, Tehran, Khartoum, Djibouti, Bogota, La Paz, Lima, Maputo, and Honiara are excluded.

Aside from the increase of q, there is no substantial change from the result of the former period (**Figure 4A**). One can see a discontinuity across the rank nine (Urumchi) and ten (Sydney). To conclude, comparison between **Figure 4A** and **Figure 4B** indicates that in contrast to the temperatures, there exists no evidence of the climatic positive feedback for the precipitations.

6) In **Figure 4C** scattergram is plotted for rank data of Period II to III versus the data of Period I to II ($r_S = 0.5183$ with $d = 1.994$ for $n = 108$). In comparison with the temperatures ($r_S = 0.7907$ for **Figure 3C**) the rank correlation coefficient reduces substantially. It can be concluded that the reduction in the rank correlation is caused by the stochastic nature of the precipitations.

Regional Analysis

Results of the temperatures and precipitations, respectively, are given in **Figures 5**, **6**. In both cases, of the four modellings (**Eqs. 2–5**) the best fit to the logarithmic function (**Eq. 5**) has been confirmed. Specifically, for the temperatures, over Period I (from 1931 to 1960) to Period II (from 1951 to 1980), $|r| = 0.9973$ with $d = 0.662$ for $q = 1.89$ ($n = 75$), while over Period II (from 1951 to 1980) to Period III (from 1981 to 2010), $|r| = 0.9883$ with $d = 0.477$ for $q = 0.91$ ($n = 75$). For the precipitations, over Period I to II, $|r| = 0.9705$ with $d = 0.666$ for $q = 3.77$ ($n = 74$), while over Period II to III, $|r| = 0.9932$ with $d = 0.540$ for $q = 2.49$ ($n = 75$). The reason why the number of dots fluctuates between $n = 74$ and 75 will be mentioned below. The top-twenty rankings of the rotation angle are listed in **Tables 3A**, **3B** for the temperatures and in **Tables 4A**, **4B** for the precipitations. With these results we remark as follows:

1) For Period I (from 1931 to 1960) to Period II (from 1951 to 1980), rank dependence of the cross angles of the monthly temperatures on the Japanese stations is shown in **Figure 5A**. The line in the figure indicates the optimized fit to **Eq. 5** ($|r| = 0.9973$ with $d = 0.662$ for $q = 1.89$ and $n = 75$). It can be seen that as has been found in the World counterpart (**Figure 3A**) the dots are linearly arranged according to the rank-size rule with several clusters in the dots' aggregations. Again, the magnitude of q becomes considerably larger than unity ($q = 1.89$), suggesting that the effect arising from the snow/ice-albedo feedback is not yet so apparent in the present period.
2) For Period II (from 1951 to 1980) to Period III (from 1981 to 2010) the rank dependence of the cross angles is given in **Figure 5B**. The line in the figure indicates the optimized fit to **Eq. 5** ($|r| = 0.9883$ with $d = 0.477$ for $q = 0.91$ and $n = 75$). It is found that although the rank-size rule is preserved, the magnitude of q decreases substantially in comparison with the former period (1.89→0.91), revealing that the snow/ice-albedo feedback becomes critical in particular on the highly latitudinal stations in Japan (for specific numeric, see **Table 3B**).
3) In **Figure 5C**, scattergram is plotted for rank data of Period II to III versus those of Period I to II ($r_S = 0.6381$ with $d = 2.125$ for $n = 75$). The dots' pattern shares a feature with the one in the World temperatures (**Figure 3C**). Namely, the envelope of the intermediate dots tends to swell out, indicating that except several spots in the vicinity of the top and bottom the ranking shows relatively high mobilities.
4) For Period I (from 1931 to 1960) to Period II (from 1951 to 1980), rank dependence of the rotation angles of the monthly distributions of precipitations on the Japanese stations is shown in **Figure 6A**. The line in the figure indicates the optimized fit to **Eq. 5** ($|r|$ = 0.9705 with

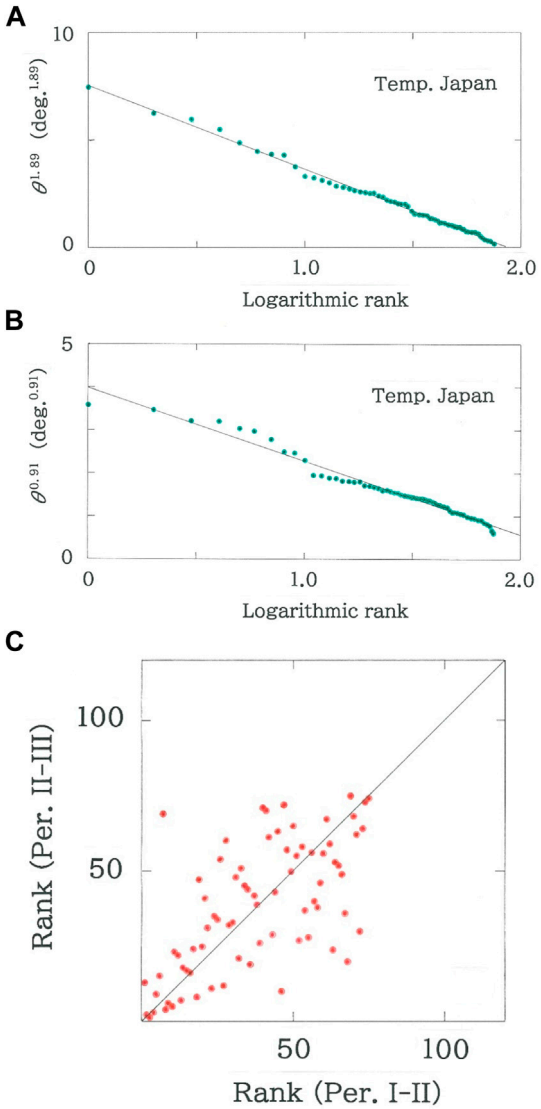

FIGURE 5 | Rank dependence of the cross angles of the monthly temperatures on the Japanese stations (**Supplementary Table S3** in Supplementary Material). **(A)** From Period I (from 1931 to 1960) to Period II (from 1951 to 1980). The line indicates the optimized fit ($|r| = 0.9973$ with $d = 0.662$ for $q = 1.89$ and $n = 75$). **(B)** From Period II (from 1951 to 1980) to Period III (from 1981 to 2010). The line indicates the optimized fit ($|r| = 0.9883$ with $d = 0.477$ for $q = 0.91$ and $n = 75$). **(C)** Scattergram of rank data of Period II to III versus the data of Period I to II ($r_S = 0.6381$ with $d = 2.125$ for $n = 75$).

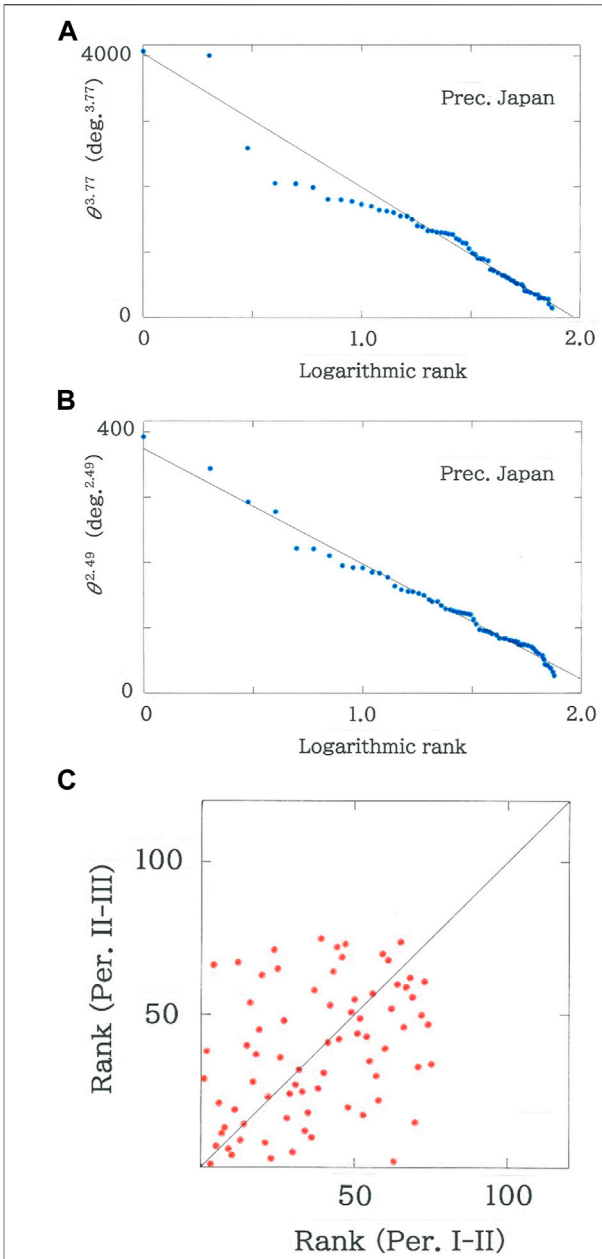

FIGURE 6 | Rank dependence of the cross angles of the monthly precipitations on the Japanese stations. **(A)** From Period I (from 1931 to 1960) to Period II (from 1951 to 1980). The line indicates the optimized fit ($|r| = 0.9705$ with $d = 0.666$ for $q = 3.77$ and $n = 74$). **(B)** From Period II (from 1951 to 1980) to Period III (from 1981 to 2010). The line indicates the optimized fit ($|r| = 0.9932$ with $d = 0.540$ for $q = 2.49$ and $n = 75$). **(C)** Scattergram of rank data of Period II to III versus the data of Period I to II ($r_S = 0.3797$ with $d = 1.992$ for $n = 75$).

$d = 0.666$ for $q = 3.77$ and $n = 74$), wherein an exceptional datum on the top ranking, Karuizawa, is foreclosed. First, it is found in the plots that in contrast to the temperatures (**Figure 5A**) the degree of fit, $|r|$, reduces substantially. As has been seen in the World precipitations the arrangement of the dots bears a sigmoid feature rather than a straight one.

5) For Period II (from 1951 to 1980) to Period III (from 1981 to 2010) the rank dependence of the precipitations is given in **Figure 6B**. The line in the figure indicates the optimized fit to **Eq. 5** ($|r| = 0.9932$ with $d = 0.540$ for $q = 2.49$ and $n = 75$). One can see a discontinuity across the rank four (Obihiro) and five (Owase). Aside from the increase in $|r|$ (0.9705→0.9932) and the decrease in q (3.77→2.49), there is no noticeable change from the result of the former period (**Figure 6A**). To conclude, comparison between **Figure 6A** and **Figure 6B** indicates that

TABLE 3A | Top-twenty Japanese stations in the intersecting angle of the monthly temperatures from Period I (from 1931 to 1960) to Period II (from 1951 to 1980).

Rank	Station	Lat. (°′)	θ (°)	Δ T (K)
01	Karuizawa	36 21 N	2.90	+0.2
02	Obihiro	42 55 N	2.64	+0.4
03	Kushiro	42 59 N	2.58	+0.3
04	Sapporo	43 04 N	2.46	+0.4
05	Aomori	40 49 N	2.31	+0.5
06	Sendai	38 16 N	2.21	+0.6
07	Tokyo	35 41 N	2.17	+0.6
08	Abashiri	44 01 N	2.16	0.0
09	Asahikawa	43 46 N	2.02	+0.3
10	Nemuro	43 20 N	1.89	+0.1
11	Yamagata	38 15 N	1.87	+0.4
12	Morioka	39 42 N	1.82	+0.3
13	Hakodate	41 49 N	1.79	+0.2
14	Akita	39 43 N	1.74	+0.3
15	Urakawa	42 10 N	1.73	+0.2
16	Sakata	38 55 N	1.70	+0.2
17	Yokohama	35 26 N	1.67	+0.6
18	Wakkanai	45 25 N	1.66	+0.1
19	Osaka	34 41 N	1.66	+0.7
20	Fukushima	37 46 N	1.64	+0.4

TABLE 4A | Top-twenty Japanese stations in the intersecting angle of the monthly precipitations from Period I (from 1931 to 1960) to Period II (from 1951 to 1980).

Rank	Station	Lat. (°′)	θ (°)	Δ H (mm)
01	Karuizawa	36 21 N	11.67	−41
02	Izuhara	34 12 N	9.06	+50
03	Tokushima	34 04 N	9.03	+118
04	Hamada	34 54 N	8.04	+85
05	Murotomisaki	33 15 N	7.56	+12
06	Takamatsu	34 19 N	7.55	−43
07	Hamamatsu	34 45 N	7.50	−5
08	Sakata	38 55 N	7.31	−33
09	Abashiri	44 01 N	7.31	−6
10	Obihiro	42 55 N	7.28	+9
11	Nagoya	35 10 N	7.23	+29
12	Fukuoka	33 35 N	7.19	−13
13	Kofu	35 40 N	7.14	−114
14	Tsu	34 44 N	7.11	+4
15	Nagano	36 40 N	7.09	−14
16	Aikawa	38 02 N	7.02	+17
17	Yokohama	35 26 N	7.01	−69
18	Kochi	33 34 N	6.93	+20
19	Saigo	36 12 N	6.83	−72
20	Ushiomisaki	33 27 N	6.82	+185

TABLE 3B | Top-twenty Japanese stations in the intersecting angle of the monthly temperatures from Period II (from 1951 to 1980) to Period III (from 1981 to 2010).

Rank	Station	Lat. (°′)	θ (°)	Δ T (K)
01	Kushiro	42 59 N	4.07	+0.6
02	Obihiro	42 55 N	3.94	+0.7
03	Sapporo	43 04 N	3.62	+0.9
04	Abashiri	44 01 N	3.60	+0.6
05	Nemuro	43 20 N	3.39	+0.5
06	Asahikawa	43 46 N	3.30	+0.6
07	Hakodate	41 49 N	3.09	+0.8
08	Wakkanai	45 25 N	2.73	+0.5
09	Aomori	40 49 N	2.71	+0.8
10	Okayama	34 40 N	2.49	+1.6
11	Takayama	36 09 N	2.08	+0.7
12	Utsunomiya	36 33 N	2.07	+0.9
13	Karuizawa	36 21 N	2.01	+0.4
14	Kagoshima	31 33 N	2.00	+1.3
15	Sendai	38 16 N	1.94	+0.5
16	Sakata	38 55 N	1.93	+0.8
17	Urakawa	42 10 N	1.91	+0.2
18	Akita	39 43 N	1.91	+0.7
19	Aikawa	38 02 N	1.81	+0.8
20	Shimonoseki	33 57 N	1.80	+1.2

TABLE 4B | Top-twenty Japanese stations in the intersecting angle of the monthly precipitations from Period II (from 1951 to 1980) to Period III (from 1981 to 2010).

Rank	Station	Lat. (°′)	θ (°)	Δ H (mm)
01	Tokushima	34 04 N	11.02	−289
02	Nemuro	43 20 N	10.44	−51
03	Urakawa	42 10 N	9.79	−110
04	Obihiro	42 55 N	9.58	−64
05	Owase	34 04 N	8.75	−269
06	Abashiri	44 01 N	8.75	−51
07	Murotomisaki	33 15 N	8.57	−198
08	Matsumoto	36 15 N	8.32	−36
09	Kofu	35 40 N	8.27	+42
10	Shimizu	32 43 N	8.26	+6
11	Hamamatsu	34 45 N	8.16	−119
12	Naze	28 23 N	8.13	−213
13	Sakata	38 55 N	8.01	+9
14	Tsu	34 44 N	7.76	−127
15	Hachijojima	33 07 N	7.64	−60
16	Kumagaya	36 09 N	7.60	+79
17	Ida	35 31 N	7.59	−70
18	Matsumoto	36 15 N	7.55	−36
19	Nagoya	35 10 N	7.48	−40
20	Wakayama	34 14 N	7.34	−137

in contrast to the temperatures, there exists no evidence of the climatic positive feedback for the precipitations.

6) In **Figure 6C** scattergram is plotted for rank data of Period II to III versus those of Period I to II ($r_S = 0.3797$ with $d = 1.992$ for $n = 75$). In comparison with the temperatures ($r_S = 0.6381$ for **Figure 5C**) the rank correlation coefficient reduces substantially. In the same way as the World precipitations (**Figure 4C**), this reduction of the rank correlation is attributable to the stochastic nature inherent in the statistics of precipitations.

DISCUSSION

Global Analysis

The results of **Figure 3** along with **Tables 1A**, **1B** indicate quantitatively that indeed the climate change has arisen in the global scale, but the circumstances are more critical in the northern countries on the Northern Hemisphere than those on the Southern Hemisphere. For the Northern Hemisphere ($n = 97$) regression analysis of the intersecting angle versus the latitude has

TABLE 5 | Comparison of optimal fitting parameters in the rank dependence of the intersecting angle of the monthly temperatures on the World stations. (a) From Period I (from 1931 to 1960) to Period II (from 1951 to 1980); (b) From Period II (from 1951 to 1980) to Period III (from 1981 to 2010).

Method	*n*	*q*	|*r*|	*d*
	(a) Period I to II			
A	115	1.61	0.9974	0.594
B	115	1.43	0.9961	0.526
C	115	1.32	0.9961	0.856
	(b) Period II to III			
A	116	1.01	0.9961	0.784
B	116	1.28	0.9969	1.088
C	116	1.44	0.9966	0.688

TABLE 6 | Comparison of optimal fitting parameters in the rank dependence of the intersecting angle of the monthly precipitations on the World stations. (a) From Period I (from 1931 to 1960) to Period II (from 1951 to 1980); (b) From Period II (from 1951 to 1980) to Period III (from 1981 to 2010).

Method	*n*	*q*	|*r*|	*d*
	(a) Period I to II			
A	106	1.21	0.9675	0.404
B	106	1.11	0.9768	0.176
C	106	1.60	0.9880	0.420
	(b) Period II to III			
A	107	1.51	0.9863	0.709
B	107	1.69	0.9924	0.415
C	107	1.83	0.9873	0.397

shown the typical exponential growth with $r = 0.8195$ ($d = 1.234$) for Period II to III, whereas $r = 0.7063$ ($d = 1.754$) for Period I to II. For the Southern Hemisphere ($n = 19$), however, the degree of fit has reduced substantially, i.e., $r = 0.5151$ ($d = 2.113$) for Period II to III, while $r = 0.5080$ ($d = 2.708$) for Period I to II, though both of them barely maintain the exponentiality. In striking contrast to the temperatures, for the results of the precipitations, no effect arising from the positive feedback has been observed (**Figures 4A, B**). Instead of the latitudinal dependence, the relations of the rotation angles as a function of the mean annual precipitations on the Entire Sphere ($n = 108$) have been shown to obey the logarithmic decay as $r = -0.7609$ ($d = 1.332$) for Period I to II, and $r = -0.6795$ ($d = 1.611$) for Period II to III. Here, as specific data of the annual precipitations, the arithmetic mean of the two subsequent periods has been adopted. The results suggest that a forthcoming large-scale rainmaking or artificial rain project using cloud seeding by spreading silver iodide [53] might make possible arbitrarily (not spontaneously) perturbing the upper ranking in the statistics of World precipitations.

Regional Analysis

For the Japanese stations ($n = 75$) regression analysis of the intersecting angle versus the latitude has shown the logarithmic growth with $r = 0.7361$ ($d = 1.976$) for Period I to II, in contrast to the exponential growth with $r = 0.7373$ ($d = 1.639$) for Period II to III. In remarkable contrast to the temperatures, for the results of the precipitations, similarly to the global counterpart, no effect due to the positive feedback has been observed (**Figures 6A,B** with **Table 4A**, **4B**). Incidentally, for the present, Japan takes no potential interest in the artificial rain project on his territory.

Comparison With Other Methods

The procedure mentioned in **Subsection 2.1** can be modified with joining the first differences [19].

$$\boldsymbol{p} = (\langle u_1\rangle, \langle u_2\rangle, \ldots, \langle u_{12}\rangle; \langle v_1\rangle, \langle v_2\rangle, \ldots, \langle v_{11}\rangle), \quad (11)$$

$$\boldsymbol{q} = (\langle x_1\rangle, \langle x_2\rangle, \ldots, \langle x_{12}\rangle; \langle y_1\rangle, \langle Y_2\rangle, \ldots, \langle Y_{11}\rangle), \quad (12)$$

$$\langle v_j\rangle = \langle u_{j+1}\rangle - \langle u_j\rangle, \quad (13)$$

$$\langle y_j\rangle = \langle x_{j+1}\rangle - \langle x_j\rangle. \quad (14)$$

Here $j = 1, 2, \ldots, 11$. Note that $\langle v_j\rangle$ and $\langle y_j\rangle$ stand for the rate of change. To discriminate this method from the original one (i.e., $\langle v_j\rangle \equiv 0$ and $\langle y_j\rangle \equiv 0$, respectively, in **Eqs. 11**, **12**), we will use the terms, Method A (original; 12 dimensions) and Method B (modified as **Eqs. 11**, **12**; 23 dimensions), respectively. The vectors can be expanded further by adding the second differences [19].

$$\boldsymbol{p} = (\langle u_1\rangle, \langle u_2\rangle, \ldots, \langle u_{12}\rangle; \langle v_1\rangle, \langle v_2\rangle, \ldots, \langle v_{11}\rangle; \langle w_1\rangle, \langle w_2\rangle, \ldots, \langle w_{10}\rangle), \quad (15)$$

$$\boldsymbol{q} = (\langle x_1\rangle, \langle x_2\rangle, \ldots, \langle x_{12}\rangle; \langle y_1\rangle, \langle y_2\rangle, \ldots, \langle y_{11}\rangle; \langle z_1\rangle, \langle z_2\rangle, \ldots, \langle z_{10}\rangle), \quad (16)$$

$$\langle w_k\rangle = \langle v_{k+1}\rangle - \langle v_k\rangle, \quad (17)$$

$$\langle z_k\rangle = \langle y_{k+1}\rangle - \langle y_k\rangle. \quad (18)$$

Here $k = 1, 2, \ldots, 10$. Note that $\langle w_k\rangle$ and $\langle z_k\rangle$ imply the 'monthly change of curvature.' To discriminate this method from other methods we will term it Method C (ultimately modified; 33 dimensions).

In **Table 5** comparison among these methods is made for optimized fitting parameters in the rank dependence of the rotation angle of the monthly temperatures on the 116 World stations. For Period I to II an exceptional spot, Urumchi, has been excluded. First, one can find, irrespective of the period as well as the method, the high degree of fit is preserved to the function of **Eq. 5**. For the optimal value of q, however, one can see a significant difference, i.e., the median of the parameter decreases in the subsequent period; this tendency is most remarkable in Method A (q: 1.61→1.01). It is interesting to investigate the results in the data of precipitations. In **Table 6** comparison among the three methods is made for optimized fitting parameters in the rank dependence of the intersecting angle of the monthly precipitations on the 108 World stations for which data on precipitations are available. Note that in addition to the eight stations the following spots that include exceptional data have been excluded: for Period I to II, Asswan and Kashgar; for Period II to III, Asswan. In comparison between **Table 5** (temperatures versus ranks) and **Table 6** (precipitations versus ranks), the degree of fit, $|r|$, reduces substantially in the latter, indicating that for the ranking of precipitations, there might be a difficulty in adopting the function

TABLE 7 | Comparison of optimal fitting parameters in the rank dependence of the intersecting angle of the monthly temperatures on the Japanese stations. (a) From Period I (from 1931 to 1960) to Period II (from 1951 to 1980); (b) From Period II (from 1951 to 1980) to Period III (from 1981 to 2010).

	(a) Period I to II			
Method	***n***	***q***	***|r|***	***d***
A	75	1.89	0.9973	0.662
B	75	1.76	0.9908	1.090
C	75	—	—	—
	(b) Period II to III			
A	75	0.91	0.9883	0.477
B	75	0.92	0.9907	0.317
C	75	0.99	0.9881	0.611

TABLE 8 | Comparison of optimal fitting parameters in the rank dependence of the intersecting angle of the monthly precipitations on the Japanese stations. (a) From Period I (from 1931 to 1960) to Period II (from 1951 to 1980); (b) From Period II (from 1951 to 1980) to Period III (from 1981 to 2010).

	(a) Period I to II			
Method	**n**	**q**	***|r|***	***d***
A	74	3.77	0.9705	0.666
B	75	2.08	0.9876	1.316
C	75	1.99	0.9942	1.377
	(b) Period II to III			
A	75	2.49	0.9932	0.540
B	75	2.57	0.9906	0.810
C	75	2.28	0.9939	0.825

of **Eq. 5**. With respect to the change of q, in **Table 6** the tendency is reversed, i.e., its value increases in the latter period. The comparative results of the regional analysis are listed in **Tables 7** and **8**. The principal features that have been confirmed in the global analysis are found to be shared with those in the domestic counterpart. Note that for the temperatures (**Table 7**), independently of the method, the value of q in Period II to III becomes smaller than unity ($q < 1$). The blanks in **Table 7** have arisen from a certain ill-posed behavior in the prosses of parameter optimization.

CONCLUSION

Independently of the period, the variation of the angles has been found to show a long-tailed decay as a function of their ranks being aligned in descending order. For the temperatures this trend has been shown to get more remarkable in the latter period, confirming that indeed the albedo feedback arises. In contrast to the temperatures (**Figure 3** and **Table 5**), no indication of the feedback has yet been found for the precipitations (**Figure 4** and **Table 6**). To examine the validity of the rank-size analysis in more detail, a regional analysis for 75 stations in Japan has been made as well. Computed results have shown a coherence with the global counterpart. To conclude, through the numerical results of this paper we have confirmed that, along with conventional applications to complex systems, the rank-size approach is useful for revealing climate change impacts not only in the global but in the regional scale. With the current pace in the warming being preserved, the worse (i.e., $q = 1.61 \rightarrow q = 1.01 \rightarrow q < 1$) for the World temperatures is anticipated for Period III (from 1981 to 2010) to the subsequent Period IV (from 2011 to 2040). The worst scenario will be $q \rightarrow 0$, in which θ versus χ obeys the power law as suggested in **Eqs. 7**, **9**.

Extension of the methodology to arbitrary circular data in climatic studies [39, 40], such as the wind direction and the animal migration, might be interesting as a future research topic.

DATA AVAILABILITY STATEMENT

The raw data supporting the conclusion of this article will be made available by the authors, without undue reservation.

AUTHOR CONTRIBUTIONS

The author confirms being the sole contributor of this work and approved it for publication.

SUPPLEMENTARY MATERIAL

The Supplementary Material for this article can be found online at: https://www.frontiersin.org/articles/10.3389/fphy.2021.687900/full#supplementary-material

REFERENCES

1. GOSAT Project, the National Institute for Environmental Studies, Japan. *A Prompt Report on the Monthly Mean Carbon-Dioxide Concentration Averaged over the Entire Atmosphere* (2019). Available at: http://www.gosat.nies.go.jp/recent-global-co2.html (Accessed July 19, 2020).
2. Metoffice. *HadCRU4 Dataset Produced by the Met Office and the Climatic Research Unit at the University of East Anglia. Global Climate In Context As the World Approaches 1 °C Above Pre-Industrial For the First Time* (2015). Available at: https://www.metoffice.gov.uk/research/news/2015/global-average-temperature-2015 (Accessed July 19, 2020).
3. TF Stocker, D Qin, GK Plattner, MMB Tignor, SK Allen, J Boschung, et al. editors. *Climate Change 2013: The Physical Science Basis (Working Group I Contribution to the Fifth Assessment Report of the Intergovernmental Panel on Climate Change)*. Cambridge: Cambridge University Press (2014).
4. Király A, Jánosi IM. Stochastic Modeling of Daily Temperature Fluctuations. *Phys Rev E* (2002) 65:051102. doi:10.1103/PhysRevE.65.051102
5. Lind PG, Mora A, Gallas JA, Haase M. Reducing Stochasticity in the North Atlantic Oscillation Index with Coupled Langevin Equations. *Phys Rev E Stat Nonlin Soft Matter Phys* (2005) 72:056706. doi:10.1103/PhysRevE.72.056706
6. Redner S, Petersen MR. Role of Global Warming on the Statistics of Record-Breaking Temperatures. *Phys Rev E Stat Nonlin Soft Matter Phys* (2006) 74:061114. doi:10.1103/PhysRevE.74.061114
7. Verdes PF. Global Warming Is Driven by Anthropogenic Emissions: A Time Series Analysis Approach. *Phys Rev Lett* (2007) 99:048501. doi:10.1103/PhysRevLett.99.048501

8. Newman WI, Malamud BD, Turcotte DL. Statistical Properties of Record-Breaking Temperatures. *Phys Rev E Stat Nonlin Soft Matter Phys* (2010) 82: 066111. doi:10.1103/PhysRevE.82.066111
9. Rossi A, Massei N, Laignel B. A Synthesis of the Time-Scale Variability of Commonly Used Climate Indices Using Continuous Wavelet Transform. *Glob Planet Change* (2011) 78:1–13. doi:10.1016/j.gloplacha.2011.04.008
10. Balzter H, Tate N, Kaduk J, Harper D, Page S, Morrison R, et al. Multi-Scale Entropy Analysis as a Method for Time-Series Analysis of Climate Data. *Climate* (2015) 3:227–40. doi:10.3390/cli3010227
11. Tamazian A, Ludescher J, Bunde A. Significance of Trends in Long-Term Correlated Records. *Phys Rev E Stat Nonlin Soft Matter Phys* (2015) 91:032806. doi:10.1103/PhysRevE.91.032806
12. Huang X, Hassani H, Ghodsi M, Mukherjee Z, Gupta R. Do Trend Extraction Approaches Affect Causality Detection in Climate Change Studies. *Physica A: Stat Mech its Appl* (2017) 469:604–24. doi:10.1016/j.physa.2016.11.072
13. Zhang F, Yang P, Fraedrich K, Zhou X, Wang G, Li J. Reconstruction of Driving Forces from Nonstationary Time Series Including Stationary Regions and Application to Climate Change. *Physica A: Stat Mech its Appl* (2017) 473: 337–43. doi:10.1016/j.physa.2016.12.088
14. Matcharashvili T, Zhukova N, Chelidze T, Founda D, Gerasopoulos E. Analysis of Long-Term Variation of the Annual Number of Warmer and Colder Days Using Mahalanobis Distance Metrics - A Case Study for Athens. *Physica A: Stat Mech its Appl* (2017) 487:22–31. doi:10.1016/j.physa.2017.05.065
15. Moon W, Agarwal S, Wettlaufer JS. Intrinsic Pink-Noise Multidecadal Global Climate Dynamics Mode. *Phys Rev Lett* (2018) 121:108701. doi:10.1103/physrevlett.121.108701
16. Hassani H, Silva ES, Gupta R, Das S. Predicting Global Temperature Anomaly: A Definitive Investigation Using an Ensemble of Twelve Competing Forecasting Models. *Physica A: Stat Mech its Appl* (2018) 509:121–39. doi:10.1016/j.physa.2018.05.147
17. Wang C, Wang ZH, Sun L. Early-Warning Signals for Critical Temperature Transitions. *Geophys Res Lett* (2020) 47:e2020GL088503. doi:10.1029/2020gl088503
18. Wang C, Wang Z-H, Li Q. Emergence of Urban Clustering Among U.S. Cities under Environmental Stressors. *Sustain Cities Soc* (2020) 63:102481. doi:10.1016/j.scs.2020.102481
19. Hayata K. Global-Scale Synchronization in the Meteorological Data: A Vectorial Analysis That Includes Higher-Order Differences. *Climate* (2020) 8:128. doi:10.3390/cli8110128
20. Kanter I, Kessler DA. Markov Processes: Linguistics and Zipf's Law. *Phys Rev Lett* (1995) 74:4559–62. doi:10.1103/physrevlett.74.4559
21. Yang AC-C, Hseu S-S, Yien H-W, Goldberger AL, Peng C-K. Linguistic Analysis of the Human Heartbeat Using Frequency and Rank Order Statistics. *Phys Rev Lett* (2003) 90:108103. doi:10.1103/physrevlett.90.108103
22. Alvarez-Martinez R, Martinez-Mekler G, Cocho G. Order-Disorder Transition in Conflicting Dynamics Leading to Rank-Frequency Generalized Beta Distributions. *Physica A: Stat Mech its Appl* (2011) 390:120–30. doi:10.1016/j.physa.2010.07.037
23. Blumm N, Ghoshal G, Forró Z, Schich M, Bianconi G, Bouchaud J-P, et al. Dynamics of Ranking Processes in Complex Systems. *Phys Rev Lett* (2012) 109: 128701. doi:10.1103/physrevlett.109.128701
24. Ausloos M. Hint of a Universal Law for the Financial Gains of Competitive Sport Teams. The Case of Tour de France Cycle Race. *Front Phys* (2017) 5:59. doi:10.3389/fphy.2017.00059
25. Morales JA, Colman E, Sánchez S, Sánchez-Puig F, Pineda C, Iñiguez G, et al. Rank Dynamics of Word Usage at Multiple Scales. *Front Phys* (2018) 6:45. doi:10.3389/fphy.2018.00045
26. Mehri A, Agahi H, Mehri-Dehnavi H. A Novel Word Ranking Method Based on Distorted Entropy. *Physica A: Stat Mech its Appl* (2019) 521:484–92. doi:10.1016/j.physa.2019.01.080
27. The National Astronomical Observatory of Japan. *Chronological Scientific Tables*, Vol. 59. Tokyo: Maruzen (1985).
28. The National Astronomical Observatory of Japan. *Chronological Scientific Tables*, Vol. 66. Tokyo: Maruzen (1992).
29. The National Astronomical Observatory of Japan. *Chronological Scientific Tables*, Vol. 91. Tokyo: Maruzen (2017).
30. Weart SR. *The Discovery of Global Warming*. Cambridge, MA: Harvard University Press (2008).
31. Berger JJ. *Climate Peril*. Berkeley, CA: Northbrae (2014).
32. Wadhams P. *A Farewell to Ice: A Report from the Arctic*. London: Penguin Books (2016).
33. von Storch H, Zwiers FW. *Statistical Analysis in Climate Research*. Cambridge: Cambridge University Press (2000).
34. H von Storch A Navarra, editors. *Analysis of Climate Variability: Applications of Statistical Techniques*. 2nd ed. Berlin: Springer (2010).
35. Chatterjee S, Hadi AS. *Regression Analysis by Example*. 5th ed. Hoboken, NJ: Wiley (2012).
36. Hayata K. Statistical Properties of Extremely Squeezed Configurations: A Feature in Common between Squared Squares and Neighboring Cities. *J Phys Soc Jpn* (2003) 72:2114–7. doi:10.1143/jpsj.72.2114
37. Hayata K. A Time-Dependent Statistical Analysis of the Large-Scale Municipal Consolidation. *Forma* (2010) 25:37–44.
38. Hayata K. Phonological Complexity in the Japanese Short Poetry: Coexistence between Nearest-Neighbor Correlations and Far-Reaching Anticorrelations. *Front Phys* (2018) 6:31. doi:10.3389/fphy.2018.00031
39. Fisher NI, Lee AJ. Regression Models for an Angular Response. *Biometrics* (1992) 48:665–77. doi:10.2307/2532334
40. Jammalamadaka SR, SenGupta A. *Topics in Circular Statistics*. Singapore: World Scientific (2001).
41. Vélez JI, Correa JC, Marmolejo-Ramos F. A New Approach to the Box-Cox Transformation. *Front Appl Math Stat* (2015) 1:12. doi:10.3389/fams.2015.00012
42. Lejaeghere K, Cottenier S, Van Speybroeck V. Ranking the Stars: A Refined Pareto Approach to Computational Materials Design. *Phys Rev Lett* (2013) 111:075501. doi:10.1103/PhysRevLett.111.075501
43. Kim K, Li TGF, Lo RKL, Sachdev S, Yuen RSH. Ranking Candidate Signals with Machine Learning in Low-Latency Searches for Gravitational Waves from Compact Binary Mergers. *Phys Rev D* (2020) 101:083006. doi:10.1103/physrevd.101.083006
44. Tsuneta Yano Commemorative Association. *Kensei: The Data Book for the 47 Prefectures in Japan*. Tokyo: Tsuneta Yano Commemorative Association (2017).
45. Federico PJ. Squaring Rectangles and Squares. In: JA Bondy USR Murty, editors. *Graph Theory and Related Topics*. New York, NY: Academic Press (1979). p. 173–96.
46. Duijvestijn AJW. Simple Perfect Squared Square of Lowest Order. *J Comb Theor Ser B* (1978) 25:240–3. doi:10.1016/0095-8956(78)90041-2
47. The Japan Tourist Agency, the Ministry of Land, Infrastructure and Transport. *Statistical Survey on Foreign Visitors* (2017). Available at: https//www.mlit.go.jp/common/001190401.pdf (Accessed March 23, 2021).
48. Merton RK. The Matthew Effect in Science. *Science* (1968) 159:56–63. doi:10.1126/science.159.3810.56
49. Price DDS. A General Theory of Bibliometric and Other Cumulative Advantage Processes. *J Am Soc Inf Sci* (1976) 27:292–306. doi:10.1002/asi.4630270505
50. Barabási A-L, Albert R. Emergence of Scaling in Random Networks. *Science* (1999) 286:509–12. doi:10.1126/science.286.5439.509
51. Érdi P. *Ranking*. New York, NY: Oxford University Press (2020).
52. Nishizawa N, Makino K. *Ranking of Japanese Given Names*. Tokyo: Shinjimbutsuoraisha (2001).
53. Bostock B. *China Is Massively Expanding its Weather-Modification Program, Saying It Will Be Able to Cover Half the Country in Artificial Rain and Snow by 2025* (2021). Available at: https://www.businessinsider.jp/post-225599 (Accessed March 23, 2021).

Conflict of Interest: The author declares that the research was conducted in the absence of any commercial or financial relationships that could be construed as a potential conflict of interest.

Advantages of publishing in Frontiers

OPEN ACCESS
Articles are free to read for greatest visibility and readership

FAST PUBLICATION
Around 90 days from submission to decision

HIGH QUALITY PEER-REVIEW
Rigorous, collaborative, and constructive peer-review

TRANSPARENT PEER-REVIEW
Editors and reviewers acknowledged by name on published articles

Frontiers
Avenue du Tribunal-Fédéral 34
1005 Lausanne | Switzerland

Visit us: www.frontiersin.org
Contact us: frontiersin.org/about/contact

REPRODUCIBILITY OF RESEARCH
Support open data and methods to enhance research reproducibility

DIGITAL PUBLISHING
Articles designed for optimal readership across devices

FOLLOW US
@frontiersin

IMPACT METRICS
Advanced article metrics track visibility across digital media

EXTENSIVE PROMOTION
Marketing and promotion of impactful research

LOOP RESEARCH NETWORK
Our network increases your article's readership